The 6th International Scientific Conference for Nanotechnology, Advanced Materials and Their Applications

ICNAMA 2-3 May 2018

المؤتمر الدولي السادس للنانوتكنولوجي والمواد المتقدمة وتطبيقاتها

2-3 آيار 2018

(Part 3)

البحوث المقبولة في المؤتمر

Proceeding Book

Accepted Manuscripts of The Conference

Special Issue

Head of Scientific Committee

Prof. Dr. Alaa A. Atiyah

Head of Preparatory Committee

Prof. Dr. Mohammad Jasim Khadim

رئيس اللجنة العلمية

أ.د.علاء عبد الحسن عطية

رئيس اللجنة التحضيرية

أ.د.محمد جاسم كاظم

م.د. علياء حسين عبد السلام - مقررا

م.د. علي عبد الوهاب عاتي - مقررا

The title	Page No.
Use of Taguchi approach to optimize Electrical Discharge Machining (EDM) process of Stainless Steel AISI 304 (23-04)	488
Numerical Study on Thermal-hydraulic Performance and Entropy Generation of Confined Slot Impinging Jet with Nanofluids	495
Geotextile by using Nano Natural Material for Iraqi Crude Oil	506
Effect of Annealing Process on a Microstructure and a Tensile Test of Aluminium – Silicon Alloy Deformed by Equal Channel Angular Pressing	512
Synthesizing α-Fe2O3/Nps by Pulsed Laser Ablation in Liquid Environment at Different Laser Energies	523
Self-Powered Photosensor Fabricated Based on ZnO/CdS/dye Nanostructure	530
Enhancement of UV photodetectors based on ZnO nanorods and Cu-doped by hydrothermal method	536
Toxicity assessment of porous silicon nanoparticles In-vivo	546
Improvement the Wear Resistance for Grinding Ball of Horizontal Cement Mill in Kufa Cement Plant	554
Synthesis and antibacterial activity of hematite α-Fe2O3 nanopowder prepared by hydrothermal process	565
Fabrication of Tri Metal Oxides Gas Detector for Medical Diagnosis Application	571
Synthesis of Photovoltaic Organic – Inorganic Perovskites Photodetctor	579
The structural and thermal properties of the Cermet system using powder technology	585
Structural and Thermal Properties In Ferromagnetic INVAR (Fe-Ni)alloys Prepared by powder Metallurgy Method	598
Preparation and Characterization of porous ZnO from ZnO pastes by Doctor-Blade Method	603
Size Dependence of Gas Sensitivity of ZnO Nanorods towards LPG	608
Burnishing technique for improvement resistance to corrosion of low carbon steel (AISI 1017) in HCl acid	616
Studying the Rheology of Water Based Nanofluid	527
Preparation and Investigation of composite coating (Ni-nano hydroxyapatite) on low carbon steel samples	634
Using Well Logging Data to determine Water Saturation in a Carbonate Reservoirs	645
Studying of Traditional Solid –Carburization and Comparison it with Laser Carburization of Low Carbon Steel	651

Cu/Multiwalled Carbon Nanotube Composite Coatings fabricated by Pulse Electrodeposition	**658**
Recovery of Metallic Lead from Cathode Ray Tube Funnel Glass using Pyrovacuum Reduction Process	**665**
Inhibition of medium carbon steel corrosion process in 1 M H2SO4 acidic medium by using aqueous and alcoholic extracted purslane	**671**
Characterization studies the influence of glancing angle on the structural and optical properties of ZnO nanostructure	**679**
Synthesis of Nano-Colloidal Titanium Oxide by Pulsed Laser Ablation Technique	**685**
Study Some Physical Proprieties for Graphene Ribbons Doped by Nitrogen Atoms	**690**
Corrosion Protection Improvement of Gas Turbine Blades by Coating with Nano Oxides	**696**
Characterization of R.F Sputtering $(SnO_2)1\text{-}x$ (TiO_2: CuO) x Films as Gas Sensor	**700**
Characterization and Electromagnetic Interference of Nickel Ferrite / polyaniline Composite	**715**
Electrical and Detection Properties of Nano and Micro Copper Oxide prepared by RPLD	**725**
Study the Effect of SiO_2 Particles on Flexural properties of Epoxy Reinforced by Glass Fiber Composites	**731**

Available online at
http://namrc.uotechnology.edu.iq/index.php/

Nanotechnology and Advanced Materials Research Centre

Proceeding Articles Book 00 (2018) 000–000

6th International Scientific Conference on Nanotechnology, Advanced Materials and its Applications

Use of Taguchi approach to optimize Electrical Discharge Machining (EDM) process of Stainless Steel AISI 304

Shukry H. Aghdeab, Ahmed Basil Abdulwahhab
Production and Mettalurgy engineering, University of Technology, Baghdad, Iraq

Abstract

Electrical discharge machining (EDM) is a widespread Non-traditional machining Processes for manufacturing geometrically complicated or hard materials parts that are very difficult to machine by traditional machining operation. EDM stratify the connotation of material removal by using electric spark erosion. The objective of this research study to discuss the optimal process parameters of EDM on AISI 304 as a work material with copper as a tool electrode. The effect of various process parameters on machining performance is investigated in this study. The input parameters considered are current; pulse on time and pulse off time are used for experimental work and their effect on Material Removal Rate (MRR). A computer program has been developed using Minitab environment to adopt Taguchi method to formulate the experimental layout to analysis the effect of input process parameters on the machining characteristics and find the optimal process parameters of EDM. The results of the present work shows that the MRR is increase with increasing in current and pulse on time and it decrease with increasing in pulse off time, and it found that the MRR predicted by Taguchi method is 40.0851 mm3/min with using the best parameters of current is 30 Ampere, pulse on time is 70 µs and lower value of pulse off time is 35 µs.

Keywords: Electrical Discharge Machining, Material Removal Rate, Taguchi method, pulse on time, pulse off time.

Introduction

Electrical discharge machining (EDM) is basically a non-conventional material removal process which is widely used in industry [1]. EDM sometimes indicate as spark machining, spark eroding, burning, die sinking or wire erosion is a manufacturing process whereby a coveted shape is obtained using electrical sparks. Material is taken away from the workpiece by a series of frequent periodic electric discharges between tool (electrode) and workpiece separate by a dielectric solution and subject to an electric voltage [2]. EDM is basically a thermal process with a complicated metal removal mechanism, include the formation of a plasma channel between the electrode and workpiece, resulting in the material removal, which also leads to surface roughness, work hardness, hole magnification, white layer, heat effected layer, surface structural changes, metallurgical transformations and cracking. These properties determine the operational behavior of the material and can be included in one term called Surface Integrity [3]. EDM process has feature over the other machining techniques because its ability to make complex parts with a higher accuracy. This operation is convenient to machine hard materials, which would be difficult to machining by other machining processes. Another advantage of EDM is its ability to machine parts on very small scale. EDM is usually used in the production of industrial tools, dies and molds, and the machining of heat treated ceramic materials such as tungsten carbides [4].

In Daneshmand et al. [5] focused on the effects of EDM parameters, discharge current, voltage, pulse on time and pulse off time on the material removal rate, tool wear and surface roughness of NiTi alloy". The results of this research were the parameters of current, voltage, and pulse on time which are effected directly on material removal rate (MRR), and with their increase, the MRR increases. Tool wear rate (TWR) decrease with the increase of pulse off time.

B. Prajapati & R. Prajapati [6] studied the performance of different electrode materials on EN-9 workpiece material with EDM process, used the tool materials were graphite, copper and brass. The important parameters were peak current, pulse on time and pulse off time. The results of this study were the graphite electrode gives higher MRR than other two electrodes. Brass electrode gives better surface finishing comparison with the others.

Chikalthankar et al. [7] studied the effect of machining parameters as voltage, current, pulse-on time and pulse off time for responses of material removal rate and surface roughness (Ra) on the EDM of AISI D2 tool steel using the copper electrode material. This study found the current is the more influential parameter affecting the material removal rate and surface roughness.

Chandramouli et al. [8] discussed the optimal process parameters of EDM on RENE80 nickel super alloy material with aluminum as a tool electrode. The input parameters considered are current; pulse on time and pulse off time are used for experimental work and their effect on MRR, TWR and surface roughness. The results of the research showed that proper selection of input parameters played a great role in EDM.

Tomadi et al. [9] investigated on the effect of the parameters (peak current, power supply voltage, pulse on time and pulse off time). The surface quality that was considered in this research was surface roughness using pertho-meter machine. MRR and electrode wear rate (EWR) in this experiment was calculated by using mathematical method. The result of the experiment then was collected and analyzed using STATISTICA software.

Rahman et al. [10] study optimized model to inspect the influence of peak current, pulse on time and pulse off time in EDM performance on MRR of titanium alloy using copper tungsten and positive polarity of the electrode. The conclusion leads to desirable MRR and economical industrial machining to optimize the input parameters.

This work was motivated by the problem of reducing number of experiments to define the machining parameters of electric discharge machining process. There are many existing approaches to finding these parameters. This work suggest using Taguchi method to develop a mathematical description way to find the optimal machining parameters for this process. Experiments show that this approach is feasible as optimization tool. In future research, we will address using this approach with other machining/objective parameters like surface roughness and micro hardness.

Materials and Method

Principle of EDM Operation

The principle of EDM operation is a non-conventional manufacturing process based on removing material from a part by means of a series of frequent electrical discharges (created by electric pulse generators at short intervals) between a tool, called electrode, and the part, calls workpiece being machined in the presence of a dielectric fluid [11]. At present, EDM is a widespread technique used in industry for high-precision machining of all types of conductive materials such as metals, metallic alloys, graphite, or even some ceramic materials [9]. The EDM is a well determined machining choice for manufacturing geometrically hard material parts that are highly difficult to machine by traditional machining processes [12]. Its unparalleled feature of using thermal energy to machine electrically conductive parts regardless of hardness has been its special advantage for manufacturing of mold, die, automotive, aerospace and surgical components [13]. Appropriate selection of the machining parameters can result in a higher material removal rate, better surface finish, and lower electrode wear ratio [14].

Several factors (current, pulse on time and pulse off time) effect on the Material Removal Rate (MRR). The experiments have done with kerosene as dielectric medium on EDM CM 323C (CNC Machine), as shown in Fig. 1, with using copper electrodes (ϕ5 mm). The work material used in this study is Stainless Steel AISI 304 with nine specimens dimensions (40 mm × 30 mm × 1.7 mm). The chemical composition and mechanical properties of the work material is given in Table 1 and Table 2 respectively.

The tool (electrode) material were used in the experimental study is copper electrode made as a rod with diameter (5 mm) and length (60 mm).

The working factors used in experimental work, as shown in Table 3.

Equation (1) is used to calculate MRR, which depends on the diameter of the hole resulting from the process of cutting by electric spark [15].

$$MRR=(Vw.p)/t \quad \ldots\ldots\ldots\ldots\ldots\ldots\ldots\ldots\ldots\ldots (1)$$

Where:

MRR= Material removal rate (mm3/min).

Vw.p = Volume of material removed from workpiece (mm3).

Vw.p = π. r2 .h

t = Time of machining (min).

r = Radius of the produced hole (mm).

h = Thickness of workpiece (mm).

The design and levels parameters of the study experiments were shown in Table 4.

The measured results were collected and analyzed through developed program using Minitab software by adopted Taguchi design method. Taguchi method is a designed experiment which helps to choose a product or process that functions more consistently in the operating environment. Taguchi designs recognize that not all factors that cause variability can be controlled. These uncontrollable factors are called noise factors. Taguchi designs help to identify controllable factors "control factors" that minimize the effect of the noise factors. During experimentation, noise factors were manipulated to force variability to occur and then determine optimal control factor settings that make the process or product robust, or resistant to variation from the noise factors. A process designed with this goal produced more consistent output. A product designed with this goal delivered more consistent performance regardless of the environment in which it is used.

1- Results and discussion

The results that obtained from experiments were shown in the Tables (5), (6), (7), and (8) respectively.

Fig. 2. shows the effect of machining parameters (current, pulse on time and pulse off time) on the material removal rate (MRR) by (response of mean), from this figure, the MRR increased to (32.71 mm3/min) with increased current (30 A) and MRR reached to (31.12 mm3/min) with pulse on time (70 µs), and obtained high MRR (32.23 mm3/min) with low pulse off time (35 µs). A high current generates a high-intensity spark and as has been inferred in the results, thus increasing the thermal flux of the internal cavity. As a result, the heat of the spark area increases sharply, which leads to a frequent melting of the contact area of the workpiece, lead to increase the MRR.

Fig. 3. shows the effect of machining parameters on the MRR by using (response of Signal to Noise Ratios), from this figure, obtained high MRR (30.07 mm3/min) with higher current (30 A), and MRR was (29.61 mm3/min) with higher pulse on time (70 µs), and obtained higher MRR (30 mm3/min) with lower pulse off time (35 µs).

The MRR predicted by Taguchi method was (40.0851mm3/min) with mean, and MRR predicted was (32.6437 mm3/min) by S/N Ratio, these values were best with parameters of higher current (30 A) and higher pulse on time (70 µs) and lower pulse off time (35 µs).

Table. 1. Chemical composition of AISI 304 work material.

Material	C%	Si%	Mn%	P%	S%	Cr%
% Weight	0.043	0.3	1.52	0.03	0.0005	19.4
Material	Mo%	Ni%	Cu%	V%	W%	Fe%
% Weight	0.222	8.60	0.33	0.064	0.059	Balance

Table. 2. Mechanical and physical properties of work materials.

Properties	AISI 304
Tensile Strength (MPa)	600
Compression Strength (MPa)	210
Coefficient of thermal expansion (°K-1)	17.2x10-6
Thermal conductivity (W/m.°K)	16.2

Electrical conductivity (1/Ω m)	11.6x107
Melting point (°K)	1644
Boiling point (°K)	1672
Electrical Resistivity (Ù.m)	$0.072x10^{-6}$
Density (g/m^3)	8.00
Modulus of Elasticity (GPa)	193
Hardness (HRB)	88
Impact Test (KV/Ku(J)(min))	203
Yield strength (MPa)	241

Table. 3. Working factors used in the experimental work.

Working Factors	Description
Workpiece	AISI 304 (40×30×1.7 mm)
Tool-electrode material	copper (5mm diameter)
Tool-electrode polarity	Negative (-)
Workpiece polarity	Positive (+)
Dielectric	Kerosene
Dielectric temperature	40-80°C
Input voltage	380V (three phase) AC
Output voltage	140V (two phase) DC
Current	10-30A
Pulse on time	50-70 µs
Pulse off time	35-55 µs

Table. 4. Design of experiment (Parameters and Levels).

Factors of consideration	Symbols	Levels		
		1	2	3
Current (A)	I	10	20	30
Pulse on time (µs)	Pon	50	60	70
Pulse off time (µs)	Poff	35	45	55

Table. 5. Taguchi matrix (3-Level Design).

No. of Experiments	Machining parameters levels		
	I	Pon	Poff
	Current (A)	Pulse on time (µs)	Pulse off time (µs)
1	1	1	1
2	1	2	2
3	1	3	3
4	2	1	2
5	2	2	3
6	2	3	1
7	3	1	3
8	3	2	1
9	3	3	2

Table. 6. Experimental results of machining parameters with Taguchi method.

Exp. No.	Current(I) (A)	Pulse on time (µs)	Pulse off time (µs)	MRR (mm3/min)	SNRA1	MEAN1
1	10	50	35	23.956	27.5883	23.956
2	10	60	45	23.574	27.4487	23.574
3	10	70	55	21.354	26.5896	21.354
4	20	50	45	24.958	27.9442	24.958
5	20	60	55	24.123	27.6486	24.123
6	20	70	35	34.810	30.8341	34.810
7	30	50	55	22.981	27.2274	22.981
8	30	60	35	37.931	31.5799	37.931
9	30	70	45	37.210	31.4132	37.210

Table. 7. Response Table for Means.

Level	Current (I)	Pulse on time	Pulse off time
1	22.96	23.97	32.23
2	27.96	28.54	28.58
3	32.71	31.12	22.82
Delta	9.75	7.16	9.41
Rank	1	3	2

Table. 8. Response Table for Signal to Noise Ratios.

Level	Current (I)	Pulse on time	Pulse off time
1	27.21	27.59	30.00
2	28.81	28.89	28.94
3	30.07	29.61	27.16
Delta	2.86	2.03	2.85
Rank	1	3	2

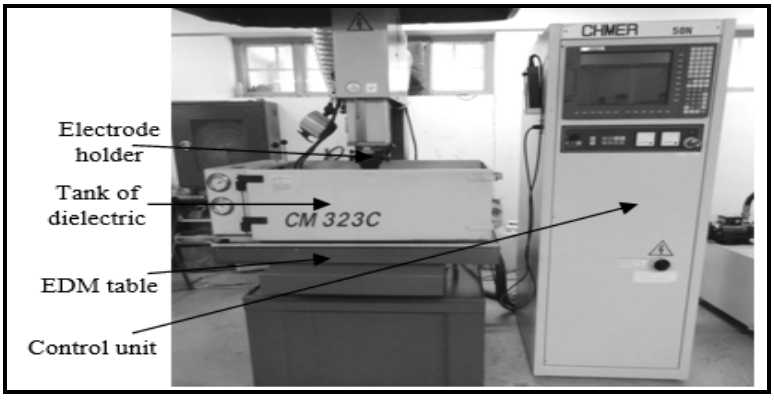

Fig. 1. EDM CM323C CNC Machine used in this work.

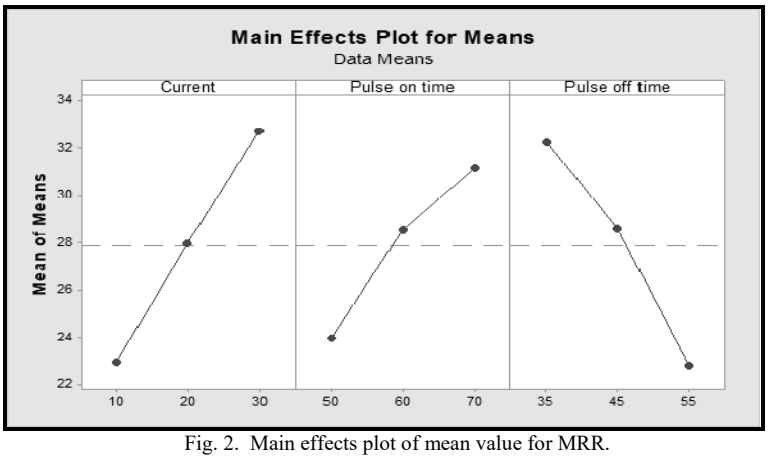

Fig. 2. Main effects plot of mean value for MRR.

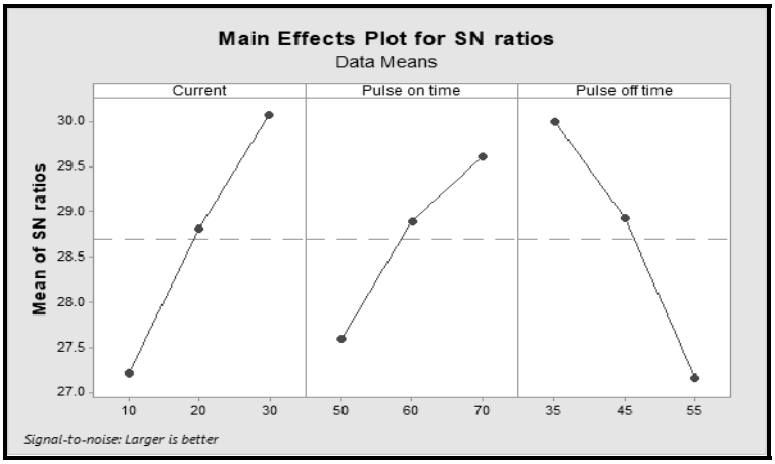

Fig. 3. Show Main effect plot of S/N ratios for MRR.

4-Conclusion

Result shows that current, pulse on time and pulse off time have significant effect on MRR. The results of this work reveal that proper selection of input parameters played a significant role in EDM. The main conclusions from this work can be summarized as follows: a) The MRR is increasing with increase in current and pulse on time.b) MRR is decrease with increase in pulse off time. c) Using Taguchi method to predicted best parameters with optimal value of MRR.

References

[1] K. Ojha, R. K. Garg, K. K. Singh, "MRR Improvement in Sinking Electrical Discharge Machining: A Review," Journal of Minerals & Materials Characterization & Engineering, 2010, vol. 9, no. 8, p. 709-739.
[2] S. B. Chikalthankar, V. M. Nandedkar, S. V. Borde, "Experimental Investigations of EDM Parameters," International Journal of Engineering Research and Development, 2013, vol. 7, p. 31-34.
[3] S. P. Arikatla, K. T. Mannan, A. Krishnaiah, "Influence of Pulse Current and Pulse on Time on Material Removal Rate and Surface Roughness in Electric Discharge Machining of AISI T1 High Speed Steel," in Proc. of Int. Conf. on Emerging Trends in Engineering and Technology, 2013, p. 178-186.
[4] Y. S. Wong, L. C. Lima, L. C., "Effect of Flushing on Electro Discharge Machined Surface," Journal of Materials Processing Technology, 1995, vol. 48, p. 299-305.
[5] S. Daneshmand, E. F. Kahrizi, E. Abedi, M. M. Abdolhosseini, "Influence of Machining Parameters on Electro Discharge Machining of NiTi Shape Memory Alloys," International Journal Electrochemical, 2013, p. 3095-3104.
[6] H. B. Prajapati, H. R. Prajapati, "Parametric Analysis of Material removal rate and surface roughness of Electro Discharge Machining on EN 9" International Journal of Research in Modern Engineering and Emerging Technology, 2013, vol. 1.
[7] S.B.Chikalthankar, V.M. Nandedkar, S.V. Borde "Experimental Investigations of EDM Parameters" International Journal of Engineering Research and Development, 2013, vol. 7, Issue 5, p. 31-34.
[8] S. Chandramouli, U. B. Shrinivas, K. Eswaraiah, "Optimization of Electrical Discharge Machining Process Parameters Using Taguchi Method" International Journal of Advanced Mechanical Engineering, 2014, vol. 4, p. 425-434.
[9] S. H. Tomadi, M. A. Hassan, Z. Hamedon, "Analysis of the Influence of EDM Parameters on Surface Quality, Material Removal Rate and Electrode Wear of Tungsten Carbide" in Proc. International Multi Conference of Engineers and Computer Scientists, 2009, vol. 2.
[10] M. M. Rahman, R. K. Ashikur, K. K. Noor, R. A. Bakar, "Modeling of Material Removal on Machining of Ti-6Al-4V through EDM using Copper Tungsten Electrode and Positive Polarity" International Journal of Mechanical and Materials Engineering, 2010, p. 135-140.
[11] P. C. Pandey, H. S. Shah, “Modern Machining Processes: An overview" in Modern Machining Processes, New Delhi, India: Tata McGraw-Hill, 1980, p. 2-6.
[12] K. H. Ho, S. T. Newman, "State of the art electrical discharge machining (EDM)" Int. J. Machine Tools Manufac., 2003, vol. 43, p. 1287-1300.
[13] K. Ponappa, S. Aravindan, P.V. Rao, J. Ramkumar, M. Gupta, "The effect of process parameters on machining of magnesium nano alumina composites through EDM" Int. J. Adv. Manufac. Technol., 2010, vol. 46, p. 1035-1042.
[14] C. L. Lin, J. L. Lin, T. C. Ko, "Optimization of the EDM process based on the orthogonal array with fuzzy logic and grey relational analysis method" Inter. J. Adv. Manuf. Technol., 2002, vol. 19, p. 271-277.
[15] Izwan N. S. L. B., Feng Z., Patel J. B., and Hung W. N., "Prediction of Material Removal Rate in Die-Sinking Electrical Discharge Machining" 44th Proceedings of the North American Manufacturing Research Institution of SME, 2016, vol. 5, p 658–668.

Available online at
http://namrc.uotechnology.edu.iq/index.php/

Nanotechnology and Advanced Materials Research Centre

Proceeding Articles Book 00 (2018) 000–000

6th International Scientific Conference on Nanotechnology, Advanced Materials and its Applications

Numerical Study on Thermal-hydraulic Performance and Entropy Generation of Confined Slot Impinging Jet with Nanofluids

M.A. Ahmed, Ibrahim. K. Alabdaly
Dept. of Mechanical engineering, College of Engineering, University of Anbar, Ramadi, Iraq
Corresponding auther:mohammed.ahmed@uoanbar.com

Abstract

In this paper, the flow and thermal characteristics of a confined slot-jet impingement with nanofluids have been numerically investigated over Reynolds number ranges of 100-1000. Four different types of nanofluids which are SiO_2, Al_2O_3, CuO and ZnO-water with volume fraction concentration from 0 to 4 % and nanoparticles diameter between 30 and 70 nm were performed. The governing equations momentum, energy, and mass are discretized by using finite volume approach based on the SIMPLE algorithm. The effect of Reynolds number, types of nanofluids, nanoparticles diameters and the volume fraction on the average Nusselt number, pressure drop, total entropy generation and thermal-hydraulic performance factor have been presented and discussed. It is observed that the average Nusselt number, pressure drop and average entropy generation increases with increasing Reynolds number and nanoparticles volume fraction and with decreasing nanoparticles diameter. Also, the thermal-hydraulic performance factor of SiO_2-water nanofluids is the highest compared with other types of nanofluids. It can be concluded that using SiO_2-water nanofluids with 30 nm nanoparticles diameters and 4% volume fraction can provide the best thermal-hydraulic performance.

Keywords: Jet Impingement, Nanofluids, Entropy generation, Thermal-hydraulic performance, Finite volume method

1. Introduction

Among various convection transport methods, the impinging jet is an especially attractive heating or cooling mechanism due to high heat transfer rates. Hence, the jet impingement technique is widely utilized in different industrial applications such as cooling the turbine blades, cooling of electronic equipment, metal annealing , paper drying and glass tempering [1-2]. There are many numerical and experimental investigations on the impinging jet. A confined air slot-jet impingement on the smooth target plate has been experimentally investigated by Hee et al. [3]. They found that the highest heat transfer enhancement at the stagnation point. Sahoo and Sharif [4] performed a numerical investigation of the flow field and heat transfer enhancement by air slot-jet impingement with a constant heat flux surface. It was observed that for a given domain of aspect ratio, the average Nusselt number increases with increasing jet exit Reynolds number. Dagtekin and Oztop [5] presented a numerical investigation on the double slot-jets impingement. They found that the average Nusselt number increases linearly with Reynolds number. Simionescu et al. [6] performed an experimental and numerical study to investigate the heat transfer enhancement using air impinging jet and it was found that the static surface pressure increased with Reynolds number. Sharif [7] numerically investigated of air slot-jet impingement on a heated surface. It is observed that the skin friction and Nusselt number increased with decreasing jet-to-surface spacing. Lam and Prakash [8] performed a numerical investigation of heat transfer enhancement and entropy generation of air jet impingement. It was observed that the average Nusselt number and entropy generation increased with increasing Reynolds number and decreasing channel height.

Manca et al. [9] performed a numerical investigation of the turbulent impinging jet with Al_2O_3-water nanofluids and it was found that the average Nusselt number increased with increasing Reynolds number and nanoparticles volume fraction. Forced convection flow using Al_2O_3-water nanofluid in a radial flow cooling system were investigated by Palm et al. [10] and Yang and Lai [11]. Results showed that the Nusselt number and pressure drop increased with the increasing volume fraction of nanoparticles. Sun et al. [12] presented an experimental investigation of heat transfer enhancement using jet impingement with copper-water nanofluids. They observed that the average Nusselt number increased with Reynolds number. Gherasim et al. [13] experimentally studied on the laminar convective heat transfer of Al_2O_3-water nanofluid flow between a flat plate and heated disk with axial coolant

injection. It was observed that the Nusselt number increased with Reynolds number and nanoparticles volume fraction and decreases with increasing the jet-to-disk distance. Manco et al. [14] numerically investigated on the laminar slot-jet impingement using Al_2O_3-water nanofluids. It was observed that the maximum heat transfer enhancement was about 36% at nanoparticles concentration of 0.05. Lv et al. [15] presented an experiential investigation on the heat transfer performance using single jet impingement with SiO_2-water nanofluids. It was observed that the heat transfer enhancement increased with increases the volume concentration of nanoparticles and Reynolds number. Lafmajani et al. [16] carried out an experiential investigation of a planner jet impinged on the convex heated surface using SiO_2-water nanofluids. They concluded that the maximum enhancement of average heat transfer coefficient about 32.78 % occurred at the nanofluids concentration of 2%. Lafouraki et al. [17] numerically investigated on the entropy generation of a confined slot-jet impingement with TiO_2 –water mnanofluid. Results showed that the total entropy generation increases with increasing nanoparticles volume fraction.

In the present study, laminar forced convection of a confined slot-jet impingement on an isothermal surface using nanofluids is numerically investigated over Reynolds number range of 100-1000. The effects of four different types of nanofluids, such as SiO_2, Al_2O_3, CuO, and ZnO-water, nanoparticles diameters of 30, 50, and 70 nm and nanoparticles volume fraction ranging from 0 to 4% on the flow and thermal characteristics have been presented and analyzed.

2- Mathematical Formulation

Problem description

Fig.1 depicts the geometry of a confined slot-jet impingement used in this study. The jet width is W=10 mm, the distance between a jet and the target surface is H, and the length of target plate is L=200 mm. The jet-to-plate spacing is constant at H/W= 1. It is assumed that the flow is uniform, laminar, steady state, two-dimensional and incompressible. The mixture of water and nanoparticles are assumed homogeneous. Due to the flow is symmetric about y-axis, only the half-domain is analyzed in this study.

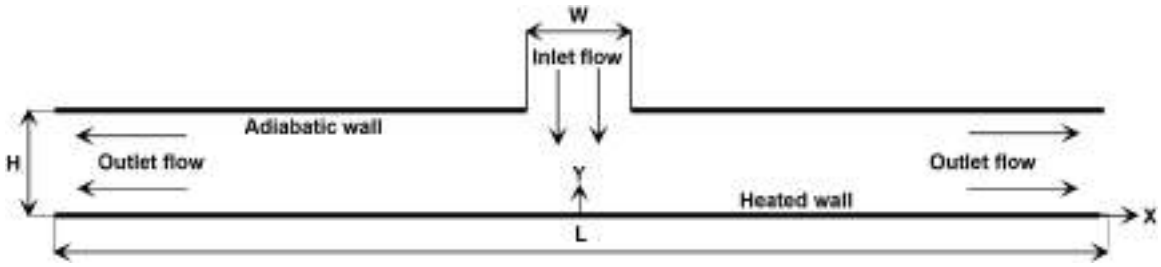

Fig. 1. The physical domain for this study.

Governing equations and boundary conditions

The non-dimensional governing equations in the body-fitted coordinates are [18]:

Continuity equation:

$$\frac{\partial}{\partial \xi}(\rho U^a) + \frac{\partial}{\partial \eta}(\rho V^a) = 0 \qquad (1)$$

X-Momentum:

$$\frac{\partial}{\partial \xi}(\rho U U^a) + \frac{\partial}{\partial \eta}(\rho V U^a) = -\frac{\partial}{\partial \xi}(Y_\eta P) + \frac{\partial}{\partial \eta}(Y_\xi P) + \frac{1}{Re}\left[\frac{\partial}{\partial \xi}\left(\beta_{11}\frac{\partial U}{\partial \xi}\right) + \frac{\partial}{\partial \eta}\left(\beta_{22}\frac{\partial U}{\partial \eta}\right) + \frac{\partial}{\partial \xi}\left(\beta_{12}\frac{\partial U}{\partial \eta}\right) + \frac{\partial}{\partial \eta}\left(\beta_{21}\frac{\partial U}{\partial \xi}\right)\right] \qquad (2)$$

Y-Momentum:

$$\frac{\partial}{\partial\xi}\left(VU^{c}\right)+\frac{\partial}{\partial\eta}\left(VV^{c}\right)-\frac{\partial}{\partial\xi}\left(X_{\eta}P\right)-\frac{\partial}{\partial\eta}\left(X_{\xi}P\right)+\frac{1}{Re}\left[\frac{\partial}{\partial\xi}\left(\beta_{11}\frac{\partial V}{\partial\xi}\right)+\frac{\partial}{\partial\eta}\left(\beta_{22}\frac{\partial V}{\partial\eta}\right)+\frac{\partial}{\partial\xi}\left(\beta_{12}\frac{\partial V}{\partial\eta}\right)+\frac{\partial}{\partial\eta}\left(\beta_{21}\frac{\partial V}{\partial\xi}\right)\right] \quad (3)$$

Energy:

$$\frac{\partial}{\partial\xi}\left(\theta U^{c}\right)+\frac{\partial}{\partial\eta}\left(\theta V^{c}\right)=\frac{1}{Re\,Pr}\left[\frac{\partial}{\partial\xi}\left(\beta_{11}\frac{\partial\theta}{\partial\xi}\right)+\frac{\partial}{\partial\eta}\left(\beta_{22}\frac{\partial\theta}{\partial\eta}\right)+\frac{\partial}{\partial\xi}\left(\beta_{12}\frac{\partial\theta}{\partial\eta}\right)+\frac{\partial}{\partial\eta}\left(\beta_{21}\frac{\partial\theta}{\partial\xi}\right)\right] \quad (4)$$

Where:

$$U^{c}=UY_{\eta}-VX_{\eta},\quad V^{c}=-UY_{\xi}+VX_{\xi},\quad J=X_{\xi}Y_{\eta}-X_{\eta}Y_{\xi},\quad \beta_{12}=\beta_{21}=-\left(X_{\xi}X_{\eta}+Y_{\xi}Y_{\eta}\right)/J,$$
$$\beta_{22}=\left(X_{\xi}^{2}+Y_{\xi}^{2}\right)/J,\quad \beta_{11}=\left(Y_{\eta}^{2}+X_{\eta}^{2}\right)/J \quad (5)$$

The equation of entropy generation in the dimensionless form is given by [19]:

$$N=\frac{1}{(T_{in}{}^{*}+\theta)^{2}}\left[\left(\frac{\partial\theta}{\partial X}\right)^{2}+\left(\frac{\partial\theta}{\partial Y}\right)^{2}\right]+\frac{Ec\,Pr}{(T_{in}{}^{*}+\theta)}\left[2\left\{\left(\frac{\partial U}{\partial X}\right)^{2}+\left(\frac{\partial V}{\partial Y}\right)^{2}\right\}+\left(\frac{\partial U}{\partial Y}+\frac{\partial V}{\partial X}\right)^{2}\right] \quad (6)$$

The non-dimensional parameters that are used in the above equations can be expressed as:

$$X=\frac{x}{W},\ Y=\frac{y}{W},\ U=\frac{u}{V_{in}},\ V=\frac{v}{V_{in}},\ \theta=\frac{T-T_{in}}{T_{w}-T_{in}},\ P=\frac{p}{\rho_{nf}V_{in}^{2}},\ T_{in}^{*}=\frac{T_{in}}{T_{w}-T_{in}} \quad (7)$$

The boundary conditions that used in this study:

i. Jet inlet section: $U=0,\ V=-1,\ \theta=0$ (8a)

ii. Outlet section: $\frac{\partial U}{\partial X}=0,\ \frac{\partial V}{\partial X}=0,\ \frac{\partial\theta}{\partial X}=0$ (8b)

iii. Target surface: $U=0,\ V=0,\ \theta=1$ (8c)

iv. Upper wall: $U=0,\ V=0,\ \frac{\partial\theta}{\partial Y}=0$ (8d)

v. Symmetry line: $\frac{\partial U}{\partial X}=0,\ \frac{\partial V}{\partial X}=0,\ \frac{\partial\theta}{\partial X}=0$ (8e)

The local and average Nusselt number at the target plate can be calculated as follow:

$$Nu_{x}=\frac{h_{x}W}{K_{nf}}=-\frac{K_{nf}}{K_{bf}}\frac{\partial\theta}{\partial Y},\quad Nu_{av.}=\frac{1}{L}\int_{0}^{L}Nu_{x}\,dx \quad (9)$$

The friction factor can be expressed as:

$$f=\Delta P\frac{W}{L}\frac{2}{\rho_{nf}V_{in}^{2}} \quad (10)$$

The thermal- hydraulic performance factor can be defined as [20]:

$$PEC=\left(\frac{Nu_{av,nf}}{Nu_{av,bf}}\right)\Big/\left(\frac{f_{nf}}{f_{bf}}\right)^{1/3} \quad (11)$$

The average entropy generation of heat transfer and fluid friction terms as follows:

$$N_{C,ave.}=\int N_{C}\,dV \quad (12)$$

$$N_{F,ave.}=\int N_{F}\,dV \quad (13)$$

And the total entropy generation is given by:

$$N_{T}=N_{C,ave}+N_{F,ave} \quad (14)$$

Properties of nanofluids:

In the present study, the thermophysical properties of Al_2O_3–water nanofluids are described as follows:

i. Density and heat capacity:
The density and heat capacity of the nanofluid are defined as [21]:

$$\rho_{nf} = (1-\phi)\rho_f + \phi\rho_p \quad (15)$$

$$(\rho C_p)_{nf} = (1-\phi)(\rho C_p)_f + \phi(\rho C_p)_p \quad (16)$$

ii. The dynamic viscosity:
The dynamic viscosity of the nanofluid is given by [22]:

$$\frac{\mu_{nf}}{\mu_f} = \frac{1}{1-34.87\left(d_p/d_f\right)^{-0.3}\phi^{1.03}} \quad (17)$$

Where d_f is the equivalent diameter of the base fluid molecule, it can be calculated as:

$$d_f = 0.1\left[\frac{6M}{N\pi\rho_{fo}}\right]^{1/3} \quad (18)$$

Where ρ_{fo} is the density of water determined at the temperature of T_o = 293 K.

iii. Thermal conductivity:
The effective thermal conductivity of the nanofluid can be given by [23]:

$$K_{eff} = K_{static} + K_{Brownian} \quad (19)$$

Where

$$K_{static} = K_f\left[\frac{(K_p+2K_f)-2\phi(K_f-K_p)}{(K_p+2K_f)+\phi(K_f-K_p)}\right] \quad (20)$$

$$K_{Brownian} = 5\times10^4\,\beta\phi\rho_f C_{pf}\sqrt{\frac{kT}{\rho_p d_p}}\,f(T,\phi) \quad (21)$$

Where

$$\beta = 8.4407\,(100\phi)^{-1.07304} \quad (22)$$

$$f(T,\phi) = (2.8217\times10^{-2}\phi + 3.917\times10^{-3})\left(\frac{T}{T_o}\right) + (-3.0669\times10^{-2}\phi - 3.91123\times10^{-3}) \quad (23)$$

Numerical method:

The governing continuity, momentum, and energy equations in the body-fitted coordinate are solved using finite volume method based on the SIMPLE algorithm [24]. The upwind scheme is employed to discretize the convection terms in the governing equations, and the central difference scheme is adopted to discretize the diffusion terms. Furthermore, a collocated grid arrangement is used in this study [25].The two-dimensional of Poisson equations were solved to generate the computation domain. The under-relaxation factor was applied to obtain the better convergence. The convergence criterion for all variables is 10^{-5}.

Code validation and grid test:

In order to validate the numerical algorthim used in the current study, the Nusselt number for a confined impinging slot jets using Al_2O_3- water nanofluid has been calculated at stagnation point and compared with the numerical study of Manco et al. [14], as shown in Fig. 2. It is found that the results are in a good agrement. To check the grid independence, the local Nusselt number along the target surface using SiO_2-water nanofluid are tested for the different five grid sizes. It is found that the grid size of 361×101 can give the grid-independence solution for all results.

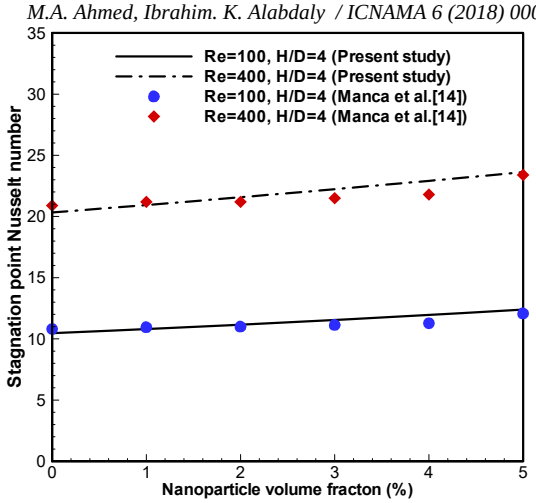

Fig. 2. Comparison stagnation point Nusselt number of the current study with previous the numerical study of Manca et al. [14].

3- Results and discussion:

The velocity vectors of SiO_2-water nanofluids for different Reynolds numbers at ϕ=4%, dp=30 nm and H/W=1 are shown in Fig. 4.

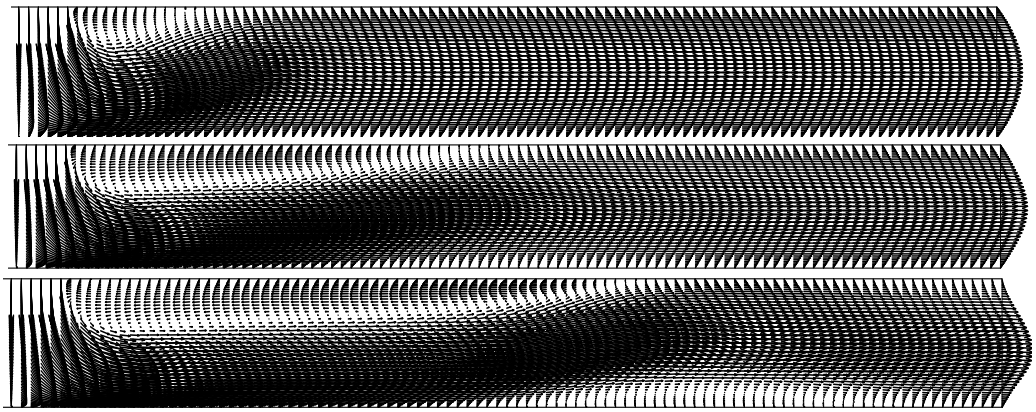

Fig. 4. Velocity vectors of SiO_2-water nanofluids for different Reynolds numbers (a)Re=100, (b)Re=500, and Re=1000 at ϕ=4% and dp=30 nm.

When a jet impinges onto the target plate, a counterclockwise primary vortex can be seen in the neighborhood the jet inlet due to the shear force caused by the jet on the fluid in the channel. When Reynolds number increases, the size of this vortex increased. At Re=1000 a clockwise secondary vortex formed at the target plate near the exit channel, which is a smaller size than the primary vortex and weaker. These results are compatible with the numerical study of Sahoo and Sharif [4].
Fig. 5 depicts the isotherms contours for different Reynolds number. It can be observed that the minimum thickness of the thermal boundary layers at the stagnation zone due to the high-velocity gradient. When Reynolds number increases, the thickness of thermal boundary layer decreases and the temperature gradient increases at the target surface.

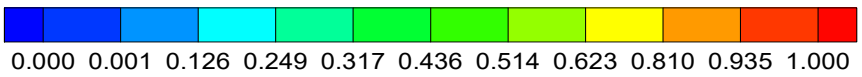

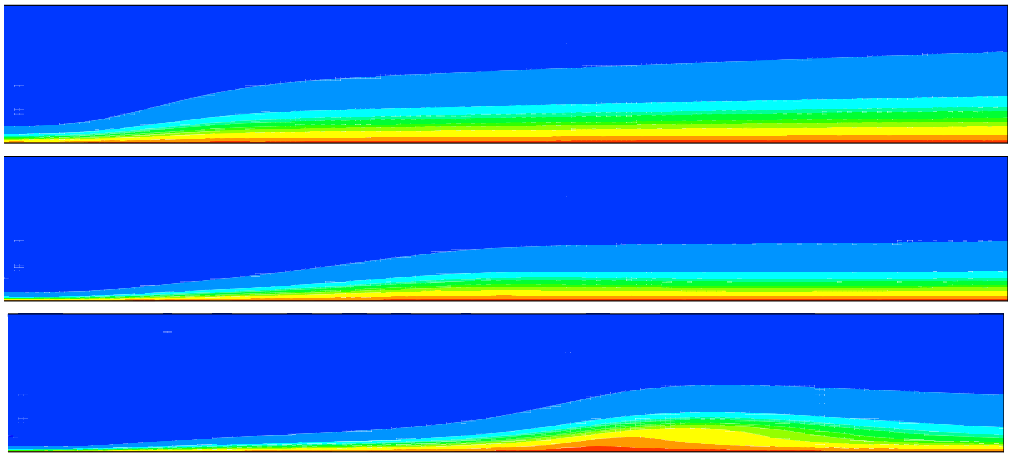

Fig. 5. Temperature contours of SiO_2-water nanofluids for different Reynolds numbers (a)Re=100, (b)Re=500, and Re=1000 at ϕ=4% and dp=30 nm.

Fig. 6. shows the contours for total entropy generation of SiO_2-water nanofluids at ϕ = 4% and dp=30 nm for different Reynolds number. It is observed that the maximum entropy generation at the stagnation region. When Reynolds number increases, the total entropy generation increases due to the irreversibilities of fluid friction and heat transfer.

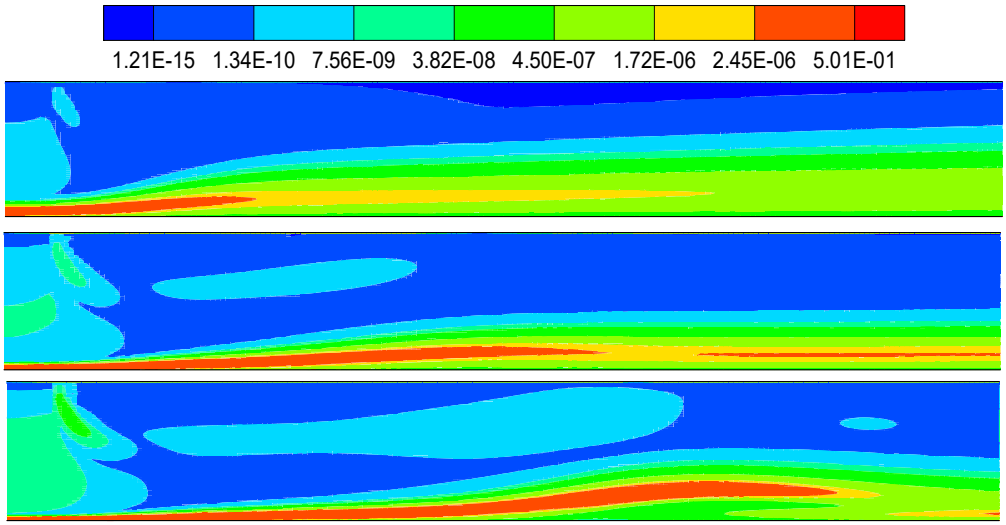

Fig. 6. Total entropy generation contours of SiO_2-water nanofluids for different Reynolds numbers (a)Re=100, (b)Re=500, and Re=1000 at ϕ=4% and dp=30 nm.

Fig. 7 (a) shows the variation of the average Nusselt number with Reynolds number for different nanoparticles volume fraction of SiO_2-water nanofluids at dp=30 nm. It is observed for a given volume fraction, the average Nusselt number increases significantly with Reynolds number due to decrease the thermal boundary layer thickness and increase the temperature gradient at the impingement surface. At a particular Reynolds number, it can be noted that the average Nusselt number increased with increasing nanoparticles volume fraction due to improving the thermal conductivity of the base fluid as well as the Brownian motion of nanoparticles. Fig. 7 (b) shows the variation of the pressure drop with Reynolds number for different nanoparticles volume fraction of SiO_2-water nanofluids at dp=30 nm. It is found that the pressure drop increase with Reynolds number because of the high-velocity gradient at the target plate. It is found that the pressure drop increases with increasing nanoparticles volume fractions due to increase the viscosity of the nanofluids. Fig. 7 (c) shows the variation of thermal-hydraulic performance factor with Reynolds number for different nanoparticles volume fraction of SiO2-water nanofluids at dp=30 nm. It is observed that the thermal-hydraulic

performance factor increases with increase nanoparticles volume fractions due to the enhancing in heat transfer is greater than the increasing in pressure losses. Fig. 7 (d) displays the variation of the average entropy generation with Reynolds number for different nanoparticles volume fraction of SiO_2-water nanofluids at dp=30 nm. It is found that the average entropy generation increases linearly with Reynolds number at a given volume fraction due to the effect of fluid friction and heat transfer irreversibilities. Furthermore, it is observed that the average entropy generation increases with nanoparticles volume fraction at a particular Reynolds number.

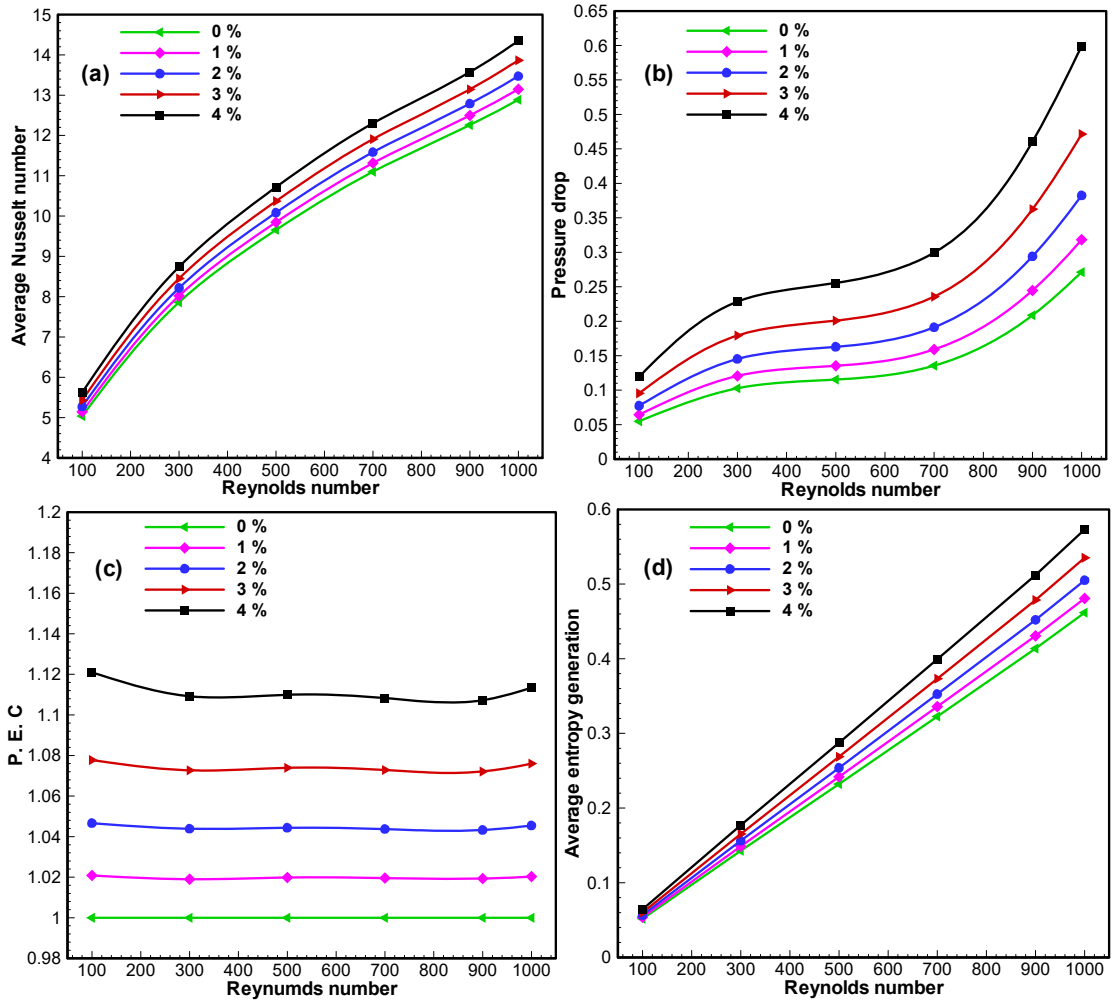

Fig. 7. The effect of nanoparticles volume fraction for SiO_2 on (a) average Nusselt number, (b) pressure drop, (c) thermal-hydraulic performance factor (d) average entropy generation at dp =30nm.

Fig. 8 (a) presents the variation of the average Nusselt number with Reynolds number for different nanoparticles diameters of SiO_2-water nanofluids at ϕ= 4 %. It is observed that the average Nusselt number increases with the deceasing in nanoparticles diameter. Fig. 8 (b) displays the variation of the pressure drop with Reynolds number for different nanoparticles diameters of SiO_2-water nanofluids and ϕ= 4%. It is found that the pressure drop increases with decreasing in nanoparticles diameter. This is because the viscosity of nanofluid increases with decreasing nanoparticles diameter. Fig. 8 (c) displays the variation of thermal-hydraulic performance factor with Reynolds number for different nanoparticles diameters of SiO_2-water nanofluids at ϕ= 4%. It is found that the value of performance factor for different nanoparticles diameters over the entire range of Reynolds number is greater than unity. This means that the increasing in the heat transfer is more than the augmentation in the pressure drop. At a given Reynolds number, it is found that the performance factor is inversely proportional to nanoparticles diameters. Fig. 8 (d) presents the variation of average entropy generation with Reynolds number for different nanoparticles diameters of SiO_2-water nanofluids at ϕ= 4%. It is observed that the average entropy generation increase as nanoparticles diameters decrease.

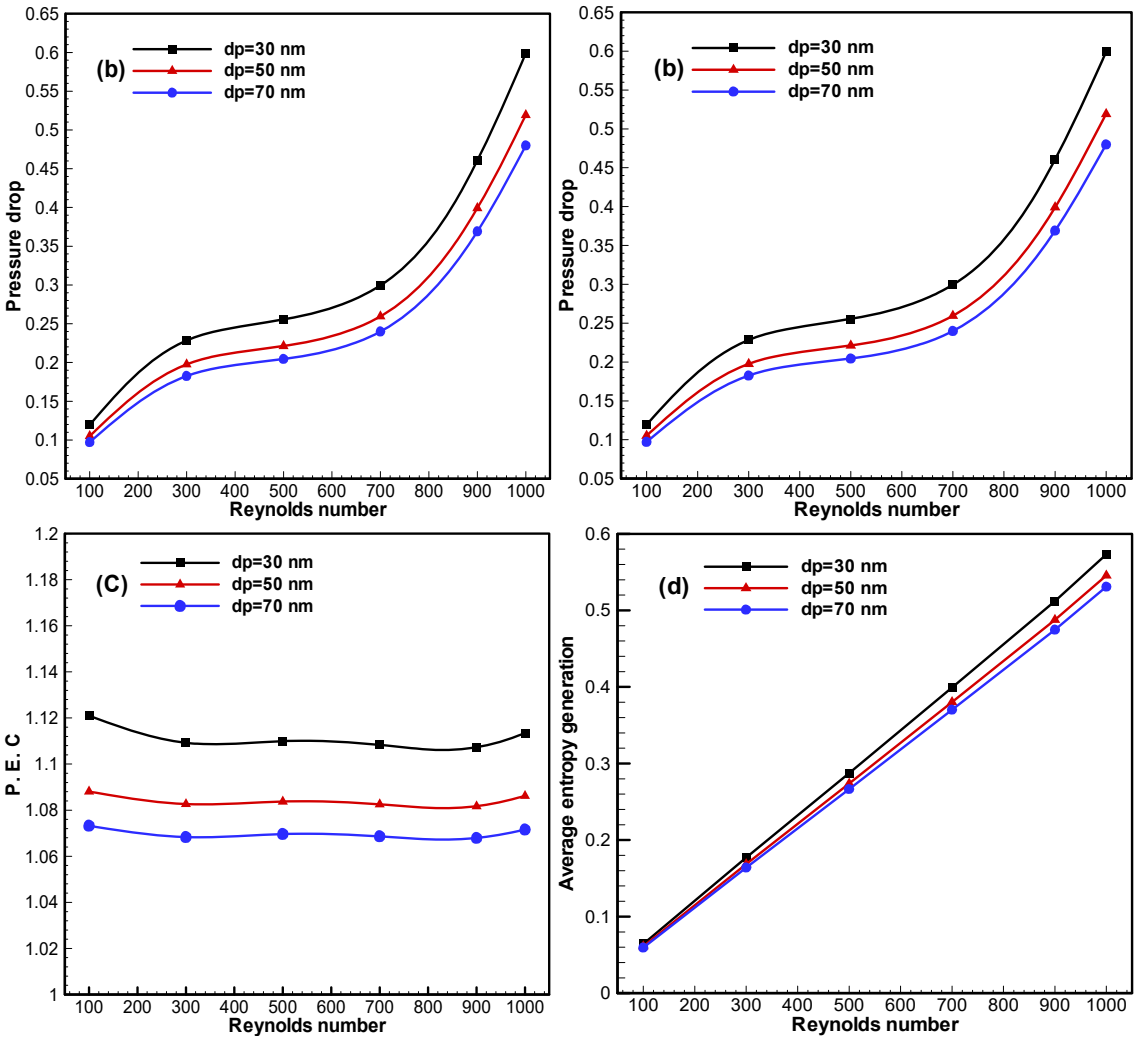

Fig. 8. The effect of nanoparticles diameter of SiO_2 on (a) average Nusselt number, (b) pressure drop, (c) thermal-hydraulic performance factor (d) average entropy generation at dp =30nm and ϕ= 4%.

Fig. 9 (a) presents the variation of average Nusselt number with Reynolds number for different types of nanofluids at dp=30 nm and ϕ= 4%. It is can found that the SiO_2–water nanofluids provids the highest Nusselt number followed by Al_2O_3, ZnO, CuO–water nanofluids as well as pure water. In addition, the pure water has the lowest Nusselt number due to the poor thermal conductivity. Fig. 9 (b) displays the variation of the pressure drop with Reynolds number for different types of nanofluids at dp=30 nm and ϕ= 4%. It can be found that the pressure drop for all types of nanofluids are higher than that pure water due to the high density and viscosity of nanofluids. Also, the SiO_2-water nanofluids displays the highest pressure drop followed by Al_2O_3, ZnO, CuO–water nanofluids. Fig. 9 (c) presents the variation of thermal-hydraulic performance factor with Reynolds number for different nanofluid types at dp=30 nm and ϕ= 4%. It is found that the performance factor for all types of nanofluids are higher than water. In addition, SiO_2-water nanofluids displays the best performance factor followed by Al_2O_3, ZnO, CuO–water nanofluids. Fig. 9 (d) presents the variation of the average entropy generation with Reynolds number for different nanofluid types at dp=30 nm and ϕ= 4%. It is found that the average entropy generation for all types of nanofluid is the higher than that for the pure water. Also, it is found that that the SiO_2-water nanofluid has the maximum average entropy generation.

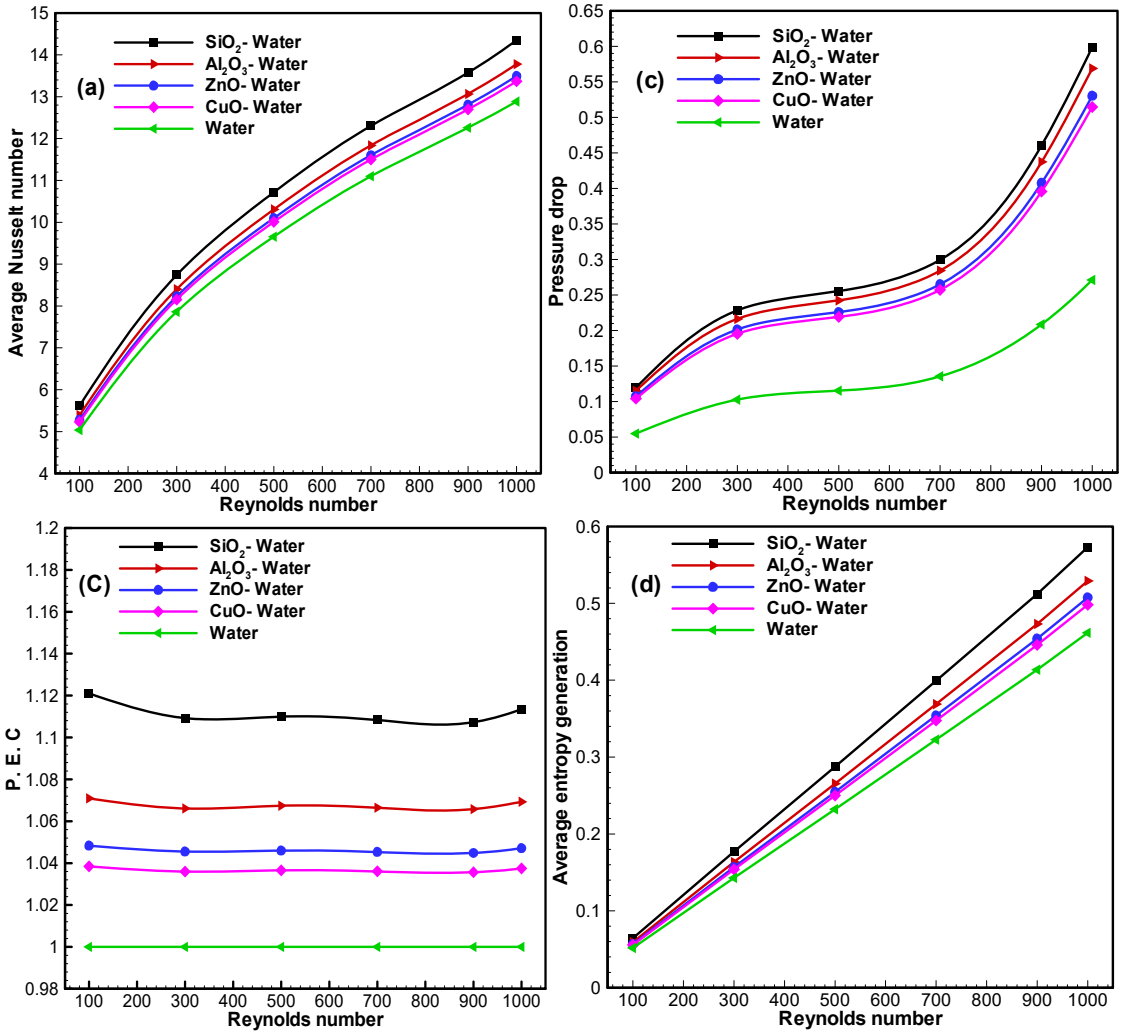

Fig. 9. The effect of nanofluid types on (a) average Nusselt number, (b) pressure drop, (c) thermal-hydraulic performance factor (d) average entropy generation at dp =30 nm and ϕ= 4%.

4- Conclusion:

In this study, the flow field and heat transfer characteristics of the laminar forced flow using confined slot-jet impingement with nanofluids have been numerically investigated over Reynolds number range of 100-1000. Four different types of nanofluids which are SiO_2, Al_2O_3, CuO, and ZnO-water, nanoparticles diameters in the range of 30-70 nm as well as nanoparticles volume friction in the range of 0- 4 % have been considered. The governing equations have been solved using finite volume method with SIMPLE algorithm technique. It was found that the average Nusselt number, pressure drop, thermal-hydraulic performance factor and average entropy generation increases with increasing nanoparticles volume fraction and with decreasing nanoparticles diameter. In addition, the thermal-hydraulic performance factor for all types of nanofluid are higher than that for water. It can be concluded that using SiO_2-water nanofluids with 4% volume fraction of nanoparticles and 30 nm nanoparticles diameters can provide the best thermal-hydraulic performance factor.

Nomenclature

H	channel height (m)	Greek symbols:	
w	jet width (m)	η, ζ	body-fitted coordinates
L	channel length (m)	β_{11}, β_{12}	transformation coefficients
h	heat transfer coefficients ($W/m^2.^oC$)	β_{21}, β_{22}	transformation coefficients
f	friction factor	ϕ	concentration of nanofluids
C_p	specific heat (J/Kg.K)	μ	dynamic viscosity ($N.s/m^2$)
K	thermal conductivity (W/mK)	θ	non-dimensional temperature
Nu	Nusselt number	ρ	density (Kg/m^3)
P	pressure (pa)	Δp	pressure drop (pa)
Pr	Prandtl number	$\mathcal{B}$	Boltzmann constant, 1.381×10^{-23} J/K
T	temperature (^oC)		
u, v	velocities components (m/s)	Subscripts:	
U, V	dimensionless velocity component	eff	effective
x, y	2D cartesian coordinates (m)	f	base fluid
X, Y	dimensionless cartesian coordinates	in	inlet
J	Jacobian of transformation	av	average value
Re	Reynolds number ($Re=\rho_{nf}\, v_{in}\, w/\mu_{nf}$)	nf	nanofluid
dp	nanoparticles diameter	w	wall
N	dimensionless entropy generation	p	particles
N_t	total entropy generation.	x	local value
N_C	entropy generation due to heat transfer.	bf	base fluid (Water)
N_F	entropy generation duo to fluid friction.		
E_C	Eckert number		

References:

[1] R. Viskanta, "Nusselt-Reynolds Prize Paper Heat Transfer to Impinging Isothermal Gas and Flame Jets," pp. 111–134, 1993.

[2] D. Hee, J. Ryeol, H. Jin, J. Sik, and P. Ligrani, "International Journal of Heat and Mass Transfer Confined , milliscale unsteady laminar impinging slot jets and surface Nusselt numbers," *Int. J. Heat Mass Transf.*, vol. 54, no. 11–12, pp. 2408–2418, 2011.

[3] D. Hee, H. Jin, and P. Ligrani, "International Journal of Heat and Mass Transfer Milliscale confined impinging slot jets : Laminar heat transfer characteristics for an isothermal flat plate," *Int. J. Heat Mass Transf.*, vol. 55, no. 9–10, pp. 2249–2260, 2012.

[4] D. Sahoo and M. A. R. Sharif, "Numerical modeling of slot-jet impingement cooling of a constant heat flux surface confined by a parallel wall," *Int. J. Therm. Sci.*, vol. 43, no. 9, pp. 877–887, 2004.

[5] I. Dagtekin and H. F. Oztop, "Heat transfer due to double laminar slot jets impingement onto an isothermal wall within one side closed long duct," *Int. Commun. Heat Mass Transf.*, vol. 35, no. 1, pp. 65–75, 2008.

[6] Ş. M. Simionescu, N. O. Tănase, D. Broboană, and C. Bălan, "Impinging Air Jets on Flat Surfaces at Low Reynolds Numbers," *Energy Procedia*, vol. 112, no. October 2016, pp. 194–203, 2017.

[7] M. A. R. Sharif, "Heat transfer from an isothermally heated flat surface due to twin oblique slot-jet impingement," *Procedia Eng.*, vol. 56, no. September 2015, pp. 544–550, 2013.

[8] P. A. K. Lam and K. Arul Prakash, "A numerical investigation of heat transfer and entropy generation during jet impingement cooling of protruding heat sources without and with porous medium," *Energy Convers. Manag.*, vol. 89, pp. 626–643, 2015.

[9] O. Manca, P. Mesolella, S. Nardini, and D. Ricci, "Numerical study of a confined slot impinging jet with nanofluids," *Nanoscale Res. Lett.*, vol. 6, no. 1, pp. 1–16, 2011.

[10] S. J. Palm, G. Roy, and C. T. Nguyen, "Heat transfer enhancement with the use of nanofluids in radial flow cooling systems considering temperature-dependent properties," *Appl. Therm. Eng.*, vol. 26, no. 17–18, pp. 2209–2218, 2006.

[11] Y. T. Yang and F. H. Lai, "Numerical investigation of cooling performance with the use of Al2O3/water nanofluids in a radial flow system," *Int. J. Therm. Sci.*, vol. 50, no. 1, pp. 61–72, 2011.

[12] B. Sun, Y. Qu, and D. Yang, "Heat transfer of Single Impinging Jet with Cu Nanofluids," *Appl. Therm. Eng.*, vol. 102, no. March, pp. 701–707, 2016.

[13] I. Gherasim, G. Roy, C. T. Nguyen, and D. Vo-Ngoc, "Experimental investigation of nanofluids in confined laminar radial flows," *Int. J. Therm. Sci.*, vol. 48, no. 8, pp. 1486–1493, 2009.

[14] O. Manca, D. Ricci, S. Nardini, and G. Di Lorenzo, "Thermal and fluid dynamic behaviors of confined laminar impinging slot jets with nanofluids," *Int. Commun. Heat Mass Transf.*, vol. 70, pp. 15–26, 2016.

[15] J. Lv, C. Hu, M. Bai, K. Zeng, S. Chang, and D. Gao, "Experimental investigation of free single jet impingement using SiO2 - water nanofluid," *Exp. Therm. Fluid Sci.*, vol. 84, pp. 39–46, 2017.

[16] N. Asghari Lafmajani, M. Ebrahimi Bidhendi, and M. Ashjaee, "SiO2 nanofluid planar jet impingement cooling on a convex heated plate," *Heat Mass Transf. und Stoffuebertragung*, vol. 52, no. 12, pp. 1–12, 2016.

[17] B. Yousefi-Lafouraki, A. Ramiar, and S. Mohsenian, "Entropy generation analysis of a confined slot impinging jet in a converging channel for a shear thinning nanofluid," *Appl. Therm. Eng.*, vol. 105, pp. 675–685, 2016.
[18] M. A. Ahmed, M. M. Yaseen, and M. Z. Yusoff, "Numerical study of convective heat transfer from tube bank in cross flow using nanofluid," *Case Stud. Therm. Eng.*, vol. 10, pp. 560–569, 2017.
[19] A. Mukhopadhyay, "Analysis of entropy generation due to natural convection in square enclosures with multiple discrete heat sources," *Int. Commun. Heat Mass Transf.*, vol. 37, no. 7, pp. 867–872, 2010.
[20] C. Qi, J. Hu, M. Liu, L. Guo, and Z. Rao, "Experimental study on thermo-hydraulic performances of CPU cooled by nanofluids," *Energy Convers. Manag.*, vol. 153, no. July, pp. 557–565, 2017.
[21] Y. Xuan and W. Roetzel, "Conceptions for heat transfer correlation of nanofluids," *Int. J. Heat Mass Transf.*, vol. 43, no. 19, pp. 3701–3707, 2000.
[22] M. Corcione, "Empirical correlating equations for predicting the effective thermal conductivity and dynamic viscosity of nanofluids," *Energy Convers. Manag.*, vol. 52, no. 1, pp. 789–793, 2011.
[23] R. S. Vajjha and D. K. Das, "A review and analysis on influence of temperature and concentration of nanofluids on thermophysical properties, heat transfer and pumping power," *Int. J. Heat Mass Transf.*, vol. 55, no. 15–16, pp. 4063–4078, 2012.
[24] Versteeg H.K & Malalasekera, An Introduction to Computational Fluid Dynamics, vol. M. 2007.
[25] J. H. Ferziger and M. Peric, *Computational methods for fluid dynamics*, vol. 46, no. 2–3. 2003.

Available online at
http://namrc.uotechnology.edu.iq/index.php/

Nanotechnology and Advanced Materials Research Centre

Proceeding Articles Book 00 (2018) 000–000

6th International Scientific Conference on Nanotechnology, Advanced Materials and its Applications

Geotextile by using Nano Natural Material for Iraqi Crude Oil

Ramzy. S. Hamied, Mayssaa Ali AL-Bidry, Hawwraa. A., Raghad A., Marwa. S.
Petroleum Technology Department / University of Technology, Baghdad, Iraq
Corresponding auther:150002@uotechnology.edu.iq

Abstract

The main environmental concern associated with crude oil is that it may cause significant hazards to human health and the earth's ecology. This study has focused on detecting the ability of Iraqi clays with different grain size (-75, 75, 150, and 300) µm and nano size as geotextile compacted liners to prevent leakage oil. The Iraqi clay was analyzed by using x-ray diffraction and atomic absorption spectroscopy. Physical properties of Iraqi crude oil: API grade (American *petroleum institute), density, viscosity,* sulphur content, and sediment content were tested. The adsorption capacity was determined of Iraqi clays. The results show that Iraqi nano - kaolinite adsorption capacity better than natural clays (kaolinite and attapulgite). Moreover, the adsorption capacity increases with increasing the grain size and increase API gravity of crude oil, therefore, it can be used as a geotextile liner either mixed with additives, bonded with geomembrane or as filler between geotextiles. Throw experimental results on the clay with different grain sizes, all experiments were successful except 300µm.

*Keywords:**G***eotextile; Nano clay;Crude Oil; Kaolinite; Attapulgite.

1- Introduction

Engineered landfills are a controlled method of refuse disposal designed to reduce the environmental and public health impacts of waste. The most important issue in landfill design and construction is to contain liquid and gas pollutants such that they do not contaminate their surroundings [1]. To limit contaminant migration to levels that will result in negligible impact on the environment, several different types of lining systems can be used for waste containment. Use of hydraulic containment in a landfill that is lined with a compacted clay liners (CCL) lends the advantage that the clay is permanently saturated, it is therefore less likely to suffer from post-emplacement desiccation, which can be a problem in conventional landfill. The simplest liner consists of either a geomembrane, a CCL or a GCL [2-5].

Geosynthetic clay liners (GCLs) are manufactured barrier layers containing high quality sodium bentonite clay attached or adhered to geotextiles or a geomembrane. The GCL's low permeability and high strength make it an ideal replacement for containment or capping projects with petroleum, storage, conveyance, or refining industries. GCLs have been used as primary or secondary containment in bulk tank farms, process fluid ponds, and pipeline liners. GCLs are also used to cap petroleum-impacted soil or waste; and used as a primary liner in bioremediation pads or constructed wetlands [6-8].

This study has focused on the heavy and light crude oil acted with Iraqi nano kaolinite and natural clays (kaolinite and attapulgite), *by adsorptions* capacity of Iraqi clays, the possibility of using Iraqi clays (geotextile compacted liners) as anti spill or geomembrane, and the effect of grain size on the efficiency of Iraqi clays as geotextile compacted liners to prevent leakage oil.

2- Materials and Method

Kaolinite was acquired from Iraqi Geological Survey Company. and grinding to - 75µm, 75µm, 150µm., 300µm, and nano size. The main mineral component of kaolin is kaolinite, and gangue minerals quartz, calcite and gypsum as determined by X-Ray diffraction. The chemical compositions of the kaolinite are given in Table 1 via atomic absorption spectrometer analysis.

Table 1.The chemical compositions of the Iraqi kaolinite.

SiO_2 %	Al_2O_3%	Fe_2O_3%	TiO_2%	CaO%	MgO%	SO_3%	Na_2O%	K_2O%	MnO%	L.O.I. %
46.48	35.45	1.62	1.6	0.56	0.14	0.19	0.16	0.48	19	13.23

Nano Iraqi kaolinite was obtained by using ceramic ball mill, where the grinding period was ten days [9]. For the preparation of the compacted and geotextile four types of liners were used

1) *Kaolinite with different grain size* (-75, 75, 150 and 300) µm.

2) 150µm kaolinite and attapulgite.

3) 300µm kaolinite and attapulgite .

4) Nano kaolinite with 150µm kaolinite and attapulgite.

While there are many types of crude oil, the oil and gas sector uses important characteristics to classify them: density (heavy crude and light crude) API degree equals (23.5 and 30).

This study has focused on the behavior of heavy and light crude oil with Iraqi kaolinite and nano kaolinite. A good example of Iraqi heavy crude comes from the AL - Ahdab field and light crude from AL-Burjsiha field.

The focus of this part: the evaluation of laboratory data Iraqi nano kaolinite and kaolinite. Adsorption capacity to heavy or light crude which can be used to compare the adsorbing capacity between Iraqi nano kaolinite, kaolinite and attapulgite to crude oil and relative cost effectiveness. The crude oil retention capacity test is a laboratory method that was developed to determine the amount of free crude oil released from a sorbent material bentonite when it is subjected to pressure. Oil retention was measured as the ratio of oil adsorbed to dry sorbent weight Eq. 1 [10]:

Oil capacity (retention) % = [(Os – On)/Os] x 100 ……(1)

where: Os = total oil adsorbed, On = net oil remaining (after oil retention test)

2-2-2 Tests of Iraqi Clays as Geotextile Compacted Liners

Ten sets of experiments were done testing the ability Iraqi nano kaolinite and mixed clays (kaolinite and attapulgite) to prevent crude oil pollution as an anti spill by using Iraqi heavy crude comes from the AL - Ahdab field and light crude from AL-Burjsiha field .

1) Compacted Kaolinite liners with different gra*in size* (-75, 75, 150 and 300)µm.

2) Geotextile liner composed from kaolinite 150µm and attapulgite 150µm.

3) Geotextile liner composed from kaolinite 300µm. and attapulgite 300µm.

4) Geotextile liner composed from nano kaolinite with kaolinite 150µm. and attapulgite150µm.

All experiments using a transparent tube with diameter 3.2cm and 30cm height, small mesh sieve and stand to fix the tube. Experiments include using 50ml of crude oil with 25g of Iraqi clays. The total height of the oil with clays was (6 - 10 cm). Each

hour the total height was measured to see how much oil was leaked into the clays and calculating the absorption volume. Contact time continued up to four weeks.

3- Results and discussion

Adsorption Capacity (AC) for Natural Iraqi Clay

Adsorption capacity (AC %) tests of crude oil (East of Baghdad and AL-Burjsiha) on Iraqi nano kaolinite and natural clays (kaolinite and attapulgite) with different grain sizes in order to test the capacity of clays to adsorb crude oil , effective grain size on adsorption capacity and possibility of using clays as anti spill are shown in Figures (1 – 5).

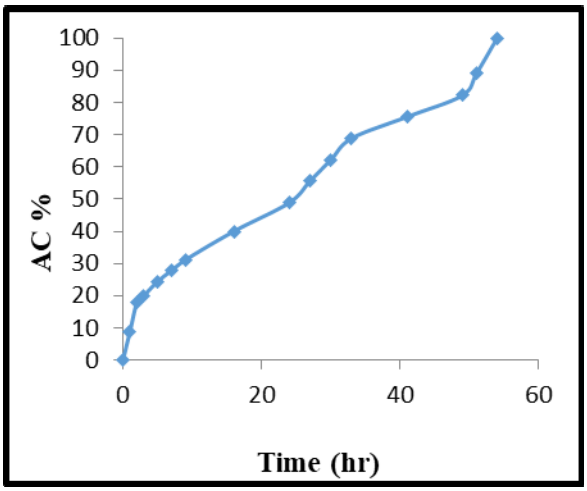

Figure 1. AC. % Vs. Time for Kaolinite -75 micron for AL - Ahdab Crude Oil.

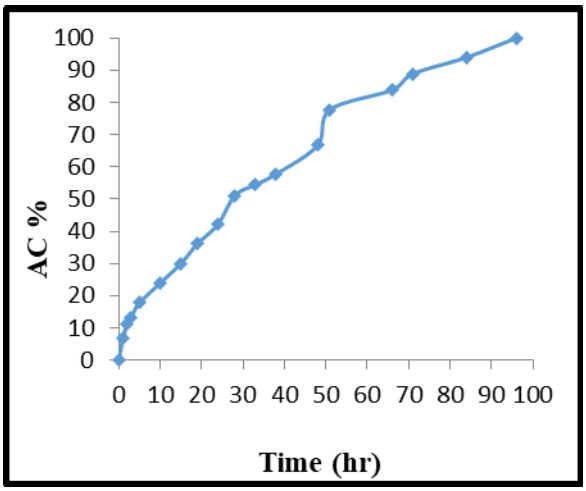

Figure 2. AC. % Vs. Time for Kaolinite 75 micron for AL - Ahdab Crude Oil.

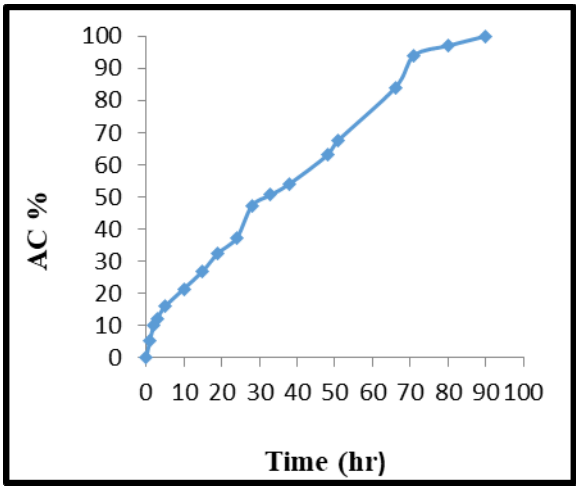

Figure 3. AC. % Vs. Time for Kaolinite 150 micron for AL - Ahdab Crude Oil.

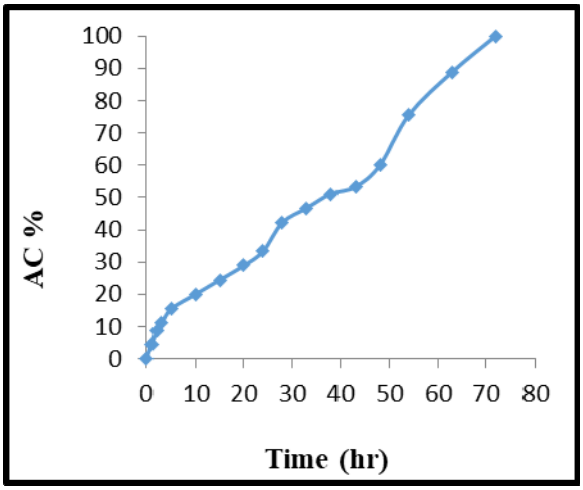

Figure 4. AC. % Vs. Time for Kaolinite 300 micron for AL - Ahdab Crude Oil.

Figures (1 - 4) shows that the adsorption capacity (AC %) increasing from (0 % to 100 %) for kaolinite of (-75, 75,150, and 300 microns) at (54, 96, 90, and 72 hour) for AL - Ahdab Crude Oil. Kaolinite can be used as a geosynthetic clay liner either mixed it with additives, bonded with geomembrane or as filler between geotextiles to reduce the hydraulic conductivity of liner because it fails to retain crude oil. Also, it can be seen that the adsorption capacity increase with increasing grain size. [11]

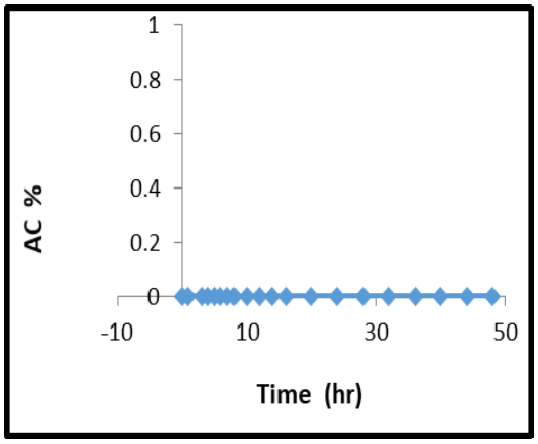

Figure 5: AC % Vs. Time (hr) of Kaolinite+ Attabulgite (150 and 300 micron) AL – Ahdab crude oil.

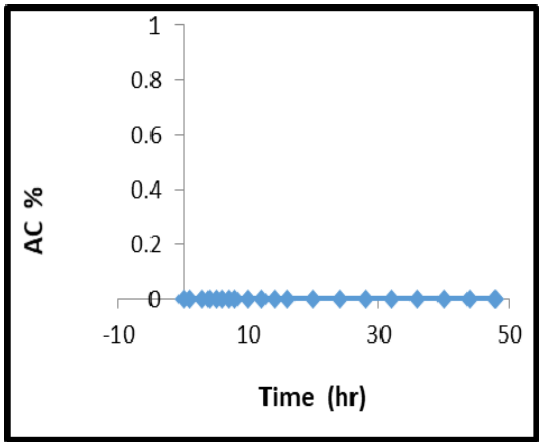

Figure 5: AC % Vs. Time (hr) of Kaolinite and (-75, 75, 150 and 300 micron) AL - Burjsiha crude oil.

Figures 5 and 6 show that the adsorption capacity (AC %) of kaolinite (-75, 75,150, and 300)µm equal to zero. Soon after the addition of crude oil to kaolinite, cracks occur that lead to the oil spill completely and thus no absorption occur. All experiment failure even if repeating experiment more than one attempt for Al–Burjsiha crude oil. Also, the adsorption capacity of kaolinite + attapulgite 150µm and 300µm, equal to zero because all exper*iment failure even if repeating.*

Adsorption Capacity (AC %) Tests for Nano Iraqi Clay

Adsorption capacity tests of Al-Ahdab crude oil on Iraqi nano kaolinite and natural clays (kaolinite and attapulgite) with grain sizes 150µm in order to test the capacity of clays to adsorb crude oil, effective grain size on adsorption capacity and the possibility of using clays as anti spill are shown in Figures. (7 ,8 and 9).

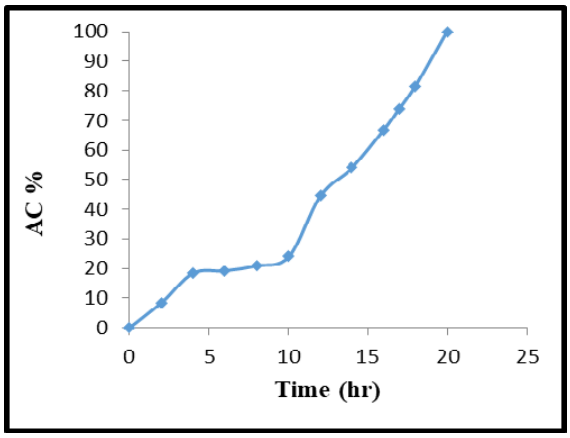

Figure 7.AC. % Vs. Time for Kaolinite+Attapulgite 150µm + Nano kaolinite for AL - Ahdab Crude Oil.

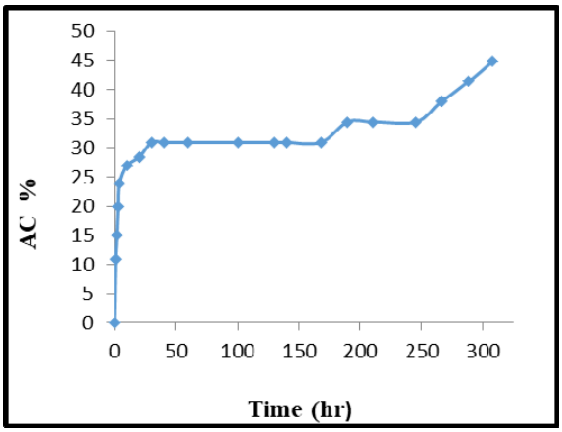

Figure 8.AC. % Vs. Time for Kaolinite 150µm + Nano kaolinite For AL - Ahdab Crude Oil.

Figure 7 show that the adsorption capacity (AC %) of Kaolinite + Attapulgite 150μm with nano – kaolinite increasing from 0 % - 100 % at 20 hours only, which mean that this experiment failure, because adding nano – kaolinite don't changing ability of clay to seal crude oil.

Figure 8 illustrates that the adsorption capacity (AC %) of kaolinite 150μm with nano – kaolinite increasing from 0 % - 45 % after 310 hours which means that nano – clay increasing ability to prevent movement crude oil through clay.

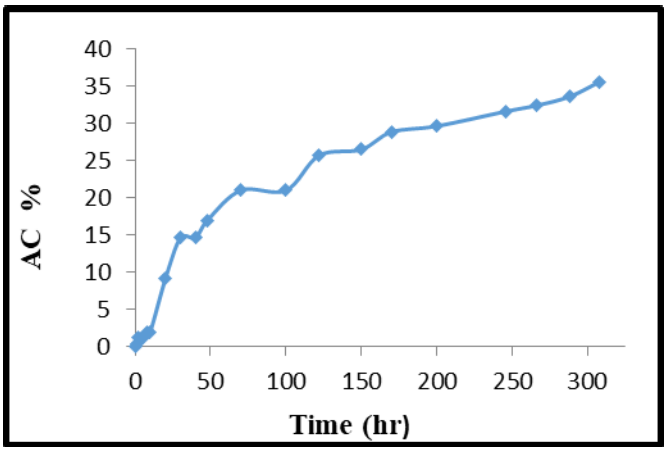

Figure 9.AC. % Vs. Time for Kaolinite 150μm. mixed with Nano kaolinite for AL-Burjsiha Crude Oil.

The result of Figure 9 shows that the adsorption capacity (AC %) of kaolinite 150 μm mixed with nano – kaolinite increasing from 0 % - 36 % after 310 hours. Clay controlling the environment provides a good seal [12] that impede and prevents movement of pollutants especially for Al – Ahdab and AL-Burjsiha Crude Oil.

4- Conclusion

The results shows that kaolinite clay adsorption capacity of crude oil increase with increasing the grain size of clay and API gravity (American petroleum institute), heavy crude oil (Al -Ahdab) adsorption capacity (AC %) reach to 100 % at 96 hours, which make this type of clay suitable for heavy crude oil.

Crude oil seepage decrease with increasing thickness of clay liner. The rate of crude oil flow decrease across the thick clay layer because high saturated of an upper part of the layer.

Iraqi nano- kaolinite liner with layers kaolinite and attapulgite, can be used as a geosynthetic clay liner either mixed with additives, bonded with geomembrane or as filler between geotextiles to reduce the hydraulic conductivity of liner since it fails to retain crude oil. On the other hand Iraqi nano - kaolinite mixed with kaolinite liner efficient engineered barrier system that can be used as a compacted liner due to the excellent seal that impedes and prevents movement of pollutants through the layer of clays since adsorption capacity reach 36 %– 45 % after two weeks.

References

1- Olsen Gregory R. 2011. Dimensional Stability of Geosynthetic Clay Liners in Landfill Applications. PhD thesis, Faculty of California Polytechnic State University, San Luis Obispo.
2- AL-Bidry Mayssaa Ali, Hamied Ramzy S, Raja Ghassan 2017. Anti Spill of Compacted Iraqi Bentonite by Using Different Iraqi Crude Oil. Emirates Journal for Engineering Research, 22 (2), 11-16.
3- Miller Brad, Fishman Stev. 2014. Geosynthetic Clay Liners for the Petroleum Storage Convenience and Refining. CETCO, Minerals Technology Company.
4- Gitipour S, Hosseinpour M A, Heidarzadeh N, Yousefi P and Fathollahi A 2015. Application of Modified Clays in Geosynthetic Clay Liners for Containment of
Petroleum Contaminated Sites. Int. J. Environ. Res. 9(1), 317-322.
5- Pengxiang Xing, Yu Wang, Hailiang Lu, Lei Lan, Xishan Wen and Shulin Zhang 2014. Potential Calculation on the Oil-Gas Pipeline with Geosynthetic Clay Liners Based on BEM. Journal of Power and Energy Engineering. 2, 594-599.
6-Meer Stephen R, Craig H Benson 2007. Hydraulic Conductivity of Geosynthetic Clay liners Exhumed from landfill Final Covers. Journal of Geotechnical and Geo-environmental Engineering 13 (5), 550-563.
7-Grim R.E. 1962. Applied Clay Mineralogy. McGraw Hill, New York.
8- Bruno Herlin 2002. Geosynthetic Clay Liners (GCLs). 4th International Pipeline Conference.
9- Dader Dena 2017. Application of Nanotechnology in Water Base Mud. Master Thesis, Petroleum Technology Department / University of Technology. Baghdad -Iraq.
10- Carmody Onuma, Frost Ray, Xi Yunfei, Kokot Serge 2007. Adsorption of HC on Organo–Clay – Implications for Oil Spill Remediation. J. Colloid and Interface Science. 305 (1), 17-24.
11- Churchman G J, Askary M, Peter P, Wright M, Raven M D, Self P G 2002. Geotechnical Properties Indicating Environments uses for Un Unusual Australian Bentonite. Applied Clay Science. 20, 199-209.
12- Fitzpatrick R W, Eggleton R A 1995. Clay Controlling the Environmental. Proceeding of the 10th International Clay Conference, Adelaide, Australia. CSIRO Publishing, Melbourne, ISBN 0.643 -05536-3.

Available online at
http://namrc.uotechnology.edu.iq/index.php/

Nanotechnology and Advanced Materials Research Centre

Proceeding Articles Book 00 (2018) 000–000

6th International Scientific Conference on Nanotechnology, Advanced Materials and its Applications

Effect of Annealing Process on a Microstructure and a Tensile Test of Aluminium – Silicon Alloy Deformed by Equal Channel Angular Pressing

Ali A. Aljubouri[a], Nurulakmal Mohd. Sharif[b]

[a] University of Technology, Department of Applied Sciences, Materials Science Branch, Baghdad, Iraq

[b] School of Materials and Mineral Resources Engineering, USM, 14300, Nibong Tebal, Penang, Malaysia

Abstract

An aluminum-silicon (Al-Si) alloy was cast in the form of solid cylindrical shapes that were machined down. Two groups of work pieces were used: the first one, the as-cast work pieces, and the second group are the cast work pieces annealed at 500 ^{O}C for 24 hours. These work pieces processed in a 90° equal channel angular pressing (ECAP) die, via route B_C (where the sample is rotated by 90° in the same direction between each consecutive pressing). Evaluation of the microstructure was done via scanning electron microscopy (SEM). Tensile testing was studied as a function of the number of passes through the die. The initial grain size of Al-Si alloy before ECAP was 40-70 μ m. Many fine dimples were observed in the work piece after ECAP was confirmed by SEM observation to be 0.5-2 μ m. The maximum stress at the maximum load increases with increasing the number of passes through the ECAP die, reaching to 275 and 230 Mpa after five passes for work pieces without annealing and annealed work pieces at 500°C respectively. The undeformed work pieces show no considerable amount of elongation in length and a slight reduction in cross-sections. While the work pieces processed by ECAP show fracture surfaces at approximately 45° to the loading axis with evidence of necking near the fracture sections for annealed work pieces.

Keywords: Al-Si alloy; ECAP; Route B_c; Tensile test.

1- Introduction

In the last two decades, many of sever plastic deformation (SPD) processing methods have been used to introduce large plastic straining and significant microstructural refinement in bulk crystalline solids. These methods include, multidirectional forging[1], accumulative roll-bonding(ARB) [2, 3], twist extrusion [4], cyclic extrusion compression[5], friction stir processing (FSP) [6], high-pressure torsion (HPT) [7, 8], constrained groove pressing (CGP) [9, 10], and ECAP) [11-13]. Most of these methods are well established to obtain ultra-fine grained materials lying typically within grain sizes range from few micron to some hundreds nanometer scale. ECAP technique has received especially attention for several reasons. First, it can be conducted to large segments. Second, it is fairly simple and cheap technique that is easily applied to many materials. Third, ECAP process can be repeated many times to accumulate high strain within the workpiece. Fourth, ECAP may be readily scaled up for the production of relatively large bulk work pieces that may be suitable for use in industrial applications. Fifth, ECAP has been combined with other metal working process to provide a more versatile procedure [14].

It is well known that an ECAP die consist of two equal cross section channels intersected at two angles as shown in figure (1), Φ is the internal angle between the two intersecting channels and Ψ is the angle subtended by the arc of curvature at the point of intersection.

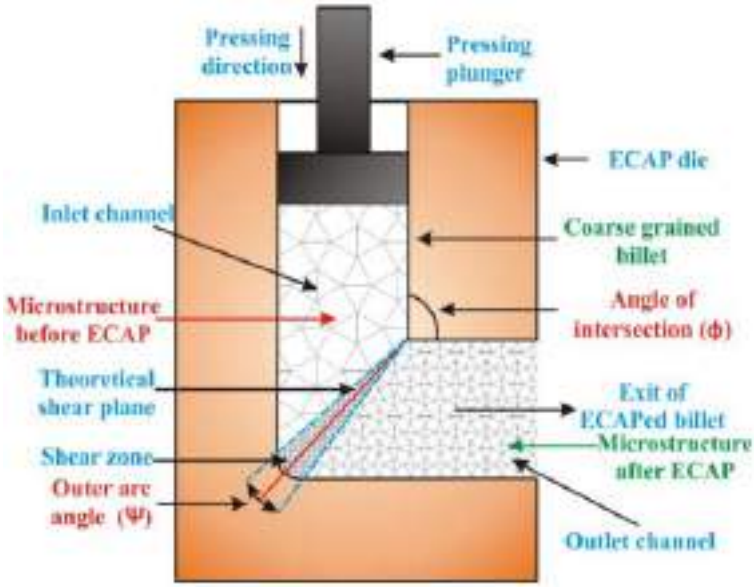

Figure 1. Angles for equal channel angular pressing and ECAPed workpiece [15].

As the material crosses the intersection of the channel, it experiences a shear deformation that induces a shear strain. Subsequently, the strain ε, after N passes through the die is given by the following equation, [16].

$$\varepsilon_N = N\left[\frac{2\cot\left(\frac{\Phi}{2}+\frac{\Psi}{2}\right)+\Psi\cos ec\left(\frac{\Phi}{2}+\frac{\Psi}{2}\right)}{\sqrt{3}}\right] \quad \ldots\ldots\ldots\ldots\ldots\ldots\ldots (1)$$

Where ε_N is the strain after N passes through the die. According to equation (1), the channel angle Φ has more influence on the strain generated during ECAP than the die corner angle Ψ [17].

The streangth of a material is generally related to the grain size, d, the following Hall-Petch equation, which relates the yield stress of a material σ_y to the grain size by the expression; [18].

$$\sigma_y = \sigma_0 + k_y d^{-1/2} \quad \ldots\ldots\ldots\ldots\ldots\ldots\ldots\ldots\ldots\ldots\ldots\ldots\ldots\ldots\ldots\ldots\ldots\ldots\ldots\ldots (2)$$

where σ_0 is the friction stress, k_y is a positive constant of yielding grains.

There are many parameters that affect the microstructural evolution in materials. Among them are, the die angle, which determines the strain introduced in the material for each deformation pass [16, 17], and the number of passes through the die, which corresponds to the total accumulated strain applied to the workpiece. Ali A. Aljubouri and Nurulakmal Mohd. Sharif [19], have been discussed the influence of the ECAP die angle and the number of passes through the die on the microhardness of Al-Si alloy. The deformation route, which involves rotating the workpiece between each successive passes, is another important parameter in microstructure development [20, 21]. In addition, the content of impurities [22], pressing speed [23], the deformation temperature [24], and the friction between the die walls and the workpiece [25], are also essential parameters.

However, different microstructures can be developed in ECAP by rotating the workpiece between extrusion cycles [26-28]. It is possible to define four distinct processing routs A, B_A, B_C and C, which are classified by how the workpiece is rotated with respect to the die after each pass around its longitudinal axis: without rotation (route A), $\pm 90^0$ (route B_A), + 90^0 (route B_C), and +180^0 (route C) [29].

In this study, The ECAP was conducted using a die with Φ =90^0 and Ψ =0^0. SEM has been used to investigate the fracture morphology, and the Instron device used for tensile test.

2- Materials and Method

X-ray fluorescence (XRF) equipment was used to determine the chemical composition of the alloy which is used in this study as shown in table (1):

Table 1. The chemical composition of Al-Si-Mg alloy

Alloying elements	Si	Mg	Fe	Cu	Mn	Zn	Ga	Ti	Al
Wt.%	1.3	0.3	0.18	0.023	0.019	0.017	0.014	0.011	base

ECAP was applied for six passes at room temperature using a die with a channel angle of Φ =90^0 and Ψ =0^0, which produce an equivalent strain of about 1.15 during each pass through the die. In this study, the ECAP die consisted of two blocks of SKD 11 tool steel, bolted together to give a die with two channels having an equal circular cross-section with the diameter of 10 mm. Route B_C is selected by rotating the workpiece 90^0 in the same direction around its longitudinal axis between each two consecutive passes. Work pieces were prepared by melting Al-Si alloy billets by a conventional furnace and cast into a circular sand molds (Φ 15 mm X 150 mm). The cast ingots were machined by lathe machine with cooling liquid to overcome the machining effect. The machined rods with dimensions of (Φ 10 mm X 50 mm) became suitable for pressing by ECAP facility. Prior to ECAP, the surface of the work pieces was polished using SiC abrasive papers with grades 100, 230, 400, 600, 800, 1000 and 1200 to reduce the friction between the workpiece and the die wall.

For tensile test two groups of work pieces were used: first, work pieces as cast, second, cast work pieces annealed at 500 ^{0}C for 24h. The work pieces were slowly heated from room temperature to 500 ^{0}C at heating rate 10 ^{0}C/min, holding at that temperature for 24 hours followed by cooling to room temperature inside the furnace. Tensile work pieces were machined from the samples before and after ECAP up to six passes with the gauge dimensions of 5mm in diameter and a gauge length of 10mm. These work pieces were pulled to failure at room temperature using the INSTRON device operating at a constant rate of cross head displacement (0.3mm/min).

The scanning electron microscope (SEM)model Supra 35VP Field Emission (FE-SEM) was used to show the micrographs of the fracture surfaces of the casted and tested annealed Al-Si work pieces at 500 ^{0}C for 24 hours: The average grain and subgrain sizes were taken from measurements made directly from the SEM photomicrographs using the linear intercept method (at least 5 different places on a sample were measured).

3- Results and discussion

Another test of mechanical properties is a tensile test, which is defined as the resistance of a material to a slowly applied force. The ECAP of the cast and annealed cast Al-Si alloy work pieces at 500 ^{0}C for 24h was conducted using a die with Φ =90^0 and Ψ =0^0. All pressing were conducted using route B_C. The failed tensile work pieces are shown in figures (2 and 3). It is observed that the undeformed work piece shows brittle fracture with no considerable amount of elongation in length and reduction in section. The work pieces processed by ECAP show fracture surfaces at approximately 45^0 to the loading axis with evidence of necking near the fracture section, which refer clearly to the ductility behaviour of the alloy.

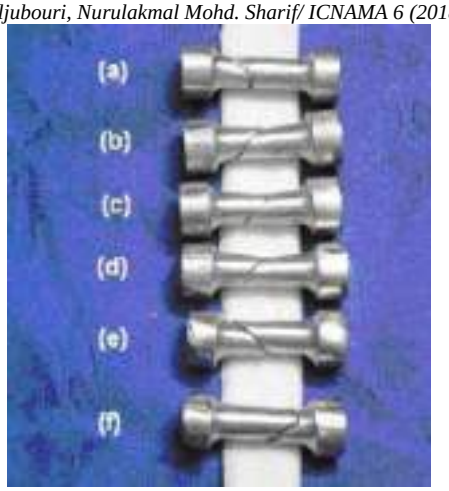

Figure 2. Tensile test at room temperature of casted and ECAPed Al-Si workpieces: (a) as cast, (b) after two passes, (c)after three passes, (d) after four passes, (e) after five passes and (f) after six passes.

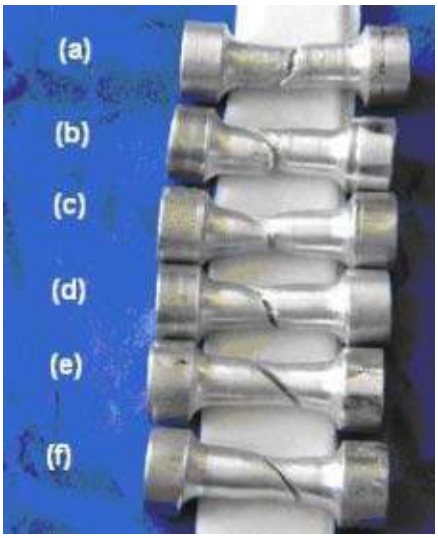

Figure 3.Tensile test at room temperature of annealed and ECAPed annealed Al-Si workpieces at 500 ^{0}C for 24h: (a) as annealed cast, (b) after one pass, (c) after two passes, (d) after three passes, (e) after four passes and (f) after five passes.

Typical strain-stress curves of cast and annealed cast Al-Si alloy at different ECAP passes are shown in figures 4and 5.

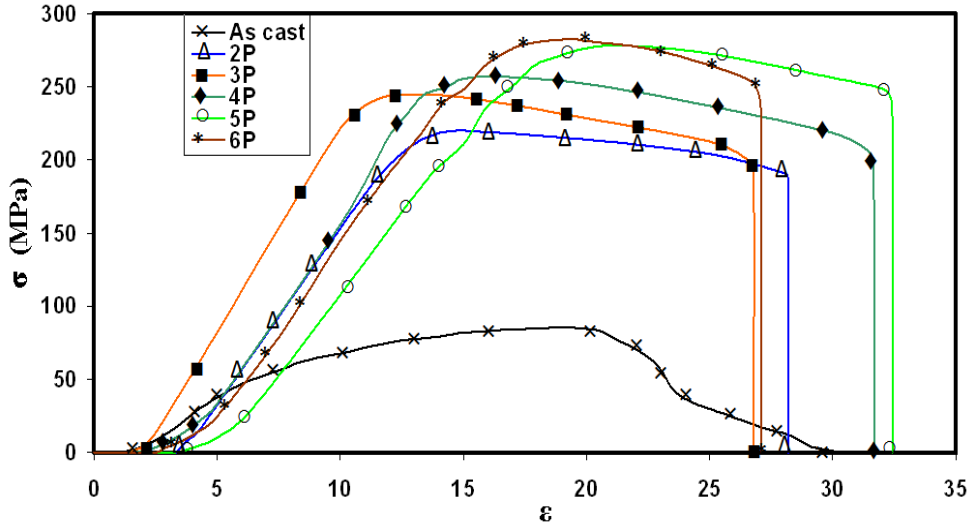

Figure 4.True stress-strain curves of Al-Si alloy at different number of passes through the die with Φ *=90⁰ and* Ψ *=0⁰.*

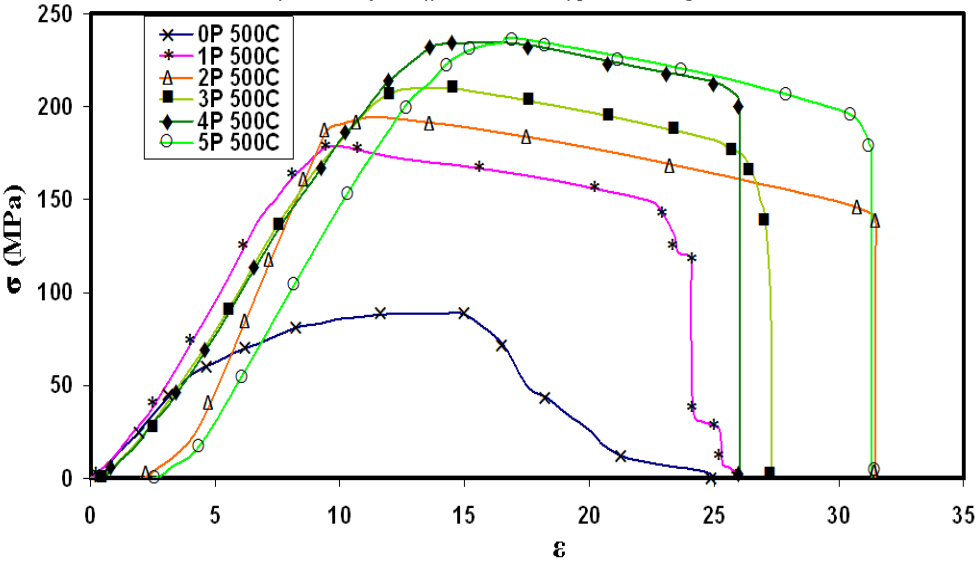

Figure 5. True stress-strain curves of annealed Al-Si alloy at 500 ^{0}C for 24h at different number of passes through the die with Φ =90^0 and Ψ =0^0.

The stress at the maximum load are extracted from figures 4 and 5, and plotted in figure (6) as a function of the number of passes through the die for as cast alloy and annealed cast alloy at 500 ^{0}C for 24h before ECAP process. The necking generation in annealed group is a result of low hardening rate. The strain hardening rate relates to the generation and accumulation of dislocations in the materials.

The stress increases with increasing the number of passes through the ECAP die. However, the increasing of stress is significant only after the first pressing, followed by a gradual increase during the subsequent passes. This trend in maximum stress with the number of passes is almost consistent with the trend of hardness as investigated in article [19], where the refined structure with high angle grain boundaries after ECAP may impede the motion of dislocations and consequently enhanced the hardness. The level of stress at the maximum load in the cast alloy was higher than that of annealed alloy at 500 ^{0}C, and this may be due to grain growth after annealing which leads to reduce the strength of the material. Figure (7) shows the comparison of the dependence of

strain on the number of passes between annealed workpieces at 500 ^{0}C for 24h and not annealed work pieces by using the ECAP die with Φ =90^0 and Ψ =0^0 . It can be seen that the strain increases after ECAP in both cases.

As the number of passes through an ECAP die increases, the dislocation density increases and the grains become extremely fine [30]. The alloy subjected to ECAP exhibits superplastic

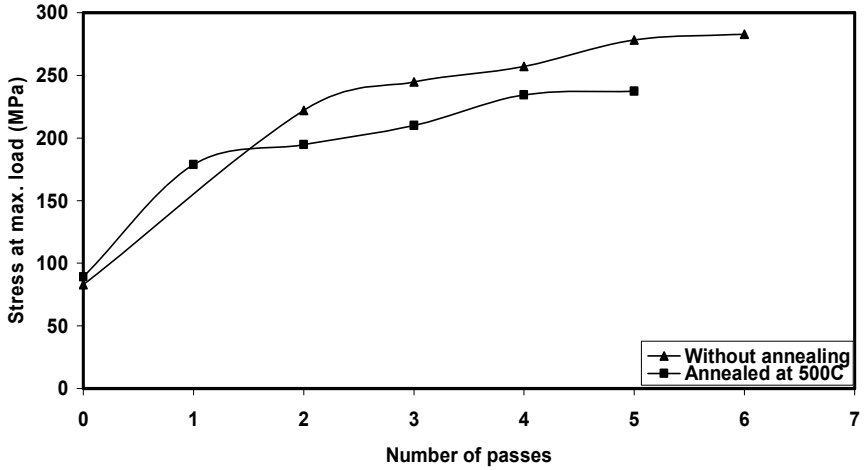

Figure 6.The effect of the number of passes on the stress at the maximum load of ECAPed casted and ECAPed annealed casted Al-Si alloy at 500 ^{0}C for 24h.

Properties with high elongation to failure. This superplastic properties are provided by high stability of ultrafine grained structure produced by ECAP [31]. The fine grains resulting from the ECAP process help maintain a good ductility even after significant straining from the cold extrusion [32]. The fluctuation of strain% during ECAP in figure (7), which attributed to some imbedded defects during Al-Si casting. The main properties of these defects are brittle and non-adhesion to the matrix. These two properties lead to failure with less elongation. Figures 8 and 9 show some imbedded defects.

The fracture surfaces of tensile Al-Si work pieces after ECAP processing for many passes are shown in figure (8). The fracture surface of the cast Al-Si alloy shows many facets (not dimples) with about 40-70 μ m in diameter as observed in the figure 8(a).

As shown in figure 8(b), many fine dimples are observed in the workpiece after three passes, although these dimples are not equal in size. Dimples are slightly elongated along tensile direction in the ECAPed samples as shown in figures (8 and 9).

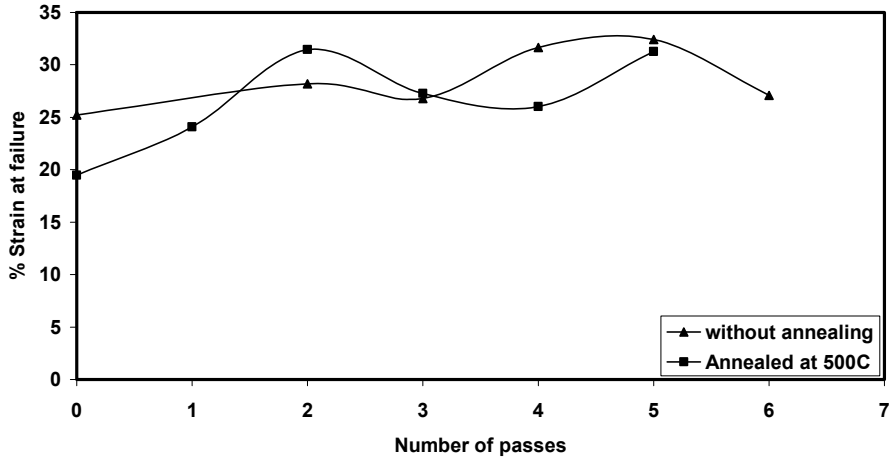

Figure 7. The effect of the number of passes on the % strain at failure of ECAPed casted and ECAPed annealed casted Al-Si alloy at 500 ^{0}C for 24h.

The elongated dimples are due to void nucleation and subsequent coalescence by strong shear deformation and fracture on the shear plane. It can be seen that the average dimple size gradually decreases with increasing number of ECAP passes becoming very fine dimples with dimensions of up to 500nm in diameter after six passes as shown in figure 8(f). The continuous decrease in the dimple size should be associated with the grain refinement of workpieces processed by ECAP.

Figure (9) shows SEM images of the fracture surface of tensile workpieces annealed at 500 ^{0}C after ECAP process carried out via the route Bc. It is found that the dimples are more uniform in size in the fracture zone, indicating a typical ductile fracture. This could be attributed to the better distribution of strain and a more homogeneous grain size in the microstructure.

Superior mechanical properties represented by a unique combination of strength and ductility in metallic materials were achieved by the grain refinement using ECAP process. Such properties are highly desirable in the development of advanced structural materials.

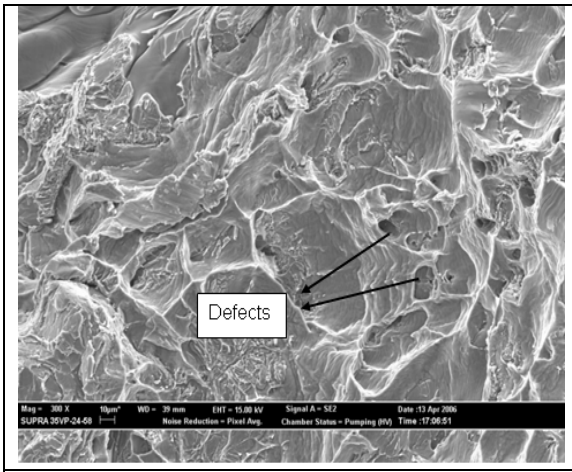

(a) As cast x300 marker 10 μ m

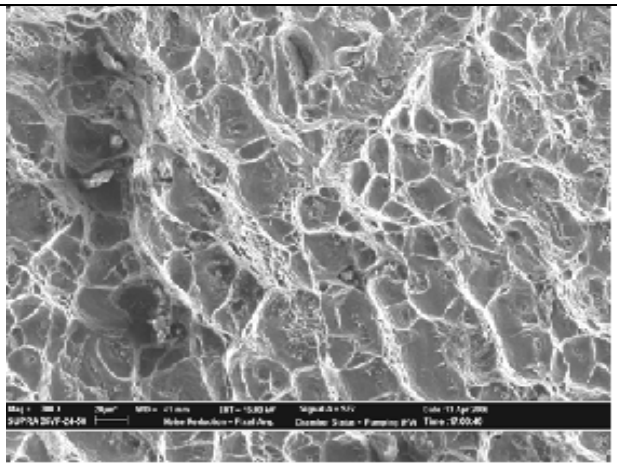

(b) 3p x300 marker 20 μ m

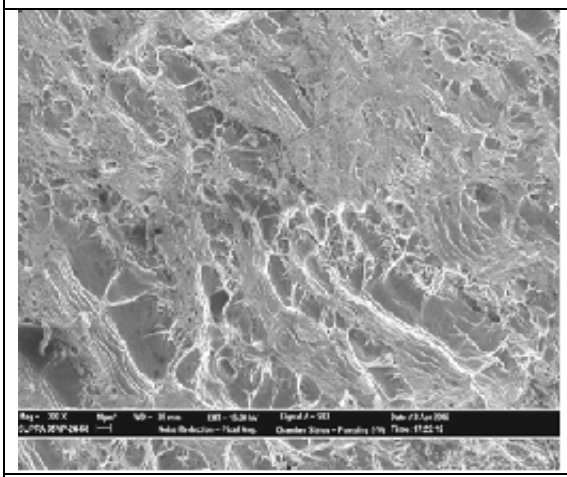

(c) 5p x300 marker 10 μ m

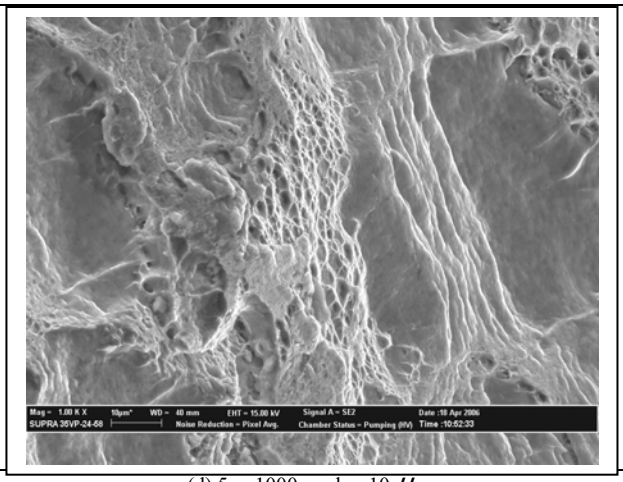

(d) 5p x1000 marker 10 μ m

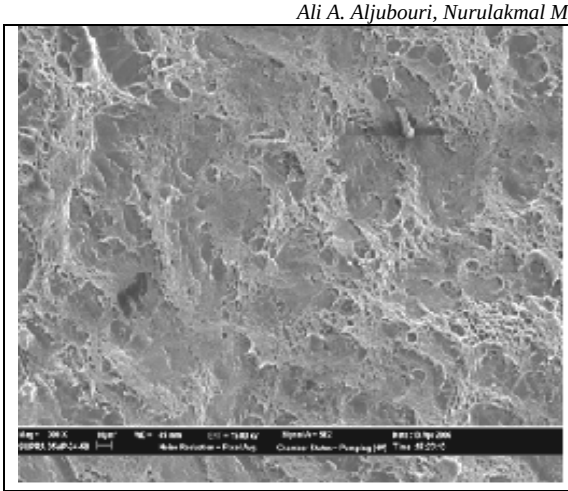

(e) 6p x300 marker 10 μ m

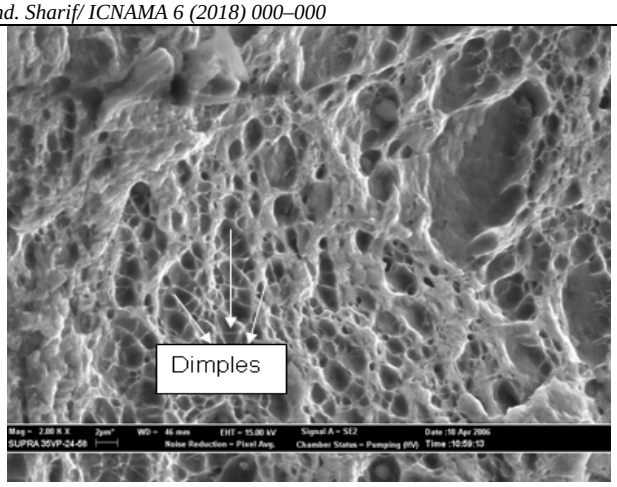

(f) 6p x2000 marker 2 μ m

Figure 8. Scanning electron micrographs of the fracture surfaces of the tested Al-Si workpieces: (a) cast alloy, (b) after 3 passes, (c & d) after 5 passes with different magnification, and (e & f) after 6 passes with different magnification.

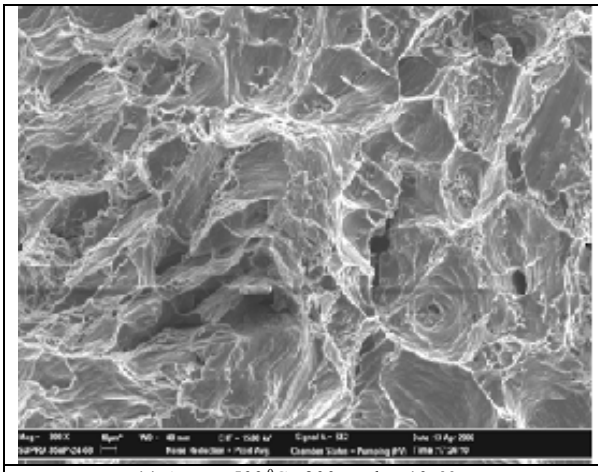

(a) As cast 500 ^{0}C x300 marker 10 μ m

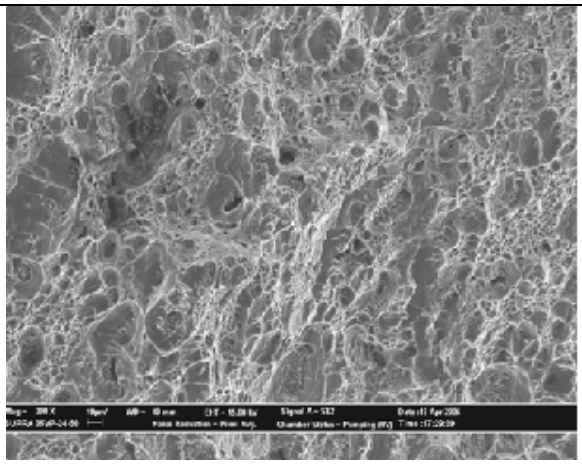

(b) 2P 500 ^{0}C x300 marker 10 μ m

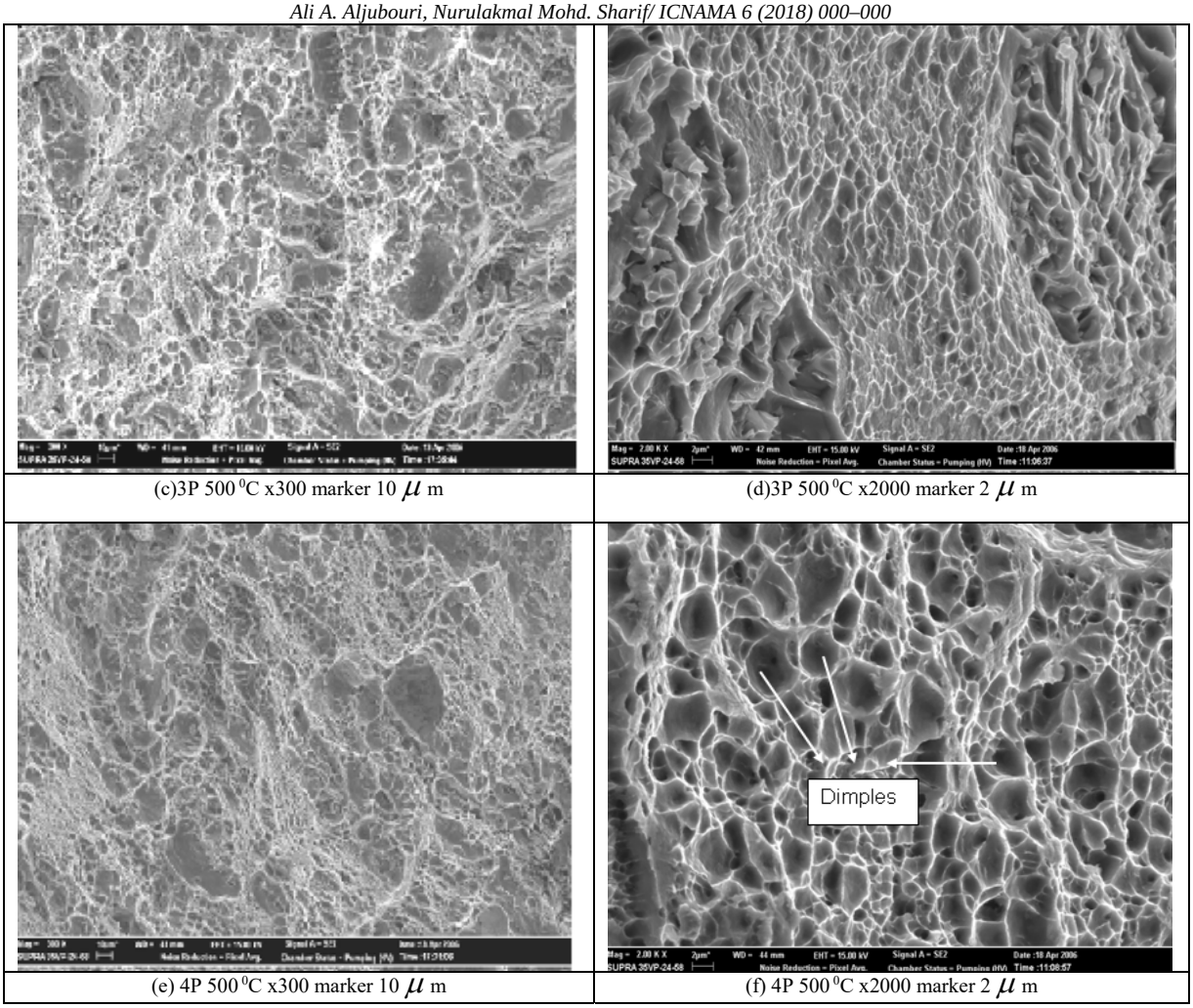

(c)3P 500 ^{0}C x300 marker 10 μ m | (d)3P 500 ^{0}C x2000 marker 2 μ m

(e) 4P 500 ^{0}C x300 marker 10 μ m | (f) 4P 500 ^{0}C x2000 marker 2 μ m

Figure 9. Scanning electron micrographs of the fracture surfaces of the tested annealed Al-Si work pieces at 500 ^{0}C for 24 hours: (a) annealed cast alloy, (b) after 2 passes, (c & d) after 3 passes with different magnification, and (e & f) after 4 passes with different magnification.

4- Conclusion

- ECAPed work pieces show fracture along a surfaces that makes an angle of approximately 45^0 with the tensile axis.
- The maximum stress after ECAP process increases sharply after the first pass followed by gradual increment with the number of passes.
- The undeformed work piece shows brittle fracture with no considerable amount of elongation in length and reduction in section.
- Maximum load for undeformed work piece is 80 MPa.
- Maximum load for deformed work pieces increases with the number of passes from 215 MPa after two passes to 275 MPa after five passes through the ECAP die.
- Maximum load for annealed deformed work pieces at 500 ^{0}C increases with the number of passes from 190 MPa after two passes to 235 MPa after five passes through the ECAP die.
- As a result of grain refinement with the number of passes through the ECAP die, the dimple size decreases gradually.
- In ultrafine grain metals processed by ECAP both strength and ductility can be improved by performing fracture tensile test.
- The elongation to failure increases after ECAP for annealed and non-annealed deformed work pieces.

References

[1] Saeed Khan, Moghanaki, MohsenKazeminezhad, RolandLogé, "Mechanical Behavior and Texture Development of Over-Aged and Solution Treated Al-Cu-Mg Alloy During Multi-Directional Forging", Materials Characterization, Vol. 135 (2018), pp: 221-227.
[2] S. H. Seyed Ebrahimi, K. Dehghani, J. Aghazadeh, M. B. Ghasemian, Sh. Zangeneh, "Investigation on Microstructure and Mechanical Properties of Al/Al-Zn-Mg–Cu Laminated Composite Fabricated by Accumulative Roll Bonding (ARB) Process", Materials Science and Engineering: A, Vol. 718, (2018), pp: 311-320.
[3] Nahed El-Mahallawy, Adel Fathy, Walaa Abdelaziem, Mohammed Hassan, "Microstructure Evolution and Mechanical Properties of Al/Al–12%Si Multilayer Processed by Accumulative Roll Bonding (ARB)", Materials Science and Engineering: A, Vol. 647 (2015), pp: 127-135.
[4] U. Mohammed Iqbal, V. S. Senthil Kumar, "An Analysis on Effect of Multipass Twist Extrusion Process of AA6061 Alloy", Materials & Design. Vol. 50 (2013), pp: 946-953.
[5] Mohamad Syahmi, Shahrom Ahmad, Razlan Yusoff, "Cyclic Extrusion Compression Back Pressure Technique for Hot Forging Process in Direct Recycling of Aluminium 6061 Machining Chip", Journal of Manufacturing Processes, Vol. 29 (2017), pp: 1-9.
[6] C. Y. Liu, H. J. Jiang, B. Zhang, Z. Y. Ma, "High Damping Capacity of Al Alloys Produced by Friction Stir Processing", Materials Characterization, Vol. 136 (2018), PP: 382-387.
[7] Yuki Ito, Kaveh Edalati, Zenji Horita, "High-Pressure Torsion of Aluminum with Ultrahigh Purity (99.9999%) and Occurrence of Inverse Hall-Petch Relationship", Materials Science and Engineering: A, Vol. 679 (2017), PP: 428-434.
[8] Pedro Henrique R. Pereira, Yi Huang, Terence G. Langdon, "Examining the Microhardness Evolution and Thermal Stability of an Al–Mg–Sc Alloy Processed by High-Pressure Torsion at a High Temperature", Journal of Materials Research and Technology Vol**.** 6, Issue 4 **(**2017**)**, pp**:** 348-354.
[9] Dong Hyuk Shin, Jong-Jin Park, Yong-Seog Kim, Kyung-Tae Park, "Constrained Groove Pressing and its Application to Grain Refinement of Aluminum", Materials Science and Engineering: A, Vol. 328, Issues 1–2 (2002), pp: 98-103.
[10] K. N. Nagaraju, A. R. Sunil, K. Sachin, H. Sujay, H. S. Siddesha, S. Anand Kumar, "Influence of Constrained Groove Pressing Passes and Annealing Characteristics on the Mechanical Properties of 6061 Aluminum Alloy", Materials today: Proceedings, Vol.5, Issue 1, Part 3 (2018), pp: 2660-2665.
[11] S. Suren darnath, Ram. Subbiah, K. Sankar anarayana samy, B. Ravi sankar, "Finite Element Simulation of Pure Aluminum Processed by ECAP Using New Die Design", Materials today: Proceedings, Vol.4, Issue 2, Part A (2017), pp: 2544-2553.
[12] Atul Dayal, K. Hans Raj, Rahul Swarup Sharma, "ECAP Die Design for Minimising Corner Gap", Materials today: Proceedings, Vol.5, Issue 1, Part 1 (2018), pp: 1686-1690.
[13] L. B. Hussain, A. A. Aljubouri, M. A. M. Gebril, Nurulakmal M. Sharif, "Spot Welding Copper–1% Cr Electrode Tips Produced Via Equal Channel Angular Pressing", IIUM Engineering Journal Vol. 9, No. 2 (2008), pp: 1-10.
[14] A. Azushima, R. Kopp, A. Korhonen, D.Y. Yang, F. Micari, G.D. Lahoti, P. Groche, J. Yanagimoto, N. Tsuji, A. Rosochowski, A. Yanagida, "Severe Plastic Deformation (SPD) Processes for Metals", CIRP Annals - Manufacturing Technology 57 (2008), pp: 716–735
[15] Ankit Sahai, K. Hans Raj, N. K. Gupta, "Mechanical Behaviour and Surface Profile Analysis of Al6061 Alloy Processed by Equal Channel Angular Extrusion", Procedia Engineering, 173 (2017), pp: 956-963.
[16] Y. Iwahashi, J. Wang, Z. Horita, M. Nemoto, T. G. Langdon, "Principle of Equal Channel Angular Pressing of Ultra-Fine Grained Materials", Scripta mater. **35** (1996), pp: 143-146.
[17] K. Nakashima, Z. Horita, M. Nemoto, T. J. Langdon, "Influence of Channel Angle on the Development of Ultrafine Grains in ECAP", Acta Mater. 46 (1998), pp: 1589-1599.
[18] M. Furukawa, Z. Horita, M. Nemoto, R.Z. Valiev, T.G. Langdon, "Microhardness Measurements and the Hall-Petch Relationship in an Al-Mg Alloy with Submicrometer Grain Size", Acta mater. 44 (1996), pp: 4619-4629.
[19] Ali A. Aljubouri, Nurulakmal Mod. Sharif, "Influence of Die Angles on the Microhardness of Aluminum Alloy Processed by Equal Channel Angular Pressing", IIUM Engineering Journal, Vol. 11, No. 2 (2010), pp: 137-149.
[20] Chao-lan TANG, Hao LI, Sai-yi LI, "Effect of Processing Route on Grain Refinement in Pure Copper Processed by Equal Channel Angular Extrusion", Trans. Nonferrous Met. Soc. China 26 (2016), pp: 1736-1744.
[21] Y. Iwahashi, Z. Horita, M. Nemoto, T.G. Langdon, "The Process of Grain Refinement in Equal-Channel Angular Pressing". Acta Mater. 46(1998), pp: 3317–3331.
[22] E. V. Avtokratova, Oleg Sitdikov, Oksana Mukhametdinova, Michael V. Markushev, Narayana Murty Svs, Prasad Mjnv, Bhagwati P. Kashyap, "Microstructural Evolution in Al–Mg–Sc–Zr Alloy During Severe Plastic Deformation and Annealing", Journal of Alloys and Compounds, 673 (2016), PP: 182-194.
[23] P. B. Berbon, M. Furukawa, Z. Horita, M. Nemoto, T.G Langdon, "Influence of Pressing Speed on Microstructural Development in ECAP", Metall. Trans. A, 30A (1999), PP: 1989-1997.
[24] L. J. Zheng, H. X. Li, M. F. Hashim, C. Q. Chen, Y. Zhang, M. G. Zeng, "Evolution of Microstructure and Strengthening of 7050 Al Alloy by ECAP Combined with Heat- Treatment". J. Mater. Processing Tech. 171 (2006), PP: 100-107.
[25] R. K. Oruganti, P. R. Subramanian, J. S. Marte, Michael F. Gigliotti, Sundar Amancherla, "Effect of friction, Backpressure and Strain Rate Sensitivity on Material Flow During Equal Channel Angular Extrusion", Mater. Sci. Eng. A 406 (2005), pp:102–109.
[26] Y. Iwahashi, M. Furukawa, Z. Horita, M. Nemoto, T.G. Langdon, "Microstructural Characteristics of Ultrafine-Grained Aluminum Produced Using Equal-Channel Angular Pressing", Metall. Mater. Trans. A29A (1998), pp: 2245–2252.

[27] Vladimir V. Stolyarov, Y. Theodore Zhu, Igor V. Alexandrov, Terry C. Lowe, Ruslan Z. Valiev, "Influence of ECAP Routes on the Microstructure and Properties of Pure Ti", Materials Science and Engineering: A, Vol. 299, Issues 1–2 (2001), pp: 59-67.
[28] L. B. Tong, M. Y. Zheng, X. S. Hu, K. Wu, S. W. Xu, S. Kamado, Y. Kojima, "Influence of ECAP Routes on Microstructure and Mechanical Properties of Mg–Zn–Ca Alloy", Materials Science and Engineering: A, Vol. 527, Issues 16-17 (2010), pp: 4250-4256.
[29] M. Furukawa, Z. Horita, M. Nemoto, T. G. Langdon, "Review: Processing of Metals by Equal-channel Angular Pressing", Journal of Material Science 36, 10, (2001), pp: 2835–2843.
[30] M. Saravanan, R. M. Pillai, B. C. Pai, M. Brahma kumar, K. R. Ravi, "Equal Channel Angular Pressing of Pure Aluminium-an Analysis", Bull. Mater. Sci., Vol. 29, No. 7 (2006), pp: 679–684.
[31] F. Musin, R. Kaibyshev, Y. Motohashi, G. Itoh, "High Strain Rate Superplasticity in a Commercial Al–Mg–Sc Alloy", Scripta Materialia 50 (2004), pp: 511–516.
[32] Young Gwan Jin, Hyun Moo Baek, Yong-Taek Im, Byung Cheol Jeon, "Continuous ECAP Process Design for Manufacturing a Microstructure-Refined Bolt", Materials Science and Engineering A, 530 (2011), pp: 462–468.

Available online at
http://namrc.uotechnology.edu.iq/index.php/

Nanotechnology and Advanced Materials Research Centre

Proceeding Articles Book 00 (2018) 000–000

6th International Scientific Conference on Nanotechnology, Advanced Materials and its Applications

Synthesizing α-Fe_2O_3/Nps by Pulsed Laser Ablation in Liquid Environment at Different Laser Energies

Ayad Z. Mohammad[1], Kadhim A. Aadim[1] May A. Abduljabbar[2]
[1]Laser and Optoelectronics Engineering Dept., University of Technology, Baghdad, Iraq
[2]Department of physics, College of Science, University of Baghdad, Baghdad, Iraq
Corresponding auther:140048@uotechnology .edu.iq

Abstract

α-Fe2O3 nanoparticles were prepared by Pulsed Laser Ablation in Liquid technique in Ethanol using 1064 nm Nd:YAG laser for 200 pulse at different laser energies (171, 201 and 263 mJ/pulse). The morphological, optical and structural properties were studied using Atomic Force Microscope (AFM), uv-vis spectrophotometer and X-Ray Diffraction (XRD), respectively. AFM results demonstrated that the increase of laser energy causes a decrease in particle size from 96.27 nm to 84.06 nm. XRD patterns showed that the synthesized films were pure and have a crystalline structure. Optical properties indicated an increase in band gap energy from 1.92 to 2.35 eV.

Keywords: α-Fe2O3, NPs, PLAL, ethanol.

1- Introduction

Iron oxides nanoparticles in its various forms were intensively investigated due to thier optical, magnetic, low cost and catalytic properties [1]. It's used in many applications depending on the type of oxide, such as development of imaging, water splitting, purifying agents, biomedical applications, photo-catalyst, and solar energy conversion [2-5]. α-Fe_2O_3 is an n-type semiconductor that has a band gap of 2.2 eV with thermally stable, high sensitivity, cheap and non-toxic metal oxide which is suitable for electrical applications such as gas sensor or solar cell applications [6-7].

Several methods are used to synthesize iron oxide nanoparticles, such as hydrothermal and high-temperature reactions, sol-gel reactions, polyol methods, flow injection syntheses reaction, electrochemical methods, aerosol/vapor methods such as pulse laser ablation [8]. Pulsed laser ablation in liquid environment (PLAL) is one of the best methods to synthesize iron oxide nanoparticles, because it's cheap, fast, efficient, provides high temperature and pressure low contamination that are difficult to obtain in other methods [2,9-10].

In this paper, an easy one step method was used to produce iron oxide nanoparticles by employing pulsed laser ablation in ethanol; and study the influence of energy change on the optical, structural and morphological properties of the produced nanoparticles.

2- Experimental part

In this work, 2g of commercial Fe_2O_3 powder (Product #: 3310DX, 99% purity, SkySpring Nanomaterials Inc, Houston TX, USA) was uniaxially pressed by a hydraulic compressor into a disc shaped mold at pressure of 10 Tons for 3 minutes. The target was 5 m high and 16 mm wide in diameter. Afterwards, it was placed at the bottom of a glass vessel, to be submerged with 2.5 ml of Ethanol (99.9%, SOLVOCHEM, UK) as shown in Fig. (1). Q-switched Nd:YAG laser (Model HF -301, Huafei technology, China) was used to ablate the target's surface at wavelength of 1064 nm, freq. of 1 Hz, 2.2 mm spot size, 10 ns pulse duration and energies of (171, 201, 263) mJ/pulse. A focal length of 12 cm was used to focus the laser beam on the target. This distance also helps to protect the laser lens from the sputtered liquid. The ethanol height above the sample was 1cm. During the laser ablation process; the vessel was rotated to prevent the produced nanoparticles from shielding the laser beam from reaching the target's surface.

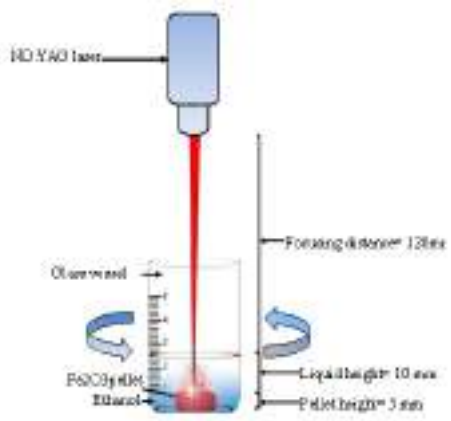

Fig.(1): Schematic representation for PLAL method.

The resulted liquid was deposited onto quartz slides by drop casting method at temperature of approximately 65ºC. The quartz slides were already cleaned via ultrasonic bath filled with de-ionized water for 30 minutes. Then, the slides were submerged in methanol for another 10 minutes. Finally, air dried to prevent any surface contaminations or impurities. After deposition process, the thin films were placed in an oven at temperature 700ºC for an hour to obtain α-Fe_2O_3 iron oxide.

3- Results and discussion

As the laser ablation takes place, it was noticed that the transparent ethanol has changed in color and it gradually became reddish brown. That gives an expectation to nano iron oxide formation. As the energy increase, the darker the liquid color has become as seen in Fig.(2).

Fig.(2): Liquid samples of iron oxide nanoparticles at different energies.

UV-vis spectrophotometer (**SP-8001 UV/Visible Spectrophotometer, Metertech, Taiwan**) device was used to study the optical properties of the resulted nanoparticles. Fig. (3) shows the absorbance as a function of wavelength at different energies, it shows high absorption in the visible region. As the laser energy increase, more particles are ablated from the target surface, which produces a higher concentration of nanoparticles suspended in Ethanol. That leads to increase the absorption spectrum.

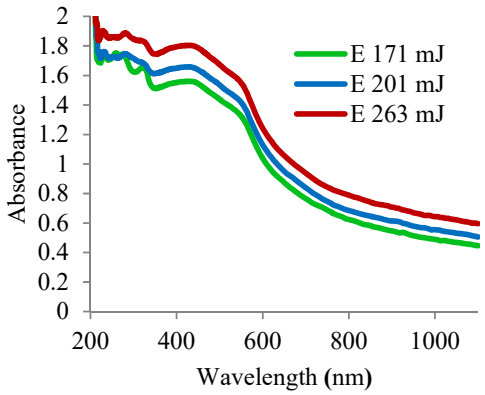

Fig.(3): Absorbance as a function of wavelength of α-Fe_2O_3 NPs.

Tauc's law was used to determine the optical band gap for direct transitions of the prepared iron oxide nanoparticles [6]:

$$(\alpha h\upsilon)^2 = A(h\upsilon - E_g)$$

Where, the absorption coefficient is (α), (E_g) is the optical energy gap, (A) is a constant and (hυ) is the photon energy of incident laight. As seen in Fig.(4), the optical band gap is effectd by the laser energy. As the laser energy for preparing the nanopartiles increase, the band gap energy shifts towards higher values. That can be attributed to the quantum confinment effect caused by the dectrease of particle size. The energy gap is listed in table (1) were similar to earlier reported reserches [11].

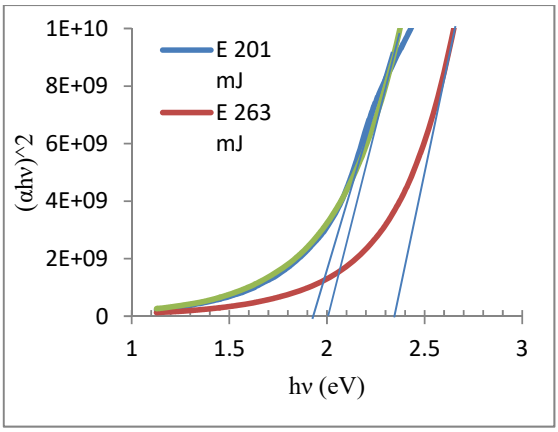

Fig. (4): The (αhυ) ^{2} versus hυ plot for α-Fe_2O_3 NPs prepared at different energies.

XRD test was used to determine the structural properties of the prepared samples (D2 phaser, Bruker, Karlsruhe, Germany). Operating with CuK_{a1} radiation at wavelength= 0.154060 nm, generated at 30 KV and 10 mA; for 2θ values between -3º to 160º.at room temperature, there was no peaks present. This indicates that the prepared thin films were of poor crystalline structure, as shown in Fig.(5). In order to enhance the crystalline structure and obtain the α-Fe_2O_3 phase, the samples were placed in a conventional electrical furnace at temp. 700º C for an hour as suggested by [6]. Fig.(6) shows the XRD spectra for the annealed samples prepared at different laser energies, which the structural peaks are well defined and correspond to the standard lines. These peaks are centered at 2θ=23.85º, 32.91º, 35.34º, 40.56º, 49.25º and 53.78º which corresponds to (110), (121), (110), (120), (220) and (231) planes that agrees with pure hematite α-Fe_2O_3 phase (JCPDS No. 13-0534). The broadening in these lines indicates the nanoparticles formation.

Table (1): The optical band gap energies at different laser energy.

Laser energy (mJ/pulse)	Band gap energy (eV)
171	1.92
201	2.05
263	2.35

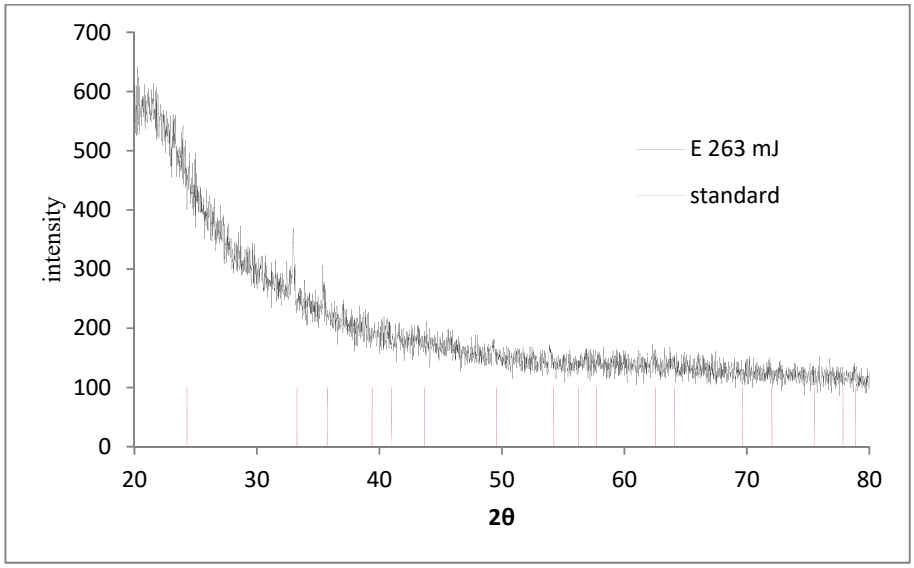

Fig.(5): X-Ray diffraction (XRD) spectra of α-Fe_2O_3 NPs at room temperature.

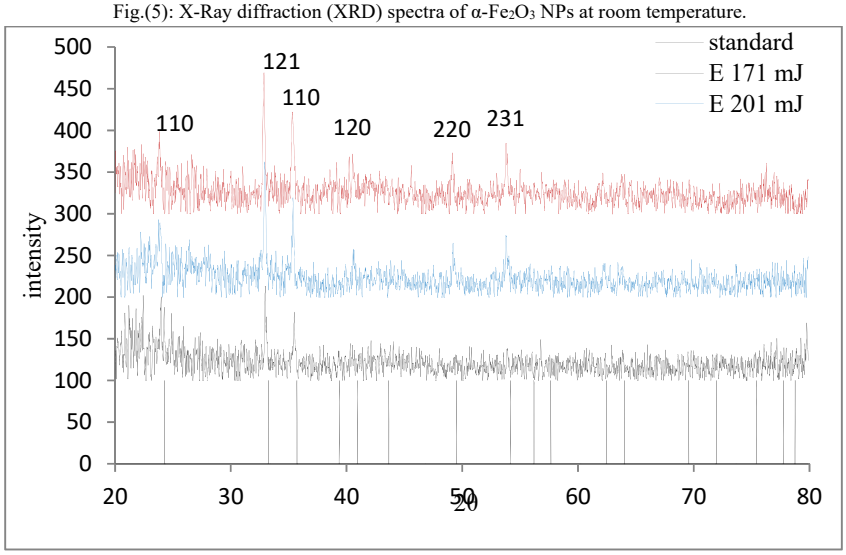

Fig.(6): X-Ray diffraction (XRD) spectra of α-Fe_2O_3 NPs prepared at different laser energies at 700º C for one hour.

The crystalline size value of synthesized samples were calculated according to Scherrer's equation [12], are listed in table (2-a,b,c).

Table 2-a: The crystalline size of α-Fe_2O_3 NPs prepared at 171 mJ/pulse

E	2θ (deg.)	(hkl)	d_{hkl} Theo.(Å)	d_{hkl} Exp.(Å)	FWHM (deg.)	Crystalline size (nm)
171 mJ	23.97	110	3.6600	3.7095	0.132	1.08
	32.98	121	2.6901	2.7138	0.167	87.54
	35.62	110	2.5101	2.5185	0.116	1.269

Table 2-b: The crystalline size of α-Fe_2O_3 NPs prepared at 201 mJ/pulse

E	2θ (deg.)	(hkl)	d_{hkl} Theo.(Å)	d_{hkl} Exp.(Å)	FWHM (deg.)	Crystalline size (nm)
201 mJ	24.01	110	3.6600	3.7034	0.411	34.87

	32.57	121	2.6901	2.7470	0.202	72.30
	35.78	110	2.5101	2.5076	0.258	57.09
	41.61	120	2.2010	2.1687	0.300	49.98
	49.24	220	1.8380	1.8490	0.202	76.34
	54.82	231	1.6900	1.6733	0.262	60.27

Table 2-c: The crystalline size of α-Fe_2O_3 NPs prepared at 263 mJ/pulse

E	2θ (deg.)	(hkl)	d_{hkl} Theo.(Å)	d_{hkl} Exp.(Å)	FWHM (deg.)	Crystalline size (nm)
263 mJ	23.85	110	3.6600	3.7279	0.398	36.00
	32.91	121	2.6901	2.7194	0.216	67.67
	35.34	110	2.5101	2.5378	0.279	52.73
	40.56	120	2.2010	2.2224	0.284	52.62
	49.25	220	1.8380	1.8487	0.354	43.56
	53.78	231	1.6900	1.7032	0.254	61.88

The surface morphology of α-Fe_2O_3 NPs was imaged by atomic force microscope (AFM) (CSPM- Scanning probe microscope). Fig.(7) demonstrates the surface morphology and size distribution are changed at different laser energies. As the laser energy increase, the average diameter decreases from 96.27 nm to 84.06 nm. This is due to increase in plasma plume temperature that generates large kinetic energy, which leads to increase the number of collisions between larger formed NPs causing the reduction in size as reported by Haider et al. [13] and Dorranian et al. [14]. Furthermore, the freed nanoparticles are suspended in the liquid that get in the way of the incoming laser pulse, absorbing some of its energy that causes further breakdown and fragmentation in these particles causing the size to reduce even more. The average diameter of α-Fe_2O_3 NPs prepared under different energies is listed in table (3).

Table (3): The average diameter and roughness of Fe_2O_3 NPs prepared under different laser energies.

Laser energy(mJ/pulse)	Average diameter (nm)	Roughness (nm)
171	96.27	9.56
201	92.86	2.16
263	84.06	15.8

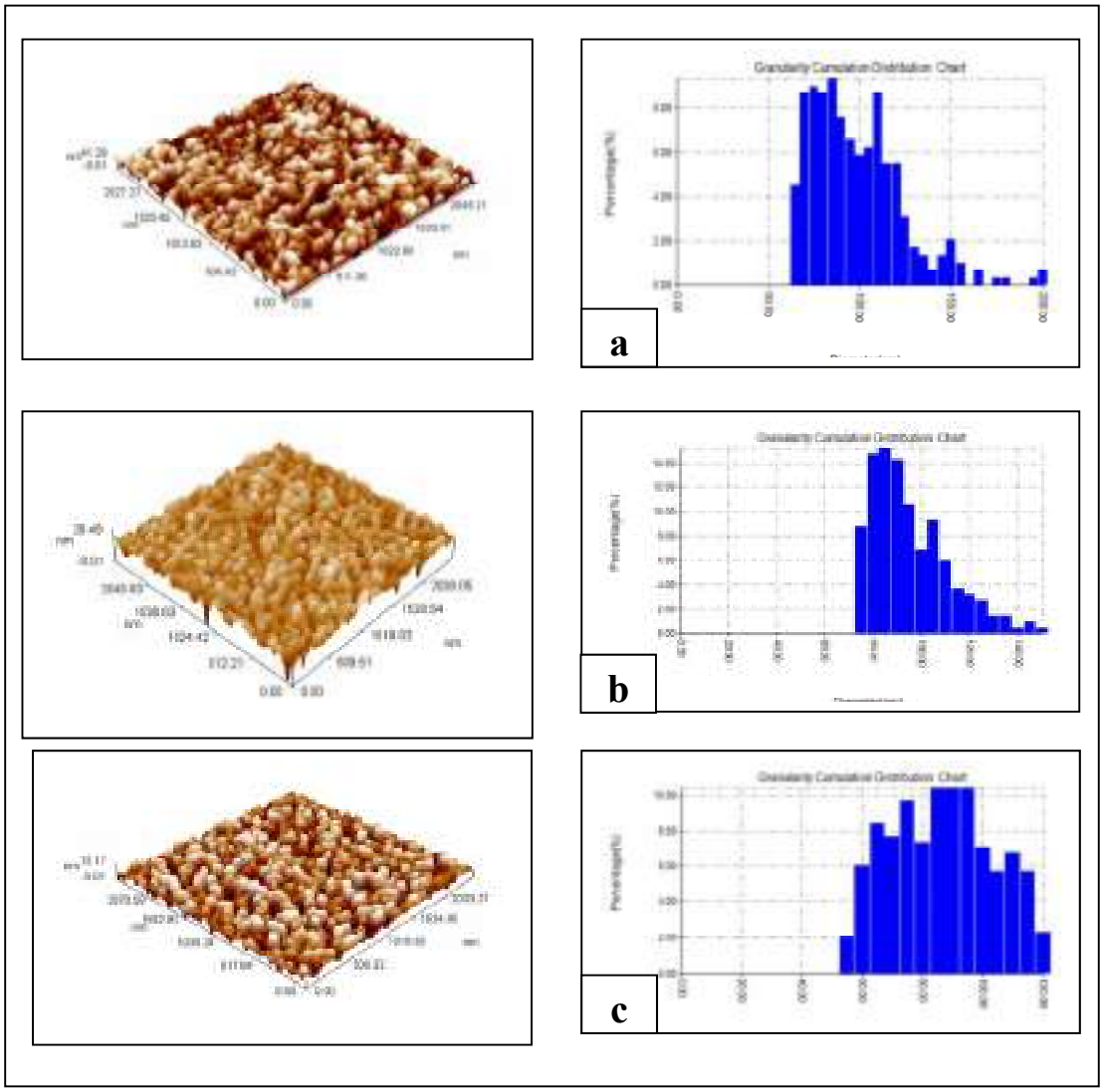

Fig.(7): 3D AFM images and size distribution of α-Fe_2O_3 NPs prepared at 700ºC, different laser energies (a) 171 mJ/pulse, (b) 201 mJ/pulse, (c) 263 mJ/pulse.

4- Conclusion

α-Fe_2O_3 NPs were successfully prepared by pulse laser ablation in ethanol at different laser energies. It's found that with increasing the laser energy causes the band gap energy to increase from 1.92 eV to 2.35 eV due to quantum confinement effect. After annealing the samples at 700º C for an hour, the XRD peaks appeared with high purity that the peak intensity increase preeportionally with increasing the ablating laser energy due to higher crystalline concentration. AFM images showed that the average nanoparticles size decrease with increasing laser energy. The size and morphology of NPs is strongly dependant on the characteristics of the induced plasma. At low laser energies, low temperature plasma is produced and large NPs are created. On the other hand, when increasing the laser energy, larger kinetic energy is generated from the high temperature plasma, which leads to increase the number of collisions between the larger formed NPs causing it to reduce in size.

References

[1] M. F. Silva et al., "Nanometric particle size and phase controlled synthesis and characterization of γ-Fe2O3 or (α + γ)-Fe2O3 by a modified sol-gel method," J. Appl. Phys., vol. 114, no. 10, 2013.
[2] P. Maneeratanasarn, T. Van Khai, S. Y. Kim, B. G. Choi, and K. B. Shim, "Synthesis of phase-controlled iron oxide nanoparticles by pulsed laser ablation in different liquid media," *Phys. Status Solidi Appl. Mater. Sci.*, vol. 210, no. 3, pp. 563–569, 2013.
[3] A. Kebede, A. V. Gholap, and A. K. Rai, "Impact of Laser Energy on Synthesis of Iron Oxide Nano-particles in Liquid Medium," *World J. Nano Sci. Eng.*, vol. 1, no. 4, pp. 89–92, 2011.
[4] E. Fazio, M. Santoro, G. Lentini, D. Franco, S. P. P. Guglielmino, and F. Neri, "Iron oxide nanoparticles prepared by laser ablation: Synthesis, structural properties and antimicrobial activity," *Colloids Surfaces A Physicochem. Eng. Asp.*, vol. 490, pp. 98–103, 2016.
[5] A. Kebede *et al.*, "Controlled synthesis, characterization, and application of iron oxide nanoparticles for oral delivery of insulin,"

Lasers Med. Sci., vol. 28, no. 2, pp. 579–587, 2013.
[6] R. A. Al-wardy, H. A. T. Al-ogaili, and S. I. Abbas, "Study of Annealing Temperature on Prepared Iron oxide Nanoparticles by Sol-Gel Method," *Int. J. Innov. Res. Sci. Eng. Technol.*, vol. 5, no. 4, pp. 5560–5567, 2016.
[7] N. V. Long, T. Teranishi, Y. Yang, C. M. Thi, Y. Cao, and M. Nogami, "Iron Oxide Nanoparticles for Next Generation Gas Sensors," *Int. J. Metall. Eng.*, vol. 1, no. December 2015, pp. 1–18, 2015.
[8] S. Laurent *et al.*, "Magnetic iron oxide nanoparticles: Synthesis, stabilization, vectorization, physicochemical characterizations and biological applications," *Chem. Rev.*, vol. 108, no. 6, pp. 2064–2110, 2008.
[9] Y. Vitta, V. Piscitelli, A. Fernandez, F. Gonzalez-Jimenez, and J. Castillo, "α-Fe nanoparticles produced by laser ablation: Optical and magnetic properties," *Chem. Phys. Lett.*, vol. 512, no. 1–3, pp. 96–98, 2011.
[10]A. M. Mostafa, S. A. Yousef, W. H. Eisa, M. A. Ewaida, and E. A. Al-Ashkar, "Synthesis of cadmium oxide nanoparticles by pulsed laser ablation in liquid environment," *Optik (Stuttg).*, vol. 144, no. July, pp. 679–684, 2017.
[11]R. Gopal, "Optical and Magnetic Property of Iron Oxide Nanoparticles Synthesized by PLA," no. March, 2015.
[12]A. S. Lanje, R. S. Ningthoujam, S. J. Sharma, and R. B. Pode, "Luminescence and electrical resistivity properties of cadmium oxide nanoparticles," *Indian J. Pure Appl. Phys.*, vol. 49, no. 4, pp. 234–238, 2011.
[13]A. F. M. Y. Haider, S. Sengupta, K. M. Abedin, and A. I. Talukder, "Fabrication of gold nanoparticles in water by laser ablation technique and their characterization," *Appl. Phys. A Mater. Sci. Process.*, vol. 105, no. 2, pp. 487–495, 2011.
[14]D. Dorranian and A. F. Eskandari, "Effect of laser fluence on the characteristics of ZnO nanoparticles produced by laser ablation in acetone," *Mol. Cryst. Liq. Cryst.*, vol. 607, no. 1, pp. 93–100, 2015.

Available online at
http://namrc.uotechnology.edu.iq/index.php/

Nanotechnology and Advanced Materials Research

Centre Proceeding Articles Book 00 (2018) 000–000

6th International Scientific Conference on Nanotechnology, Advanced Materials and its Applications

Self-Powered Photosensor Fabricated Based on ZnO/CdS/dye Nanostructure

Haider Abdulelah Abdulwahid[1,*], M.A. Mahdi[1], Gh.M. Jabbar[1], J.J. Hassan[1], Basil Ali[1], S.J. Kasim[1], H.F Al-Taay[2]

[1]Department of Physics, College of Science, University of Basrah, Basrah, Iraq.
[2]Department of Physics, College of Sciences for Women, University of Baghdad, Baghdad, Iraq
* Corresponding author**:** haiderabdulelah@yahoo.com

Abstract

Preparation and characterization of photosensors are received a lot of attention in recent years due to the important application**.** In the present work, ZnO nanorods array have been grown successfully onto fluorine doped tin oxide FTO/glass substrate by microwave assisted chemical bath deposition (MACBD) method. CdS nanocrystalline thin films are deposited onto ZnO nanorods using same method. The mechanism of formation of ZnO nanorods and CdS nanocrystalline thin films is explained. Then, ZnO nanorods/CdS nanocrystalline thin films are immersed for 24 hours in different types of dyes (Rhodamine B **and** Cresyl violet perchlorate) to form nanostructures ZnO/CdS/dye devices. The surface morphology, optical properties and current-time characterization of the fabricated devices are investigated under zero bias voltage. Under **low illumination intensity (3 mW/cm^2),** ZnO/CdS/Cresyl violet perchlorate device shows the highest sensitivity of 2900% and faster response compared by other synthesized devices**.**

*Keywords***:** ZnO, photosensor, dye, CdS.

1- Introduction

Photosensor is a device that senses and converts some of incident light photons into an electrical signal [1,2]. Generally, the physical principle of photosensors is based on the interaction of incoming photons with the atomic lattice of the material and cause generation photocurrent inside of the device. The efficiency of a photosensor depends on the optical absorption process, charge carrier separation and transport, and charge extraction into the electronic circuit system [3]. ZnO nanostructures, as a wide direct band gap 3.37 eV compound semiconductor has been widely used for its potential applications in optoelectronic devices [4-8]. In the nearly some decades, 1D nanostructures have been over a large area investigated due to their unusual in an interesting way physical and chemical properties, such as large surface to volume ratio [11-14], extremely good light absorption [15]. For that reason, many researchers are study to synthesize different of 1D nanostructures with controllable size, Various 1D nonostructures including nanorods (NRs), nanowires, nanobelts and nanotubes [16,17]. 1D nanostructured semiconductor exhibited extended application in light-emitting diode, transistors, lasers, solar cells, panel displays, field emitters, and photodetector devices [18-20]. As a significant II–VI semiconductor, Cadmium sulfde (CdS**)** is an n-type semiconductor with a wide band gap of 2.42 eV at room temperature [21-25]. The unique characteristics of CdS such as excellent photoconductivity, good chemical stability, low work function (4.2 eV), and the working in visible spectrum [26].

Photodetectors based on ZnO nanostructures have given considerable attention due to their high sensitivity in the UV range [27-30]. Heretofore, a large diverse of semiconductor nanostructures have been used in photodetectors and some mechanisms include have also been partly revealed [31-33]. In the past few years, it has been achieved that ZnO-based hybrid **nanostructures** can show photoresponse without any external bias rendering the devices as self-powered [34-36].
S. Sarkar and et al.[37] studies ZnO Nanorods/CdS/PEDOT:PSS device under zero bias condition and found that good performance responsive to both UV and visible lights. K.T. Lam and et al. [38] synthesized ZnO Nanorods/CdS heterostructures and found that the sensitivity device in the UV range is 146 under 5V bias. K.P. Kim and et al.[39] using Aluminum-doped zinc oxide (AZO) nanowire/TiO2 nanoparticle device as photodetector in the UV range and found that the sensitivity is 25 under external 5 bias.
In this letter, we demonstrated a self-powered white light based on ZnO/CdS/dye. The built-in potential separates the electron–hole pairs generated by white light and makes the photosensor generate photocurrent without any external bias. The morphology, optical and current-time characteristics of the fabricated photosensors was investigated.

2- Materials and Method

2. Materials Preparations

2.1 Synthesis of seed materials

Seed layer solution was prepared using Sol-Gel method**.** Firstly, FTO/glass was cleaned by sonication in acetone, ethanol, and hot distilled water. Then, 1.5gm of zinc Acetate (ZnAc) was dissolved in 75ml ethanol and vigorously stirred and drop wise in aqueous solution of diethanolamine (DEA) at room temperature for one hour. Zinc ions will be attached with OH^- groups of DEA backbone chains. Finally, the solution was spin coated onto FTO/glass substrates with four layers and each layer at 2000 rpm for 30s. After that, the heat treatment was done at 380 ^{0}C for two hours.

2.2 Synthesis of ZnO Nanorod

ZnO nanorods were grown onto Seed layer/FTO coated glass substrates by microwave assisted chemical bath deposition method (MW-CBD). 0.5g of zinc nitrate [$Zn(NO_3)_2$] was dissolved in 50ml distilled water, another hand use beaker contains 1g of hexamethylenetetramine complex (C6H12N4) dissolved in 50ml distilled water. Immerse the slides containing the seed layer vertically in**to** solution and add dropwise of both $Zn(NO_3)_2$ and C6H12N4 at 90 ^{0}C for one hour and ZnO nanorods will be formed.

2.2.1 Reaction Mechanism of Formation ZnO Nanorod

In this study, the growth of ZnO nanorods underwent a process of hydrolysis and condensation of precursors [40]. At that stage, the reaction vessel containing the aqueous solution of zinc nitrate hexahydrate acts as a source of zinc cations and hexamethylenetetramine complex ($C_6H_{12}N_4$) acts as a slow release of OH-anions. In that state, the typical reactions were according to the following equations [41].

$$C_5H_{12}N_4 + 6H_2O \rightarrow 6HCHO + 4NH_3 ...(1)$$

$$NH_3 + H_2O \rightarrow NH_4^+ + OH^- ...(2)$$

$$Zn(NO_3)_2 \rightarrow Zn^{2+} + 2NO_3^- ...(3)$$

$$2OH^- + Zn^{2+} \rightarrow Zn(OH)_2 ...(4)$$

$$Zn(OH)_2 \triangleq ZnO + H_2O ...(5)$$

2.3 Preparation CdS Nonocrystalline Thin Film

Nanocrystalline CdS thin **fi**lm was deposited onto ZnO nanorods substrates using MW-CBD method in an alkaline aqueous solution. 0.05M of cadmium nitrate[$Cd(NO_3)_2$] was dissolve in 50 ml distilled water (DW). Then, add 0.1M of thiourea [CS(NH2)2] to the solution to use it as a Cd^{2+} and S^{2-} ions source, respectively. Ammonium acetate [NH_4CH_3COO] with 1 M is added as a buffer solution to control the reaction rate. Ammonia solution was added to adjust the pH to 10 and the total volume was 100 ml. After stirred the solution for 5 min, the ZnO nanorods substrates are immersed vertically in the beaker and then transferred the solution to the microwave oven under 2.45 GH_z frequency and the temperature is **fi**xed at 75 °C the preparation temperature of 75 °C for 30 minute. Finally, the samples are taken out of the solution and washed by distilled water to remove any contaminants.

2.3.1 Reaction Mechanism of Formation CdS Thin Films

Adding ammonia solution to the water produces ammonium and hydroxide ions as shown below:

$$NH_3 + H_2O \longleftrightarrow NH_4^+ + OH^- \quad \ldots 6$$

The dissolution of $Cd(NO_3)_2$ in water provides free cadmium ions (Cd^{2+}). These ions react with hydroxide ions to create cadmium hydroxide [$Cd(OH)_2$], which finally react with ammonia to produce cadmium tetramine complex $[Cd(NH_3)_4]^{2+}$ as shown in the reactions below [42]:

$$Cd^{+2} + 2\ OH^- \longleftrightarrow Cd(OH)_2 \quad \ldots 7$$

$$Cd(OH)_2 + 4NH_3 \longleftrightarrow Cd(NH_3)_4]^{+2} + 2OH^- \quad \ldots 8$$

Adding thiourea to the solution leads to the productionn of free sulfur S^{2-} ions, as shown in the equations below:

$$(NH_2)_2CS + OH^- \longleftrightarrow SH^- + CN_2H_2 + H_2O \quad \ldots 9$$

$$SH^- + OH^- \longleftrightarrow S^{-2} + H_2O \quad \ldots 10$$

Finally, the CdS thin film is formed by the reaction of $[Cd(NH_3)_4]^{2+}$ complex with S^{2-} ions as shown below:

$$[Cd(NH_3)_4]^{+2} + S^{-2} \longleftrightarrow CdS + 4NH_3 \quad \ldots 11$$

3- Results and discussion

3.1 Surface Morphology

Figure 1A shows field emission scanning electron microscopy (FE-SEM) images of the ZnO nanorods array at 3 k x magnification. Images magnified top-view (fig. 1B) shows that the ZnO is grown on the surface of FTO-glass substrate as a nanorod structure with an average diameter of 400 nm at 50 k x magnification.

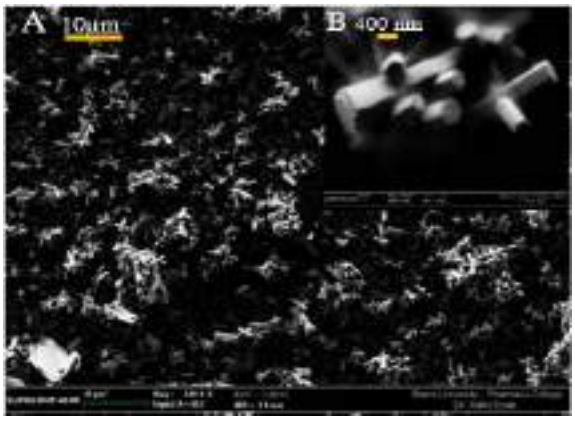

Figure 1: FE-SEM micrograph of ZnO nanorods, Inset high magnification of thin film

3.2 Optical Absorption

The absorption spectra of the ZnO nanorods/CdS nonocrystalline thin film **is** investigated from 340nm to 800nm, and dyes are investigated in the wavelength range of 300-900nm. Figure (2) **shows** that two edges of optical absorbance of ZnO nanorods/CdS nonocrystalline thin film**.** First absorbance peak return **to** ZnO nanorods appears at 380 nm and second peak of CdS thin films is

appears at 504 nm in the visible light region. Similar absorption spectrum was observed by Y. Tak et al**. [43].** All dyes have absorption peak wavelength fall at visible region. Optical absorbance peak of Rhodamine B dye appeared at around 551 nm while Cresyl violet perchlorate dye contains absorbance peak located at 578 nm [22].

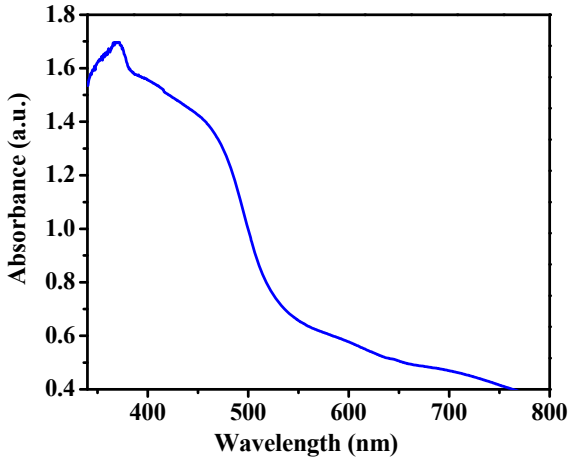

Figure 2: Optical absorbance ZnO nanorods/CdS nanocrystalline thin film prepared onto FTO/glass substrate.

3.3 Current-Time Characterization

The Sensitivity (S) of the photosensors devices were calculated using the relationship [44].

$$S = \left[\frac{I_{ph} - I_D}{I_D}\right] X100\%$$

Where I_{ph} is the photocurrent and I_D the dark current.

Figures 3 and 4 shows that the reproducible on/off switching times. The ZnO nanorods/CdS/ Rhodamine B (R) device show the lowest raise time of 0.18s while the ZnO nanorods/CdS/ Cresyl violet perchlorate (C) was the highest raise time of 0.275s. The photosensor R device give the highest decay time of 0.5s while the photosensor C was lowest decay time of 0.195s. The sensitivity of device C is 2900% greater than device R (36%). However, many reasons of the limiting the sensitivity of C photosensor compared by R device. Range optical properties of device C is one of them. There is a remarkable range of work reported in the literature on organic–inorganic hybrid photodsensors with good response both in the UV and/or visible region [44-50].

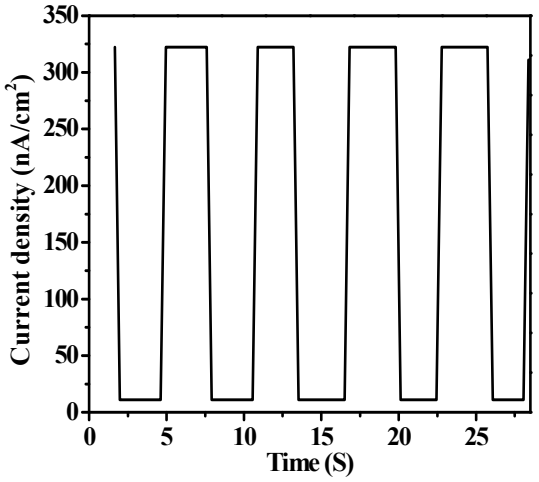

Figure 3**:** Transient response of the photocurrent of ZnO **nanorods/ CdS/Cresyl violet perchlorate** under zero bias voltage

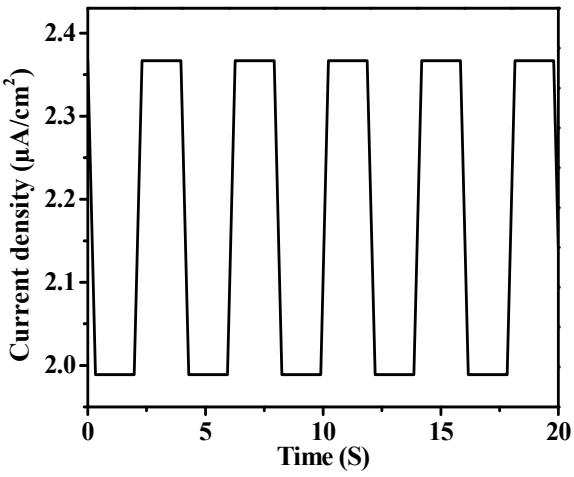

Figure 4**:** Transient response of the photocurrent of **ZnO nanorods/CdS/**Rhodamine B under zero bias voltage

4- Conclusion

We are reporting, for the first time, a self- powered white light photosensor based on a ZnO/CdS/dye nanostructure. ZnO nanorods has been successfully deposited onto FTO/glass substrate using MW-CBD method. There is very important advantage to use ZnO nanorods in photosensors due to its have high surface to volume ratio that leads to increased exposed area to light. The maximum sensitivity of 2900% was obtained from the ZnO nanorods/CdS/ Cresyl violet perchlorate.

References

1] M.M. Ombaba, H. Karaagac, K.G. Polat, M.S. Islam, Nanowire enabled photodetection, Photodetectors, 87-120, 2016
[2] N. Bahram. Photodetectors: Materials, Devices and Applications. Woodhead Publishing, 2015.
[3] D. Kufer, Photodetectors based on low-dimensional materials and hybrid systems,Ph.D thesis, The Institute of Photonic Sciences Barcelona, 2016.
[4] J.J. Hassan, M.A. Mahdi, A. Ramizy, H.A. Hassan, Z. Hassan, Fabrication and characterization of ZnO nanorods/p-6H–SiC heterojunction LED by microwave-assisted chemical bath deposition, Superlattices and Microstructures, 53, 31-38. 2013.
[5] J.J.Hassan, M. A. Mahdi, S. J. Kasim, N. M. Ahmed, H. Abu Hassan, Z. Hassan. High sensitivity and fast response and recovery times in a ZnO nanorod array/p-Si self-powered ultraviolet detector, *Applied Physics Letters,* 101, 261108, 2012.
[6] N. S. Ramgir, Y. Yang, and M. Zacharias, Nanowire-Based Sensors Small 6, 16, 1705-1722, 2010.
[7] H. Abdullah, N.P. Ariyanto, S. Shaari, B. Yuliarto, S. Junaidi, Study of porous nanoflake ZnO for dye-sensitized solar cell application.,American Journal of Engineering and Applied Sciences, 2(1), 2009.
[8] H.Q. Li, X. Wang, J.Q. Xu, Q. Zhang, Y. Bando, D. Golberg, Y. Ma, T.Y. Zhai, One-Dimensional CdS Nanostructures: A Promising Candidate for Optoelectronics. Advanced Materials, *25*(22), 3017-3037,2013
[9] J. S. Jie, W. J. Zhang, I. Bello, C. S. Lee, S. T. Lee, One-dimensional II–VI nanostructures: synthesis, properties and optoelectronic applications, *Nano today,* 5(4), 313-336, 2010.
[10] G. H. Li, Y. Jiang, Y. G. Zhang, X. Z. Lan, T. Y. Zhai, G. C. Yi, High-performance photodetectors and enhanced field-emission of CdS nanowire arrays on CdSe single-crystalline sheets, Journal of Materials Chemistry C ,(2),39, 8252-8258, 2014.
[11] W. Zhao, , L. Liu, M. Xu, X. Wang, T. Zhang, Y. Wang, Z. Zhang, S. Qin, Z. Liu, Single CdS Nanorod for High Responsivity UV–Visible Photodetector. Advanced Optical Materials, *5*(12), 2017.
[12] Z. Y. Fan, J. G. Lu, Chemical sensing with ZnO nanowire field-effect transistor, IEEE transactions on nanotechnology, 393-396. 5.4 (2006).
[13] X. Wang, F. Sun, Y. Duan, Z. Yin, W. Luo, Y. Huang, & J. Chen, Highly sensitive, temperature-dependent gas sensor based on hierarchical ZnO nanorod arrays. Journal of Materials Chemistry *C*, *3*(43), 11397-11405, 2015.
[14] X.W. Fu, Z.M. Liao,Y.B. Zhou, H.C. Wu, Y.Q. Bie, J. Xu, D.P.Yu Graphene/ZnO nanowire/graphene vertical structure based fast-response ultraviolet photodetector, Applied physics letters,100, 223114, 2012.
[15] L. Y. Cao, J. S. White, J. S. Park, J. A. Schuller, B. M. Clemens, M. L. Brongersma, Engineering light absorption in semiconductor nanowire devices, Nature materials 8(8), 643, 2009.
[16] C.J. Jia, L.D. Sun, Z.G. Yan, L.P. You, F. Luo, X.D. Han, C.H. Yan, Single-Crystalline Iron Oxide Nanotubes, Angewandte Chemie 117(28) ,4402-4407, 2005.
[17] Z. W. Pan, Z. R. Dai, Z. L. Wang, Nanobelts of semiconducting oxides, Science, 291,(5510), 1947-1949.,2001.
[18] L. Li, P. C. Wu, X. S. Fang, T. Y. Zhai, L. Dai, M. Y. Liao, Y. Koide, H. Q. i. Wang, Y. Bando, D. Golberg, Single-crystalline CdS nanobelts for excellent field-emitters and ultrahigh quantum-efficiency photodetectors." Advanced Materials, 22 (29), 3161-3165, 2010.
[19] Y. F. Lin, J. H. Song, Y. Ding, S. Y. Lu, Z. L. Wang, Alternating the output of a CdS nanowire nanogenerator by a white-light-stimulated optoelectronic effect." Advanced Materials 20(16), 3127-3130, 2008.
[20] M. A. Mahdi, J. J. Hassan, S. S. Ng, Z. Hassan, N. M. Ahmed, Synthesis and characterization of single-crystal CdS nanosheet for high-speed photodetection, Physica E: Low-dimensional Systems and Nanostructures, 44(7-8), 1716-1721, 2012.
[21] Haider Abdulelah, B. Ali, M. A. Mahdi, J. J. Hassan, H. F. Al-Taay, P. Jennings. "Fabrication and characterization of nanowalls CdS/dye sensitized solar cells." Physica E: Low-dimensional Systems and Nanostructures, 90,104-108, 2017.
[22] H. Abdulelah,B. Ali, M.A. Mahdi, A.Q. Abdullah, J.J. Hassan, H.F. Al-Taay, P. Jennings, Fabrication and characterization of porous CdS/Dye sensitized solar cells, J. Sol. Energy 2016 (2016) 7.
[23] M. A. Mahdi, Z. Hassan, S. S. Ng, J. J. Hassan, and S. K. M. Bakhori, Structural and optical properties of nanocrystalline CdS thin flms prepared using microwave-assisted chemical bathdeposition," *Thin Solid Films*,520(9),3477–3484, 2012.
[24] M. A. Mahdi, J. J. Hassan, Z. Hassan, and S. S. Ng, Growth and characterization of $Zn_xCd_{1-x}S$ nanoflowers by microwave-assisted chemical bath deposition, Journal of Alloys and Compounds, 541,227-233,2012.
[25] W. H. Strehlow, E. L. Cook ,Compilation of energy band gaps in elemental and binary compound semiconductors and insulators, Journal of Physical and Chemical Reference Data, 2(1) , 163-200. 1973.

[26] K. T. Lin, S. C. Tseng, H. L. Chen, Y. S. Lai, S. H. Chen, Y. C. Tseng, T. W. Chu, M. Y. Lin, Y. P. Lu, Ultrahigh-sensitivity CdS photoconductors with instant response and ultralow power consumption for detection in low-light environments, Journal of Materials Chemistry C, 1(27),4244-4251, 2013.
[27] B. Cao, W. Cai, Y. Li, F. Sun, L. Zhang, Ultraviolet-light-emitting ZnO nanosheets prepared by a chemical bath deposition method. *Nanotechnology*, *16*(9), 1734, 2005.
[28] S.E. Ahn, J.S. Lee, H. Kim, S. Kim, B.K. Kang, K.H. Kim, G.T. Kim Photoresponse of sol-gel-synthesized ZnO nanorods, Applied Physics Letters, *84*(24),5022-5024,2004
[29] Q.H. Li, T. Gao, Y.G. Wang, T.H. Wang, Adsorption and desorption of oxygen probed from ZnO nanowire films by photocurrent measurements, Applied Physics Letters, 86(12), 123117, 2005.
[30] A. Manekkathodi, M.Y. Lu, C.W. Wang, L.J. Chen (2010) Direct growth of aligned zinc oxide nanorods on paper substrates for low-cost flexible electronics. Advanced materials, *22*(36), 4059-4063, 2010.
[31] Y. Li, V.F. Della, M. Simonnet, I. Yamada, J.J. Delaunay, High performance UV detector made of ultra-long ZnO bridging nanowires. Nanotechnology 20(4):045501, 2009.
[32] F. Teng, L. Zheng, K. Hu, H. Chen, Y. Li, Z. Zhang, X. Fang, A surface oxide thin layer of copper nanowires enhanced the UV selective response of a ZnO film photodetector. Journal of Materials Chemistry C, 4:8416, 2016
[33] H. Li, X. Wang, J. Xu, Q. Zhang, Y. Bando, D. Golberg, Y. Ma, T. Zhai, Onedimensional CdS nanostructures: a promising candidate for optoelectronics. Advance Mater 25:3017,2013.
[34] Z. Y.Zhan, L. X. Zheng, Y. Z. Pan, G. Z. Sun, L. Li, Self-Powered, Visible-Light Photodetector Based on Thermally Reduced Graphene Oxide-ZnO (RGO-ZnO) Hybrid Nanostructure. Journal of Materials Chemistry, 22, 2589-2595, 2012.
[35] S. M. Hatch, J. Briscoe, S. Dunn, A Self-Powered ZnO-Nanorod/CuSCN UV Photodetector Exhibiting Rapid Response. Advance Mater, 25, 867-871, 2013,
[36] O. Game, U. Singh, T. Kumari, A. Banpurkar, S. Ogale, ZnO(N)-Spiro-MeOTAD Hybrid Photodiode: An Efficient Self-Powered Fast-Response UV (Visible) Photosensor, Nanoscale, 6, 503-513,2014, 2014.
[37] S., Sanjit, and Durga Basak, Self Powered Highly Enhanced Dual Wavelength ZnO/CdS Core–Shell Nanorod Arrays Photodetector: An Intelligent Pair, ACS applied materials & interfaces, 7.30, 16322-16329, 2015.
[38] K.T. Lam, Y.J. Hsiao, L.W. Ji, T.H. Fang, H.K. Hsiao, T.T. Chu, High-Sensitive Ultraviolet Photodetectors Based on ZnO Nanorods/CdS Heterostructures, Nanoscale research letters, *12*(1), 31, 2017.
[39] K.P. Kim, D. Chang, S.K. Lim, S.K. Lee, H.K. Lyu, D.K. Hwang, Effect of TiO_2 nanoparticle modification on ultraviolet photodetection properties of Al doped ZnO nanowire network. Japanese Journal of Applied Physics, 50(6S), 06GF07, 2011.

[40] J. J. Hassan, M. A. Mahdi, C. Chin, Z. Hassan, H. A. Hassan, Microwave assisted chemical bath deposition of vertically aligned ZnO nanorods on a variety of substrates seeded by PVA–Zn $(OH)_2$ nanocomposites, Applied Surface Science, 258 (2012),4467–4472.
[41] Q. Li, V. Kumar, Y. Li, H. Zhang, P. T. Robert, H. Chang, Fabrication of ZnO nanorods and nanotubes in aqueous solutions, Chemistry of Materials, 17 (2005) 1001-1006.
[42] M. A. Mahdi, S. J. Kasem, J. J. Hassen, A. A. Swadi, S. K. J.A l-Ani, Structural and Optical Properties of Chemical Deposition CdS Thin Films, Nanoelectronics and Materials, 2(2009) 163-172.
[43] Y. Tak, S. J. Hong, J. S Lee, Yong, K. Solution-Based Synthesis of a CdS Nanoparticle/ZnO Nanowire Heterostructure Array, Crystal Growth and Design, 9(6), 2627-2632, 2009.
[44] B. Yuan, X.J. Zheng, Y.Q. Chen, B. Yang, T. Zhang, High photosensitivity and low dark current of photoconductive semiconductor switch based on ZnO single nanobelt. Solid-State Electronics, *55*(1), 49-53,2011.
[45] M.J. Deng, S.L. Shen, X.W. Wang, Y.J. Zhang, H.R. Xu, T. Zhang, Q. B. Wang, Controlled synthesis of $AgInS_2$ nanocrystals and their application in organic–inorganic hybrid photodetectors. CrystEngComm,15(33), 6443-6447., 2013.
[46] S. Mridha and D. Basak, ZnO/polyaniline based inorganic/organic hybrid structure: Electrical and photoconductivity properties. Applied Physics Letters, 92(14), 142111., 2008.
[47] C. J. Novotny, E. T. Yu, P. K. L. Yu, InP nanowire/polymer hybrid photodiode, Nano Letters, 8, 775–779,2008.
[48] J.J. Wang, Y.Q. Wang, F.F. Cao, Y.G. Guo, L.J. Wan, Synthesis of monodispersed wurtzite structure $CuInSe_2$ nanocrystals and their application in high-performance organic− inorganic hybrid photodetectors. Journal of the American Chemical Society, *132*(35), 12218-12221., 2010.
[49] X. F. Wang, W. F. Song, B. Liu, G. Chen, D. Chen, C. W. Zhou, G. Z. Shen, High-performance organic-inorganic hybrid photodetectors based on P3HT: CdSe nanowire heterojunctions on rigid and flexible substrates. Advanced Functional Materials, *23*(9), 1202-1209,2013.
[50] D.J. Xue, J.J. Wang, Y.Q. Wang, S. Xin, Y.G. Guo, L.J. Wan, Facile synthesis of germanium nanocrystals and their application in organic–inorganic hybrid photodetectors, Advanced materials, *23*(32), 3704-3707, 2011.

Available online at
http://namrc.uotechnology.edu.iq/index.php/

Nanotechnology and Advanced Materials Research Centre

Proceeding Articles Book 00 (2018) 000–000

6th International Scientific Conference on Nanotechnology, Advanced Materials and its Applications

Enhancement of UV photodetectors based on ZnO nanorods and Cu-doped by hydrothermal method

Hussein Abdullah Hameed[1], J. J. Hassan[2], H. L. Saadon[2]

[1]Physics Department, College of Science, University of Kufa, Najaf, Iraq [2]
Physics Department, College of Science, University of Basra, Basrah, Iraq

Abstract

Copper-doped zinc oxide (ZnO: Cu) nanorods (NRs) were prepared by hydrothermal method deposited on glass substrates. The synthesized pure ZnO and Cu doped ZnO were investigated by using, XRD, FE-SEM, EDX, photoluminescence and UV absorption techniques. X-ray diffraction analysis demonstrates a decrease in the lattice parameters of Cu doped ZnO NRs. Photoluminescence studies on pure and Cu-doped ZnO NRs shows that the near band edge. MSM UV detector devices were fabricated for pure ZnO and Cu doped ZnO. Responsivity, detectivity, Quantum efficiency, and sensitivity were measured for all devices at biased voltage of 5 V for UV radiation of wavelength (365, 385) nm and have intensity equal 40 μ watt/cm^2. All sensing properties were enhanced for Cu doped ZnO nanorods device. The highest responsivity was 2.93681 A/W by using the Cu-doped ZnO nanorod arrays.

Keywords: hydrothermal method, MSM UV detector, ZnO nanorods, Responsivity, Cu doped ZnO

1-Introduction

Due to their wide band gap of 3.37 eV at room temperature, zinc oxide nanorods have promising applications in solar cells, photodetectors and sensors devices[1-3]. Although there are many studied regarding ZnO in the past decades, there are several reports focused on efforts to control the properties of ZnO by adding the transition metal impurities such as Mg[4], Al [5], Co[6], Ni [7], and Cu [8, 9]. Doping work to control and adjust the band gap, which greatly contribute to increase the efficiency and power n in many applications, such as Light emitting diodes, laser diodes, solar cells, transparent electrodes, thin film transistors and optical sensors. [10-12].

This work has discussed the fabrication of Metal Semiconductor Metal (MSM) UV photodetector using pure and Cu doped ZnO nanorods arrays via a simple technique using hydrothermal method at high temperature. The importance of this study is the amplification of (MSM) UV detectors performance using ZnO nanorods arrays, resulting in a low-cost, time-saving fabrication process. It has also discussed the performance of (MSM) UV detectors fabricated using Cu-doped ZnO nanorods that produce the highest responsivity, quantum efficiency and others parameters comparing to pure ZnO.

2-Experimental

Hydrothermal method was used to prepared a pure and Cu doped ZnO nanorods arrays as reported by several researchers[13, 14]. First, the glass substrates were cleaned by an ultrasonic cleaner with Acetone, Ethanol and propanol for 10 min, then cleaned with deionized water and dried. Zinc acetate dehydrates 0.5 M was first dissolved in the ethanol with stirring at 60 C° for (2-3) h until a clear and transparent homogeneous solution was formed. The solution was spin coated at a rate of 2500 rpm for 30 s using a spin coater for 5 times. The as-deposited thin film was heated in an oven at (140-150) C° for 10 min to remove the solvent, and annealing at (350-400) C° in the furnace for 2 h [1, 15] to obtain the ZnO seed layer. After the formation of seed layer, ZnO nanorods arrays were formed through hydrothermal method. The substrates with a seed layer were putting verticality inside Teflon vessels filled with the aqueous solution of 0.05 M zinc nitrate hexahydrate ($Zn(NO_3)_2{\cdot}6H_2O$; 98% purity) and 0.05 M Hexamethylenetetramine (HMT; $C_6H_{12}N_4$; 99% purity; Aldrich), sealed and heated at (110-120) C° for 3 h. Then, the substrate removed from Teflon vessel, cleaned with distilled water, and dried. Next, the Cu-doped ZnO nanorods arrays were grown on the seed-layer-coated glass substrate using aqueous solutions of 0.05 M zinc nitrate hexahydrate ,0.05 M Hexamethylenetetramine and the ratio atoms Cu/Zn (0.025, 0.05) Copper(II) nitrate trihydrate ($Cu(NO_3)_2{\cdot}3H_2O$; 98%purity). These reagents were dissolved and reacted in Teflon vessel with

temperature of (110-120) C° for 3 h. Following, the substrate was rinsed with distilled water and all the samples were annealed for 2 h in furans at 350 C°.

Then, aluminum (Al) contacts were deposited on the nanorods films using a thermal evaporator technique to produce a metal–semiconductor–metal (MSM)-type UV photoconductive detector. The deposition of metal contacts was performed at chamber pressure of 9.5 × 10^{-5} Pa. The separation between the metal contacts was fixed at 0.05 mm for all samples using a metal mask as showed in Table 1.

3-Results and discussion

3.1 Structural studies

Pure and Cu doped ZnO nanorods possess polycrystalline hexagonal wurtzite structures are shown in Fig. 1. It is noted that the intensity of diffraction peaks of the ZnO deposition appear at 31.4839, 34.169 and 35.9584, which correspond to the (1 0 0), (0 0 2) and (1 0 1) plane, respectively. The peak positions of all samples corresponding to ZnO according to the standard JCPDS card with hexagonal wurtzite structure[16]. It was also observed that with increasing Cu concentration the (0 0 2) peak positions 2θ of the doped sample were shifted from 34.16 to 34.199 and 34.22 for Cu- doped. This shift in the (0 0 2) peak for Cu-doped ZnO might be due to the substitution of Zn by Cu in the hexagonal lattice. These shifts agree with previous reports[9, 10]. No change in the crystalline structure was detected. The inter planar spacing, the lattice constant (a, c) and the micro-strain (ε) can be found by the equations (1-3) [9, 10, 12].

$$2d\sin\theta = n\lambda \quad , \quad \frac{1}{d^2} = \frac{4}{3(h^2 + hk + k^2/a^2)} + \frac{l^2}{c^2} \quad \text{and} \quad \varepsilon = \frac{\beta\cos\theta}{4} \tag{1-3}$$

where *h, k* and *l* are miller indices, Show Table 2.

3.2 SEM Analysis

The surface morphology of the grown pure and Cu-doped ZnO nanorods (A B2) was investigated by the field-emission scanning electron microscope (FESEM). The results can be shown in Fig. 2 with hexagonal rod shapes at diameters ranging from 30- 80 nm. The chemical composition at different concentrations of 0, 0.025, and 0.05 (A, B1, and B2) ratio atoms Cu/Zn were measured by using EDX shown as in Fig. 3.

3.3 Optical properties

The optical absorption spectrum of undoped and Cu-doped ZnO nanorods is shown in Fig.4 at room temperature. It showed that all samples have sharp absorption edges in the UV region. The Absorption band edge was observed at 380 nm, 398 nm, and 413 nm for A, B1, and B2, respectively. Because of the band-to-band transition and Cu doped ZnO shows that the absorption edge shifted to a long wavelength with an increasing in the doping ratio due to quantum-size effects. The optical bandgap of ZnO was estimated using the fundamental relation [1, 17, 18]

$$(\alpha h\upsilon) = B(h\upsilon - E_g)^n \tag{4}$$

where α is the absorbance, υ is the frequency in every unit of a wavelength, h is Planck's constant, Eg the optical band gap energy and k, n =1/2 for direct allowed transition and B is the proportionality constant. The optical band gap of the A, B1, and B2 was observed equal to 3.27, 3.184, and 3.146 eV, respectively, as shown in Fig. 5. All the estimated band gap energies were below the theoretical band gap value of 3.37 eV. However, it was noted that with Cu doping a decrease in the band gap of pure ZnO with a red shift that can be attributed to that the new ion (Cu^{+2}) energy level formed in the band gap, thereby decreasing the ZnO band gap. The photoluminescence (PL) spectra for undoped and Cu-doped ZnO nanorod samples with excitation at a wavelength of 320 nm are depicted in Fig. 6, which compares the photoluminescence (PL) spectra of samples (A B1 B2) and shows characteristic UV emission peak at (385.5,388.3, 389.8) nm is attributed to the near band edge emission from the recombination of free excitons through an exciton–exciton collision process[18, 19], to surface states (V_{Zn}) or band tail states in ZnO [18, 20]. Weak blue band at (436.5 431 438.4) nm, a strong blue band at (444,445.8, 454.2) nm, a strong green band at (543.05, 543.04, 542.4) nm. The range of wavelength 450–550 nm deep level visible emission region (DLE) is usually recognized to intrinsic defects such as V_{Zn}, Zn_i, and V_O, O_i, as well as extrinsic impurities [18, 21, 22].

3.4 Device Fabrication Process

The UV photodetector device with dimension of 1 cm x 1 cm for the structure of Al/ZnO/Al was fabricated by MSM. The Al electrode was deposited onto samples (A, B1, B2) and the annealed films using a mask through thermal evaporation technique. The current-voltage (I-V) curves of the fabricated MSM under dark and UV (365, 385) nm with power density of 40 μW/cm^2 were measured for all samples. The results can be shown in Fig. 7. It showed a linear response of the photocurrent curve; that can be attributed to an ohmic contact between the ZnO film and Al electrodes. The ohmic behavior is very important to the photodetector properties because the sensitivity of photodetectors or the ratio of electrical resistance under illumination to dark condition can be maximized when the metal-semiconductor junction is ohmic or has a negligible junction resistance. The slope of the I-V curve measured under UV illumination increases suggested a decrease in the electrical resistance of the film; it was due to a change in the carrier density of the structure, as compared to the I-V curve in the dark. In addition to that, the responsivity (R), quantum efficiency (η), detectivity (D) and sensitivity (S) can be calculated by the Eq's (5-8) [3, 23, 24]

$$R = \frac{I_{ph} - I_{dark}}{P_{opt}} \ , \ \eta = R\frac{hc}{e\lambda} \ , \ D = \frac{\lambda\eta e}{hc}\left(\frac{RA}{4kT}\right)^{1/2} \quad \text{and} \quad S = \frac{I_{ph} - I_{dark}}{I_{dark}} * 100\ \% \tag{5-8}$$

Where I_{ph} is the photocurrent, I_{dark} is the dark current and P_{opt} is the optical power of the UV source, c, e and λ are blank constant, light speed, electron charge and wavelength used, respectively. According to the relations (5-8), the results can be found in Tables 3-6, at wavelength of 365, 385 nm is as a function applied voltage.

It is to be noted that voltage was chosen for getting the highest and best in the different responsivity samples of cu doped and undoped at wavelength of 365 nm as illustrated in Table 3.The results can be shown in Table 7. Fig. 8 shows the photoresponse of UV photodetector at wavelength of 365 and 385 nm. The ON-OFF switching UV time duration characteristics was at 2 and 5 min for the samples A, B1, and B2, respectively, with intensity of 40 μ W/cm^2 at 5V applied bias. Upon UV illumination, the photocurrent rapidly increased and then drastically decreased to its initial level when the light was turned off, indicating that excellent stability and reproducible characteristics of the photodetector. According to [1, 25], the sensor sensitivity was closely related to oxygen adsorption and desorption processes. In the dark, oxygen molecules tend to adsorb onto nanorod surfaces by capturing free electrons and producing adsorbed oxygen ions, as shown by following equation:

$$O_2 + e^- \rightarrow O_2^- \tag{9}$$

In which O_2 is the oxygen molecule, e^- is the free electron, and O_2^- is the adsorbed oxygen ion on the nanorod surface. The adsorbed oxygen ions create a barrier near the surface generates a low current before UV illumination. When UV light is irradiated onto the nanorods, an electron–holes pairs are generated at the surface according to the following equation:[26]

$$h\nu \rightarrow h^+ + e^- \tag{10}$$

Where $h\nu$ the photon energy of UV light, h+ is the photo generated hole in the valence band, and e^- is the photo generated electron in the conduction band. The photo generated holes recombine with adsorbed oxygen ions on the surface, producing oxygen molecules; this reaction also eliminates the barrier near the nanorod surface. This process is described by the following equation:

$$O_2^- + h^+ \rightarrow O_2 \tag{11}$$

At the same time, desorption of adsorbed oxygen ions on the nanorod surface leaves photo generated electrons in the conduction band, increasing the film conductivity and contributing to the photocurrent. When the UV light is switched off, oxygen starts to adsorb once again onto the nanorod surface, decreasing the conductivity of the sensor. When the nanorods array, the surface area increases, enabling UV light to be absorbed more effectively and to generate more electron–hole pairs. The responsivity is defined as the generated photocurrent per unit power of incident light on the effective area of the photodetector and external quantum efficiency (η) is nothing but the number of electron-hole pairs generated due to the one absorbed photon of energy hν .The responsivity and quantum efficiency of a device has been at 1V applied bias which calculated by equations 5 and 6 as a function of wavelength. The results are depicted Fig. 9 by using the relation (12) [27]

$$Responsivity\ ratio = \frac{R_{doped}}{R_{undoped}} \tag{12}$$

It is observed that the responsivity of devices cu-doped ZnO (B1 B2) shows higher and shifted at low wavelength, there are based UV photodetector device is highly responsive in UV region and prominently does not show photoresponse to visible region, which is credited to the wide band gap energy of ZnO so that no charge carrier is excited at low energy visible photons.

Table 1: represent as name and ratio Cu-doped ZnO for samples used in this paper		
samples	element	atoms ratio Cu/Zn doped ZnO
A	pure ZnO	0
B1	Cu	0.025
B2	Cu	0.05

Table 2: The crystalline size, inter planar spacing, lattice… synthesized for the all samples							
names	h k l	2 θ°	FWHM 2 θ°	d (A)	a (nm)	c (nm)	ε
A	1 0 0	31.4839	0.2362	2.84159	3.04767895	---	0.056837464
	0 0 2	34.169	0.1181	2.62418	---	5.24836	0.028223447
	1 0 1	35.9584	0.0984	2.4976	---	---	0.023399956
B1	1 0 0	31.5573	0.1574	2.83514	3.05461248	---	0.037868761
	0 0 2	34.1996	0.1378	2.6219	---	5.2438	0.032928637
	1 0 1	36.0164	0.1968	2.4937	---	---	0.046792227
B2	1 0 0	31.01	0.0694	2.88153	3.00543601	---	0.01671922
	0 0 2	34.2232	0.1378	2.62015	---	5.2403	0.032926552
	1 0 1	36.089	0.1574	2.48885	---	---	0.037416564

Table 3: represent the changing Responsivity A/W as a voltage of w. (365 385) nm for all samples						
Voltage (V)	UV-365 nm			UV-385 nm		
	A	B1	B2	A	B1	B2
1	0.09903	0.6875	**0.83333**	0.07319	0.21528	**0.27083**
5	0.24097	1.71389	**1.84722**	0.13792	**0.59583**	0.51389
10	1.37361	2.86458	**2.93681**	0.96715	**0.97917**	0.79444

Table 4: represent the change quantum efficiency as a voltage at w. (365 385) for all samples						
Voltage (V)	quantum efficiency % UV-365 nm			quantum efficiency % UV-385 nm		
	A	B1	B2	A	B1	B2
1	0.33676	2.33797	**2.8339**	0.23598	0.69406	**0.87317**
5	0.81947	5.8284	**6.28182**	0.44465	**1.92098**	1.65679
10	4.67122	9.74155	**9.98715**	3.11813	**3.15686**	2.56131

Table 5: represent the change sensitivity as voltage at (365 385) nm for all samples						
Voltage (V)	sensitivity % UV-365 nm			sensitivity % UV-385 nm		
	A	B1	B2	A	B1	B2
1	312.83582	1514.28571	**1807.14286**	257.31343	542.85714	**650**
5	401.34607	1723.68421	**1871.71053**	272.47069	**664.47368**	608.55263
10	702.03926	2064.28571	**2119.04762**	523.89286	**771.42857**	650

Table 6: represent detectivity ($Hz^{1/2}$ W^{-1}) as function voltage for all samples						
voltage (V)	UV 365 nm			UV 385 nm		
	A	B1	B2	A	B1	B2
1	2.16534E6	1.82303E6	7.87231E6	14550.63116	8.59084E6	5.02044E6
5	2.18054E7	1.7771E7	6.73166E7	147911.53757	7.46923E7	4.04761E7
10	5.05351E7	3.51028E7	1.50956E8	348000.48282	1.56133E8	7.61756E7

Table 7: represent the optimum ratio Responsivity (B1, B2) - Responsivity (A) for all samples

Voltage (V)	Responsivity B1- Responsivity A		Responsivity B2 - Responsivity A	
	UV 365 nm	UV 385 nm	UV 365 nm	UV 385 nm
1	0.58847	0.14208	0.73431	0.19764
5	**1.47292**	**0.45792**	**1.60625**	**0.37597**
10	1.49097	0.01201	1.56319	-0.17271

Table 8: result parameters of devices are measured at 5 v applied biases of all samples								
sample	UV 365 nm				UV 385 nm			
	Responsivity	quantum efficiency	sensitivity	detectivity	Responsivity	quantum efficiency	sensitivity	detectivity
A	0.24097	0.81947	401.34607	2.18054E7	0.13792	0.44465	272.47069	147911.53757
B1	1.71389	5.8284	1723.68421	1.7771E7	0.59583	1.92098	664.47368	7.46923E7
B2	1.84722	6.28182	1871.71053	6.73166E7	0.51389	1.65679	608.55263	4.04761E7

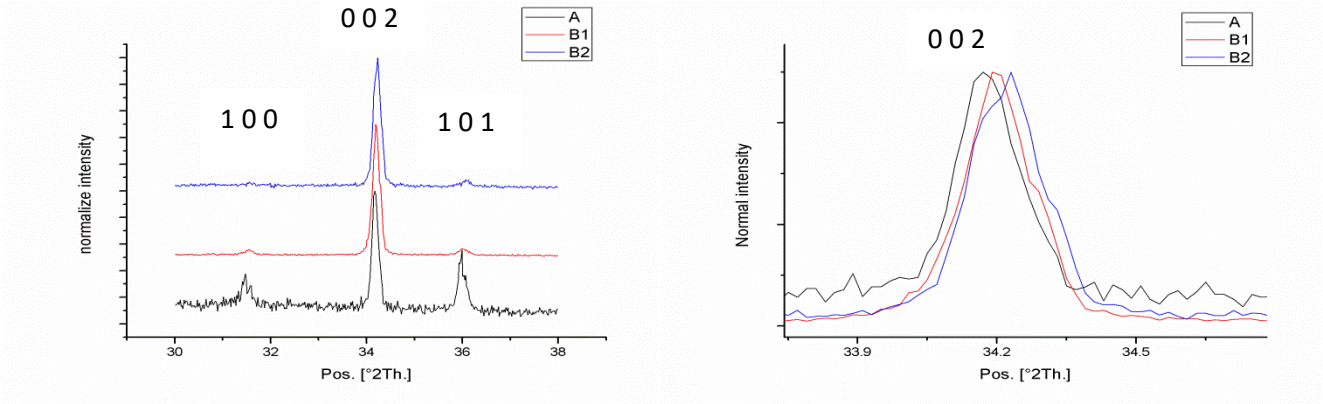

Fig. 1. XRD patterns (1 0 0), (0 0 2) and (1 0 1) peaks taken for pure ZnO and (0.025, 0.05) Cu-doped ZnO nanorods on glass substrates

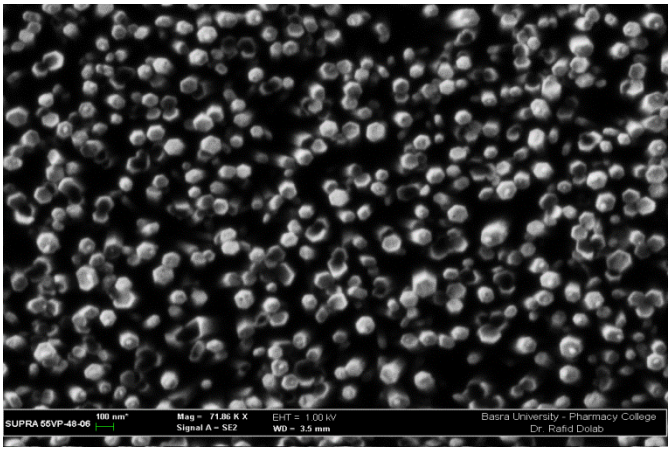

a

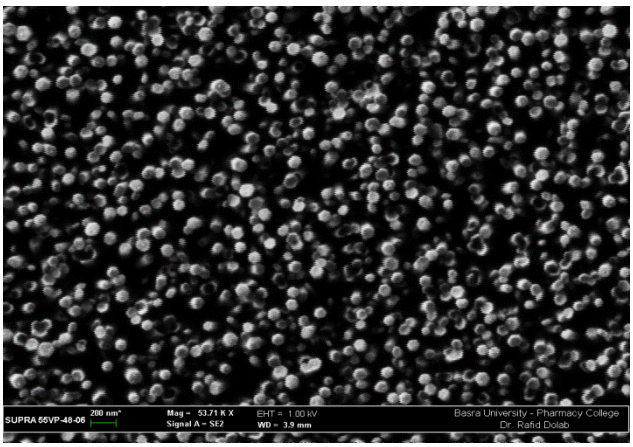

d

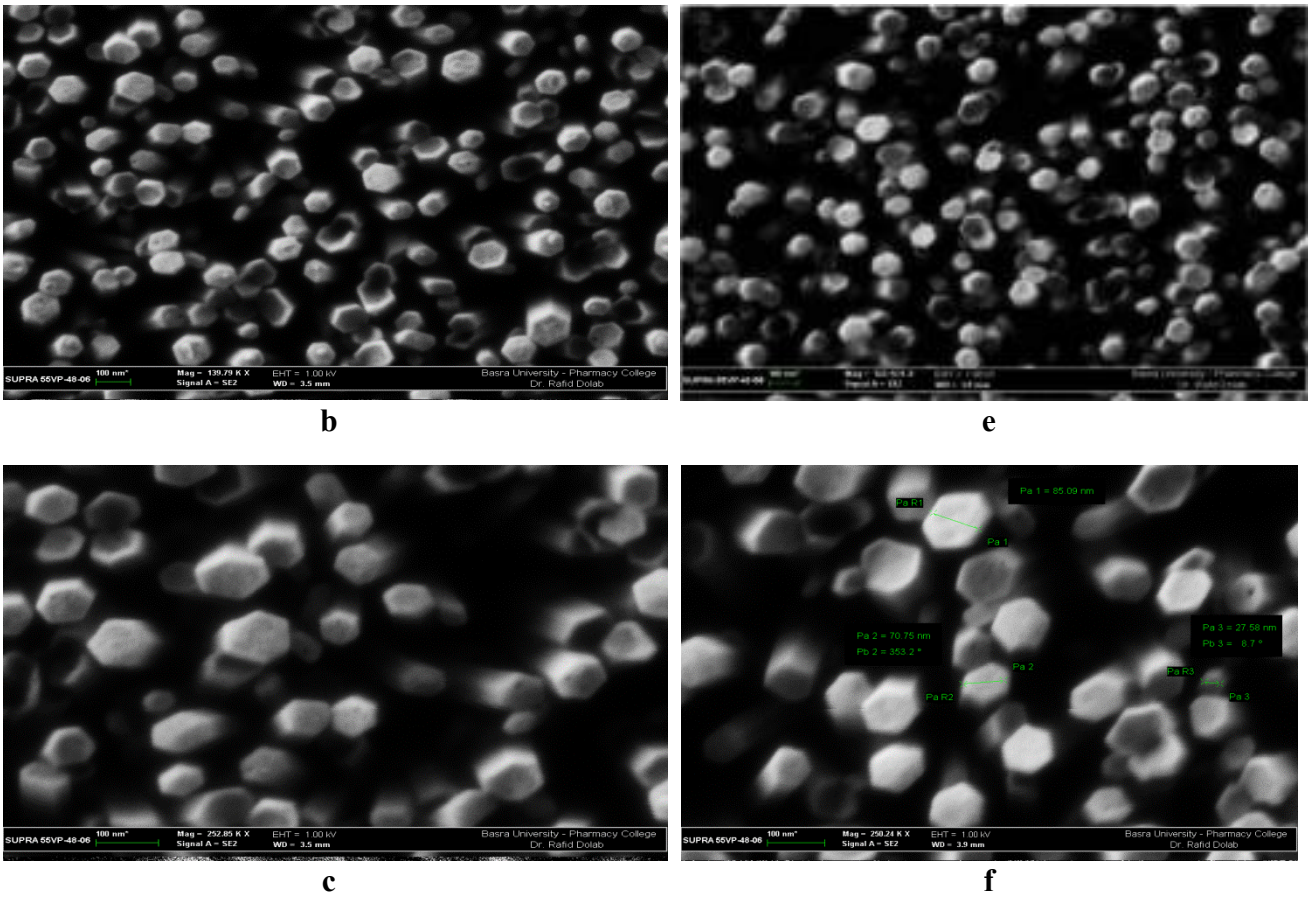

Fig.2 the FE-SEM image (a b c) of pure ZnO nanorods, (d e f) the FE-SEM image of (0.05) Cu doped nanorods**.**

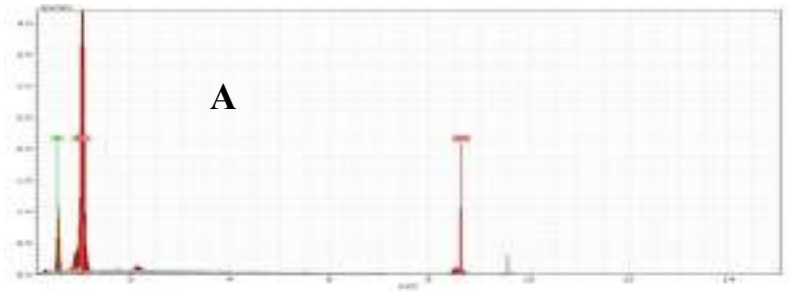

Spectrum: Acquisition

Element	Series	unn. C [wt.%]	norm. C [wt.%]	Atom. C [at.%]	Error (1 Sigma) [wt.%]
Zinc	L-series	72.94	75.20	42.60	4.69
Oxygen	K-series	24.05	24.80	57.40	4.06
	Total:	97.00	100.00	100.00	

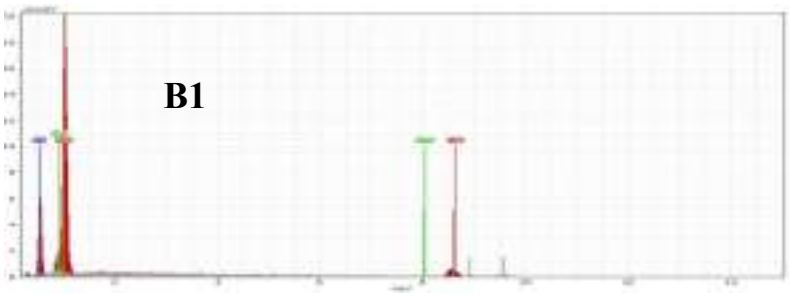

Spectrum: Acquisition

Element	Series	unn. C [wt.%]	norm. C [wt.%]	Atom. C [at.%]	Error (1 Sigma) [wt.%]
Zinc	L-series	68.68	73.67	41.74	4.49
Copper	L-series	1.45	1.56	0.91	0.67
Oxygen	K-series	23.09	24.77	57.35	4.41
	Total:	93.23	100.00	100.00	

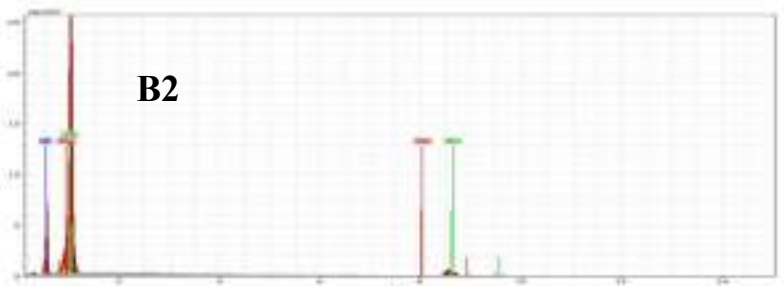

Spectrum: Acquisition

Element	Series	unn. C [wt.%]	norm. C [wt.%]	Atom. C [at.%]	Error (1 Sigma) [wt.%]
Copper	L-series	4.01	3.38	2.00	1.34
Zinc	L-series	86.15	72.71	41.81	5.62
Oxygen	K-series	28.33	23.91	56.19	5.37
Total:		118.49	100.00	100.00	

Fig. 3: EDX spectrum of Cu-doped ZnO (A B1 B2)

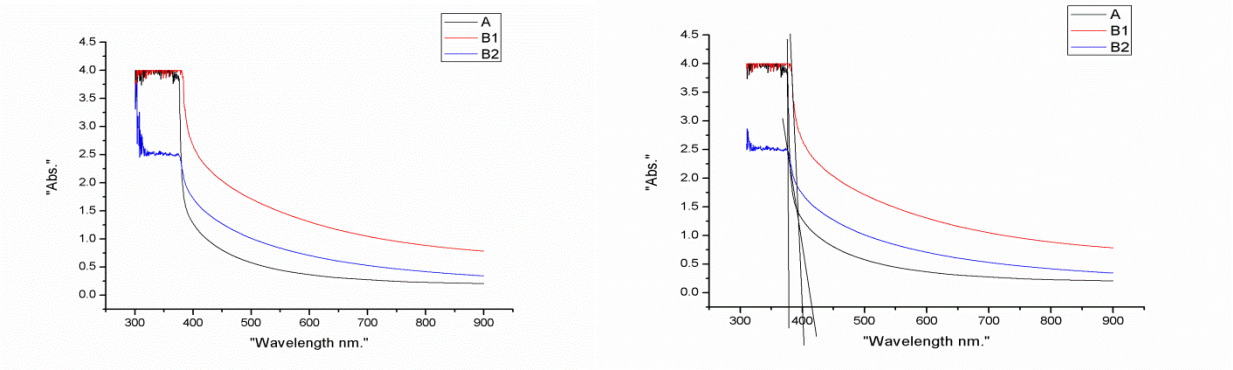

Fig. 4 Absorption spectra of pure and Cu-doped ZnO nanorods at different concentrations

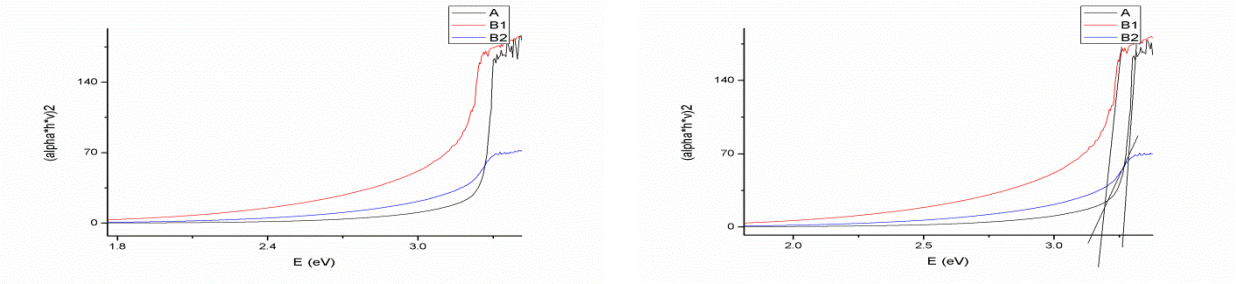

Fig. 5: Plot to determine the band gap energy for pure and different atoms ratio Cu-doped ZnO.

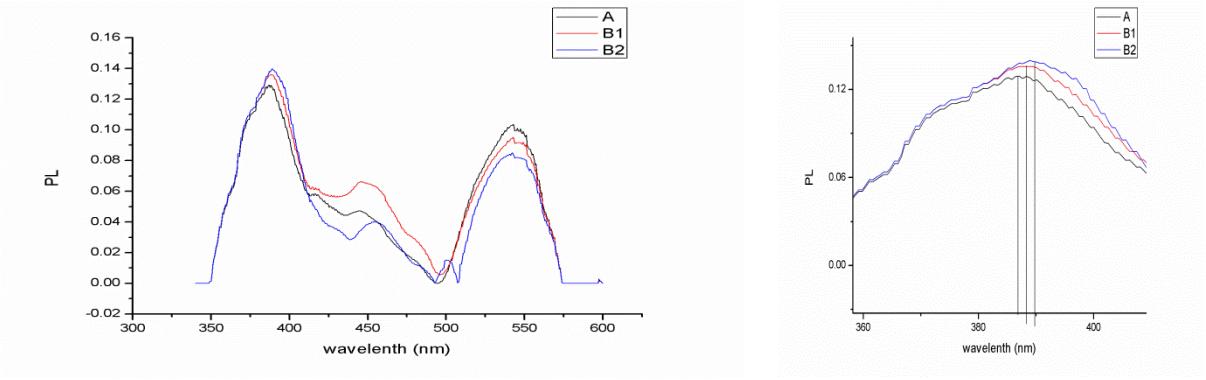

Fig. 6. R.T. PL spectra of undoped ZnO and Cu doped ZnO nanorods excited radiation with a 325nm

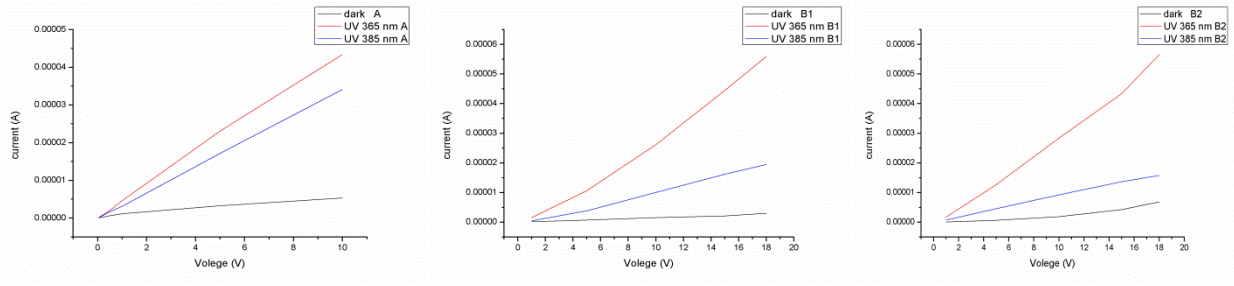

Fig 7 I–V characteristics of the ZnO MSM UV detector showing the dark current and photocurrent at 365 385 nm (power intensity = 40 μW/cm2).

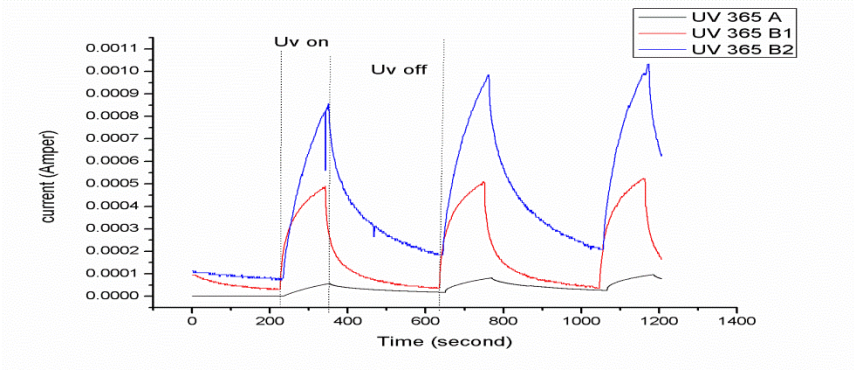

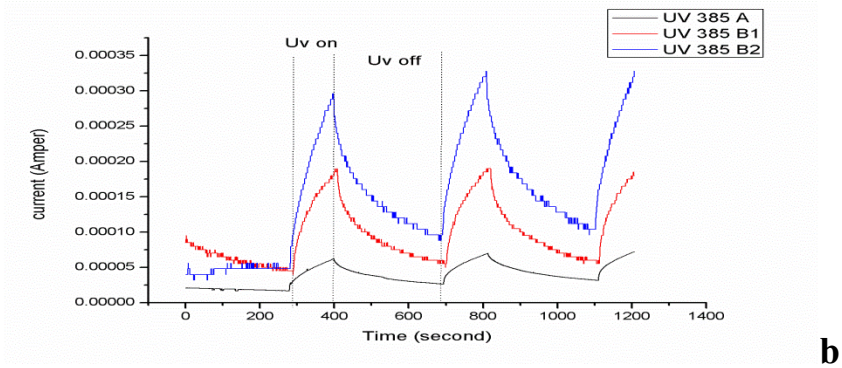

Fig. 8 Photoresponse of UV photodetector under (on off)(2 5) min a) UV 365 light b) UV 385 light

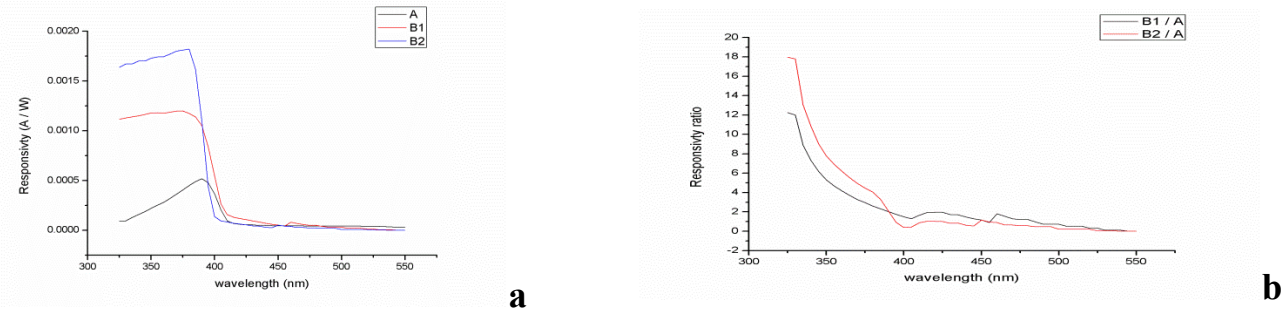

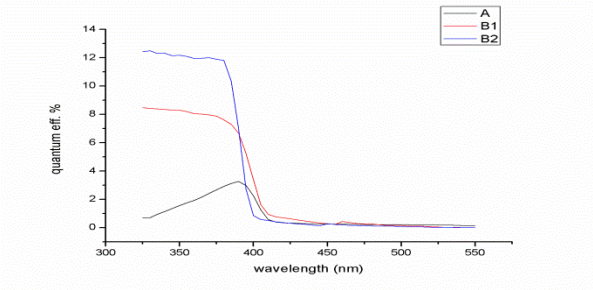

Fig.9 a) responsivity as wavelength (330-550) nm.
b) the ratio R of cu doped ZnO (B1 B2) onto R pure ZnO
c) Quantum eff. As wavelength (330-550) nm

4. Conclusions

In this work, pure and Cu doped nanorods of ZnO were successfully synthesized by hydrothermal method. The MSM UV has been fabricated and based on a pure and Cu-doped ZnO thin film. The photoresponse properties under UV illumination were studied at room temperature, the performance of the photodetector can be improved with respect to photocurrent, contrast ratio, dark current and detectivity. The MSM UV based on a Cu-doped ZnO has showed enhanced responsivity and quantum efficiency and others parameters show in Table 8 compared to that pure ZnO at shifted low wavelength.

References

1. Ali, G.M. and P. Chakrabarti, ZnO-based interdigitated MSM and MISIM ultraviolet photodetectors. Journal of Physics D: Applied Physics, 2010. 43(41): p. 415103.
2. Mamat, M., et al., Fabrication of an ultraviolet photoconductive sensor using novel nanostructured, nanohole-enhanced, aligned aluminium-doped zinc oxide nanorod arrays at low immersion times. Sensors and Actuators B: Chemical, 2014. 195: p. 609-622.
3. Zhou, H., et al., The investigation of Al-doped ZnO as an electron transporting layer for visible-blind ultraviolet photodetector based on n-ZnO nanorods/p-Si heterojunction. Materials Science in Semiconductor Processing, 2015. 38: p. 67-71.
4. Garcés, F., et al., Structural analysis of ZnO (: Al, Mg) thin films by X-ray diffraction. Procedia Materials Science, 2015. 8: p. 551-560.
5. Özgür, Ü., et al., A comprehensive review of ZnO materials and devices. Journal of Applied Physics, 2005. 98(4): p. 11.
6. Djurišić, A., A. Ng, and X. Chen, ZnO nanostructures for optoelectronics: material properties and device applications. Progress in quantum electronics, 2010. 34(4): p. 191-259.
7. Wu, C., et al., Effects of growth conditions on structural properties of ZnO nanostructures on sapphire substrate by metal–organic chemical vapor deposition. Nanoscale research letters, 2009. 4(4): p. 377.
8. Thaweesaeng, N., et al., Structure properties of as-synthesized Cu-doped ZnO nanopowder synthesized by co-precipitation method. Energy Procedia, 2013. 34: p. 682-688.
9. Singhal, S., et al., Cu-doped ZnO nanoparticles: synthesis, structural and electrical properties. Physica B: Condensed Matter, 2012. 407(8): p. 1223 1226.
10. Mohan, R., K. Krishnamoorthy, and S.-J. Kim, Enhanced photocatalytic activity of Cu-doped ZnO nanorods. Solid State Communications, 2012. 152(5): p. 375-380.
11. El Hallani, G., et al., Comparative study for highly Al and Mg doped ZnO thin films elaborated by sol gel method for photovoltaic application. Journal of Applied Physics, 2017. 121(13): p. 135103.
12. Fu, M., et al., Sol–gel preparation and enhanced photocatalytic performance of Cu-doped ZnO nanoparticles. Applied Surface Science, 2011. 258(4): p. 1587-1591.
13. Liu, J., et al., One-step hydrothermal synthesis and optical properties of aluminium doped ZnO hexagonal nanoplates on a zinc substrate. CrystEngComm, 2011. 13(5): p. 1283-1286.
14. Lupan, O., et al., Synthesis and characterization of Ag-or Sb-doped ZnO nanorods by a facile hydrothermal route. The Journal of Physical Chemistry C, 2010. 114(29): p. 12401-12408.
15. Habibi, M. and M.K. Sardashti, Structure and morphology of nanostructured zinc oxide thin films prepared by dip-vs. spin-coating methods. Journal of the Iranian Chemical Society, 2008. 5(4): p. 603-609.
16. Chow, L., et al., Synthesis and characterization of Cu-doped ZnO one-dimensional structures for miniaturized sensor applications with faster response. Sensors and Actuators A: Physical, 2013. 189: p. 399-408.
17. Jiang, D., et al., Ultraviolet Schottky detector based on epitaxial ZnO thin film. Solid-State Electronics, 2008. 52(5): p. 679-682.
18. Chakraborty, M., A. Ghosh, and R. Thangavel, Experimental and theoretical investigations of structural and optical properties of copper doped ZnO nanorods. Journal of Sol-Gel Science and Technology, 2015. 74(3): p. 756-764.
19. Xia, C., et al., Room-temperature ferromagnetic properties of Cu-doped ZnO rod arrays. Bulletin of Materials Science, 2011. 34(5): p. 1083-1087.
20. Palni, P.P., et al., Effect of annealing on high quality zinc oxide nanowires synthesized by catalytic vapor-deposition. Nano Trends: J Nanotechnol Appl, 2007. 3: p. 1-6.
21. Yılmaz, S., et al., Effects of Cu diffusion-doping on structural, optical, and magnetic properties of ZnO nanorod arrays grown by vapor phase transport method. Journal of Applied Physics, 2012. 111(1): p. 013903.
22. Wang, J. and L. Gao, Hydrothermal synthesis and photoluminescence properties of ZnO nanowires. Solid State Communications, 2004. 132(3-4): p. 269-271.
23. Jun, J.H., et al., Ultraviolet photodetectors based on ZnO nanoparticles. Ceramics International, 2009. 35(7): p. 2797-2801.
24. Hsu, C.L. and S.J. Chang, Doped ZnO 1D nanostructures: synthesis, properties, and photodetector application. Small, 2014. 10(22): p. 4562-4585.

25. Ali, G.M., S. Singh, and P. Chakrabarti, Fabrication and characterization of ZnO photodetectors with high gain. Journal of Nanoelectronics and Optoelectronics, 2009. 4(3): p. 316-320.
26. Sharma, P., K. Sreenivas, and K. Rao, Analysis of ultraviolet photoconductivity in ZnO films prepared by unbalanced magnetron sputtering. Journal of Applied Physics, 2003. 93(7): p. 3963-3970.
27. Chey, C.O., et al., Synthesis of Fe-doped ZnO nanorods by rapid mixing hydrothermal method and its application for high performance UV photodetector. Journal of Nanomaterials, 2014. 2014: p. 222.

Available online at
http://namrc.uotechnology.edu.iq/index.php/

Nanotechnology and Advanced Materials Research Centre

Proceeding Articles Book 00 (2018) 000–000

6th International Scientific Conference on Nanotechnology, Advanced Materials and its Applications

Toxicity assessment of porous silicon nanoparticles In-vivo

Majid S. Jabir [1], Kareem H. Jwaid[2], Uday M.Nayef [1], Zainab J. Taqi[1], Nada R. Ahmed[3], ButheniaAbd-Alhamza[1]

[1]Departent of Applied Science, University of Technology, Baghdad, Iraq
[2]Department of medical Engineering, University of Technology, Baghdad, Iraq
[3]Department of biology, University of Baghdad, Baghdad, Iraq

Abstract

Nanoparticles are a special group of materials with unique features and extensive applications in many biomedical and chemicals fields. In the present study porous silicon nanoparticles are prepared by electrochemical etching method and pulse laser ablation Nd:YAG laser and their toxicity are tested using lab. Animal model. We confirmed the synthesis of porous silicon nanoparticles using UV-Vis spectrophotometer, and XRD. The toxicity effect of these nanoparticles on animals body weight, kidney, and liver function parameters were studied by injected of porous silicon nanoparticles in the intraperitoneal cavity at concentration (125, 250, 500 µg\kg). The results of biochemical assay (GOT, GPT, Creatinine and Urea Blood) compared with the control groups, for a period of four weeks. shows PSNs had no toxic effect in body weight, and kidney and liver function.

Keywords: PS nanoparticles, Kidney, liver function, toxicity.

1- Introduction

Porous silicon nanoparticles (PSNPs) have been widely used for variety biomedical applications, such as anti- cancer cell agent, biosensors, novel drug delivery, radiotherapy and others because of their easy surface modification as well as optical properties and electronic [1]. Recently PSNPs have been used in the treatment of rheumatoid arthritis and tumors [2]. Nanoparticles have single properties unlike from bulk-sized materials, involved volume ratios to large surface area, strong interaction with biological conditions, in height reactivity, and related to their less size. The toxicity of PSNPs has been described in vitro and in vivo [3]. There are different results have been demonstrated, depending on experimental conditions, such as size of particle, time to exposure, concentration, and animal models [4]. There is study demonstrated the toxicity of PSNPs with size (13.5 nm) using mice after injected them intraperitoneal, or oral and intravenous, respectively, the results of this study show that tail vein injection of PSNPs had fewer toxicity effects compared oral or intraperitoneal injection [5]. Other study demonstrated that the toxicity of PSNPs by intravenous injection, and intraperitoneal, although its toxicity, the results has not been widely explored [6]. This study was designed to evaluate toxicity PSNPs after intraperitoneal dose injection to mices and some of biomedical parameters are measured.

2- Materials and Method

Preparation of PSNPs

Porous silicon (PS) samples have been prepared by the electrochemical etching method using silicon wafers (100) oriented boron doped of diameter 7.6 cm resistivity (1.5-4) Ω.cm, thickness (550±50) nm and has central circular of 5.5cm^2. The electrolyte was 1:1 (v/v), hydrofluoric acid (24%) and ethanol (99.9%). The PS films were obtained by anodizing the silicon wafers for etch time (40) min. with current etch density of (80) mA/cm^2. Where the HF container made from Teflon because the Teflon has high resistance to HF and to avoid any chemical reaction with HF. The way was utilized for removing the porous layer from Si substrate by using current etch density of (250) mA /cm^2 for (30) sec. Next the sample was rinsed with pentane and ethanol and dried film was then milled with ball mill to obtain NPs. The nanoparticles then dissolved with deionized water and put into the ultrasound device for (4) hrs. The nanoparticles were then produced through a filter that passed nanoparticles size up to the 0.22 µm. Finally, nanoparticles prepared was

treated with post-laser under the conditions of *Nd–YAG* laser of wavelength1064 nm and laser energy (350) mJ for the purpose to obtaining smaller size of PSNPs.

Laser system

A pulsed Q-switched, *(Nd:YAG*) laser system at 1064 nm wavelength with maximum energy 350 mJ per pulse was used for the treatment of the samples. The output pulse duration was (9) ns and repetition rate of (1) Hz. Beam diameter of 2.4 mm was used for post laser. Figure (2) explain the details of laser system.

Characterization of PSNPs

UV-Vis spectrophotometer

spectrophotometer (Metertech,SP8001spectrophotometer, Japan) was employed for the optical analysis of PSNPs at within the spectral range (250-1250) nm for PSNPs.

X – ray Diffraction (XRD)

XRD (Philips. PW, Japan) was used to confirm the structure. It was scanned in the range of 2θ (20˚- 80˚).

Toxicity of PSNPs *in – vivo*

The toxicity of PSNPs *in-vivo* was studied using experimental animals (mice) at age of (8) weeks and weight ranged from (20-25) grams were randomly divided into five groups and three mice for each group:

- **First group:** the mice are injected intraperitoneal with the physiological phosphate solution (PBS) as a negative control.
- **Second group** injected with 125 µg/kg with PSNPs and left for a week.
- **Third group** injected with 250 µg/kg with PSNPs and left for two weeks.
- **Fourth group** injected with 500 µg/kg of PSNPs and left for three weeks.
- **Fifth group** injected with 500 µg/kg with PSNPs and left for four weeks. The mice were weighted before and after the injection of PSNPs. After that the animals were anesthetized by exposure to a quantity of ethyl ether $(C_2H_4)_2O$. Blood withdrawn from the heart through the heart puncture to obtain the largest quantity of blood. Blood samples were collected in test tubes free of anticoagulant and left for (15-20) min at room temperature and then centrifuged for 5min at 5000 rpm for collect serum samples [9] .

Study of biochemical parameters

To measure the effect of PSNPs on the liver functions have been done according to instruction of (Randox Company). Alanine Amino-Transferase (GPT), Aspartate Amino-Transferase GOT (AST) and Alkaline Phosphatase (ALP) were investigated. To measure the effect of PSNPs on renal function (Creatinine and blood urea), this tests were done using (BioMerieux. French). The OD was reading on a wavelength of 500,520 nm.

Statistical Analysis

The grouped data analysis were investigated by Graph Pad prism software for windows (version5.0,GraphPadSoftwere,Inc.San Diego,CA) [13].

3- Results and discussion

UV-Visible of PSNPs

Figure (1) shows the effect of using high-power laser on the PSNPs preparation by electrochemical method. It has been shown that the material became more nanoparticles and its effect appears in different concentrations 500 and 750 µg / ml. The first, second and third curves have a wavelength of 448 nm which have the highest absorption intersecting 1,0.85 and 0.7 respectively. The absorptions of curves were 0.9, 0.8 and 0.63 respectively. From this we conclude that the increase in concentration is due to increasing absorption. Thus increasing the laser energy causes a shift in optical absorption towards long wavelengths (red shift).The difference in absorption is also due to the percentage of crystalline concentrations and the defects in the material. The results indicates the important of laser in reducing the size of nanoparticles We also showed the energy gap values increased to high values from 1.85 to 2.5 nm than after the laser treatment. This indicates the size of PSNPs due to quantum confinement effect. Figure (2) and Table (1) represent the results of the optical power gap and particle size by different concentrations

Table (1): result Energy gap (eV) and Gran size (nm) at different concentrations 250, 500 and 750 µg/ml.

Concentration (µg/ml)	Gran size (nm)	Energy gap (eV)
250	5.2	2.5
500	5.8	2.3
750	5.6	1.85

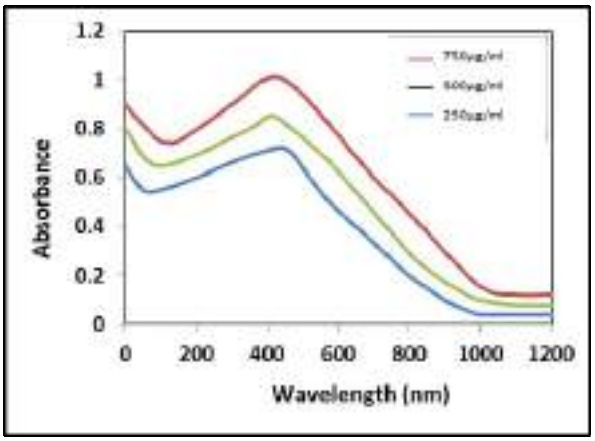

Fig (1): UV-Vis spectroscopy PSNPs by electrochemical etching method and high-power laser at different concentrations.

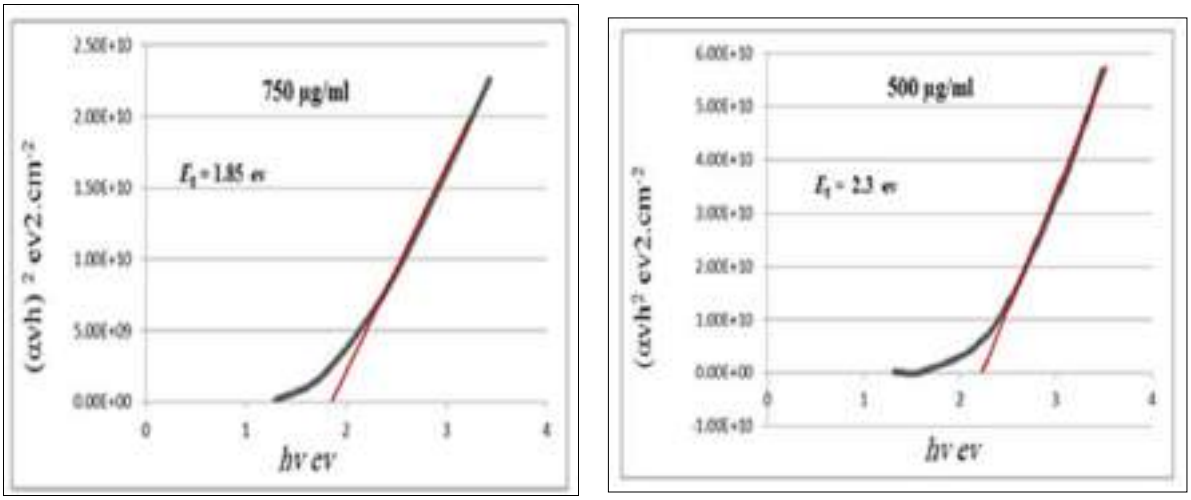

Fig (2): The optical band gap of the PSNPs prepared by electrochemical etching method use high-power laser at different concentrations 500 and 750 µg/ml.

X–Ray Diffraction

X-ray diffraction analysis of PSNPs prepared by electrochemical etching method and using high- power laser at different concentrations 250, 500 and 750 µg/ml. as shown in Figure (3), the results of X-ray diffraction of high-power laser treated PSNPs with energy of 350 mJ. We observed that the material became a smaller size and its effect is clear in different concentrations 250, 500, 750 µg/ml. Figure (3) shows at concentration of 250 µg/ml, a change in the intensity of the peaks and it increases in width when the diffraction angle 2θ is 28.5° and 47.4° corresponding to (111) and (220) where the particle size is 25.5° nm. Also, Figure (3) shows at concentrations of 500 µg/ml that intensity of the peak is sharp compared to the concentration of 250 µg/ml. The diffraction angle 2θ is 28.6° and the corresponding is (111) where the nanosize is about (36.6) nm. At a concentration of 750 µg/ ml indicates that the peak strength is sharper than the concentration of 500 µg/ml and the diffraction angle 2θ is 28.11° and the corresponding is (111) indicating that the nanometer is 55 nm. Increasing the laser energy increases the width of the peak and thus leads to a reduction in the nanoscale size as shown in table (2).

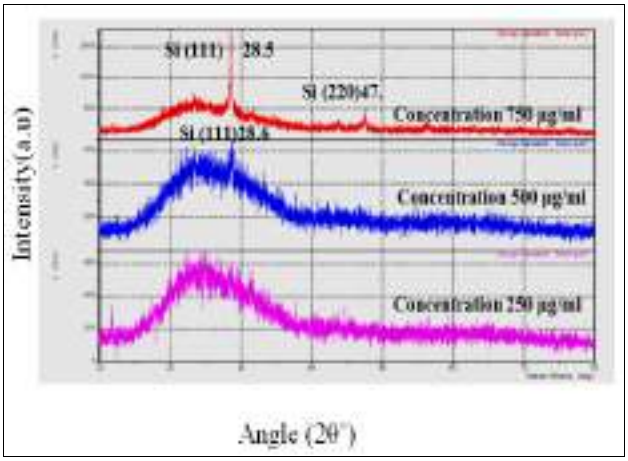

Fig (3): X-Ray diffraction of PSNPs preparation by electrochemical etching method and used high-power laser at different concentration.

Table (2): Show (d) inter-plane distance (a) lattice constant (L) nanosize for PSNPs at concentrations 250, 500 and 750 µg/ml.

Concentrations (µg/ml)	2θ (deg.)	FWHM (deg.)	d′ (nm)	a (nm)	L (nm)	phase
250	28.54	0.2322	0.3138	0.5435	25.5	111
500	28.54	0.2322	0.3138	0.5435	28.11	111
750	28.54	0.2322	0.3138	0.5435	55	111

Study the toxicity of PSNPs

The lab. Animals body weights were measured before and after injected with PSNPs. The results of the body weight showed no significant differences in the body weight among the treatment groups as shown in Figure (4).

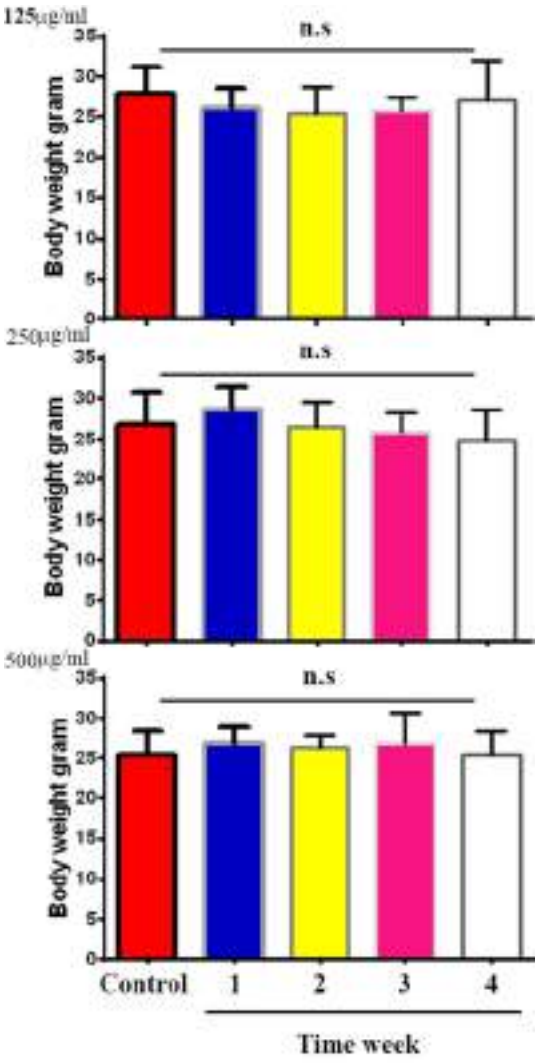

Fig (4): Effect of PSNPs in body weight of animal compared with control group.

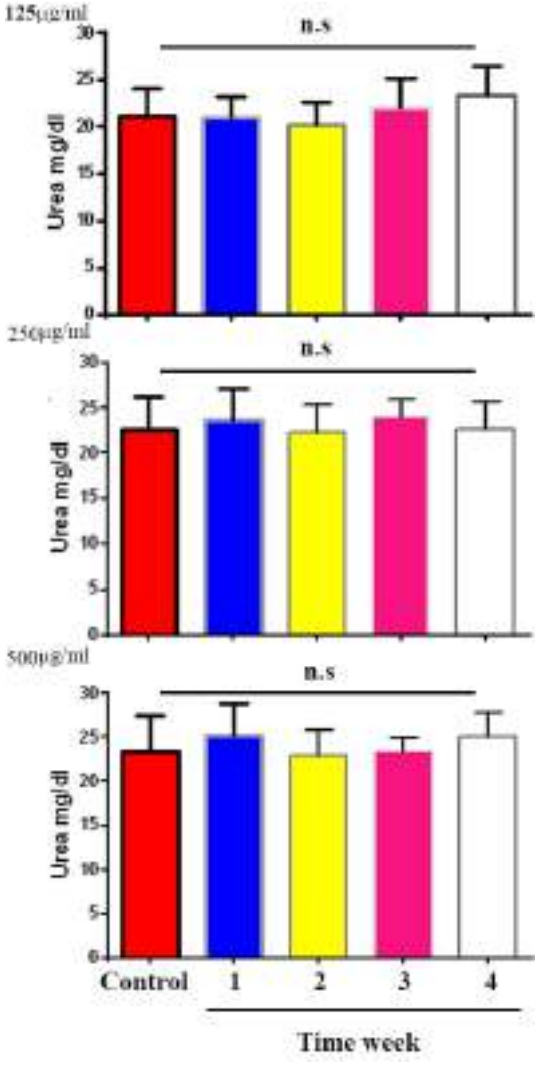

Fig (5): Effect of PSNPs in urea concentration.

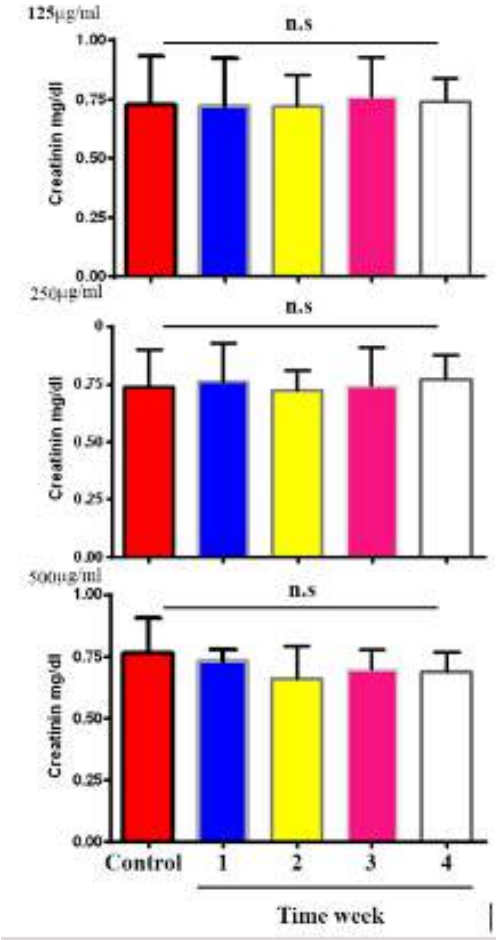

Fig (6): Effect of PSNPs in creatinine concentration.

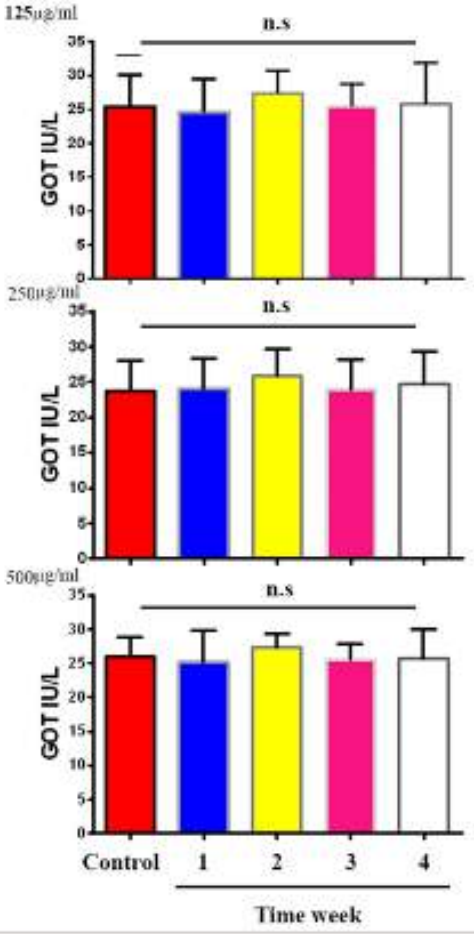

Fig (7): Effect of PSNPs on GOT concentration.

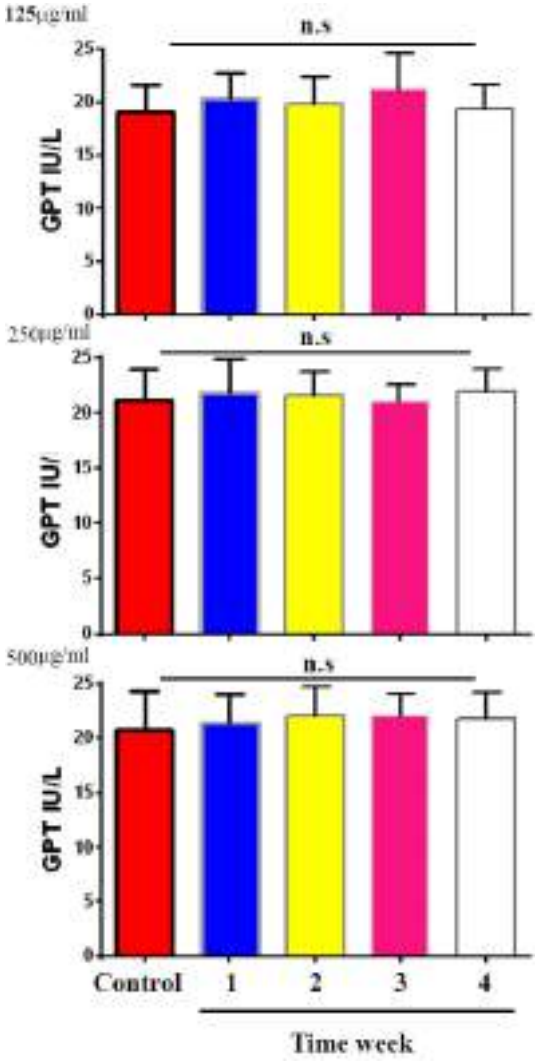

Fig (8): Effect of PSNPs on GPT concentration.

The results of the biochemistry tests of both kidney and liver functions were shown after injected of animals with PSNPs as indicated time and concentration. Kidney function tests for both urea and creatinine showed no significant differences between the treatment groups and the control group. This indicates that there is no toxicity to renal activity as shown in figure (5, 6), respectively. While the results of PSNPs toxicity on liver function had no significant differences between all groups as shown in figures (7,8) respectively. The use of high-power laser (1064) nm helped to reduce the size of nanoparticles by fragmenting nanoparticles into smaller size. This was proved by UV, and XRD tests, as the increases of the concentration mean an increases of the nanoparticles size. PSNPs had on side effects *in-vivo* using animal model.

4- Conclusion

SNPs had on side effects in-vivo using animal model. PSNPs were prepared using electrochemical etching method with a high-power laser. These particles are characterized by the fact that the ratio of surface to size increases millions of times, changing the physical and chemical properties compared to the material in its (bulk).

References

[1] Xie, J.; Lee, S.; Chen, X., Nanoparticle-basedtheranostic agents. Adv Drug Deliver Rev . 62, 1064-79, 2010.
[2]Couvreur, P., Nanoparticles in drug delivery: past, present and future. Adv Drug Deliv Rev . 65, 21-3, 2013.
[3] Choi, H. S. Renal clearance of quantum dots. Nature Biotech. 25,1165-1170 , 2007.
[4]Wang, R. B.; Billone, P. S.; Mullett, W. M., Nanomedicine in action: an overview of cancer nanomedicine on the market and in clinical trials. J Nanomater. 629-681, 2013.
[5]Liu, Z. Circulation and long-term fate of functionalized, biocompatible single-walled carbon nanotubes in mice probed by Raman spectroscopy.Proc. Natl Acad. Sci. USA . 105, 1410-1415, 2008 .
[6] Ballou, B., Lagerholm, B. C., Ernst, L. A., Bruchez, M. P. & Waggoner, A. S.Noninvasive imaging of quantum dots in mice. BioconjugateChem .15,79-86, 2004 .
[7] Ghassan.M. S., Majid S. J., Anaheed H. H., Nanoscale modification of chrysin for improved of therapeutic efficiency and cytotoxicity, Artificial cells, nanomedicine, and biotechnology, 1, 1-13 , 2018.
[8] Majid S. J., Gassan M. S., Zainab J. T., Dong L, Iraqi propolis increases degradation of IL-1β and NLRC4 by autophagy following Pseudomonas aeruginosa infection, Microbes and infection, 20, 89-100, 2018.
[9] Pinon-Lataillade,G.; Thoreux- Manaly, A.; Coffigny,H.; Masse,R. And Soufir,J.C" Reproductive toxicity of chronic lead exposure in male and female mice". Hum. Experiment. Toxicol., 14: 872-878,1995.
[10]Camargo M. M. P., and Martinez C. B. R., " Histopathology of gills,kidney and liver of a Neotropical fish caged in an urban stream" .Neotrop. Ichthyol., 5,327-336, 2007.
[11] Majid S. J., Ali A. T., Usama I. S., Zainab J. T., Ahmed M., Alyaa S. S., Novel of nano delivery system for linalool loaded on gold nanoparticles conjugated with CALNN peptide for application in drug uptake and induction of cell death on breast cancer cell line, Materials science and engineering C, 94, 949-964, 2019.
[12] Corina C., Flaviu T., Ioana I., Cristian M., Cornel I., Lucian M., Teodora " Assessment of silver nanoparticles toxicity in human red blood cells using ELISA and immunofluoresence microscopy technique " BIOTEC. MOLE. BIOL. NANOMED.,1 (1) , 2330-9318, 2013.
[13]Majid,S.:Neil,D.:DongLi,Hannah,K.:Panagiotis,T.:Daniel,P.:Alison.:Lee,H.:Anna,S.:Clare,B.:and ThomasJ" Caspase-1 Cleavage of the TLR adaptor TRIF Inhibits Autophagy andb-InterferonProduction during Pseudomonas aeruginosa Infection".CellHost&Microbe 15:214-227, 2014.
[14] Khawla S. Khashan, Majid S. Jabir,Farah A. Abdulameer. "Carbon Nanoparticles decorated with cupric oxide Nanoparticles prepared by laser ablation in liquid as an antibacterial therapeutic agent",Materials Research Express, 2018.
[15] Jabir, M. S., Taha, A. A. , Sahib, U. I. Linalool loaded on glutathione-modified gold nanoparticles: a drug delivery system for a successful antimicrobial therapy, Artificial Cells, Nanomedicine, and Biotechnology, 1,1-11, 2018.
[16]Lenshin A.S., Kashkarov V.M., Spivak Y. M.,Moshnikov V.A., "Investigations of Nanoreactors on the Basis of p-Type Porous Silicon: Electron Structure and Phase Composition", Materials Chemistry and Physics, Vol. 135, 293-297, 2012.

Available online at
http://namrc.uotechnology.edu.iq/index.php/

Nanotechnology and Advanced Materials Research Centre

Proceeding Articles Book 00 (2018) 000–000

6th International Scientific Conference on Nanotechnology, Advanced Materials and its Applications

Improvement the Wear Resistance for Grinding Ball of Horizontal Cement Mill in Kufa Cement Plant

Ali SadiqYasir[1], OdayKhadem Mohammed[2]
[1] College of Engineering, University of Kufa, Kufa, Iraq
[2] Ministry of Industry and Minerals, Kufa Cement Plant, Kufa, Iraq

Corresponding author: OdayKhadem@gmail.com

Abstract

The aim of the research is to reduce the wear rate of the grinding wheels used in horizontal cement mills the increase in the consumption rates of the grinding mill designed at 200 g / ton clinker. The samples of white cast iron were manufactured by specialized companies, Treadmill, ASTM 532 and DIN1695 German, micro hardness test, rigidity, wear test, chemical composition , SEM Due to lack of system and cost of processing from outside the country, HVOF high velocity oxy fuel system has been manufactured and used to coating the samples with thickness of (50,70,80μm) by tungsten carbides (WC). Samples were tested with wear test (pin on disc),and micro hardness test .The results show that presence of nano coating on sample surface will reduce the consumption rates for what by 50% and increase the survival of the grinding ball of cement mill for a period of approximately 2 years to 5 years with the possibility of non-replacement and repainting more than once and at a lower cost studied economically.
Keywords : High chromium cast white irons **;** Tungsten carbide Nano particles (WC) ; HVOF system; wear test.

1- Introduction

Cement grinding in two-compartment cement mills, the first, coarse grinding compartment is provided with a step lining that is suitable for large grinding media and ensures optimum lifting of the mill charge. The shell lining in the second compartment or in a one-compartment cement mill is a corrugated lining designed to obtain maximum power absorption and grinding efficiency. For special applications a classifying shell lining may be supplied for fine grinding in the mill. The ball charge mill consists of grinding media in various sizes (5mm) to ensure optimum grinding efficiency and easy maintenance. The size distribution of the grinding media in the coarse grinding compartment is designed to just crush the coarsest particles in the mill feed material and to ensure adequate fineness of the material passing the diaphragm[1]. For fine grinding, the charge consists of small balls, which ensures the best possible grinding efficiency without obstructing the material flow through the ball charge. The stone diaphragm between the grinding compartments effectively screens the material passing.

2- Materials and Method

Grinding Media:

Rotation of the mill causes the charge consisting of grinding media and feed material to be lifted over some distance by fraction between the media and the lining [2]. As Figure is shown (1)grinding media The height to which the charge is lifted depends on certain factors including:

1-Circumferential velocity of the mill.
2-Shape, size, and weight of the grinding media.
3-Friction between the lining and the grinding media.
4-Internal friction mill charge

Figure (1): Grinding Media

Material used

High chromium white cast irons (HCCIs):

In the form of castings heat treated are the alloys used to improved wear resistance and equipment longevity [3]. High chromium white cast irons (HCCIs casing and impellers, in piping components exposed to high wear such as bends, elbows and reducers, and also in breaker screens, wear liners, nozzle inserts, and cyclones. They generally Table **(1)** chemical composition high-chromium white cast iron ranging from 12 to 17 wt.% Cr and 2.3 to 3.4 wt.%C, with those two elements comprising the principal alloying additions .

Table (1) chemical composition high-chromium white cast iron

Element	C%	Si%	Mn%	P%	S%	Cr%	Mo%	Ni%	Al%	Co%	Cu%	Fe%
HCCI	2.3	0.867	o.67	0.03	0.o4	17	0.1	0.194	0.03	0.18	0.15	Bal.

Tungsten carbide Nan particles (WC)

Black hexagonal crystals; Melting point 2870 ° C, Boiling point 6000 ° C; Dissolved in mixed acid of nitric acid and hydrofluoric acid, also in aqua region; Insoluble in cold water; The relative density of 15.63; Strong acid resistance; High hardness, High elastic modulus; Use for the production of various alloys[4]. Producing high capability nano-crystalline or super fine horniness alloy, hard-face abrasion resistant spraying and petrochemical cracking catalyst; Chinless forming tools; Cutting tools; Mining tolls; Nano-composites (for enhanced hardness, strength, and wear resistance); Erosion-resistant coatings; Wear-resistance coatings; [5] Corrosion-resistant coatings; Wear-resistant parts .

Experimental work

The materials used in the production of the surface layer using thermal coating technique by Flame spraying technology. the equipment used in the coating process and the practical method used in coating samples of high-chromium white cast iron .There are three axes of practicality manufacturing models manufacturing thermal coating system and examination of models

Manufacturing of thermal coating system(HVOF) and Coating method:

The HVOF system was manufactured in the Laboratory of Applied Mechanics and the Nanotechnology; Department of Mechanical Engineering at Kufa University. The HVOF system was manufactured in the Laboratory of Applied Mechanics and the Nano technology. The coating was applied to the samples after the operation of the system. The oxygen rate to the acetylene was (2-1) and the flow rate of nano particle and the distance between the sample and nozzle was 10cm Figure (2) System dives (HVOF) [6]

Figure (2): System dives (HVOF)

HVOF Thermal Spray Technology

HVOF (High Velocity Oxygen Fuel) thermal spray technology allows us to apply coatings with extremely low porosity and high bond strength. A mixture of fuel and oxygen are combusted within a thermal spray gun producing temperatures near 6000¹F (3300 C).Powder particles are injected into the high-pressure gas stream created by the combustion and accelerate down the barrel of the spray gun at several times the speed of sound. At these speeds and temperature conditions, semi-molten particles adhere to the substrate with superior bond strength exceeding (10 Mpa). [7] During coating application, the product rotates methodically in front of the HVOF thermal spray gun until the coating builds to the specified thickness (50,70,80) by SEM test micrometer. This process creates the strongest bond and highest hardness value as compared to any other thermal spray process Figure (3) Process diagram.

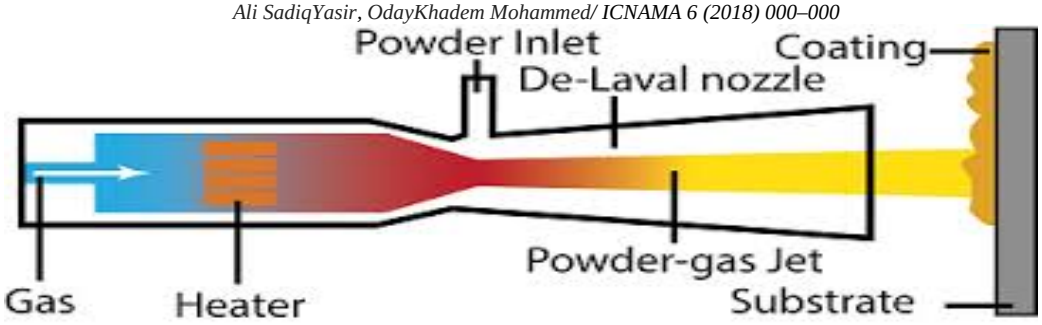

Figure(3):Process of coating with HVOF method

Manufacturing of wear pin-disc samples

The Samples of wear are manufacturing according to ASTM (G99-05) [8] with dimensions According to the dimensions of the American system pin &disc of metal white cast iron (Gx-26-Cr 17) as shown in the Figure(4) for a disk samples. The material of pin samples are made from white cast iron (Gx-26-Cr 17) by Silvan Turkish company. The chemical compositions of pin materials were tested in KARAMA general company, Baghdad as indicated as shown in the Figure(5)

1.Procedure the lathing of the samples to reach the required dimensions

2.The surface of the sample is smoothed to achieve the smoothness required for coating and testing at the Faculty of Engineering, University of Kufa.

figure (4): Sample of dick

figure (5): Sample of Pins

Method press coating

1. The samples by emery paper made of silicon carbide with a thickness of P120.
2. Place the samples at a suitable distance of 100 mm from the nozzle
3 - Install the samples on the surface of the thermal bricks
4 - Operation of the discharge system and the introduction of (Ar) gas into the spray chamber.
5. Operating the flame system with oxygen and acetylene ratios (2: 1) to heat the samples to 800 ° C
6. Spray the nanoparticles of tungsten carbide with three different times: 5, 10 and 15 seconds
7. Heat treatment where the samples were heated to 1100 ºC and a60-minute fixation time to ensure adhesion and homogeneity of the coated layer. Indicate the spray coating procedures.

Wear test of the pin on disk samples

Wear is a process of removal of material from one or both of two solid surfaces in solid state contact. As the wear is a surface removal phenomenon and occurs mostly at outer surfaces, it is more appropriate and economical to make surface modification of

existing alloys than using the wear resistant alloys.The pin was held against the counter face of a rotating disc is made from white cast iron (GX-260 Cr 17) according ASTM G99-05 as shown in the Figure(6)and (7).

Figure (6):Disc samples

Figure (7): divas test

The specimen is weighted after the test and the weight difference is calculated (w1-w2)and then calculating the wear rate using the relation

Wear rate $= \frac{dw}{sd}\left(\frac{g}{cm}\right)$ …… (1) (Firas Q. Mohmmad 2007)

Where;

Δw : the weight difference (g)

$$\Delta w = w1 - w2 \quad \text{…….(2)}$$

sd=The sliding distance (cm)and it is calculated using the relation

$$sd = 2\pi * r * n * t \quad \text{……3)}$$

3- Results and Discussion

Wear Test:

This test carried out according ASTM G99-05 for 12 samples without coating as indicated in the Table (2) and shown in the Figure (8) with angular velocity (400 and 600 r.p.m) and load 20, 40 and 60 N with test time 10 min. The samples were weighted before and after tests the weight loss were calculated. The best of weight loss percentage in samples without coating is (0.003798 %) at 400 r.p.m by 20N. while, the best of weight loss percentage in samples with coating thickness 70µm is (0.0020855 %) at 400 rpm by 20N with coating time 10 seconds. The coating thicknesses 50 and 80 µm were neglect because there is ablation coating layer in 80 µm and there is no enough thickness to wear test process.

Table (2):Wear test without coating.

no. sample	N (rpm)	force (N)	initial weight before wear(g)	final weight after wear(g)	weight loss	Weight loss %
wo1	400	20	72.2023	72.1995	0.0028	0.003877993
wo2		20	72.6177	72.615	0.0027	0.003718102
Wo3		40	73.2857	73.2811	0.0046	0.006276804
wo4		40	73.0966	73.0919	0.0047	0.006429848
wo5		60	74.902	74.8945	0.0075	0.010013084
wo6		60	73.4588	73.4511	0.0077	0.010482066
wo7	600	20	72.965	72.9612	0.0038	0.005207976
wo8		20	72.75	72.7463	0.0037	0.005085911
wo9		40	74.2221	74.2139	0.0082	0.011047922
wo10		40	73.2999	73.2919	0.008	0.010914067
wo11		60	74.0624	74.0522	0.0102	0.01377217
wo12		60	73.903	73.8922	0.0108	0.01461375

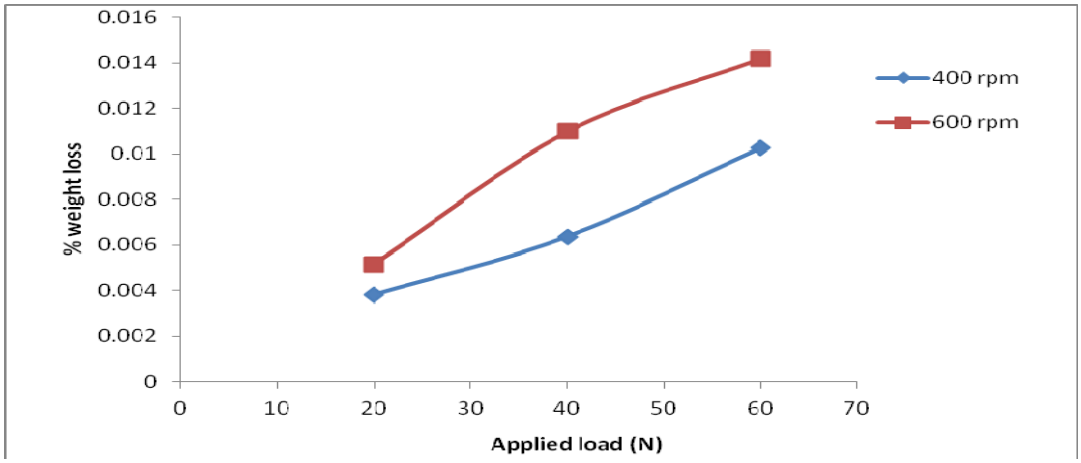

Figure (8) Applied load-% weight loss for specimens without coating.

Table (3) : Wear test for 10 sec

no. sample	N (rpm)	force (N)	initial weight befor coat (g)	initial weight after coat(g)	final weight after wear(g)	weight loss	Weight loss %
1	400	20	73.526	73.5285	73.5269	0.0016	0.002176
2		20	75.183	75.1855	75.184	0.0015	0.0019951
3		40	76.234	76.2366	76.2348	0.0018	0.0023611
4		40	73.989	73.9915	73.9898	0.0017	0.0022976
5		60	76.1877	76.1902	76.1883	0.0019	0.0024938
6		60	75.1814	75.1835	75.1815	0.002	0.0026602
7	600	20	73.526	73.5284	73.5267	0.0017	0.002312
8		20	76.3002	76.3025	76.3008	0.0017	0.002228
9		40	73.5112	73.5137	73.5117	0.002	0.0027206
10		40	74.4006	74.4031	74.4009	0.0022	0.0029569
11		60	75.4218	75.4238	75.4211	0.0027	0.0035798
12		60	76.2344	76.237	76.2344	0.0026	0.0034104

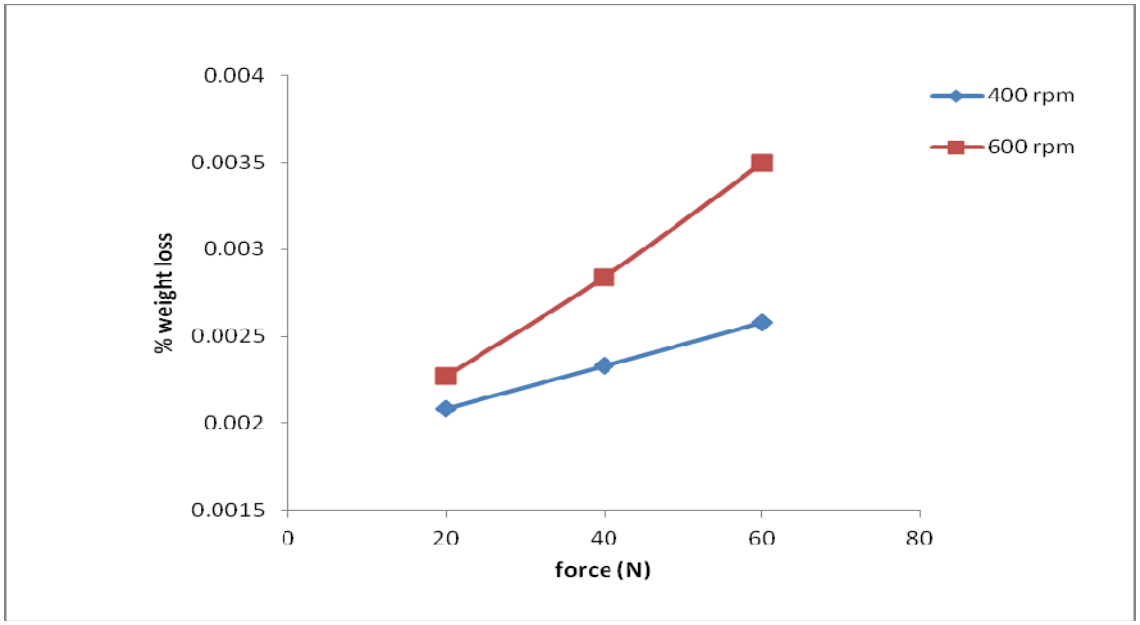

Figure (9) force-weight loss relation for specimens with 70µm coating thickness.

Table(4) :Wear test result

Force	without coating		with coating 5 sec		with coating 10 sec		with coating 15 sec	
	wear at N=400 without coat	wear at N=600 without coat	wear at N=400 with 5 sec coat	wear at N=600 with 5 sec coat	wear at N=400 with 10 sec coat	wear at N=600 with10 sec coat	wear at N=400 with15 sec coat	wear at N=600 with15sec coat
20	0.00275	0.00375	0.00155	0.0017	0.001275	0.001475	0.00115	0.001275
40	0.00365	0.00595	0.00175	0.0021	0.0016	0.001775	0.0013	0.0014
60	0.00465	0.0081	0.00195	0.00265	0.00185	0.00205	0.001575	0.00165

The test was carried out for pin and the disc for three types of samples, with different layers of paint, where the first group was 50, 60 and 80, and the feeding rate was a, and the coating time was 5, 10 and 15 seconds.

Relationship between Coating Thickness and Spray Time

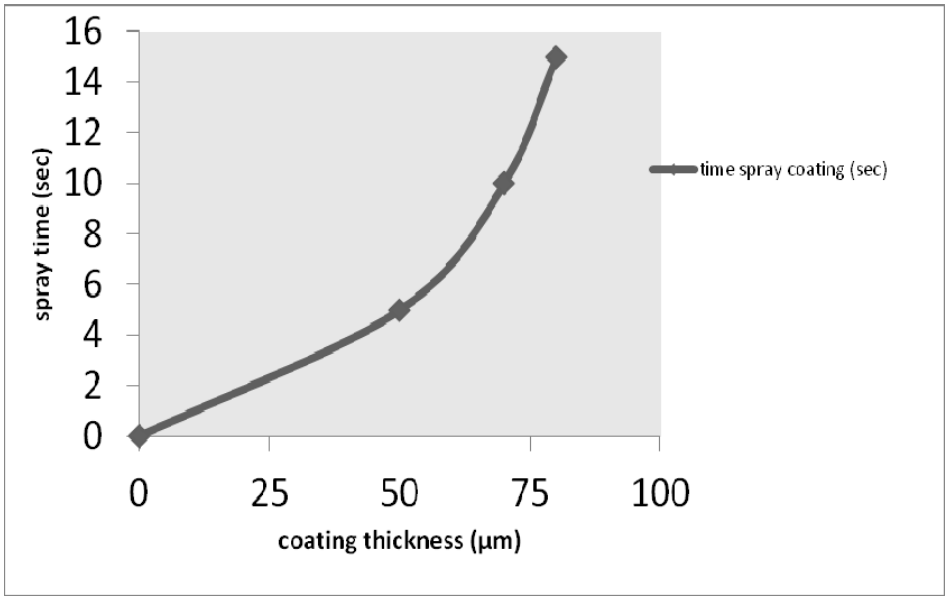

Micro Hardness test:

The micro hardness of samples carried for 8 samples as indicated in the table (5) and figures (5) with coating thickness 50, 70 and 80 µm. The used load was 4.905N and 10s (33%)for coated sample
Max-Min/Max…….(4)

Table(5) : Micro hardness HV

number	HV hardness without coating	HV hardness coating of spray time5 sec	HV hardness coating of spray time10 sec	HV hardness coating of spray time15 sec
1	554.9	600.3	669.1	740.2
2	556.4	585.2	671.4	742.1
3	555.8	595.4	670.9	737.2
4	556.4	580.7	674.1	733.4
5	554.9	579.4	671.6	734.8
6	556.1	582.1	678.2	742.2
7	554.7	577.4	674.6	743.7
8	557	578.2	676.8	740.8
total	4446.2	4678.7	5386.7	5914.4
average	555.775	584.8375	673.3375	739.3

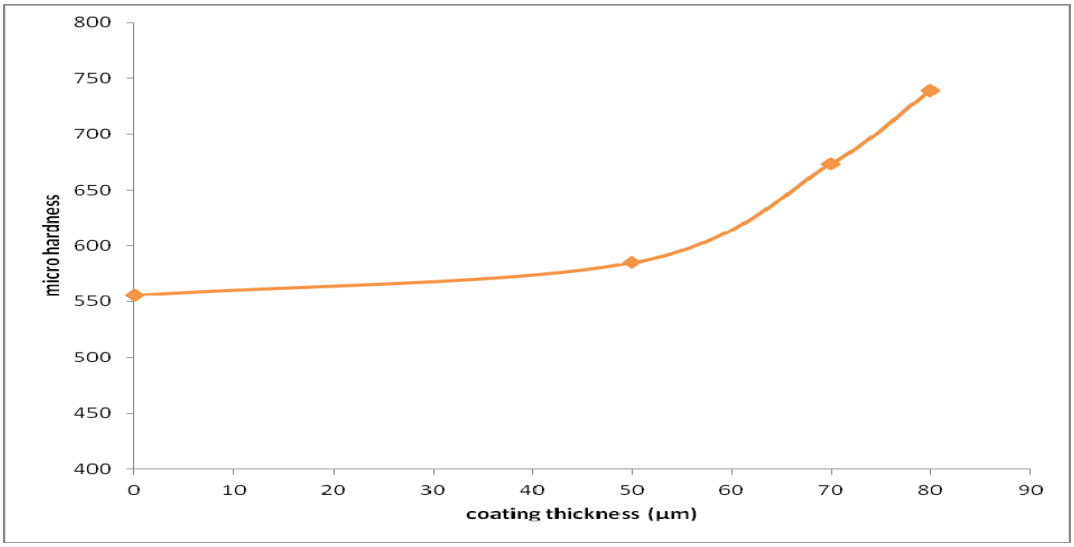

Figure(10):Micro hardiness spray time

Microstructure of Coated Samples:

The SEM test were done to calculate the thickness of coating layer for specimens for different coating time (5, 10, and 15)sec. This test were done for several specimens for each coating time .The measuring of coating thickness(70µm) the EDS . The percentage of the weight of tungsten was 13.74%.

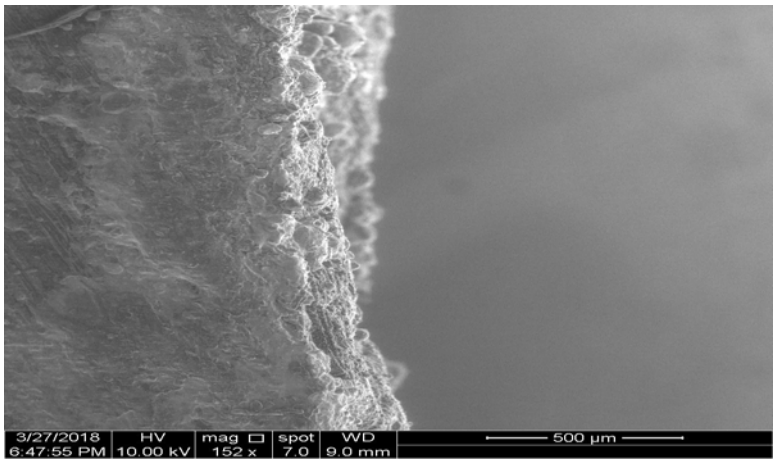

Figure (11) SEM morphology of layer thickness

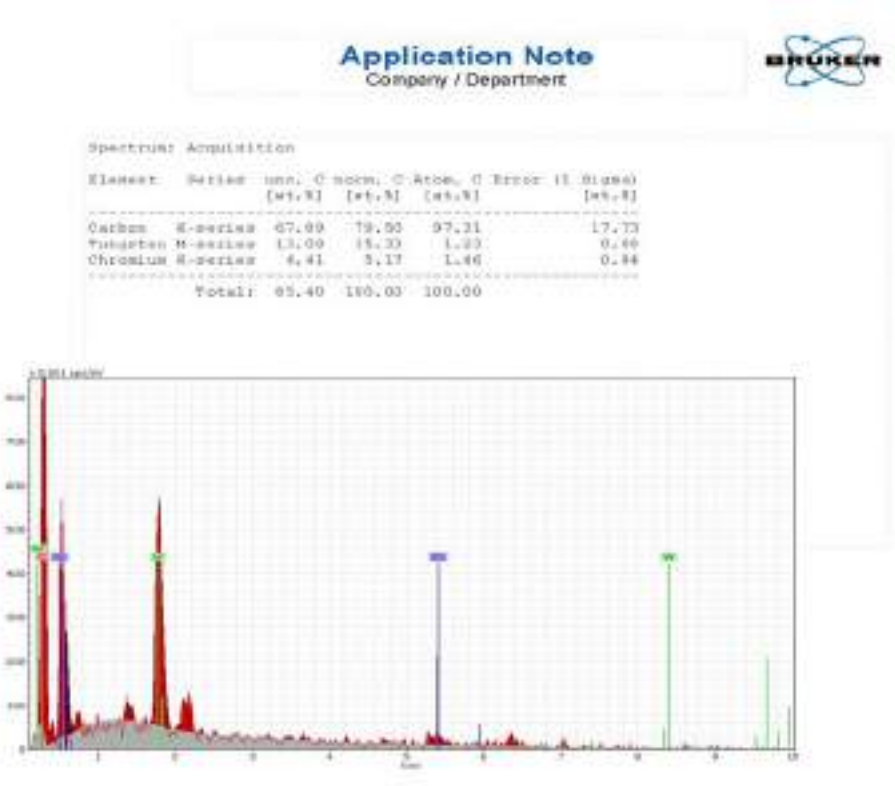

Figure (12):EDS spectrum for70 µm coating thickness.

4- Conclusion

1- The use of spraying flame on the surface of the lining of iron cast iron high chromium using advanced nanomaterials with high mechanical properties to improve the mechanical properties, including increased resistance to mechanical wear of the surface High-chromium white cast iron Gx-260 Cr17 and that lead to improving the wear resistance after coating about (50-66%).

2- The high temperature of the flame used in the coating process has sometimes led to the melting of part of the surface layer of the base metal at certain points. Thus increasing the bonding of the metal coating with the base metal.

3- As the thickness of the nano coating increases, there is an increase in micro hardness reach to (33%)for coated sample

References

[1] J.D. Gates, G.J. Gore, M.J-P. Hermand, M.J-P. Guerineau, P.B. Martin, J. Saad, "The meaning of high stress abrasion and its application in white cast irons", Wear 263 (2007) 6–35.

[2] M.S. Powell, N.S. Weerasekara, S. Cole, R.D. LaRoche , J. Favier ," DEM modeling of liner evolution and its influence on grinding rate in ball mills", Minerals Engineering 24 (2011) 341–351.

[*3*] D. Kopyciński, S. Piasny, M. Kawalec, A. Madizhanova, " The Abrasive Wear Resistance of Chromium Cast Iron", archives of found engineering volume e 1 4 , issue 1 / 2014 , 63 - 66

[4] A Santos, C Gonzalez and Z Y Ramirez, "Characterization of Tungsten Carbide coatings deposited on AISI 1020 steel", Journal of Physics: Conference Series 786 (2017) 012011

[5] Cecilio A. da Cunha, Nelson Batista, Jose Roberto M., Ana Helena de A. meida, Armando Fernando p. Lalgudi V. Ramanathan," Microstructure and Mechanical Properties of Thermal Sprayed Nanostructured Cr3C2-Ni20Cr Coatings", Materials Research, (2008) 11, (2), 137-143.

[6**]** Firas Q. Mohmmad, " studying the effect of some powders used in thermal spraying by flame one some of the mechanical properties of medium carbon steel", MS.c thesis in metallurgy engineering of universty of technology (2007).

[7] Magdy M. El Rayes, , Hany S. Abdo, and Khalil Abdelrazek Khalil," Review paper Erosion - Corrosion of Cermet Coating" *Int. J. Electrochem. Sci.,* 8 **(2013)** 1117 - 1137 .

[8] American standard of testing and material (ASTM), " Standard Test Method for Wear Testing with a Pin-on-Disk Apparatus " G 99 – 04 (2004).

Available online at
http://namrc.uotechnology.edu.iq/index.php/

Nanotechnology and Advanced Materials Research Centre

Proceeding Articles Book 00 (2018) 000–000

6th International Scientific Conference on Nanotechnology, Advanced Materials and its Applications

Synthesis and antibacterial activity of hematite α-Fe_2O_3 nanopowder prepared by hydrothermal process

Rashed T. Rasheed , Sariya D. Al-Algawi, Hadeel S. Mansoor, Zeena R. Rhoomi
[1] School of Applied Sciences department, University of Technology, Baghdad, Iraq
Corresponding auther: r_awsy@yahoo.com

Abstract

The iron oxide nanopowder hematite type (α-Fe_2O_3) have been prepared by hydrothermal technique at annealing temperature 400℃, and characterized by X-ray diffraction (XRD), atomic force microscopy (AFM), surface morphology by scanning electron microscopy (SEM), spectroscopy of Ultra-violet/visible and FT-IR spectra. The effect of Fe_2O_3 was tested against Gram-positive; *Staphylococcus aureus* and Gram-negative; *Escherichia coli*, has been studied. This study showed that Fe_2O_3 powder has efficient antibacterial activity, and can use as an antibacterial agent for different purposes.

Keywords: α-Fe_2O_3, X-ray Diffraction, Morphology, hydrothermal method, antibacterial properties.

1- Introduction

Iron oxides are of great scientific and technological importance in fields of catalysts, pigments and gas sensors [1]. α-Fe_2O_3 is an n-type semiconductor, having a small band gap (2.1 eV) [2] and is the most stable iron oxide under ambient conditions. Because of its small band gap, hematite can absorb about 40% of the sunlight [3] which is an important advantage for its use in solar energy conversion, a hexagonal structure, exhibit paramagnetic behavior and semiconducting properties under ambient conditions, Hematite is the most researched and most frequently polymorph in nature and its wide technological importance in pigments, catalysis, electrode materials, strong catalytic activity, widely and easily available, and are extremely environment friendly. Iron oxide particles are synthesized by different methods such as the sonochemical route [4], coprecipitation [3], solid-state chemical reaction [5], hydrothermal methods [2], sol-gel [6] and mechanical methods [7]. It was observed that the nanoparticles manifested very different physical and chemical properties depending on their microstructure, such as size uniformity and crystallinity. Therefore, developing a synthesis method that can maintain size uniformity and crystallinity is critical for the application of these nanoparticles [8].The hydrothermal method in wet methods is easy to operate, plus its reaction conditions are simple to handle. So it is a relatively simple preparation method in terms of technical equipment the hydrothermal process proceeds with aqueous and/or non-aqueous systems as the reaction medium and is environmentally friendly since the reactions are carried out in a closed system. The phase, particle size and crystallinity can easily be controlled by hydrothermal conditions [9]. In particular, the particles prepared by hydrothermal synthesis are expected to have the uniform-sized large surface area, smaller crystallite size and higher stability than those obtained by other methods.

2- Materials and Method

Iron oxide nanopowder was synthesized by hydrothermal method inside an autoclave, via the reaction of ferric chloride anhydrous ($FeCl_3$) with urea(NH_2CONH_2). Ferric chloride anhydrous (2.5 g) was dissolved in distilled water (20 ml). The solution was kept at 25˚C for 10 min. in a beaker to ensure complete dissolution. Meanwhile, (1.4 g) of urea, was dissolved in distilled water (10 ml.) on a magnetic stirrer at 25°C for 10 min. Until it became colorless. The two solutions were mixed and stirred with a magnetic stirrer at 25°Cfor 20 min. The mixed solutions were then put into an autoclave (as mentioned above), without the adding any of structure directing agents. Then placed in the oven and heated to 200°C for 12 h. Then, allowed the autoclave cool to room

temperature naturally. The reddish-brown sediment is wash in water distillery (about 5 times) then collected by centrifugation, then washed with ethanol (2 times), and then the precipitate was dried in an oven at 100°C for 120 min. Dark red color precipitate convert when annealing at 400°C.

The reaction took place between iron chloride and urea as following steps:

1. $3NH_2CONH_2 + 9H_2O \rightarrow 6NH_4OH + 3CO_2$ …….…..…. (1)
2. $2FeCl_3 + 6\ NH_4OH \rightarrow 2Fe(OH)_3 + 6NH_4Cl$ ……..……. (2)
3. $2Fe(OH)_3 \xrightarrow{Heat} Fe_2O_3 + 3H_2O$ …….…… (3)

The final equation is:

$2FeCl_3 + 3NH_2CONH_2 + 6H_2O \xrightarrow{Heat} Fe_2O_3 + 6NH_4Cl + 3CO_2$ …… (4)

3- Results and discussion

3.1 Characterization of nanopowder

The XRD is employed for the identification and understanding the crystalline growth nature of α-Fe_2O_3 nanoparticles prepared by hydrothermal method at annealing temperature 400℃, Fig. (1) shows the diffraction peaks for the planes (012) , (104) , (110) and (113) at (2θ = 24.1, 32. 9, 35.6 and 40.8) that conformity to the α-Fe_2O_3 hematite phase in the cards [JCPDS No. 13–534], and agreement with references [10], and based on that the grain size for that peak alone calculated, using the Debye - Scherer formula [11]:

$$D = k\lambda / \beta\cos\theta \qquad \text{…….(5)}$$

Where k is the constant (0.9), λ is the wavelength of X-ray (1.54nm), β is the full width half maximum (FWHM) of the peak and θ is the reflection angle.

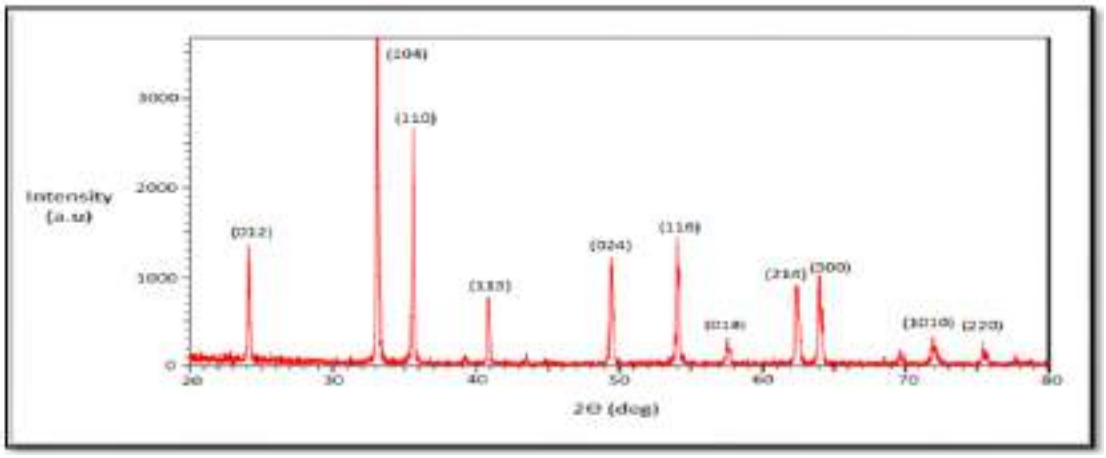

Figure (1): XRD pattern of α-Fe_2O_3annealed at 400°C for 120 min.

3.2 Effect of Annealing Temperature on FT-IR.

The FTIR spectrum of the iron oxides annealing at 400°C for 120 min showing in Fig. (2), the peak at 3361 and 1640 cm^{-1} agree to water of hydration. The peaks at 547 and 474 cm^{-1} correspond to the metal–oxygen (Fe-O) vibration modes [12].

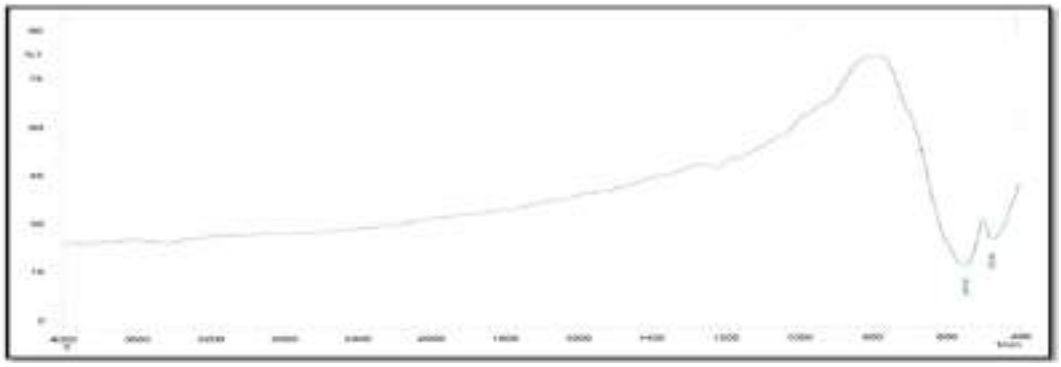

Figure (2): FTIR transmittance spectrum of α-Fe_2O_3 annealing at 400°C for 120 min as a function of wave number.

3.3 Morphology of Fe_2O_3 nanopowder

3.3.1 Surface Morphology Atomic Force Microscopic (AFM)

The surface morphology of α-Fe_2O_3 nanopowder was analyzed using atomic force microscopy. Fig. (3) shows a typical two and three dimensional AFM image and the granularity accumulation distribution chart of α-Fe_2O_3 powders which annealing at 400°C. The grain size of the α-Fe_2O_3 powder was 61.53 nm and roughness 0.198 nm.

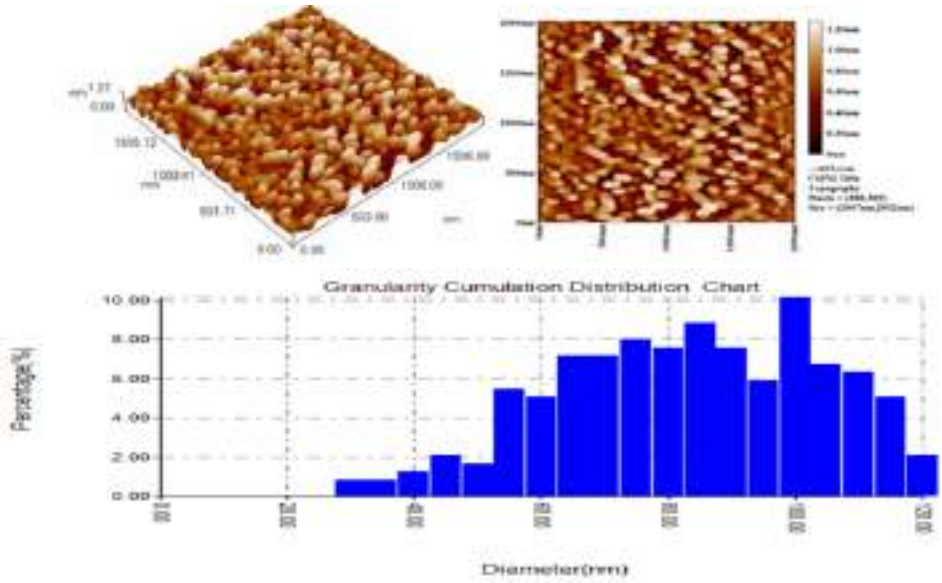

Figure (4): 2 and 3- D AFM image for the α-Fe_2O_3 annealing at 400°C.

3.3.2 Surface Morphology by (SEM)

The SEM images of the α-Fe_2O_3 nanopowder prepared by hydrothermal method with annealing temperature 400°C for (120min) have been shown in Fig. (5), for magnification's (1μm and 500nm) respectively. As seen, nanoparticles have been grown as individual clusters with few conglomerates over the surface, the obvious faces expected hexagonal micro pyramid which belonged to α-Fe_2O_3 as matching with the XRD patterns results.

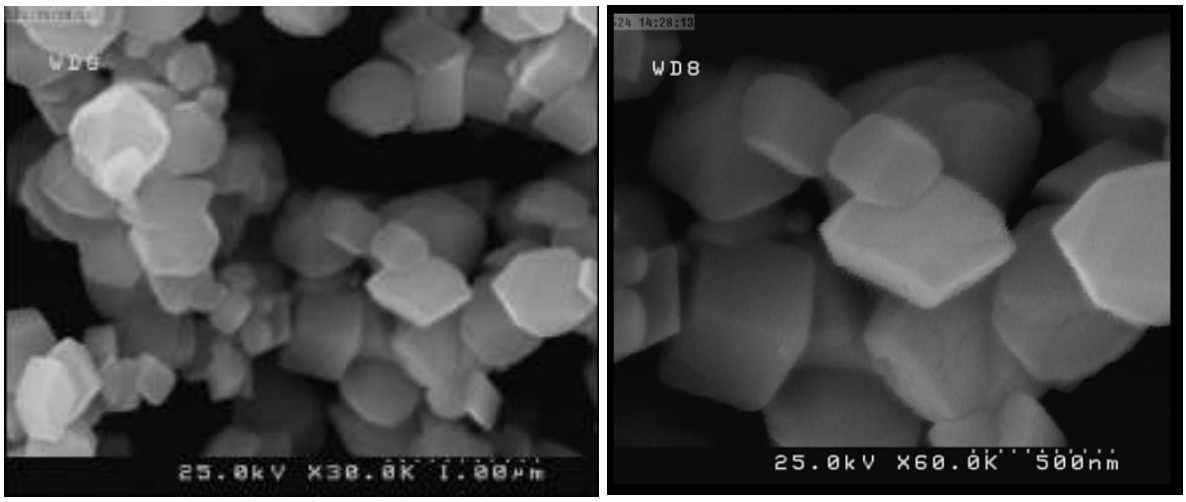

Figure (5): SEM images of α-Fe_2O_3 powder at 400°C for (a) at1µm and (b) at 500nm magnification.

4. Absorption of Fe_2O_3 nanopowder

The UV−VIS absorption spectra of the Fe_2O_3 powder at annealing temperature 400°C for 120 min are presented in Fig. (6). the light absorption threshold for pure Fe_2O_3 is almost 490 nm, interview to the band gap of Eg = 2.1 eV, this fact can be attributed to the presence of the amorphous state of iron and/or to the quantum size effect. The pure Fe_2O_3 exhibits a very slight absorption at the tail of its absorption edge in the region of 470 nm < λ < 540 nm.

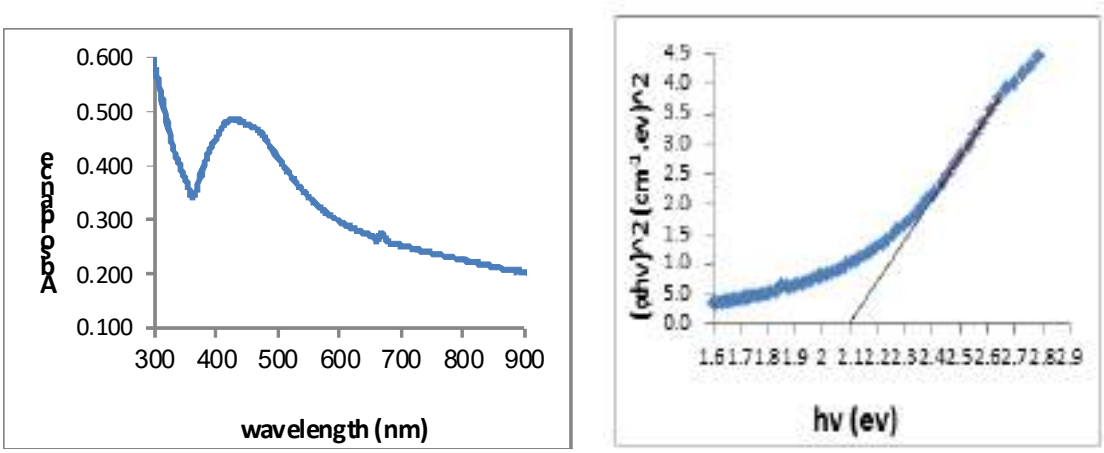

Figure (6): UV–vis absorption spectra and the optical band gap energies for α-Fe_2O_3 were annealed 400°C for 120 min.

5. Antibacterial activity for α-Fe_2O_3 nanopowders

Antimicrobial activities of the synthesized α-Fe_2O_3 nanopowder were performed against both *E. coli* and *S. aurous* bacteria. Fig. (7,8) are showing the relationship between various concentrations of α-Fe_2O_3 nanopowder with *S. aurous* and *E. coli* bacteria living cells after 24 h in 37°C of contact. The gram-positive bacteria have a relatively thick wall composed of many layers of

peptidoglycan polymer, and only one membrane (plasma membrane). The gram-negative bacteria have only a thin layer of peptidoglycan and a more complex cell wall with two cell membranes, an outer membrane, and a plasma membrane [13]. Table (1) against *S. aurous* and *E-Coli* shows α-Fe_2O_3 powder at annealing temperature 400˚C in the zone of inhibition studies. It is observed that the inhibition zone was increased slightly as the concentricity of α-Fe_2O_3 powder increase in all types of tested Pathogens, the 1000 μg ml^{-1} were the perfect concentration of α-Fe_2O_3 powder for inhibiting the growth of both bacteria strains. This result showed that Fe_2O_3 powder was effective for inhibiting both gram-positive and gram-negative bacteria [14]. The antibacterial activity against *S. aurous* was stronger than that against *E. coli*, may be due to the different structure and thickness of the membrane cell wall between *S. aurous* and *E. coli*.

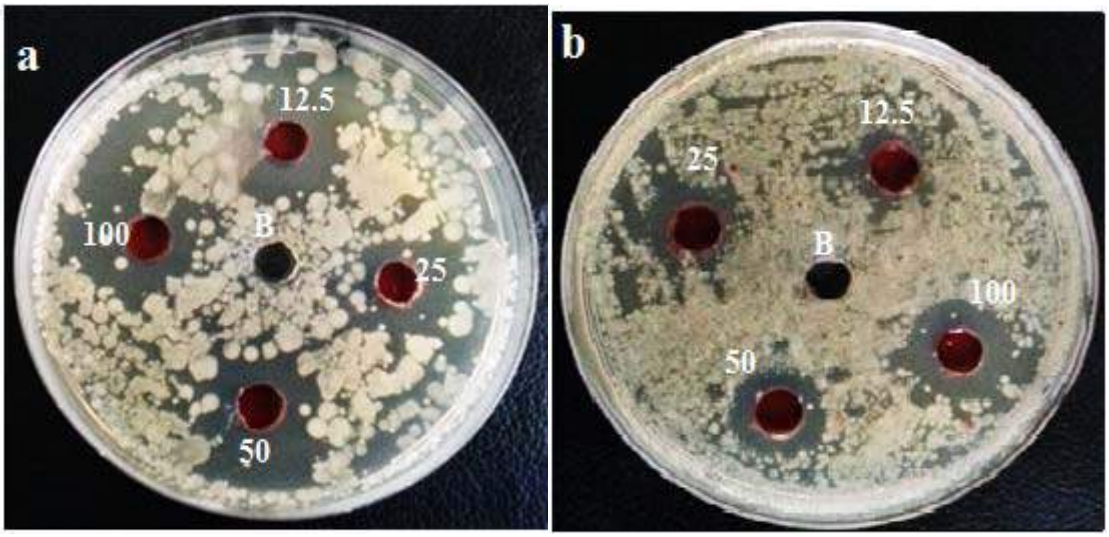

Figure (7): Photo image of (a) *S. aurous* and (b) *E-coli* bacterial in contact at different concentrations for α-Fe_2O_3 powder annealed at 400 ˚C.

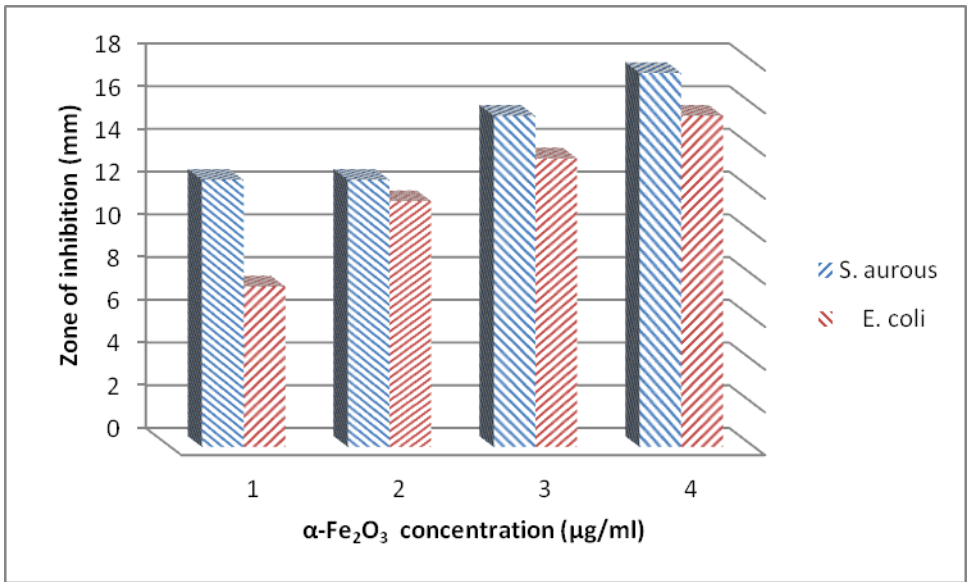

Figure (8): Antibacterial efficiency at: (1) 12.5, (2) 25, (3) 50 and (4) 100 μg/ml of α-Fe_2O_3 nanopowder as anti-bacterial (*E.coli* and *S. aurous*) activity.

Table (1): antibacterial screening of synthesized α-Fe_2O_3 nanopowder

Organism	α-Fe_2O_3 concentrations			
	12.5 µg/ml	25 µg/ml	50 µg/ml	100 µg/ml
S. aurous	12.5	12.5	15.5	17.5
E. coli	7.5	11.5	13.5	15.5

4- Conclusion

The XRD result reveals that α-Fe_2O_3 nanopowder has well crystalline at annealing temperature 400°C, high-intensity peak (104) for α-Fe_2O_3 hematite phase. The AFM study shows that the grain size of the powder is (61.53 nm). The SEM images of α-Fe_2O_3 matching with the XRD patterns results. The more efficient phase as antibacterial agent α-Fe_2O_3 powder was effective and sensitive with *S. aurous* more than *E. coli*.

References

1- Caihua, W., Linlin, W., and Kaibin, T. "Synthesis of Mesoporous Fe_2O_3 Nanorods and Their Electrochemical Performance", Int. J. Electrochem. Sci., (2013), 8: p.4543-4550.

2- Batin, M. N., Popescu, V. "Synthesis and characterization of iron oxide powders", Powder Metallurgy Progress, (2011), 11(3-4): p.201-205.

3- Boumaza, S., Boudjemaa, A., Omeiri, S., Bouarab, R., Bouguelia, A., and Trari, M. "Physical and photoelectrochemical characterizations of hematite α-Fe_2O_3: Application to photocatalytic oxygen evolution", Solar Energy, (2010), 84(4): p.715-721.

4- Batin, M. N., Popescu, V. "Synthesis and characterization of iron oxide powders", Powder Metallurgy Progress, (2011), 11(3-4): p.201-205.

5- Karami, H. "Synthesis and Characterization of Iron Oxide Nanoparticles by Solid State Chemical Reaction Method", Journal of Cluster Science, (2010), 21(1): p.11-20.

6- Teja, A. S., and . Koh, P.Y. " Synthesis, properties, and applications of magnetic iron oxide nanoparticles", Progress in Crystal Growth and Characterization of Materials, (2009), 55(1-2): p.22-45.

7- Arbain, R., Othman, M., and Palaniandy, S. "Preparation of iron oxide nanoparticles by mechanical milling", Minerals Engineering, (2011), 24(1): p.1-19.

8- Rong-Sheng, Cai., Shang, Lei., Xue-Hua, Liu., Wang, Yi-Qian., Yuan, Lu., and Zhou Guang-Wen. "New modulated structure in α -Fe_2O_3nanowires", Chin. Phys. B, (2013), 22(10): p.107401-4.

9- Basavaraja, S., Balaji, D. S., Bedre, M. D., Raghunadan, D., Prithviraj Swamy, P. M., and Venkataraman A. "Solvothermal synthesis and characterization of acicular α-Fe_2O_3 Nanoparticles" , Bull. Mater. Sci., (2011), 34(7): p.1313-1317.

10- Debajeet, K. B., Artur, B., Selma, E., Olga, S., Thomas, G., and Edwin, C. C. "Evolution of structural properties of iron oxide nanoparticles during temperature treatment from 250°C -900°C: X-ray diffraction and Fe K-shell pre-edge X-ray absorption study", Original Research Article, (2012), 12(3): p.817–825.

11- Shakeel, A. A., Mohammad O., Rukhsana S., Anish K., Syed I. A., Mohammad A. J. , Syed K. Z., Mohammad H. A. " Antibacterial activity of iron oxide nanoparticles synthesized by co- -precipitation technology against Bacillus cereus and Klebsiella pneumonia", Pol. J. Chem. Tech., (2017), 19(4): p. 110—115.

12- Basaraja, S., Balaji, D. S., Mahesh Bedre, D., Raghunandan, D., Prithviraj Swamy, P. M., and Venkataraman, A. "Solvothermal synthesis and characterization of acicular α -Fe_2O_3Nanoparticles", Bull. Mater. Sci., (2011), 34(7): p.1313-1317.

13- Reddy, R., Manorama , K. M. S.V., and Reddy, A. R. "Band gap studies on iron oxide nanoparticles", Materials Chemistry and Physics, (2002), 78: p.239-245.

14- Ismail , R. A., Sulaiman, G. M., Abdulrahman, S. A., Marzoog, T. R. "Antibacterial activity of magnetic iron oxide nanoparticles synthesized by laser ablation in liquid", Mater Sci. Eng. C Mater Biol. Appl., (2015), 53: p.286-97.

Available online at
http://namrc.uotechnology.edu.iq/index.php/

Nanotechnology and Advanced Materials Research Centre

Proceeding Articles Book 00 (2018) 000–000

6th International Scientific Conference on Nanotechnology, Advanced Materials and its Applications

Fabrication of Tri Metal Oxides Gas Detector for Medical Diagnosis Application

Farhad M.Othman, Alaa A.Abdul-hamead, Zena Abd-Alameer Salman
University of Technology/Materials Engineering Departments, Baghdad, Iraq

Corresponding author:zena_eng87@yahoo.com

Abstract

In this article we propose tri-metal oxides gas sensor that could be a diagnostic tool handheld breath analyzer providing information about ammonia gas content in the expired human breath that act as biomarker of the renal disease, namely called the kidney failure. Gas sensor made of mixed metal oxides obtained by using special spray pyrolysis technique via employed double nozzle instead of single nozzle. Tungsten salt and tin salt spray on heated substrate (Si_{100} n-type) at 600 °C with three different compositions. Structural properties, including x-ray diffraction XRD, scanning electron microscopy SEM and atomic force microscopy AFM, were examined. Moreover, the gas sensing property toward ammonia gas at a concentration of (10) ppm was investigated. Experimental results show that the micro wires and rods structures of $WSnO_4$ oxide were achieved from using this technique, these structure have been recognized as one of the most efficient microstructures for gas sensor due to their large specific surface area.

Keywords: disease diagnosis, breath analysis, renal failure, bio marker, tri metal oxides, semiconductor gas sensor

1- Introduction

Detecting technology has been advanced for identification of gases in various application areas: environmental, industrial, medical, and scientific applications. In medical application related breath analysis is very exciting application area for gas detectors, the capability to monitor diseases and recognize exposure to poisons by means of breath test would revolutionize current human healthcare [1]. Breath smells used to identify diseases case before long time to current -day for medical diagnosis such as; a sweet odor related to diabetes, fish odor regards liver problems, and urine odor related to renal failure [2]. The human breath is a combination of nitrogen oxygen carbon dioxide with some inert gases and other trace gases, the last one contains inorganic gases like ammonia, mono-carbon oxide and volatile organic compounds (VOCs) like isoprene and methane, the anomaly concentration of certain trace gases, so-called biomarkers, could potentially provide information to diagnose corresponding diseases [3]. Renal failure considered to be detected by high ammonia concentration in human breath, and that related to high content of blood urea nitrogen [1], for that reason excessive concentration of ammonia in exhaled air may be used to reveal of diseases of renal failure [4], figure (1) explain breath markers and their usual content in normal persons (green bars) in contrast to these at some stage in disorder (gray bars).

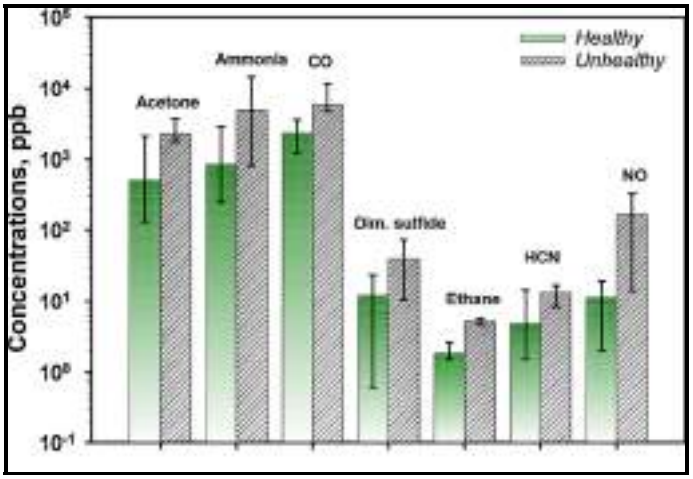

Figure (1) breathe markers and their common concentrations for healthy and unhealthy people [5].

Metal oxides, such as SnO_2, WO_3, ZnO, TiO_2 and Co_3O_4 based gas sensors have attracted extremely good care in field of analysis of volatile organic compounds because of unexpansive, actual time of detection, curable and portable [6]. WO_3 has fascinated scholars since the 18th century, and is widely used today. In addition to its optical and electrical properties WO_3 is a usually utilized as a commercial compound for sensors based on semiconductor [1]. Tin oxide SnO_2 is an n-type semiconductor with an energy band gap of 2.6 eV and it is one of the very promising and widely-studied sensing materials, [7]. The oxides SnO_2 and WO_3 conceded to be most important materials in the area of semiconductor gas-sensor and they have used in industrial sensor instrument. A combination of SnO_2 and WO_3 oxides formed stannous tungstate $SnWO_4$ compound used to be first stated in 1972. Alpha form of $SnWO_4$ is obtained at temperature below 670 ºC, it is orthorhombic crystal structure considered be n-type, has diamagnetic characterize. Both metal atoms have distorted octahedral oxygen coordination's as in SnO_2 and WO_3, and in the α-$SnWO_4$, structure the SnO_2 tin shows in divalent form, Sn^{2+} [8].

Considering the effectiveness of WO_3 and SnO_2 oxides for sensing different gases, we report fabrication of $SnWO_4$ oxide using special spray pyrolysis technique, and detect ammonia gas level in human breath to investigate the possibility of the existence of renal disease.

2- Materials and Method

1. Sensing Film Preparation

The stannous tungstate oxide film prepared by advance spray pyrolysis method using double nozzle by mixing aqueous solutions $(NH_4)_2WO_4$ and $SnCl_2$ with molarity (0.1 M) at three composition are summarized in table (1).

Table (1) mixing percentages of salts.

Salts	Mix 1 (%)	Mix 2 (%)	Mix 3 (%)
	S1	S2	S3
$(NH_4)_2WO_4$	3	1	1
$SnCl_2$	1	1	3

The salts were dissolved after knowing the molecular weights in a certain volume of distilled water and put on the magnetic stir for a period of (20 min) to ensure completion of the solvent, so we get a homogeneous solution, then mix equal volumes of both the two solutions to be the total volume of the mixture (20 ml). The solution was sprayed on the heated silicone (n-type) substrates at 600 ˚C, the other parameters like pressure, spray rate and spray distance technique are summarized in table (2). After the deposition, the prepared samples were annealed for one hour at 500 ˚C and let the samples cooling inside furnace.

Table 2. Process parameters.

Process Conditions	Range
Pressure	7 bar
Air flow rate	8 cm^3/sec
Spray Distance	25 ±1 cm
spray solution size	20 ml
Feeding rate	2.5 ml/min
Spatter number	20
Period between Spatter	1-2 min

2.2 Sensing Film Characterizations

The crystal structure of the sensing films were characterized by X-ray diffraction inspection with radiation CuKα (λ=1.5406 °A), the microstructures of the samples were investigated by Scanning Electron Microscopy (SEM) and the surface morphology of samples was observation by Atomic Force Microscopy (AFM). The gas sensing properties were carried out in a custom made gas test set up, contain gas source and an airtight test chamber with dimensions (20 × 20) cm collect with a heater and thermocouple to adjust the sensor temperature, the chamber has an inlet for allowing the tested gas to flow in, the chamber contain also multi pin for electrical connections. A digital multi-meter of type UNI-T UT81B and Laptop PC are used to register the variation of the sensor resistance when a mix ratio of air/gas flow, the test gas and air passes through a flow meter and needle valve arrangement. The gas sensor samples with aluminum electrodes are placed inside the airtight test chamber, the resistance measured in air first and the NH_3 gas at (10 ppm) concentration pumped in chamber, then resistance measured with time. The testing system for the proposed gas sensors was used to measure the sensitivity through the use of the equation below [9], where S (sensitivity), Ra (resistance in air) and Rg (resistance in NH_3 gas).

$$S\% = \left[\frac{R_a - R_g}{R_a}\right] \times 100\% \qquad \ldots(1)$$

3- Results and discussion

3.1. X-Ray diffraction Examination

Figure (2) exhibits the XRD patterns of sample (S1) after annealing, orthorhombic (α-$SnWO_4$) peak can be notice with high crystalline intensity 100 % at (2θ =28.33º) oriented (121), and Hexagonal phase (h-WO_3) has appeared in low crystalline peak intensity, where the highest peak intensity at (2θ = 24.33º) oriented (210), no characteristic peaks for SnO_2 due to its low percentage. Figure (3) reveals the XRD patterns of sample (S2) after annealing, indicated to (α-$SnWO_4$) at high intensity with more peaks, and (h-WO_3) appear at low intensity peaks comparing to sample (S1) due to equal ratio of salts that allows for the formation of (α-$SnWO_4$).

Figure (4) shows the XRD patterns of sample (S3) after annealing, inducted of Cubic SnO_2 with the highest intensity100% at (2θ = 31.45) oriented (111), due to its high percentage and can find also peaks for (α-$SnWO_4$) at low intensity, that's compatible with [8].

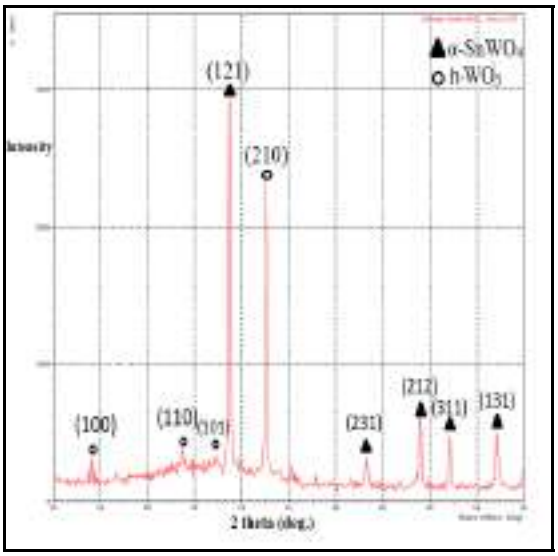

Figure (2) the XRD pattern (S1).

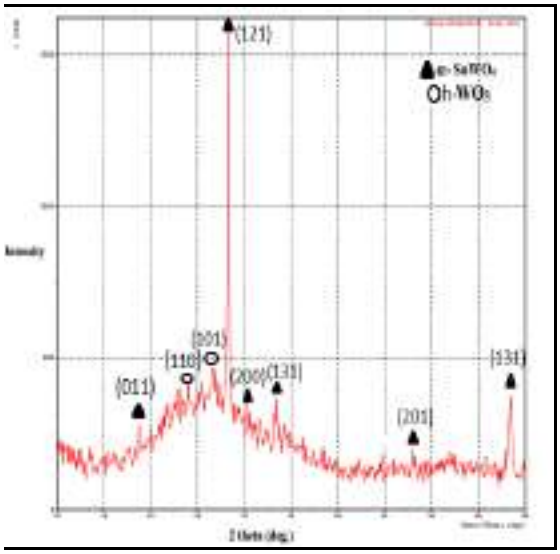

Figure (3) the XRD pattern (S2).

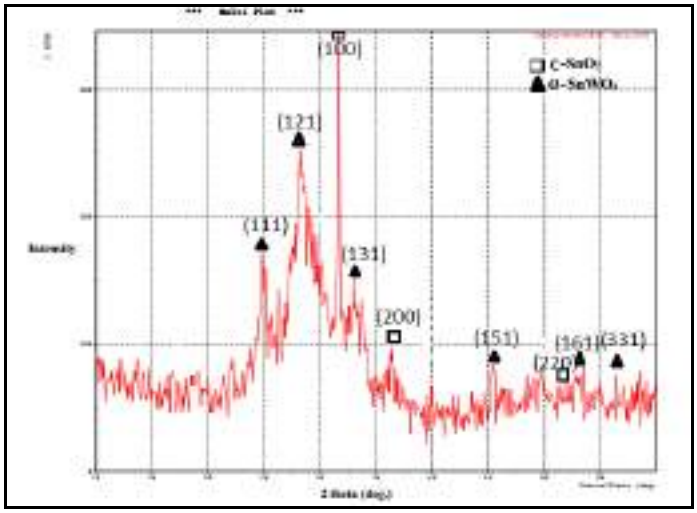

Figure (4) the XRD pattern (S3).

3.2. SEM Examination

Microstructural evolution for the films deposited on silicone substrate were investegated by SEM, in figures (5) the micostructure of (S1) is found to be self-assembled to near-microplates aggregates of $SnWO_4$ oxide that have low density due to low percent of Sn salts. Figure (6) the image of (S2) reveals rich density of a micro-wire of $SnWO_4$ that exhibit uniform structure with size (1-1.5)µm in width and (9-10)µm length. In figure (7) SEM image of sample (S3) shows micro-rodes with size (2-3)µm in width and (10-15)µm length, is relatively rough as compared to (S2) due to different the ratio of Sn salt, , nearly agree with [10].

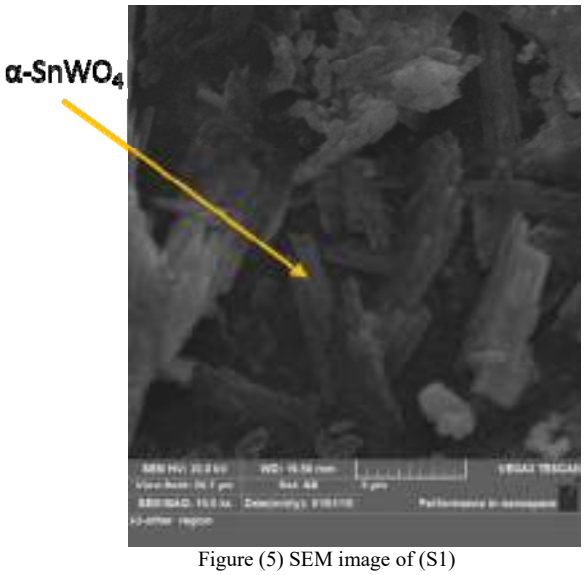

Figure (5) SEM image of (S1)

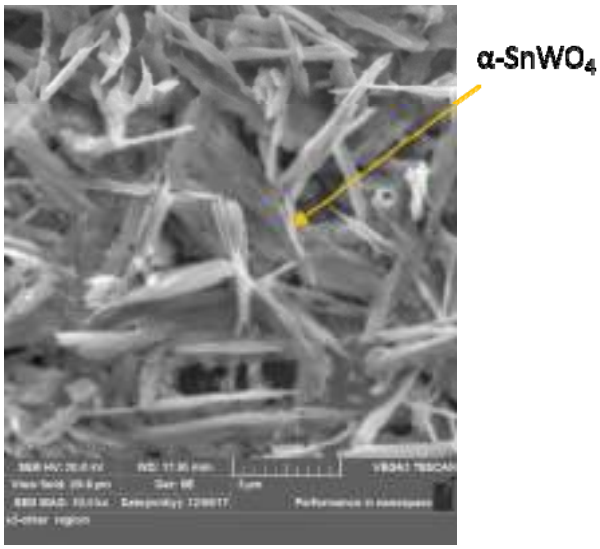

Figure (6) SEM image of (S2)

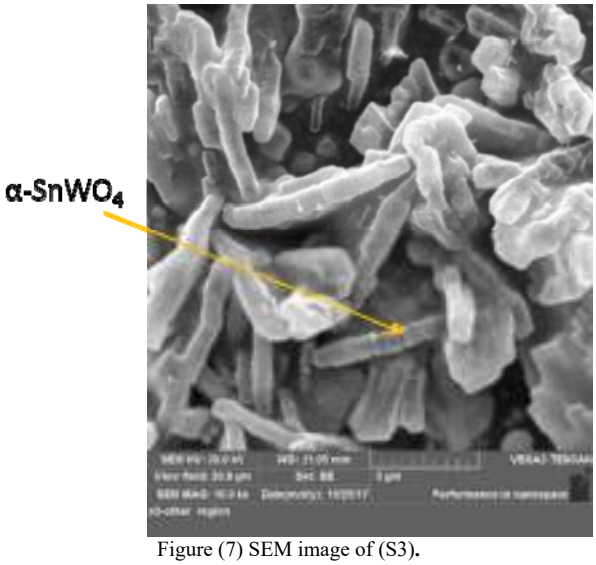

Figure (7) SEM image of (S3).

3.3 AFM Examination

The morphology of the annealed samples were investigated using AFM at nano-scale. In figure (8) show root mean square (0.899 nm) with average diameter (89.55 nm) of (S1).The image in figure (9) reveals surface homogeneity with root mean square (0.185 nm) and have average diameter (77.95 nm) for (S2), and figure (10) show smooth surface with root mean square only (0.0599 nm) with average diameter (74.40 nm) of (S3).

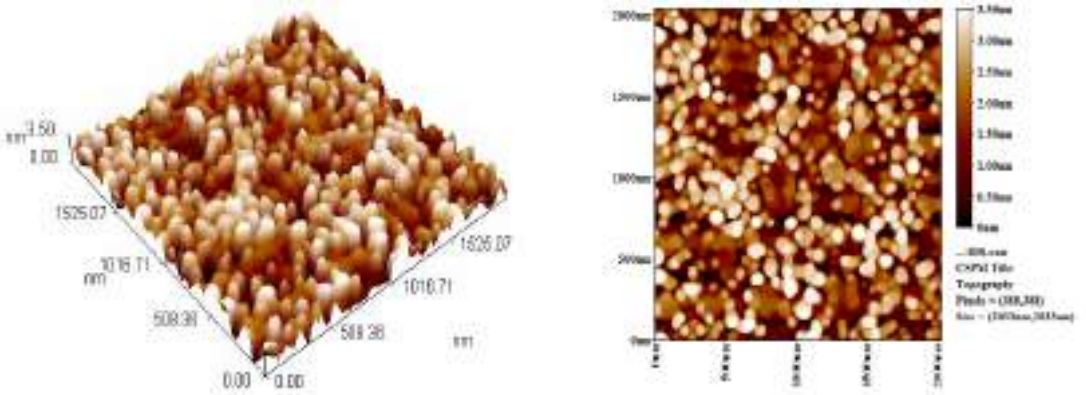

Figure (8) AFM images 2 and 3D of the (S1).

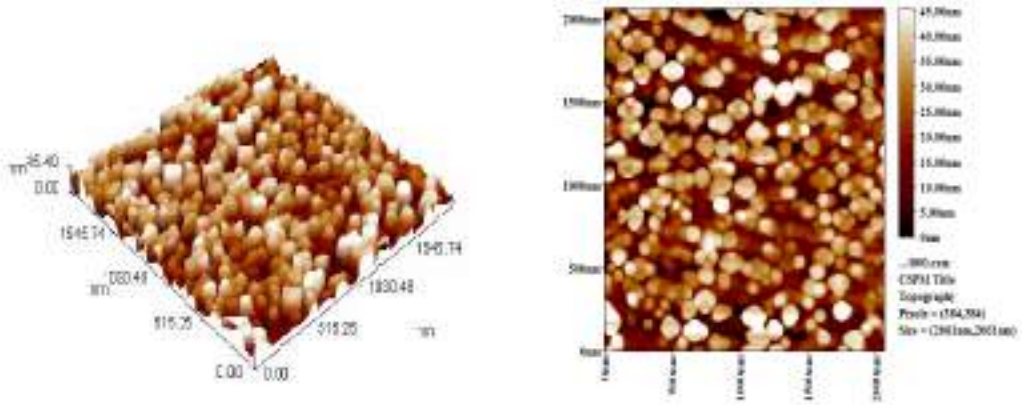

Figure (9) AFM images 2 and 3D of (S2).

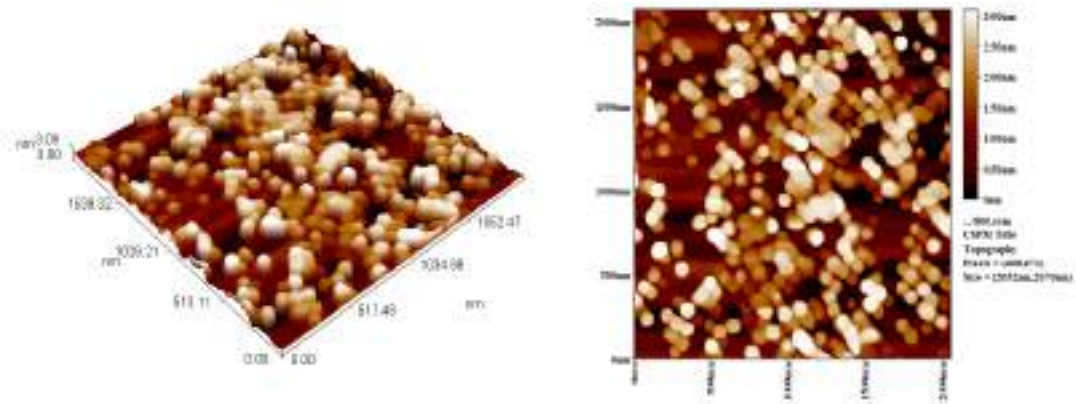

Figure (10) AFM images 2 and 3D of the (S3).

3.3 Gas Sensor Characteristics

Figures (11) show the relation between the sensitivity and time at (10 ppm) of ammonia gas at 25 and 100 °C, it could be notice the sensitivity increase with increasing temperature from 25 to 100 °C significantly more than (30 %) of S1, (25%) of S2 and (10%) of S3. In figure (11, A) shows during the first ten seconds the sensitivity rise to around (50%) of their final value, where observe the highest sensitivity (60%) of the S2 sample at (1 minute). In figure (11, B), S2 show the highest sensitivity is (85%) at the same time and this is due to support of operation temperature to increase the sensitivity of semiconductor metal oxides. The sample S2 exhibits high sensitivity than S1 and S3 due to narrow energy gap (1.64 ev) [11] of the compound (α-$SnWO_4$) that is the major compound comparing with samples S1 and S3, where SnO_2 and WO_3 oxides rise the energy gap because they both have high energy gaps (3.1 ev) [12] and (3.8 ev) [13] respectively compared to (α-$SnWO_4$).

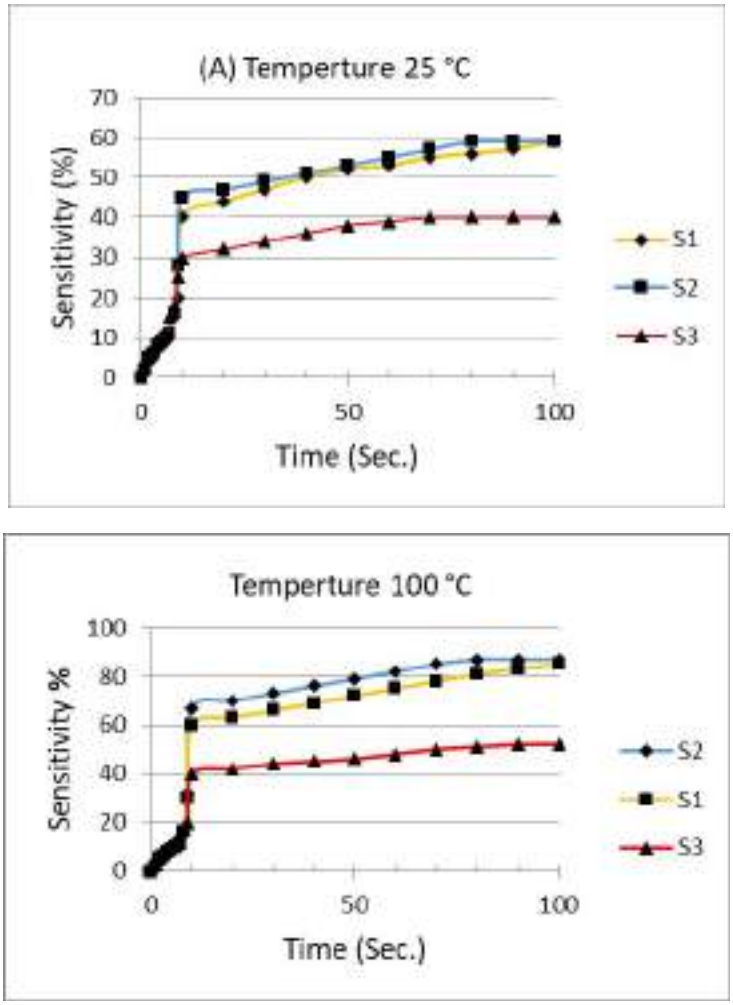

Figure (11) Sensitivity of S1, S2 and S3 of NH_3 gas, A) at temperature 25 °C, B) at temperature 100 °C

4- Conclusion

It could conclude that the deposition temperature is suitable to obtain (α-$SnWO_4$).
Spray pyrolysis technique using double nozzles offer different design to microstructure and this improves the sensitivity to gases.

Increasing the tin ratio has changed the shape topography and microstructure of the films oxides this is reflected in the changing proportions of the phases formed with different percentages of Tin salts.
Best performance was obtained for sample (S2) show highest value of sensitivity at room temperature making it be chose to use in preparation the biomedical detector.

References

1. Staerz, U. Weimar and N. Barsan, "Understanding the Potential of WO_3 Based Sensors for Breath Analysis", Sensors, 2016, 16, p.1815.
2. O. Lawal, W. M. Ahmed, T. M. E. Nijsen, R. Goodacre and S. J. Fowler, " Exhaled breath analysis: a review of 'breath-taking' methods for off-line analysis", Metabolomics, 2017, 13(10): p.110.
3. P. Gouma and M. Stanacevic, "A selective nanosensor device for exhaled breath analysis", Procedia Engineering, 2011, 25, p. 1557-1560.
4. O. Essiet, "Diagnosis of Kidney Failure by Analysis of the Concentration of Ammonia in Exhaled Human Breath" Emerging Trends in Engineering and Applied Sciences, 2013, 4(6): p. 859-862.
5. M. Righettoni, A. Amann, and S. Pratsinis, "Breath analysis by nanostructured metal oxides as chemo-resistive gas sensors", Materials Today, 2015, 18(3): p.163-171.
6. W.T. Koo1, S. J. Choi1, J. S. Jang and D. Kim, " Metal-Organic Framework Templated Synthesis of Ultrasmall Catalyst Loaded ZnO/$ZnCo_2O_4$ Hollow Spheres for Enhanced Gas Sensing Properties" Scientific Reports, 2017, 7, p. 45074.
7. Li, M. Lv, J. Zuo and X. Huang, "SnO2 Highly Sensitive CO Gas Sensor Based on Quasi-Molecular-Imprinting Mechanism Design", Sensors, 2015, 15, p. 3789-3800.
8. J.L. Solis and V. Lantto, "A study of gas-sensing properties of sputtered α-$SnWO_4$ thin films", Sensors and Actuators B Chemical, 1995, 25(1): p. 591-595.
9. Chowdhuri, V. Gupta, K. Sreenivas, R. Kumar, S. Mozumdar and P. K. Patanjali, "Response speed of SnO_2-based H_2S gas sensors with CuO nanoparticles", Applied Physics Letters, 2004, 84 (7): p. 1180-1182.
10. K. J. Pyper, T.C. Evans and B. M. Bartlett, "Synthesis of α-$SnWO_4$ thin-film electrodes by hydrothermal conversion from crystalline WO_3", Chinese Chemical Letters, 2015, 26, p. 474–478.
11. Kuzmin, A. Anspoks, A. Kalinko, J. Timoshenko and R. Kalendarev, "Extended x-ray absorption fine structure spectroscopy and first-principles study of $SnWO_4$", Royal Swedish Academy of Sciences, 2014, 89, p. 5.
12. Miglio, R. Saniz, D. Waroquiers, M. Stankovski, M. Giantomassi, G. Hautier, G.-M. Rignanese and X. Gonze, "Computed electronic and optical properties of SnO_2 under compressive stress", Optical Materials, 2014, 38, p. 161–166.
13. P. González-Borrero, F. Sato, A. N. Medina, M. L. Baesso, A. C. Bento, G. Baldissera, C. Persson, G. A. Niklasson, C. G. Granqvist, and A. Ferreira da Silva, "Optical band-gap determination of nanostructured WO_3 film", Applied Physics Letters, 2010, 96, p. 061909-3.

Available online at
http://namrc.uotechnology.edu.iq/index.php/

Nanotechnology and Advanced Materials Research Centre

Proceeding Articles Book 00 (2018) 000–000

6th International Scientific Conference on Nanotechnology, Advanced Materials and its Applications

Synthesis of Photovoltaic Organic – Inorganic Perovskites Photodetctor

Aref S. Baron, Sattar J. Qasim
Physics department, College of science, Basrah University, Basrah, Iraq
Physics department, College of science, Kufa University,Kufa, Iraq
Corresponding author: arif.aljuburi@uokufa.edu.iq

Abstract

One of the important electronic applications in the recent years its organic – inorganic perovskite materials characterized by the tunable optical properties , in this work we focused at this property to synthesis of photovoltaic photodetctor devises by preparation of two types of perovskites , $MAPbCl_3$ and $MAPbBr_2Cl$ where the best responsively at the wavelengths 400 nm , 460nm in addition this perovskites have a short raise time and fall time specially in the wavelengths 400 nm where t_{rise}=0.262 s , t_{rise} =0.282s and t_{fall} =0.528 s t_{fall}=0.262 s for $MAPbCl_3$ and $MAPbBr_2Cl$ respectively.

Keyword: Photovoltaic , Perovskits,TiO_2 nanocrystal ,Photodetctor

1-Introduction

The great attention has recently been raised in the organic-inorganic perovskites for the last ten years as an intervention of field-effect transistors, light-emitting diodes, sensors, photodetectors, and photovoltaic cells, because of their tunable optical properties, long-ranged balanced electron and hole transport, facile deposition techniques, low cost and high-efficiency[1-3].The organic -inorganic perovskite compounds discovered by the German mineralogist Gustav Rose in the year 1839 then characterized by Russian mineralogist L.A. Perovski, which derives the name of the chemical structure formula of ABX_3 [4, 5] where A is a bulky cation which occupies a cubo-octahedral site shared with 12X anions e. g. $CH_3NH_3^+$ or $HC(NH_2)^+$, and B is a smaller cation stabilized in an octahedral site shared with 6X anions e.g. Pb^{+2}, Sn^{+2} and X is anion halogen e.g. halides chloride Cl^-, bromide Br^- and iodide I^-, respectively ,Figure 1 shows the basic structural arrangement[6, 7] .Methyl ammonium lead halide perovskites ($MAPbX_3$, MA = methyl ammonium) hybrid organic-inorganic attention has recently increased with these structure in particular as photovoltaic devices, which have bandgap easily and effectively adjusted by changing the cation, the metal or the halide and the power conversion efficiency (PCE) has been boosted from 3.8% to more than 20% within 10 years [2, 8] .

The formability of Perovskite structure is based on its geometric tolerance factor (t) which is the ratio of the (A–X) distance to the (B–X) distance

$$t = \frac{(R_A + R_X)}{\sqrt{2}(R_B + R_X)} \qquad (1)$$

Where R_A, R_B and R_X are the effective ionic radii for A, B and X ions, respectively. t = 1 for ideal cubic perovskite while octahedral deformation is expected when t < 1 . Symmetry of perovskite decreases for t < 1, which may affect electronic properties . Halide perovskite of alkali metal is determined in the range 0.813 < t < 1.107 [9, 10] .The radii cations for Perovskite structure between 1.60 A˚ and 2.50 A˚ and methyl ammonium cation is suitable for lead halide perovskite because its ionic radius is 1.8 A˚ and effective ionic radii for its t = 0.8 and t = 1 .

The optical properties of perovskites $MAPbX_3$) explain that $MAPbX_3$ have a direct bandgap of 1.55 eV ,2.2 eV and 3.0 eV for $MAPbI_3$,$MAPbBr_3$ and $MAPbCl_3$ respectively, moreover the absorption edges of $MAPbX_3$ perovskites have different values where the $MAPbI_3$ have great value while the $MAPbBr_3$ and $MAPbCl_3$ less than ,this effect at the highest occupied molecular orbital (HOMO) and the lowest unoccupied molecular orbital (LUMO) energy levels for $MAPbX_3$ perovskites as the table1[11, 12].

When two halide elements are mixed with controlled ratios, we get a perovskite have optical properties are different at the $MAPbI_3$, $MAPbBr_3$ and $MAPbCl_3$.and also we can control of the bandgap from the ETM (electron transport material) like TiO_2,ZnO, CdS etc. which act as n-type semiconductors [11]. In this study ,we focused at the optical properties for $MAPbCl_3$ and $MAPbBr_{3-x}Cl_x$ perovskites to manufacturing the photovoltaic photodetctor devices .

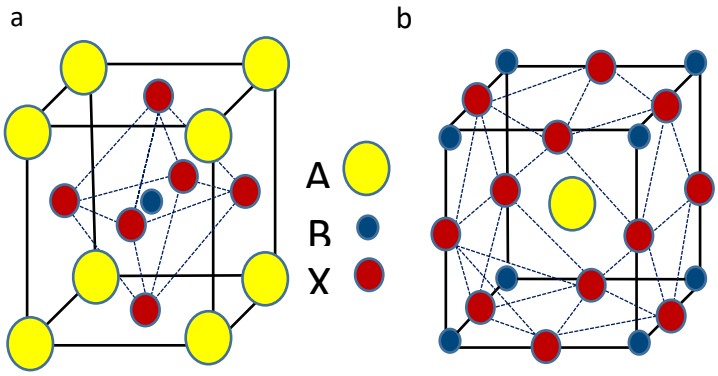

Figure 1,Crystal structural of perovskite ,(a

Table 1.The types of main perovskites

perovskites	Bandgap	HOMO	LUMO
$MAPbI_3$	1.55 eV	-5.23 eV	-3.66 eV
$MAPbBr_3$	2.2 eV	-5.6 eV	-3.4 eV
$MAPbCl_3$	3.0 eV	-5.8eV	2.8eV

2-Experimental

The Materials

FTO glass , acetone, 2-propanol ,titanium(IV) butoxide,$TiCl_4$, Methylamine CH_3NH_2 (MA) , hydrobromic acid (HBr), hydrochloric acid (HCl 36 wt%) ,lead bromide ($PbBr_2$), lead chloride ($PbCl_2$) and dimethyl formamide DMF.

Preparation of TiO_2 Nanocrystal: TiO_2 Nanocrystal (TiO_2Ncs) prepared by hydrothermal method , firstly the FTO glass cleaned by acetone ,2-propanol subsequently using the ultrasonic bath . Immersed FTO in the Teflon stainless steel autoclave contain the precursor of titanium perpend from adding 15 ml HCl , 15 ml deionized water and 0.25 ml titanium(IV) butoxide . The autoclave conducted for 7 hours at 170˚C with a temperature controlled furnace[18]. After hydrothermal process, the samples were cleaned with in deionized water and annealing at 450c° for 45 min .The resulting of TiO_2Ncs treatment with $TiCl_4$ by immersed in $TiCl_4$ aqueous (0.57 ml $TiCl_4$ with 100 ml deionized water) at 80c° for 30 min then annealed at 450 c° 30 min again. [13,14]

Sample preparation : MAX (X= Br, Cl) were synthesized according to[15] .Briefly reacting 30 ml from CH_3NH_2 with 20 ml from HCl (MACl) in round-bottom flask beaker in the ice about 0 C° for 2h with stirring. The precipitates were recovered by rotary vacuum evaporation at 60 C° for 1h to remove the solvents .The crystals were washed using diethyl ether and ethanol several times then dried by evaporated for several hours to produce crystal powder which was stored it in dark dry place.

Perovskites Preparation

MAPbCl3 preparation : mixing (0.25g) MACl , $PbCl_2$(3.08 g) with 2 ml from DMF and stirring several hours at 60C° ,by spin-coating we dropped the solution at TiO_2Ncs for 1500 rpm/5 sec ,2500 rpm/45 at sequentially, then annealed at 120 C° for 30min.

MAPbBr2Cl preparation : mixing equal molar ratio from MACl (0.27 g) and PbBr2(1.5g) dissolved in 2ml from DMF at room temperature with stirring several hours , then dropped the solution at TiO_2Ncs substrate with spin-coating for 1500 rpm/5 sec then 2500 rpm/45 sec ,finally the film annealed at 120 C° for 30 min .

3-Result and Discussion

The perovskites $MAPbCl_3$ and $MAPbBr_2Cl$ was fabricated to design a photodetctor device, First we distinguish the crystallization of perovskites by XRD were there are many peaks for $MAPbCl_3$, the most important at 15.4, 21,9,31.3 and 35.1peaks and the indexed (100), (110),(200) and (210) respectively while the $MAPbBr_2Cl$ have many peaks at 15, 21,30,34 and 46 for indexed (100), (110), (200) , (210), and (300) respectively. The phase of the $MAPbBr_2Cl$ it was single phase ,the space group (*pm3m*) and unit cell a=5.95 Fig. 2 [16,17]

Fig.3a shows the absorption spectrum of the perovskites , we found the absorption edge for the $MAPbCl_3$ equal 405nm and nearly 520nm for $MAPbBr_2Cl$ [19,20] and this clearly in the band gaps were calculated by using Kubelka –Munk method where the direct band gap about 2.95 eV for $MAPbCl_3$ and 2.48 eV for $MAPbBr_2Cl$ Fig.3b, and here, it turns out that the energy gap can be tuning by controlling the component ratios of the

halogens, where the energy gap approaching the values of the main compositions ($MAPbI_3$,$MAPbBr_3$ and $MAPbCl_3$) depending at the I, Br and Cl ,in this work the ratio equal 1:1 for MACl:$PbBr_2$.

The schematic diagram of the perovskite device structure shows in the Fig.4a , its consist of FTO/TiO_2Ncs/$MAPbX_3$/Ag , the TiO_2Ncs/$MAPbX_3$ act as n-type and the $MAPbX_3$/Ag act as p-type when the light incident through the FTO glass substrate .The morphology of surface devices were measured by SEM show in the Fig. 4b for TiO_2Ncs, Fig. 4c to the $MAPbCl_3$ and Fig.4d for the $MAPbBr_2Cl$ perovskite.

We further studied the spectral response of the Perovskite device through illuminated its by two different light incident wavelengths (400 nm and 460 nm) have same power (0.9 mW cm-1) and this lights were in the form of pulses , per half cycle equal 70 s for each wavelengths. When the photocurrent increase from 10% to 90% or decrease from 90% to 10% of the peak value this represented the rise time (t_{rise}) and fall time (t_{fall}) [18-20]. The temporal photoresponse of the devices showed in the Fig. 5 , the photocurrent resulting from the $MAPbCl_3$ Perovskite device equal I_{light}=0.16 □A when the light incident have a wavelength 400 nm then decay until equal I_{dark}=1 nA for one cycle ,while the photocurrent decrease when used wavelength 460nm for the same device where its reach to less than I_{light} =0.02 □A see Fig.5a , this is because if the light incident has a higher energy than the bandgap of the device, the number of excitations increases and therefore the photocurrent will increase, and this also impact at the time of responsively while decrease from t_{ries}=0.262s when □=400 nm to t_{rise}=0.650s at the □□=460nm and also from t_{fall} =0.528s to the t_{fall} =2.923s for □=400 nm and □=460 nm respectively Fig.5b and table 2 .For the $MAPbBr_2Cl$ device, the situation is similar but the value of the photocurrent I_{light} =1.37□□A to the □=460nm is higher when we compared it's with same wavelength was using in the $MAPbCl_3$, because of the energy gap of the $MAPbBr_2Cl$ device less than energy gap of the $MAPbCl_3$ device ,but that photocurrent still less than wavelength 400nm , was equal I_{light} =1.9 □A.

This result correspond to behavior of responsivity as function to the wavelength of these devices which showed in the Fig.6 .

There are a number of important parameters used to calculate the of photodetctor, the Photoresponsivity *R* which can be calculated by

$$R = \frac{I_{light} - I_{dark}}{PA} \qquad (2)$$

where *P* the incident light intensity (W.cm^{-2}), *A* the effective area of the device (cm^2),we found the Photoresponsivity *R* ranges from 0.013 to 0.17 A.W^{-1}, and the high values of *R* realize when the wavelength of incident light equal 400nm and that depends on at the energy gap of device which affected at TiO_2 bandgap and perovskite bandgap, from the photoresponsivity *R* can calculate the detectivity $D^*$and the external quantum efficiency (EQE), where

$$D^* = \frac{R}{\sqrt{2qJ_{dark}}} \qquad (3)$$

q, the elementary charge (col) , J_{dark} dark current density (A.cm^{-2}),D^* nearly between 4x10^{+11} to 8 x 10^{+11}Joens, while EQE(□□□can be calculate□□from□

$$\eta = R\frac{hv}{q}100\% \qquad (4)$$

hv are the responsivity, the value of the elementary charge ,the high value of photoresponsivity *R* 0.17A.W^{-1} corresponding the high value of □ equal 53% in the wavelength 400 nm (table 2) [21,22] .

Table 2. The values of perovskite photodetctor parameters

Perovskite	Wavelength nm	t_{rise} (s)	t_{fall} (s)	R A.W^{-1}	Q %	D Jones
$MAPbCl_3$	454	0.650	2.923	0.013	3.59	4.3 x10^{+11}
	400	0.262	0.528	0.171	53.04	5.5 x10^{+11}
$MAPbBr_2Cl$	454	0.267	0.272	0.076	20.5	6 x10^{+11}
	400	0.282	0.262	0.105	32.7	8.3 x10^{+11}

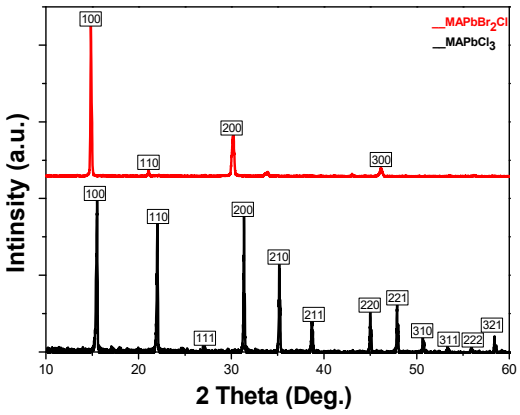

Figure 2 XRD pattern for the $MAPbCl_3$ and $MAPbBr_2Cl$ perovskites

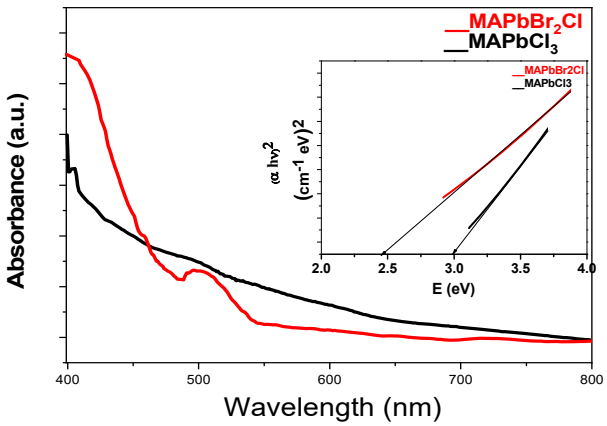

Figure 3(a) Absorbance spectrum to the $MAPbCl_3$ and $MAPbBr_2Cl$ (b) The energy of band gap

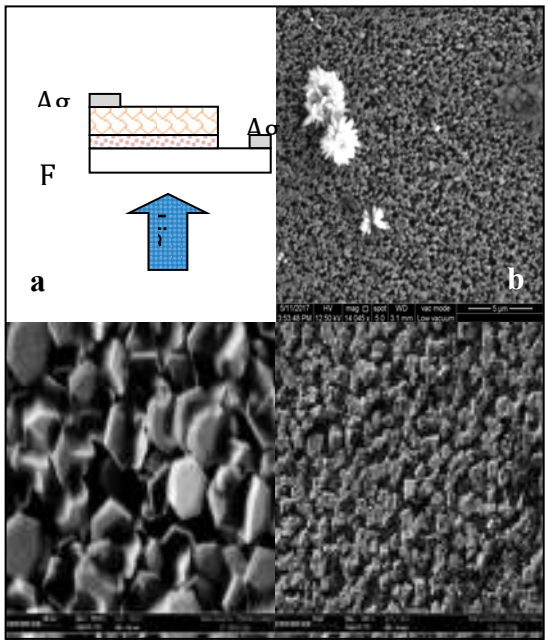

Figure 4,(a) Schematic diagram of the perovskite device structure (b) SEM image for TiO_2 Ncs (c) SEM image for $MAPbCl_3$ (d) SEM image to the $MAPbBr_2Cl$

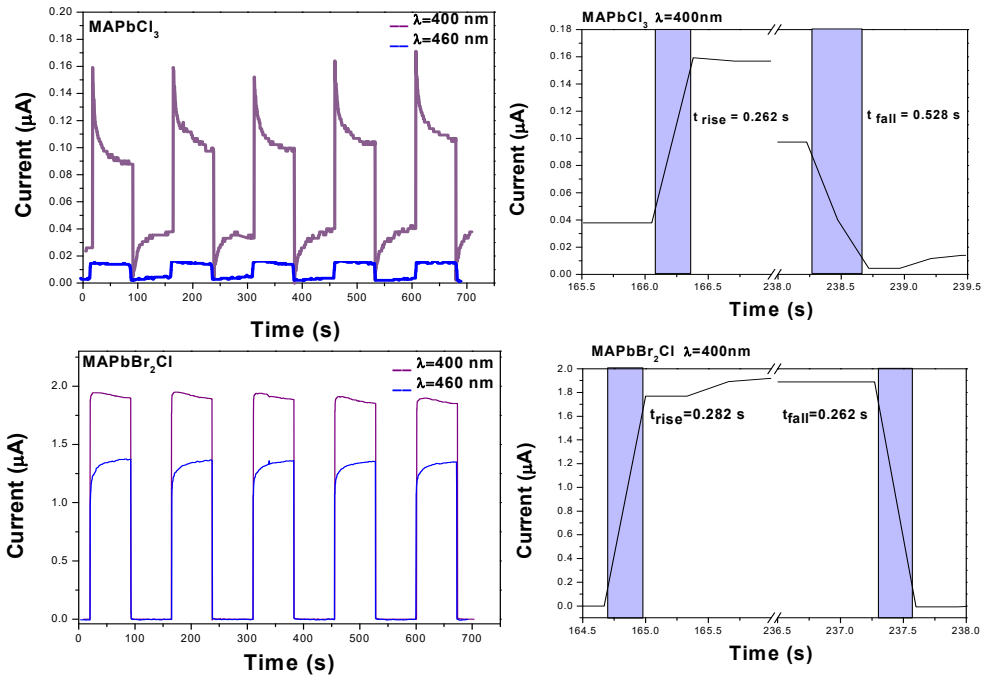

Figure 5 (a) (b)The current as function of time and rise - fall time for $MAPbCl_3$.(c)(d) The current as function of time and rise - fall time for $MAPbBr_2Cl$

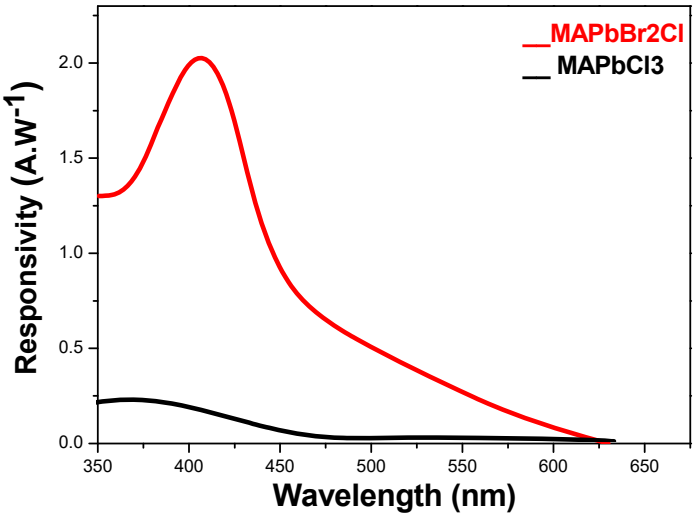

Figure 6 The Responsivity as a function to th wavelength for the $MAPbCl_3$.and $MAPbBr_2Cl$

4. Conclusion

The photovoltaic photodetctor devices designed after the preparation of two types organic-inorganic perovskites $MAPbCl_3$ and $MAPbBr_2Cl$, and tuning of device bandgap to synthesis photodetectors by changing the ratio and kind of halogen I,Br and Cl, and addition of TiO_2 Ncs .These photodetectors have a fairly high speed time for rise and fall time specially at the wavelength 400nm where the t_{rise}=0.262 s , t_{rise} =0.282s and t_{fall} =0.528 s t_{fall}=0.262 s at the 0v voltage applied .This kind of materials allow to design a photodetectors operating in a wide region from UV to IR regions.

Reference

1.Cai, B., et al., High performance hybrid solar cells sensitized by organolead halide perovskites. Energy & Environmental Science, 2013. **6**(5): p. 1480-1485.

2.Zhou, H., et al., Interface engineering of highly efficient perovskite solar cells. Science, 2014. **345**(6196): p. 542-546.

3.Makhsud I. Saidaminov, Ahmed L. Abdelhady, Banavoth Murali, Erkki Alarousu, Victor M. Burlakov, Wei Peng, Ibrahim Dursun, Lingfei Wang, Yao He, Giacomo Maculan, Alain Goriely, Tom Wu, Omar F. Mohammed & Osman M. Bakr , High-quality bulk hybrid perovskite single crystals within minutes by inverse temperature crystallization. Nature communications, 2015. **6**.

4.Etgar, L., Hole Conductor Free Perovskite Based Solar Cells. 2016: Springer.

5.Salim M., Shahdat M. H., Hossain M. S., A Micro-Review on Prospects and Challinges of Perovskite Materails in Organic-Inorganic Hybrid Solar Cell Applicatins . Digest Journal of Nanomaterials and Biostructures, 2015. **10**(4): p. 1289-1302.

6.Gao, P., M. Grätzel, and M.K. Nazeeruddin, Organohalide lead perovskites for photovoltaic applications. Energy & Environmental Science, 2014. **7**(8): p. 2448-2463.

7.Naresh K. K., Madhvendra N. T., Umesh W., and Dinesh K., Structural, Optical, and Electronic Properties of Wide Bandgap Perovskites: Experimental and Theoretical Investigations. The Journal of Physical Chemistry A, 2016. **120**(22): p. 3917-3923.

8.Niemann R. G., Athanassios G. K, Dimitrios P., Efstratios I. K., Andreas K., Federico B., Polycarpos F., and Petra J. C., Halogen effects on ordering and bonding of $CH_3NH_3^+$ in $CH_3NH_3PbX_3$ (X= Cl, Br, I) hybrid perovskites: a vibrational spectroscopic study. The Journal of Physical Chemistry C, 2016. **120**(5): p. 2509-2519.

9.Park, N.-G., Perovskite solar cells: an emerging photovoltaic technology. Materials Today, 2015. **18**(2): p. 65-72.

10.Li C., Lu X, Ding W, Feng L, Gao Y, Guo Z., Formability of ABX_3 (X= F, Cl, Br, I) Halide Perovskites. Acta Crystallographica Section B: Structural Science, 2008. **64**(6): p. 702-707.

11.Qin P., Sanghyun P., Ibrahim M. D., Norman P., Jaejung K., Michael G., and Mohammad K. N., Perovskite solar cells with 12.8% efficiency by using conjugated quinolizino acridine based hole transporting material. Journal of the American Chemical Society, 2014. **136**(24): p. 8516-8519.

12.Cui D., Zhou Y., Dong Y., Xiaodong R., Yucheng L., Qingbo W., Haibo F., Jinghui Z., and Shengzhong F. L., Color-Tuned Perovskite Films Prepared for Efficient Solar Cell Applications. The Journal of Physical Chemistry C, 2015. **120**(1): p. 42-47.

13. Onur A., E. Şennik,, N. Kılınç, Z. Ziya . Gas sensor application of hydrothermally growth TiO2 nanorods, ScienceDirect, 120 (2015) 1162 – 1165.

14. Luo J.,L. Ma,T. He,C. Fan,S. Wang,H.Sun,and H.J. Fan, TiO_2/(CdS, CdSe, CdSeS) Nanorod Heterostructures and Photoelectrochemical Properties, The Journal of Physical Chemistry C, 2012, 116, 11956−11963.

15. Guo W., C. Xu, X. Wang, S. Wang ,C. Pan,C. Lin, and Z. L. Wang, Rectangular Bunched Rutile TiO_2 Nanorod Arrays Grown on Carbon Fiber for Dye-Sensitized Solar Cells, Journal of the American Chemical Society, 2012, 134, 4437−4441.

16. Lee M., J. Teuscher,T. Miyasaka,T. N. Murakami,H. J. Snaith Efficient Hybrid Solar Cells Based on Meso-Superstructured Organometal Halide Perovskites, Science, 2012 , **338**, 643-647

17 Rong Y., Z. Tang,Y. Zhao,X. Zhong, S. Venkatesan, H. Graham, M. Patton, Y. Jing, A. Guloy and Y. Yao, Electronic Supplementary Material (ESI) for Nanoscale. 2015.

18. Bryan A. Rosales, L. Men, Sarah D. Cady, Michael P. Hanrahan, Aaron J R., and J. Vela,rsistent Dopants and Phase Segregation in Organolead Mixed-Halide Perovskites,Chem. Mater, 2016

19. Yang D., C. Xie, X. Xu, P. You, F. Yan, and S. Fung Yu, Lasing, Characteristics of $CH_3NH_3PbCl_3$ Single-Crystal Microcavities under Multiphoton Excitation, Adv. Optical Mater. 2017,1-6 .

20. Tan Z., Y. Wu, H. Hong, J. Yin, J. Zhang, L. Lin, M. Wang, X. Sun, L. Sun, Y. Huang, K. Liu, Z. Liu, and H. Peng, Two-Dimensional $(C_4H_9NH_3)_2PbBr$ Perovskite Crystals for High-prformance Photodetector, J. Am. Chem. Soc.,2016.

21. Li D.,G. Dong,W. Li , and L. Wang , High performance organic-inorganic perovskite- optocoupler based onlow-voltage and fast response perovskite compound photodetector, Scientific Reports ,2015,1-6.

22. Zhang H.,Z. Zhang,Y. Zhang,H. Dai,X. Song,J. Yang,Y. Yu,G. Zhang,Y. Che,M. Cao,and J. Yao ,Highly Photosensitive Vertical Phototransistors Based on a Poly(3hexylthiophene) and PbS Quantum Dot Layered Heterojunction, American Chemical Society,2017, 4, 584−592.

Available online at
http://namrc.uotechnology.edu.iq/index.php/

Nanotechnology and Advanced Materials Research Centre

Proceeding Articles Book 00 (2018) 000–000

6th International Scientific Conference on Nanotechnology, Advanced Materials and its Applications

The structural and thermal properties of the Cermet system using powder technology

Salih Y.Darweesh[1], Ismael .K. Jassim[2], Amer. SH. Mahmood[2]
[1] Physics Department, College of Education, Tikrit University, Tuzkormato, Iraq
[2] Physics Department, College of Education and Pure science, Tikrit University, Iraq
Corresponding auther: Salih.youns@gmail.com

Abstract

In this study, basalt powders were prepared as a base material and supported by aluminium powder with a percentage of reinforcement (0,10,20,30,40,50)%. The powders were mixed and formed by an electric press at (4) tons and for two minutes. of Oxygen at (1000℃) and for only two hours. microstructural tests included (XRD) and (SEM) microscopy. Thermal tests included (thermal conductivity, thermal effusion, thermal diffusion, thermal capacity, thermal resistance). X-ray diffraction was found in four basalt rocks with crystalline systems (Cubic, Monoclinic and Triclinic), followed by sludge (Al_2O_3) with the(Rhombohedral) system and SiO_2 (SEM) showed a superficial homogeneity and significant atomic interconnectivity, while the thermal test showed a clear improvement in the compound and an increase in thermal conductivity values to (3.7 w / m.k) and thermal diffusion to (3.1643 mm^2 / sec) and the thermal effusion to (2080 $w.s^{1/2}$ / m^2.k) with the increase of the ratio of aluminium added to the ratio of 50% aluminium while the values of thermal capacity and resistance decreased Thermal with an increase ratio of 50% reinforced aluminium .

Keywords:Cermet, powder technology, structural, thermal properties

Introduction

Technical advances and evolution have prompted the need for new engineering materials with unique properties, which has led to the emergence of materials called composite materials. It is a term called material consisting of two or more different types of materials, and they are bonded together uniformly so that one of them is known as the base material of the other material known as the reinforcing material. Where the pure metals and alloys are known to be unable to achieve the qualities and properties that must be provided by the products, so that the materials (compound) is one of the most recent alternatives are low cost with the availability in the market and high mechanical properties with the possibility of development or change in addition to light weight and ease Transfer [1]. Powder metallurgy technology is one of the most important technologies of overlapping materials. It dates back thousands of years BC and is known as the lost art and was known during the early stages without sintering until it was known in Europe at the end of the 18th century when different methods were recorded in the production of platinum powder. Production of powders was not known but could be obtained by granulation after melting of the metal. It was preferred to lower fusion temperature and high oxidation resistance as in gold powder because of the low availability at that time. Metal powders such as aluminium , bronze, copper, gold and some oxides were known as ceramic decoration materials and as a basis for paints, inks and cosmetics. Gold powder was also used to decorate manuscripts. These powders are used in modern science to solidify and strengthen solids by pressing and heating to temperatures below the melting temperature of the base metal as the use of powders for decorative purposes and dyes has become a thing of the past. In 2010, the researcher (Q.Wang) and his group studied the effect of wear friction on the behavior of basalt, graphite and silica nanoparticles. They found that the graphite with basalt was more useful in improving the properties of BFC, (3) (S.Nncik) and(V.Kmecova) studied in 2013 the effect of basalt powder on the properties of basalt compounds on the properties of cement complexes. The researchers found that adding basalt has a positive effect on Density of cement and increase of hardness and strength of overlays [4] In 2015 the researcher (P.Reiterman) and total Its study of the physical and mechanical properties of compounds made of basalt fiber and aluminium at high temperatures, where researchers

found that the increase in fiber basalt gives high compressive strength and density and withstand thermal ranges and features high mechanical and physical high [5].

2- Materials and Method

1- Raw materials used

The material used in the current research was composed of Indian aluminium with a density of (2.7 g / cm^3) with a granular volume of(≥ 44 μm) and used as a supporting material. The base material was of German basalt powder with a density of (2.8 g / cm^3) and granular size less than (≤100 μm).

2- Method of preparation

After weighing the granular size of the powders used, these powders were weighed using the weight ratios to prepare all the overlays. The weights and weight ratios of the aluminium and basalt were weighted using a sensitive electrical balance (Sartorius) at (0.0001g). It is of great importance to influence the amount of overlap in each sample. The basalt rock was then brought from the Geological Department \ Faculty of Science \ University of Baghdad, and the main location of the rock is the state of Rhineland-Palatinate. After the rock was cleaned, dried and then crushed first with a regular brow for the purpose of reducing the size of the rock to an appropriate size to granules by less than 8mm and then the granule plate produced by a special type (Mortar Grinder RM 200) in the laboratory of the Research and Materials Department \ Ministry of Science and Technology, Rock for 48 hours until

access to fine powder when granular size (≤100 μ m). After the weight of the raw materials, mix well with Mortar with a mortar of fine agate to get a homogeneous mixture and a fine granular size of homogeneous sizes. The importance of this process lies in obtaining homogeneous powders that affect the reaction rate of these materials, The mixing process is very necessary in order to ensure the distribution and homogeneity of the powder granules in full because of the varying densities between the base material and the supporting material as well as the importance of mixing well in the physical properties of the final product. The resulting powders are then dried in an electric drying oven (100 °C) for half an hour to remove the moisture. After this process, the bonding material (PVA) is added by 2% of the total weight of the model. The mixture is to be bonded during the process of removal from the mold and no distortion or surface defects of the model. This ratio does not affect the main components. Final heating. After the completion of the weight and homogeneity of the samples, the cylindrical cylinder with diameter (2cm) was prepared. The compression process was done using an electric screw type (FYD-40MTI) of existing German origin piston in the Ministry of Science and Technology \ Materials Research Department - Powder Technology Center. The specimen were cylindrical (2 cm) and (3 mm) high for all tests, except for compressive strength, where the pressure was obtained. The sampling process was carried out in the Ministry of Science and Technology / Materials Research Department through the use of an electric oven (the use of an electric oven) Electric Muffle Furnace) Type [CARBOLITE] English origin (1200 °C). The Argon gas bottle is connected to the furnace to prevent failure and oxidation of the models because the material of the reinforcement is aluminium from the metal, which is fast oxidation and interaction with oxygen, knowing that the Argon gas is inert and when injected into the oven, (5°C/ Min.) and to keep the sample in the oven for two hours, then turn off the furnace and cool the compresses inside the furnace slowly and cool to room temperature, ie to the morning The next day.

3- Measurements

First: X-ray spectroscopy (XRF)

Before mixing the powders, the components of these powders must be checked. They are the aluminium powder supported and Basalt base powder. This test was conducted at Baghdad University \ Faculty of Science \ Geological Department. Using a German X-Ray Fluoridation device.

Second: x-ray diffraction (XRD)

X-rays are electromagnetic rays, mono-wavelengths and short wavelengths that produce x-rays by colliding electrons with metal within the X-ray tube. The X-ray beam is in all directions when it falls on levels (consisting of aligning the atoms in clusters within the crystal)), And to determine the distance between the crystalline levels during X-ray diffraction examination, the following relationship is applied [6, 7].

$$2d\ \sin\theta = n\lambda \quad \text{--- (1)}$$

Where:

d : Distance between atomic levels

θ : Diffraction angle (Barak angle) :

wave length :λ

n: An integer represents the order of the diffraction peak

X-ray diffraction of the precipitation was examined using a Japanese type XRD-6000 SHIMADZU device. The tubes used were Cu (kα). The tests were conducted at room temperature. We were provided with the values of the interstitial levels of the atomic levels (d) for each perforated and obtained the phases by comparing the values of the interstitial (d) with the radiance and the angle (2θ) According to standard schedules for materials used to obtain Miller transactions.

Third: Scanning electron microscopy (SEM).

The examination of the samples was carried out by the Ministry of Science and Technology / Materials Research Department, using the electron microscope (TESCAN) type (Vega III) of the origin, shown in Figure 3.16. Electrons instead of light waves, which gives a detailed picture three-dimensional and magnified and the image in black and white because it does not rely on light waves, and the samples to be examined inside the empty column of air in the electronic microscope through the entrance or seal closure where the samples are painted silver Or gold to be his Viability of electrical conductivity [8].

Fourth: thermal conductivity tests.

The third generation of Mathis TCi technology in the Ministry of Science and Technology / Materials Research Department is characterized by wide thermal conductivity capabilities, including non-sampling tests. The device also gives a very accurate and simple description of the thermal conductivity and thermal flow. It does not need to calibrate or prepare samples to measure its thermal conductivity. It also measures the conductivity of W / mk (0-100) and a wide range of temperatures (-5 to to 200CC). The device is equipped with one or two sensors to help analyze the accuracy of solids, liquid, powders and pastes in a time of only 5 minutes. Because the device is non-contagious, the samples remain intact and usable after the test [9]. This device relies on the technique of (MTPS) any sensor from the side of the side sample, where it releases the heat to the sample and at the same time measures the thermal conductivity and flow through a program linked to the device, and Figure (1) shows the shape of the device (MathiTC i).

Figure (1) the shape of the device (Mathis TC i).

use the device can be included in the following steps: To

The materials used (the sample) may be solid, liquid, powdered or paste.1-

A stream is given to the sensor to be supplied with a small amount of heat.2-

3-The supplied heat output increases the interaction temperature between the probe and the sample and is usually less than 2 ° C. The high temperature in the probe and sample interface stimulates and changes the voltage of the sensor.

4-The voltage increase rate of the sensor is used to determine the physical and thermal properties of the sample element.

Thus, thermal conductivity and its variants can be calculated from the following relationships [10,11].

$$Q = \frac{dH}{dt} = -\lambda A \frac{dT}{dx} \quad \text{.....(4)}$$

whereas:

) Q: The amount of heat for the time unit (watt

) H: Heat (J

t: Time (sec).

λ: thermal conductivity (w / m.k).

T: Temperature (K).

X: High test sample (m).

A: The area of the cross section of the sample (m^2).

The thermal diffusion equation (m^2 / s) is:

$$\delta = \frac{\lambda}{C_p \cdot \rho} \quad \text{.....(5)}$$

)Cp: Specific thermal capacity (J / g.k

) ρ: Sample density (g / cm^3

The thermal flow relationship Ɛ ($W.S^{1/2}$ / m^2 K) is:

$$\varepsilon = \sqrt{\lambda \cdot \rho \cdot C_p} \quad \text{.....(6)}$$

The thermal resistance R (m^2.K / W) is:

$$R_{thermal} = \frac{\Delta x}{\lambda} \quad \text{.....(7)}$$

4- Results and discussion

First: X-ray Fluorescence (XRF)

After the aluminium powder and the basalt powder were tested by the X-ray machine, the ratio of aluminium was (99%), while the highest percentage of basalt was found to be about 39% for silica SiO_2. This is expected for basalt rocks with the highest percentage of silica oxide. The two tables below (1), (2) illustrate the results of the chemical analysis of both extractors.

Table (1) Chemical analysis of aluminium powder.

% concentration	Element
0.5	Fe
0.03	Pd
0.0005	Ar (Arsenic)
Rem.	Al

Table (2) Chemical Analysis of Basalt Powder.

Element	% concentration
SiO2	39.18
MgO	5.77
Al2O3	10.82
P2O4	1.122
K2O	1.343
CaO	12.96
TiO2	3.072
Fe2O3	12.32
MnO	0.184
WO3	0.140
Trace	——

Second: X-ray diffraction test results (XRD)

1- X - ray diffraction results for basalt powder

Figure(2) shows the X-ray diffraction of basalt rock after milling and is largely consistent with the study of the researcher [12]. (XRF). These oxides are composed of four compounds. The first compound, CaMg $(SiO_3)_2$, is monoclinic, consisting of (MgO, CaO (SiO_2)), which is highly concentrated in the base powder, especially SiO_2, which greatly helps to increase the hardness of basaltic rocks, while the second compound is ($CaAl_2Si_2O_8$) with Triclinic, where the most concentrated is silica and the third compound $CaSO_4.2H_2O$ (Gypsum), Monoclinic and finally Fe_2O_3 (Cubic). When we observe the four components of the basalt we find that more The coefficients are the silica (SiO_2) and the Monoclinic (Meloclinic) .Miller coefficients were found by comparing the values of (d) at the angle values (2θ) of the Peaks with the standard tables of the ASTM card and that the standard scale numbers for the four compounds are(0318-17), (1486-41), (0311-33),(1346-39). [13].

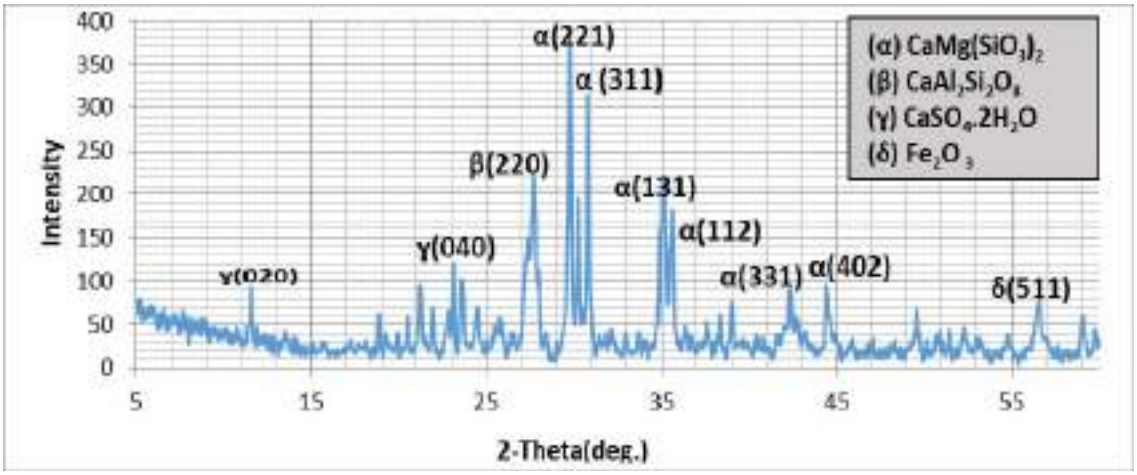

Figure (2) X-ray diffraction of basalt rock.

2- X - ray diffraction results for aluminium powder

Figure 3 shows the X-ray diffraction spectra of the aluminium powder. We observe from the test that the type of powder used is Cubic. It is noted from the peaks of the diffraction that the coefficients of meler (hkl) are either individual or odd even if any:
h2 + k2 + l2 = 3,4,8,11……
This means that the values of Miller's coefficients will be within the crystal structure (F.C.C):
…...(311) ,(220) ,(200) ,(111)
It is the same structure studied by researcher [14]. This is evident as the aluminium of the metal system (F.C.C) is a clear indication of the high purity of the aluminium powder used.

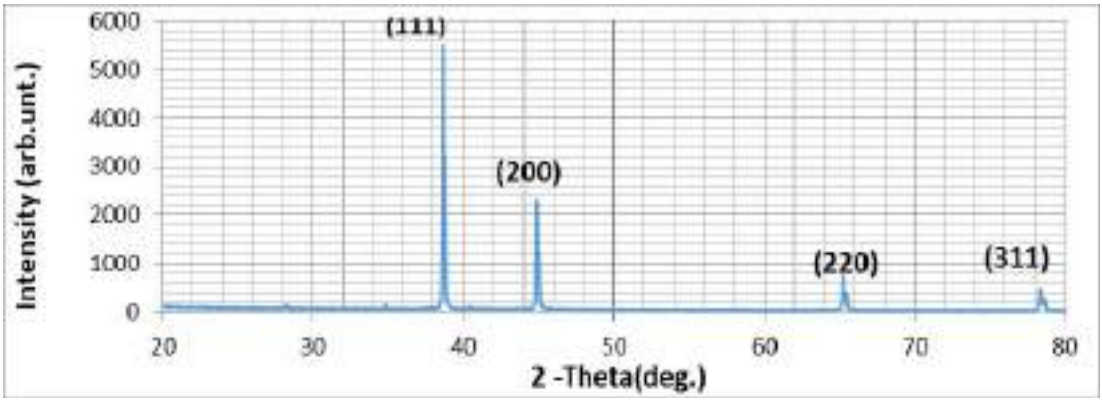

Figure (3) X-ray diffraction of aluminium powder before sintering.

3- X-ray diffraction results after formation and sintering

Figure (4), (5), (6), (7), (8) shows the results of X-ray diffraction spectroscopy after sintering at (1000 1000) for only 2 hours. Alumina (Al_2O_3) (25.6 = 22), (65.5 = 22), and we observe the emergence of (Si) with Cubic at the two peaks (28.45 = 22), (47.32) = 22). Also, we notice a large aluminium spread with increasing the added support rates as shown in the following forms, with a deviation of some angle positions of the basalt complexes. The spread of the aluminium can be observed after each reinforcement. The appearance of alumina is evidence of increased hardness. This is what was obtained when the hardness tests and compressive strength were observed, ie, there is a clear improvement in the increase in the intensity of the diffraction peaks, which indicates the crystalline growth and the homogenization of the crystalline structure and the improvement of all the physical properties. This is true with microstructure and electron microscopy (SEM) The temperature of sintering has a significant effect on the melting of

aluminium granules and formation of the liquid phase, which helped fill the blanks or pores generated during mixing and formation. This is evident when observing ratios 40% and 50% aluminium for Al (Al_2O_3, SiO_2). The combination of basalt oxides and aluminium granules at 50% produces a ceramic compound which is characterized by high hardness and resistance.

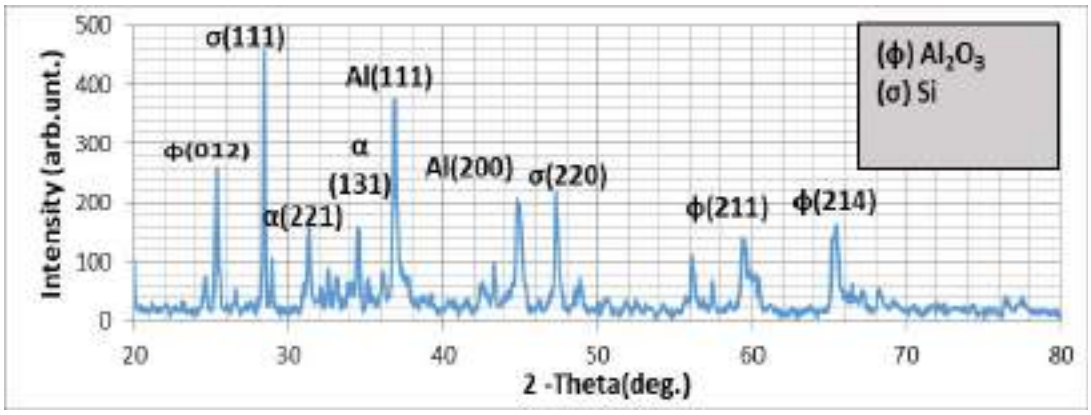

Figure (4) X-ray diffraction at 10% reinforcement after formation and after sintering.

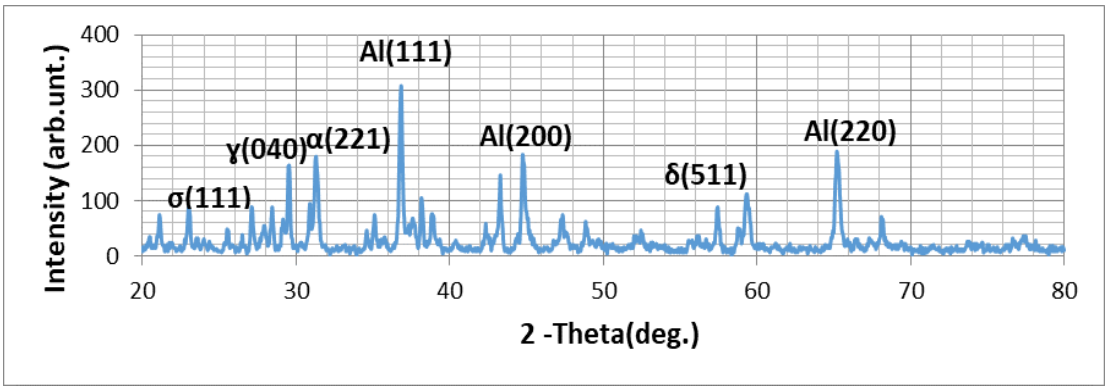

Figure (5) X-ray diffraction at 20% reinforcement after formation and after sintering.

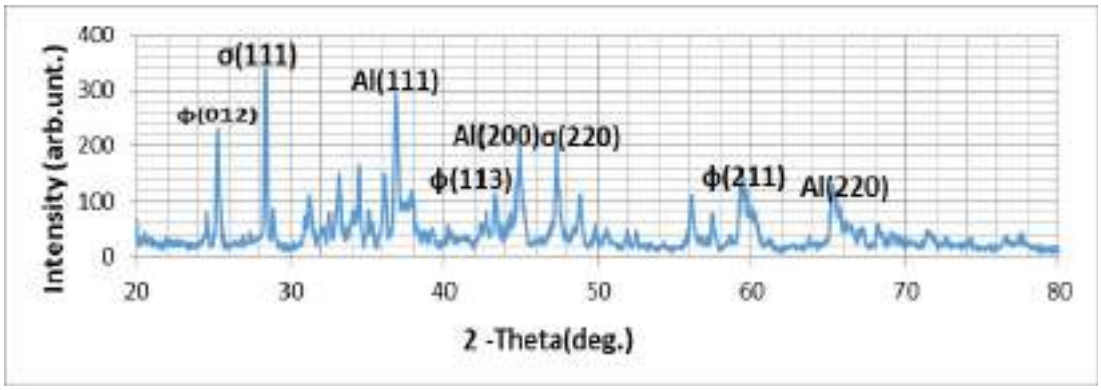

Figure (6) X-ray diffraction at 30% reinforcement after formation and after sintering.

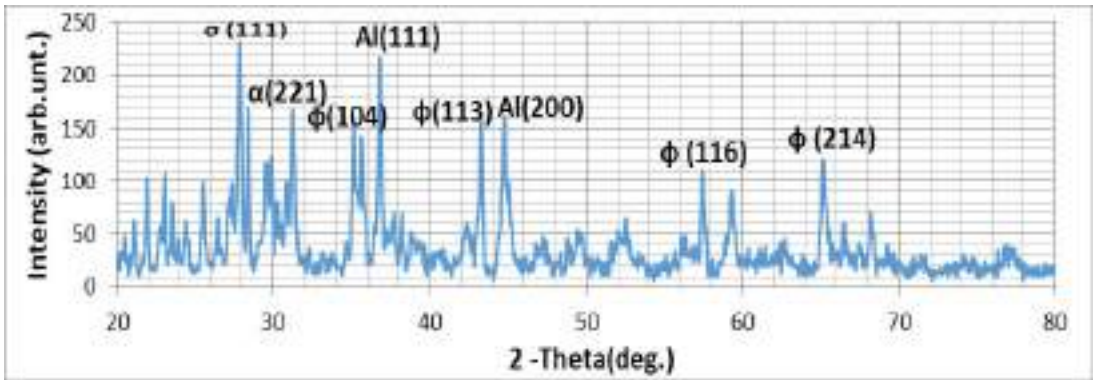

Figure (7) X-ray diffraction at 40% reinforcement after formation and after sintering.

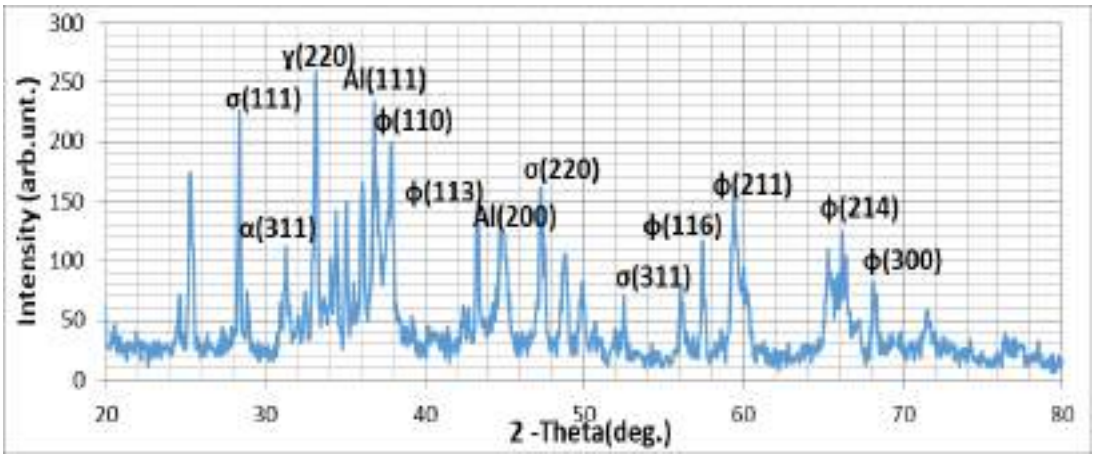

Figure (8) X-ray diffraction at 50% post-forming and post-fertilization ratio.

Third: Results of Scanning Electron Microscopy (SEM)

Through the images of the electron microscopy microscope (SEM) shown in Figure (9) of the compound (Basalt-Al and at 10 µM), and with a magnification force (5KX) for all samples, we observe what is coming In the form (9 / A) with a percentage of reinforcement (0% aluminium) after thermal treatment, we notice that the bond between the basalt components is homogeneous but somewhat random, but the effect of the heat is apparent through the cohesion of the granules with each other. Microstructure. It is also noted that there are low density and high density areas that lead to the spacing of elements and their heterogeneity, and (9/ B) where the aluminium reinforcement ratio is 50%. We find that the temperature of sintering at (1000 °C) and the ratio of large aluminium has a clear effect on the distribution and fusion of the full aluminium between the basalt compounds with a clear disappearance of pores and a lack of surface defects, a re-crystallization of aluminium grains bonding the eight basalt oxides.

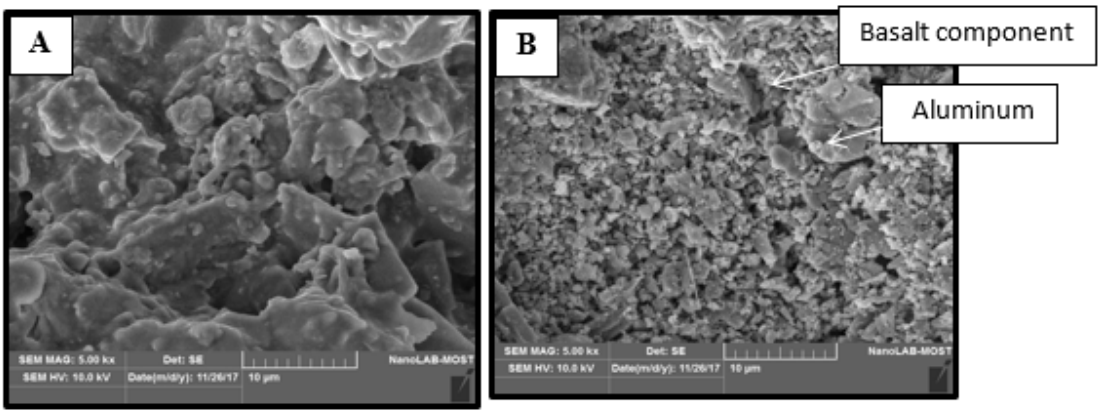

Figure (9) The images of the scanning electron microscopy (SEM) at (10μm) and the magnification force (5 KX) where :(A) 0% Al , (B) 50% Al.

Fourth: the results of thermal tests

1-Effect of the content of the particles on the thermal conductivity

Figure (10) and Table (3) show the relationship between the effect of the aluminium content on thermal conductivity and the increase in thermal conductivity from (w / mk 0.76) to (3.7w / mk) Respectively, ie, the linearity between the thermal conductivity (λ) and the increasing support ratios. This is due to the fact that the basalt has a very low thermal conductivity because it is a group of oxides. The aluminium component is very high thermal conductivity. The other reason is the method of preparing the aggregate and the process of particle distribution and homogeneity during the process of formation and segregation. In addition to the opposite effect of both density and porosity on the increase of thermal conductivity, pores act as heat transfer insulators. Thus, the heat transfer process is converted from the base material (basalt) [15] To conduction to Convection. Low porosity values have a significant effect on increasing thermal conductivity, which is inversely proportional.

Table (3) Thermal conductivity with change in basalt-Al.

Sample No.	Sample Code	Thermal Conductive(λ)
1.	100%Basalt+0%Aluminium	0.76
2.	90%Basalt+10%Aluminium	0.97
3.	80%Basalt+20%Aluminium	1.3
4.	70%Basalt+30%Aluminium	1.81
5.	60%Basalt+40%Aluminium	2.8
6.	50%Basalt+50%Aluminium	3.7

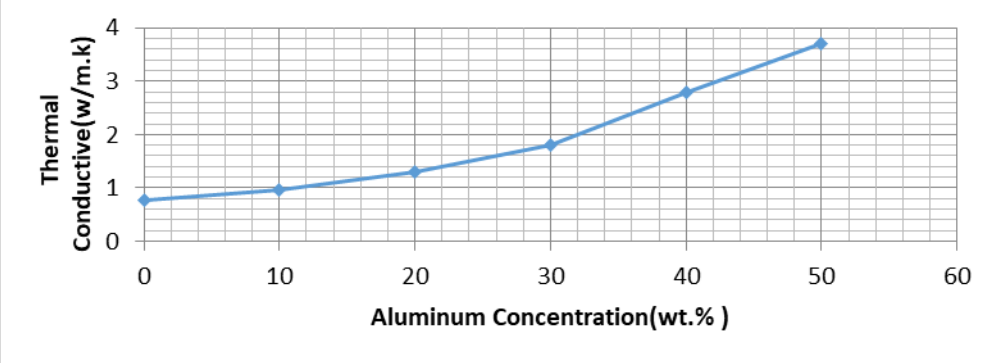

Figure(10) The relationship between the increase of the weight ratio of aluminium particles and thermal conductivity.

2- Effect of the particles' content on thermal Effusion

Figure (11) and Table (4) show the relationship between the effect of the aluminium content on the thermal flow and the increase in thermal flow from (1101w / $s^{1/2}$ / m^2.k) to (2080W. $S^{1/2}$ / m^2.k) (0%) to (50%) respectively, ie, a direct correlation between the weight ratios of the reinforcement and the thermal flow (ε). There is a significant improvement in the thermal flow values with the increase of the aluminium due to the improvement of thermal conductivity and density after the frying. As the high thermal conductivity of aluminium significantly facilitated the flow of heat between the parts of the compound and with the increase of the reinforcement ratios we notice the clear difference between the values of the increasing effusion.

Table (4) Thermal Flow with Basalt-Al Modification Ratio.

Sample No.	Sample Code	) Thermal Effusion (ε
1.	100%Basalt+0%Aluminium	1101
2.	90%Basalt+10%Aluminium	1209
3.	80%Basalt+20%Aluminium	1380
4.	70%Basalt+30%Aluminium	1590
5.	60%Basalt+40%Aluminium	1830
6.	50%Basalt+50%Aluminium	2080

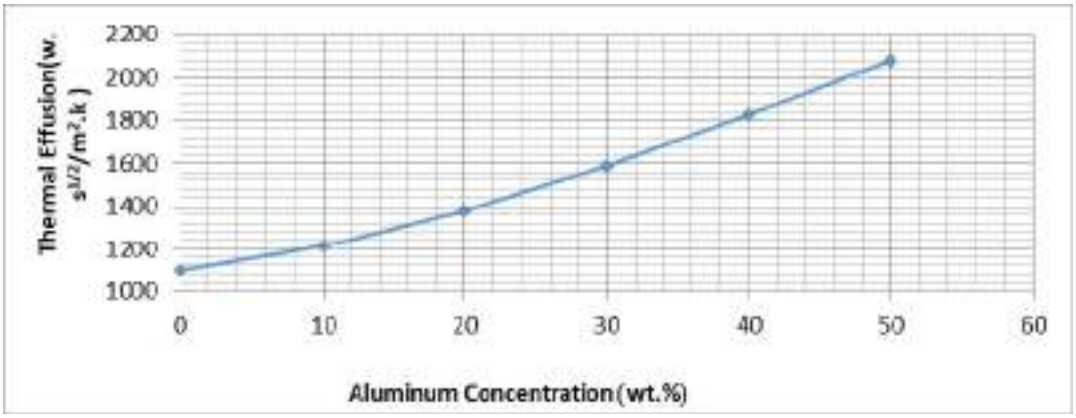

Figure (11): The relationship between the increase of the weight ratio of the aluminium particles and the thermal effusion.

3- Effect of the content of the particles on the spread of thermal

Figure (12) and Table (5) show the relationship of the effect of the aluminium content on thermal diffusion where where we observe the increase of thermal spread from (0.4665mm^2 / sec) to (1.1643mm^2 / sec) (50%) respectively, which is also a linear fit between the weight ratios of the material and the thermal spread, which was found by thermal conductivity and thermal flow in the two paragraphs above, as well as the values of high density and thermal conductivity after sintering and the accompanying changes in the crystalline pattern (spike) Significant increase in heat propagation values is very evident through the high conductivity of aluminium Aluminium granules scattered through pores also helped to increase thermal diffusion.

Table (5) Thermal diffusion with Basalt-Al Composite Ratio.

Sample No.	Sample Code	) Thermal Diffusion (
1.	100%Basalt+0%Aluminium	0.4665
2.	90%Basalt+10%Aluminium	0.6033
3.	80%Basalt+20%Aluminium	0.8874
4.	70%Basalt+30%Aluminium	1.2958
5.	60%Basalt+40%Aluminium	2.3411
6.	50%Basalt+50%Aluminium	3.1643

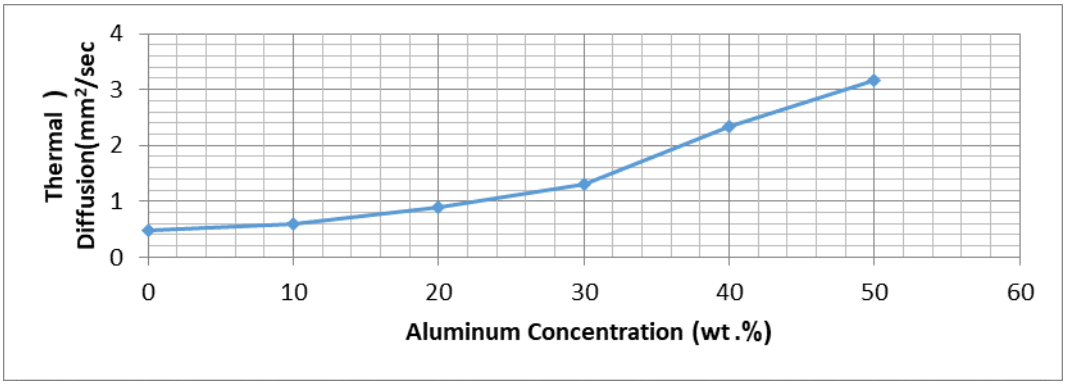

Figure (12) The relationship between the increase of the proportion of the aluminium particles and the thermal diffusion.

4-Effect of the content of the particles on the thermal capacitance

Figure (13) and Table (6) show the relationship between the effect of the aluminium content on the thermal capacity and the decrease in the thermal capacity from (656.3791 J / kg.k) to (444.5997J / kg.k) (50%), respectively. The reason for the decrease in thermal capacity (Cp) with the increase of the added percentages of the aluminium alloy powder due to the behavior of the composites as a conductor of any composite of a basalt and a conductive material. The result is a semi- This is consistent with the researcher [16].

Table (6) Thermal capacity with change in basalt-Al.

Sample No.	Sample Code	Thermal Capacity (Cp)
1.	100%Basalt+0%Aluminium	656.3791
2.	90%Basalt+10%Aluminium	640.5758
3.	80%Basalt+20%Aluminium	570.0089
4.	70%Basalt+30%Aluminium	538.6580
5.	60%Basalt+40%Aluminium	458.2512
6.	50%Basalt+50%Aluminium	444.5997

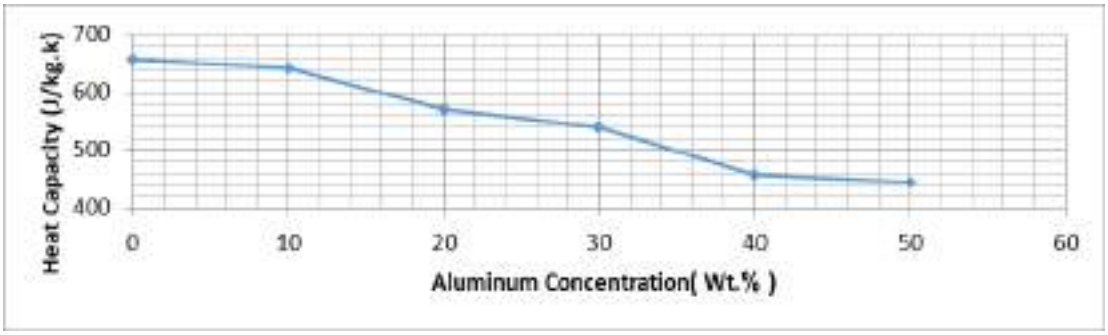

Figure (13): The relationship between the increase of the weight ratio of the aluminium particles and the thermal capacity.

5- Effect of the content of the reinforcing particles on thermal resistance

Figure (14) and Table (7) show the relationship between the effect of the aluminium content on thermal resistance (R). We observe the reduction of thermal resistance from (0.00422 m^2.k/w) to (0.00087 m^2.k / w) (0%) to (50%), respectively, any process that is inversely proportional to the thermal resistance with the increase of the content of the aluminium and it is expected from the compound because the insulators show resistance to the transfer of heat during them but by increasing the content of the material (aluminium) any conductive material to fill the gaps) Between the granules, which facilitates the work of a physical way of heat transfer during the compound, ie, proportional to the porosity and vice versa with the thermal conductivity.[17].

Table (7) Thermal resistance with change in basalt-Al.

Sample No.	Sample Code	Thermal Resistance (R)
1.	100%Basalt+0%Aluminium	0.00422
2.	90%Basalt+10%Aluminium	0.00332
3.	80%Basalt+20%Aluminium	0.00243
4.	70%Basalt+30%Aluminium	0.00146
5.	60%Basalt+40%Aluminium	0.00106
6.	50%Basalt+50%Aluminium	0.00087

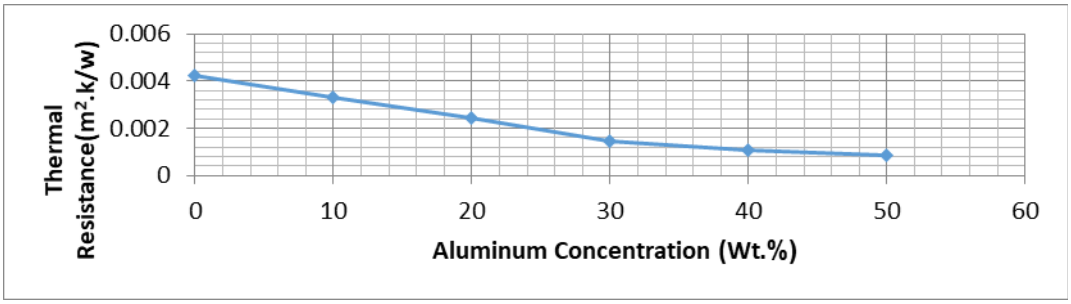

Figure (14) The relationship between the increase of the weight ratio of aluminium particles and thermal resistance.

4- Conclusion

1- XRF showed 99% purity of aluminum and 39.18% of SiO2.
2- SEM scans showed the homogeneity of the overlays with each other, especially 50% aluminium.
3- The results of X-ray diffraction showed that there were four compounds in basalt rocks with crystalline systems (Cubic, Monoclinic, Triclinic), and after the sintering, the Rhombohedra (Al_2O_3) compound and the FCC (Si).
4- Increasing the thermal conductivity from (0.76 w/ m.k) to (3.7w / m.k) from the percentage of reinforcement (0%) to (50%), respectively. As well as increased thermal flow from (1101w. $S^{1/2}$ / m^2.k) to (2080w $s^{1/2}$ / m^2.k) from the percentage of reinforcement (0%) to (50%), respectively.
5- Increasing the thermal spread from (0.4665mm^2 / sec) to (1.1643mm^2/ sec) from the percentage of reinforcement (0%) to (50%), respectively.
6- Decrease in thermal capacity from (656.3791J / kg.k) to (J / kg.k444.5997) from the reinforcement percentage (0%) to (50%), respectively. (m^2.k / w 0.00422) to (0.00087m^2.k /w) from 0% to 50% respectively.

References

[1] A. L. Samarrai, "Plastics and Composites", First Edition, 2010.
[2] P. W. Lee " Powder Metal Technologies and Applications " published in 1998 as Volume 7 of ASM Handbook , The Volume was Prepared Under the Direction of the ASM Handbook Committee. , Copyright 1998 by ASM International .
[3]Q.Wang, X.Zhang, X.Pei , "study on the friction and wear behavior of basalt fabric composites filled with graphite and nano-SiO_2"Materials and Design, Vol.31, Issue 3, Pages (1403-1409), 2010.
[4]S. Uncik, V. Kmecova, "The effect of basalt powder on the properties of Cement composite", procedia engineering 65, Page (51-56), 2013.
[5]P. Reiterman, O. Helcapek, M. Jogl, P.Konvalinka," physical and mechanical properties of composites made with aluminous cermet and basalt fiber developed for high temperature application", hindawi publishing corporation advances in materials science and engineering, Vol.10, article ID 703029, 2015.
[6] B.D. Cullity, S.R. Stock “Elements of X-Ray Diffraction "PP.346-565, ADDISON-WESLEY PUBLISHING COMPAN , Copyright @ 1956 .
[7] F. M. Mahdi , Raed N. Razooqi , Saif S. Irhayyim "Effect of Graphite Content and Milling Time onPhysical Properties of Copper Graphite Composites Preped by Powder Metallurgy Route" Australian Journal of Basic and Applied Sciences , Vol. 7 , No. 12 , PP. 245-255 , Oct. 2013.
[8] D. M. Mullan, "scanning electron microscopy 1928-1965". P.(175-185), 17(3), 2006.
[9] D. Edison. Selvaraj, "Partial discharge characteristics of enamel filled with micro and nano composite of SiO2 and TiO2." International Journal of Science and Engineering Applications 1.2: pp.95-101. (2012).
[10] E1952, “Method for Thermal Conductivity and Thermal Diffusivity by Modulated Temperature Differential Scanning Calorimetric”, ASTM International, West Conshohocken, PA.(2008).
[11] Mateusz B., “Carbon Nan tube Networks in Epoxy Composites and Aero gels", PhD. Thesis, University of Pennsylvania, (2007).
[12] A. Prstic, Z. Acimovic-Pavlovic, L. Pavlovic, L. Andric, A. Terzic," The Application Of Basalt In The Manufacturing Of Ceramic Glazes", Journal Of Mining And Metallurgy, 43 A (2007) 53 – 60.

[13]S..I.,polytechna, Foreign Trade Corporation ,panska, Czchoslovakia, ICDD Grant-in-Aid.(1990).
[14] C. hai Jiang*, Chang-qing Ye and Bo Hong," X-ray Diffraction Analysis of the Recrystallization Behavior of SiCw/Al Composite at High Temperature", Materials Transactions, Vol. 46, No. 10 (2005) pp. 2125 to 2128. 2005 The Japan Institute of Metals.
[15] Jose Sebastian, Eby T.Thachil, Jobin,Job and Macdhavan;" Enhancement in the electrical and thermal properties or Ethylene Vainly Acetate by zinc oxide Nano particles", open Journal of composite materials, India, Vol.5, PP.(79-91), 2015.
[16] Edison Selvaraj, D. and Sivaprakash," Characteristics of electrical and thermal properties of enamel filled with CNT", proceedings of the third International conference on trends in Information, New York (2013).
[17] I. .K. Jassim, A. F. Abdul Aziz, F. K. Farhan ,Salih Y.Darweesh "Characteristics of the Electrical Conductivity of the Basalt-Aluminum System Manufactured by Powder Technology", Journal of University of Babylon, Vol.26, No.2,pp.(288-300), 2018.

Available online at
http://namrc.uotechnology.edu.iq/index.php/

Nanotechnology and Advanced Materials Research Centre

Proceeding Articles Book 00 (2018) 000–000

6th International Scientific Conference on Nanotechnology, Advanced Materials and its Applications

Structural and Thermal Properties In Ferromagnetic INVAR (Fe-Ni)alloys Prepared by powder Metallurgy Method

Salih Y.Darweesh[1], Ismael .K. Jassim[2],Abdullah M.Ali[2]
[1] Physics Department, College of Education, Tikrit University, Tuzkormato, Iraq
[2] Physics Department, College of Education and Pure science, Tikrit University, Iraq
Corresponding auther:Salih.youns@gmail.com

Abstract

In order to understand the invar effect in 3D transition metal alloy, the ($Fe_{1-x}Ni_x$) alloys with (x= 35, 50, 70)wt.% have been chosen. Experiments have made on structural and thermal properties to study the physical origin of invar characteristics such as thermal expansion, phase transition and curie temperature (T_c) which are closely related to its ferromagnetism. (Fe_{65} Ni_{35}) shows an anomalously small thermal expansion coefficient below the curie temperature with (FCC) structure. This behaviour has not been found in other combination. The structure results show the (BCC) phase occurs above (50wt.% Ni) and does not affect the invar behaviour.

K*eywords*: phase transitions, Invar alloys, thermal expansion, material engineering, powder metallurgy magnetism.

1- Introduction

Powder metallurgy is used in the production of soft magnetic materials for direct current applications and for permanents .In many of these applications ,parts are produce by powder metallurgy ,because this method permits production to final shape with a minimum subsequent machining and grinding while at the sometime achieving desirable magnetic properties[1]. Nickel is soluble in iron in all proportions. Nickel helps to prevent excess grain growth at high temperatures and enables fine a grain steels to be produced more easily [2].

Nickel may be present in the steel up to 50% percent. In the range of 2 to 5 percent nickel contributes great strength and hardness with high elastic limit, good ductility and a good resist acre to corrosion and a decrease Mach inability [3]. In the range of 30 to 40 percent nickel lowers the coefficient of thermal expansion 9 and it increases magnetic permeability large amounted of nickel gives resistance to oxidation at high temperature Invar has practically zero thermal expansion coefficient ,which is quite useful for engineering application. Thermal expansion is a normally associated with the onset of ferromagnetism in certain, notably (Fe_{1-x} Ni) with is kno 25 the Invar effect [4].

Many experimental and theoretical studies of Invar alloys have been under taken in percent years using ultrasonic ,neutron scattering [5,6] and other techniques to elucidate the microscopic origin of the effect , but as yet no clear understanding has been reached. Never the less in all models of the Invar effect it is recognized that the relation between magnetic and atomic volume in tetratomic distance plays a critical role[7]. The Fe-Ni system is also is of fundamental important from the structure point of view since Ni has a(FCC)structure and Fe is (BCC) at room temperature. As an example of ferromagnetism, the (Fe_{1-x} Ni) alloy system was chosen with (x=0.35,0.50,0.70) to study the thermal and structural properties to understand the Invar effect in 3D transition metal alloys Fe with Ni.

2- Materials and Method

Pure Fe and Ni Powders supplied by (B DH LTd) was used to prepare the alloys as a cylindrical sample of 10mm diameter and 30 mm height. These percentages of Ni are added to Fe and mixed with ball mills for 24 hr. The powder union alloy pressed at 100 (Kgf). Sintering was carried out at temperature of 1050 ºC for 2hr of 10 ºC /min heating rate .

The metallic element ratio of the alloys are determined by atomic absorption spectroscopy and induction coupled plasma (p) techniques. This measurement indicates no evince of any impurties .the samplefor x-ray diffraction (XRD) and differential thermal analyses (DTA) were obtained powder alloys down to 3000 μr mesh grains.

x-ray diffraction at RT type Philips Pw 1877 was used .to obtain lattice parameters more accurately , the Nelson –riley extrapolation was used . The specific heat measurements at high temperatures obtain from the differential thermal analysis (DTA type Net 25ch 409) where a 1100 ºC furnace was used with a heating rate of 10 ºC /min . the weights of sample used were about 500 mg .the specific heat determined from the depends on the mass (m) and the heat reaction or the enthalpy change (ΔH) ; then by using the equation [8] .

$$C_P = [\Delta H/dT].(1/m) \dots\dots\dots (1)$$

Where , dT is the differen in temperature between a sample (5) daintier reference (r) .A Cylindrical specimens ≅ 3 cm in length is used for the thermal expansion as a function of temperature in range 300 to 100 K.

3- Results and discussion

Alloys which exhibit Invar behavior have a small thermal expansion coefficient below the curie temperature .Fig(1) shows the thermal expansion coefficient versus temperature cures. for the alloys in the (Fe_{1-x} Ni_x) system (x=0.35,0.50 and 0.70), the composition ($Fe_{0.65}$ $Ni_{0.35}$) shows negative thermal expansion below curie temperature (T_c) with more Invar effect than in ($Fe_{0.50}$ $Ni_{0.50}$). Both alloys have a(fcc) ɣ-phase structure . the system ($Fe_{0.30}$ $Ni_{0.70}$) has a (bcc) α-phase structure where there is no Invar behavior as shown in figure (1).

Table(1) shows the important physical properties of the three samples .

The negative thermal expansion of the sample($Fe_{0.65}$ $Ni_{0.35}$) below T_c is due to the interaction between the lattice Vibration and magnetic degrees of freedom .

Increasing the temperature tends to produce expansion , but because of special strong magnetic attraction between atoms in this alloys , a sample net expansion takes place .However , above curie temperature the alloy expands normally .these results are identical with the spontaneous magnetization of the alloys which shows anomalies such as deviation of the magnetic moment curve Fe concentration [8] the specific heat result for (Fe_{1-x} Ni_x) alloys are shown in Figure(3a,b,c)which reveal an anomalous temperature dependence .

At ($Fe_{0.50}$ $Ni_{0.50}$) , Cp-curve is character by two distinct maxima , one at about 780K and the second revels an anomalous maximum at about 540K .the position of this anomalous maxima is only slightly concentration depended where there is a strong decrease of the curie temperature as well as of the magnetic heat of transformation occurs with decreasing nickel content so that the alloy with 35% Ni reveals only a single maximum composed of both curie peak and the maximum caused by the anomalous excess heat .similar effects have been seen in other Invar alloys such as $Fe_{0.80}$ Ni_x Cr_{50} system [9,10].the lattice parameter for $Fe_{0.65}$ $Ni_{0.35}$ (111) lines position using Bragg's law for a cubic system with smallest error (∓ 0.1) due to incorrect values of 20 angle diffraction .figure(3)present the change of the lattice parameter (a) versus milling time for the ball milling process of $Fe_{0.65}$ $Ni_{0.35}$ .the value of lattice parameter increased from a=3.60 ºA for 24 hr to a=3.79 ºA for 96 hr .such change of (a) when milling time increase was because of the small difference between the atomic size of the Ni and Fe atoms .the structural result fit well and agree with the data reported in Ref [4,6] to obtain a deeper understanding of the Invar phenomena ,it is helpful to collect microscopic information by scanning Electron microscopic (SEM) about the physical properties .more detailed discussion of these phenomena will be given in future work.

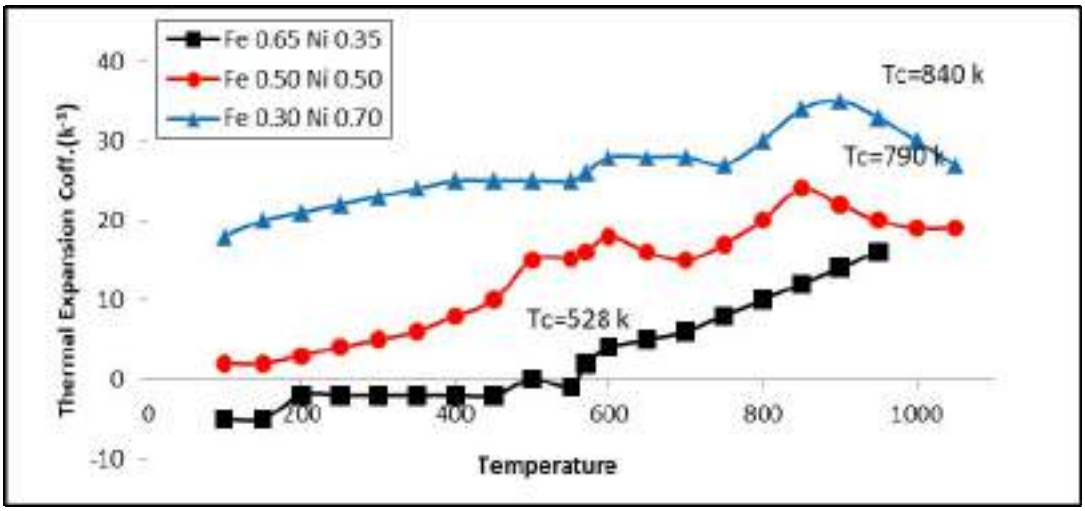

Figure (1): The Relation between thermal expansion coefficients and temperature.

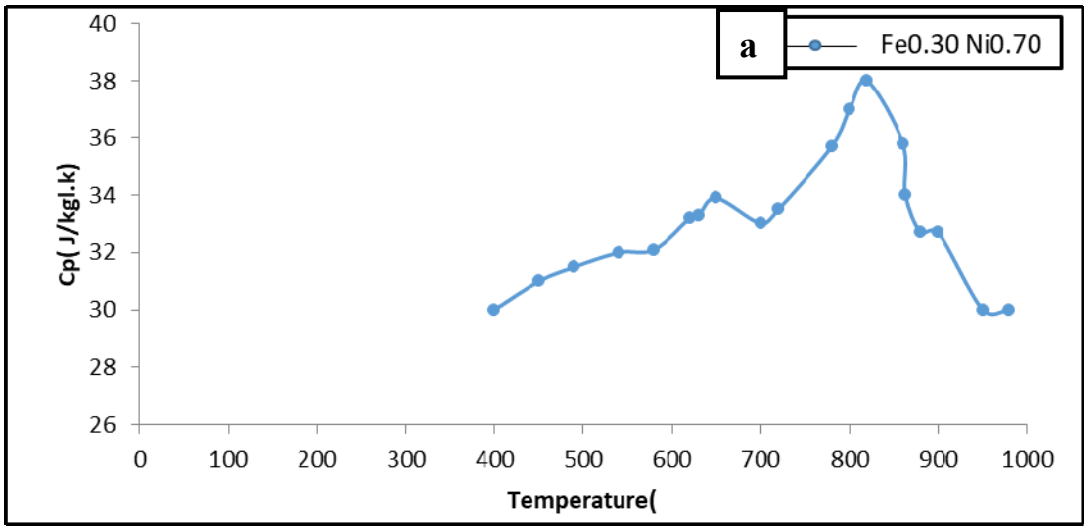

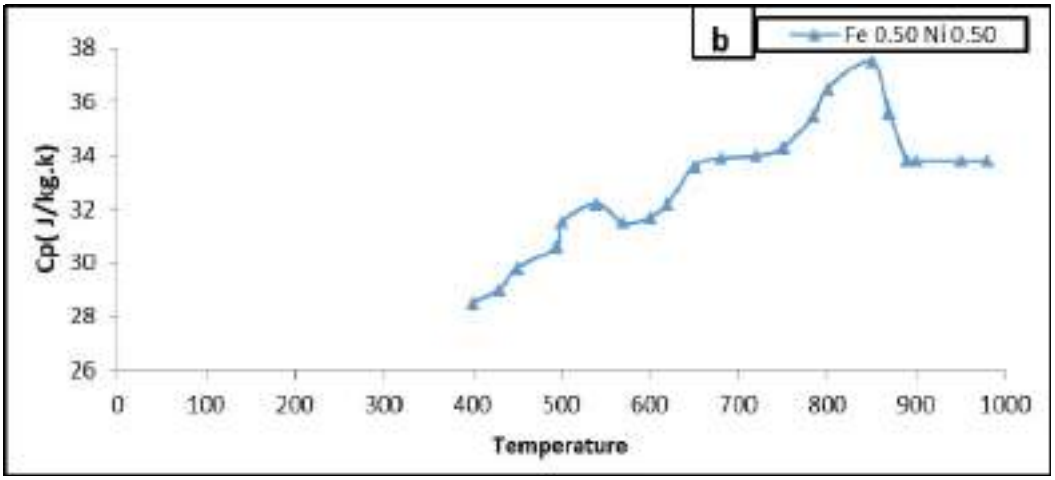

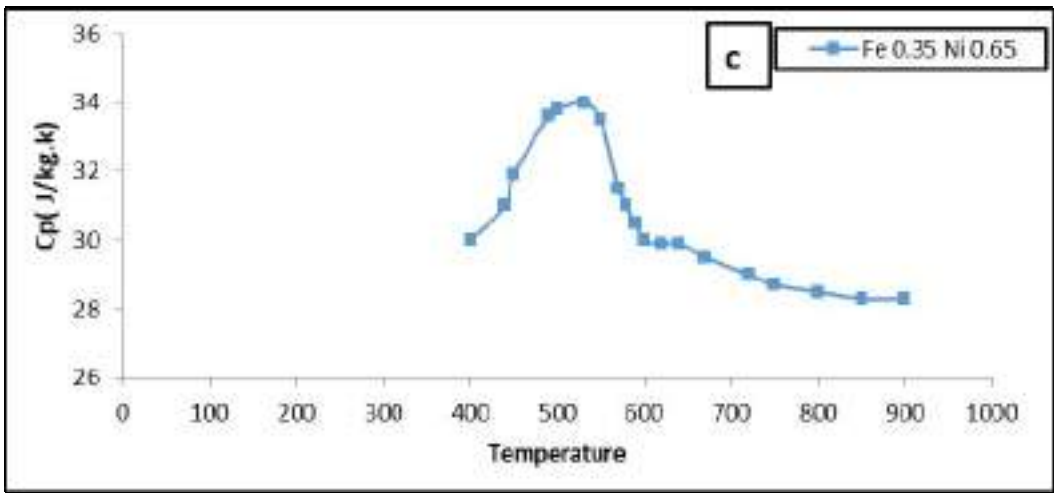

Figure (2.a, b, c): The Relation between specific heat (C_p) and temperature.

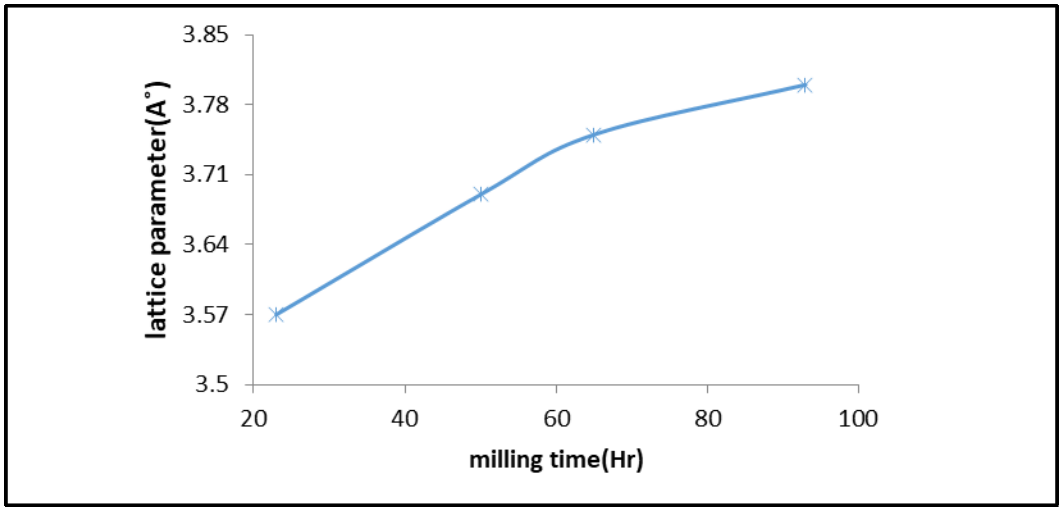

Figure (3): Lattice Parameters of Fe.Ni Versus milling time (Hr).

4- Conclusion

In this work ,we investigate the effect of nominal composition on thermal and structural properties of Invar Fe_{1-x} Ni_x alloys with(x=0.35,0.5,0.70).It was found that :

1- $Fe_{0.65}$ $Ni_{0.35}$ shows Negative thermal expansion below curie temperature T_c due to interaction between lattice vibration and magnetic degree of freedom .

2- the specific heat result revel an anomalous temperature depended with x-content with strong deposes of T_c and heat transformation with decreasing Ni%

3- $Fe_{0.65}$ $Ni_{0.50}$ shows more Invar effect than in $Fe_{0.50}$ $Ni_{0.50}$ Both alloys an Fcc(ɣ-phase)structure while $Fe_{0.30}$ $Ni_{0.70}$ has bcc(α-phase) structure when there is no Invar behavio

References

[1] S.V.Grigoriev , S.V. Maloyev and G.kozik , APPl.phys.A74 719-721 (2002)
[2] P.J.Brown , I.k. Jassim ,physica B , 161,9(1989)
[3] J.W.Lynn , N.Rosov ,J.APPl.Phys ,75(10), 6069(1994)
[5] P.J.Brown , I.k.Jassim , Journal de Physique , C8, P307 NO 12(1988).
[5] I.k.Jassim , J.B Al-dabbagh ,International Journal of Engineering and scince ISSN:2278-4721, vol 7, P47(2012).
[6] J.Wittenauer ,the Invar effect Metals and Materials Society (1997)
[7] I.K.Jassim ,J.Al-dabbagh,R.Abbss, Journal Iraq of physics ,Vol 2, (2004)
[8] J.crangle,G.C.Hallam,Pro.Roy.soy, A272,119(1963).
[9] W.Bendick,H.H.Ettwing and W.PePPehof ,J.Phy.F.Meta phys,8,2525(1978).
[10] Y.End,Y.Noda and.Y.Ishika ,soild stat Common ,23,951(1977).

Available online at
http://namrc.uotechnology.edu.iq/index.php/

Nanotechnology and Advanced Materials Research Centre

Proceeding Articles Book 00 (2018) 000–000

6th International Scientific Conference on Nanotechnology, Advanced Materials and its Applications

Preparation and Characterization of porous ZnO from ZnO pastes by Doctor-Blade Method

Abdulla M. Ali[1], Kawkab D. Salim[2]

Physics Department, College of education for pure science, Tikrit University, Tikrit, Iraq

Abstract

The porous zinc oxide ZnO thick film was prepared by doctor- blade method. The structural, morphological of ZnO have been studied. XRD anaylsis assure that the ZnO thin film were of a hexagonal crystal structure with 16 nm particle size. AFM investigations showed that the produced ZnO particles have rod-shape with good disposability and 3.03nm rms.

1. Introduction

It is well known that nanostructures have very good sensitivity with respects to size, shape, type of material, and preparation techniques. Thus, ZnO is a good promising for recent and future application due to its wide band gap(3.2) eV, high conductivity, and it can be easily formed in a different shapes like rods, tubes, particles, wires, needles, etc[1]. The porous ZnO is a part from these structures, and it has a good advantages like the high area of surface, chemical stability, shape selectivity, and uniformity in pore size. The advantage of surface high area makes its surface has a high active, this would increase the interaction of gases with material of semiconductors. In brief words, it can be said that ZnO thin film must be high specification and porous to obtain high conversion in photovoltaic applications [2-5]. Doctor blade is a simple technique to produce thick films from its pastes, and it is a good method to fabricate the (DSSc) solar cell because it is ensuring us that the desired amount of pastes is metered on substrates at room temperature. Also its important to know the glueyness is varying according to the nature of substrate and the kind of product [6]. Amal kahlout was deposited ZnO paste on fluorine-doped SnO2-(FTO)-coated glass substrates using the "doctor blade" technique to form 0.5 × 0.5 cm layers. The layers were dried at 100 °C for one hour, followed by heating in air at various temperatures ranging from 200 to 500°C [7]. S.Sarker was deposited highly viscous titanium dioxide (TiO2) paste on a glass substrate coated with fluorine doped tin oxide (FTO) by using a doctor-blade method [8].

2. Experimental

ZnO photoanodes were engineered for flexible (DSCs) by doctor blade bloding a ZnO gel. To achieve good adhesion to substrate and inter particle connection, 1.2 gm zinc oxide (ZnO) nanoparticle powder (commercial P25 Degussa ZnO nanoparticles) with ethyl- cellulose as a binder for mixture components, then the mixture is dissolved in 4.5 ml of terpineol solution. The ZnO paste was coated on to glass substrate by docore- blade method with obtained thickness of (2-12 µm). then it was heated at 550ºC for 30 minutes, ethyle-cellulose and terpinoel were burned, lefting porous Zno just behind them . After deposition of porous ZnO, the films could be easily removed by ammonia surface activation without using high temperature.

3- Results and discussion

3-1Morphology of porous ZnO

Figures (1) and (2) show the AFM image of the porous ZnO that obtained by doctor-blade method, which is very simple way to produce ZnO paste, it exhibited perfect morphology with good crystal quality. Obtained porous ZnO has nanorods shape and the nanoparticles show a dens packing which is not good factor for absorption. The surface roughness analysis shows the ZnO film has 3.03nm rms and 2.47nm roughness average.

3-2 X-Ray diffraction Analysis

XRD pattern of the prepared porous ZnO film is shown in Fig. 3. It is clear from the figure that it has a hexagonal shape all the diffraction peaks are highly crystalline as well as the diffraction peaks are well defined and in accordance with the typical wurtzite hexagonal structure. We have ten major diffraction peaks were seen at figure(3), (31.79º, 34.44º, 36.26º, 47.55º, 56.60º, 62.88º, 66.41º, 67.96º, 69.04º, 72.72º) which can be assigned to diffraction from (100), (002), (101), (102), (110), (103), (200), (112), (201), (004) planes respectively, according to the data base in JCPDS card (00-036-1451). This revealed that the particle of porous ZnO with a hexagonal wurtzite structure (a=3.249Å, c=5.621Å) as in the table (1). The grain size was calculated by using Debye-Scherre formula. Figure (4) shows that there is a decrease in the value of grain size when the full width at half the maximum (FHWM) has increased. The calculated grain sizes are ranging between (16nm-10nm) table(2), this is a normal result according to the Debye-Scherrer equation as below:

$$D = \frac{0.9\lambda}{\beta_{FHWM}\cos\theta} \qquad \ldots\ldots(1)$$

Where D is the grain size, λ is the wavelength of incident X- ray (λ=0.1540nm),β_{FHWM} is the integral half width, and θ is Bragg angle [9]. Both of figs (5) & (7) declare an increasing in dislocation density and the strain with increasing of (FHWM). Also we had calculated the Zn-O bond length by using the formula [10]:

$$L = \sqrt{\left(\frac{a^2}{3} + \left(\frac{1}{2} - u\right)^2 c^2\right)} \quad \text{.....(2)}$$

Where u is positional parameter in hexagonal structure, it has given by[11]:

$$u = \frac{a^2}{3c^2} + 0.25 \quad \text{.....(3)}$$

Fig (7) explains the relation between Zn-O bond length and the volume of unit cell (V) which calculated by[11],

$$V = \frac{\sqrt{3}}{2} a^2 c \quad \text{.....(4)}$$

4- Conclusion:

Doctor- blade is a simple method to obtain porous zinc oxide, and it is suitable to fabricate DSSc solar cell, and grain size of 16 nm was calculated by Debye- Scherre equation.

Table (1): XRD parameters analysis forporouse ZnO

2θº	counts	FWHM	(rad)β	hkl	d*=(2sinθ/nλ)nm
31.7893	842	0.4977	0.008686504	100	0.355791193
34.4424	596	0.4556	0.00795172	002	0.382953636
36.266	1302	0.5275	0.009206612	101	0.403906758
47.5594	278	0.56	0.009773844	012	0.5240848
56.6088	450	0.5733	0.010005973	110	0.615898538
62.8805	302	0.6192	0.010807079	013	0.678569565
66.4139	54	0.5633	0.00983144	200	0.716423209
67.9603	264	0.6429	0.011220722	112	0.724532422
69.0495	172	0.656	0.01144936	201	0.736526243
72.72	46	0.656	0.01144936	004	0.769943922

Table (2): Some of structural parameter of porous ZnO

2θ	a	c	D(nm)	σ (line/nm^2)	ϵ	L(Å)	V (Å)
31.8	3.249292	5.621275	16.02735	0.003893	0.002089	1.47	51.3
34.3	3.018823	5.222564	17.39541	0.003305	0.0019	1.27	41.2
36.24	2.862218	4.951638	14.94371	0.004478	0.002188	1.14	35.1
47.6	2.205882	3.816176	13.55143	0.005445	0.002236	0.68	16.1
56.62	1.877045	3.247288	12.73698	0.006164	0.002202	0.50	9.9
63	1.703686	2.947377	11.42105	0.007666	0.002304	0.40	7.4
66.96	1.613668	2.791646	12.28113	0.00663	0.00205	0.36	6.2
67.82	1.595607	2.760401	10.70684	0.008723	0.002328	0.35	6.05
69.1	1.569624	2.71545	10.41359	0.009221	0.002358	0.34	5.7
72.72	1.501498	2.597592	10.18191	0.009646	0.002305	0.31	5

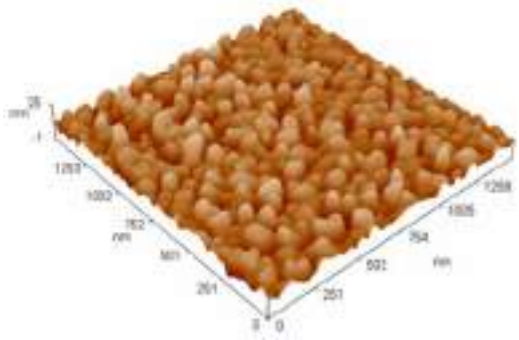

Fig(1): The AFM image of porous ZnO

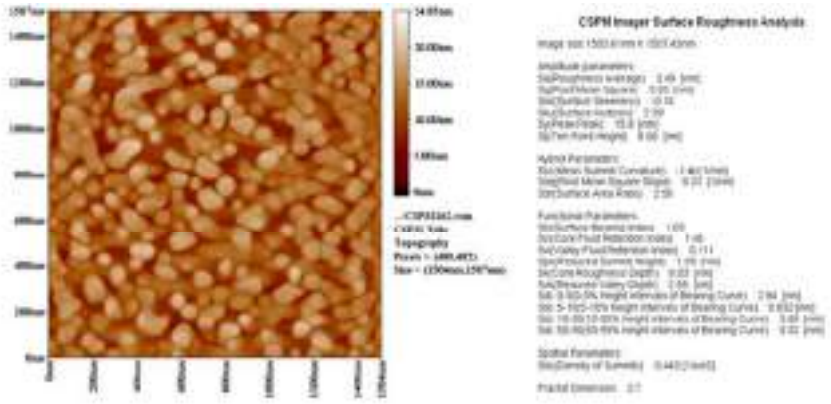

Fig(2): The full description of ZnO morphology

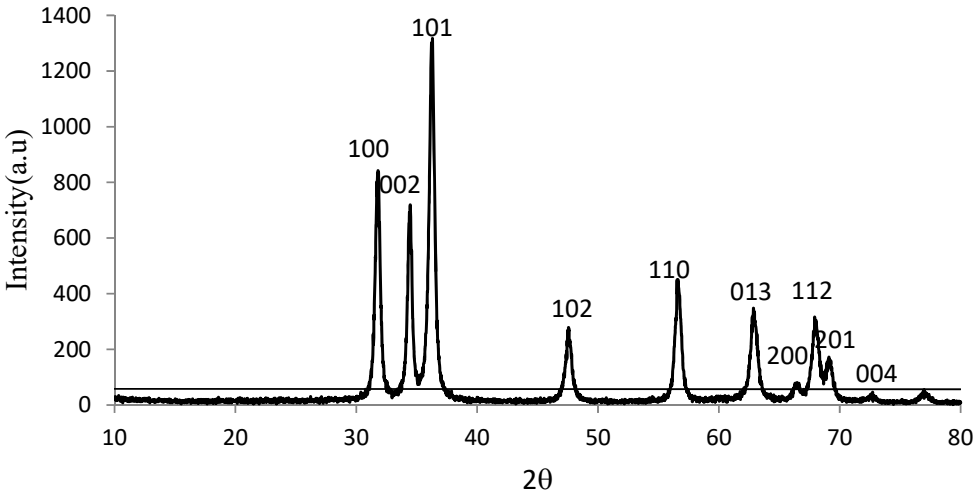

Fig.(3): XRD pattern of porous ZnO.

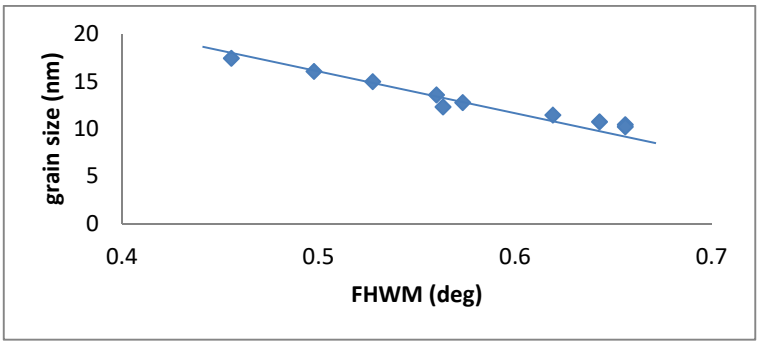

Fig.(4): The variable of grain size with FHWM

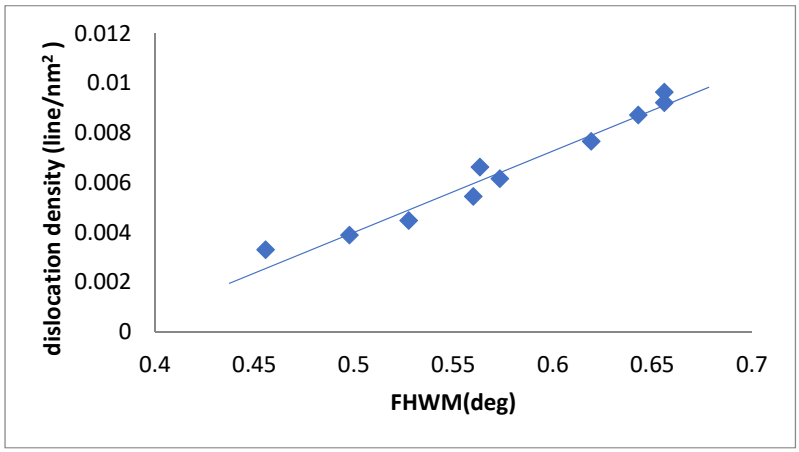

Fig(5): The variable of grain size with FHWM

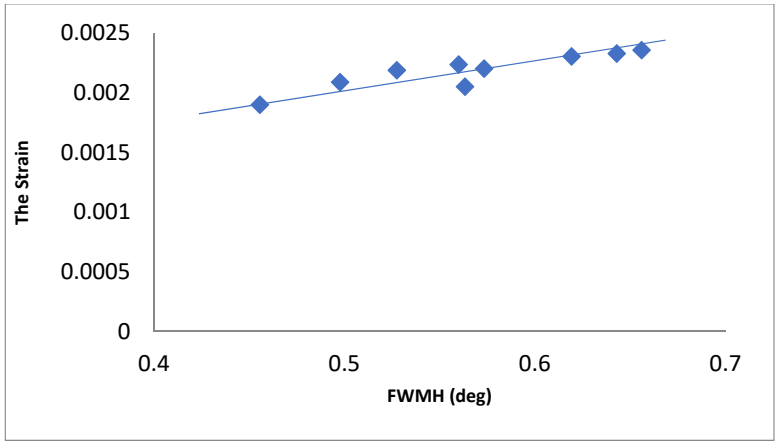

Fig(6): The variable of Strain with FHWM

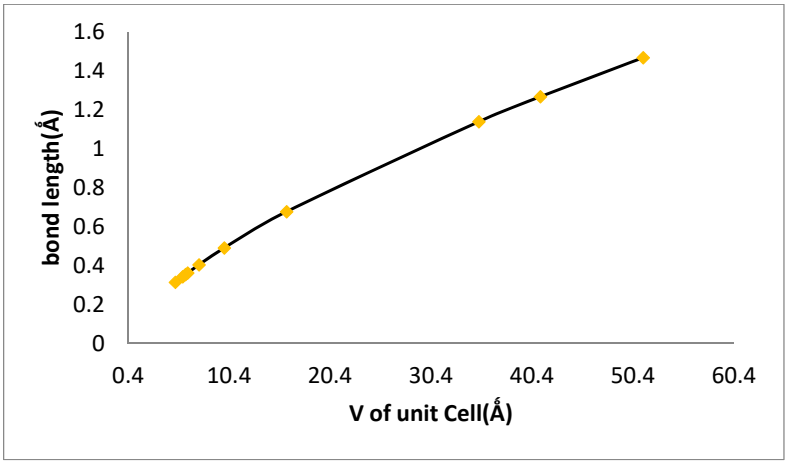

Fig(6): the relation between the Zn-O bond length and the volume of unit cell.

References

1- K. Sowri babu, A. Ramachandra Ready, CH. Sujatha, K. Venugopal Redddy, A. N. Malika, " Synthesis and optical characterization of porous ZnO", Journal of Advanced Ceramics, Vol.2 , No.3, PP.260-265, 2013.
2- C. Lei, M. Pi, C. Jiang, B. Cheng, J. Yu, " Synthesis of hierarchical porous zinc oxide (ZnO) microspheres with highly efficient adsorption of Congo red", J Colloid Interface Sci,;No. 490, PP.242-251, 2017 Mar 15.
3- M. Karyaoui, A. Ben Jaballah, R. Mechiac, and R. Chtourou "The porous of nature of ZnO thin films deposited by sol- gel spin coating technique",IOP conf. Series: Material Sceince and engineering 28 (2012) 012019
4-M. Rani, S. K. Tripathi" Synthesis and photosensitive performance of nanostructured ZnO/dye hybrid film for energy conversion", International Journal of Modern Physics: Conference Series, Vol. 22 (2013) 18–23 World Scientific Publishing Company
5-M. Saito & Sh.Fujihara," Fabrication and photovoltaic properties of Dye-Sensitized ZnO thick films by a facile doctor-blade printing method using nanocrystalline pastes", Journal of ceramic society of Japan, Vol.7 ,No. 117, PP. 823- 827, 2009.

6- NPCS Board of consultant and engineering (2009), Asia Pacific Business press Inc.
7- Amal Al-Kahlout, " Thermal treatment optimization of ZnO nanoparticles-photoelectrodes for high photovoltaic performance of dye-sensitized solar cells", Journal of the Association of Arab Universities for Basic and Applied Sciences (2015) 17, 66–72.
8- S. Sarker, NC. Nath, MM. Rahman, SS. Lim, AJ. Ahammad, WY. Choi, JJ.Lee," TiO2 paste formulation for crack-free mesoporous nanocrystalline film of dye-sensitized solar cells", J Nanosci Nanotechnol. 2012 Jul;12(7):5361-6.
9- P. Bindo& S. Thomas" Estimation of lattice strain in ZnO nanoparticles: X-ray peak profile analysis", J Theor Appl Phys,(2014) 8: 123-134.
10- Kawkab D. Salim, "Preparing and studying the properties of MgxZn1-xO/Si nanostructure by chemical spry pyrolysis for photovoltaic applications" 2017, (PhD thesis, Tikrit University, Iraq.
11-. A.K. Srivastava, R. Gakhar1, P. Dua, K. Senthil, J.S.Tawale1, K.N. Sood and K. Yong," Structural determination of Zn-O dumbbells in facetted nano-particles", Microscopy: Science, Technology, Applications and Education/Díaz (Eds), pp. 1820-1823, © FORMATEX (2010).

Available online at
http://namrc.uotechnology.edu.iq/index.php/

Nanotechnology and Advanced Materials Research Centre

Proceeding Articles Book 00 (2018) 000–000

6th International Scientific Conference on Nanotechnology, Advanced Materials and its Applications

Size Dependence of Gas Sensitivity of ZnO Nanorods towards LPG

Ali J. Almudhafer, J.J. Hassan

Physics Department, College of Science, University of Basrah, Basrah, Iraq

Abstract

In this research, Zinc oxide nanorods were prepared by chemical bath deposition method (CBD) through using raw materials on the glass substrate. The crystalline structure, surface morphology, elemental composition and optical properties of ZnO were studied by X-ray diffraction (XRD), field emission scanning electron microscopy (FESEM), energy dispersive spectrometers (EDS), and UV-vis spectrophotometer, respectively. The sensing properties of the ZnO nanorod arrays for LPG were determined for different average nanorods diameter. The results indicate that the smaller diameters of ZnO nanorods have good sensitivity and stability when compared with other larger nanorods diameter.

Keywords: Zinc Oxide (ZnO); Nanorod arrays; Chemical bath deposition (CBD); LPG sensor.

1-Introduction

The improvement in the semiconductor metal oxides properties make them valuable for more application in various fields[1]. Direct wide band gab (~3.37 eV) and a large free-exciton binding energy of about (~60 meV) make ZnO as promising material in excitonic emissions and lasing applications above room temperature compared with other materials[2-4]. In addition, ZnO is usually an n-type semiconductor because of the presence of oxygen vacancy in ZnO and it acts as electron donor[5].

On the other hand, ZnO has been synthesized in various nanostructures such as nanowires [6], nanobelts, nanotubes[7], and nanorods[6], etc. These different nanostructures make ZnO the best candidate in various applications especially in solar cell, and gas sensor due to the high ratio of the surface to volume.

Recently, several studies have been conducted to improve the performance of ZnO sensors in order to enhance sensitivity and response time and to decrease the working temperature [8]. Many synthesis methods have been employed to prepare ZnO nanorods[9], such as vapor-liquid-solid [10], metal organic chemical vapor deposition [11], laser ablation-catalytic growth [12], pulsed laser deposition [13], hydrothermal [14], and chemical bath deposition (CBD) method [15, 16]. Recently, chemical bath deposition (CBD) method has been widely adopted because of it does not need vacuum system or high temperature. Moreover, CBD method is a simple and economical approach for the growth nucleation of zinc oxide (ZnO) and it can achieve many different morphologies and different properties for ZnO nanostructures.

In this paper, ZnO nanorods arrays were fabricated with aligned irregular diameter on glass substrates using a chemical bath deposition method at normal atmospheric pressure without any metal catalyst. The ZnO nanorods sensors show disparate sensitivity response and recovery time depending on the characteristics of the nanorods diameters.

2-Materials and Method

a. Materials and Sol Formation

In this research, all chemical reagents were purchased commercially and utilized without further purification. ZnO nanorods were synthesized from the cost-effective zinc acetate dehydrate $(C_2H_3O_2)_2$ Zn $2H_2O$. Initially, amount of zinc acetate was dissolved in 50 ml of ethanol by stirring for 1 hr at room temperature to obtain a homogenous solution. Then some of Diethanolamine was added to the obtained homogeneous solution and then mixed by a magnetic stirrer for 15 min at maintained room temperature.

b. Seed Layer Preparation

The seed layers were coated on a clean glass substrate by means of sol-gel method, which started with spin-coating process. Seed sol is used to synthesize the thin seed layers. The glass substrates were cleaned with HCl, Acetone, ethanol and deionized water by

a utilized ultrasonic instrument and dried at room temperature. The coating process was done with rotation around 2700 rpm within 1 min for each once. After coating each spin, all the films were dried at 200°C for 2 min. Then, many layers were deposited on each substrate to obtain the desired thickness. Finally, all films were annealed at 350°C for 2 hr to convert (ZnAc) to ZnO nucleation arrays.

c. Growth of ZnO nanorods

The chemical bath deposition method has employed to a growth of ZnO nucleation. The precursor solutions were combined as amount of Zinc nitrate hexahydrate (Zn (NO3)2 6H2O, 99.9% purity) and amount of hexamethylenetetramine (HMT, C6H12N4, 99.9% purity) that individually dissolved into 20 ml distilled water at room temperature with magnetic stirrer for 30 minutes. The seeded substrates were placed vertically in a bath at 90 °C into quartz beaker containing 50ml deionized water on the hot plate for 2h. Then, the growth process started through mixing the two solutions by dipping in the beaker. This growth process continued for 2 hr. All the details of the samples inserted in Table 1.

Table 1. the details of the samples.

Sample	Zinc acetate in ethanol Molarity	Amount of Diethanol-amine ml	Zinc nitrate in water Molarity	Hexamie in water Molarity	Layers
S1	0.13	8	0.05	0.05	8
S2	0.09	4	0.05	0.05	4
S3	0.09	2	0.05	0.05	4

d. Fabrication of Electronic Gas Testing System

Nowadays, the most important thing to start the study of gas sensor application requires how can build testing system able to test the samples. Therefore, it is very necessary to construct an electronic system that tests the samples with significant advantages, such as high accuracy and low cost. Electronic sensor system was constructed in the unit of nanotechnology laboratory at physics department/ college of Science at the University of Basrah to measure the sensitivity of ZnO nanorod arrays samples for various types of gas, such as LPG and CO2 gas as shown in figure 1.

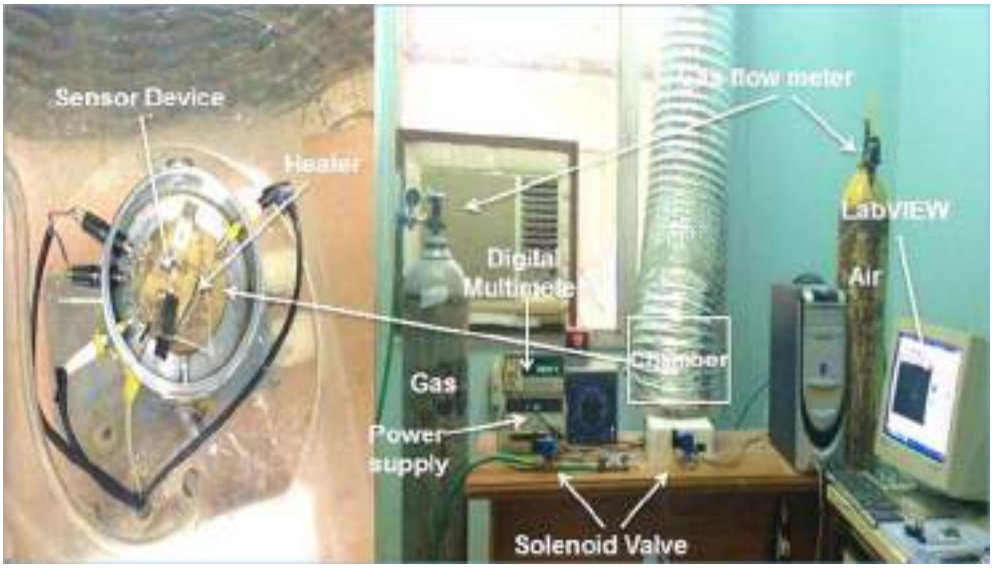

Figure 1: Photograph of Electronic Gas Sensor Testing System.

The sensor system includes: pressure regulators, sensing chamber, silica tube air dryer, gas cylinder, heated sample holder, mass flow controller, and required electronics (solenoid valve). These elements are used to control the gas flow and time inside the test chamber as shown in Figure 1.
The sensor response was measured by the following equation [17], as LPG belongs to the category of reducing gasses:

$$S = \frac{I_g - I_a}{I_a} \times 100 = \frac{\Delta I}{I_a} \times 100 \qquad (1)$$

Where (S) is the sensitivity of ZnO nanorod arrays sensor, I_a is the value of the current in the presence of air and I_g is the value of the current after exposure to the gas. The sensor signal acquisition was automated and performed through the dedicated Lab-VIEW software code developed in-laboratory. The Lab-VIEW software in coordination with Hewlett-Packard Interface Bus (GPIB)/ Universal Serial Bus (USB) interface enables to reception and transfer data between the computer and digit multimeter.
The current–time measurements were performed at various working temperature using digit multimeter (FLUKE 8808 used for current measurement) and a voltage current source.

1.1 Characterization Methods

The nanomaterial was investigated as-synthesized by X-ray diffraction (XRD) using a X'pert Modular Powder. Diffractometer equipped with CuKα wavelength of radiation (λ = 1.54056 Å). The morphological details of nanostructure were characterized by field-emission scanning electron microscopy (FESEM, Zeiss Supra, Germany). The elemental composition of ZnO nanorods was studied by utilization energy-dispersive spectrometers (energy-dispersive X-ray spectroscopy EDXS). Furthermore, the optical properties of ZnO nanorods were reveal by using UV-vis spectrophotometer.

3-Results and discussion

The XRD patterns of the ZnO nanorods/nanotubes are studied with the diffraction angle in the range of 20˚- 70˚. All The diffraction peaks in the XRD patterns are matching with the ZnO hexagonal phase according to JCPDF No.36-1451.
Figure 2 shows the XRD pattern of vertically aligned ZnO nanorod arrays grown on glass substrate. There are no other characteristic impurities peaks appeared, this figure also indicates that the obtained product is in a pure phase. The intensity of the peak assigned to the (0 0 2) plane of wurtzite ZnO was markedly large due to the peak intensity is related to vertically aligned of ZnO nanorods [18]. On the other hand, the diffraction peaks of other crystal planes almost disappeared or were very weak compared by the (0 0 2) plane that is strongly oriented perpendicularly to the substrate surface. Thus, the columnar rods composing the layer are formed through elongation along the c-axis. Further, absence of diffraction peaks related to any other impurities and the sharpness of the peaks related to ZnO indicated that the prepared ZnO nanorods have high crystallinity.
In addition, the lattice constants (a) and (c) of ZnO nanorods grown on glass substrate is calculated by using the following equation [2]:

$$\frac{1}{d_{hkl}^2} = \frac{4}{3}\left(\frac{h^2 + hk + k^2}{a^2}\right) + \frac{l^2}{c^2} \qquad (2)$$

The lattice constants (a and c) and c/a ratio of ZnO nanorods grown on glass substrate are 3.214, 5.249 and 1.633, respectively.
Where all the diffractions could be indexed to hexagonal wurtzite structure of ZnO with lattice parameters of a = 3.214 Å and c = 5.249 Å, which have good matching with the reported data for wurtzite ZnO (a = 3.249 Å, c = 5.205 Å, JCPDS File 5-664).
Figure 3(a), (b) and (c) shows the FESEM pictures of ZnO nanorods that grown on a glass substrate. Where it is clear from this pictures that the ZnO nanorods have hexagonal shapes with irregular diameter and growth vertically along the c-axis with high distribution density on the surface of the substrates and the diameter range of ZnO nanorods for each samples about (290-530 nm), (80-320nm), and (60-280nm) respectively. In contrast, the average diameters of samples S1and S2 and S3 were 362, 186 and 162 nm, respectively.

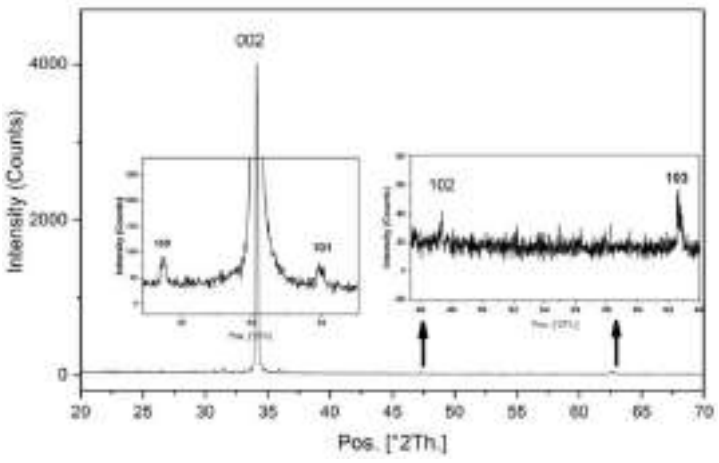

Figure 2: XRD spectrum of vertically aligned ZnO nanorods array on glass substrate.

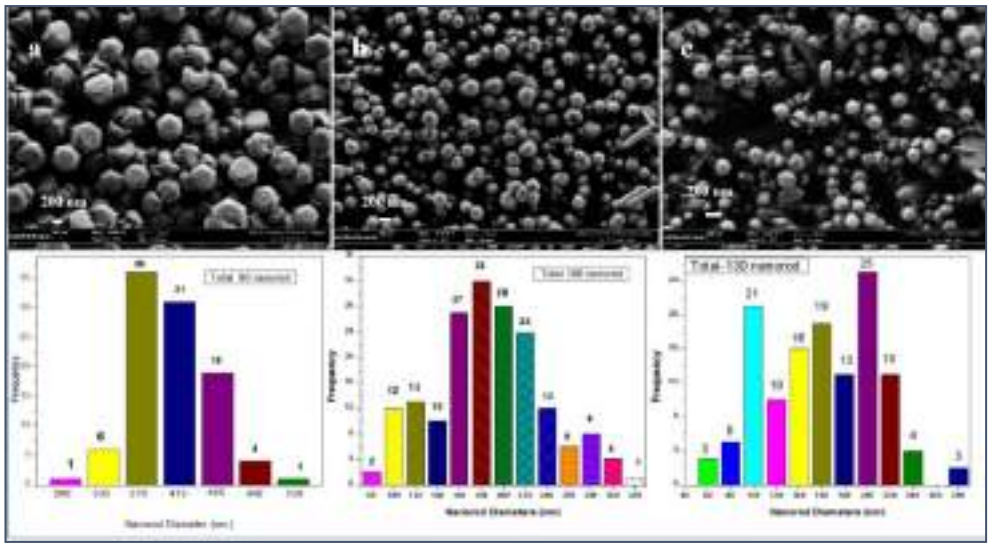

Figure 3: FESEM images of ZnO nanorod arrays grown onto a glass substrate for sample (a) S1 (average nanorods diameter 364 nm) (b) S2 (average nanorods diameter 186 nm) and (c) S3 (average nanorods diameter 162 nm).

Figure 4: epresents to The (EDX) spectrum analysis of the ZnO nanorod arrays sample shows only Zn and O signal peaks. The elemental composition of ZnO nanorods approximate atomic ratio of zinc and oxides is found to be 42.11: 57.89

Figure 4: The energy-dispersive X-ray spectroscopy (EDAX) Analysis of the ZnO Nanorod arrays.

I-V characteristics of ZnO nanorods were drawn in the presence of air at room temperature conditions. Figure 5 shows the I-V characteristics of ZnO nanorod arrays sample is symmetrical behaviour, indicating ohmic nature of aluminium contacts. It was taken after annealing the ZnO nanorods at 350°C.

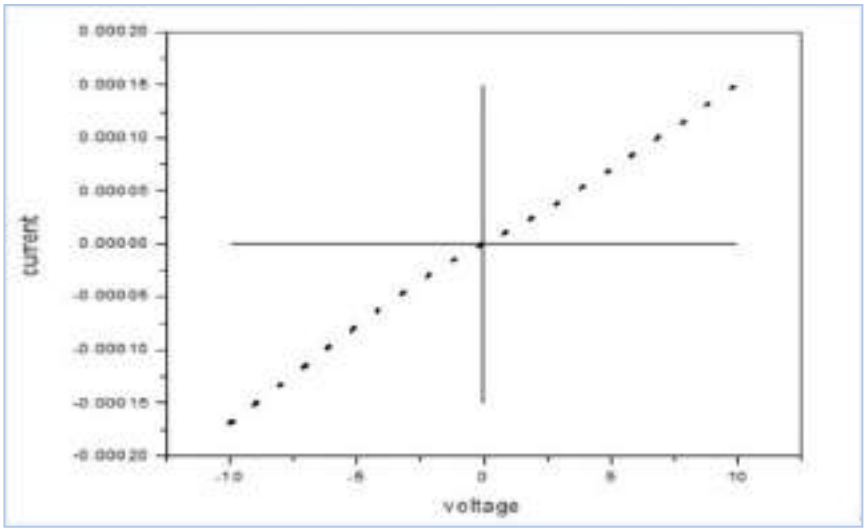

Figure 5: Room Temperature I-V Curve of Al Grid Showed Ohmic Behavior between Grid and Semiconductor.

Figure 6 shows UV-V absorption of ZnO Nanorod arrays grown on glass substrate. The adsorption edge of ZnO Nanorod arrays is about 400 nm that related to optical band gap of ZnO. This adsorption spectrum describe the high transmission of ZnO Nanorod at energies lower than energy gap of ZnO nanorods. The optical energy gap can be estimated by calculating the optical absorption coefficient (α), which depends on the absorbance and film thickness of the sample as given in the following equation.

$$\alpha = 2.303A/t \qquad (5)$$

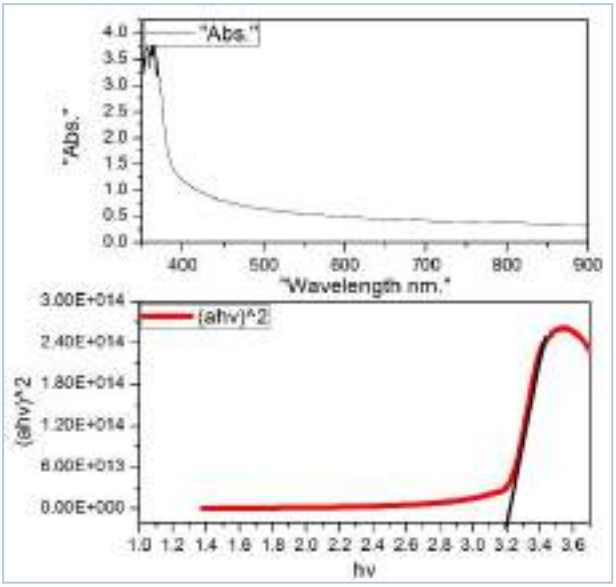

Figure 6: (a) UV-Visible Absorption Spectra of ZnO Nanorod Arrays (b) Plot of (αhν) ^ 2 versus (hν) for determination of band gap of ZnO nanorods.

Where (α) is the optical absorption coefficient, which can be calculated from absorbance and thickness of the sample using: (a=2.303A/t); and (hν) can be calculated form wavelength using: (hν = 1240/wavelength). The energy band gap (Eg) was calculated using figure 6 (b). The value of the optical band energy was found to be 3.2 eV.

In the absence of target gas, oxygen is always adsorbed on the surface of the semiconducting metal oxide upon exposure to the ambient air components, bound in empty sites and pick up electrons from the conduction band and form chemisorbed oxygen on the surface of the semiconductor material to produce negatively charged chemisorbed oxygen, such as O2- and O- which creates a depletion layer at the surface of the individual nanorods, given as[19-21]

$$O_{2(gas)} + e^- \rightarrow 2O^-_{(ads)} \qquad (3)$$

When the sensor is exposed to the gas molecules, the molecules of gas interact with the adsorbed oxygen ions present on the surface of the sensor as shown in Eq.(3) and released the trapped electrons back to the conduction band. This leads to an increased carrier concentration of ZnO and increasing the current of the sensor. The overall reaction of LPG molecules with the adsorbed oxygen species can be explained based on the following reactions[22]:

$$C_nH_{2n+2} + 2O^-_{(ads)} \rightarrow H_2O + C_nH_{2n}{:}\ O + e^- \qquad (4)$$

$$C_nH_{2n}{:}\ O + O^-_{(ads)} \rightarrow CO_2 + H_2O + e^- \qquad (5)$$

Where, CnH2n+2 represents the hydrocarbons of LPG, propane (C3H8), and butane (C4H10).

Figure 7: shows the sensitivity of ZnO nanorods at operating temperature 275ºC, for three different samples at the same temperature. Where the black, blue, and red line represents the sensitivity of sample S1, S2 and S3 respectively. The figure indicates that the ZnO nanorods for sample S3 gives highest sensitivity more than compared with the sensitivity in samples S1 and S2. The ability of the sample S3 to sense more than S2 and S1 because of it is has smaller nanorods diameter more than with the other samples so this reason gives it high surface to volume ratio.

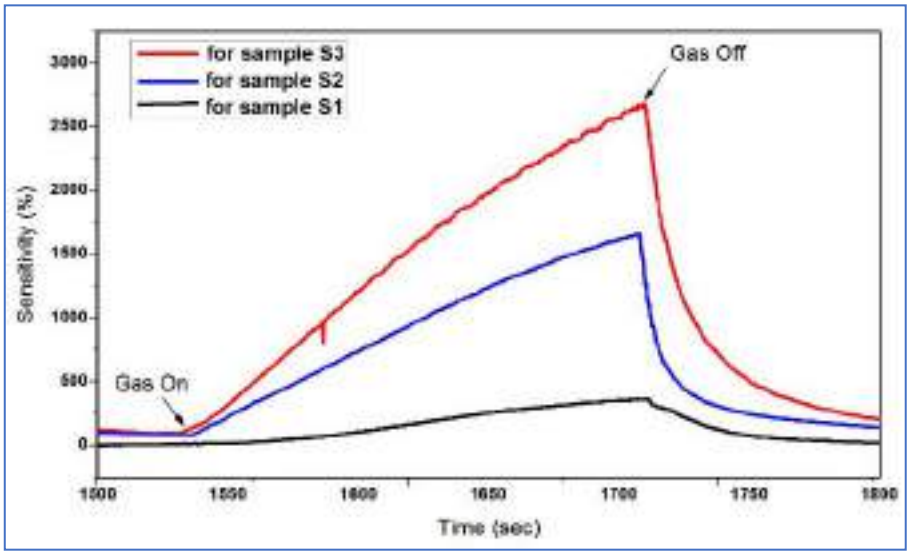

Figure 7: sensitivity as a function of time of ZnO nanorods for sample S1, S2 and S3 at 275 ºC

Table 2 shows that the LPG sensitivity of the sensor in the present work (this work) is 2703%. Which is much more high as compared to 3% recorded in [23], 8.02 recorded in [24] and other reported in [5], [25], and [26]. the larger sensitivity that has achieved in the present work may be because of the nanostructure has the Large surface area to volume ratio due to the nanorods have small diameters i.e. more atoms able to interaction with the gas molecules, as well as small diameters means that the depletion layer increase compares with the conductive channel.

Table 2. Comparison of LPG sensing properties of previously recorded with the sensor in the present work

Material	Temperature (ºC)	Concentration	Response time	Recovery time	Sensitivity (S)	Ref.
ZnO nanorods	332	200 ppm	10 sec	30 sec	3%	[23]
ZnO thick films	350	100 ppm	…..	…..	8.02	[24]
ZnO nanorods	300	2600 ppm	…..	…..	37%	[5]
ZnSnO3: ZnO nanowire	room temperature	4000 ppm	…..	…..	67.52%	[25]
ZnO nanostructure	450	0.7 %	…...	…..	160	[26]
ZnO nanorods	275	3 lit/min	135 sec	27 sec	2703%	This work.

4-Conclusion

ZnO nanorods sample could be prepared on glass substrate using inexpensive and simple chemical bath deposition technique. The smaller ZnO nanorods sensor in the present work showed remarkable enhancement of LPG response over the other large ZnO nanorods diameters films and other oxide thick films. In addition, The ZnO nanorods have a high sensitivity to LPG and as well as exhibits rapid response and recovery time which is one of the main features of this sensor.

Acknowledgements

The authors gratefully acknowledge support of the university of Basrah/ Collage of Science.

References

1.Priya SM, Geetha A, Ramamurthi K: Structural, morphological and optical properties of tin oxide nanoparticles synthesized by sol–gel method adding hydrochloric acid. Journal of Sol-Gel Science and Technology 2016, 78(2):365-372.
2.Hsu J-C, Chiang Y-S: Influence of oxygen on zinc oxide films fabricated by ion-beam sputter deposition. ISRN Materials science 2013, 2013.
3.Janotti A, Van de Walle CG: Fundamentals of zinc oxide as a semiconductor. Reports on progress in physics 2009, 72(12):126501.
4.Hassan J, Mahdi M, Chin C, Hassan Z, Abu-Hassan H: Microwave assisted chemical bath deposition of vertically aligned ZnO nanorods on a variety of substrates seeded by PVA–Zn (OH) 2 nanocomposites. Applied Surface Science 2012, 258(10):4467-4472.
5.Gurav K, Deshmukh P, Lokhande C: LPG sensing properties of Pd-sensitized vertically aligned ZnO nanorods. Sensors and Actuators B: Chemical 2011, 151(2):365-369.
6.Huang MH, Wu Y, Feick H, Tran N, Weber E, Yang P: Catalytic growth of zinc oxide nanowires by vapor transport. Advanced Materials 2001, 13(2):113-116.
7.Sun Y, Fuge GM, Fox NA, Riley DJ, Ashfold MN: Synthesis of aligned arrays of ultrathin ZnO nanotubes on a Si wafer coated with a thin ZnO film. Advanced materials 2005, 17(20):2477-2481.
8.Park S-H, Ryu J-Y, Choi H-H, Kwon T-H: Zinc oxide thin film doped with Al 2 O 3, TiO 2 and V 2 O 5 as sensitive sensor for trimethylamine gas. Sensors and Actuators B: Chemical 1998, 46(2):75-79.
9.Hassan J, Mahdi M, Kasim S, Ahmed NM, Abu Hassan H, Hassan Z: High sensitivity and fast response and recovery times in a ZnO nanorod array/p-Si self-powered ultraviolet detector. Applied Physics Letters 2012, 101(26):261108.
10.Klimovskaya A, Ostrovskii I, Ostrovskaya A: Influence of growth conditions on morphology, composition, and electrical properties of n-Si wires. physica status solidi (a) 1996, 153(2):465-472.
11.Yazawa M, Koguchi M, Muto A, Ozawa M, Hiruma K: Effect of one monolayer of surface gold atoms on the epitaxial growth of InAs nanowhiskers. Applied Physics Letters 1992, 61(17):2051-2053.
12.Duan X, Lieber CM: Laser-assisted catalytic growth of single crystal GaN nanowires. Journal of the American Chemical Society 2000, 122(1):188-189.
13.Guo X-L, Choi J-H, Tabata H, Kawai T: Fabrication and optoelectronic properties of a transparent ZnO homostructural light-emitting diode. Japanese Journal of Applied Physics 2001, 40(3A):L177.
14.Wu W, Hu G, Cui S, Zhou Y, Wu H: Epitaxy of vertical ZnO nanorod arrays on highly (001)-oriented ZnO seed monolayer by a hydrothermal route. Crystal Growth and Design 2008, 8(11):4014-4020.
15.Tian ZR, Voigt JA, Liu J, Mckenzie B, Mcdermott MJ, Rodriguez MA, Konishi H, Xu H: Complex and oriented ZnO nanostructures. Nature materials 2003, 2(12):821-826.
16.Xu S, Wang ZL: One-dimensional ZnO nanostructures: solution growth and functional properties. Nano Research 2011, 4(11):1013-1098.
17.Dhawale D, Dubal D, More A, Gujar T, Lokhande C: Room temperature liquefied petroleum gas (LPG) sensor. Sensors and Actuators B: Chemical 2010, 147(2):488-494.
18.Nayeri FD, Narimani K, Kolahdouz M, Asl-Soleimani E, Salehi F: Surface structure optimization for cost effective field emission of zinc oxide nanorods on glass substrate. Thin Solid Films 2014, 571:154-160.
19.Dehkordi HA, Dastafkan K, Moshaii A, Mokhtari A: Thermal post-annealing and gas concentration effect on liquid petroleum gas sensing characteristics of nanocrystalline zinc oxide thin films. Journal of Materials Science: Materials in Electronics 2015, 26(5):3134-3142.
20.Sonker RK, Singh M, Kumar U, Yadav B: MWCNT doped ZnO nanocomposite thin film as LPG sensing. Journal of Inorganic and Organometallic Polymers and Materials 2016, 26(6):1434-1440.
21.Dhawale D, Lokhande C: Chemical route to synthesis of mesoporous ZnO thin films and their liquefied petroleum gas sensor performance. Journal of Alloys and Compounds 2011, 509(41):10092-10097.
22.Sivapunniyam A, Wiromrat N, Myint MTZ, Dutta J: High-performance liquefied petroleum gas sensing based on nanostructures of zinc oxide and zinc stannate. Sensors and Actuators B: Chemical 2011, 157(1):232-239.
23.Jiaqiang X, Yuping C, Daoyong C, Jianian S: Hydrothermal synthesis and gas sensing characters of ZnO nanorods. Sensors and Actuators B: Chemical 2006, 113(1):526-531.
24. Patil D, Patil L: Cr 2 O 3-modified ZnO thick film resistors as LPG sensors. Talanta 2009, 77(4):1409-1414.
25.Fu Y, Nie Y, Zhao Y, Wang P, Xing L, Zhang Y, Xue X: Detecting liquefied petroleum gas (LPG) at room temperature using ZnSnO3/ZnO nanowire piezo-nanogenerator as self-powered gas sensor. ACS applied materials & interfaces 2015, 7(19):10482-10490.
26.Latyshev V, Berestok T, Opanasyuk A, Kornyushchenko A, Perekrestov V: Nanostructured ZnO films for potential use in LPG gas sensors. Solid State Sciences 2017, 67:109-113.

Available online at
http://namrc.uotechnology.edu.iq/index.php/

Nanotechnology and Advanced Materials Research Centre

Proceeding Articles Book 00 (2018) 000–000

6th International Scientific Conference on Nanotechnology, Advanced Materials and its Applications

Burnishing technique for improvement resistance to corrosion of low carbon steel (AISI 1017) in HCl acid

Zeyad D. Kadhim, Mohammed Abdulraoof Abdulrazzaq, Suha Q. Alshahrabally
Materials Engineering Department, Al-Mustansiriyah University, Baghdad, Iraq
Mechanical Engineering Department, Al-Mustansiriyah University, Baghdad, Iraq
Materials Engineering Department, Al-Mustansiriyah University, Baghdad, Iraq
Correspondence author: mohammedraof415@yahoo.com

Abstract

It has been investigated burnishing influence on the resistance to metallic corrosion of low carbon steel. In burnishing technique a stainless steel roller pressed against a rotatory rod, this process formed a plastic deformation on the external surface. The effect for two variables of burnishing process on the corrosion resistance of the steel in1 moles of HCl acid has been studied, one of them is the burnishing feed which changed as 0.6, 0.9, 1.5, 2, and 3mm/rev at constant speed of 125 rpm and the other is the burnishing speed which changed as 85, 125, 370, 800 and 1200 rpm at a constant feed of 2mm/rev. The corrosion test was carried out using potentiostate device at room temperature. Also, the results showed that the burnishing process lead to improvement in metal corrosion resistance, surface roughness and hardness. It was recorded that the best corrosion resistance for this alloy in HCl acid using a feed rate 2 mm/rev and rotational speed 1200 rpm. Where, the corrosion rate became 20.26mpy. The highest hardness value was 240 HV at feed rate and rotational speed 2mm/rev, 1200rpm respectively. However, the best surface roughness was 0.6 µm.

Keywords**:** *Burnishing process, corrosion test, mild steel.*

1- Overview

Many metal experience some interaction kind with a great number of diverse surroundings. Often, such interactions injury a material's utility as an effect of the deterioration of its mechanical features (e.g., ductility and strength), appearance and other properties. Sometimes, to the design engineer chagrin, the material degradation behavior for certain application is ignored, with the adverse consequences. Mechanisms of deteriorative are different for the material types. In metal, there is actual injury in metal either by form a scale, film layer on the surface (oxidation) or by corrosion [1, 2]. Corrosion of metals is resulted from the deterioration of certain metals or alloys because of its interaction with surrounding mediums [3, 4]. The driving force for metals to oxidize is its free energy of oxidation and the energy will released when the metallic materials react with the oxygen[5, 6].

Steel which consist of iron and carbon in certain amount is regarded the greatest common engineering material, it is applied in an extensive range of application like automobile, steel play a major role in machine design for base plates, housings, chutes, countless machine components and structural members [7, 8]. Carbon content in low carbon steel is between 0.15% and 0.35%, and it is regarded the most common kind of steel, where its properties is satisfactory for many applications. It is neither brittle nor ductile and that because of its low amount of carbon content. It has lower tensile strength and it is regarded malleable [9, 10].

Burnishing technique is an effective method used for improvement in the surface of metals; it is include pressing hardened steel balls or rolls into the work piece surface and imparting a feed motion to the same as indicated in Figure (1). During burnishing process, residual compressive stresses are formed in the work piece surface and thereby advance the properties of material. This technique will smooth and harden the surface of metallic material, burnishing technique produce a finished surface which has longer life than the metals which they do not burnished [11, 12]. All surfaces which subjected to machining operations have arrangements of many peaks and valleys which is not regular in spaces and tallness, plastic deformation formed by burnishing technique is a displacement of the peaks into the valleys under the action of pressure. This result in tough, work hardened, wear resistance and corrosion resistance metallic surface [13, 14].

Burnishing operation affected by certain factors these are:

1. Feed rate.
2. Depth of penetration.
3. Burnishing speed.
4. No. of passes which used in burnishing technique.
5. Size of burnishing tool [15, 16].

Benefits of burnishing technique can be summarized in:

1. Highly productive process, simple technique which may be done by conventional machines.
2. Possibly replace more complex operations like honing, lapping and grinding.
3. Wants low torque and energy because pressure load is comparatively little.
4. Doesn't yield shavings, chips, turnings or filings.
5. Provides close-fitting dimensional tolerances.
6. When compared with any operations, wear of tool is moderately less [17, 18].

2- Experimental work

Steel specimens at a temperature of 25.5°C and moister rate of 25% was tested, it becomes clear that its type was (AISI 1017). The reason for chosen low carbon steel is because of its several applications in field of industry, low cost, good ductility and easy to fabricate. Chemical test was carried out by (Thermo ARL 3460, optical emission spectrometer). The results were contrasted with the standard of America to determination the type of steel (Table 1). The steel was placed for 3 hours in the furnace at 200°C to relieve stresses as shown in Figure (2).

2.1- Microstructure examination

1. The samples were grind by using smoothing device, abrasive paper was changed to grinding samples regularly and papers which were used for grinding were (200, 400, 800, 1000, 1200, 1500 and 2000) respectively.
2. Then the process of grinding followed by polishing operation by using gloss cloth and diamond paste in order to polishing the specimen.
3. Immersed the sample for twenty second in etching solution (contain 98% Methanol alcohol and 2% HNO_3 acid) then the sample was washed with purified water and finally dried to make the samples ready for microstructure test.
4. To notice the microstructure of low carbon steel before cold working operation, optical microscopic was used. It consists of dark areas (pearlite) and light areas (ferrite). The lens zoom of the device was X 200. The details of this test are explained in Figure (3).

2.2- Burnishing process

The specimens that was used were burnished with burnishing tool and it was done by applying lathe machine as indicate in Figure (4). during burnishing technique 2 variables were used; these were speed and feed of burnishing. The process was done on 10 corrosion specimens. First collection consists of held the speed and change feed of burnishing, where burnishing speed was 125 rpm and burnishing feeds were (0.6, 0.9, 1.5, 2 and 3) mm/rev. 2nd collection includes held the feed of burnishing and change burnishing speed, where burnishing feed was 2mm/rev and burnishing speeds were (85, 125, 370, 800 and 1200) rpm.

2.3- Corrosion specimen's preparation

Corrosion specimen was too small and it is difficult to make burnishing technique on it, so to make the standard specimen for corrosion test and to making the burnishing technique on it, the following point was done:

1. Eliminate the shaft of metal to (10 mm) for each case (feed, speed).
2. Then making the burnishing process on it as indicate in Figure (5).
3. Then cutting the rod from the region of burnishing to (12mm) length to make the corrosion specimens, hole drilled with diameter □□□□□ mm and thread it to M3 (ISO 4032) as indicate in Figure (6).
4. Finally, samples were grinding with sandpaper 1200 and cleaned by applying acetone before making tests.

2.4- Corrosion test

Corrosion examination was used to know the corrosion rate for the samples by using Gamry series (G300) potentiostat device as indicate in Figure (7), the tests carried out by Tafel test. corrosion test was done in 1Moles of HCl acid at 23°C. Before doing the tests, the device should be calibrated to obtain an accurate data, by connecting the device cable with calibration kit, this procedure take a few minutes. Three electrodes are existing in corrosion device as shown in Figure (8): The first electrode was working electrode and its specimen name that is being tested, The second electrode was the graphite and it was used as an auxiliary electrode, The third electrode was the saturated calomel electrode (Standard electrode). The results will appear on the screen monitor which shows corrosion rate data and curves.

2.5- Measurement of surface roughness

Surface roughness of the samples was measured before and after burnishing process because this process improve surface roughness of metals and it is effect on the corrosion resistance of metals, this measurement is done via applying surface roughness measurement apparatus shown in Figure (9), the sample was placed on V holder and the sensor measured the surface roughness.

2.6- Micro hardness test

Vickers hardness examination was done on samples before and after burnishing technique. The samples before the test should be polish in order to obtain best results. The load was holding for fifteen seconds and the device is shown in Figure (10).

3- Results and discussion

3- 1 Results of corrosion tests

Corrosion test was the first test done on carbon steel before and after burnishing technique. This examination was done in 1M of HCl solution at 23℃. Figure (11) show Tafel tests for carbon steel samples in 1moles of HCl acid. It was obvious that there were small differences in cathodic reactions, fastest reaction was for the specimen without making burnishing technique on it which means it has the highest rate of corrosion, while the slowest reaction was in the test of specimen that burnished with a 2mm/rev feed and 1200 rpm speed, this shows that it has the lowest rate of corrosion. It was clear that when burnishing feed increase, the rate of corrosion decrease until reach to certain magnitude, after that magnitude, the resistance to corrosion improved but at magnitude lower than the highest magnitude that was obtained and when burnishing speed increase, the rate of corrosion decrease until reach to the lowest magnitude of corrosion rate which means better resistance to corrosion, this was due to the plastic deformation on the metallic surface, where there were rearrangement of grains at the surface, the result was indicated in both Tables (2 and 3) and Figures (12 and 13).

3.2- Results of micro hardness tests

It was evident from the results that the burnishing operation leads to improvement in surface hardness of metal. When we were increasing burnishing feed, the surface hardness increase until reach definite magnitude, the surface hardness after that magnitude enhanced but at magnitude less than the highest magnitude that was gained and when increasing burnishing speed this lead to increasing surface hardness until reach to the highest value of surface hardness, this was due to the plastic deformation on the surface, where the grains rearranged at the surface, the result is indicated in both Tables (4 and 5) and Figures (14 and 15).

3.3- Results of surface roughness tests

It was evident from the results that the burnishing operation leads to improvement in surface roughness of the metal. When we were increasing burnishing feed, the surface roughness was decrease until reach to certain magnitude, after that magnitude, the surface roughness improved but at magnitude lower than the highest magnitude that was gained and when increasing burnishing speed this lead to decreasing surface roughness until reach to the highest magnitude of surface roughness, this was due to the plastic deformation on the metallic surface, where there was rearrangement of grains at the surface, the result is indicated in both Tables (6 and 7) and Figures (16 and 17).

4- Conclusion

Applying burnishing operation as a cold working operation on (AISI 1017) carbon steel yielded great improvement on the properties of the steel, these improvements was:

1. Enhancement in resistance to corrosion of the steel in 1moles of HCl acid was 80% at 2mm/rev feed and 1200 rpm speed.
2. Enhancement in surface roughness of the steel was 75% at 2mm/rev feed and of 1200 rpm speed.
3. Enhancement in surface hardness was 43% at 2mm/rev feed and 1200 rpm speed.

Table (1) Result of steel chemical composition test.

Elements	Actual value	Standard value
Fe %	Bal.	99.11 - 99.56
Mn %	0.585	0.3 – 0.60
C %	0.174	0.14 – 2.0
S %	0.022	≤ 0.050
P %	0.009	≤ 0.040
Cr %	0.165	-
Si %	0.185	-
Ni %	0.062	-
Mo %	0.009	-
Cu %	0.130	-
Al %	0.021	-
W %	0.046	-
V %	0.001	-

Table (2) Corrosion test result before and after technique of burnishing (changing feed of burnishing).

Sample	$I_{corrosion}$ (μA)	$E_{corrosion}$ (mV)	Corrosion rate (mpy)
Without burnishing	1220	-488.0	105.5
Feed 0.6 mm/rev, Speed 125rpm	774.0	-508.0	66.93
Feed 0.9 mm/rev, Speed 125rpm	705.0	-485.0	60.98
Feed 1.5 mm/rev, Speed 125rpm	644.0	-463.0	55.69

Feed 2 mm/rev, Speed 125rpm	382.0	-451.0	33.04
Feed 3 mm/rev, Speed 125rpm	502.0	-473.0	43.39

Table (3) Corrosion test result before and after technique of burnishing (changing speed of burnishing).

Sample	$I_{corrosion}$ (μA)	$E_{corrosion}$ (mV)	Corrosion rate (mpy)
Without burnishing	1220	-488.0	105.5
Feed 2 mm/rev, Speed 85rpm	502.0	-478	43.37
Feed 2 mm/rev, Speed 125rpm	382.0	-451.0	33.04
Feed 2 mm/rev, Speed 370rpm	292.0	-432.0	25.27
Feed 2 mm/rev, Speed 800rpm	264.0	-500.0	22.80
Feed 2 mm/rev, Speed 1200rpm	234.0	-498.0	20.26

Table (4) Result of micro Vickers hardness (HV) test before and after technique of burnishing (changing feed of burnishing).

Sample	Micro Vickers hardness (HV)
Without burnishing	167
Feed 0.6 mm/rev, Speed 125rpm	178.7
Feed 0.9 mm/rev, Speed 125rpm	188.6
Feed 1.5 mm/rev, Speed 125rpm	200.3
Feed 2 mm/rev, Speed 125rpm	210.1
Feed 3 mm/rev, Speed 125rpm	203

Table (5) Result of micro Vickers hardness (HV) test before and after technique of burnishing (changing speed of burnishing).

Sample	Micro Vickers hardness (HV)
Without burnishing	167
Feed 2 mm/rev, Speed 85rpm	201.7
Feed 2 mm/rev, Speed 125rpm	210.1
Feed 2 mm/rev, Speed 370rpm	222.5
Feed 2 mm/rev, Speed 800rpm	231.2
Feed 2 mm/rev, Speed 1200rpm	240

Table (6) Result of surface roughness test before and after technique of burnishing (changing feed of burnishing).

Sample	Surface roughness (μm)
Without burnishing	2.51
Feed 0.6 mm/rev, Speed 125rpm	2.1
Feed 0.9 mm/rev, Speed 125rpm	1.8
Feed 1.5 mm/rev, Speed 125rpm	1.75
Feed 2 mm/rev, Speed 125rpm	1.2
Feed 3 mm/rev, Speed 125rpm	1.5

Table (7) Result of surface roughness test before and after technique of burnishing (changing speed of burnishing).

Sample	Surface roughness (μm)
Without burnishing	2.51
Feed 2 mm/rev, Speed 85rpm	1.64
Feed 2 mm/rev, Speed 125rpm	1.2
Feed 2 mm/rev, Speed 370rpm	0.91
Feed 2 mm/rev, Speed 800rpm	0.83

	Feed 2 mm/rev, Speed 1200rpm	0.6

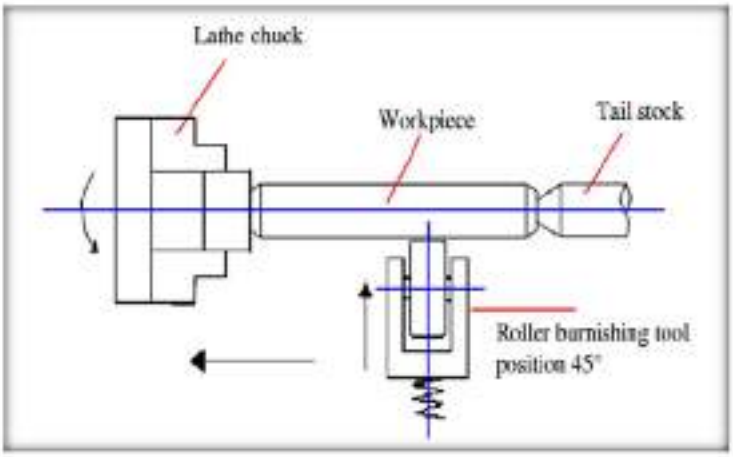

Figure (1) Roller burnishing process [13].

Figure (2) Furnace used for stress relieve heat treatment.

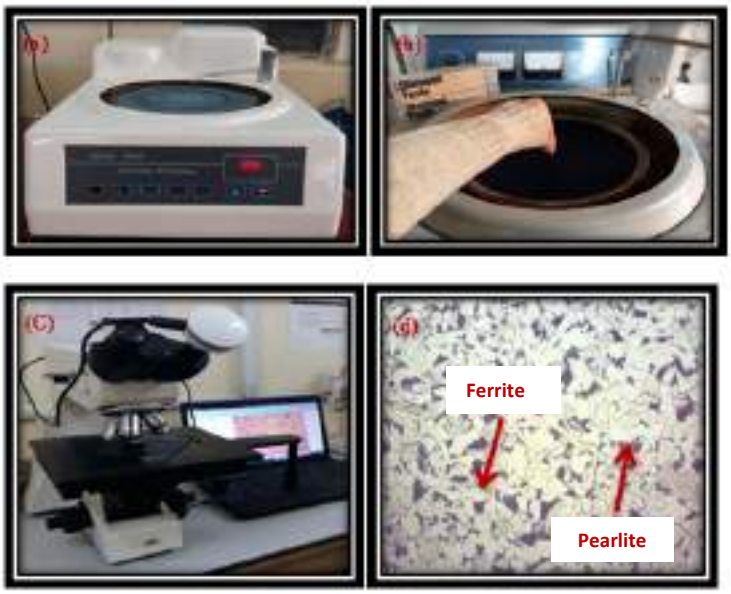

Figure (3) a) Grinding machine b) Polishing machine c) Optical microscope d) Steel microstructure.

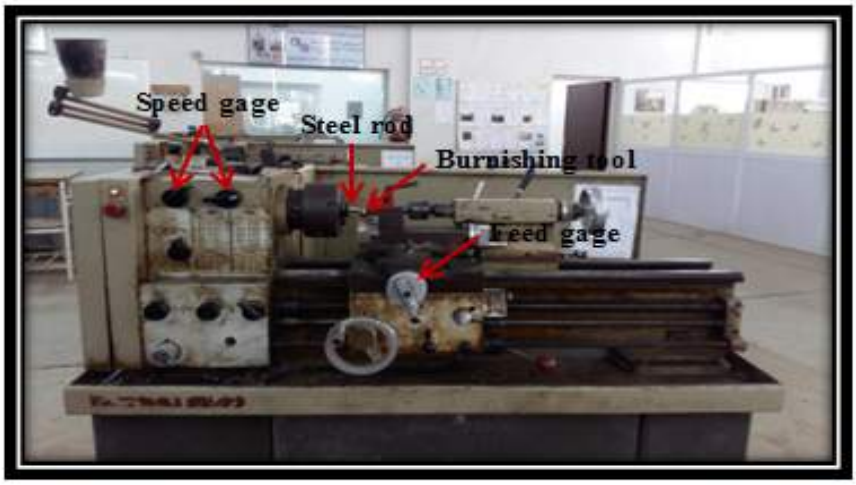

Figure (4) Lathe machine applied for burnishing technique.

Figure (5) Rods before and after burnishing process.

Figure (6) Standard corrosion specimen and its holder in corrosion cell.

Figure (7) Corrosion testing device (potentiostat).

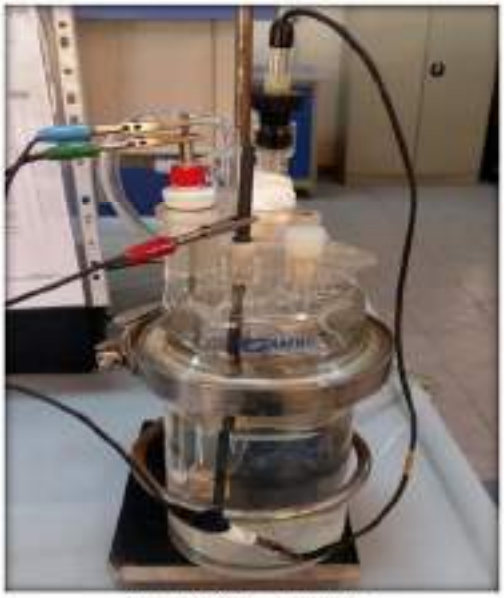

Figure (8) Cell of corrosion .

Figure (9) Surface roughness measurement device.

Figure (10): Digital micro Vickers hardness tester.

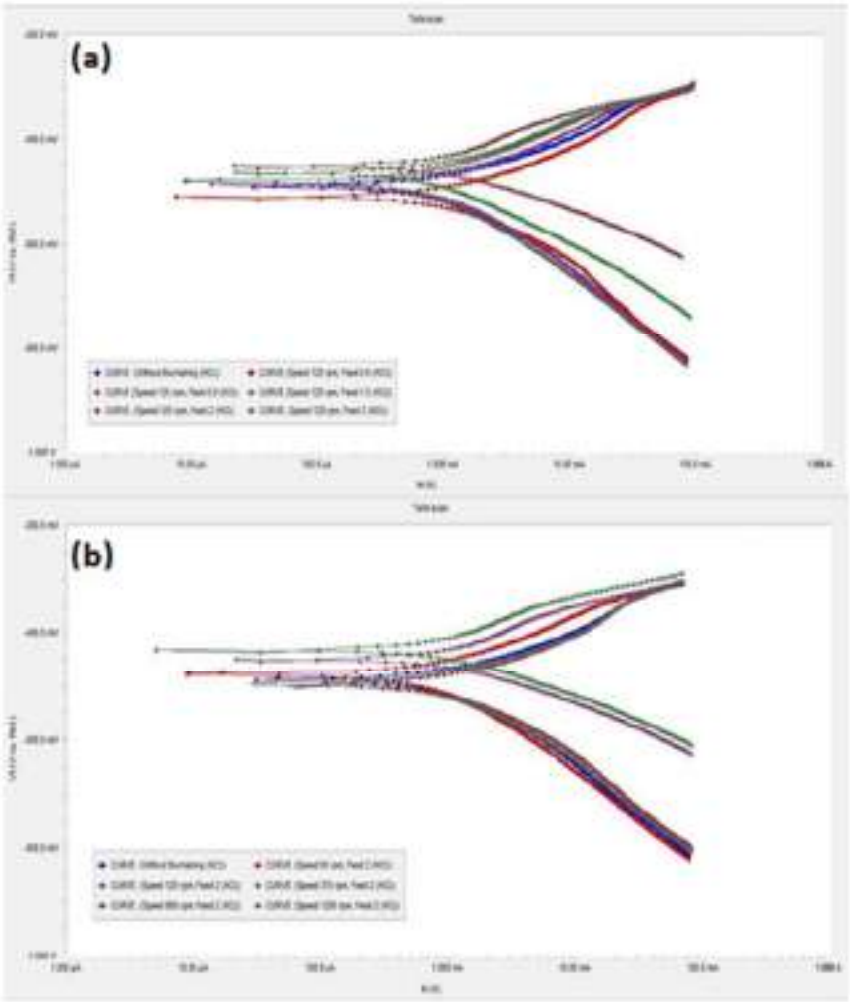

Figure (11) Tafel tests for a) case of changing burnishing feed b) case of changing burnishing speed.

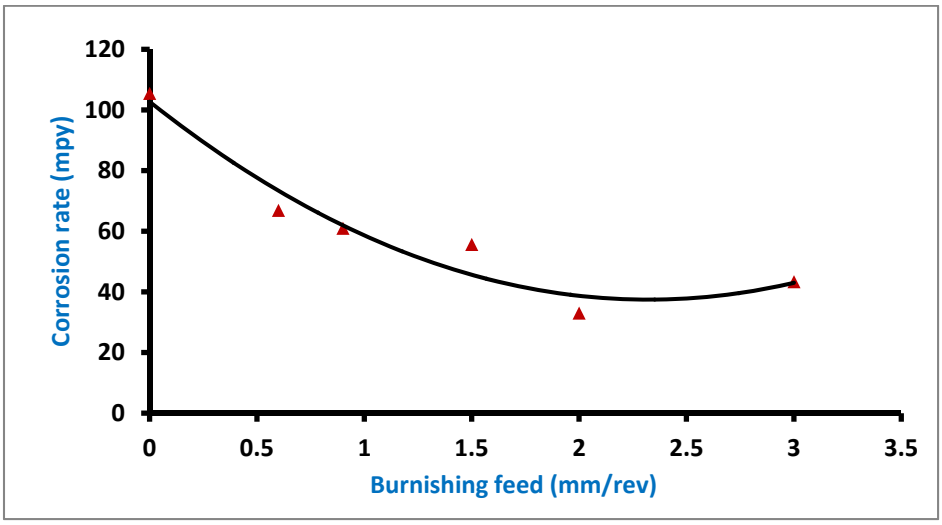

Figure (12) Relationship between burnishing feed and corrosion rate.

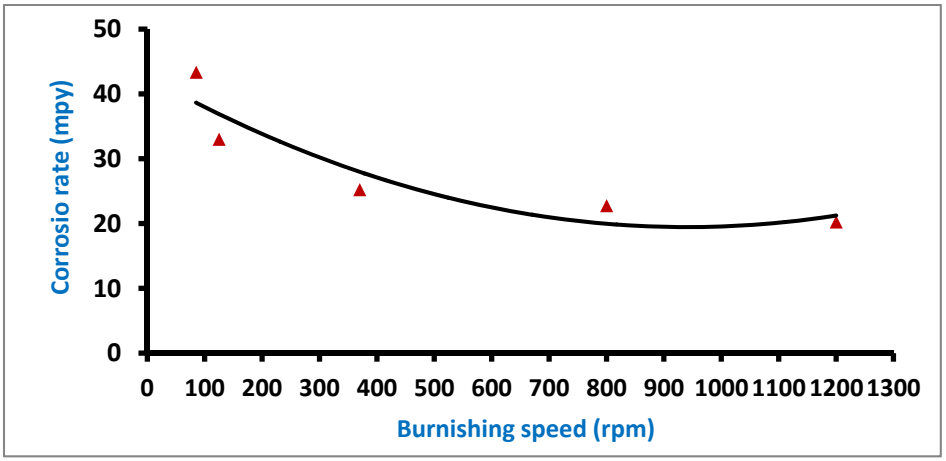

Figure (13) Relationship between burnishing speed and corrosion rate.

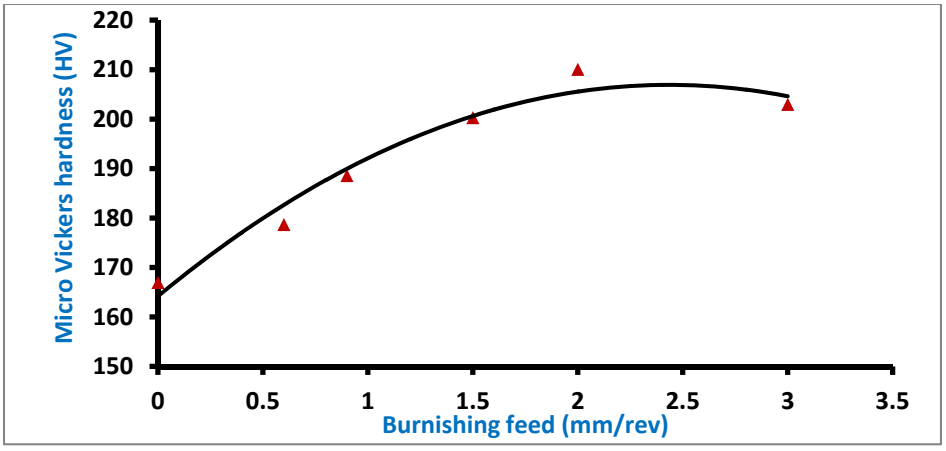

Figure (14) Relationship between burnishing feed and surface hardness.

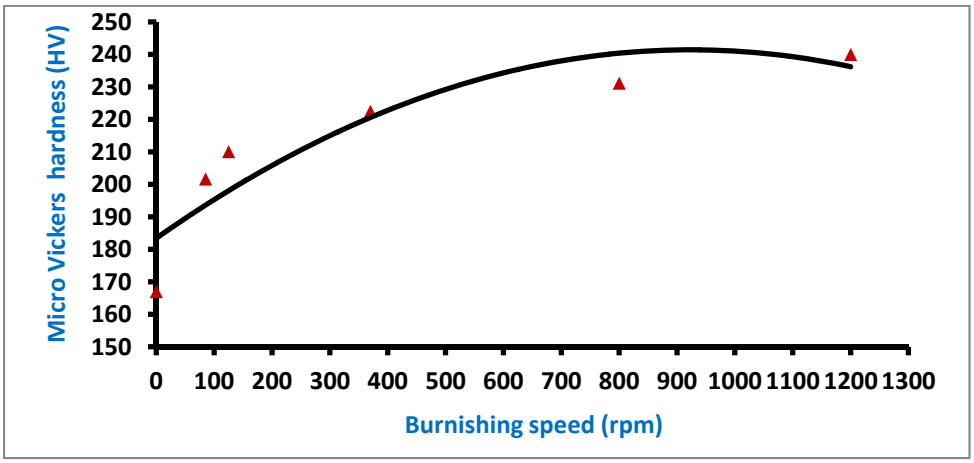

Figure (15) Relationship between burnishing speed and surface hardness.

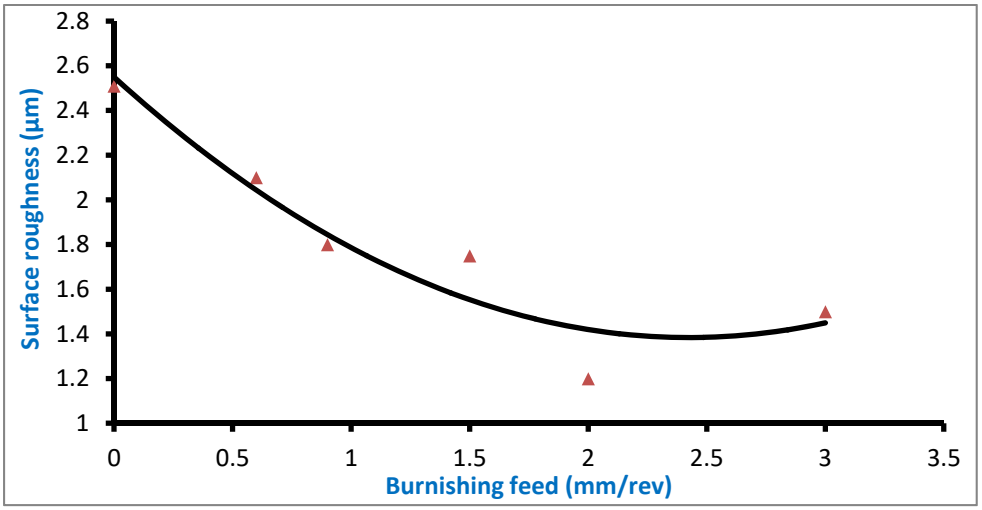

Figure (16) Relationship between burnishing feed and surface roughness.

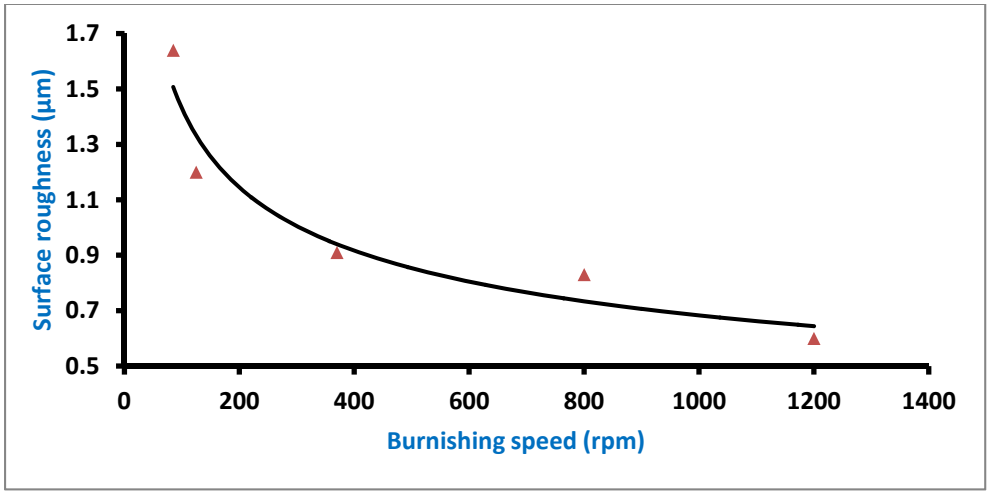

Figure (17) Relationship between burnishing speed and surface roughness.

References

[1] William D. Callister, Jr., "Material Science and Engineering", (2003), pp.570, United State of America, John Wiley & Sons, Inc., sixth edition.
[2] E.E. Stansbury and R.A. Buchanan, "Fundamental of electrochemical and corrosion", (2000), p.1, United State of America, ASM International.

[3] Al-Sultani Kadhim F., Alseroury F. A., Duaa A. Ali, "Use Eco-Friendly Materials to Steel Corrosion Inhibition", International Journal of Advances in Science Engineering and Technology, (2016), Volume 4, Issue 4, pp.40-44.
[4] Yuantai Ma, Ying Li and Fuhui Wang, "Corrosion of low carbon steel in atmospheric environments of different chloride content", Journal of corrosion science at science direct, 51 (2009), pp. 997-1006.
[5] Michael Ashby, Hugh Shercliff and David Cebon, "Materials, engineering, science, processing and design", (2007), p.390, UK, Elsevier.
[6] Junwen Tang and Fuhui Wang, "Corrosion behavior of carbon steel in different concentrations of HCl solutions containing H_2S at 90 ^{O}C", Journal of corrosion science at science direct, 53 (2011), pp. 1715-1723.
[7] Kenneth G. Budinski and Michael K. Budinski, "Engineering Materials, properties and selection", (2010), p.393-434, New Jersey, Pearson Education.
[8] Osarolube, E., Owate, I. O and Oforka, N. C., "Corrosion behavior of mild and high carbon steels in various acidic media", Journal of Scientific Research and Essay, June (2008), Vol.3 (6), pp. 224-228.
[9] J. Dossett and G.E. Totten, "Steel Heat Treating Fundamentals and Processes", (2013), p.2- 259, United State of America, ASM International, Volume 4A.
[10] Abd Alkader Ibrahim, Tamer Khalil, Tarik Tawfeek , " Study the influence of a new ball burnishing technique on the surface roughness of AISI 1018 low carbon steel", International Journal of Engineering & Technology (2015), Vol 4 (1), pp. 227-232.
[11] Deepak Mahajan and Ravindra Tajane, "A Review on Ball Burnishing Process", International Journal of Scientific and Research Publications, (2013), Volume 3, Issue 4, p.1-8.
[12] Murali Krishna R., "An investigation of the effect of the process parameters on the material properties of burnished components", Thesis (Doctor), July (2012), Faculty of Mechanical Engineering, Hyderabad University, India.
[13] Ashutosh Verma and Dalgobind Mahato, "Roller Burnishing-A Literature Review of Developments and Trends in Approach to Industrial Application", Asian Journal of Engineering and Technology, (2013), Volume 01, Issue 03, p.68-83.
[14]Tadeusz Hryniewiez and Krzysztof Rokosz, " Corrosion behavior of C45 carbon steel after roller burnishing", Journal of Hradec nad Moravici (2005), Vol. 5 pp. 24-26.
[15] N. M. Qureshi, Vaibhav B. Patil, Basavaraj D. Teli, "Analysis of Effect of Ball and Roller Burnishing Processes on Surface Roughness on EN8 Steel", International Journal of Engineering Research and Technology, (2015), Volume 4, Issue 06, p.311-315.
[16] Hamadache Hamid, Taamallah Wahiba, Zemouri Zahia," Characterization layers hardened burnished steel AISI/SAE 3115", International Journal of Mechanics and Applications (2014), Vol. 4 (1), pp. 13-19.
[17] Davinder Saini., Manish Kapoor, C. S Jawalkar, "Parametric Analysis of Mild Steel Specimens Using Roller Burnishing Process", International Refereed Journal of Engineering and Science, (2017), Volume 6, Issue 3, p.45-51.
[18] J. N. Malleswara Rao, Chennakesava Reddy Alaval, P. V. Rama Rao, "The effect of roller burnishing on surface hardness and surface roughness on mild steel specimens", International Journal of Applied Engineering Research, Dindigul (2011), Vol. 1 No. 4.

Available online at
http://namrc.uotechnology.edu.iq/index.php/

Nanotechnology and Advanced Materials Research Centre

Proceeding Articles Book 00 (2018) 000–000

6th International Scientific Conference on Nanotechnology, Advanced Materials and its Applications

Studying the Rheology of Water Based Nanofluid

Thamer Jasim Mohammed, Ellaf Khaled Abbass

Chemical Engineering Department, University of Technology, Baghdad, Iraq
Corresponding Author: thamer_jasim58@yahoo.com

Abstract

This research deals with experimental study of the rheological behavior of nanofluid. Suspension of selected nanoparticles in a base fluid can generate a nanofluid which is one of the most popular fluids in scientific community. The thermophysical properties such as viscosity have important effects on fluid flow and heat transfer characteristics as they affect the pumping power and workability of the fluid. In this paper, the rheological behavior (as shear stress and viscosity with respect to shear rate) of SiO_2_water and TiO_2_water were examined for different concentrations at room temperature (35ºC ±1). Stable and homogeneous suspensions, with concentrations ranging from50 to 250 ppm were prepared by dispersing dry SiO_2 and TiO_2 nanoparticles in a liter of distilled water. The rheological properties of these materials were investigated using a Brookefield digital viscometer with range between 20-250 rpm.

The viscosities are performed at the shear rates ranging from (24.46 s^{-1} to305.8 s^{-1}) for each nanofluid sample. The results showed that the nanofluids appeared as a non-Newtonian fluid with shear thickening or dilatant behavior with a power law index of higher than unity (n >1). As the concentration of nanofluid increased the flow behavior index (n) was in the range between 1.5 -1.75 at 35°C. Correlations were developed that describe the effect of nanofluid concentration on flow behavior index for each material used in this study and presented in a linear form.

The work concluded that shear stress and viscosity increased with increasing shear rate and decreased with increasing concentration and the diminution was higher in TiO_2–water compared to SiO_2–water nanofluid for both shear stress and viscosity.

Key words: Rheology, Nano fluids, Viscosity, Shear thickening.

1. Introduction:

It is clear that adding nano-sized materials to the fluids alters their other thermo-physical properties such as viscosity which measures the interfacial friction, that is the internal resistance of the fluid layers. It is an important parameter for all applications involving fluid flow [1]. The rheological behavior of the fluid flow is needed to obtain the required pumping power. Therefore, a great number of research have been conducted to investigate the viscosity and rheological behavior of different nanofluids.

Nanofluids preparation methods [2], particles shapes and sizes [3], particles concentrations, temperatures, surfactants and properties of base fluids affect the rheological behavior of nanofluids.

A summary of such studies for the viscosity of nanofluids based on Newtonian behavior is presented. These studies revealed that the viscosity of nanofluids enhances by increasing the particle concentration, and decreases with an increase in temperature. However, a few studies have been reported on non-Newtonian nanofluids. Among these studies, the study of the rheological behavior of TiO2–ethylene glycol nanofluids was performed by Cabaleiro et al. [4]. They determined the viscosity of the nanofluid at nanoparticle mass concentrations up to 25% for temperature ranging from 283.15 K to 323.15 K. They also repeated the experiments at various shear rates and showed that the nanofluid exhibited a non-Newtonian behavior according to the Ostwald–de Waele model.Later, Chen et al. [5] reported that particle shape had great impact on viscosity. They also observed that the nanofluids displayed shear thinning behavior above concentrations of 2 vol%. Similarly, Hojjat et al. [6] observed pseudo plastic (shear thinning) behavior for c-Al_2O_3, TiO_2 and CuO nanoparticles which were dispersed in a 0.5 wt% aqueous solution of carboxymethyl cellulose (CMC). Moreover, Garg et al. [7] found that MWCNT–water nanofluids showed a shear thinning behavior. Based on the available data from literatures, it is concluded that some nanofluids exhibit Newtonian behavior [8-16] while others demonstrate non-Newtonian behavior [6, 7, 10–26]. Therefore, there is a need for more experimental work on rheological behavior of nanofluids. However, interestingly, Sahoo et al. [16] experimentally found that Al_2O_3 nanofluids behaved like a non-Newtonian fluid at lower temperatures (0-35ºC) but it displayed Newtonian behavior at higher temperatures (0–90ºC). They tested 1–10% volume concentrations prepared by 53 nm Al_2O_3 nanoparticles dispersed in a base fluid of 60% (by mass) of ethylene glycol and water.

Maré et al. [27] have studied experimentally the thermal-hydraulic performance of Al_2O_3 and carbon nanotubes (CNT) aqueous based nanofluids in a plat heat exchanger at low temperatures. Their results show that the impact of viscosity and pressure drop is important and has to be taking into account before to use nanofluids. Due to high viscosity of SiO_2/water based nanofluids at high particles concentration, Ferrouillat et al. [28] reported that the pumping power is very high and that the practical benefits of using nanofluids is not significant compared to base fluid. Ngyuen et al. [29] have investigated on particle size effect for Al_2O_3 aqueous based nanofluids and observed that the particle size effects on viscosity are more significant for high particles concentration. Numburu et al. [30] studied the rheogical behavior of SiO2/water and SiO2/Ethylene Glycol based nanofluids for a range of -35°C to 50°C. Their results show that the nanofluid is Newtonian for high temperatures and shear thinning for low temperatures. Kulkarni et al [31] studied the effect of temperature for a range from -35°C to 50°C for CuO, Al_2O_3 and SiO_2 Ethylene Glycol and water based nanofluids. They reported that viscosity decreases exponentially with the increase of temperature. Kole et al. [32] investigated Al2O3-car engine coolant nanofluid and found that the Brownian motion of the nanoparticles in the fluid plays an important role in understanding the viscosity of nanofluids.

Paritosh et al. [33] studied the effect of dispersing energy (ultra-sonication) on viscosity of multi walled aqueous based nanofluids MWCNT. They showed that CNT exhibit a shear thinning behavior and that the Non-Newtonian character may not be solely attributed to the presence of the surfactant (Gum Arabic).

On the other hand, Newtonian or non-Newtonian behavior of nanofluids plays an important role in thermal and fluid flow applications. Hence, there is a key need to the examination of the rheological behavior of nanofluids. Therefore the aim of the present work was to study the rheological behavior of two types of nanofluids: SiO_2_water and TiO_2_water which were examined for different concentrations at room temperature. In this regard, the nanofluid samples were prepared at various solid concentrations and were experimented under different shear rates.

2. Experimental Procedure

2.1. Materials and Preparation

SiO_2 (20-30 nm) TiO_2 nanoparticles were suspended in water (base fluid) in this investigation. These nanoparticles were chosen because they are produced in large scale in industry and are chemically more stable, easily available and not harmful for human being.

Nanofluids with different particle concentrations were prepared by adding distilled water to the defined amounts of nanoparticles. In this method, known as the two-step method, the nanoparticles are purchased as dry powder and then dispersed in the liquid medium. The solid content is expressed in terms of ppm which represents the weight of solid in milligram respect to a liter of distilled water. The characteristics of SiO_2, TiO_2 nanoparticles are presented in Table 1. [34]

In the present work, to make stable samples of nanofluid the suspensions were mixed with a high-speed mechanical stirrer at a power of 400W and rotational speed of 2000 rpm for about 20 minutes before the viscosity tests were carried out. This process was applied to break down the agglomeration between the particles, which leads to achieving a uniform dispersion and a stable suspension.

In order to obtain a characterization of the nano-sized materials, the structural properties of the dry SiO_2 nanoparticles were measured by using Atomic force microscopes (AFM) as shown in Fig.1

Table 1 Characteristics of SiO_2 and TiO_2 nanoparticles: [34]

Property	SiO_2	TiO_2
Purity	99.8%	99.9%
Color	Whit	White
Size outer diameter	20-30(nm)	100(nm)
Specific surface area	180-600m^2/g	85m^2/g
Bulk density	<0.10 g/cm^3	0.65 g/cm^3
True density	2.4 g/cm^3	3,9 g/cm^3

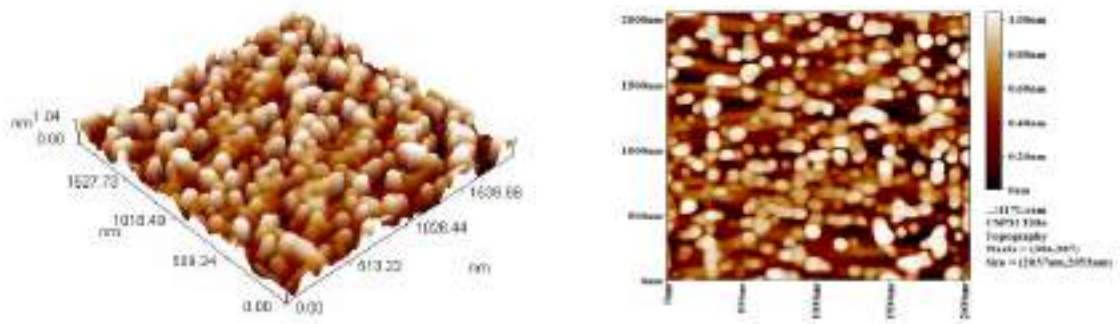

Fig.1. Atomic force microscopes (AFM) photographs of SiO2 nanoparticles

2.2. Rheological Property Measurements:

Rheological properties of the nanofluid with solid concentrations of 50,100,150,200 and 250 ppm were measured in the room temperature (35ºC ±1). The Brookfield ISO9001 digital viscometer, was employed to measure the viscosities of the nanofluid samples. The spindle of the viscometer was submerged into the nanofluids. The rheometer was connected with the computer into which (rheocalcT) software had been installed to obtain the rheological data of water based nanofluids. The major application of this device was to verify the mechanical resistance of the samples before they were tested in the pipeline (closed-loop liquid circulation). It was also used to identify the samples which produced the desired viscosity. In this case, the rheology was tested for different materials of different concentrations. (A schematic diagram of the experimental set up is shown in Fig 2.

The viscosity measurement range of this equipment is mPa s. In this experiment, the viscosity and shear stress data of all samples were measured within a shear rate range of 24.46 s^{-1} to305.8 s^{-1} while the spindle rotation was 20–250 rpm with a total time period of 180 s for each rheology calculation. All data were recorded for three times and the corresponding averaged values were plotted.

Fig.2. Graphical image of a Brookfield viscometer for rheological behavior measurement.

3. Results and discussion:

3.1. Torque Measurements:

Figure 3 illustrates the effect of rotational speed on the torque of different concentrations of SiO_2 nano particles in comparison with the torque of pure water (as reference). It could be seen that the torque decreased slightly with increasing SiO_2 concentration compared to the torque of pure water. The torque of pure water at 250 rpm was 67.4% while the torque of SiO_2 suspension of 250 ppm was 51.1% at the same rpm. This indicates that increasing the nanofluid concentration affects its drag reduction efficiency.

Figure 4 shows the relationship between the torque and the rotational speed for different concentrations of TiO_2. It is obvious that the torque decreased a little when the concentration of TiO_2 is increased.

3.2. Rheological Properties Measurements:

To evaluate the rheological behavior (Newtonian or non-Newtonian) of the nanofluid, all experiments were repeated at different shear rates for each concentration. For the lowest shear rates (typically at24.6 s^{-1} some fluctuations of viscosity were observed, especially in the case of the less viscous solutions (while increasing the concentration).

Figure 5 shows the variation in the nanofluid viscosity as function of the shear rate and nanoparticles concentration for the case of silica nanoparticles. Figure 6 shows similar results for the case of TiO_2 nanoparticles. Suspensions of different concentrations show an increase in viscosity with the increase in shear rate. This is a typical behavior for a shear thickening fluid (Dilatant behavior). For these nanofluids, viscosity decreases with particles concentration. Figs. 7 and 8 Show the shear stress as

function of shear rate, concentration for SiO_2 and TiO_2 nanoparticles suspensions, respectively. In Fig.5, fluids are shown to exhibit non-Newtonian flow behavior. This relationship can be represented by the power law or Ostwald-de-Wale equation:

$\tau = k \gamma^n$

Where τ is shear stress (dyne/cm^2), γ is shear rate (s^{-1}), k is the power law constant (consistency index), n is constant (flow behavior index). Dividing the power law equation through by γ gives an expression in terms of viscosity :

$\eta = k \gamma^{n-1}$

n is less than 1 for pseudoplastic fluids, greater than 1 for dilatants fluids, and equal to 1 for Newtonian fluids. For the case of TiO_2 and SiO_2 nanoparticle suspensions (Figs. 7&8), as the particles concentration increases from 50 to 250 ppm the fluids non- Newtonian characteristics (Dilatant behavior) intensify. However, suspensions with TiO_2 nanofluid show more decrease in viscosity and shear rate with respect to SiO_2 nanofluid. (Figs. 9&10)

The shear thickening effect may be related to a transition of suspension structure from an ordered state to a rather disordered state. Increasing the shear stress is so that the particles or clusters are displaced from their equilibrium position to become a disorder structure which dissipates more energy during flow leading to the increase of the mixture viscosity.

Table 2 shows the calculated power law index (for the test cases in Figs. 6 and 7) to vary from 1.57 to 1.65 for TiO_2 nanoparticles and 1.53 to 1.74 for SiO_2 nanoparticles revealing shear thickening behavior.

Table 2 shows the calculated power law index for TiO_2 nanoparticles and SiO_2 nanoparticles

Material or nanofluid	Concentration (ppm)	Power Law Index n	Consistency k ($x10^3$)	Least Square Fit, R^2
Distilled water	-------	1.669	0.35	0.999
TiO2	50	1.641	6.57	0.896

TiO2	100	1.629	0.38	1.000
TiO2	150	1.571	0.47	0.998
TiO2	200	1.607	0.40	0.999
TiO2	250	1.649	0.32	0.998
Nano silica	50	1.641	0.37	1.000
Nano silica	100	1.537	0.63	0.998
Nano silica	150	1.713	0.25	1.000
Nano silica	200	1.735	0.20	0.999
Nano silica	300	1.723	0.23	0.996

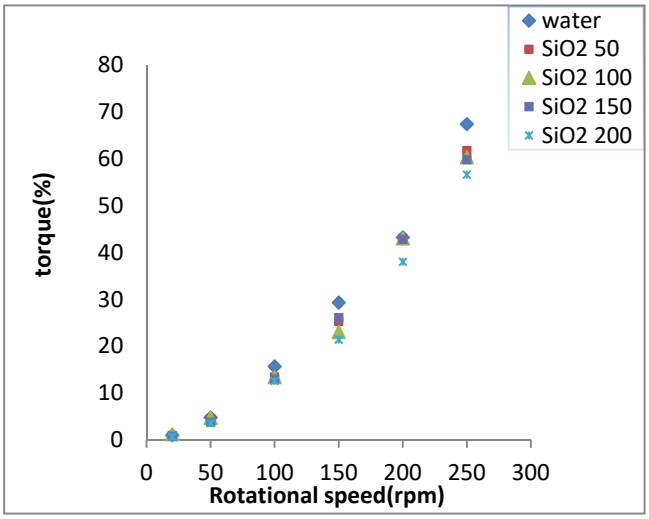

Fig.3 Effect of rotational speed on the torque of different concentrations of nano SiO_2

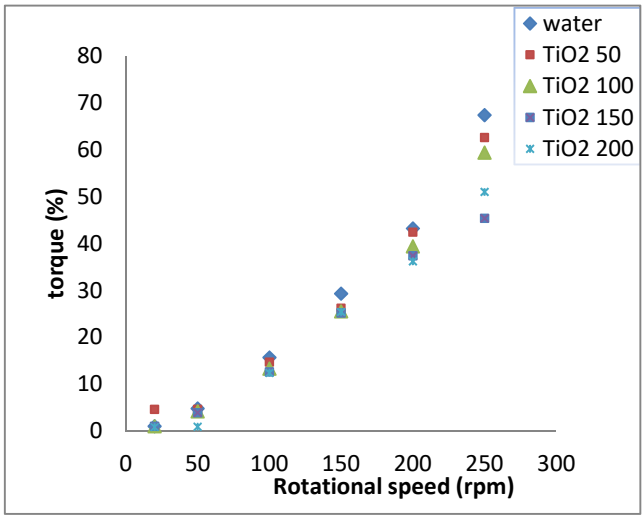

Fig.4 Effect of rotational speed on the torque of different concentrations of nano TiO_2

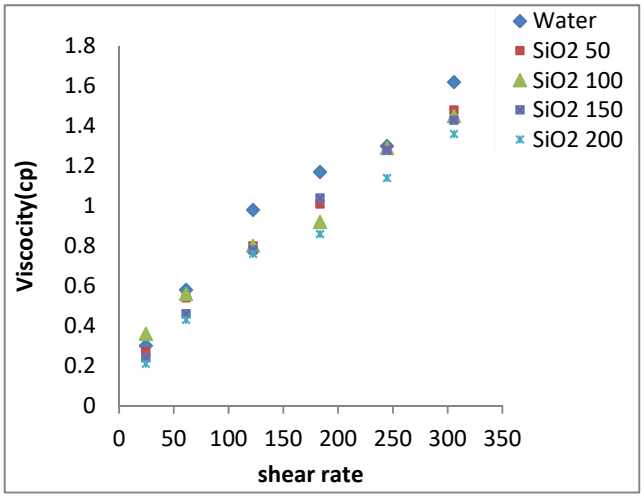

Fig.5. Viscosity versus shear rate for various nano SiO2 samples

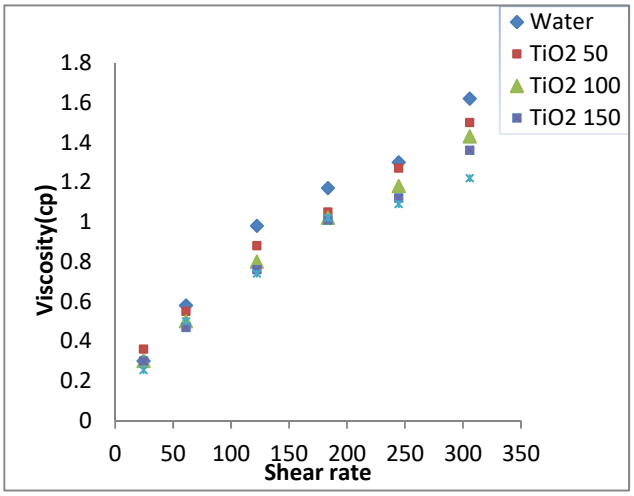

Fig.6. Viscosity versus shear rate for various nano TiO2 samples.

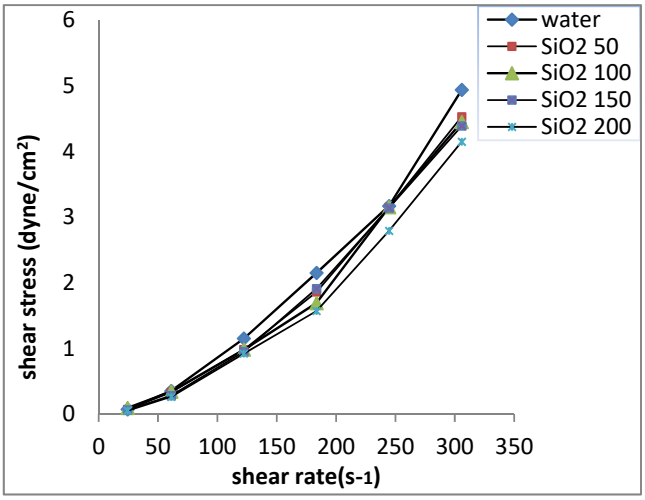

Fig.7 Shear stress versus shear rate for various of nano-SiO_2 samples.

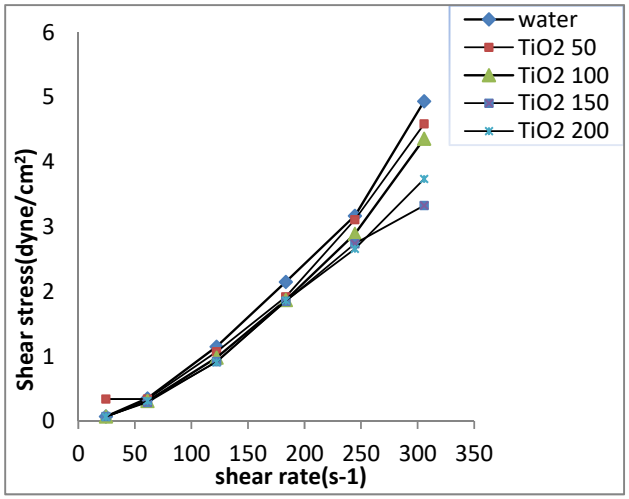

Fig.8. Shear stress versus shear rate for various of nano-TiO_2 samples.

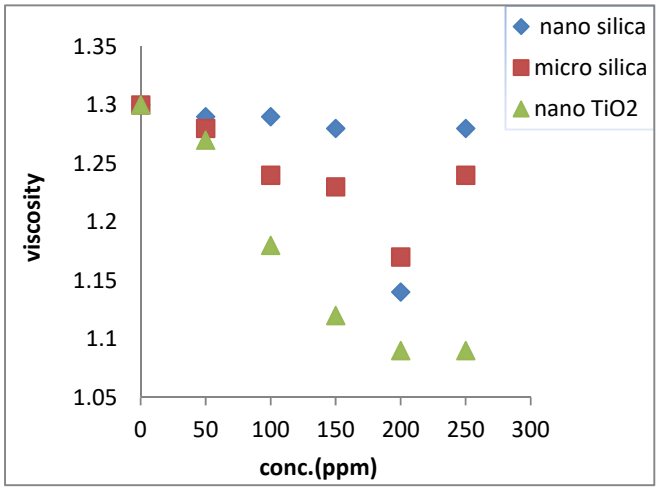

Fig.9 Comparison of viscosity obtained for various of nanofluid samples at 200 rpm

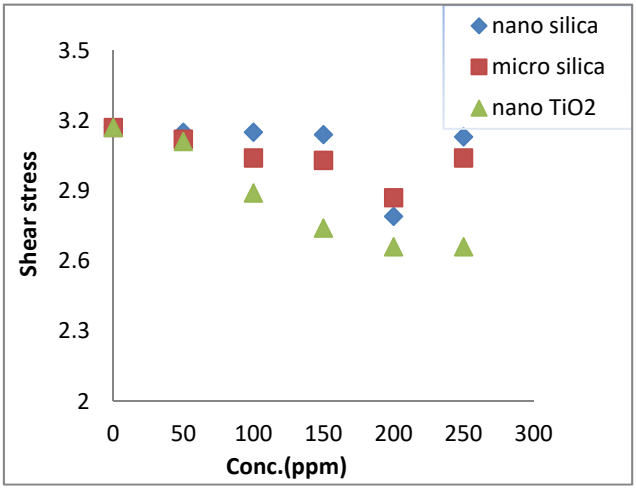

Fig.10 Comparison of shear stress obtained for various nanofluid samples at 200rpm

4. Conclusions:

Rheological tests on suspensions using TiO_2 and SiO_2 nanoparticles show an increase in viscosity and shear stress with the increase in shear rate (shear thickening or dilatant behavior). The increase in viscosity is by about a factor of 6 as shear rate increases by a factor of 12.5. Nanoparticles concentrations also affect shear stress and viscosity. They decreased with an increase in concentration. TiO_2–water nanofluids showed lower shear stress and viscosity over SiO_2–water at the same concentrations.

The highest diminution of viscosity was found to be 30% over the base fluids at 250ppm for TiO_2–water and SiO_2-water nanofluids.

References:

[1] C.T. Nguyen, F. Desgranges, G. Roy, N. Galanis, T. Maré, S. Boucher, H. Angue Mintsa, Temperature and particle-size dependent viscosity data for water based nanofluids – hysteresis phenomenon, Int. J. Heat Fluid Flow 28 (6) (2007) 1492–1506.
[2] X. Wang, X. Xu, S.U.S. Choi, Thermal conductivity of nanoparticle–fluid mixture, J. Thermophys. Heat Transfer 13 (4) (1999) 474–480.
[3] J. Chevalier, O. Tillement, F. Ayela, Rheological properties of nanofluids flowing through micro channels, Appl. Phys. Lett. 91 (23) (2007). 233103-233103-233103.
[4] D. Cabaleiro, M.J. Pastoriza-Gallego, C. Gracia-Fernández, M.M. Piñeiro, L. Lugo, Rheological and volumetric properties of TiO2-ethylene glycol nanofluids, Nanoscale Res. Lett. 8 (2013) 286 (13 pages).
[5] H. Chen, Y. Ding, Y. He, C. Tan, Rheological behavior of ethylene glycol based titania nanofluids, Chem. Phys. Lett. 444 (4–6) (2007) 333–337.
[6] M. Hojjat, S.G. Etemad, R. Bagheri, J. Thibault, Rheological characteristics of non-Newtonian nanofluids: experimental investigation, Int. Commun. Heat Mass Transfer 38 (2) (2011) 144–148.
[7] P. Garg, J.L. Alvarado, C. Marsh, T.A. Carlson, D.A. Kessler, K. Annamalai, An experimental study on the effect of ultrasonication on viscosity and heat transfer performance of multi-wall carbon nanotube-based aqueous nanofluids, Int. J. Heat Mass Transfer 52 (21–22) (2009) 5090–5101.
[8] H. Chen, Y. Ding, C. Tan, Rheological behavior of nanofluids, New J. Phys. 9 (10) (2007) 367.
[9] J. Chevalier, O. Tillement, F. Ayela, Structure and rheology of SiO2 nanoparticle suspensions under very high shear rates, Phys. Rev. E 80 (5) (2009) 051403.
[10] U. Teipel, U. Förter-Barth, Rheology of nano-scale aluminum suspensions, Propellants Explos. Pyrotech. 26 (6) (2001) 268–272.
[11] R. Prasher, D. Song, J. Wang, P. Phelan, Measurements of nanofluid viscosity and its implications for thermal applications, Appl. Phys. Lett. 89 (13) (2006). 133108-133108-133103.
[12] P.K. Namburu, D.P. Kulkarni, D. Misra, D.K. Das, Viscosity of copper oxide nanoparticles dispersed in ethylene glycol and water mixture, Exp. Therm. Fluid Sci. 32 (2) (2007) 397–402.
[13] F. Boschini, A. Rulmont, R. Cloots, R. Moreno, Rheological behaviour of BaZrO3 suspensions in non-aqueous media, Ceram. Int. 35 (3) (2009) 1007–1013.
[14] H. Chen, S. Witharana, Y. Jin, C. Kim, Y. Ding, Predicting thermal conductivity of liquid suspensions of nanoparticles (nanofluids) based on rheology, Particuology 7 (2) (2009) 151–157.
[15] D.P. Kulkarni, D.K. Das, R.S. Vajjha, Application of nanofluids in heating buildings and reducing pollution, Appl. Energy 86 (12) (2009) 2566–2573.
[16] B.C. Sahoo, R.S. Vajjha, R. Ganguli, G.A. Chukwu, D.K. Das, Determination of rheological behavior of aluminum oxide nanofluid and development of new viscosity correlations, Pet. Sci. Technol. 27 (15) (2009) 1757–1770.
[17] D.P. Kulkarni, D.K. Das, G.A. Chukwu, Temperature dependent rheological property of copper oxide nanoparticles suspension (nanofluid), J. Nanosci. Nanotechnol. 6 (4) (2006) 1150–1154.
[18] W.J. Tseng, C.-N. Chen, Effect of polymeric dispersant on rheological behavior of nickel–terpineol suspensions, Mater. Sci. Eng. A 347 (1–2) (2003) 145–153.
[19] W.J. Tseng, K.-C. Lin, Rheology and colloidal structure of aqueous TiO2 nanoparticle suspensions, Mater. Sci. Eng. A 355 (1–2) (2003) 186–192.
[20] K. Kwak, C. Kim, Viscosity and thermal conductivity of copper oxide nanofluid dispersed in ethylene glycol, Korea-Aust. Rheol. J. 17 (2) (2005) 35–40.
[21] K. Lu, Rheological behavior of carbon nanotube–alumina nanoparticle dispersion systems, Powder Technol. 177 (3) (2007) 154–161.
[22] M. Kole, T.K. Dey, Viscosity of alumina nanoparticles dispersed in car engine coolant, Exp. Therm. Fluid Sci. 34 (6) (2010) 677–683.
[23] T.X. Phuoc, M. Massoudi, Experimental observations of the effects of shear rates and particle concentration on the viscosity of Fe2O3–deionized water nanofluids, Int. J. Therm. Sci. 48 (7) (2009) 1294–1301.
[24] H. Chen, Y. Ding, A. Lapkin, X. Fan, Rheological behavior of ethylene glycoltitanate nanotube nanofluids, J. Nanopart. Res. 11 (6) (2009) 1513–1520.
[25] H. Chen, W. Yang, Y. He, Y. Ding, L. Zhang, C. Tan, A.A. Lapkin, D.V. Bavykin, Heat transfer and flow behavior of aqueous suspensions of titanate nanotubes (nanofluids), Powder Technol. 183 (1) (2008) 63–72.
[26] H. Chen, Y. Ding, A. Lapkin, Rheological behavior of nanofluids containing tube/rod-like nanoparticles, Powder Technol. 194 (1–2) (2009) 132–141
[27] Maré T, Halelfadl S, Sow O, Estellé P, Duret S, Bazantay F. Comparison of the thermal performances of three nanofluids at low temperature in a plate heat exchanger. Exp Thermal Fluid Sci. 2011;35:1535-1543.
[28] Ferrouillat S, Bontemps A, Ribeiro JP, Gruss JA, Soriano O. Hydraulic and heat transfer study of SiO2/water nanofluids in horizontal tubes with imposed wall temperature boundary conditions. Int J Heat Fluid Flow 2011;32:424-439
[29] Nguyen CT, Desgranges F, Roy G, Galanis N, Maré T. Temperature and particles-size dependent viscosity data for water-based nanofluids – Hysteresis phenomenon. Int J Heat Fluid
Flow. 2007;28:1492-1506.
[30] Numburu PK, Kulkarni DP, Dandekar A, Das DK. Experimental investigation of viscosity and specific heat of silicon dioxide nanofluids. Micro Nano Lett 2007;2:67-71
[31] Kulkarni DP, Debendra KD, Ravikanth SV. Application of nanofluids in heating buildings and reducing pollution. App Energy 2009;86:2566-2573.
[32] Kole M, Dey TK. Thermal conductivity and viscosity of Al2O3 nanofluid based on car engine coolant. J Phys D Appl Phys 2010;43:315501.
[33] Paritosh G, Jorge LA, Marsh C, Carlson TA, Kessler DA, Annamalai K. An experimental study on the effect of ultrasonication on viscosity and heat transfer performance of multi-wall carbon nanotube-based aqueous nanofluids. Int Journal Heat Mass Transfer 2009;52:5090–5101
[34] US Research Nanomaterials, Inc, The advanced nanomaterial provider.

Available online at
http://namrc.uotechnology.edu.iq/index.php/

Nanotechnology and Advanced Materials Research Centre

Proceeding Articles Book 00 (2018) 000–000

6th International Scientific Conference on Nanotechnology, Advanced Materials and its Applications

Preparation and Investigation of composite coating (Ni-nano hydroxyapatite) on low carbon steel samples

Nabaa Sattar Radhi, Zainab S. Al-Khafaji
University of Babylon, Babylon, Iraq
Al-Mustaqbal University College, Babylon, Iraq

Abstract

This work presents an attempt to produce a further improvement for the properties of Nickel coatings, by addition HA particle to electrodeposited solution. Low carbon steel samples were coated with Nickel and (Ni- HA) with two different nanoscale particles size of hydroxyapatite the first one is (20 nm) and the second one is (40 nm). After producing electroplating, these samples were tested in Hank's solution in order to study the corrosion behavior. Then testing the micro-hardness, surface roughness, and topographic for Nickel coating and (Ni-HA) with (20 and 40) nm.

Keywords: Hydroxyapatite, orthopedic implant, biocompatibility, electrodeposited, nanoscale and Hank's solution

1. Introduction

Coating is a wide chemical industrial use process providing many benefits such as: preventing rust, corrosion resistance, heat resistance, electrical conductivity, and resistance for wear. Besides these functions, paint could be adding for decoration and beauty purposes. However, the coating process are releasing a high concentrations of mineral-containing wastewater, which severely affects the environment. So if the purpose of coating is to improve the implants properties which will placed inside human body, in this condition that materials that used for coating should by non-toxic in order to prevent the bad effect for these metals, [1]

Nickel is one of the metals that wide-commonly used in electroplating so as to enhance the usefulness, value and overall sales promotion for consumer goods and manufacturing of products, **[1].** Moreover, nickel coating is also used to enrich the physical characteristics like resistance of wear, heat and corrosion. Therefore, Nickel coatings are used in many important applications due to the ability of this coating to improve the resistance of the metal against corrosion with an improving in the functional properties as well as providing a decorative shape, **[3-5].**

1.2 Bio-active Coating

Bio-active materials is a term usually referring to the materials that will be active inside the human body and in interact with the surrounded bones or with the soft tissue. And in some cases, these materials are depending on the Bioactivity Index (I_B) which introduced by (Hench) as shown in below to measure the level of bio-activity**:**

$$I_B = 100/ t\ 0.5bb$$

Whereas: t 0.5bb = the required time to get bonding interface for more than 50%. And this usually occurs during the time depending on kinetic modification of the surface, generated by implantation of the bio-active material inside the live bone. Due to the reaction between the bio-active materials which inside the live bone and the surrounding body fluids there will be an ion exchange. And this ion exchange will lead to produce of a biologically active carbonate apatite (CHA) coat on the bioactive object which is equivalent to the bone mineral phase chemically and crystallographically. And the main examples for bio-active materials are synthetic hydroxyapatite (HA), and Bio-glass [6].

1.3 Hydroxyapatite

Hydroxyapatite (HA), usually written as $Ca_{10}(PO_4)_6(OH)_2$ is one of ceramics member for apatite group. And the terms of apatite refers to deceit or deception and the main origin for this term is the Greek word (a pate) and the cause of this name return to the variation of the shape and colour [7]. It was chosen several times as an artificial bone due to the similarity for its nature with live bone nature in spite of lacking of the organic constituents like polysaccharides and collagen. The chemical similarity of HA to bone and its excellent biocompatibility and bioactivity have attracted the attention of medical professionals **[8, 9].**

HA was manufactured and used to manufacture different implants forms (porous and solid) and as a layer of coating on other implants **[10].**

2. Experimental part:

2.1 Electroplating Process

The samples were low carbon steel (L.C.S.) with chemical composition as presented in Table (1). The chemical analysis was performed by a spectroscopy device for metal.

The samples that used in all the tests were prepared by using cylindrical moulds and the finals samples have disc shape with the following dimension (thickness = 2mm and diameter = 15mm) as well as the surface area for these samples are (447.667 mm^2).

On the other hands, the samples surface was prepared as following:

1-Grinding the sample surface by using Grit silicon carbide papers which carried these grade (220,240,400,600,800,1000,1200). Then the sample surface will clean by using brines and acids to be ready for Electroplating process depending on the required period for each sample.

2-Electroplating process was carried out by using basin produced from polythene and has a rectangular shape (29x21x18 cm) as shown in figure (1); and power supply which can give the current up to (6Amp) and The voltage given up to (20 Volt).

2.2 Composition of Electroplating Baths:

The Watts Nickel Plating Solution, the majority of plating solutions that cotain nickel , particularly those used in the design paint, are based on the "Watts" formula which developed by Professor Oliver P. Watts in 1916. The electrolyte of Watts combines nickel sulphate, chloride of nickel and boric acid. While the ratios might be differ depending on the required application, Table 2 is shown in typical formulation with operating parameters.

2.3 Tests:

In the research, the following tests were carried out to evaluate the performance of the coating layers:

2.3.1. Thickness Test

The thickness measuring device was used to measure the thickness of Ni and Ni-HA films, in (Babylon/College of Material Engineering/University of Babylon).

2.3.2. Light Optical Microscope (LOM)

Involved identification and measurement of the phases, shape and grain size are some characteristics of grain boundaries. Each of these has distinct characteristics. The microstructure evaluated with (100x) magnification using Olympus microscope manufactured by Japan.

2.3.3. Hardness Test

Vickers Hardness (TH-717 Digital Micro Vickers Hardness Tester) was measured the hardness of Ni and Ni-HA films, at load (200N) and holding time 20 seconds in (college of Material engineering /University of Babylon).

1.3.4. surface roughness test

The surface roughness of a nickel-coated steel sample (Ni-nHAP) was measured by using the (TR-100 surface roughness tester), which is located at the University of Babylon, Faculty of Materials Engineering. The device passes on the sample surface to measure the surface roughness. The device has a sensor that records the roughness of the sample surface and takes the reading directly from the device screen. The accuracy of the device (± mμ0.01).

2.3.5. Electrochemical Test

The corrosive behaviour of low carbon steel studied in the solution of Hank. Where the Hank's solutions chemically composited from the components which illustrated in Table (3) and pH of it at 37C° was 7.4.

2.3.5.1 Open Circuit Potential (OCP)

The experimental arrangement for the measurement of open circuit potential is described. A 500 ml capacity glass electrolytic cell is used. The tests were performed with the specimen submerged in a Hanks solution. The working potential for the electrode is calculated in regarding with a Saturated Calomel electrode (SCE).

2.3.5.2 Potentiostatic Polarization

Electrochemical experiments were performed in three electrode cell containing and electrolytes for solution of Hank which chemically composited from the components that demonstrated in table (3), [10].

The test was carried out by stepping the possible using a scanning ratio 0.4 mV/s from the first potential (250 mV) below the potential of open circuit and the scanning continuous up to 250 mV above the potential of open circuit. Corrosion rate measurement is got by applying the following equation [11].

Corrosion rate (mpy) = 0.13icorr(E.W.)/A.ρ …(1)

Where:

E. W. = equivalent weight (g/ eq)

A = area (cm^2)

ρ =density (g/ cm^3)

0.13 = metric and time conversion factor.

icorr. = current density (μA / cm^2).

The improvement percentage is calculated for coated samples, using the following equation **[11]**:

Improvement percentage =$(CR^0 - CR / CR^0)$, 100 …(2)

Where:

CR° =the corrosion rate of master sample (without coated).

CR =the corrosion rate of coated sample (with Ni or (Ni-HAP)).

3. Discussion of the experimental Results:

3.1 Thickness Results

For Ni specimen the thickness is 25.7μm, while the thickness increased to (47.5, 48.7) μm for (Ni-20nHaP) samples with 10 and 20 g/L , and then the thickness reach to it is high value (49.7, 50.5) μm for (Ni-40nHaP) samples with 10 and 20 g/L. These results indicated that the deposit rates of last two coating layers are greatly faster than for (Ni). This can be attributed to the high diffusivity of the species caused by the presence of HaP. Anyhow with increasing amount and particles size of HAP, the rate of thickness increased also as shown in Table (4).

3.2 Light Optical Microscope (LOM)

The optical microscope is shown the topography behaviour of coating layer for Ni and (Ni-HAP) as illustrated in figure (2(a,b,c,d,e)). From these figures can illustrated the smooth morphology at Ni layer in figure (2.a), less smooth in figures (2 (b&c)) for Ni added HaP at (10&20)g with 20nm particles size, while figures(2 (d&e)) for Ni added HaP at (10&20)g with 40nm particles size shown the rough surface, because the addition of particles with different size.

3.3. Hardness results

The hardness test was performed to determine the effect of (Ni) coating on the hardness values 200 of low carbon steel. And finding out the effect of adding (HAP) in two different particles size on the hardness values of (Ni) coating and the low carbon steel values. Table (5) shows the results of hardness test for of the carbon steel sample, the Ni-coated steel sample, the Ni-20nHAP layers and the Ni-40nHaP layer. The difference in hardness values observed between Ni-20nHAP and Ni-40nHAP is due to the difference in the volume of hydroxide uptake in both layers. The material hardness is clearly affected by the size of the particles, and mathematically can explain it by Hall-Petch relationship, which states, [5]:

$$HV = H_O + K/\sqrt{d}$$

Where as:

H_V: Hardness of material with small granular size.

Ho: Hardness material is multi-size granular (polycrystalline grain size).

K: Constant, represents the slope of the Hv hardness when drawing against, and it depends on the type of material.

$1/\sqrt{d}$: Diameter of the particle.

Hall-Petch relationship is one theory that explains why ultra-fine microstructures have higher hardness values 344 when compared to the coarser-grained ones and the same hardened material.

3.4 Surface roughness results

It is clear from table (6) the roughness of (Ni-40nHAP,20g) is the highest. This may be attributed to the bigger HAP particles size. This is idea is supported by the fact that (Ni) layer which is free of HAP particles possesses the lowest value of surface roughness. The roughness of surface for the deposited layers are presented in table (6).

3.5 Corrosion Tests

3.5.1 The Potential of Open Circuit (OCP) - Time Measurements

The OCP - time was calculated in regarding with SCE in the solution of Hank at 37°C for uncoated samples and coated samples (Ni and Ni-HA Coating). The data of OCP are shown in Table (4).

3.5.2 Potentiostatic Polarization

This test was done by using the Potentiostatic polarization test in Hank's solution) for uncoated, Ni and Ni-HA coated samples at 37 °C, as shown in table (7) and figure(3).

These results indicate stability behavior of HA coating layer. Along with an improvement of corrosion resistance, this HA coating is able to change the characteristics of the surface on the materials without affecting the characteristics of the bulk **[13, 14]**. Also, the availability of HA in coatings can increase resistance of the coated implant in biological solutions against corrosion which means decreasing of the releasing of metal by promoting the fixation by the chemical bonding **[13, 15].**

Porosity however, seems to follow the same sequence, i.e porosity of (Ni) layer is once again has the lower value. As can be seen in table (8) the porosity increases when HaP particles of nano-size increasing were added. This increase expected since it is associated with the large particles of HaP. This explanation is supported by the fact that nano-size particles significantly lower both the porosity and corrosion current density. This is due to possible filling the pores by these fine particles. When HaP particles were incorporated into (Ni), the nano-size HaP reduces the corrosion current density to the lowest value, table (8).

However when the samples were coated with (Ni) deposit, a significant reduction in current density occurred, table (7)

It is found throughout this work that the optimum thickness (20μm) more than this thickness the deposited layer crack in this spalled. If the layer thickness is less than (20μm), it is no longer protective.

Spalling may be the thick layers may be attributed to the defects, internal and loss of adhesion.

Table (1) Chemical composition of the sample used.

C	Si	Mn	Cr	Fe
0.12	0.17	0.65	0.04	Rem

Table (2) Components of plating solution, [2].

Solution	Chemical composition	Condition of Deposition
Ni	NiSO4.6H2O=240 g/l	pH = 3.5
	NiCl2.6H2O=45 g/l	Temp=55°C .
	H3BO3=25 g/l	Coating time= 60 min.
		Nickel Anodes=(99.9%)
		Current density=2.5 (Amp/dm²)
Ni-nHAP	NiSO4.6H2O=240 g/l	pH = 3.5
	NiCl2.6H2O=45 g/l	Temp=55°C .
	H3BO3=25 g/l	Coating time= 60 min.
	HAP=10 g/l	Nickel Anodes=(99.9%)
	Nano scale , d (20) nm	Current density=2.5 (Amp/dm²)
Ni-nHAP	NiSO4.6H2O=240 g/l	pH = 3.5
	NiCl2.6H2O=45 g/l	Temp=55°C .
	H3BO3=25 g/l	Coating time= 60 min.
	HAP=20 g/l	Nickel Anodes=(99.9%)
	Nano scale , d (20) nm	Current density=2.5 (Amp/dm²)
Ni-nHAP	NiSO4.6H2O=240 g/l	pH = 3.5
	NiCl2.6H2O=45 g/l	Temp=55°C .
	H3BO3=25 g/l	Coating time= 60 min.
	HAP=10 g/l	Nickel Anodes=(99.9%)
	Nano scale , d (40) nm	Current density=2.5 (Amp/dm²)
Ni-nHAP	NiSO4.6H2O=240 g/l	pH = 3.5
	NiCl2.6H2O=45 g/l	Temp=55°C .
	H3BO3=25 g/l	Coating time= 60 min.
	HAP=20 g/l	Nickel Anodes=(99.9%)
	Nano scale , d (40) nm	Current density=2.5 (Amp/dm²)

Table (3): Chemical Analysis for Hank's Solution [11]

NO.	CONSTITUENT	(mg/l)
1	NaCl	8
2	CaCl2	0.14
3	KCl	0.4
4	NaHCO3	0.35
5	Glucose	1
6	Mg Cl2.6H2O	0.1
7	Na2HPO4. 2H2O	0.06
8	KH2 PO4	0.06
9	Mg SO4. 7 H2O	0.06

Table (4): The Thickness of Ni and (Ni-HAP) Layer Coating.

Samples	Thickness (μm)
Ni	25.7
Ni-20nHAP,10g	47.5
Ni-20nHAP,20g	48.7
Ni-40nHAP,10g	49.7
Ni-40nHAP,20g	50.5

Table (5) the hardness value

Layer coating	Hardness value
L.C.S	200
Ni	251
Ni-20nHAP,10g	304
Ni-20nHAP,20g	344
Ni-40nHAP,10g	295
Ni-40nHAP,20g	306

Table (6) Surface roughness value

Layer coating	Roughness value
L.C.S	-
Ni	0.153
Ni-20nHAP,10g	0.265
Ni-20nHAP,20g	0.57
Ni-40nHAP,10g	0.293
Ni-40nHAP,20g	0.775

Table (7): The Potential of Corrosion (Ecorr.), Current of Corrosion (Icorr.) and Improvement Percentage of coated Samples in the solution of Hank at 37 °C

Samples	Icorr. µA/cm2	Ecorr. (-mV)	Corrosion rate (mpy)	Improvement percentage%
L.C.S	24.51	506.3	46.533	-
Ni	6.49	344.2	12.321	73.522
Ni-20nHAP,10g	1.35	255.1	2.563	94.492
Ni-20nHAP,20g	0.556	24.2	1.055	97.732
Ni-40nHAP,10g	1.47	354.8	2.79	94.004
Ni-40nHAP,20g	0.984	199.4	1.868	95.986

Table (8) The effect of HaP size on corrosion current.

Layers coated	Current density(μA/cm^2)
Ni	6.49
Ni-20nHAP,10g	1.35
Ni-20nHAP,20g	0.556
Ni-40nHAP,10g	1.47
Ni-40nHAP,20g	0.984

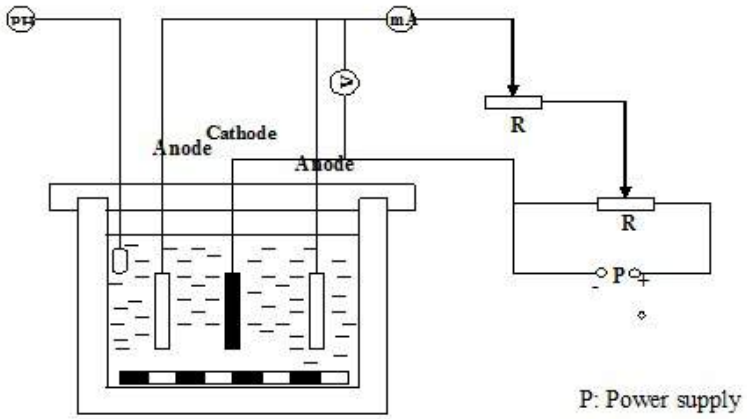

Figure (1) electroplating cell.

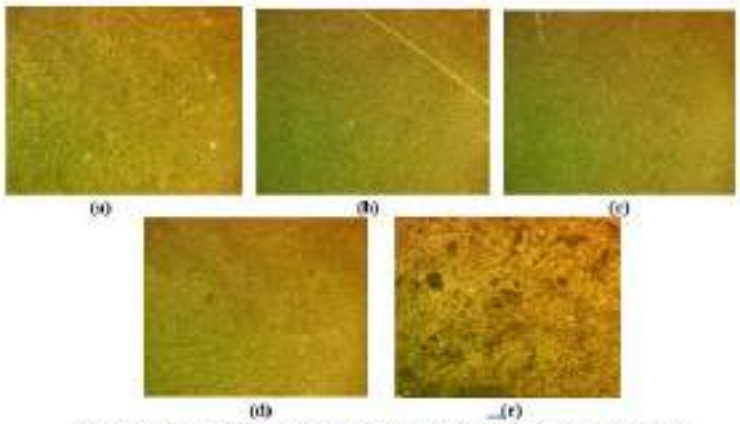

(a): Ni coating layer, (b): Ni 20nHAP,10g coating layer, (c): Ni 20nHAP,20g,
(d): Ni 40nHAP,10g, (e): Ni 40nHAP,20g
Figure (2) topographic morphology for coating layers at (100x) magnification.

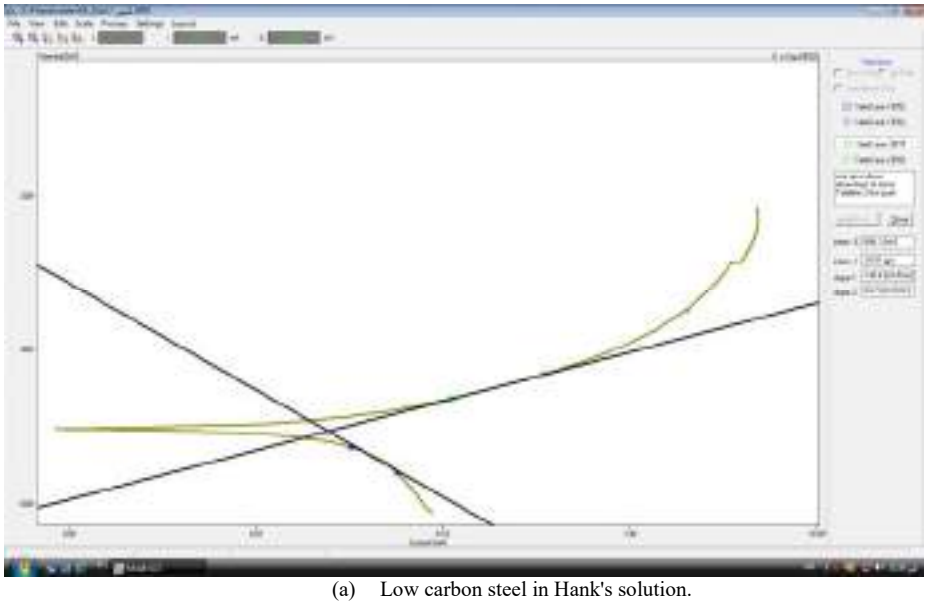

(a) Low carbon steel in Hank's solution.

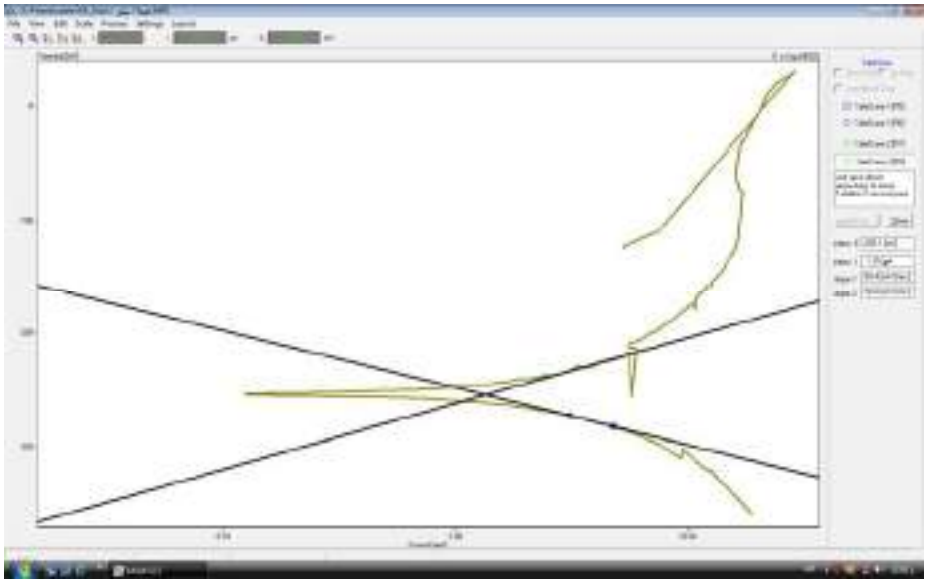

(b)Low carbon steel coating with Nickel layer in Hank's solution.

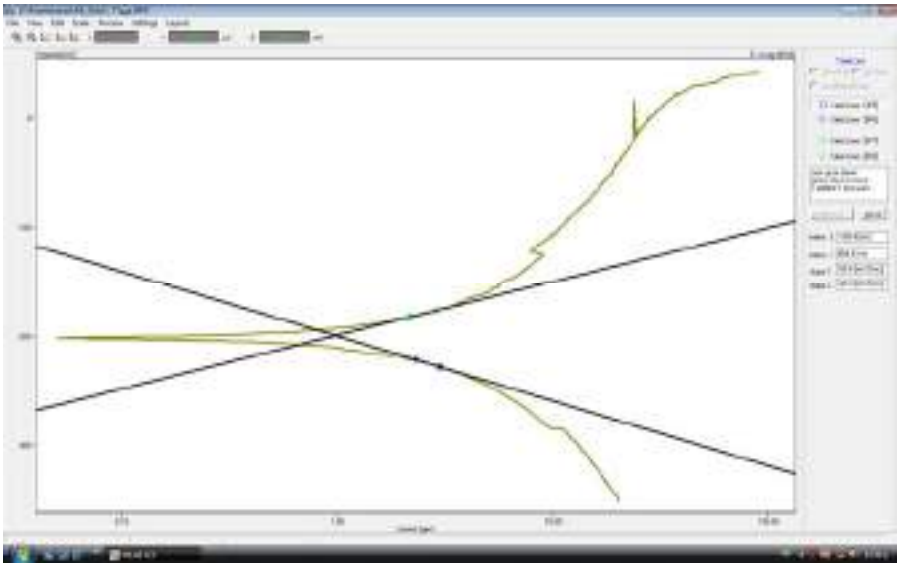

(c) Low carbon steel coating with (Ni-40nHAP,10g/L) in Hank's solution.

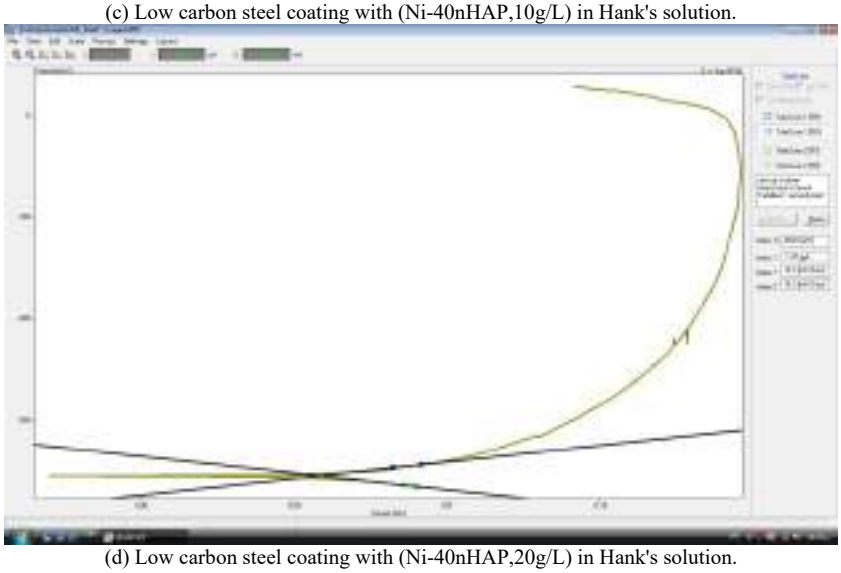

(d) Low carbon steel coating with (Ni-40nHAP,20g/L) in Hank's solution.

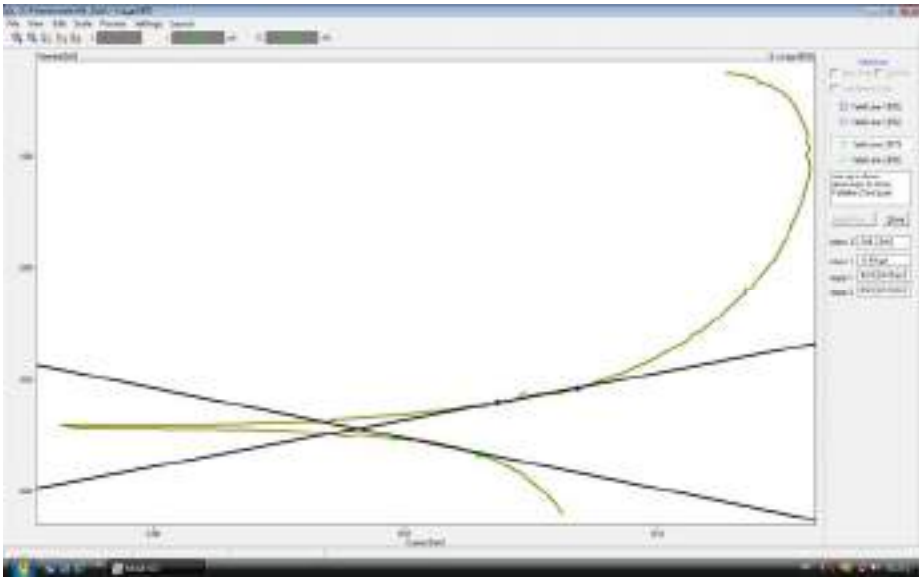

(e) Low carbon steel coating with (Ni-20nHAP,10g/L) in Hank's solution.

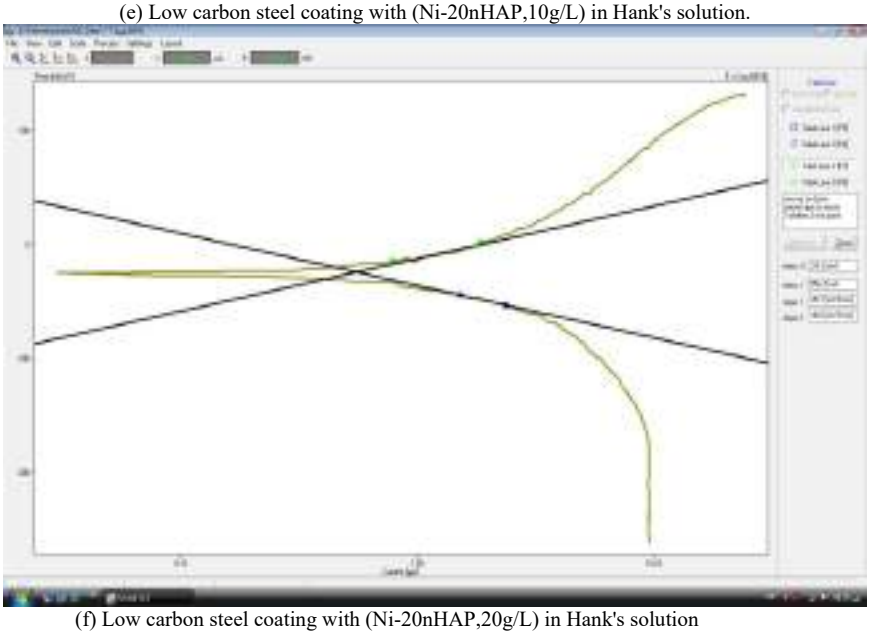

(f) Low carbon steel coating with (Ni-20nHAP,20g/L) in Hank's solution

4- Conclusion:

1. The adding of hydroxyapatite to the electrolytic coating of metal (Ni) makes the coating layer has good properties.
2. Ni-20nHAP, 20 g/L) showed better results than (Ni-40nHAP, 20) because of the hydroxyapatite particles size which is very small, which support the crystal structure by the interaction with the crystalline structure.
3. The coating layer (Ni-20nHAP, 20 g/L) showed hardness and good corrosion resistance because hydroxyapatite is a chemically inert and has high hardness so as to it properties are reflected on the Ni coating layer. The results of the coating layer (Ni-20nHAP, 20 g / L) was much better than the results of the coating layer (Ni-40nHAP, 20 g / L) due to the small size of hydroxyapatite, which enter deeply in the alloy and its small size near the distance between the atoms in the crystal structure makes it as supporting particles for this Composition.

References

1. Teodosiu C, Barjoveanu G, Sluser BR, Popa SAE, Trofin O (2016) Environmental assessment of municipal wastewater discharges: a comparative study of evaluation methods. Int J Life Cycle Assess 21:395–411
2. NICKEL PLATING HANDBOOK 2014.
3. Dr.Abdalwahid K. Rajih, Dr.Jaleel K. Ahmed, Dr.Nabaa S. Radhi,"INVESTIGATION SOME PROPERTIES OF (Zn-Ni-SiC) COMPOSITES COATING ON LOW CARBON STEEL",The Iraqi Journal for Mechanical – and Materials Engineering, 2018.
4. Dr.Jaleel K. Ahmed, Dr.Nabaa S. Radh, "Protective the carbon steel from corrosion by coating (Zn-Ni) alloy", The Iraqi Journal For Mechanical And Material Engineering, Vol.11, No.1, 2011.
5. Dr.Jaleel K. Ahmed, Dr.Nabaa S. Radh, "Improvement the Hardness and Wear of (Zn-Ni) Coating Layer by Adding Silicon Carbide", The Iraqi Journal For Mechanical And Material Engineering, Vol.11, No.3, 2011.
6. Yadava A.A., Masumdara E.U., Moholkar A.V., Neumann-Spallartc M., Rajpured K.Y., and Bhosaled C.H.(2011)‘ Effect of substrate temparature on the crystal growth orientation and some physical properties of SnO_2:F thin films deposited by spray pyrolysis technique’ Journal of Alloys and Compounds 448, 350–355.
7. Okner, R. G. and andler , D. M .(2011)‘ Electrochemical coating of medical implant applications electrochemistry and nanotechnology in biology and medicine’, springer science and business media ,LLC,pp.1-13.
8. Silva, M. H., limos , A. F. and ferreira, J.(2010) ‘Mechanical characterization of porous glass reinforced Hydroxyapatite ceramic –bonelike’,Material researcher.Vol.2,pp. 98-102F.
9. Farah Sami Rasheed Abood," Surface Modification by HA of 316 L S.S for Biomedical Applications", MSC thesis, University of Babylon Collage of Materials Engineering, 2018.
10. Park, J. ‘bioceramics, properties, characterization and application’, springer.
11. Wang, N .li and Rae , G.(2007)'Stress corrosion cracking of Ni Ti in artificial saliva', dental materials ,vol. 23,pp.133-137.
12. K. W.NG, H. C. Man and T.M.Yue(2011)'characterization and corrosion study of Ni Ti laser surface alloyed with Nb or Co',vol. 257,Isaue.8,32 G9.
13. Ajay, S. and Abhinandan, R.(2010) ‘Study of hydroxyapatite and hydroxyapatite-chitosan composite coatings on stainless steel by electrophoretic deposition method’, National Institute of Technology.
14. Shalabi, M. M.,Wolke, J. G. and Jansen, V. M.(2007)‘Evaluation of bone response to titanium – coated polymethacrylate resin (PMMA)implants by X-ray tomography’J. Mater sic. Mater Med, vol.18,pp.2033-2039.
15. Roether, J. A. and Deb, S. (2004) ‘The effect of surface treatment of hydroxyapatite on the properties of bioactive bone cement ’Journalof materials science ,material in medicine , vol.15,pp.413-418.

Available online at
http://namrc.uotechnology.edu.iq/index.php/

Nanotechnology and Advanced Materials Research Centre
Proceeding Articles Book 00 (2018) 000–000

6th International Scientific Conference on Nanotechnology, Advanced Materials and its Applications

Using Well Logging Data to determine Water Saturation in a Carbonate Reservoirs

Fadhil Sarhan Kadhim, Salam Al Rbeawi
Petroleum Technology department, University of Technology, P.O. Box35010, Baghdad, Iraq
METU Northern Cyprus Campus
Corresponding auther:fadhilkadhim47@yahoo.com

Abstract
the accurate determination of water saturation in complex carbonate reservoirs is the most challenging aspects of well log analysis. Water saturation is calculated by many models that developed over the years based on known physical principles or on empirically derived relationships. The complex formation under study is Yamamma carbonate formation which is one of the deepest hydrocarbons bearing zone in the Nasiriya oilfield in south of Iraq. The available scanned copes of well logs are digitalized by using Neurolog software. Schlumberger charts 2005 had been used for environmental corrections. These correction charts are supplied in the Interactive Petrophysics software. Simple Archie equation, Dual water model, and Indonesia model have been used to calculate water saturation of Yamamma carbonate formations. After making the environmental corrections, the porosity interpretation shows that the logging tools have a good quality of data reading. From Indonesian model, the water saturation for Yamamma formation is ranged from 0.25 to 0.41. This study is provided water saturation values with depth that should use to calculate original oil in place and detect the perforation zones in the pay zone using Interactive Petrophysics software.

Keywords: Porosity, Water Saturation, Carbonate Formation, Yamamma Formation

1- Introduction

The behaviour of petrophysical properties of complex carbonate reservoirs is a highly nonlinear because these reservoirs are a heterogeneous in nature. In carbonate petroleum reservoirs, many forms of heterogeneity in rock properties are present. Estimation of the volume of hydrocarbons and their flow patterns depend on porosity, permeability and fluid saturation which are the key variables for characterising a reservoir. Porosity can be determined by using different logging devices. For example, if a density logging tool is to be used, the rock matrix density must be known in order to determine the porosity. Likewise, using sonic log for porosity determination, the known parameter must be the matrix travel time and for neutron log, the parameter that must correspond to the rock type is the matrix setting for the neutron logging tool. Formation density log, sonic log or neutron log all, can determine the values of porosity (kadhim et al., 2015).
Fluid flow through heterogeneous carbonate reservoirs (limestone and dolomite) is a substantially different process from the flow through the homogeneous sandstone reservoir. This variation is largely cause to the fact that carbonate rocks tend to have a more complex pore system than sandstone (Chilingar et al., 1979; Mazzullo, 1986). In terms of rock types, carbonate reservoirs are very heterogeneous. Therefore, in order to define average values and trends of petrophysical parameters in the reservoir rocks, the reservoir should be split into layers on the basis of the dominant rock type (Kadhim, et al., 2013).

The density log is a continuous record of a formation's bulk density. It is used mainly for the determination of porosity, and the differentiation between liquids and gases (when used in combination with neutron log). When organic content is present, density is low. Variation of density indicates porosity changes. For example, low density indicates high porosity (Akinyokun, 2009). The density tool responds to the electron density of the material in the formation. Formation bulk density (RHO_B) is a function of matrix density, porosity, and density of fluids in the pores (salt water, fresh water mud, or hydrocarbons). The formula for calculating density-derived porosity is (Darwin and Julian 2007; Hamada, 1999):

$$PhiD = \frac{2.71 - RHO_B}{2.71 - RHO_f} \quad \text{.....(1)}$$

Where: RHO_B: is the bulk (matrix) density, [2.71 (gm/cc) for limestone, 2.87 (gm/cc) for dolomite and 2.65 (gm/cc) for sandstone]. RHH_f: is the fluid density (gm/cc) [fresh water mud = 1, for salt water mud 1.1].

Neutron logs are porosity logs that measure the hydrogen concentration in a formation. In clean formations (shale-free), where the pores are filled with water or oil, therefore hydrogen is concentrated in the fluid-filled pores, energy loss can be related to the formation porosity. Whenever shale is part of the formation matrix the reported neutron porosity is greater than the actual formation porosity (Asquith and Krygowski, 2004). The neutron log is used mainly for lithology identification, porosity evaluation, and the differentiation between liquids and gases when used in combination with density log. On cross-plot of neutron and density logs, pure shale can be recognized by the high neutron value relative to the density value which gives a large positive separation to the logs while gas stands out distinctly giving a large negative separation (Akinyokun, 2009).

The sonic log is a porosity log that measures interval transit time (Δt or DT) of a compressional sound wave traveling through the formation, the interval transit time depends upon both lithology and porosity. Wyllie time-average equation may be written as follows (Etnyre, 1989):

$$PhiS = \Phi s = \frac{\Delta t_{\log} - \Delta t_{mat}}{\Delta t_f - \Delta t_{mat}} \quad \text{.....(2)}$$

Where: Φs is sonic-derived porosity, fraction, Δt_{ma}: is the interval transit time in the matrix [Its value is 47.6μsec/ft for limestone and 43.5 μsec/ft, for dolomite], Δt_{log}: is the interval transit time in the formation, μsec/ft., Δt_f: is the interval transit time in the fluid within the formation [For fresh water mud = 189 (μsec/ft); for salt-water mud = 185(μsec/ft)].

One of the most controversial problems in the formation evaluation is the clay effect to reservoir rocks (Hamada, 1999). Shale is usually more radioactive than sand or carbonate, gamma ray log and other logs can be used to calculate volume of shale in porous medium. The volume of shale expressed as a decimal fraction or percentage is called shale volume (V_{shale}) (Asquith and Krygowski, 2004). The volume of clay can be calculated from gamma ray log, the minimum value of clay (V_{clay}) is the closest to the truth (Susan and Robert, 1990; Schlumberger, 2008).

The total natural radioactivity of the formation are provided by the spectral gamma ray (SGr) measurements. The spectral gamma ray tool detects the naturally occurring gamma rays and defines the energy spectrum of the radiations. Because Potassium (K), Thorium (Th) and Uranium (UR) are responsible for the energy spectrum observed by the tool, their respective elemental concentrations can be calculated (Schlumberger, 2008):

$$V_{clay} \le \frac{SGr - SGr_{\min}}{SGr_{\max} - SGr_{\min}} \quad \text{.....(3)}$$

$$(V_{clay})_{UR} \le \frac{UR - UR_{\min}}{UR_{\max} - UR_{\min}} \quad \text{.....(4)}$$

$$(V_{clay})_K \le \frac{K - K_{\min}}{K_{\max} - K_{\min}} \quad \text{.....(5)}$$

$$(V_{clay})_{Th} \le \frac{Th - Th_{\min}}{Th_{\max} - Th_{\min}} \ldots\ldots\ldots\ldots\ldots\ldots\ldots\ldots\ldots\ldots (6)$$

Since the Uranium is associated with radioactive minerals other than those found in clay (i.e. Organic materials), so it is generally not a reliable clay indicator. By eliminating the uranium contribution from the total gamma ray response and defining the Corrected Gamma Ray GrC (i.e., sum of thorium and potassium only) (Hamada, 1999):

$$V_{sh} \le \left[\frac{GrC - GrC_{\min}}{GrC_{\max} - GrC_{\min}} \right] \ldots\ldots\ldots\ldots\ldots\ldots\ldots\ldots\ldots\ldots (7)$$

Where: GrC: Corrected gamma ray logs reading in the zone of interest (API units), GrC_{min}: Corrected gamma ray logs reading in a 100 % clean zone (API units), GrC_{max}: Corrected gamma ray logs reading in 100% shale (API units).

Resistivity logs were used to determine values of water saturation and consequently, hydrocarbon saturation. It is also used in conjunction with lithology logs to identify hydrocarbon bearing intervals and to estimate the net pay thickness (peters, 2011). True resistivity (Rt) may be obtained from Deep Induction Log (DIL) or Deep Lateral Log (DLL), so any invasion correction should be applied to obtain the true resistivity which will lead to good interpretation for water saturation (Toby, 2005).

The standard practice in oil and gas fields for calculating water saturation is by using different saturation models. But these models should be tuned to the area of work which requires the estimation of parameters in the laboratory. There is always more than one fluid phase occupying the pore space in a petroleum and gas reservoirs. The fluid saturation is the petrophysical property that describes the amount of each fluid type in the pore space. It is defined as the fraction of the pore space occupied by a fluid phase. One of the most troublesome aspects of log analysis is the calculation of water saturation (S_w).There are many equations and empirical correlations have been developed over the years to calculate the (S_{wi}). Resistivity and conductivity are common methods to calculate water saturation. In the earliest days of well logging resistivity logs are the most commonly used measurements to determine (S_w). A high resistivity log reading in porous medium can be indicated of the presence of hydrocarbon (Jackson, et al., 2008; Adeoti, et al., 2009). While the principle of conductivity method depend on sodium cations concentration, that can be calculated in term of Cation Exchange Capacity (CEC), expressed in mille equivalents per gram of dry clay.
Archie in 1942 was introduced equation, which based on laboratory experiments on clean sands, water wettability and non- vugy carbonates. The earliest research established that for a formation with constant porosity and water salinity, an increase in resistivity indicated the presence of hydrocarbons. Archie qualified this relationship as shown in the following equation; Archie, 1942):

$$Sw^n = \frac{a.Rw}{Rt.\Phi^m} \ldots\ldots\ldots\ldots\ldots\ldots\ldots\ldots\ldots\ldots (8)$$

In1971, Poupon and Leveaux introduced Indonesia model. This model was derived based on the fresh waters saturation and clay volume that present in many oil reservoirs in Indonesia. Conductivities of the shale and formation water are affected by the relationship between true resistivity and water saturation in this model. The Indonesia formula can be written as follows (Amin, et al., 1987):

$$S_w^{0.5} = (R_t)^{-0.5} \left[\frac{V_{cl}^d}{R_{cl}^{0.5}} + \frac{\Phi^{0.5m}}{(aR_w)^{0.5}} \right] \ldots\ldots\ldots\ldots (9)$$ Where: d=1-0.5 V_{cl}

Conductivity models are improved the water saturation results by matching well log data with laboratory measurements. The most commonly used cation exchange capacity model is a Dual-Water model. The dual-water model is modified from Waxman-Smits model by calculation the conductivity of free water away from clay surface and relative volume of clay bound water for double-layer. This model is given by two types of formation water as follows (Coates, et al., 1983; Clavier, et al., 1984):

A- Bound Water Saturation S_{WB}, which defined as the fraction of total porosity occupied by bound water.

B- Free Water Saturation S_{WF}, which defined as the fraction of total porosity occupied by free water.

$$S_{wT} = Y + \left[\frac{R_{wT}}{\Phi_T^2 R_t} + Y^2 \right]^{1/2} \ldots\ldots\ldots\ldots\ldots\ldots (10)$$

Where:

$$Y = \frac{S_{wB}(R_{wB} - R_{wF})}{2R_{wB}} \quad \text{.....(11) And;}$$

R_{wT} is a resistivity of free Water, S_{wT} is total water saturation, R_{wB} is a resistivity of bound water.

The field under study is located in the north of Arabian platform in the Middle East between latitudes (34°80`- 34°60` N) and longitudes (57°50`- 60°10` E). It is anticline structure with northwest- southeast general trend. Three reservoir units contain most of the oil within the reservoir; the Yamamma, Nahr Umr, and Mishrif formations[15] which consist mainly of limestone. Yamamma formation is one of the deepest and important reservoir unit due to rudist deposits (Amnah, 2009; Jassim and Goff, 2006; Aqrawi, et al., 1998) .
In this study, water saturation of Yamamma carbonate formation is determined using corrected well log data and compared with core data which obtained from NS-2 well (INOC, 1985). The accurate determination the saturation values with depth should improve the oil in place calculation and consequently detected the perforation zones.

2- Methodology

Cross-plot techniques are employed in the analysis of well log data. A set of log data from the NS-2 in the Nasiriya oil field was used as the base data for the research reported in this paper. Neura-Log software (V5, 2008) was used to digitize the scanned copies of logs in which the results as LAS files were loaded to the Interactive Petrophysics software (IP, V3.5, 2008) where the reading measurements were taken as one reading per 0.1524 meters. The log curves are checked to be for depth with each other. Environmental corrections were made using the current Schlumberger charts (SLB, 2005), which are supplied to (IP) as the environmental correction module. Actual mud properties, calliper log, hydrostatic pressure and temperature gradient were provided for accurate corrections. Depending on well log data the Interactive Petrophysics software had been used to calculate the porosities and determine the lithology cross-plots.

3- RESULTS AND DISCUSSION

Using IP software, corrections were achieved per 0.1524 m of depth to avoid erroneous results in water saturation interpretations. The correction charts (SLB, 2005) were supplied to the software as the environmental correction module. NS-2 is the well under study in the NS oil field. The environmental corrected results for porosity from density, sonic, and neutron logs are shown in Figure 1. Computer Processed Interpretation (CPI) results of effective porosity (PHIE) are closed to the core data analysis as shown in Figure 2 and Table 1 that means the porosity interpretation by porosity logging tools have good quality after making the environmental correction. The relationship between core and CPI porosity is shown in Figure 3. From this figure the corrected equation for effective porosity was produced. This equation was used to correct the CPI value of the effective porosity. The main reason that leads to differences between the porosity value from core and log is the varying between properties of formation water and the mud filtrate (Amin, et al., 1987)**.** The

Ferro Chrome Lignite - Chrome Lignite (FCL-CL) was used as drilling mud in the studied well [18]. The (FCL-CL) mud contains barite as a weighting agent and characterized by a high ratio of free phase (water), which lead to a high diameter of invasion zone (more than 50 in) ,that mean the investigation zone

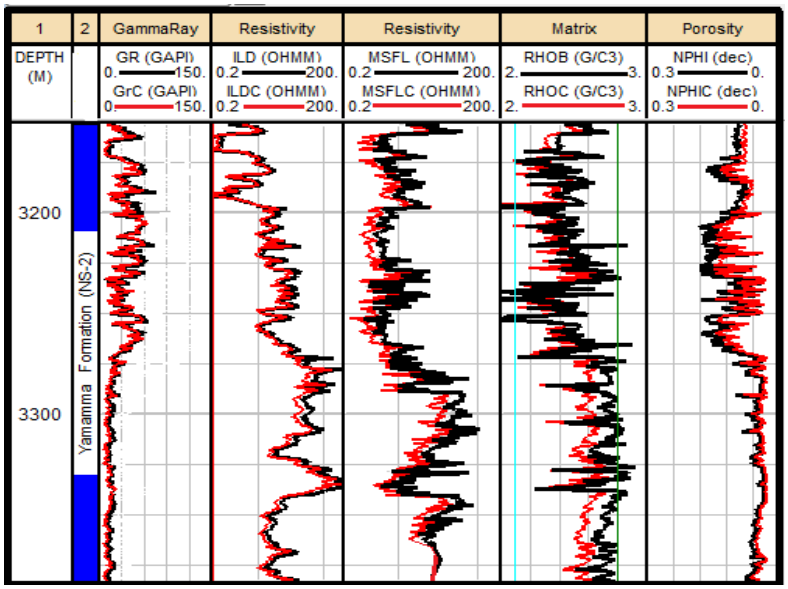

Figure 1 environmental correction of porosity, for logging tools was invaded by barite (Kadhim, et al., 2015).

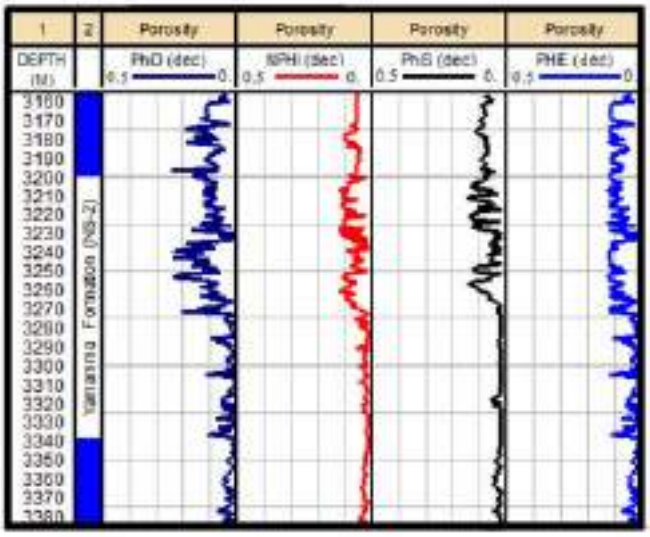

Figure 2 porosity results from well logs.

Table 1 comparison results of porosity between core and CPI

Unit	Depth Interval (m)	Avg. PHI $_{CORE}$ ((INOC, 1985))	Avg. PHIE $_{CPI}$	% Error
Y-A1	3157.0-3169.4	0.06	0.09	33.3%
Y-A2	3169.4-3204.0	0.07	0.08	12.5%
Y-B1a	3220.4-3227.5	0.06	0.08	25.0%
Y-B1b	3227.5-3246.7	0.15	0.11	26.6%
Y-B2	3266.0-3306.4	0.10	0.08	20.0%
Y-B3	3341.7-3384.0	0.07	0.05	28.5%

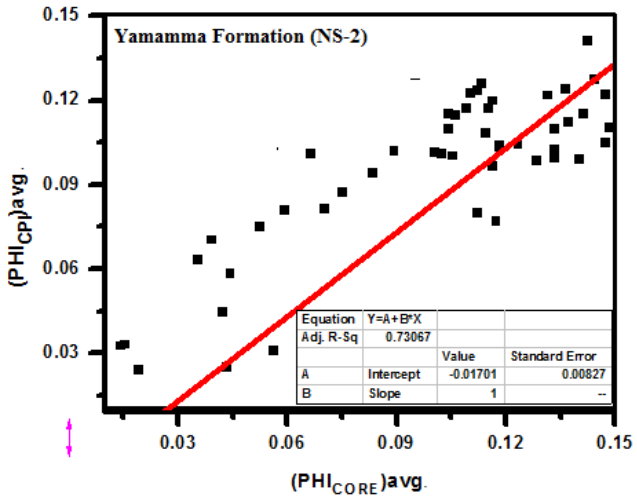

Figure 3: Φ_{CPI} and Φ_{CORE} relationship

Figure 4 shows the results of apparent water resistivity (R_{wa}), true resistivity (R_t), and clay volume from gamma ray ($V_{CL\text{-}Gr}$). Water saturation results from dual water, Archie and Indonesian models are shown in Figure 5 as well the comparison of these models results with core saturation are listed in Table 2. From this table the water saturation results from Indonesian model are more regular in comparison with Archie and dual water models. Moreover, Indonesian model results are closed to core saturation which means this model gives the results of water saturation.

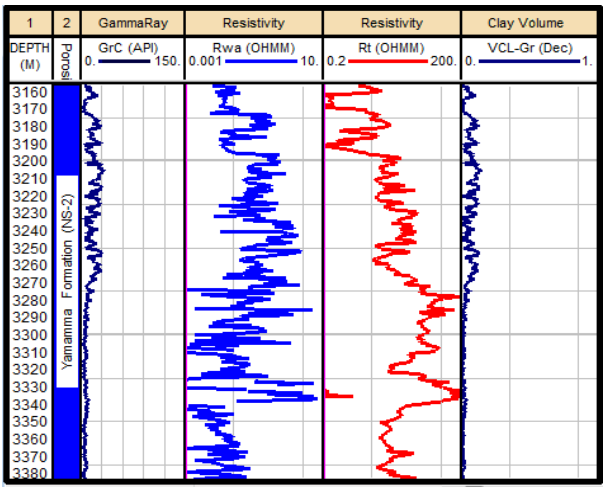

Figure 4 resistivity and clay volume results

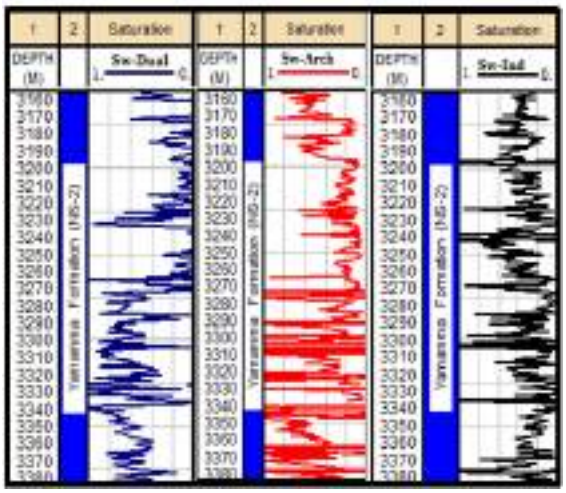

Figure 5 water saturation results from Dual water, Archie and Indonesian models for Yamamma formation (NS-2

Table 2 comparison of water saturation models and core saturation results

Unit	Depth Interval (m)	Sw Dual	Sw Arch.	Sw Ind.	Sw core
Y-A1	3157.0-3169.4	0.31	0.62	0.38	0.42
Y-A2	3169.4-3204.0	0.25	0.55	0.41	0.45
Y-B1a	3220.4-3227.5	0.40	0.4	0.25	0.31
Y-B1b	3227.5-3246.7	0.42	0.38	0.41	0.40
Y-B2	3266.0-3306.4	0.57	0.64	0.33	0.43
Y-B3	3341.7-3384.0	0.51	0.78	0.31	0.38

Archie formula gives a misleading result that ranged from 0.38 to 0.78 because it assumes that the formation water is the only electrically conductive material in the formation, which is not true for the case of shaly formation. The shale effect on various log responses depends on the type, the amount, and the way is distributed in formation (Akinyokun, 2009).

In shaly formations, it is generally accepted that the Dual water conductivity model which using total porosity gives water saturation results that are more consistent than Archie's equation (Amin, et al., 1987). However the conductivity models have inherent problem which is the total porosity cannot be measured without calibration with core analysis since the dry clay matrix points does not exist in nature and is therefore not seen by the logs.

Conclusion

The accurate determination of water saturation results gives reliable of hydrocarbon reserve calculations as well as accurate detection of perforation zones. The environmental correction for sonic, density and neutron logs gives accurate values of porosity and the average effective porosity for Yamamma formation is almost between 0.05 and 0.15.The Indonesian model gives water saturation results that are more consistent than other type equations and closet to the core saturation. The average water saturation value of this model for studied formation is located between 0.25 and 0.41.

Acknowledgement:

The authors would like to thank the Ministry of Higher Education (MOHE) in Iraq for providing a research grant.

References

A. A. Aqrawi, G.A. Thehni, G. H. Sherwani, B. M. Kareem 1998. *Iraqi Journal of Petroleum Geology*. 21(1): 57-82

A. Asquith, D. Krygowski. 2004. Basic Well Log Analysis. The American Association of Petroleum Geologists Tulsa, Oklahoma, AAPG Methods in Exploration, Series No.16.

A.T Amin, M. Watfa, M. A. Awad. 1987. *Accurate estimation of water saturation in complex carbonate reservoir*, SPE-15714-MS: Society of Petroleum Engineers, presented at the 5th SPE Middle East Oil show in Bahrain

C. Clavier, G. Coates, J. Dumanior.1984. SPE 6859-PA: 1153-168.

D. Toby, 2005. Well Logging and Formation Evaluation. Elsevier, USA

E. J. Peters, 2011. Petrophysics. University of Texas, Austin, Published by: Hadi Al-Sinan.

F.S. Kadhim, S. Samsuri, A. Idris. 2013, Life Sci. J, 10(4):2451-2458

F.S Kadhim, A. Samsuri, A.Kamal, H. Alwan, and M. Hashim, Investigation of petrophysical properties for Yamamma carbonate formation, *Modern Applied Science*, Vol.(9), No.(6).Pp 36-47, 2015

G. Coates, Y. Boutemy, C. Clavier, C.1983. SPE 10104-PA.

G. E. Archie. 1942. SPE-942054-G.

G.M. Hamada 1999. An Integrated Approach to Determine Shale Volume and Hydrocarbon Potential in Shaly Sand in the Gulf of Suez. Society of Petrophysicists and Well Log Analysts, SPWLA-V40, No3

Iraqi National Oil Company (INOC) 1985. NS-2 Unpublished Final Well Report.

G.V. Chilingar, H.G. Bissell, K.H., Wolf. 1979 *Diagenesis of carbonate sediments and epigenesis (or catagenesis) of limestone*, Larsen, G., and Chilingar,G.V. (Editiors), Diagensis in sediments and sedimentary rocks ,developments, in sedimentology.25 A. Elsevier, Amesterdam, Pp 247-422.

L Adeoti, E.A. Ayolabi, P.L. James.2009. The World Applied Sciences Journal. 7 (4): 448- 452.

L.M. Etnyre. 1989. Finding Oil and Gas from Well Logs. Van Nostrand Renhold, New York. Pp21-25.p.16.

L. M. Susan, R. S. Robert. 1990. Canadian Journal of Exploration Geophysics. Vol.26: 94-103

M.H. Amnah. 2009. Iraqi Journal of Science. 50(1):67 – 74.

O.C Akinyokun, P.A. Enikanselu, AdeyemoA.B., A. Adesida. 2009. The Pacific Journal of Science and Technology. 10 (1): 507-517.

P.D. Jackson, J.F. Williams, M.A. Lovell, A. Camps, C Rochelle, A.E. Milodowski. 2008. An Investigation of The Exponent in Archie's Equation: Comparing Numerical Modeling with Laboratory Data: Towards Characterizing Disturbed Samples from the Cascadia Margin. The 49th Annual Logging Symposium, 25-28 May, Austin, Texas, SPWLA-2008-HHH.

Schlumberger, 2008. The IP Interactive Petrophysics, V-3.5, Manual

S.J. Mazzullo. 1986. Geol. J., 21:265-28.

S.z. Jassim, J.C. Goff. 2006. Geology of Iraq, Dolin, Prague and Moravian Museum, Brno. Pp.341.

V. E. Darwin, M. s. Julian. 2007. *Well Logging for Earth Scientists*,2ndEdition, Springer, pp 62.

Available online at
http://namrc.uotechnology.edu.iq/index.php/

Nanotechnology and Advanced Materials Research Centre

Proceeding Articles Book 00 (2018) 000–000

6th International Scientific Conference on Nanotechnology, Advanced Materials and its Applications

Studying of Traditional Solid –Carburization and Comparison it with Laser Carburization of Low Carbon Steel

Abd ulkhaliq Fawzy Hamood

Production and Metallurgy Engineering, University of Technology, Baghdad, Iraq

Abstract

In this study two methods selected to employ (traditional carburization, laser carburization). Studying of mechanical, surface, metallurgical properties for each coated systems and makes a comparison among treated systems. Low carbon steel alloy has been selected as a substrate. Studying of specified properties including hardening depth and (decarburization properties at high temperature) and comparison the results of each treatment with other treatment results. XRD method also has been employed to the two methods in order to determine the compression residual stresses role in the variation of studied properties.

Keywords: Laser carburization,Low carbon steel, Solid carburization.

1- Introduction

The service conditions of many steel components such as gears, cams, valves etc, make it necessary for them to possess both hard and wear resistant surfaces but tough and shock resistant cores [1]. A low carbon steel of approximately 0.1% carbon will be tough while a high carbon steel of about 0.9% or more will possess adequate hardness (and inherently low toughness) when suitably heat-treated. The combination of hard, wear resistant surface and tough core required in the aforementioned components involves the treatment of a shock- resistant steel so as to alter the nature of the surface in order to increase the hardness while the core remains more or less unaltered.

There are two major processes through which such an alteration of the surface layers of steel components may be carried out, namely, (i) processes which impart surface hardness by changing the microstructure of the surface skin without changing the chemical composition of the surface. Such steel must not have a carbon content of less than 0.4% for them to be amenable to hardening (by any of flame, induction, laser, and electron beam hardening) (ii) processes which impact surface hardness by changing the surface chemistry of the steel by diffusing carbon, nitrogen or both carbon and nitrogen into its surface.

Steels for this process may have a carbon content of about 0.1%. Examples of this latter process include carburizing, nitriding, cyaniding, diffusion coating, and hard surfacing. The method of carburizing was selected for this investigation because it has the advantages of ease of operation, adaptability and portability of the equipment required, ability to heat-treat component after surface-finishing (since there is little oxidation, decarburization or distortion), and the ease of producing deeper zones of case depth. It is known that the inward diffusion of the carbon takes place at a rate which depends on the chemical composition of the steel, the carburizing temperature and the chemical composition of the carburizing mixture [2, 3]. Established is a concentration gradient in respect of carbon from the skin to the core of the steel. With increase in the carburizing activity of the carburizing compound, the concentration is made steeper; the depth of penetration is not however increased to the same extent.

In general, the case depth is controlled by the adjustment of the carburizing time and temperature. There is a limit to which temperature can be increased in case hardening. At high temperatures, the structure of the core deteriorates. It badly affects the diffusion too. At elevated temperature, the rate at which the diffusing element is deposited on the surface of the specimen is greater than the rate at which it diffuses towards the core of the steel. This leads to uneven distribution of the concentration of the element and a high concentration which may lead to the formation of networks of chemical compounds such as carbides and nitrides, which

impacts high brittleness to the surface layer. The yield strength of the core of a carburized component may be exceeded, particularly as the core is in a state of tensile stress [4].

Although the stress is within the fatigue limit, the stress in the case is due both to the increased strength of the surface layer and to the development of favourable compressive residual stresses close to the surface. For a successful carburization, a control of all these parameters; the carburizing temperature, carburizing time, and chemical composition of the carburizing compound must be effected [5,6,7].

Laser Surface Alloying (LSA) consists of simultaneous melting and mixing of the alloying and the alloyed (substrate) material. The action and pressure of the laser beam cause both materials to melt; a pool of molten material isformed in which intensive mixing, due to convection and gravitational movements, form a flash at the pool surface..

2- Materials and Method

In this part we illustrate the steps and procedures of practical part from the alloys (substrates) selection, and passing on a full description about the specimens manufacturing which consist from (wear ,hardness)specimens ,then illustrate the pack carburization requirements [constituents ((charcoal ,activator,)),pack container ,fire clay],experimental set ups and procedures ,finally the test and inspections which are accomplished in the research

The alloys which are selected in our research will be low carbon steel, Spectrometer inspection and chemical composition determination results as in table.

Table (1) chemical composition of selected alloy.

INGREDENT	C%	Si	Cr	Mn	Ni	Fe
PERCENT	0.197	0.025	0.270	0.564	0.100	98.4077

Specimens manufacturing: Wear samples has been manufactured according to the standard specification of test samples, in order to inspect by wear test machine with the application of tangential load .

Preparation of pack carburization Process Requirement: carburization process include many requirement starting from pack constituents and passing on the choice of temperature, suitable container fire clay, furnace and finished with the experimented set-ups and procedures.

Selection of Pack carburization Constituents : Choice of the charcoal in order to provide a source of carburization carbon source were used. Also Choice of the Activator .In the this study, our selection has been lied on the Barium Carbonate .

Preparation of Pack carburization Constituents: first of all the Preparation of the (charcoal) Carbon source -(charcoal has been received in aggregate foam with a size range (1-***7cm)*** so the following steps were performed in order to reduce the particle size and increase the surface area.

1. Crushing Process: - Laboratory jaw crusher will used in order to reduce particle size to ***(0.5-2mm)***.
2. Grinding Process: - Laboratory motor was used in order to reduce particle size to ***(0.1-1mm)***.
3. Milling Process: - Laboratory Ball Mill was used in order to reduce particle size to ***(0.01-0.5mm)***.

Preparation of Pack carburization Mixture: Constituents percentage determination

In this study the calculation of constituents percentage has been carried out in order to determine the required weight from each constituents to provide a suitable pack to a carburization process , table (2)give the constituent percentage of prepared mixtures.

Table (2) Constituent percentage of prepared mixture.

Run 1	
$BaCo_3$	charcoal
5%	95%
Run 2	
$BaCo_3$	charcoal
10%	90%
Run 3	
$BaCo_3$	charcoal
15%	85%

Pack Mixture Volume determination:-

In order to determine the sufficient volume which is required from each mixture to do the process, measurement of manufactured container dimensions has been performed, and container volume was calculated, the volume of pack mixture represent (90%)from container volume, in order to permit the passing of reaction gases above the pack mixture.

Weighting of the Pack constituents:-
Weight From each has been prepared according to the desired percentage In table (2).
Mixing of the Determined Constituents Weights:-

Laboratory Bill-Mill. (but in this process the cylinder Mill volume occupied by grinding balls is less than that volume in Milling process). Fig.(1) show Bill Mill, and grinding media and fig. (2) show the container.

Figure (1) show Bill Mill Preparation of Container The container is made of Heat resisting stainless steel

Figure (2) The container heat resisting steel container.

Experimented Set-Ups and Procedures:-

For the pack carburization process, the specimens were previously cleaned in acetone and immersed in Ethanol in order to prevent the environmental attack, the specimens then give up and dried from Ethanol, the samples were embedded in pack mixture as in the following steps.

1. Lay- out the internal surface of container by pack mixture to a depth equal to ***(20mm)*** .
2. Embedded the samples in the pack .
3. Lay-out of the samples must give space among each other for a ***(10mm)***.
4. Sealed the container cover with a fire clay paste (Fig. 2-7).
5. The ambient heated to ***(200 °C for 1 hr.)*** in order to dry the sealing fire clay paste and remove any remaining humidity
6. After words the coating temperature was reached ***(950 °C)***.

For a given time ***(8hr.)***, the heating rate was chosen ***(7 C/min.)*** After the pack carburization treatment period accomplished 7.After the full process accomplished, and Furnace cooling.

Furnace door was opened and the carburized samples were given from the pack and clean them with a smooth brusher with Ethanol in order to give up the pack mixture traces. Then immerse the carburized samples in Ethanol in order to protect them from environmental attack and when we want to inspect them we can give up them.

Inspections and Testing : Micro structure examination, Hardness Test, Wear Inspection

Laser Carburization

Results and Discussions:

This chapter In our study was include the observation of practical part result is which consist from tests and inspections stating from the external appearance of pack carburization treated samples and passing through micro hardness test, wear test, microstructure for the treated systems of low carbon steel which treated by pack carburization with different activator weight percentage {10,20,30%} barium bicarbonate and laser carburization treatment for the surfaces.

External Appearance Test:-

From the observation of external appearance for the treated systems, we can notice that the succesfulling of the surface hardening process for all the selected coating methods .

Micro Hardness Inspection

From the results of micro hardness Vickers test type, We can observe an increment in hardness value , From figures (3) , formation of hardness profile which indicate increase in hardness at the sample edge this attributed to role of hard phases like carbides phases in carburization treatment. The hardness was increase as a result of diffusion surface hardening layer formation.

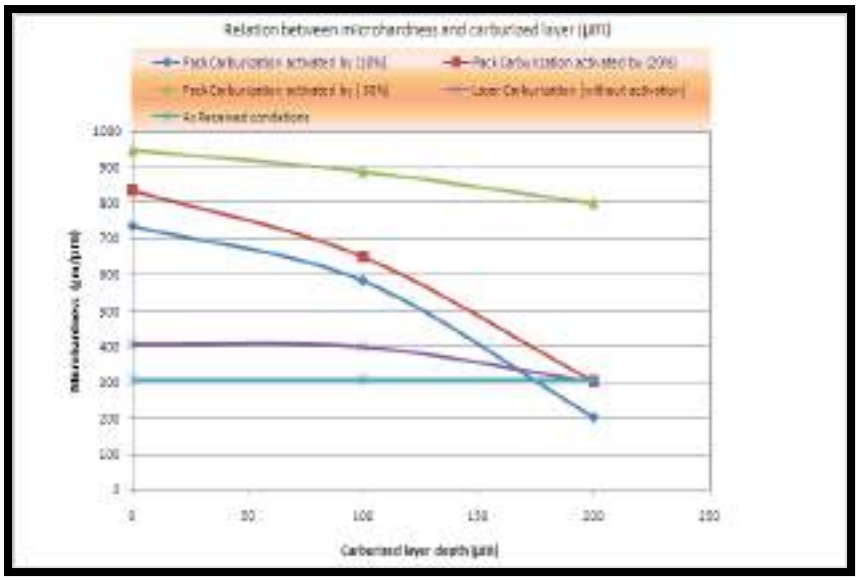

Fig. (3) Micro hardness profiles curves for all the selected treatments.

Surface hardness for the surface only is represented n the Fig. (4) ,A block diagram showed the increment in activator weight percentage lead to the improvement of hardness.

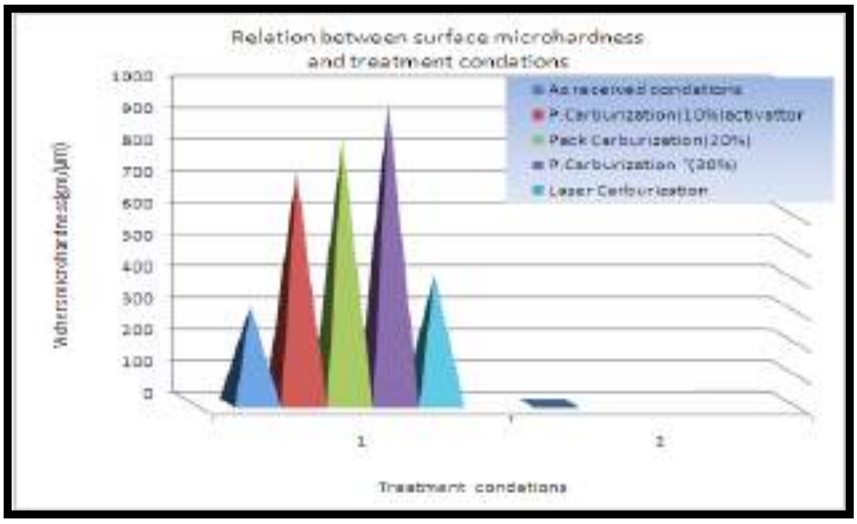

Fig. (4) Surface micro hardness block diagram for all the selected treatments.

3.3 Wear Test Results:-

From the observation of wear test results in figure (5), ,all the selected pack carburization and laser treatment were improve wear resistance this will attributed to the formation of hard surface which help the increment in surface hardness as illustrate in micro hardness discussion , this behavior was established by images which demonstrate the establishment of successful surface hardening layer as a thick layer at all treatment , all the illustrated phases lead to increase in resistance and reduction in wear

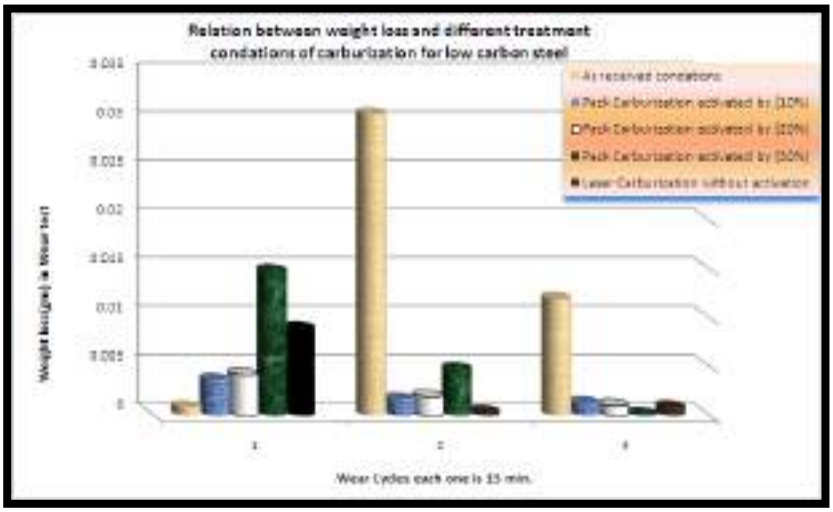

Fig. (5) a block diagram illustrating surface treatment influence on a wear rate of different coated systems of stainless steel alloy in pack cementation treatment.

Also from the above fig. (5) the optimum improvement in wear rate resistance which ensure the importance of this treatment is laser and pack carburization {activated with10%} treated systems ,who give optimum reduction in wear rate and improved the wear resistance. '[-

3 .6 Micro Structure Inspection Results:-

For the pack carburization surface treated systems observation of a clear dark coating layer starting from surface , also the obvious grains of microstructure has been appeared in images of microstructures in fig. (6).

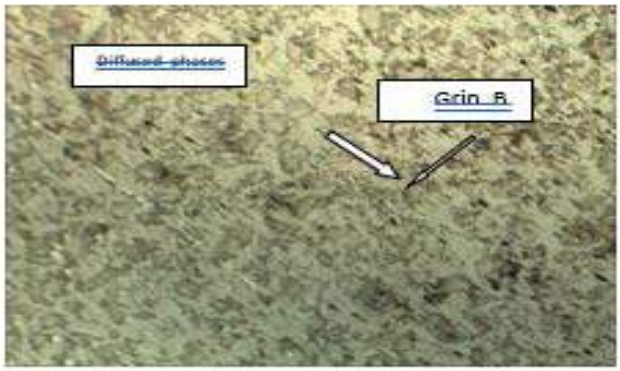

Image (a) Micro structure for stainless steel 316 core X400.

Image (b) Micro structure for stainless steel 316 core X400.

Fig. (6)microstructure of carburized low carbon steel.

Conclusion

1/ All the selected treatments help in the improvement surface and mechanical properties.
2/ Formation of diffusion surface hardening layer have a gradient character from the surface to the core and their concentration will reduce with the depth.
3/ Pack carburization surface hardening have better functional properties.
4/Laser surface treatment give improvement in surface properties for the selected inspected properties.
5/ Increment in surface hardness values as a result of hard new phase's formation.
6/ Pack carburization surface hardened systems were having better wear, micro hardness properties than the substrate(low carbon steel).
7/ Pack carburization surface hardened systems were having carbides formation, this will give the cause of wear resistance improvement.

References

[1] America Society of Metals(1964); Metals Hand book, Heat-treating, cleaning and finishing. 8th ed.
[2] M.A. Majid ad H.C. Child; Effect of carburizing on unidirectional bending fatigue strength of low alloy steel. (1983). Journal of Metals Technology, Vol. 10 page 173.
[3] Lakhtin,Yu.M(1977); Engineering Physical Metallurgy and Heat Treatment. Mir Publishers, Moscow.
[4] Smith, W.F(1970); Principles of Materials Science and Engineering. 2nd ed. Mc GrawHill Int. ed.
[5] Simon, E.N(1974); Dictionary of Metal Heat Treatment. Frederic Muller Ltd, London.
[6] Prabhudev K.H (1997) Handbook of Heat treatment of Steels. 4th ed. Tata Mc GrawHill Publishing Company Ltd. New Delhi.
[7] George S.Brady and Henry R. Clauser(1989) Materials Handbook.12th ed. Mc Graw-Hill Publishing Company, New York.
[8] Bakish, R.: Electron beam melting, refining and surface treatment: II. Industrial Heating, September 1985, pp. 26-28.
[9] Wang, H., Fen, Y., and Tang, Ch.: The effect of element Ti on the modification of microstructure by laser surface alloying. Jinshu Rechuli Xuebao (Transactions of Metal Heat Treatment), Vol. 14, No. 1, 1993, pp. 25-29.
[10] Hansen, R.C.: A comparison of high energy beam systems - electron beam/laser beam. Proc.: The Lasers vs. the Electron Beam in Welding, Cutting and Surface Treatment. State of the Art - 1985. Reno, part II. Edited by R. Bakish, Bakish Materials Corp., Englewood, N.Y., 1985, pp. 255-259.
[11] Kriszt, B., Ebner, R., Major, B., and Ciach, R.: Vanadium carbide laser surface modification of SW7M (AISI M2) high speed steel. Proc.: I Polish Conference on Surface Treatment, Kule, 13-15 Oct. 1993, pp. 97-105.

Available online at
http://namrc.uotechnology.edu.iq/index.php/

Nanotechnology and Advanced Materials Research Centre

Proceeding Articles Book 00 (2018) 000–000

6th International Scientific Conference on Nanotechnology, Advanced Materials and its Applications

Cu/Multiwalled Carbon Nanotube Composite Coatings fabricated by Pulse Electrodeposition

Shahad Adil Kamal, Mofeed A.L. Jaleel,
Applied Sciences, University of Technology, Baghdad, Iraq
Corresponding auther:shahad_uot93@yahoo.com

Abstract

Copper (Cu) coatings containing multiwalled carbon nanotubes (MWCNT) composite with 50 μm thickness were obtained by direct current (DC) and pulse current (PC) mode electrodeposition in acidic sulfate bath in order to improve the microhardness of coatings. The composite coatings were prepared with varying current density (0.01- 0.05 A/cm^2), different MWCNT particle loading (PL) (0.5- 5 g/L) , pulse current frequency in DC deposited (25, 50 and 75 Hz) and solution temperature at (30±2°C). The result of optical microstructure shows that the current density is increase in deposition .Will the increasing in PL lead to increasing the quantity of MWCNT deposited with Cu. The X-Ray diffraction shows that the deposition with PC had small crystal size compared the DC deposition which reflected on the Microhardness results where the PC had a high microhardness compared to the DC deposition.

Keywords: Multiwalled Carbon Nanotube; copper; Composite; Coatings; Electrodeposition

1- Introduction

Electrocodeposition is a process by which particles are entrapped during electroplating to produce a metal matrix composite. Small particles are dispersed in the electrolyte bath to be codeposited with the metal matrix film .Other methods for producing particle reinforced metal matrix films include thermal spraying, powder metallurgy, and stir casting .A large variety of composite films have been deposited by electrocodeposition. For example, matrix materials such as Au, Cu, Ni, and Co have been plated. Particle reinforcements have included SiC, Al_2O_3, TiO_2, carbon nanotubes, and organic particles [1]. Electrocodeposition has several advantages in developing Metal matrix composite coatings among other coating processes such as, uniform depositions on complexly shaped substrates, low cost, good reproducibility and the reduction of waste [2]. The structure and properties of composite coatings not only depend on the concentration, size, distribution, and nature of the reinforced particles, but also indirectly on the type of electrolyte used and deposition parameters (current density, pulse parameters in case of pulsed deposition, temperature, pH value, etc.). It is worth mentioning that in case of pulsed deposition; the controlling parameters, leading to better control on the coating and its properties when compared with the conventional direct current. Pulse current electrodepositions have higher mechanical and tribological properties than direct current platings [3]. Hayashi et al. proposed that the amount of metal ions adsorbed on particles has an important influence on the codeposition behavior. Roos and coworkers also developed a mathematical model for codeposition [4] Mehmet Uysal et al. were deposited Nickel/multiwalled carbon nanotubes (MWCNT) metal matrix composite coatings by pulse electrocodeposition method from a Watt's type electrolyte[5]. Carbon nanotubes (CNTs) show a better combination of electrical, mechanical, thermal, optical and structural properties. Carbon nanotubes (CNTs), in particular, exhibit great advantages as a matrix-reinforcing phase for composite coatings in high wear environments owing to their extremely high strength, stiffness and lubricity [6]. The aim of this work, we examined the effect of electrodeposition conditions on the surface morphology and microstructure of Cu– MWCNT composite plating coatings produced using a sulfuric bath. Furthermore, physical properties, such as hardness, of the composite coatings were characterized.

2- Materials and Method

The plating electrolyte used for the process was an acidic sulfate type electrolyte. The electrolyte bath is composed with 200 g/L $CuSO_4$_$6H_2O$ and 15 ml/L H_2SO_4. The MWCNTs did not disperse uniformly in the base bath; however, a homogeneous dispersion of MWCNTs was achieved by the addition of a dispersant (polyacrylic acid), mean molecular weight 5000, (PA5000)[7] to the base bath with stirring. The coating electrolyte temperature was controlled at 30 °C (±2) and the pH fixed at 1 (±0:2). Which corrected by using sodium hydroxide. The plating time was changed for various current density levels to ensure that all coatings were approximately

(50 μm) thick. A pure Cu plate with an exposed surface area of 16 cm^2 (4 X 4)cm^2 was used as the substrate. A copper plate used as an anode. The amount of MWCNTs in the electrolyte was studied at 0, 0.5, 1, 3, and 5 g/L. MWCNTs were suspended in the electrolyte, ultrasonically agitated for 1:30 min just before electroplating to enhance the wettability of particles, and to achieve uniform dispersion of reinforcement particles in the electrolyte. During the electrodeposition, a magnetic stirring for 1h was done continuously to avoid settling down of MWCNT. After co-deposition The morphology of Cu-MWCNT composite were studied by using Optical microscope from Carl Zeiss Company, with magnification X100 (100 times magnified), a scanning electron microscope (SEM) (INSPECT S50 (FEI) made in Netherlands) was used to observe the surface and microstructures of the deposits. X-ray diffraction (XRD) analysis was carried out with (XRD-7000, Shimadzu)model XRD with Cu K_α radiation of wavelength 1.5405 Å, and a scan speed of 8.0000 (deg/min). The Crystallite size of the material of matrix was calculated for pure copper , and Cu-MWCNT composite coatings from the (XRD) pattern results, and by using Scherrer's equation[1], given by:

$$D=\frac{0.9\lambda}{\beta \cos\theta} \quad (1)$$

where *D* is the main grain size of obtained coating, λ is the wavelength of Cu Kα radiation (0.154nm), β is the full width at half maximum (FWHM) of the films in radian, and θ is the Bragg diffraction angle. Microhardness test of the coatings was measured using a Vickers microhardness a LARYEE microhardness tester (model HVS-1000, made in China) with a load of 100 g for 15 s. The hardness values were taken at 5 different places on the surfaces and average of these values were considered in the results.

2- Result and Discussion

Morphological

The optical surface images result show that the MWCNT particles are homogenously dispersed in the composite coating. The surface samples surface prepared at different PLwith, CD=0.03 A/cm^2 and at different PL was observed increase of MWCNT content dark point with increasing PL as shown in Figure 1.At low current density (C.D) this homogeneity mainly because at low C.D low deposition rate with low throwing power fills the spaces between the fibers and it appears the deposit in an organized manner, at high C.D the deposition rate increases with the increase in the throwing power, leading to aggregation increasing the carbon content of the compounds that increase the grain sizes. Co-deposition of MWCNTs increased with increasing nanotubes content in the plating bath and reached to a high value in the 5 g/L MWCNTs in the electrolyte show in Figure 2

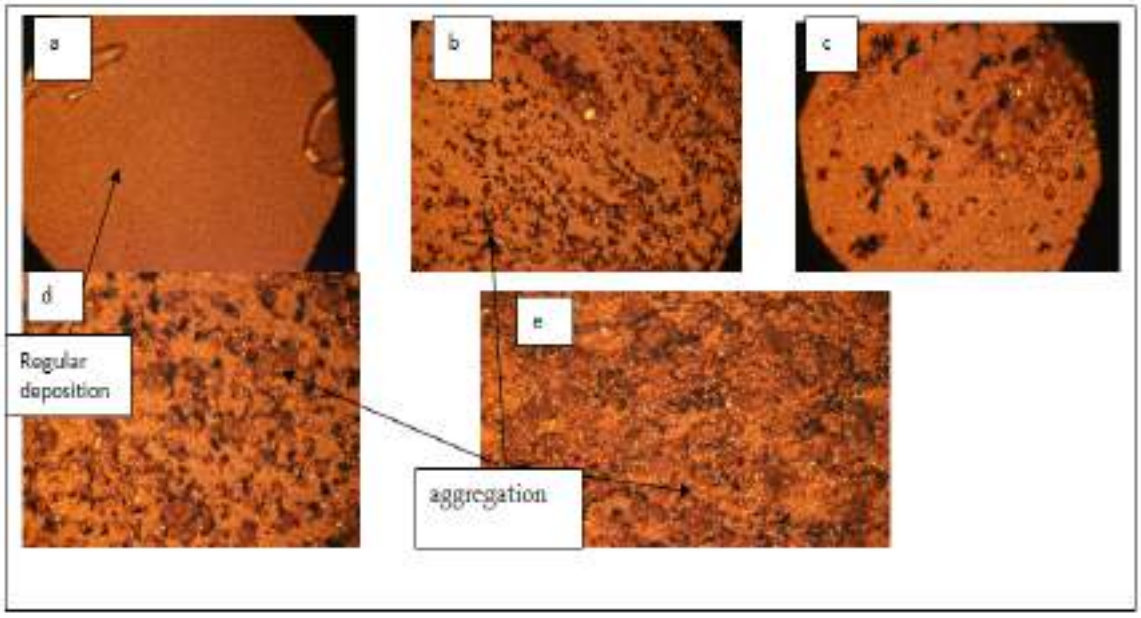

.

Figure 1:The morphology of Cu/MWCNT composite at C.D=0.03 A/cm^2, with different particle loading:(a) pure, (b)0.5,(c) 1, (d)3, (e)5 g/L, magnification 100x

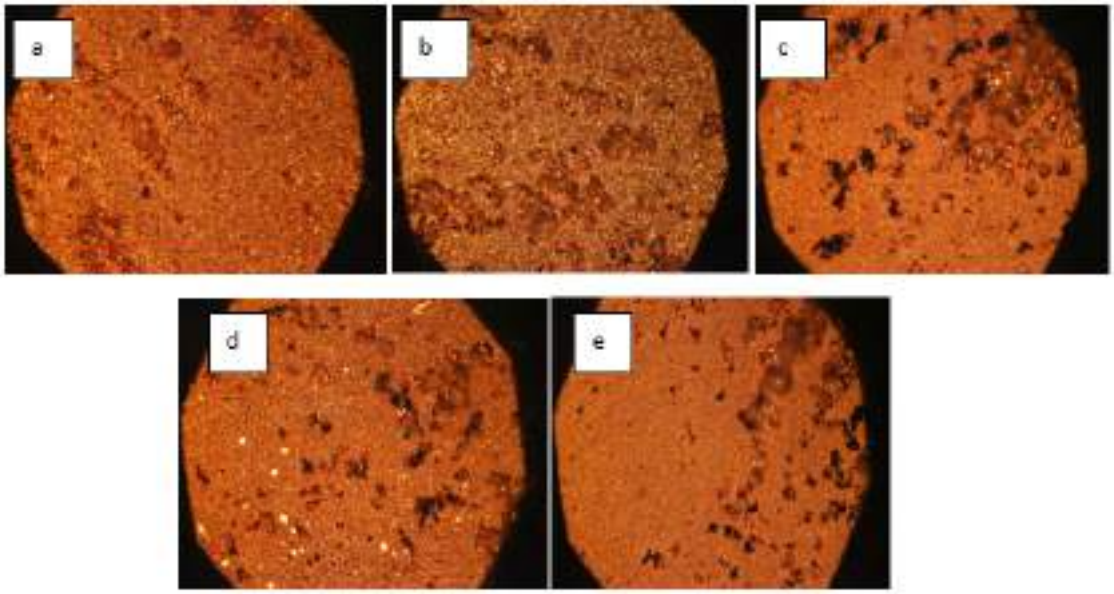

Figure 2:The morphology of Cu/ MWCNT composite at PL(1)g/l ,with different current densities(A/cm^2): (a) 0.01, (b) 0.02, (c) 0.03, (d) 0.04, (e) 0.05 ,magnification 100x

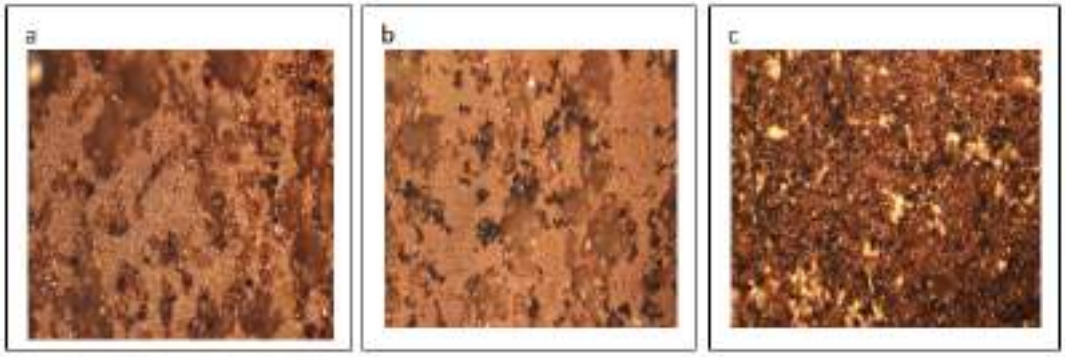

Figure 3: The morphology of Cu/ MWCNT composite at PL(1)g/L ,C.D =0.04 A/cm^2 ,with pulse rate different:(a) 25, (b) 50, (c) 75 HZ, magnification 100x

In Figure 3 the pulse deposition mode increase the MWCNT Vol% in the composite. This increase may be due to that the ON time current the deposited will processed in an ordinary manner. But at Off time deposited will stop (no Cu ion deposited on cathode) lead to increase the quantity of MWCNT that accumulate at the cathode, and when the current back a gene (ON) the deposited will continue the deposited the Cu ion and the accumulated MWCNT.

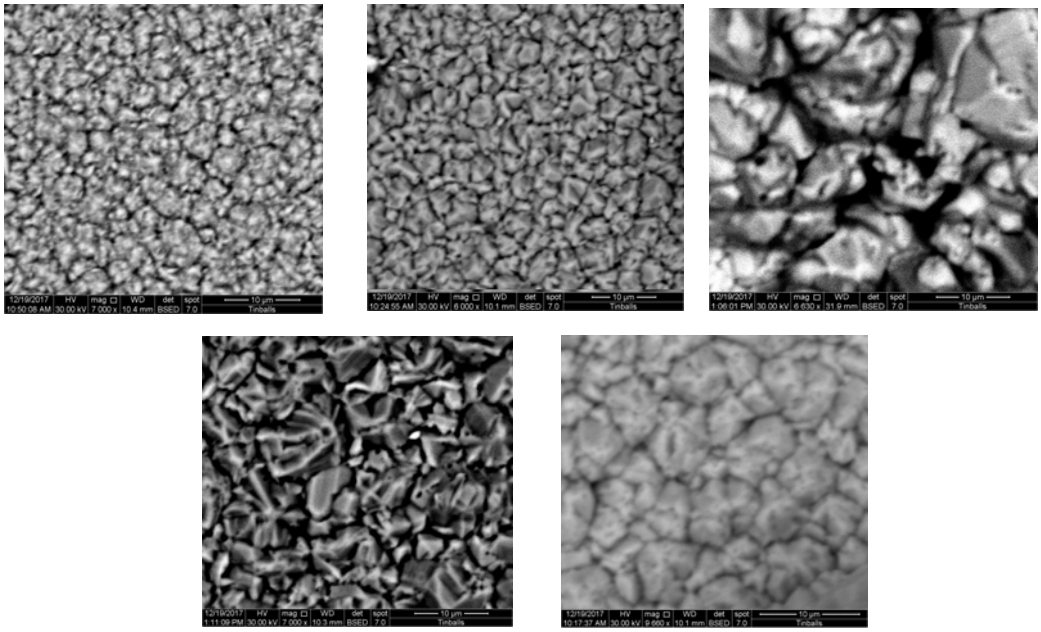

Figure (4) The microstructure by SEM of Cu/MWCNT composite with different PLs: (a)Pure (b)0.5 g/l (c) 1g/l (d) 3 g/l,(e) 5 g/l at CD=0.03(A/cm^2).

Increasing the MWCNT content in the electrolyte resulted in increasing the grain size with increasing content nanotubes, which were also confirmed by SEM analysis. Figure 4 shows the SEM microstructures of Cu/MWCNT composite coatings. The results showed an increment of the MWCNTs in the deposited Cu layer by increasing MWCNT content in the electrolyte. The amount of embedded MWCNTs was reached to a high value at 5 g/L MWCNT content.

XRD Diffraction

XRD analysis was used to determine the degree of crystallinity of the phases and the effect of MWCNTs on the preferential growth of copper coating. The peak intensity ratio of the Cu crystal planes were somewhat different from each other. To clarify this difference, i.e. the difference in the orientation of the Cu films, the orientation index of each crystal plane was calculated. All diffraction peaks were assigned to face-centered cubic Cu, and no peaks attributed to the MWCNTs were observed. The peak strength of the MWCNTs is considered to be very weak, thus, these patterns show only diffractions of the Cu matrix component of the Cu/MWCNT composite films before and after dissolution Figure 5 .XRD patterns of pure Cu and Cu/MWCNT nanocomposites. The intensity of the diffraction peak of (220) copper in the nanocomposite coating is lower, and the peak width is broader than that of the copper coating. The Cu/MWCNTs nanocomposite has exhibited increasing (111) and (200) diffraction lines with an attenuation of (220) line. This was attributed to the decrease in the grain size of the nanocomposite coating with the addition of nanoparticles in the plating bath. The nanoparticles provided more nucleation sites and retarded crystal growth, resulting in a smaller crystal size for the metal matrix in the composite coating [8].

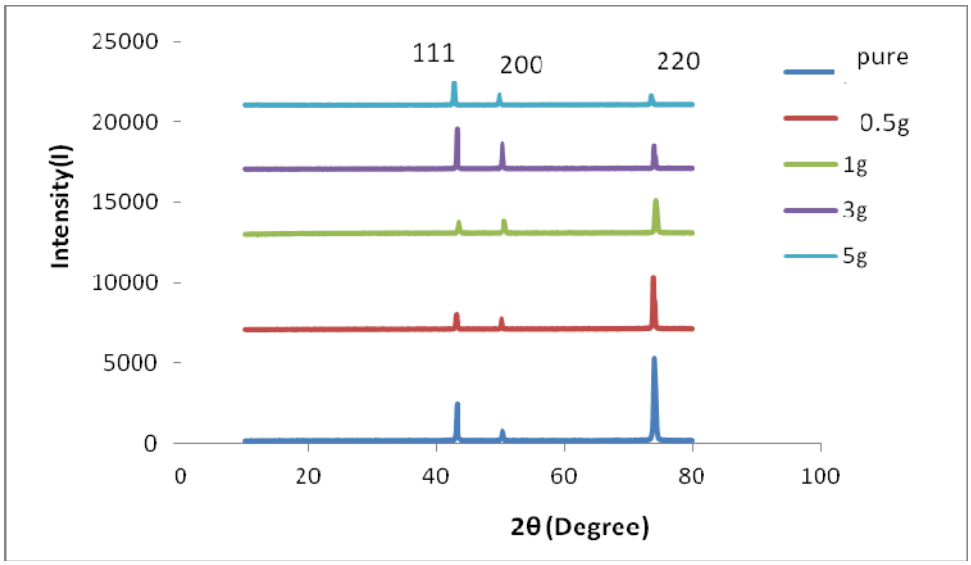

Figure 5: The XRD patterns of the deposited obtained at 0.03A/cm^2 for pure copper and composite coatings with different MWCNTs content in the electrolyte.

case of coating deposited in pulse noted the same behavior at case of coating deposition in direct current ,pulse where low intensity of the diffraction peak of (200) and increase intensity of diffraction peak of (220).

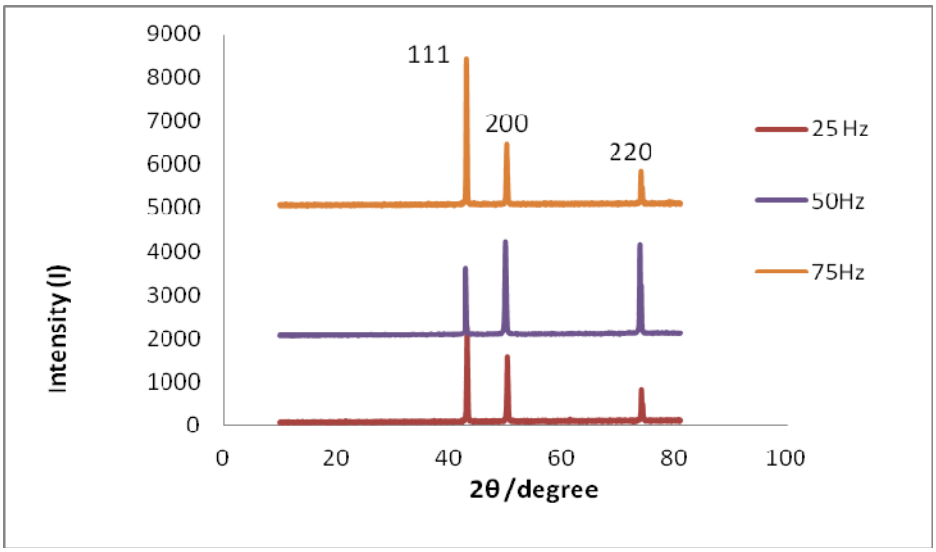

figure 6: The XRD patterns of deposition obtained at CD=0.03 A/cm^2 , PL=1g at pulse variation of 25, 50 and 75 Hz for pure copper and composite coatings .

Microhardness

Figure 7 shows microhardness of pure Cu and Cu/ MWCNTs nanocomposites. The effect of MWCNT content in the electrolyte on hardness of the unreinforced copper coating is found to be great and no regular behavior was noted on the effect of current density .The increasing current density resulted in an improved microhardness of the nanocomposite coatings. The hardness of the composite

coatings can be affected by grain size , coating composition or phase structure[9]. increase MWCNT content increase Of the cohesion of copper granules because nano carbon works on reinforcement copper granules and copper granules Building on nanocarbon This increases the amount of hardness. The increase in the hardness of the composite coatings can be attributed to the reduction in the grain size. In this case, the presence of finer grains, which indicate an enlargement of the grain boundaries, hinders the dislocation motion resulting in an improvement in hardness.

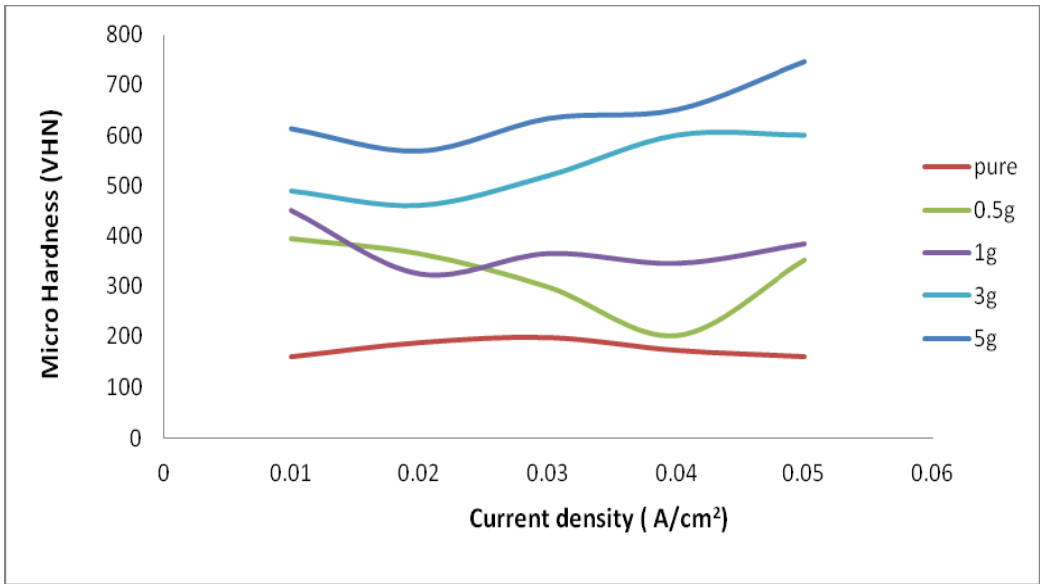

Figure 7: Variation of microhardness with Current density for pure and composite coatings, at temp= 30 ℃ ± 2

in Figure 8 shows increase hardness with increase frequency for all particle loadings work in pulse current increase the regularity of the deposit with a clear indication of increased carbon content in the deposit

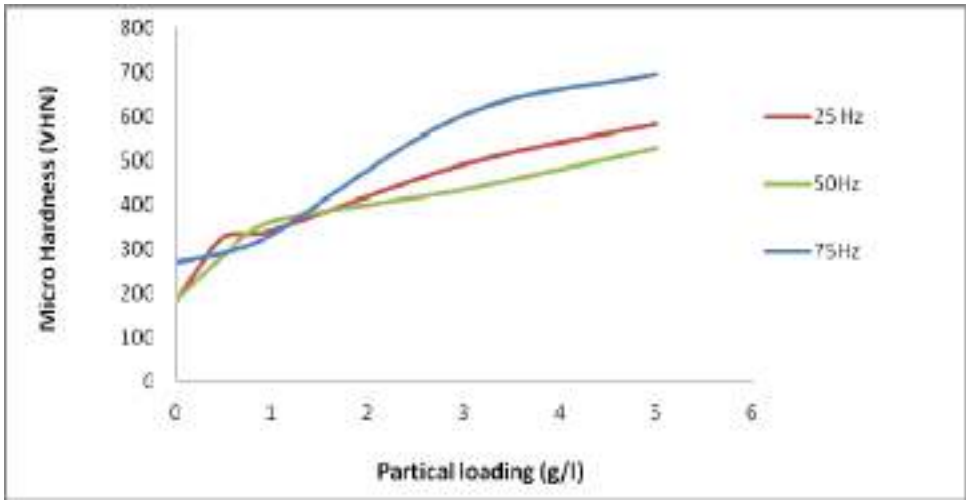

Figure 8: PC Variation of microhardness with P.L for pure and composite coatings

3- Conclusion

Based on experimental results presented in this work, it was possible to draw the following conclusions:

1- Copper electro co-depositions, reinforced with MWCNTs were successfully produced by using direct current and pulse current electrodeposition method. The results revealed that adding MWCNTs into the electrolyte resulted in increasing the amount of MWCNTs in the copper electrodeposited layer.
2- At low MWCNT concentration in the electrolyte revealed more homogeneous and in high MWCNT content revealed agglomeration.
3- Increasing MWCNTs in the electrolyte produced increased microhardness values.

References

1. Osborne, Steven J, " Electrocodeposition of nanoparticle composite films using an impinging jet electrode" (2006), (PhD thesis, UNIVERSITY OF CALIFORNIA, SAN DIEGO).

2. Ashok Akarapu, " Surface Property Modification of Copper By Nanocomposite Coating "(2011), (MSc thesis, Department of Metallurgical & Materials Engineering National Institute of Technology, Rourkela).

3. H. Güla, M. Uysalb, H. Akbulutb and A. Alpb," Tribological Behavior of Copper/MWCNT Nanocomposites Produced by Pulse Electrodeposition" , ACTA PHYSICA POLONICA A, (2013), 125: p.254-256 .

4. Susumu Arai and Akihiro Kato, " Mechanism for Codeposition of Multiwalled Carbon Nanotubes with Copper from Acid Copper Sulfate Bath", Journal of The Electrochemical Society, (2013), 160 :p.380-385 .

5. Chien-TeHsieh[a]HsishengTeng[b]Wei-YuChen[a]Yu-ShunCheng[a], "Synthesis, characterization, and electrochemical capacitance of amino-functionalized carbon nanotubes/carbon paper electrodes" , Carbon,(2010), 48:p. 4219-4229

6. T.CasagrandeG.LawsonH.LiJ.WeiA.AdronovI.Zhitomirsky, "Electrodeposition of composite materials containing functionalized carbon nanotubes", Materials Chemistry and Physics, (2008), 111:p.42-49.

7. Susumu Arai, Yoriyuki Suwa, and Morinobu Endo, " Cu/Multiwalled Carbon Nanotube Composite Films Fabricated by Pulse-Reverse Electrodeposition", *Journal of The Electrochemical Society*, (2011), 158 :p.49-53 .

8. C.R.CarpenterP.H.ShipwayY.Zhu., "Electrodeposition of nickel-carbon nanotubes nanocomposite coatings for enhanced wear resistance ", Wear, (2011), 271:p.2100-2105.

9. M. Kartal, M. Uysal1, H. Gul, A. Alp and H. Akbulut," Pulse electrocodeposition of Ni/MWCNT nanocomposite coatings" ,Research Gate, (2015), 00:p. 1-7.

Available online at
http://namrc.uotechnology.edu.iq/index.php/

Nanotechnology and Advanced Materials Research Centre

Proceeding Articles Book 00 (2018) 000–000

6th International Scientific Conference on Nanotechnology, Advanced Materials and its Applications

Recovery of Metallic Lead from Cathode Ray Tube Funnel Glass using Pyrovacuum Reduction Process

Muna K. Abbass, Abdulkaliq F. Hmood , Salam Z. Abbas
Production Engineering and Metallurgy , University of Technology, Baghdad, Iraq
Corresponding auther:Salam_eng2008@yahoo.com

Abstract

The handling of waste cathode ray tube (CRT) glass is an environmental problem in the worldwide especially after appearance of new technologies such as liquid crystal display (LCD) . The CRT glass is considered as an hazardous waste due to its containment of lead oxide . In this study, pyrovacuum process was used for the recovery of lead oxide which present in the CRT funnel in form of metallic lead after passing through a series of operations i.e. reduction, evaporation and condensation by carbothermic process, all of these processes occur within an evacuated system designed for this purpose. The experimental parameters are temperature range of 700, 800, 900 & 1000 °C , carbon content i.e. 0, 3, 6, 9 & 12 wt% , pressure (10^{-1} mm Hg) and holding time (5h) . After conducting many of physical and chemical tests of both residues and recovered metal and chemical and structural analysis using atomic absorption and XRD showed that the best lead recovery rate has reached was 99.03 % at 900 °C and 9 wt% carbon content with a purity of the obtained lead was 99 % . It is worth mentioning that the residue of funnel glass became a harmless material and suitable for construction application such as foam glass.

Keywords: CRT; funnel glass ; pyrovacuum reduction process; recovery of lead

1- Introduction

Since the middle of the twentieth century CRT has been widely used in television and computer as a display part . In that time, its production grew with increased demand for television and computer **[**1**]** . After the introduction of liquid crystals displaying (LCD) and lights emitting displaying (LED), CRT has losted its acceptability of users because of their large size, heavy weight, energy consumption, and radiation emission **[**2**]** . A large amount of CRT devices (television and computer screens) fell into disuse, generating very large quantities of scrap containing many types of materials **[3]** . The waste of CRT glass is considered as environmental pollution because it contains dangerous chemicals such as lead, barium, antimony, and strontium .

These elements harm the environment, human health and other living organisms if they are not treated properly **[**4**] .** Some countries, such as China, United States and Taiwan annually disposed an estimated 5 million, 3.2 million and 1 million computer screens and televisions, respectively**[**5**]** . The CRT glass unity is made of three various parts each one performs a different work made of different glass composition as shown in Figure 1 .

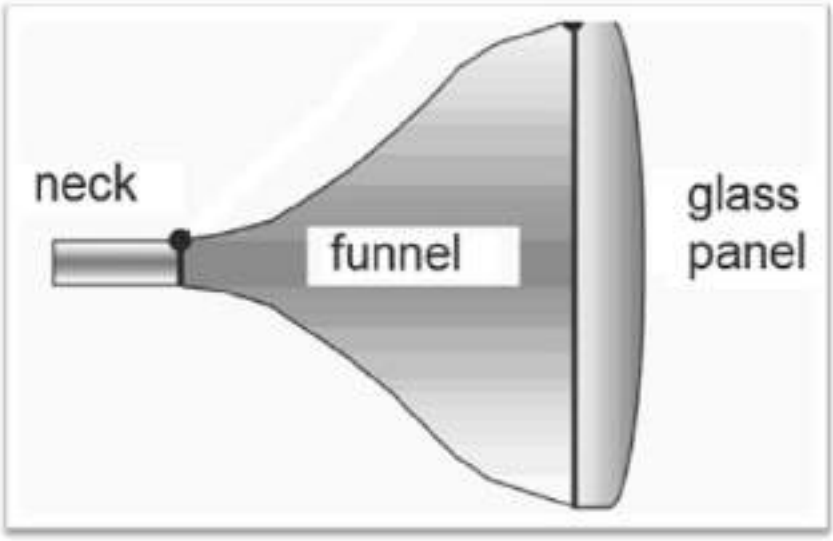

Figure 1 The main components of cathode ray tube glass

Screen or panel glass contains a large amount of the barium oxide and does not contain lead . The funnel and neck glass contains a large amount of lead oxide for protection from the x-ray radiation . The funnel glass contains about 20-25 % lead oxide while neck glass contains about 40 % lead oxide [6] . Funnel glass is the biggest part of (CRT) glass representing about one-third from all weight of (CRT) . This part is considered as toxic waste because it contains high quantity of lead [7] . Lead is a toxic metal and its effects to human health and its impact on the environment have been a great concern to the society for a long time, perhaps more than the other metals [8] .The most serious case, the direct disposal of lead glass in the landfills has become one of the most dangerous things, because it will contaminate the soils and therefore would contribute to the environmental pollution [9] . In recent years the researchers have tried various methods of lead separation from leaded glass and they address the problem . The researchers studied the effect of temperature and time on lead recovery from waste CRT funnel glass by pyrovacuum reduction process .The parameters of this process are holding time (1, 2, 3, 4& 5 h) and temperature (700, 800 & 900 °C) with other fixed conditions such as pressure (10^{-1} mm Hg) and carbon adding amount (9 %) . The maximum pure lead recovery has reached 99.03 % at 900 °C and 5 h (best conditions) [10] . In other studies, the researchers studied the effect of chlorinating volatilization process on scrap funnel glass for detoxification. After testing various parameters on the lead separation from this glass, the optimum conditions were established of temperature, time, and pressure: 1000 °C, 2 h, and 600 ± 50 Pa respectively . The maximum evaporation rate was 99 % [11] . The aim of this work is to study the effect of pyrovacuum reduction process parameters (temperature and carbon adding amount) on the lead recovery from (CRT) funnel glass, possibility of converting the residue glass resulted from this process to other industries such as foam glass .

2- Materials and Method

Sample Preparation

Sample was prepared mechanically from waste CRT glass (old television) . The funnel glass was dismantled from the other (CRT) glass parts (screen and neck) . Then the glass coating was removed by wet scrubbing . The funnel glass was crushed into smaller particle sizes (around 3cm) by using jaw crusher type (Retsch – BB200 rostfrei) . Then grinding the funnel glass by using dry ball mill type (Retsch − PM100) was done . Sieving process was carried out by using auto sieve shaker type (Impact, ISO 3310-1:2000) , in order to get the desired particle size (-53 µm) for the glass powder. The sample of the glass was analyzed by x-ray fluorescence (XRF) type (SHIMADZO,EDX-7000), in order to determine the initial lead concentration before starting the pyrovacuum process as shown in **Table1.**

Table 1: Chemical composition of CRT funnel glass by XRF after sieving process to size (-53 µm).

Oxide	SiO_2	PbO	K_2O	Na_2O	Al_2O_3	SrO	BaO	CaO	MgO	Fe_2O_3	P_2O_5	ZrO_2
wt%	48.68	24.45	9.88	5.32	4.40	2.10	1.96	1.81	1.28	0.20	0.08	0.05

Pyrovacuum Process

This process was carried out in a special system built up for this purpose as shown in **Figure 2** . The system consists of tube chamber which does the following processes : thermal reduction, evaporation and condensation . The milled glass powder (5 g) of particle size (-53 µm) was mixed with carbon powder of particle size (-53 µm) as a reducing agent . This mixture was dried at 100 °C for 24 h . After drying, the mixture was placed in a quartz crucible and placed in the tube chamber and closed this tube. Before starting the vacuum process, inert gas was pumped into the tube and then discharge it, to expel the air from the system. The temperature was raised for various temperatures (700, 800, 900 and 1000 °C) , for various carbon adding amount (0, 3, 6, 9 & 12 wt%), in order to determine the optimum parameters (temperature and carbon ratio) at constant pressure (10^{-1} mm Hg) and holding time (5h). After the end of the testing time, the system was cooled down to room temperature, then the tube chamber was released to the ambient pressure .

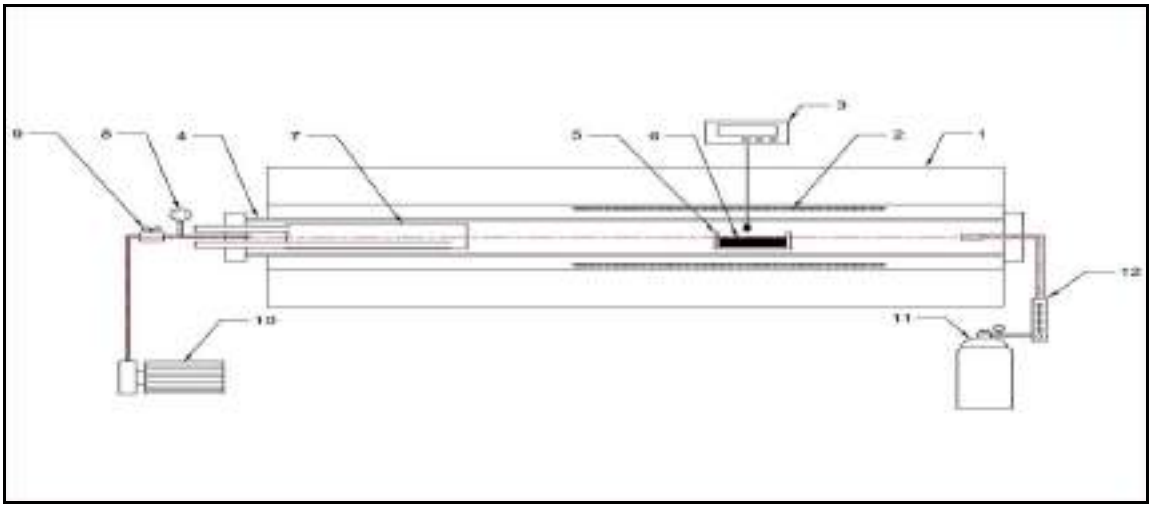

Figure 2 Schematic diagram of the lead recovery system : 1. block of the system 2. spiral heaters 3. thermal control device 4. vacuum tube 5. crucible 6. funnel glass powder 7. air cooling device 8.vacuum gauge 9. screw valve 10. vacuum pump 11. argon gas 12. flow meter .

XRD Analysis

Characterization of the metallic lead was done by X-ray diffraction (XRD) using (Rigaku MiniFlex II difractometer) with CuKa radiation of λ=1.540A°, current = 15 mA, voltage = 30 kV. Figure 3 illustrates that no phase except metallic lead could be observed in the (XRD) analysis. After the end of each experiment of the pyrovacuum process, the residue of the funnel glass was analyzed by using flame atomic absorption spectroscopy . The atomic absorption type (Phoenix-986) has shown that the lead concentration of the residue varies in different proportions according to the experimental conditions . The atomic adsorption analysis was also showed the purity of recovered metallic lead was (99%). Figure 4 illustrate the image of glass residue surface by the Scanning Electron Microscopy (SEM) type (TScanVEGA3LMU) ,the funnel glass is converted to a porous material after lead separating .

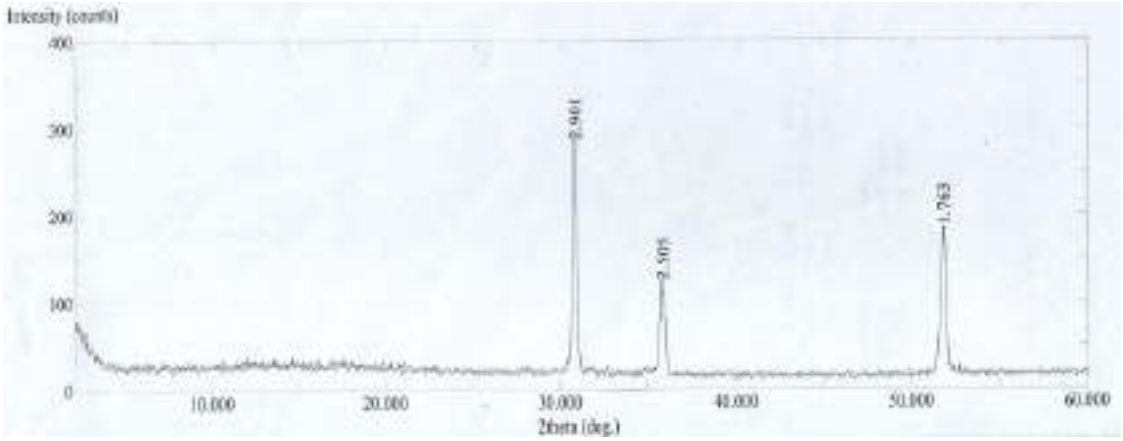

Figure.3 XRD pattern of the recovered metallic lead

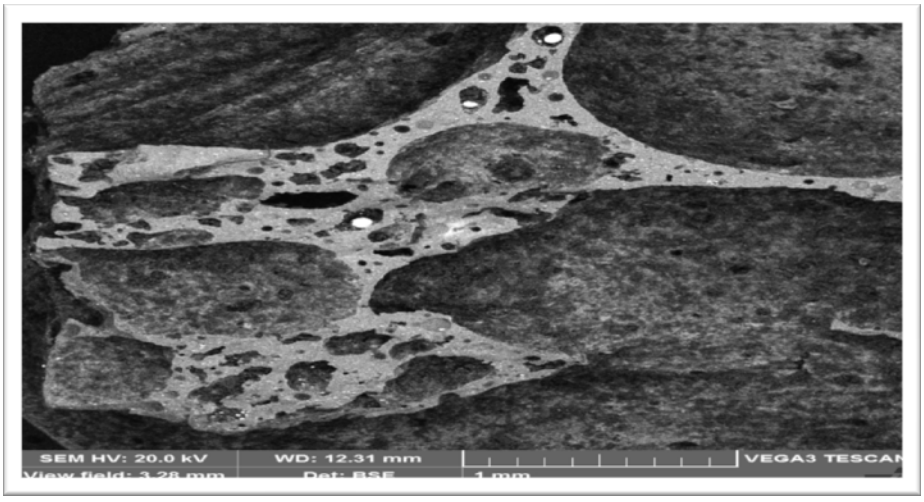

Figure 4 SEM micrograph for the glass residue

3- Results and discussion

3.1. Effect of Temperature on the Lead Recovery

Temperature is a very effective factor in the reduction of lead oxide, evaporation of lead metal and condensation of this vapor as shown in the Table 2 which explains the temperature and carbon amount adding variables and their effect on the rate of lead recovery with constant pressure (10^{-1} mm Hg) and time (5 h) . Figure 5 illustrates that increasing temperature has a very positive effect on the lead recovery rate especially above 800 °C whereas, lead recovery was increased sharply from 75.76% at 700 °C and 5h to 98.28% at 800°C and 5 h . Increment rate might be ascribed to the vapor pressure of lead element (saturation pressure = 10^{-1} mmHg or 13Pa) is almost equal to operation pressure at 800 °C, while at 700 °C saturated vapor pressure of the lead metal is merely about 0.1Pa [12] . Similar trend was obtained by Mengium Chen et al .2008 [13] . The lead recovery rate was calculated according to lead concentration in the funnel glass before and after the pyrovacuum process as shown in equation 1.

Lead recovery % $= \frac{C_1 - C_2}{C_1} \times 100\%$ (1)

C_1 : Lead concentration in the funnel glass before the thermal process .
C_2 : Lead concentration in the residue after the thermal process.

Table 2 Effect of temperature and carbon adding amount on the lead recovery rate.

Temperature °C	Carbon %	Lead %in residue	Recovery rate %
700	9	5.51	75.76
800	9	0.39	98.28
900	9	0.22	99.03
1000	9	0.48	97.88
900	0	3.59	84.17
900	3	2.51	88.93
900	6	0.48	97.88
900	12	0.41	98.19

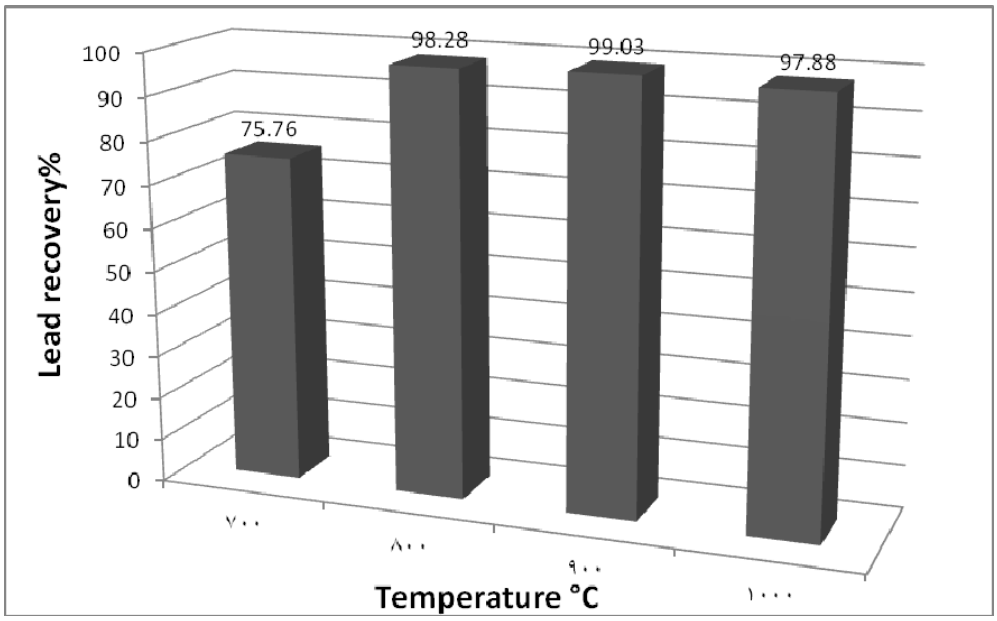

Figure 6 Relationship between lead recovery and carbon adding amount at T = 900 °C, t = 5h %, and P = 10^{-1} mmHg.

5.2. Effect of Carbon Amount Adding on the Lead Recovery

Figure 6 shows the relationship between the carbon amounts and the lead separation rate, after carbon adding amount of 6% C the behavior becomes semi stable until reaching to 9% C , then the recovery ratio suffers a slight decrease . The best carbon adding amount was 9% C which coincided with the highest lead recovery rate of 99%. It was noted that the lowest ratio of lead recovery was 84% even without carbon addition , in another meaning only melting of the funnel glass, since there is already carbon

on the surface of the glass (coated the glass particles) and it can act as a reducing agent . Similar procedure was obtained by Mengium Chen et al .2008 .

4- Conclusion

Pyrovacuum reduction process has satisfied the removing of lead oxide from the CRT funnel glass . The glass residue has become a non toxic material and it is possible to utilize it in foam glass industry and other fields. Pyrovacuum reduction process gave a maximum lead recovery of (~99 %) at the best recovery conditions which are temperature (900 °C) and carbon adding amount (9 wt%) with constant pressure (10^{-1} mm Hg) and (5 h) contact time. Separated metallic lead has been satisfied with 99% purity .

References

[1] N.Singh, J.Wang, J.Li. Waste cathode rays tube : an assessment of global demand for processing . The tenth international conference on waste management and technology (ICWMT), vol 31: 465-474(2016).

[2] G.Grause, N.Yamamoto, T.kameda, T.Yoshioka . Removal of lead from cathode ray tube funnel glass by chloride volatilization . International Journal of Environmental Science and Technology, vol 11: 959-966 (2014) .

[3] B.Hu, S. Zhao, S. Zhang . Removal of lead from cathode ray tube funnel glass by generating the sodium silicate . Journal of the Air & Waste Management Association, vol 65:106-114(2015) .

[4] P.Ledwaba, N.Sosibo. Cathode ray tube recycling in South Africa . MDPI.vol 2:1-18(2017) .

[5] I.C.Nnorom, O.Osibanjo, M.O.C.Ogwuegbu . Global disposal strategies for waste cathode ray tubes . Resources Conservation and Recycling , vol 55:275-290(2011) .

[6] R. Kukla, T. Vítěz, P. Junga, P. Mach . Leachates analysis of glass from black and white and color television sets, vol 6:205-210(2012).

[7] X.Lu,K.Shih,C.Liu,F.Wang. Extraction of metallic lead from cathode ray tube (CRT) funnel glass by thermal reduction with metallic iron .Environmental Science and Technology, vol.47,pp.9972-9978,(2013) .

[8] R.J.Sinclar. The Extractive Metallurgy of Lead.Australasian Institute of Mining and Metallurgy,(2009).

[9] N.Hiroyoshi, H.Prin, Y.Takaya, M.Ito. Application of reductive melting process of CRT glass for recovering valuable metals from PCB waste resources recycling. The 11th International Conference on Mining, Materials and Petroleum Engineering, pp.33,(2013).

[10] M.K.Abbass,A.F.Hmood,S.Z.Abbas. Effect of temperature and time on lead recovery from waste cathode ray tube funnel glass by pyrovacuum reduction technique. American International Journal of Research in Science, Technology, Engineering & Mathematics: 50-54(2017).

[11] A.Erzat, F.S.Zhang. Detoxification effect of chlorination procedure on waste lead glass. The 8th International Conference on Waste Management and Technology,vol.16,pp.623-628,(2014).

[12] N.Yoshimura. Vacuum Technology. Springer,(2008).

[13] [M.Chen, F.S.Zhang, J.Zhu. Lead recovery and the feasibility of foam glass production from funnel glass of dismantled cathode ray tube through pyrovacuum process .Journal of Hazardous Materials, vol.161,pp.1109-1113,(2008).

Available online at
http://namrc.uotechnology.edu.iq/index.php/

Nanotechnology and Advanced Materials Research Centre

Proceeding Articles Book 00 (2018) 000–000

6th International Scientific Conference on Nanotechnology, Advanced Materials and its Applications

Inhibition of medium carbon steel corrosion process in 1 M H2SO4 acidic medium by using aqueous and alcoholic extracted purslane

Layla Abdul Rahman juber*, Abd ulkhaliq fawzy hamood**, Munaf Khalf Mahmood*
*college of education, University of Tikret, Tikret, Iraq
**Production and Metallurgy Engineering department, University of Technology, Baghdad, Iraq

Abstract

Recent study the corrosion and corrosion inhibition of medium carbon steel in 1.0 M H_2SO_4 by purslane extracts (aqueous extract and alcoholic extract) has been studied using mass loss (ML)) . Samples prepared with a dimensions (2.4*2*0.4)cm , grinded with different grinding papers (160.200,400,600,800,1000) and polished , The effect of acid concentration on the corrosion rate of medium carbon steel increases with acid concentration (0.25-1 M) , showing first order corrosion reaction without changing the reaction mechanism.

Results has been showed that the optimum inhibition efficiency in astatic medium for aqueous extracted are (99.3% at 20 °C ,99.2% at 40°C) for 2 hrs , but for alcoholic extracted are (75.5%at 20 °C ,68.9% at 40°C) for 2 hrs ,also studying of reaction throwing time showed the metal corrosion inhibition process obeyed pseudo first order .

Keywords: corrosion, Inhibition, medium carbon steel, purslane.

1- Introduction

Corrosion is defined as the damage of metals and alloys as a result of their chemical or electrochemical reaction to the surrounding environment. The properties of the substance change gradually and are transformed into compounds such as oxides, hydroxides, carbonates, sulfides and sulphides.[1]

electromotive force for the completion of the corrosion reaction is the change in the free energy of the substance as a result of its transformation into compounds . These compounds have a lower free energy than the metals that are formed. Thus, they are formed automatically if the metal is exposed to the appropriate environment and the compounds are more uniform than the metal.[2]

Medium carbon steel approximately 0.3–0.8% carbon content.[3] Balances ductility and strength and has good wear resistance; used for large parts, forging and automotive components.[4-5]

The medium carbon steel is exposed to the attack of acid solutions during industrial processes such as acid cleaning, pickling and descaling this results to easy corrosion of the medium steel, thereby necessitating the use of inhibitor[6] . The many organic compounds are used as corrosion inhibitors for medium steel in acidic environments in a conjugated system and function via adsorption of the molecules on the metal surface[7]. There are many of methods for con-trolling the corrosion of metals but the use of inhibitors is still one of the best methods of protecting metals against corrosion [8-10]. Many Organic compound inhibitors are more effective with iron and so good corrosion inhibitors for acidic solutions of metals.

Numerous studies have been conducted on the use of natural plant extracts as inhibitors of metal corrosion . The aqueous and alcoholic extract for purslane was used as an inhibitor for the corrosion of medium carbon steel in the acid medium (H_2SO_4 0.25-1 M).[11]

The objective of this research is to find a natural inhibitor to get rid of metals corrosion, and found the reaction kinetic by fiend reaction order at tracing metals corrosion change with time passage.

2- Materials and Method

Preparation of samples

Chipping: The samples were cut in the shape of regular cubes with dimensions (2 cm) length, (2.4 cm) width and (0.4 cm) thickness and cut samples using appropriate cutting tool .
Smoothing: The samples were softened using silicon carbide-type paper with several gradients (1000,500,320,180), respectively .
Polishing: After washing the samples and cleaning them with water, the samples were imitated with alumina with a granular size (0.3) microns available in the same laboratory in which it was cleaned. The samples were then washed and dried with tissue .
Saveting : Samples were saved in the ethanol inside the containers tightly closed.

Chemical Analysis

The samples were chemically analyzed for the extract purslane of the kind (aqueous and alcoholic) according to the method Onyeka and Nwabekwe [12] . using a device atomic absorption

Table (1) The chemical composition of the purslane plants

Chemical composition%	K	Fe	Ni	Zn	Mn
Analytical	98.0	25.1	25.1	25.1	25.1

Table (2) The chemical composition of the medium Carbone steel.

Chemical composition%	K	Fe	Ni	Zn	Mn	Mg	Cr	Cu
Analytical	0.01	Rem 99	0.03	0.5	0.03	0.003	0.032	0.045

Preparation of **purslane** Extracts (Inhibitor**):**

Collection of plants sample

Include the sample purslane that was gained after clean from dust by using faucet water and put it in shadow for drying with laboratory temperature (20-30) for period more than 13 days and crushed the purslanes plant paper by electrical crusher for gain a powder purslane and presence in container inside laboratory for using in extracted plant after labeling with signs of plant .

Preparation of extracted plants

Was prepared extracted for purslane plane by using organic solvent petroleum ether (40-60%) and polar solvent (water and alcohol) and as :

- Preparation of extracted organic for purslane paper
  Was prepare extracted organic for sample purslane plant by take (50gm) from powder in conical flask and mixed with (250 ml) from petroleum ether for a period (72h) by using magnetic bar . After that filtrate the solution and drying the precipitate for disposal from organic material .Then preserve the filtrate in container glass and put in fridge with temperature 4 .
  1- Preparation of extracted alcohol for purslane paper plant :
  Was prepare extracted alcohol for sample purslane plant by take precipitate drying for sample plant prepared and mixed with (250 ml) from ethanol with concentrated 99% for period (72h) by using magnetic bar . After that filtrate the solution. Vapor the solvent under pressure rune by using roundabout vapor with 40 temperature and the remaining pressure for using
  2- Preparation of extracted water for purslane paper plant :
  3- Was prepare extracted alcohol for sample purslane plant by take precipitate drying for sample plant prepared and mixed with (250 ml) from distilled water for period (72h) by using magnetic bar after filtrate the solution . Vapor the solvent under rune pressure by using roundabout vapor with 40 temperature and the remaining pressure for using.

For the preparation of aggressive H2SO4 acid solutions H2SO4 were used. Approximate concentration of acids of 3, and 4 M H2SO4 solutions were prepared using double distilled water. Inhibitor purslane concentrations ranging from 0.2 to 1 wt % 3 and 4 M H2SO4 solutions were prepared. Inhibitor of average molecular weights of 1500, 4000, and 6000 g mol-1 were used in this study. The weight loss measurements were carried out at various experimental conditions plan .

3- Results and discussion

1- Found the reaction order for inhibiter

During the reaction for purslane inhibiter with 1M H2SO4 fined the reaction obey pseudo first order . show the figure (1) .

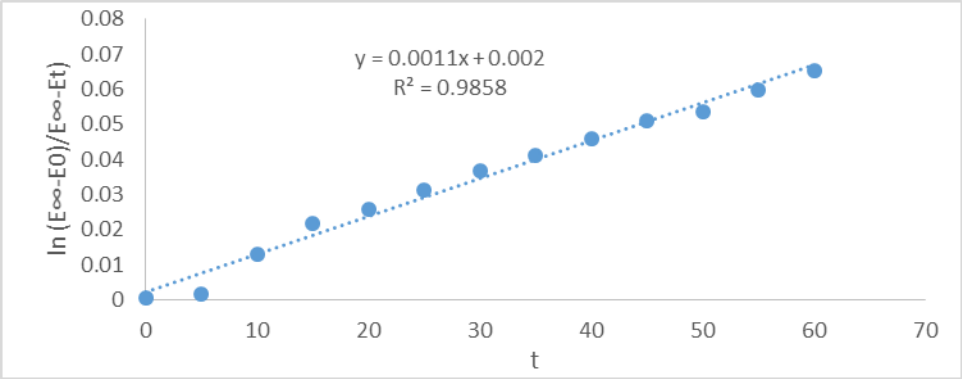

Fig.(1) : pseudo first order plot volte inhibiter during the time

2- Weight loss corrosion

Weight loss corrosion tests were carried out on the medium carbon steel in 1.0M H2SO4 in the absence and presence of (purslane) over an immersion period of 6 hours. **Table 1** represents the corrosion rates [mg.cm-2.h-1], and the percentage efficiencies [%] for the studied inhibitor with concentrations varying from $1.0x10^{-7}$ M up to $1.0x10^{-4}$ M at 293 and 313 K, respectively. The percentage efficiency was calculated according to the following expression:

$$\%E = \frac{W_{un.} - W_{inh.}}{W_{un.}} x\ 100$$

$W_{un.}$= corrosion rate without inhibitor
$W_{inh.}$= Corrosion rate with inhibitor.

Table (3) : Effect of concentration of purslane on the corrosion rate (mg.cm-2.h-1) and percentage efficiency of medium carbone steel in 1.0 M H2SO4 at various temperatures.

Inh. Time	Concentration of Inhibitor	Temperature (K)			
		293		313	
		aqueous extract			
		Corr. R	% Efficieny	Corr. R	% Efficieny

0	1.0 M H2SO4	8.39×10^{-2}	---	5.92×10^{-2}	-----
15	1.0 M H2SO4 + 1.0×10^{-7} M	6.04×10^{-2}	99.2	5.64×10^{-2}	98.9
30	1.0 M H2SO4 + 1.0×10^{-6} M	4.46×10^{-2}	98.9	5.25×10^{-2}	99.2
45	1.0 M H2SO4 + 1.0×10^{-5} M	3.40×10^{-2}	99.2	4.61×10^{-2}	99.6
60	1.0 M H2SO4 + 1.0×10^{-4} M	3.38×10^{-2}	99.6	4.43×10^{-2}	99.8
Inh. Time	Concentration of Inhibitor	Temperature (K)			
		293		313	
		Alcoholic extract			
0	1.0 M H2SO4	8.39×10^{-2}	------	5.53×10^{-2}	-----
15	1.0 M H2SO4 + 1.0×10^{-7} M	6.63×10^{-2}	69	5.509×10^{-2}	64
30	1.0 M H2SO4 + 1.0×10^{-6} M	6.41×10^{-2}	73.2	5.07×10^{-2}	66.7
45	1.0 M H2SO4 + 1.0×10^{-5} M	5.71×10^{-2}	85.9	4.81×10^{-2}	66.9
60	1.0 M H2SO4 + 1.0×10^{-4} M	4.27×10^{-2}	99.6	4.65×10^{-2}	81

The plots of the corrosion rate of purslane vs. acid without inhibiter and with inhibiter concentration in aqueous extract and alcoholic extract . is show the corrosion rate is decrease with increase temperature and increase concentration and the % Efficieny is increase . show the figure (1)

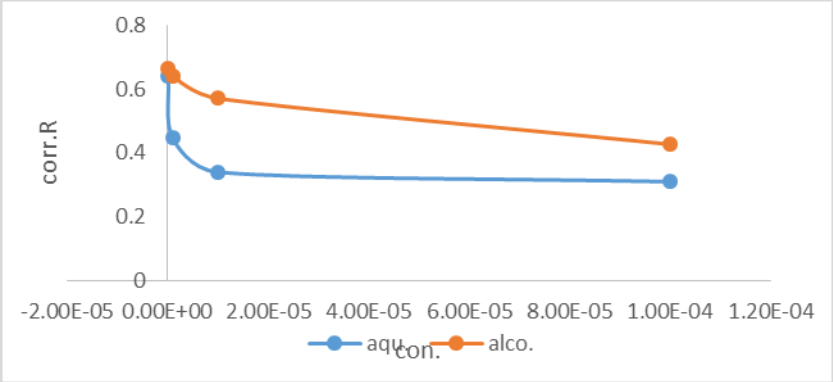

Fig (2) : Effect of concentration of purslane on the corrosion rate (mg.cm-2.h-1) of medium steel in 1.0 M H2SO4 at T=293 in aqueous extract and alcoholic extract

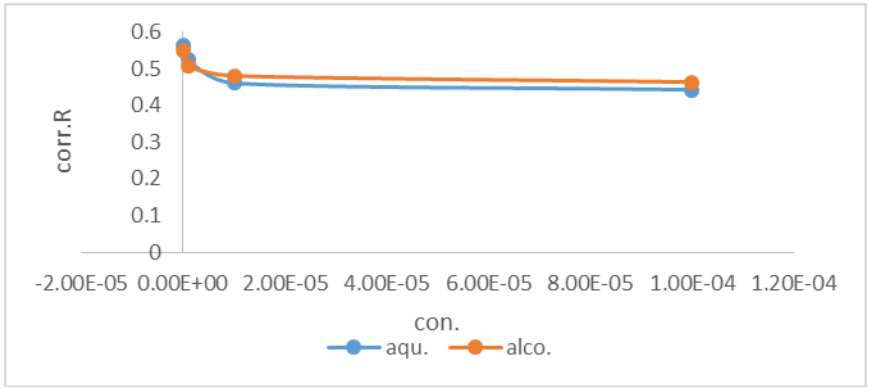

Fig (3) : Effect of concentration of purslane on the corrosion rate (mg.cm-2.h-1) of medium steel in 1.0 M H2SO4 at T=313 in aqueous extract and alcoholic extract

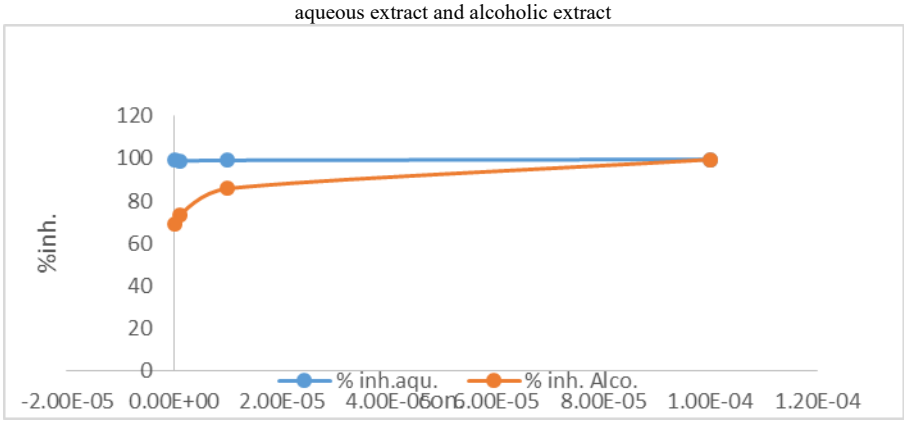

Fig (4) : Effect of concentration of % inhibiter on the corrosion rate (mg.cm-2.h-1) of medium steel in 1.0 M H2SO4 at T=293 in aqueous extract and alcoholic extract

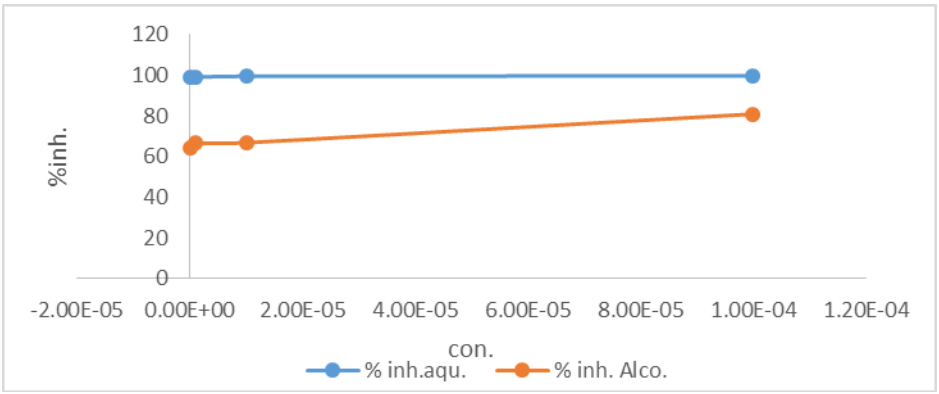

Fig (5) : Effect of concentration of % inhibiter on the corrosion rate (mg.cm-2.h-1) of medium steel in 1.0 M H2SO4 at T=313 in aqueous extract and alcoholic extract

3- Effect of temperature on inhibiter

This figure (6) showed that the % inhibition was sufficiently affected by the increase of temperature (293 to 313K), when all concentrations ($1.0x10^{-7}$ to $1.0x10^{-4}$ M) of inhibitors were employed; and the presence of the inhibitor has greatly increased the %

inhibition at all temperatures. The data obtained from the weight loss measurements **(Table 4)** were plotted in accordance to Arrhenius equation:

$$ln\ corrosion\ rate = -\frac{Ea}{RT} + \text{constant}$$

Table (4) The Data obtained from the weight loss measurements for Arrhenius Equation: (1/T) against Ln Corrosion Rate.

$1/Tx10^{-3}$	Ln corrosion rate				
	aqueous extract				
	1.0 M H2SO4	1.0 M H2SO4l + $1.0x10^{-7}$ M	1.0 M H2SO4l + $1.0x10^{-6}$ M	1.0 M H2SO4l + $1.0x10^{-5}$ M	1.0 M H2SO4l + $1.0x10^{-4}$ M
3.412	0.02127	0.01798	0.014951	0.012237	0.01217
3.194	0.01778	0.01729	0.01658	0.015282	0.0148830
Ea kcal.mol-1	22.1	21.29	21.24	21.24	21.25
	Alcoholic extract				
	1.0 M H2SO4	1.0 M H2SO4 + $1.0x10^{-7}$ M	1.0 M H2SO4 + $1.0x10^{-6}$ M	1.0 M H2SO4 + $1.0x10^{-5}$ M	1.0 M H2SO4 + $1.0x10^{-4}$ M
3.412	0.021270	0.0189160	0.0185785	0.0174221	0.014516
3.194	0.0171018	0.017063	0.0162334	0.0157069	0.015368
Ea kcal.mol-1	22.24	21.20	21.24	21.22	21.227

represents the Arrhenius plot of the corrosion of medium carbon steel in 1.0 M H2SO4 solution (Ln corrosion rate vs.(1/T) with and without the presence persulane at concentrations ranging from $1.0x10^{-7}$ to $1.0x10^{-4}$M. From this Figure, the slope ($-\frac{Ea}{R}$) of each individual line was determined and used concentration of (inhibiter) (from $1.0x10^{-7}$ to $1.0x10^{-4}$M), increased the activation energies for the corrosion of medium carbon steel in 1.0 M H2SO4 ( ) . The increase in the activation energies for the corrosion is attributed to a decrease in the adsorption of the inhibitor on the metal surface as the temperature increased; and subsequently, an increase in the corrosion rate will result due to the greater exposed area of the metal surface to the acid. to calculate the activation energy according to **equation 2**, and taking R = 1.987x10-3kcal.mol-1 **(Table 4)**. The increase of R Ea

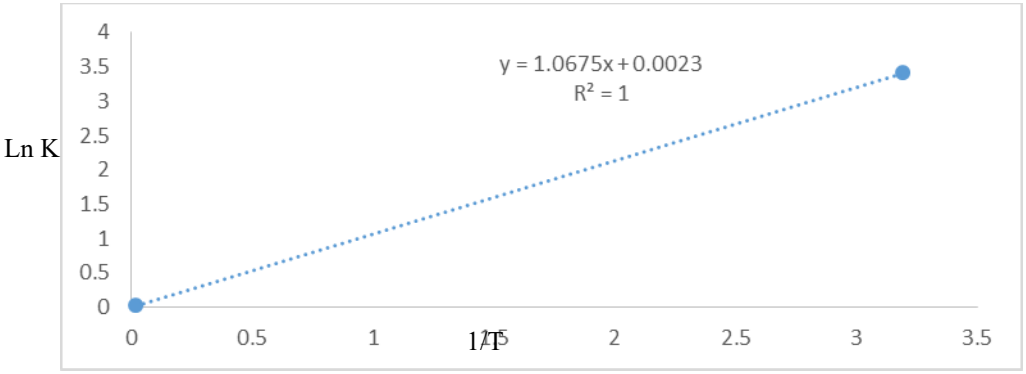

Fig.(6) : Effect of temperature on the corrosion rate of medium carbon steel in 1.0 M H2SO4 solution without perslane inhibiter

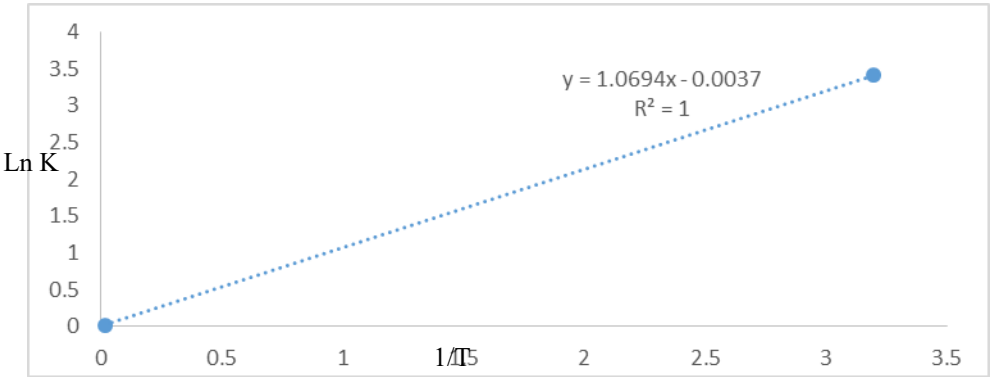

Fig. (7) : Effect of temperature on the corrosion rate of medium carbon steel in 1.0 M H2SO4 solution with perslane inhibiter in aqueous extract.

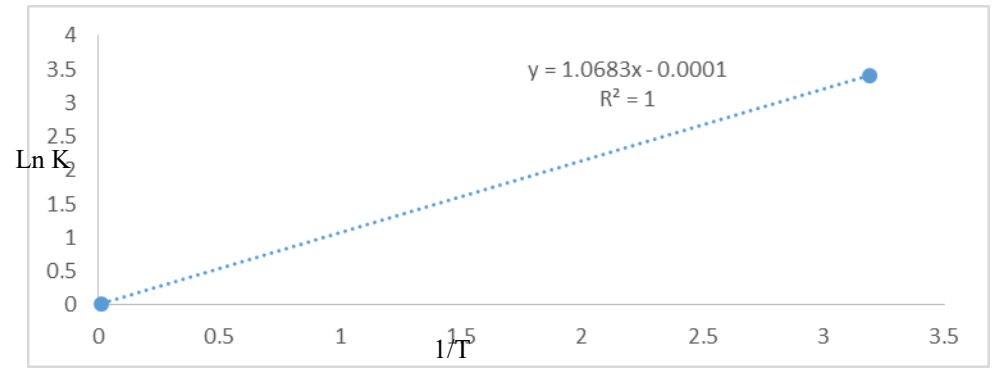

Fig. (8) : Effect of temperature on the corrosion rate of medium carbon steel in 1.0 M H2SO4 solution with perslane inhibiter in Alcoholic extract.

The figures (6-8) and table (4) that the activation energy (Ea) for the corrosion of medium carbon steel in the presence of the inhibitor are higher compared to the activation energy in the absence of inhibitor at all concentrations ranging from $1.0x10^{-4}$ M to $1.0x10^{-7}$ M in aqueous extract (from about 21.24to 21.29kcal.mol-1) while in Alcoholic extract is (from about 21.20 to 21.24) . This can be attributed to the fact that higher values of Ea in the presence of inhibitor compared to its absence are generally consistent with a persulen , while unchanged or lower values of Ea in inhibited solution suggest charge sharing or transfer from the organic inhibitor to the metal surface to form coordinate covalent bonds .

4- Conclusion

In this research we conclude:

1 - The corrosion rate of medium carbon steel increases with acid concentration
2 - The use of the plant (purslane), a natural inhibitor in its forms (aqueous and alcohol extracted), it was found that the aqueous extract is more efficient than the alcohol extract at low temperatures. At high temperatures, the alcohol extract is efficient higher than the aqueous extract.
3 - As a result of the study of kinetics with time to metal corrosion inhibition process obeyed pseudo first order

References

1- Abiola, O.K., "Studies on the inhibition of aluminum alloy (35R) corrosion by (4-amino-2-methyl-5-pyrimidinyl methylthio) acetic acid and its precursor in hydrochloric acid (HCl) solution" Corrosion and Materials, Vol. 32 (11), 2007,10-15.

2- Hugel, G., Corrosion Inhibitors—Study of their Activity Mechanism, in 1st European Symposium on Corrosion Inhibitors, Ferrara, Italy, U. of Ferrara, 1960.

3- Nishimura, Naoya; Murase, Katsuhiko; Ito, Toshihiro; Watanabe, Takeru; Nowak, Roman. "Ultrasonic detection of spall damage induced by low-velocity repeated impact". Central European Journal of Engineering. 2 (4): 650–655.

4- Alvarenga HD, Van de Putte T, Van Steenberge N, Sietsma J, Terryn H (Apr 2009). "Influence of Carbide Morphology and Microstructure on the Kinetics of Superficial Decarburization of C-Mn Steels". Metal Mater Trans A

5- O. M. Abo- Elenien , Novel Corrosion Inhibition for Carbon Steel Alloy:Synthesis and Characterization, Tikrit Journal of Pure Science Vol. 11 No.(1) 2006.

6- Jafar Ghani Majeed; Basim Ajel Sadkhan, Comparison Of The Corrosion Inhibition Efficiencies Of Low Carbon Steel In Different Acidic Mediums Using Some Polyethylene Glycols, Journal of Engineering and Development, Vol. 17, No.4, October 2013, ISSN 1813- 7822.

7- U. J. Ahile1, S.O. Adejo1, J. A. Gbertyo1, F. F Idachaba , R. L. Tyohemba1 and S. O. Ama , ' Ethanol Stem Extract Of Mucuna Pruriens As Green Corrosion Inhibitor For Corrosion of Aluminium In H2SO4, Journal of Applicable Chemistry 2014, 3 (5): 2039-2046 .

8- Joseph Tagbo Nwabanne*, Vincent Nwoye Okafor, Adsorption and Thermodynamics Study of the Inhibition of Corrosion of Mild Steel in H2SO4 Medium Using Vernonia amygdalina, Journal of Minerals and Materials Characterization and Engineering, 2012, 11, 885-890

9- Rachna Jain, Abhilash Kotha, Manish Kr. Bhadu1, Shyam K. Choudhary, Pickling inhibition efficiency of extracts of Azadirachta indica and Momordica charantia acidic medium on steel, Tata Search, 2014 .

10- I.B.Obot, N.O.Obi-Egbedi , Anti-corrosive properties of xanthone on mild steel corrosion in sulphuric acid: Experimental and theoretical investigations, Current Applied Physics, Volume 11, Issue 3, May 2011, Pages 382-392

11- Aisha M. Al- Turkustani , Corrosion and Corrosion Inhibition of Mild Steel in H2SO4 Solutions by Zizyphus Spina-Christi as Green Inhibitor, International Journal of Chemistry , Vol. 2, No. 2; August 2010 .

12- Noor Hatem Khorsheed , Inhibition of carbon steel corrosion in acid medium using Citrus aurantium leaves extract, A Thesis of Master, University of Diyala, 2016

Available online at
http://namrc.uotechnology.edu.iq/index.php/

Nanotechnology and Advanced Materials Research Centre

Proceeding Articles Book 00 (2018) 000–000

6th International Scientific Conference on Nanotechnology, Advanced Materials and its Applications

Characterization studies the influence of glancing angle on the structural and optical properties of ZnO nanostructure

Wafaa K. Khalef, Amenah A. Salman
Applied Science Department, University of Technology,Baghdad, Iraq
Corresponding uther:drwafaa1980@gmail.com

Abstract

In oblique angle deposition technique (OAD), the vapor of zinc metallic atoms traveling a fixed substrate at angle (Ɵº from50º-70º) with regard to the surface normal of the substrate. Zinc oxide nanowires (ZnO NWs) deposited on a quartz substrates were successfully synthesized via an oblique angle deposition technique. The effect of angle on thermally evaporated zinc metal films on a quartz substrate, then oxidize at temperature 650˚C for 4 hours to produce zinc oxide (ZnO NWs) has been investigated. ZnO NWs films produced was characterized by x-ray diffraction method (XRD), scanning electron microscope (SEM), UV –Visible spectrophotometers. The crystal structure calculations have confirmed the growth of Wurtzite crystalline structures of ZnO NWs and the peak intensity increases with increasing deposition angle. High-density nanowires in oblique deposition films Ɵº=50º and 70 º as compared with normal deposition Ɵº=0º.The deposition angle has a great effect on the optical properties. Absorption spectra show a peak position at in the ultraviolet region, with band gap increase with increasing deposition angle.

Keywords: Oblique deposition; Zinc oxide NWs, glancing angle deposition, GLAD method.

1- Introduction

Transparent conductive oxide (TCO) has good electrical conductivity properties and high transparency in a visible region of an electromagnetic spectrum. Essential technological applications of transparent conductive oxide (TCO) , such as light emitting diodes [1],transparent solar cells [2],for liquid crystal displays[3], low thermal emissivity coatings [4],electro chromatic windows [5].

Zinc oxide is promising material for fabricating optoelectronic devices, that operate in the UV region, owing to its large exciton binding energy of 60 m eV and wide band gap energy of 3.37 eV at room temperature [6].

Different techniques were used to prepare ZnO thin films such as pulsed laser deposition [7], sputtering [8], chemical bath deposition [9-10], sol-gel [11], plasma-assisted molecular beam epitaxy [12], chemical spray pyrolysis techniques [13] and thermal oxidation of vacuum-deposited metallic films [14]. Oblique angle deposition (OAD) allows the growth of the nanostructures with different shapes [15, 16].

In this study, we study the enhancement of deposition angle on the structural and optical properties of ZnO NWs. We have also presented the characterization of ZnO NWs from the literature and from our own measurements.

2- Materials and Method

The high purity zinc metal film deposited on a clean quartz substrate by physical vapor deposition (PVD) at normal incidence Θ˚= 0˚and oblique Θ˚=50 ˚, and 70º, then oxides in convention furnace type (Nabertherm) at 650˚C for 4 hours. Quartz slides used were held at an angle (Θ˚) to the direction of evaporation source. The evaporation of zinc metal was carried out on the substrates at room temperature in a vacuum of about (1*10-6) torr from a molybdenum boat heater, which was clean, and located at a distance of 15 cm from the substrate. After that, the ZnO NWs samples were characterized using a scanning electron microscope (JOEL JSM-6480LV). The structure properties of the ZnO NWs studied by X-ray diffraction (SHIMADZU JAPAN, XRD – 6000) with Cu Kα radiation (λ = 1.542 Aº) was used. The optical characterization of the ZnO NWs film was investigated by using a double beam UV-Vis spectrophotometer (CECIL C.7200) (France).

3- Results and discussion

3.1 Structural properties

3.1.1 XRD analysis

The X- ray diffraction patterns of the ZnO NWs films which are deposited on a quartz substrate at different angles Θº=0º and Θº=70º shown in figure 1 (a and b) respectively. It's clear from the figures, that both normal and oblique samples have the polycrystalline Wurtizite structure with sharp and strong peaks observed at diffraction angles (2Θº) of (31.83, 34.49º,36.32) and (31.58, 34.77, 36.07) corresponded to the (100),(002),(101) planes respectively . In addition, the intensity of the (002) plane decreases with increasing incidence angle, and becomes less intense with deposition angle (70◦), this is may be due to columnar growth in the direction of the evaporation source, while the intensity of the (100),(101) planes increases with increasing incidence angle θ, and becomes more intense with deposition angle (70◦) this results agree with paper [17]. This shows an improvement in the structural properties observed which have a better degree of crystallinity as compared with the normal deposition. In addition, it's clear in both normal and oblique ZnO NWs patterns, the very small peaks observed at angles (2θ) (48.9 and 57.2) corresponded to the (102) and (110) plans has intensity increased with increasing deposition angle as shown in figure 1 (a and b). The structure, properties such as (hkl) and interplanar distance and grain size of ZNONWs are listed in the table (1). The XRD peaks of ZnO NWs films good agreement with the standard ASTM (American Society of Testing Materials) cards. The grain size (GS) of the polycrystalline material can be calculated from the X-ray result by means of Full Width at Half Maximum (FWHM) method [18]. It's clear from the table, that the decreases in the value of grain size from 81.4 to 8 nm when deposition angle increases from (0˚ to 70˚), this behavior lead to the large surface area to volume for ZnO nanostractural films and large energy conservation in a detector and solar cell. This shows the structure enhancement in the oblique deposition as compared with the normal deposition (conventional deposition).

Table 1.Comparison between experimental and ASTM dhkl and average grain size (nm) of preferred orientation (100),(002) and (101) ZnONWs films oxides at temperature 650˚C for 4 hours.

deposition Angle	Oxidation temperature (˚C)	(hkl)	d_{hkl} ASTM (Å)	d_{hkl} Exp. (Å)	2θ ASTM. (degree)	2θ Exp. (degree)	FWHM (deg)	Avarge grain size (D)nm
0˚	650	100	2.81	2.80	31.819	31.83	0.512	81.43
		002	2.61	2.59	34.330	34.49	0.53	
		101	2.46	2.47	36.494	36.324	0.52	
		100	2.81	2.83	31.819	31.58	0.53	7.7

70˚	002	2.61	2.613	34.330	34.77	0.49
	101	2.46	2.48	36.494	36.07	0.80

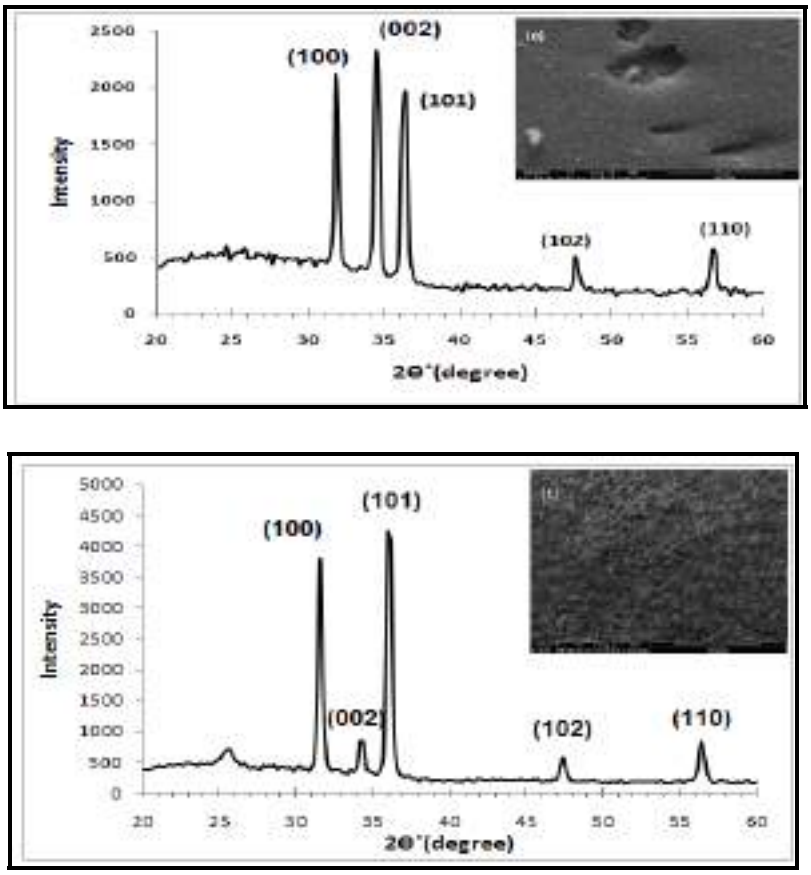

Fig.1 XRD pattern of ZnO NWs deposited at a) Θ˚=0˚ and b) Θ˚=70˚ by OAD technique at 650 ˚C.

3.1.2 SEM analysis

The morphology of the normally Θº=0 and obliquely Θº=50˚, 70˚ ZnO NWs film is shown in figure 2 (a, b and c) respectively. Where high purity Zn metal thermally evaporated at different angles (0˚,50˚ and 70˚) on clean quartz substrates, then oxides in the air at 650ºC for 4houre to produce ZnO nanostructure. Figure2.a, shows the smooth surface image of the normal zinc oxide film, while the short nanowires started to grow with minor distributed nanowires at deposition angle Θº equal 50˚ and 70˚ as shown in Figure.2b and c respectively. The nanowire was grown with density increased with increasing incident angles, this results in good agreement with J.Chu et al [17]. High-density wires like structure in oblique deposition films Θº=50º and 70 º as compared with normal deposition Θº=0º, due to the shadowing effect [19].

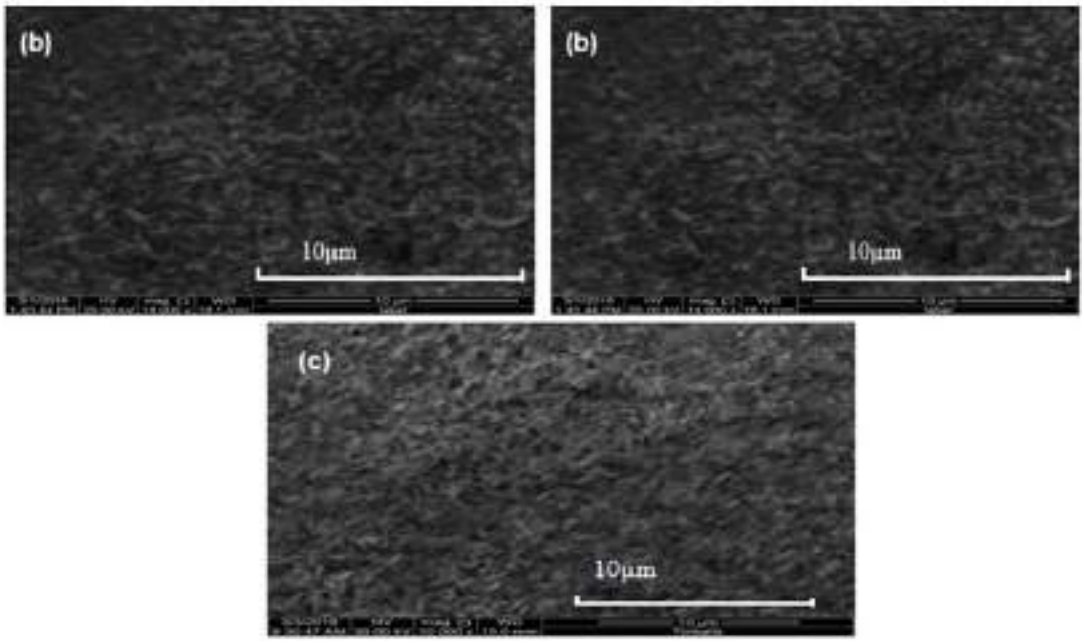

Fig 2 The top sectional SEM images of ZnO NWs grown by oblique angle deposition (OAD) technique on quartz substrates, where(a) incident angle =0˚, b)=50˚ and c)=70˚ respectively.

4. Optical properties

Absorbance spectra recorded for the normal and oblique ZnO NWs films as a function of wavelength range350-1000nm is shown in Figure3 (a and c). It is clear that the peak position around (366) nm and the absorbance increase with an increase deposition angle. This result may be due to, rod-like stricture accompanies by oblique deposition which was suitable for the absorption layer of the solar cell application. The typical plots of $(\alpha h\upsilon)2$ versus ($h\upsilon$) for ZnONWs news for normal and oblique deposition on the quartz substrate as shown in Figure 3(b and d) respectively. It is observed that the increase in the deposition angle of ZnO NWs let to increase in the optical band gap from (3.1 to 3.3) eV. These results are in agreement with the previous values, calculated for films prepared by other method [20].

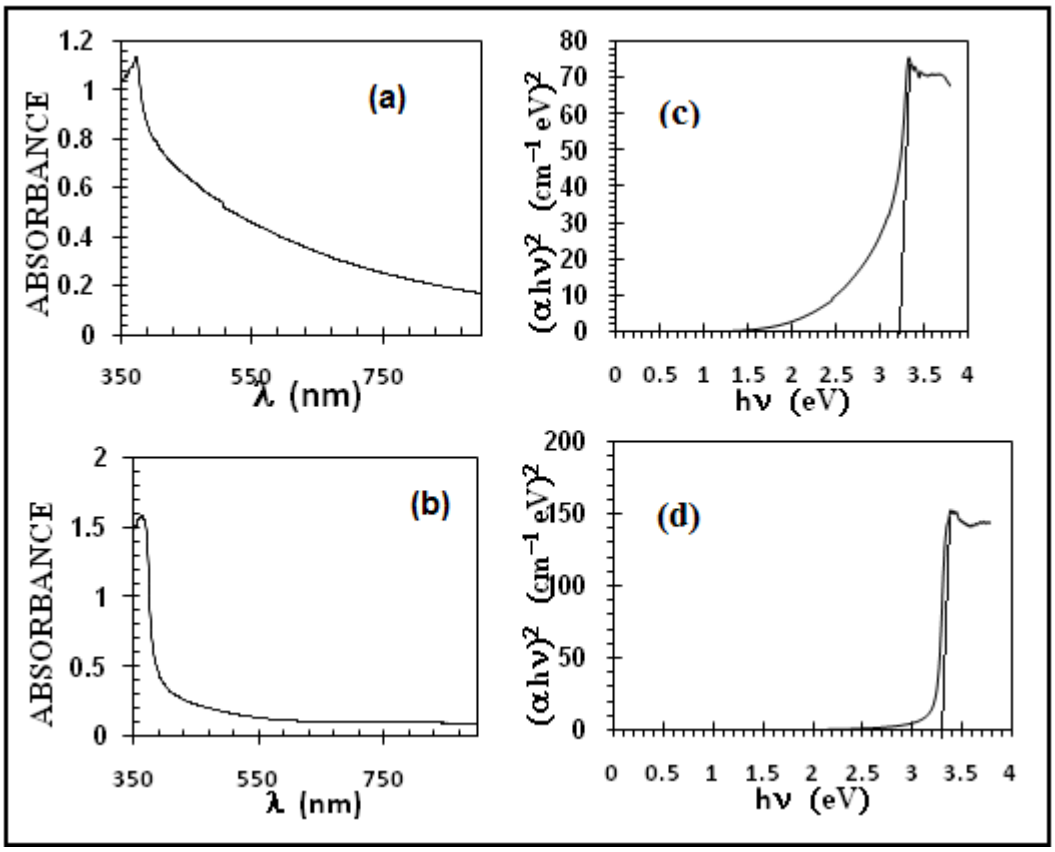

Fig.3The absorbance and energy gap of the ZnONWs normally deposition (a) Θ˚=0˚ and obliquely (b) Θ˚=70˚ at 650 C for 4 hours respectively.

4- Conclusion

In this work, an oblique-angle deposition technique led to prepared ZnO nanowire with high density as compared with the normal incident ($\Theta^o=0^o$). From XRD results, polycrystalline Wurtizite crystalline structures of ZnO NWs and the peak intensity corresponding the (100) and (101) plans to increase with increasing deposition angle. From optical results, an absorption peak position in the ultraviolet region around 366nm, with a band gap increased with increasing deposition angle.

References

[1]A.Porch,D.V.Morgan,R.M.Perks,M.O.Jones, P.P. Edwards."Transparent current spreading Layers For Optoelectronic Devices", J. Appl. Phys, 2004, 96 (8):P.4211.
[2] A.Porch, D.V.Morgan, R.M.Perks, M.O. Jones, P.P. Edwards. "Electromagnetic Absorption in Transparent Conducting Films", J. Appl. Phys, 2004, 95(9): P.4734.
[3]A.N.Tiwari,G.Khrypunov,F.Kurdzesau,D.L.Bätzner,A.Romeo,H. Zogg."CdTe solar cell In A Novel Configuration, Prog. Photovoltaics", Res. Appl.,2004, 12(22):P.33 .
[4] G.S. Chae." A Modified Transparent Conducting Oxide For Flat Panel Displays Only", Jpn.J. Appl. Phys,2001, 40(13):P.1282–1286.
[5] I. Hamberg, C.G. Granqvist. "Evaporated Sn-Doped In_2o_3 Films: Basic Optical Properties and Applications To Energy-Efficient Windows", J. Appl. Phys .,1986, 60(11): R123.
[6] S. M.H. Al-Jawad." Annealing Effect On Structure And Optical Properties Of ZnO thin Films Prepared By Spray Pyrolysis", Eng&Tech. Journal,2015,Vol.33(1):P.160-171.

[7] Jong-Hoon Kim, Byung Du Ahn, Choonghee Lee, Kyung Ah Jeon, Hong Sengkang, And Sang Yeol Lee. "Effect Of Rapid Thermal Annealing On Electrical and optical properties of Ga Doped ZnO Thin Films Prepared At Room Temperature",Journal of Applied Physics, 2006,100(11):P. 113515.
[8] F. Couzinié-Devy, N. Barreau, And J. Kessler."Dependence Of ZnO: Al
Properties On The Substrate To Target Position In Rf Sputtering", Thin Solid Films, 2008,Vol.516:P. 7094-7097.
[9] ZhiguangWang, Minqiang Wang, Zhonghai Lin, Yaohuixue, Gehuang, Andiamo."Growth And Interconversion Of ZnO Nanostructure Films On Different Substrates",Applied Surface Science2009, 255(9):P .4705 4710
[10] V.R. Shinde, C.D. Lokhande, R.S. Mane, Sung-Hwan Han."Hydrophobic And Textured ZnO Films Deposited By Chemical Bath Deposition: Annealing Effect", Journal Of Applied Surface Science,2005, 245 (1-4): P. 407-413.
[11] R. Ghosh, D. Basak, And S. Fujihara." Effect Of Substrate-Induced Strain On The Structural, Electrical, And Optical Properties Of Polycrystalline ZnO Thin Films",Journal Of Applied Physics,2004, 96(5):P.2689.
[12] Shujie Jiao, Youming Lu, Zhengzhong Zhang, Binghui Li, Bin Yao, Jiyingzhang, Dongxu Zhao, Dezhenshen, And Xiwu Fan." Optical And Electrical Properties Of Highly Nitrogen-Doped ZnO Thin Films Grown By Plasma-Assisted Molecular Beam Epitaxy", Journal Of Applied Physics,2007, 102(11):P.113509.
[13] Sh. U. Yuldashev, A. G. N. Panin, And T. W. Kang, R. A. Nusretov And I. V.Khvan." Electrical And Optical Properties Of ZnO Thin Films Grown On Si Substrates", Journal Of Applied Physics,2006, 100(1): P013704.
[14] Lisheng Wang And Xiao Zhongzhang."Synthesis Of Well-Aligned ZnO Nanowires By Simple Physical Vapor Deposition On C-Oriented ZnO Thin Films With Outeatalysts Or Additives ", Appl.Phys, 2005,86: P.024108.
[15] H. Cansizoglu, M.F. Cansizoglu, M. Finckenor, T. Karabacak. "Optical Absorption Properties of Semiconducting Nanostructures With Different Shapes", Adv. Opt. Mater.,2013,1(2):P. 158-166.
[16] D-X Ye1, T Karabacak, BK Lim, G-C Wang And T-M Lu."Growth Of Uniformly Aligned Nanorod Arrays By Oblique Angle Deposition With Two-Phase Substrate Rotation", Nanotechnology,2004, 15(7):P. 817-821.
[17]J.Chu, X.Peng, M.Sajjad, B.Yang, P.X.Feng."Nanostructures And Sensing Properties Of ZnO Prepared Using Normal And Oblique Angle Deposition Techniques",Thin Solid Films,2012,520(9):P.3493-3498.
[18]A. D., H. B., A. M. Azzam, BelayachiAnd M. Abd-Lefdil." Structural, Optical And Electrical Properties of Transparent Conducting Oxide Based On Al-doped ZnO Prepared By Spray Pyrolysis", Sensors & Transducers,2014, 27:P. 156-160.
[19] Chen, L.C., Chen, C.C., Sung, Y.T., Hsu, Y.Y." Oblique-Angle Sputtering Effects On Characteristics OfNanocolumnar Structure Anisotropic Indium Tin Oxide Films" J. Electrochem. Soc., 2009, 156, P.H471–H474.
[20]S. Y. Al-Dabag, S. S. Ahmed, W. J. Taher. " Investigation Of Structural, Optical And Electrical Properties Of ZnO Prepared Thin Film By Pld", Eng. &Tech.Journal, 2015, 33(1):P. 838-847

Available online at
http://namrc.uotechnology.edu.iq/index.php/

Nanotechnology and Advanced Materials Research Centre

Proceeding Articles Book 00 (2018) 000–000

6th International Scientific Conference on Nanotechnology, Advanced Materials and its Applications

Synthesis of Nano-Colloidal Titanium Oxide by Pulsed Laser Ablation Technique

Mohsin Talib Mohammed[1], Abbas Ali Diwan[2], Sabah Abbas Malik[3]

[1]Mechanical Engineering Department, Faculty of Engineering, University of Kufa, Najaf, Iraq

[2]Nanotechnology and Advanced Materials Research Unit, Faculty of Engineering, University of Kufa, Najaf, Iraq

[3]Department of pharmaceutical chemistry, Faculty of Pharmacy, University of Kufa, Najaf, Iraq

Corresponding auther: Mohsint.alyasiri@uokufa.edu.iq

Abstract

In this paper, pulsed laser ablation (PLA) technique was applied for synthesis of colloidal nanoparticles of titanium (Ti) oxide from pure Ti target in ethanol as liquid medium. The characteristics of ultraviolet visible (UV) absorption, Fourier transformation infrared radiation (FTIR) and scanning electron microscope (SEM) were used to investigate the produced colloidal. The parameters used for PLA technique were selected to be 200 pulses at 900 mJ per pulse in 20 ml of 99.9% purity ethanol at wavelength 532 nm. The distance between laser beam and the Ti target is adjusted to be 150 mm. The results showed that ethanol is an appropriate liquid medium for synthesis nano-colloidal Ti oxide with an UV absorption peek at 200 nm.

Keywords: Nanoparticles, Laser ablation, Titanium oxide, Nano-colloidal.

1- Introduction

Titanium oxide has a wide range of many different applications, such as biomedical, solar energy, photo catalysis, toothpaste, white pigments and gas sensors, due to its outstanding mechanical and chemical properties. The synthesis of Ti dioxide can be made using many approaches such as chemical reduction, electrolysis and laser ablation [1, 2]. The type of the synthesis techniques is considered as a main parameter for controlling nanoscale size properties of Ti oxide nanoparticles. The characteristics of nanoparticles are normal consequence of the crystal structure and the nanoparticles morphology [3].

It is well known that anatase, brookite and rutile are the main phases of Ti oxide. The most phase stable in bulk form and ambient conditions among these phases is rutile phase. The final phase of Ti oxide is influenced by the method of preparation. There are different methods for producing Ti oxide nanoparticles such as hydrothermal method [4], radiofrequency induction plasma [5], laser pyrolysis [6], sol–gel process [7], etc. Many of these methods involve chemical reactions associated with defects that require purification in other complicated procedures that may affect the properties of the nanoparticles produced. The use of the PLA method is safe and easy procedure since it keeps the nanoparticles inside the liquid without contemned particles. The main reason for using this method is to obtain a homogenous and spherical shape within the liquid due to the equal pressure of fluid around the ablated particles from the target, forming a homogeneous globular shape [8]. Furthermore, the agglomeration and aggregation can be avoided since the particles are formed within the solution using an ultrasonic mixing manner [9]. Previous investigations display that Ti oxide nanoparticles can be produced by the laser ablation process of Ti target in a suitable liquid. For example, ablation of Ti target in water results in the formation of colloidal Ti oxide nanoparticles with different morphology, size, structural and optical properties. [10, 11]. It very important to mention here that the characteristics of nanoparticles produced by PLA depend mainly upon many parameters like wavelength of laser beam, distance between laser nozzle and target, energy of laser beam, and the focusing

spot of laser [12]. In the present work, the nano-scale Ti oxide colloidal was synthesized in ethanol medium using PLA method. The characteristics of the prepared nanoparticles were also investigated using different characterization techniques.

2- Materials and Method

A target of Ti plate was cleaned and immersed in ultrasonic cleaner for 15 min in high purity ethanol. The pure Ti target were placed in a glass vessel and filled with ethanol up to 2 ml (1cm over the upper surface). The ND-YAG laser was used to prepare Ti oxide nanoparticles by ablating the Ti target immersed in ethanol as shown in the Fig. 1(a). Two hundred laser pulses were applied in this study with laser energy of 900 mJ/pulse and wavelength of 532 nm at frequency of 5 Hz. The distance between the target and the laser beam was kept at 150 mm. Fig. 1(b) shows the schematic illustration of PLA method used in this study. After ablation process, the produced nano-scale Ti oxide colloidal was examined using ultraviolet visible (U.V), Fourier transformation infrared radiation (FTIR) and scanning electron microscope (SEM).

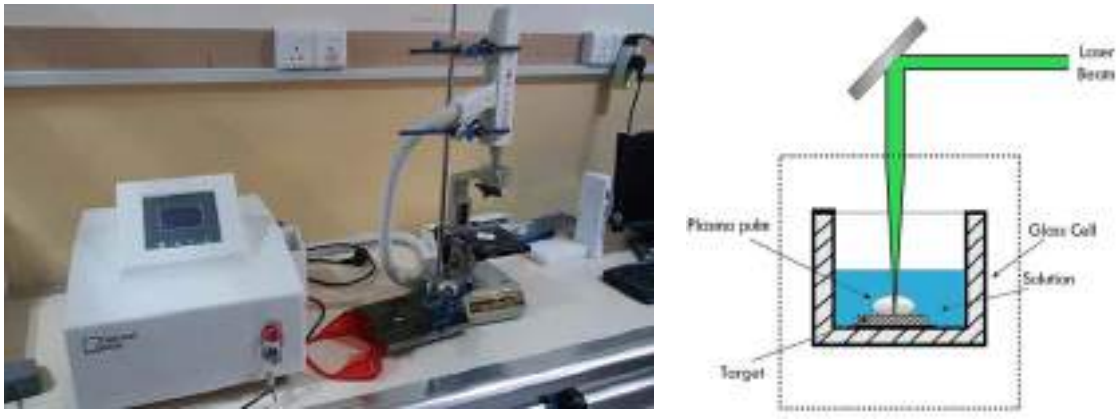

Fig. 1 (a) ND-YAG laser device used and (b) schematic of PLA method.

3- Results and discussion

The Nanoparticles of Ti oxide were obtained using PLA method by direct ablation of pure Ti target submerged in ethanol media. The morphology and size of the nanoparticles produced are governed by laser parameters and the presence of the ethanol solution. In this work, UV spectra was recorded in order to investigate the formation of Ti oxide nanocolloids,. Fig. 2 shows the U.V spectrum of the Ti oxide colloidal. It is very clear from the figure that the peak of the maximum absorption at 200 nm is related to the formation of Ti oxide. The laser ablation can be occurred only throughout the prominent edge of the pulse. This result is in well agreement with the results of the literature [13].

Fig. 3 shows the FTIR spectrum of the nano-scale Ti oxide colloidal produced. The peaks indicated at 475 and 1030 cm^{-1} are assignable to the C=O stretching vibrations. Another strong peak appears at 1300 cm^{-1} is due to the extending vibrations of Ti-O. The peak at 1639 cm^{-1} is assignable to the oscillation vibrations C=C. The last peak appears at 3410 cm^{-1} is owing to the strong stretching vibrations of C≡C-H, these peaks supporting a good formation about Ti oxide. This result has a good approximation with [14].

Fig. 4 shows the SEM images of TiO nanoparticles produced by PLA and deposited on the Si substrate. The figure clearly indicates the formation of crystalline Ti oxide nanoparticles with different grain size characteristics. This SEM test confirms the results obtained by UV spectra, i.e. the formation of Ti oxide nanoparticles during the selected conditions of PLA method through this study. It can be seen that it is easy to differentiate each individual particle. The morphology of the produced Ti oxide nanoparticles has a definite boundary and characters an irregular spherical shape. It should be mentioned here that the laser wavelength and liquid medium have a substantial effect on the morphology of the produced nanoparticles. In addition, some outsized particles are existing in the ethanol liquid. This is might be created by the agglomeration of smaller particles. The noticeable agglomeration in the structure of Ti oxide nanoparticles was appeared which is related to the formation of the nanoscale particles. It well known that the nano-sized particles tend to decrease their high surface energy by developing many agglomerated particles (clusters) during the laser ablation process. Two main mechanisms, nucleation and crystals growth, can be occurred during

the progress of the plasma plume in a liquid, which are responsible on generating different sized clusters. Therefore, an extensive nanoparticle size distribution is achieved (see Fig. 4a).

The information of EDS spectrum test (Fig. 5b) of Ti oxide was also obtained which promotes the formation of Ti oxide particles. The significant peaks related to Ti, oxygen and silicon were achieved, which support this result. The EDS analyses demonstrates that the ablation process resulted in pure and crystalline nanoparticles of Ti oxide with no other impurity phases. This means that the produced nanoparticles of Ti oxide preserve the real Ti target structure and composition. These results are highly anticipated in this study since the induced mechanism of laser ablation is non-reactive.

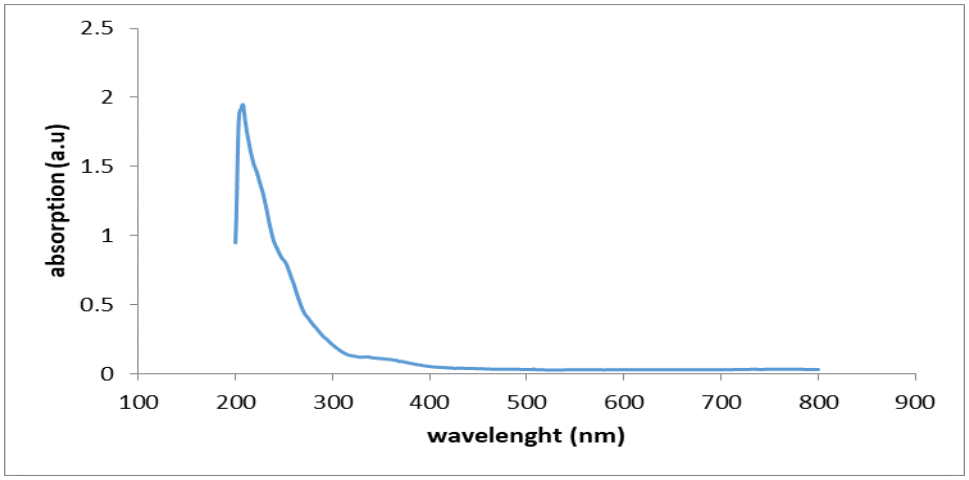

Fig. 2 U.V visible spectrum for Ti oxide colloidal produced in this study

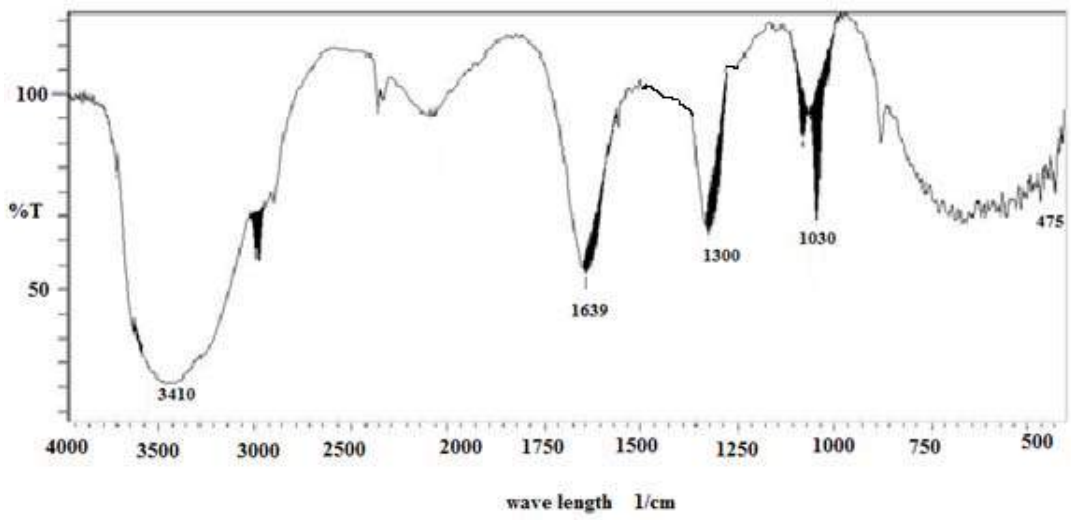

Fig. 3 FTIR spectrum of nanoscale Ti oxide colloidal produced in this study

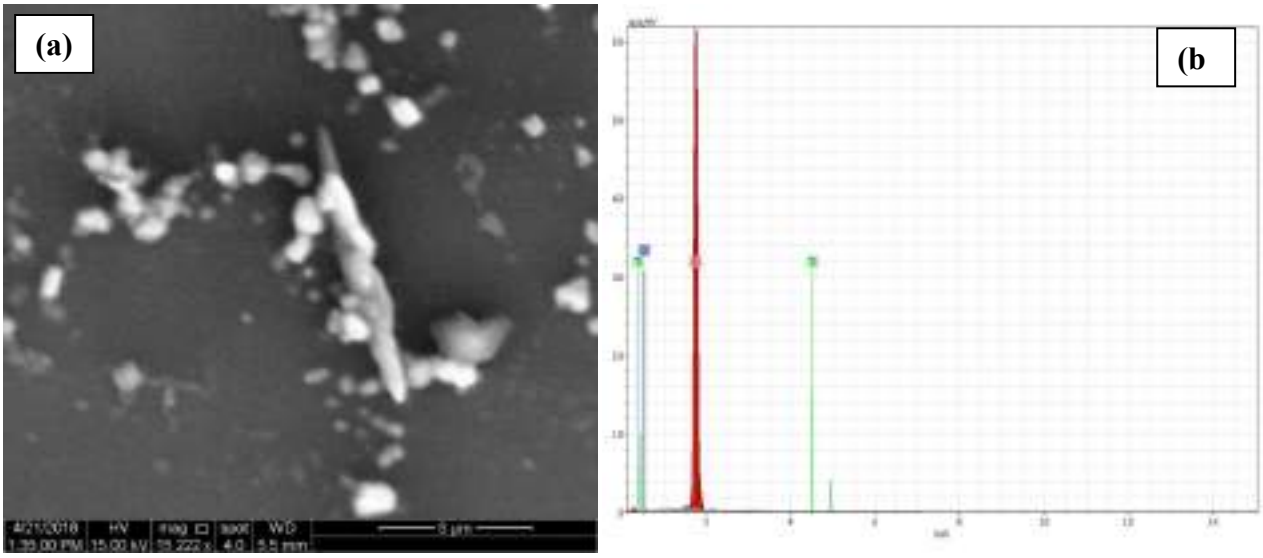

Fig. 4 SEM micrograph (a) and EDS spectrum (b) of Ti oxide nanoparticles

4- Conclusion

The Ti oxide nanoparticles can be synthesized successfully in ethanol media by PLA technique under suitable conditions. The U.V visible spectrum, FTIR and SEM investigations proved the better formation of Ti oxide nanoparticles produced by PLA method. The created Ti oxide nanoparticles were in shape of spherical and semi spherical shapes with different gain size characteristics.

Acknowledgements

The authors would like to thank Dr. Nawfal Hussein Aldujaili at Faculty of science, University of Kufa for his support in providing SEM test.

References

1] Jill E. Millstone, David F. J. Kavulak, Claire H. Woo, Thomas W. Holcombe, Erik J. Westling, Alejandro L. Briseno, Michael F. Toney and Jean M. J. Frechet, Synthesis properties, and electronic applications of size-controlled poly(3-hexylthiophene) nanoparticles, Langmuir 26 (16) (2010) 13056–13061.
[2] OV Salata, A review of Applications of nanoparticles in biology and medicine, Journal of Nanobiotechnology. 2 (3) (2004) 1–6.
[3] Hong wang Zhang , Yi Liu , Shou-heng Sun , Synthesis and assembly of magnetic nanoparticles for information and energy storage applications, Frontiers of Physics in China 5 (4) (2010) 347–356 .
[4] Yoshiyuki Yamamoto,Takahiro Miura, Yutaka Nakae, Toshiharu,Teranishi,MikioMiyake,Hidenobu Hori, Magnetic properties of the noble metal nanoparticles protected by polymer, Physica B:Condensed Matter 329–333 (2003) 1183-1184
[5] Huimin Su, Yingshun Li, Xiao-Yuan Li, and Kam Sing Wong, Optical and electrical properties of Au nano particles in two-dimensional networks: an effective cluster model, Optics Express 17 (24) (2009) 22223-22234.
[6] Yuguo Li, RuiqinPeng, XianwuXiu, XueleiZheng, Xiaosen Zhang, GuannanZhai, Growth of SnO_2nanoparticles via thermal evaporation method, Super lattices and Microstructure, 50 (2011) 511–516.
[7] Zaheer Khan, Shaeel Ahmed Al-Thabaiti, Abdullah YousifObaid, A. Al-Youbi, Preparation and characterization of silver nanoparticles by chemical reduction method, Colloids and Surfaces B: Bio interfaces 82 (2011) 513–517.

[8] E. Moncada, R. Quijada, J. Retuert, Nanoparticles prepared by the sol–gel method and their use in the formation of nano composites with polypropylene, Nanotechnology 18 (33), (2007) 335606–335611.
[9] *Bing Xian Chung, Chuan, PuLiu, Synthesis of cobalt nanoparticles by DC magnetron sputtering and the effects of electron bombardment, Materials Letters 58 (9), (2004) 1437–1440.*
[10] A.S. Nikolov, P.A. Atanasov, D.R. Milev, T.R. Stoyanchov, A.D. Deleva, Z.Y. Peshev, Synthesis and characterization of TiOx nanoparticles prepared bypulsed-laser ablation of Ti target in water, Appl. Surf. Sci. 255 (2009) 5351–5354.
[11] G. García Guillén, S. Shaji, M. I. Mendivil Palma, D. Avellaneda, G.A. Castillo, T.K. Das Roy, D.I. García Gutiérrez, B. Krishnan, Effects of ablation energy and post-irradiation on the structure and properties of titanium dioxide nanomaterials, Appl. Surf. Sci. 405 (2017) 183–194
[12] Haibo Zeng, Xi Wen Du , Subhash C. Singh , Sergei A. Kulinich , Shikuan Yang , Jianping He , WeipingCai, A review; Nano materials via laser ablation/irradiation in liquid, Advance Functional Material 22 (2012) 1333–1353.
[13] A. Nath, S.S. Laha, A. Khare, Effect of focusing conditions on synthesis of titanium oxide nanoparticles via laser ablation in titanium–water interface, Applied Surface Science 257 (2011) 3118–3122.
[14] Jaiveer Singh, Ravi Rathore, NetramKauravand G. S. Okram ,FT-IR and Zeta Potential Measurements on TiONanoparticles, AIP Conference Proceedings 1731, 140067 (2016).

Available online at
http://namrc.uotechnology.edu.iq/index.php/

Nanotechnology and Advanced Materials Research Centre

Proceeding Articles Book 00 (2018) 000–000

6th International Scientific Conference on Nanotechnology, Advanced Materials and its Applications

Study Some Physical Proprieties for Graphene Ribbons Doped by Nitrogen Atoms

Hayder M. Abduljalel, Saif Mohammed Nemea, Mohammed A. Mejbel*
Department of Physics, Collage of Science, University of Babylon, Babylon, Iraq
Corresponding auther:*wellmsc@gmail.com

Abstract

In this paper study structural and electronic proprieties of graphene ribbons by doping (n-types) semiconductor atoms to modify band gap of ribbons. Result showed that all bond length are agreement with experimental calculation. The band gap varies from conductor region to semiconductor by adding (n-type) atoms in different position from ribbon.. showed that ability to use these ribbons as hetro structure semiconductor device. All calculation is employed by using Density Function Theory (DFT).

Keyword: Density Functional Theory, Ionization Potential, Electron Affinity, Energy Gap, Higher Occupied Molecular Orbitals and Lower Unoccupied Molecular Orbitals.

1- Introduction

The discovery of graphene, a single layer of Carbon atoms has added a new class of materials to the material family, that of one-atom thick two- dimensional materials [1]. Graphene was discovered in 2004, when Geim and co-workers at Manchester University isolated single - layer samples from graphite[2].The electronic, mechanical and thermal properties of graphene are very sensitive to lattice imperfections; therefore study of changing in this material is critically important. Furthermore, the other graphene allotropes such as carbon nanotubes (armchair, zigzag and chiral) and fullerenes have been investigated enormously [3]. Ideal graphene is a semimetal contains a vanishing density of states at the Fermi energy with remarkably high carrier mobility at room temperature and therefore a single-layer graphene can be considered as a semiconductor with zero energy gap or behave as semimetallic material [4]. Doped graphene received a huge attention from scientists and researchers to understand the properties of their properties (electrical and mechanical), especially doping graphene by Boron and Nitrogen or both and also the possible applications of this doped material [5]. Doping is a powerful way to modify the properties of graphene-like materials. The electronic properties of mentioned materials could be tailored by controlling doping parameters. Spectroscopy and microscopy have been used to characterize doped graphene. Doped graphene could be used in electronics, energy storage, and bio-devices [6]. Doping of semiconductor is necessary for various device applications. Exploiting chemistry at its reactive edges was shown to be an effective way to dope an atomically thin (GNR) for realizing new devices in recent experiments [7].

Theoretical Background

The Schrödinger equation, which was proposed by Erwin Schrödinger in 1925, is central to the development of the theory of quantum mechanics. Any problem in the electronic structure of matter is covered by Schrödinger equation [6]:

$$\hat{H}\Psi = E\Psi \qquad (1)$$

Where Ψ is the wave function, it expresses the mathematical form of the de Broglie wave associated with the particle, $\hat{H}$ is the Hamiltonian operator, and E is the total energy of the system. Once the Schrödinger equation is solved, all electronic properties of the system can be calculated. The Hamiltonian operator, H, consists of two terms the kinetic energy of the electrons and the nuclei (T) and potential energy components (V) [7]:

$$\hat{H} = \hat{T} + \hat{V} \qquad (2)$$

$$\hat{H} = \hat{T}_e + \hat{T}_n + \hat{V}_{ne} + \hat{V}_{ee} + \hat{V}_{nn} \qquad (3)$$

Where ($\hat{T}_e$) and ($\hat{T}_n$) are the kinetic energy operators of the electrons and nuclei, respectively. ($\hat{V}_{ne}$) the coulomb attraction between the nuclei and electrons, ($\hat{V}_{ee}$) the coulomb repulsion between electrons, ($\hat{V}_{nn}$) the coulomb repulsion between nuclei [8]. The kinetic energy operators are represented as:

$$\hat{T}_e = -\frac{\hbar^2}{2m_e}\sum_i \nabla_i^2 \quad (4)$$

$$\hat{T}_n = -\frac{\hbar^2}{2M_A}\sum_A \nabla_A^2 \quad (5)$$

Where: m_e and M_A are the electron and nuclear mass, respectively, ∇_i^2 is the laplacian operator of i electrons, which in Cartesian coordinates has the form:

$$\nabla_i^2 = \frac{\partial^2}{\partial x_i^2} + \frac{\partial^2}{\partial y_i^2} + \frac{\partial^2}{\partial z_i^2} \quad (6)$$

The potential energy operators are represented as:

$$\hat{V}_{ne} = -\sum_A \sum_i Z_A \frac{e^2}{r_{Ai}} \quad (7)$$

$$\hat{V}_{ee} = \sum_{i<j} \frac{e^2}{r_{ij}} \quad (8)$$

$$\hat{V}_{nn} = \sum_{A<B} Z_A Z_B \frac{e^2}{R_{AB}} \quad (9)$$

Where $r_{ij} = |\vec{r}_i - \vec{r}_j|$ and Z_A is the charge of nuclei A, r_{Ai} is the distance between nucleus and electron, r_{ij} is the distance between i electron and j electron and R_{AB} is the distance between A nucleus and B nucleus [9].

The first major step in simplifying the general molecular problem in quantum mechanics is the Born-Oppenheimer approximation. This approximation is based on the fact that the nuclear masses are much greater than those of the electrons. Therefore, nuclei move much more slowly and they are nearly
fixed compared with the electrons motion [10].

Computational Details.

- **Geometrical proprieties**

Geomatrical proprieties are employed by using Density Functional Theory (DFT) with large basis set 6-31G with hybrid function B3ylp. The calculation of bond length for ribbons under study, the bonds C-C, C=C, C- - C, C-H, N-N and C-N varies in values [1.4594-1.5123], [1.3554-1.3769], 1.3915-1.4466], 1.0837-1.0857], [1.4032-1.4505] and [1.3874-1.4392] on series agreements with previous study [11][12]. Figure (1-1) show the ribbons under study.

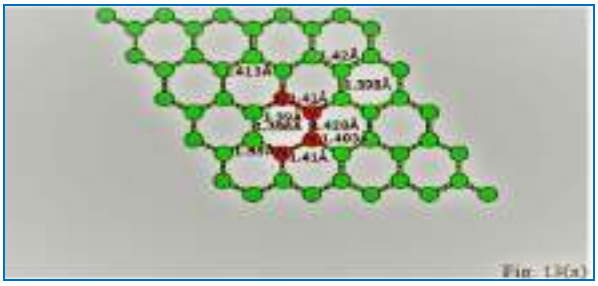

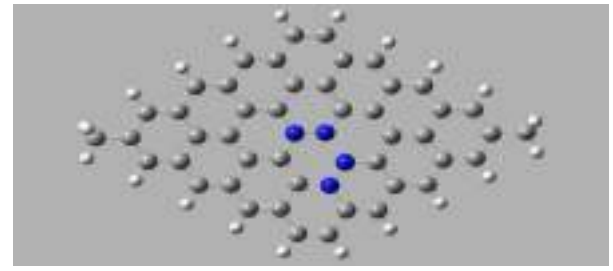

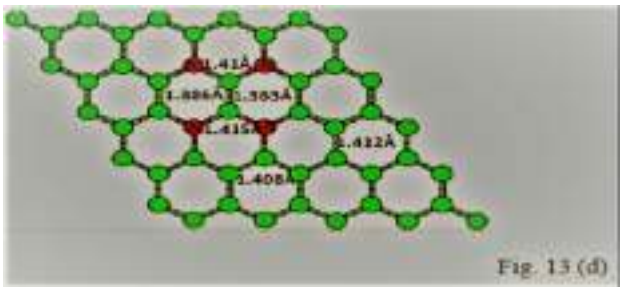

Fig. 13 (d)

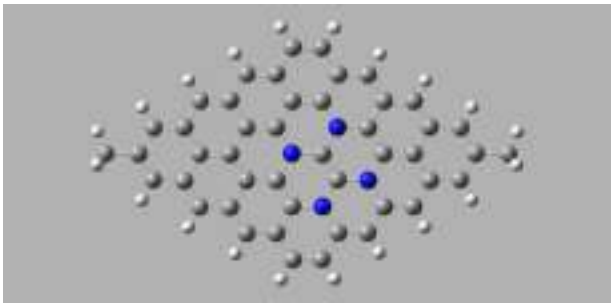

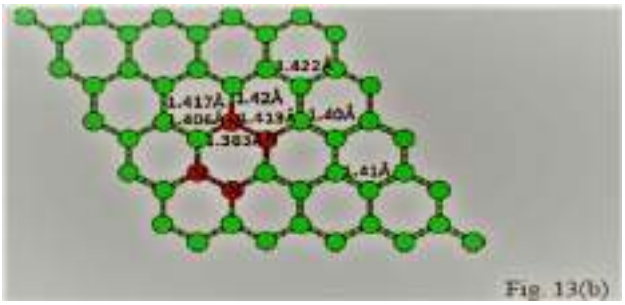

Fig. 13(b)

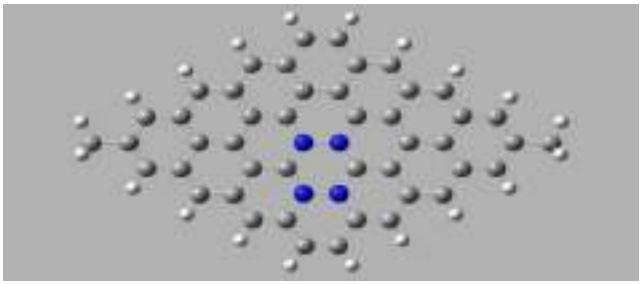

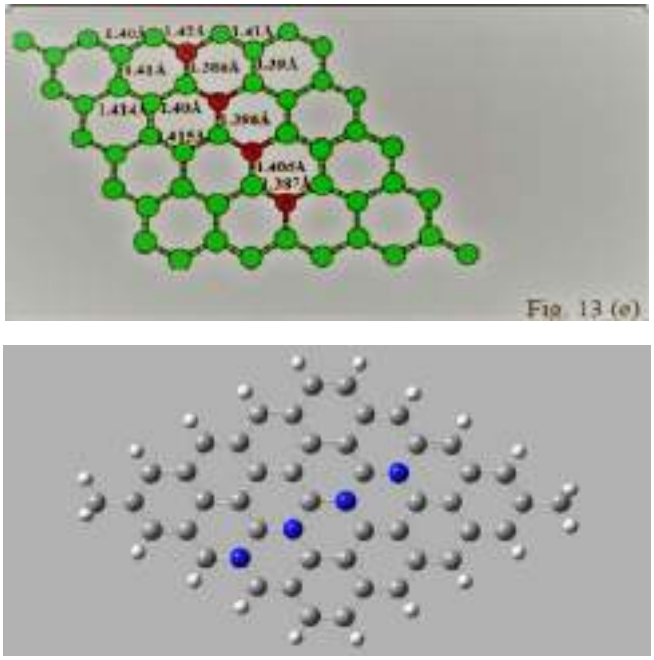

Figure (1-1) show the geometrical structure for present and previous study

- **Electronic Properties**

In this study we use the Nitrogen atoms to doping ribbon by using special positions in graphene nanoribbon, the electronic properties (H, S. IP, EA and Eg) the values of energy gaps compration with [India]. All these calculation was employed by using DFT at basis set 6-31G with hybrid function B3YLP. Table 1 show the values of energy gap, HOMO and LUMO for present study compared with reviewer study measured in electron volt unit (e.V). Calculation explain that ribbons doping in nitrogen atoms have same behaver when we using (DFT) approximation, the gap in values resulting back to types of approximation used in calculation.

Table (1-1) HOMO, LUMO and Energy Gap for ribbons under study

1.1.1. Samples	1.1.2. HOMO e.V	1.1.3. LUMO e.V	1.1.4. Present Energy Gap e.V	1.1.5. Reviewer Energy Gap e.V[13]
1.1.6. 1	1.1.7. -3.7328	1.1.8. -3.02831	1.1.9. 0.70	1.1.10. 0.04
1.1.11. 2	1.1.12. -3.74532	1.1.13. -2.46178	1.1.14. 1.28	1.1.15. 0.29
1.1.16. 3	1.1.17. -3.54042	1.1.18. -2.28055	1.1.19. 1.25	1.1.20. 0.5
1.1.21. 4	1.1.22. -3.57471	1.1.23. -2.21742	1.1.24. 1.35	1.1.25. 0.54

The electronics states was change with replacing the atom of carbons by doped atoms, this changes is important to determine amount of energy needed to change transition of electron from HOMO to LUMO, generally HOMO > LUMO to raise an electrons that transition through band gap. The values of energy gap all in ranges of semiconductor region this result back to from bonding between (C-N) raise one free electron that make in changes in energy gap states.

The property of ionization energy and electron affinity determine amount of energy that ribbons needed to denoted or acceptation of an ions for atoms that built graphene nanoribbon, from tables (2) show the values of ionization energy and electronic affinity from ribbons under study in electrons volt unit. From the result ribbon 4 have small value of ionization energy that mean have small amount of energy to denote or acceptation an electron and becomes an ions.

Table (1-2) shows IP and EA for ribbons under study in electron volt unit.

1.1.25.1. Samples	1.1.25.2. IP	1.1.25.3. EA
1.1.25.4. 1	1.1.25.5. 3.732805	1.1.25.6. 3.028312
1.1.25.7. 2	1.1.25.8. 3.745322	1.1.25.9. 2.461779
1.1.25.10. 3	1.1.25.11. 3.540423	1.1.25.12. 2.280554
1.1.25.13. 4	1.1.25.14. 3.574709	1.1.25.15. 2.217424

Figure (2) shows curve IE and EA for ribbons under study in electron volt unit.

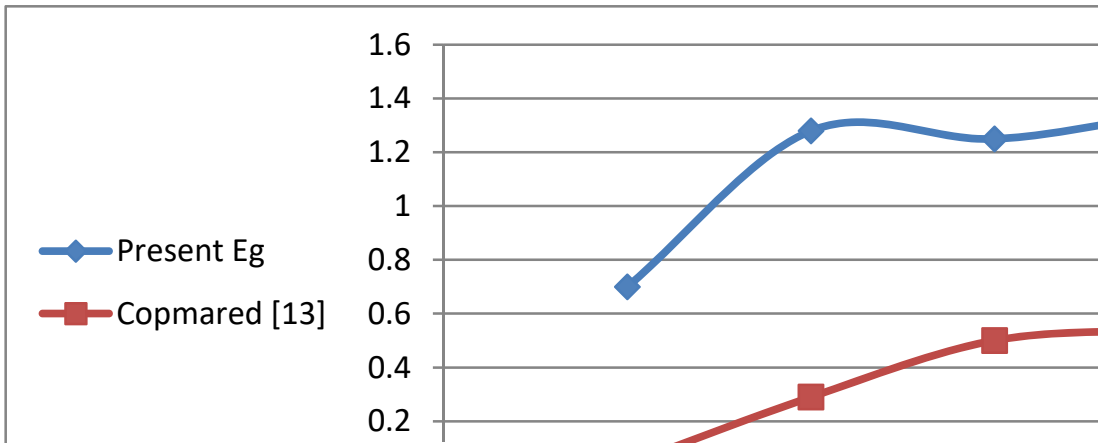

Figure (1-2) show the curve of energy gap for present study and [13].

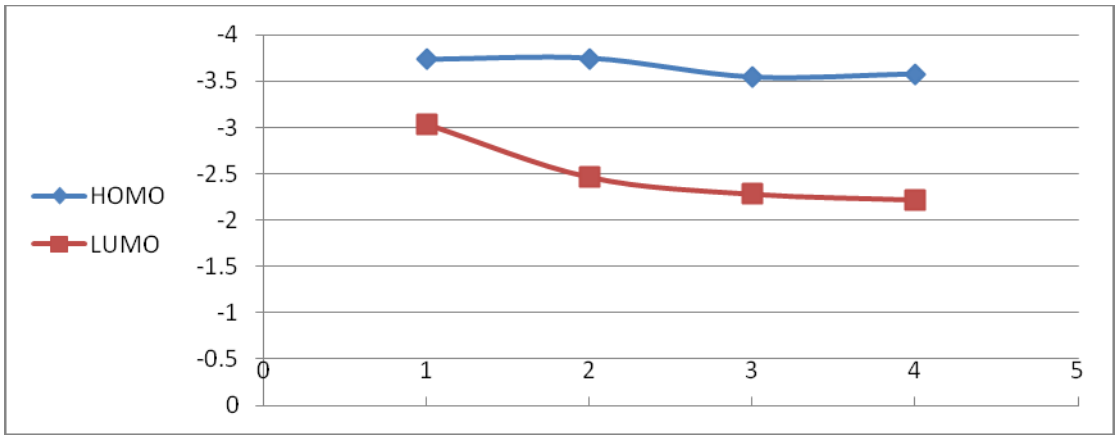

Figure (1-3) the value of HOMO and LUMO for ribbons under study

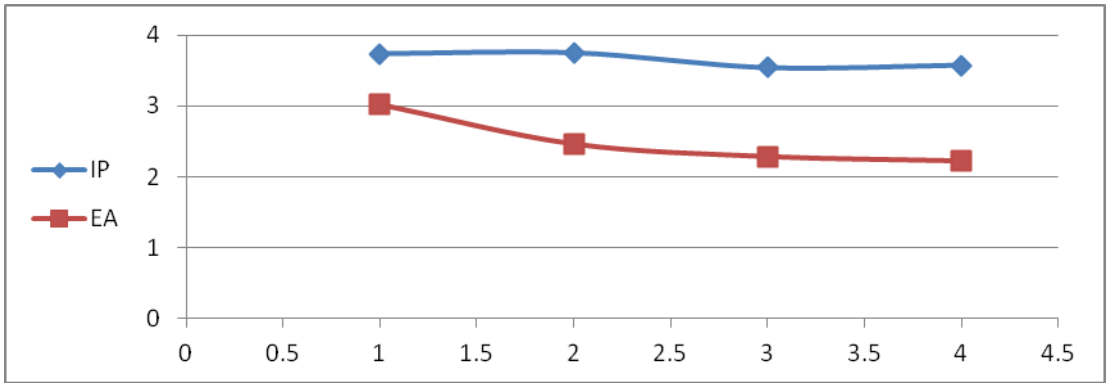

Figure (1-4) the value of IP and EA for ribbons under study

2- Conclusion

1- All geometrical proprieties are agreements with previous study this mean all structure have good relax.
2- The present band gaps are agreement with previous study in behavier and this result is expectable.
3- Graphene – Nitrogen ribbons lie in nanostructure with value –V/T is equal 2.0054.
4- The electronic properties change from semimetal to semiconductor when we change position of nitrogen atoms and this clear in ribbon (4).

Future work

1- Use CASTP package to study optical properties.
2- Use Dmol3 to calculate (I_V) proprieties.
3- Use Phosphorus atom instead of nitrogen and study electronic properties.

Study the vibrational and thermodynamics proprieties for same ribbons.

References

1. K. S. Novoselov, A. K. Geim, S. V. Morozov and D. Jiang, Science 306, 666-669 (2004).
2. A. K. Geim and K. S. Novoselov, Nature Mater. 6, 183-191(2007).
3. P. Avouris, Chen Z and V. Perebeinos Nat. Nanotechnol. 2, 605 (2007).
4. A. H. Castro Neto, F. Guinea, N. M. R. Peres, K. S. Novoselov and A. K. Geim, Rev. Mod. Phys.81, 109–162 (2009).
5. Daniel R. Cooper, Benjamin D'Anjou, Nageswara Ghattamaneni, Benjamin Harack, Michael Hilke, Alexandre Horth, Norberto Majlis, Mathieu Massicotte, Leron Vandsburger, Eric Whiteway, and Victor Yu, ISRN Condensed Matter Physics, 2012, 501686 (2012).
6. C. L. Tang, "Fundamentals of Quantum Mechanics for Solid State Electronics and Optics", NY publishes, Ithaca, (2004).
7. H. F. Hameka, "Quantum Mechanics: A Conceptual Approach", Leiden University, John Wiley & Sons, Inc., (2004).
8. A. Cox., "Introduction to Quantum Theory and Atomic Structure", Lecture in Organic Chemistry, University of Oxford, (1995).
9. D. D. FITTS*," Principles of Quantum Mechanics: as Applied to Chemistry and Chemical Physics"*, Cambridge University Press, New York, (2002).
10. P. A. Cox, ***"introduction to Quantum Theory and Atomic Structure"***, Oxford University Press Inc., New York, (1996).
11. Hamid Ibrahim Abbood and Ramla Abdulnaby Abdulzahra, " Density Functional Theory Calculations of donor- σ-bridge -acceptor Molecules" Babylon university, 2013
12. Dr. Hayder M. Abduljalil and Saja Majeed Mohammed, " A Study of the Effect of Various Substituents on the Electronic and Thermal Properties of Cyclopentane", Babylon university, 2015.
13. Pooja Rani and V.K. Jindal1, " Designing band gap of graphene by B and N dopant atoms", Panjab University, 2016.

Available online at
http://namrc.uotechnology.edu.iq/index.php/

Nanotechnology and Advanced Materials Research Centre

Proceeding Articles Book 00 (2018) 000–000

6th International Scientific Conference on Nanotechnology, Advanced Materials and its Applications

Corrosion Protection Improvement of Gas Turbine Blades by Coating with Nano Oxides

Ali Hassan Saleh, Khairia Salman Hassan, Ahmad Mohammad Salman
Middle Technical University- Institute of Technology, Baghdad, Iraq
University of Technology, Baghdad, Iraq
* Corresponding Author E-mail, Ali_aljibury1956@yahoo.com

Abstract

In this study corrosion behavior of gas turbine blades was investigated. Blade material is nickel-based superalloy Inconel 738LC. Blades were coated with Nano TiO_2 of different percentages (0.2, 0.4& 0.6%) using electroplating technique. Electrochemical test rig with potential state (cycling test) is adopted for this purpose. Corrosion current was determined to calculate corrosion rate by Tafel-equation. Nano ZrO_2 with percentage 0.4% was also used for comparison. The results showed that TiO_2 improves the corrosion resistance for blades whenever percentage of oxide increases. Corrosion rate of specimens coated with 0.6% Nano TiO_2 and 0.4% Nano ZrO_2 decreases by 3.84 and 4.48 times respectively compare to the specimen without coating.

Keywords: corrosion, gas turbine, blades, Nano oxides, Coating.

1- Introduction

Mechanical power can be received from gas turbine engine. The operation of gas turbine includes receiving of air from atmosphere by compressor blades, then the power is received by working fluid causing the pressure and temperature increase rapidly. The air to be send to the combustion chamber creating combustion and producing high temperature up to 1400ºC–1500ºC. Corrosion is considered one of the main damage types of gas turbine blades which can be occur as internal and external surface damage [1,2]. Ash deposits of low melting point creates in liquid fuel because of presence trace metal impurities such us (Na, K, S & V) and lead to blade corrosion. Na and K impurities causes occurring of high temperature corrosion which known as sulfidation attack. Hot section component suffers inter-granular pitting when sodium sulfates creates and reacts with sulfur in the fuel. Lower melting point ash deposits can form, when both vanadium and sodium impurities are present, further increasing the risk of corrosion. Recently many researchers studied the corrosion state of gas turbine blades and proposed solutions of this problem. Carlos A Estrada M.(2007)[3] presented and discussed improvement of materials using a new technologies to increase the emissions, performance, and reliability in gas turbines blades. He used several methods to apply ceramic coating to the surface of the turbine blade. Besides the technology aimed to produce better coats, to obtain high temperature gap in locations especially sensible for gas turbine operation. Mehdi T. Naeem, et al.(2008)[4] used blades of gas turbine made of nickel-base alloy to study the failure analysis of them. They found that the corrosion and erosion are the main problem of blades. They observed that the thermal fatigue crack initiates from crack on both sides of blade coating. Creep mechanism causes in initiation and propagation of the substrate intergranular crack. Yasmina A., et al.(2008)[5] estimated the safe life of first stage high pressure gas turbine blades. They found that advanced stress occur due to several parameters involving complex mechanisms of damage, such as corrosion caused on the stressed elements. Barry Ruggiero (2011)[6] discussed the presence of a corrosion threat within Trans Canada's system of hot end components. He found some characterization of the nature of the corrosion itself on power turbine discs. Julian D. Osorio, et al. (2012)[7] studied the thermal barrier coatings as thermal isolation and protection against corrosion and high temperature erosion. The authors used two different thermal barrier coatings and concluded that the life of a coating is governed by the Thermally-Grown Oxide (TGO) thickening, which is influenced by the surface defects and roughness of the Bond Coat (BC). V. Naga Bhushana Rao, et al (2014)[8] analyzed the failure of gas turbine blade used in marine applications, and they found that the blade might have suffered both corrosion and erosion in addition the blade can be weakened because of hot corrosion which reduced the thickness of the blade material. M. Nicolaus, et al (2015)[9] proposed two procedures to repair turbine blades: cladding and/or high temperature brazing. They concluded that the use of a microstructure similar to the original shape, reduce the crack formation in further operations and lead to a new-like material behavior of the repaired material. M. Sohaciu, et al.(2016)[10] studied the material used in the construction of two hydroelectric turbines on the river Olt. They concluded that the most important source of corrosion was the quality of material (inclusions, discontinuities) resulting from the elaboration and casting process and the corrosion behavior of steel T8NCuMC130 was much better than steel G-X4CrNi13-4. In the current study

improvement of corrosion behavior of gas turbine blades by coating them with two Nano high melting oxides was investigated in order to determine the suitable oxide and its percentage.

2- Experimental procedure:

2.1- Material

The material of gas turbine blade employed in Baghdad South Electrical Station is nickel-based superalloy Inconel 738LC. It was adopted as a material in this study as shown in fig.1. Chemical composition analysis of the blade material was carried out in the Engineering Industries Specialize Institute as shown in table (1).

2.2- preparation of test specimens

According to G71-30 ASTM standard, specimens of corrosion test (15x15x3mm) were cut from blade and prepared for coating through several steps, firstly sequence grind by emery paper of grades (180-250-400-500-800-1000) with water using rotary grinder. Then the specimens were polished using special cloth with solution of Al_2O_3 of grain size 0.3µm. In order to obtain microstructure of blade material two specimens were treated with solution contains 5%HNO_3 and 4%HCL for 3 minutes. Fig.(2) illustrates the microstructure of blade material that obtained using Nikon ME-600 optical microscope supplied with Nikon camera DXM-1200F.

2.3- Classification of samples

The specimens of corrosion test were categorized into five samples as shown in table 2.

2.4- Coating process

Coating of specimens carried out in solid chromium solution contains metal ceramic materials. The preparation of this solution includes 275g/L CrO_3 and 2.75g/L H_2SO_4. For coating with Nano TiO_2, three different percentages (0.2,0.4 &0.6%) of this oxide with 25nm grain size were added to the solution separately to get three groups of specimens coated with three different percentages of Nano TiO_2. One group of specimens were coated with Nano ZrO_2 by addition 0.4% of this oxide of 25nm grain size to the solution independently and this selection of percentage was considered as a medium value of TiO_2 percentages. Electrical current of 25A/100cm^2, mixing velocity 500rpm and 45min time were adopted as parameters of coating. Before coating, mixing of Nano oxides with solution was carried out using magnetic mixing method for 15 minute at 1500rpm.

2.5- Cell preparation

Coating cell is a cubic container of dimensions (20x20x20cm). It contains two electrodes made of lead and 7% antimony in addition coating solution. Specimen join with anode for one minute, then coating was carried out through join the specimen with cathode while anode joined with power supply of DC current.

2.6- Corrosion test

Solution of 3.5% NaCl was used as a media of corrosion test. PH of solution was measured using PH meter and found 6.7. Corrosion test was carried out on potentiostat at velocity rate 3mv/sec using electrochemical cell of three electrodes as shown in fig. 3. Corrosion potential (Ecorr) and corrosion current (Icorr) were measured to determine corrosion rate using Tafel equation (eq. 1) [11].

$$C.R\ (m.p.y) = 0.13 * I_{corr} * eq.wt / \rho \quad \text{----------} \quad (1)$$

Where :
C.R = corrosion rate
m.p.y= mille per year
I_{corr}= current of corrosion (mA)
eq.wt = equivalent weight of the material subjected to corrosion
ρ= density of the material subjected to corrosion (g/cm^3).

3- Results and discussion

Corrosion rate of all specimens were calculated using Tafel equation depending on values of (I_{corr}) and (E_{corr}) measured experimentally as shown in table 3. Fig.(4) shows the relationship between current and potential obtained from corrosion test for all specimens. It is clear that the values of those parameters varied according to the corrosion rate of each specimen. The results showed that the corrosion resistance improved for all specimens coated with Nano TiO_2 and Nano ZrO_2. Also the results indicate that the corrosion rate decreases as percentage of Nano TiO_2 increases in coating solution. Improvement of corrosion resistance of specimen coating with Nano ZrO_2 is better than all percentages of Nano TiO_2. The reason of that belongs to the high melting temperature of ZrO_2. Corrosion rate at value of 0.4%ZrO_2 close to the value of 0.6%TiO_2. Corrosion rate decreases 3.84 times and 4.48 times of specimens coated with 0.6% TiO_2 and 0.4% ZrO_2 respectively. Fig. (5) shows the pitting occurs in microstructure of specimens and the difference between them is clear because of corrosion rate of each one. From the above results it is obvious that coating oxides applied to the gas turbine blades give these blades ability to resist the corrosion during their operation in the environment contains harmful elements in the fuel such as (Na, S, V) which lead to create ash of low melting temperature causes corrosion when adhesive to

the blade [12], so the layer of high melting temperature oxide helps in raise the melting temperature of ash and results in protect the blades from corrosion and increase their lifetime[13].

4- Conclusions

1. Gas turbine blades can be protected from corrosion by coating them with Nano TiO_2 or Nano ZrO_2.
2. Corrosion rate decreases with increase of oxide percentage in coating solution.
3. Nano ZrO_2 improves corrosion resistance of blades more than Nano TiO_2.
4. 0.4% Nano ZrO_2 decreases corrosion rate by 4.48 times compare to blade without coating.
5. 0.6% Nano TiO_2 decreases corrosion rate by 3.84 times compare to blade without coating.

Table 1: Chemical composition of blade.
Material (Inconel 738LC)

element	C	Co	Ti	Cr	Al	W	Cu
Wt%	0.03	4.8	5.2	12.7	0.01	3.5	0.4
element	Mn	S	P	Mo	Fe	Ni	
Wt%	0.7	0.002	0.04	1.7	0.4.	Base	

Table 2: Classification of samples.

Code of sample	Description
A	Specimens without coating
B	Specimens coating with 0.2%Nano TiO_2
C	Specimens coating with 0.4%Nano TiO_2
D	Specimens coating with 0.6%Nano TiO_2
E	Specimens coating with 0.4%Nano ZrO_2

Fig.1: Employed gas turbine blade.

Table 3: Corrosion parameters and corrosion rate.

Symbol	Ico mA	ECor.mv	Corrosion Rate m.p.y.
A	0. 0613	-151.3	0.22
B	0. 295	-198.3	0. 129
C	0.198	-130.6	0.087
D	0.167	-227.2	0.07
E	0.14	-131.5	0.06

Fig.2: Microstructure of blade material.

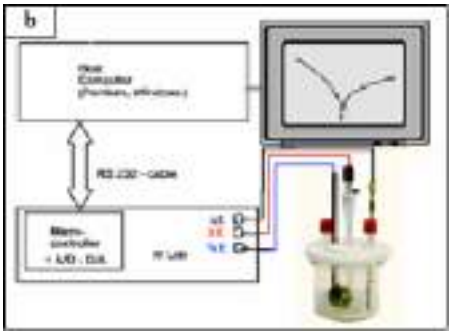

Fig.3: a) Corrosion test device, b) Electrodes map.

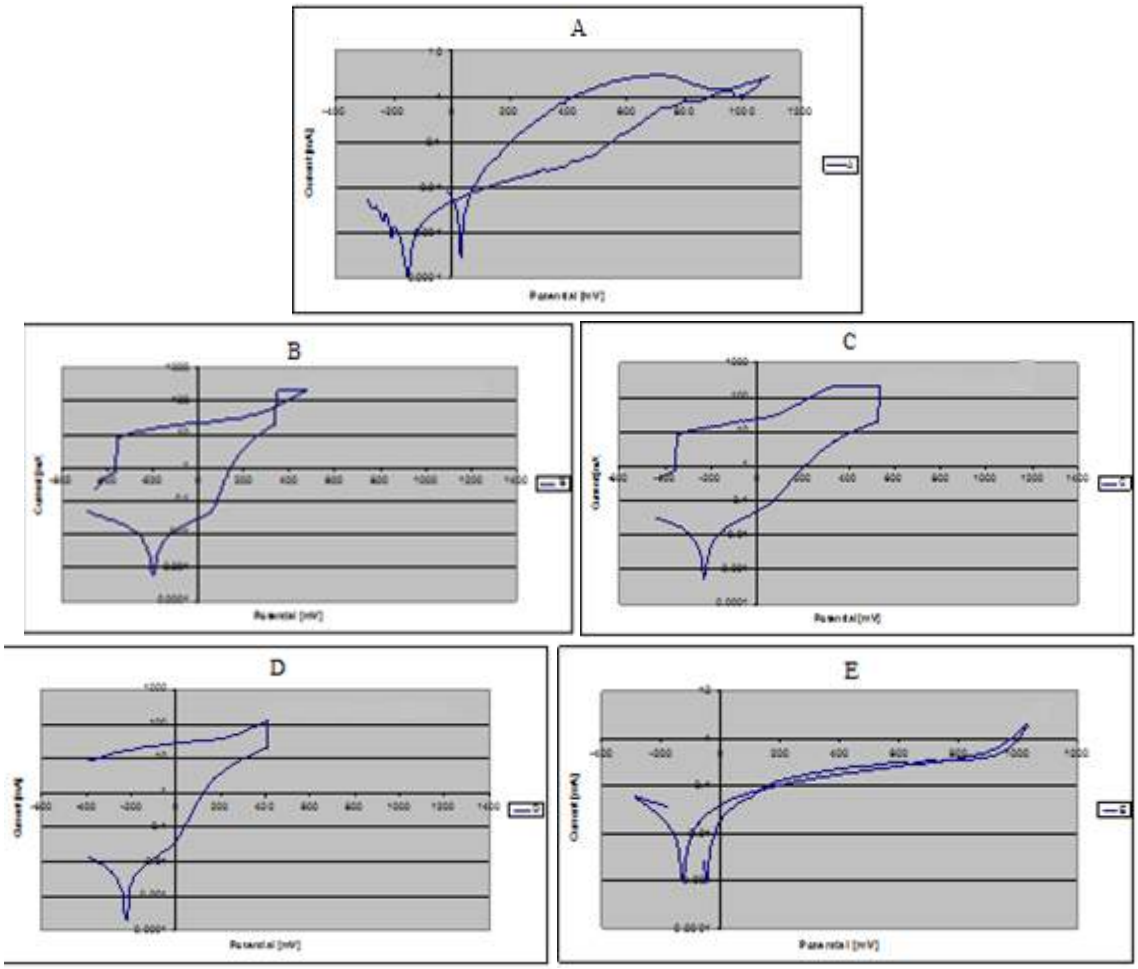

Fig. 4: Relationship between current and potential through corrosion test.

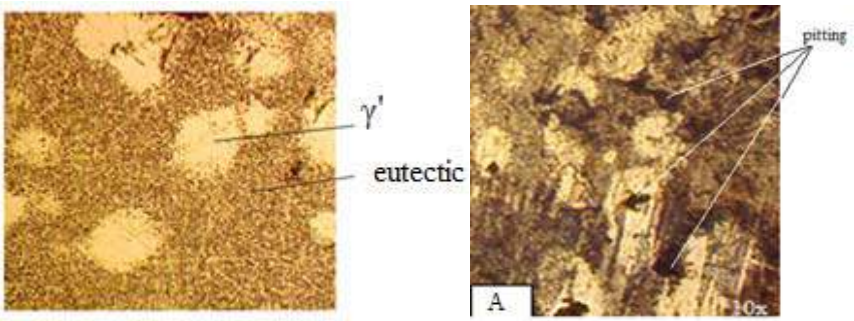

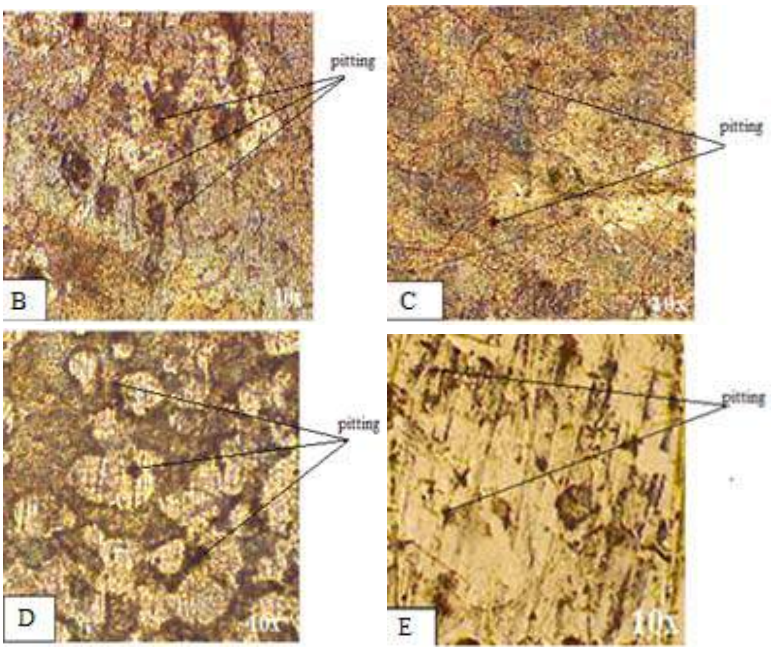

Fig. 5: Microstructure of specimens according to the code of sample after corrosion test.

References

1- Kurt H. Stern Metallurgical and Ceramic Protective Coatings ISBN 0412544407 Chapman & Hall
2- H. I. H. Saravanamuttoo, Gordon Frederick Crichton Rogers, Henry Cohen Gas turbine theory ISBN 013015847X Prentice Hall
3- Carlos A Estrada M.," New Technology Used In Gas Turbine Blade Materials", Scientia et Technica Año XIII, No 36, Septiembre 2007.
4- Mehdi Tofighi Naeem, Seyed Ali Jazayeri, Nesa Rezamahdi," Failure Analysis of Gas Turbine Blades" Proceedings of the 2008 IAJC-IJME International Conference ISBN 978-1-60643-379-9.
5- Yasmina Assoul, Samira Benbelaid, Vera Šijački - Žeravčić, Gordana Bakić, Miloš Đukić," Life Estimation of First Stage High Pressure Gas Turbine Blades" Scientific Technical Review, Vol.LVIII , No.2 , 2008.
6- Barry Ruggiero," Operator Experience With Non-Gas Path Power Turbine Disc Corrosion as an Emergent Equipment Integrity Threat"19 th Symposium of the Industrial Application of Gas Turbines Committee Banff, Albert, Canada, October 17-19, 2011.
7- Julian D. Osorio, Alejandro Toro, Juan P. Hernandez-Ortiz, "Thermal Barrier Coatings For Gas Turbine Application: Failure Mechanisms And Key Microstructural Features" Dyna, year 79, No. 176,. Medellin, December, 2012, pp. 149-158.
8- V. Naga Bhushana Rao, I. N. Niranjan Kumar, K. Bala Prasad," Failure Analysis of Gas Turbine Blades in a Gas Turbine Engine Used For Marine Applications" International Journal of Engineering, Science and Technology Vol. 6, No. 1, 2014, pp. 43-48.
9- M. Nicolaus, B. Rottwinkel, K. Möhwald, C. Nölke, S. Kaierle, H. J. Maier, V. Wesling," Future Regeneration Processes For High Pressure Turbine Blades" Deutscher Luft- und Raumfahrtkongress 2015.
10- M. Sohaciu, S. Ciuca*, D. Savastru, G. Coman, A. Predescu, A. Berbecaru, C. Cotrut, E. Matei, I. A. Gherghescu, C. Predescu," Influence of turbine blades fabrication conditions on their lifetime" Optoelectronics and Advanced Materials – Rapid Communications Vol. 10, Iss. 3-4, March - April 2016, pp. 257 – 261.
11- Rana Afif Majed, "Effect of Molybdate Anions on Corrosion Behavior of Stainless Steel 304 in 0.1M NaCl Solution", Eng. & Tech. Journal, Vol. 27, No.16, 2009.
12- Kadhim Finteel Al-Sultani, "A pilot System for Evaluation of Hot Ash Corrosion Inhibition in Power Generation Boilers",Ph.D.Thesis The Technology University, 2003.
13- Abd ALWahed, Kadhum Fantel, Zainab Mohammed, "Inhibition Vanadic Corrosion by Using Magnesium Oxide in Oil Fired Boilers" The Iraqi Journal For Mechanical And MaterialEngineering, Special Issue (C), January 2016.

Available online at
http://namrc.uotechnology.edu.iq/index.php/

Nanotechnology and Advanced Materials Research Centre

Proceeding Articles Book 00 (2018) 000–000

6th International Scientific Conference on Nanotechnology, Advanced Materials and its Applications

Characterization of R.F Sputtering $(SnO_2)_{1-x}$ $(TiO_2: CuO)_x$ Films as Gas Sensor

Bushra A. Hasan, Sara S.Mahmood, Aws F. Rauuf
University of Baghdad, College of Science, Department of Physics
**Ministry of Science and Technology
Corrosponding auther:bushra_abhasan@yahoo.com

Abstract

Radio frequency sputtering technique were used to prepare thin films $(SnO_2)_{1-x}$ $(TiO_2: CuO)_x$ with different compositions at different substrates like glass and silicon wafer. Different techniques were subjected to analyze the structure, morphology and composition the prepared thin films like x-ray diffraction and atomic force microscope. The structural investigation showed that tin oxide films were polycrystalline while the composites films are amorphous convert to polycrystalline by annealing at 873K . The average grain size increases from 82.79 nm to 90.85 nm with increase tin oxide ratio from 0 to 80 % and decreases to 68.03nm with the increase of tin oxide ratio to 50% samples. The optical properties such as optical energy gap , refractive index extinction coefficient , and real and imaginary parts of dielectric constants are measured using the transmittance spectra in the wavelength range (200- 1100) nm. The maximum sensitivity 66.24 % for $(SnO_2)_{60}(TiO_2:CuO)_{40}$. The results explained in term of grain size variation accompanied the addition of titanium and copper oxide.

Keywords: Gas Sensors, R.F-Sputtering, SnO_2 Thin Films.

1- Introduction

Metal oxide semiconductor (MOS) are used as gas sensors based on the principle of the variability of electrical conductivity of metal oxides when exposed to the gas. The various parameters that affect the function of the solid state gas sensors include the adsorption ability, electro physical - chemical properties, catalytic activity, as well as the adsorption /desorption properties of the surface [1].

The surface characteristics with specific catalysts have resulted in major advances in sensor technology where both reactivity and selectivity in a material's responses were improved [2].

Tin oxide SnO_2 is a special oxide material because it has a suitable physicochemical properties and lower cost compared to actual available materials.

It has been found that certain semiconductor additives improve the performance of tin oxide in terms of sensitivity and selectivity, compared to bare tin oxide [3].

CuO (p-type) and TiO_2 (n-type) can be used to enhance the gas sensor response of (n-type) oxides SnO_2 which have been extensively investigated as gas sensing materials, the mixing structure was used for increased the number of surface electrons and to obtain the optimal oxygen vacancy density [4]. The conduction band of SnO_2 is lower than TiO_2 which causing electrons to pass from TiO_2 to SnO_2 when the film is formed [5]. $(SnO_2)_{1-x}(TiO_2:CuO)_x$ thin films used as Nitrogen dioxide (NO_2) gas sensor, (NO_2) is oxidizing gas and strongly electronegative that will react with the oxygen ion and keep the electrons at the surface that means the electron concentration in the metal oxide will decrease, resulting in an increase of the depletion layer thickness and an increase of the electronic resistance [6] .

The aim of this study to evaluate the advantages of combining SnO_2 with CuO and TiO_2 films and comparing their gas sensitivity to those of SnO_2 film.

2- Materials and Method

Metal oxide thin films have been deposited using the sputtering method, which is one of the most extensively used techniques for the films deposition.

Sputtering can be defined as a non-thermal vaporization process where surface atoms are ejected from a solid surface by momentum transfer from an atomic-sized energetic bombarding particle which is usually a gaseous ion accelerated by the plasma and Sputtered atoms that condensed on a substrate to form a solid film[7,8].

Interactions of particle with surface of target depends on the type of ions (charge, mass, impact angle and ion energy), the nature of the target surface atoms. An advantage of sputtering technique is relatively cheap deposition method, low substrate temperatures, uniformity, good adhesion of films on substrate and high density [9].

Sputtering is performed in a vacuum chamber (Fig. 1),

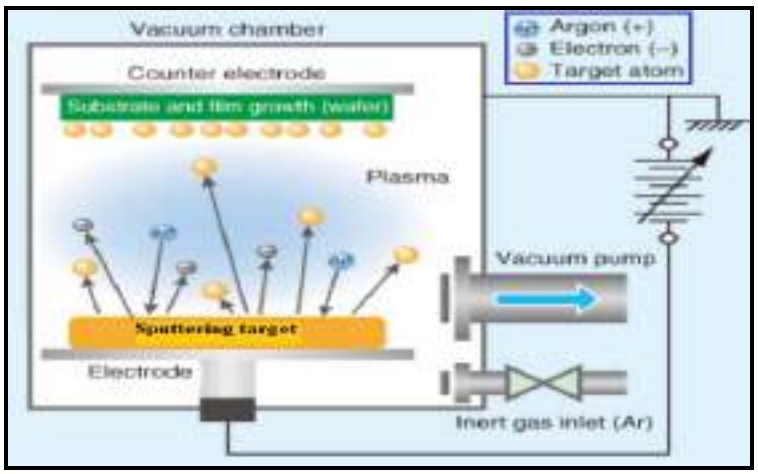

Figure (1):.rf- Sputtering process in a vacuum chamber [11]

after evacuation of air, an inert gas, such as argon or helium. A high voltage DC or AC power supply is attached to the cathode (target), which is fabricated of the material which deposited on the sample. The kinetic energy of the ions is sufficiently high to free atoms from the target surface. Hence, the escaped sputtered atoms deposit on the surface of the sample [10].

In this study, we selected a semi conductive metal oxide material as tin oxide (SnO_2)and $(SnO_2)_{1-x}(TiO_2{:}CuO)_x$ thin films were deposited by using RF- sputtering technique on glass and Silicon substrates using a pure SnO2 and $SnO_2{:}TiO_2$: CuO target. The target is mixed different stoichiometry of powder form ($90SnO_2$-$5CuO$-$5TiO_2$),($80SnO_2$-$10CuO$-$10TiO_2$),($70SnO_2$-$15CuO$-$15TiO_2$),($60SnO_2$-$20CuO$-$20TiO_2$) and($50SnO_2$-$25CuO$-$25TiO_2$)% as a ratios. Initially the single/multi- chemicals component were calcinated at 1273K for 2 hrs. in air atmosphere in furnace. The components are mixed together in an acetone for 1/2 hrs. to form medium homogeneous mixture. The mixture is heating at 373K for one hour duration. After the calcinations, the fine powder was formed by using Agate Mortar and pressed in bulk pellet form (Diameter 5cm, 2cm high) as sputtering targets for thin film preparation. The target to substrate distance was kept fixed at 7.5 cm and a power of 100 Watt was supplied to the target ,the temperature was maintained at 373Kand the working pressure was kept at 8×10^{-5} torr For a period of time 3 hour.

The thickness of the film ranged between 100 and 150 nm. All of these samples were annealed at 873K for 1 hr. in a pure air atmosphere after deposition.

Instruments:

1-Thickness of films:

The thicknesses can be determined using optical interference fringe method was calculated by using equation [12]

$$t = \frac{\Delta x}{x} x \frac{\lambda}{2} \quad \ldots\ldots\ldots\ldots (1)$$

Δx: The displacement of the fringe system across the film substrate step

λ: is the wavelength of the monochromatic light , x:is the fringe spacing

2- Structure properties:

The deposited thin films were characterized by X-ray diffraction (XRD), using CuKα radiation with a wavelength λ = 1.5418 °A at 2θ values between 20◦ and 80◦. The average of crystallite size (D) was evaluated using the Scherrer equation as follows:

$D = 0.9\lambda/\beta \cos\theta$ …… (2)

where λ, β, and θ are the X-ray wavelength, the full width of half maximum (FWHM) at the diffraction peak, and Braggs diffraction angle, respectively. The lattice constants (a, b, and c) for crystal can be determined by the equation for tetragonal .

$$\frac{1}{d^2} = \frac{(h^2 + k^2)}{a^2} + \frac{l^2}{c^2} \quad \text{…… (3)}$$

where d and (hkl) are the inter planar distance and Miller indices, respectively[13].

Atomic force microscopy (AFM) is a widely used for investigating quantifies surface topography and the surface microstructure (surface roughness and the grain size). The criterion of operation is measuring repulsive or attractive forces between the tip (cantilever) and the sample surface in constant height.

3-Optical Properties:

Optical absorbance and transmittance were limited in the wavelength range (300-1100nm) using UV-VIS spectrophotometer at room temperature. The transmission T is given by:

$$T = A\exp(-\frac{4\pi kt}{\lambda}) \quad \text{…… (4)}$$

Where (*A*) is a constant, (k) is the extinction coefficient and (t) is the thickness. The absorption coefficient (α) could be calculated using the relation:

$$\alpha = \frac{2.303\ A}{t} \quad \text{…… (5)}$$

Where (t) is the film thickness and (A) is the absorption, optical band gap calculated from equation which is known as Tauc relation is:

$$\alpha h\nu = B(h\nu - E_{opt})^r \quad \text{…… (6)}$$

where (hν) is the absorbed light energy, (n) is the parameter that distribution of the density of states and (B) is a constant or Tauc parameter , here (r = 1/2) for direct and (r = 20 for indirect transitions. In order to calculate the optical constant refractive index (n) and the extinction coefficient (k) of the films at different wavelengths, we can use the relations:[12]

$$R = \frac{(n-1)^2 + k^2}{(n+1)^2 + k^2} \text{ ....(7)}$$

$$k = \frac{\alpha\lambda}{4\pi} \text{ ....(8)}$$

The values of (n) and (k) were used to calculate both(ε_r)and imaginary (ε_i) parts of the dielectric constant were obtained by the formulas:

$\varepsilon_r = n^2 - k^2$ ……(9)

$\varepsilon_i = 2nk$ ……(10)

Where (ε_r) determines the maximum energy that can be stored in the material,(ε_i) is called the loss factor and represents the absorption of electrical energy by a dielectric material [12,14] .

4-Gas sensing properties:

•The sensitivity (S) is defined as S = (Ra − Rg)/Rg, where(Ra) the film resistance in dry air and (Rg) is the resistance in presence of test gas , measured at respective temperatures. A positive value of S implies film resistance decreases on gas exposure and vice versa.

• The selectivity of a sensor is defined as (sensitivity of sensor for interfering gas) / (sensitivity towards desired gas).

•The response time is the time interval over which resistance attains a fixed percentage (usually 90%) of final value when the sensor is exposed to concentration of the gas. A small value of response time is referring to a good sensor.

• The recovery time is the time interval over which resistance reduces to 10% of the saturation value when the sensor is exposed to concentration of the gas and then placed in clean air. A good sensor should have a small recovery time so that sensor can be used again and again [15,16,17].

The Al electrodes were formed by used thermal evaporation which active area of the sensor was about 1cm square. The sensors were placed on top of a hot plate in a test chamber atmosphere. The hot plate was heated to 373, 473 and 573K for the experiment.

3- Results and discussion

1-3 Structural Properties

Figure (2) X-ray diffraction patterns for pure SnO_2 and $(SnO_2)_{1-x}(TiO_2{:}CuO)_x$ thin films with different mixing ratios x=0.1, 0.2, 0.3, 0.4 and 0.5 were prepared by RF sputtering technique at 373K and annealed at 873K for 1 h.

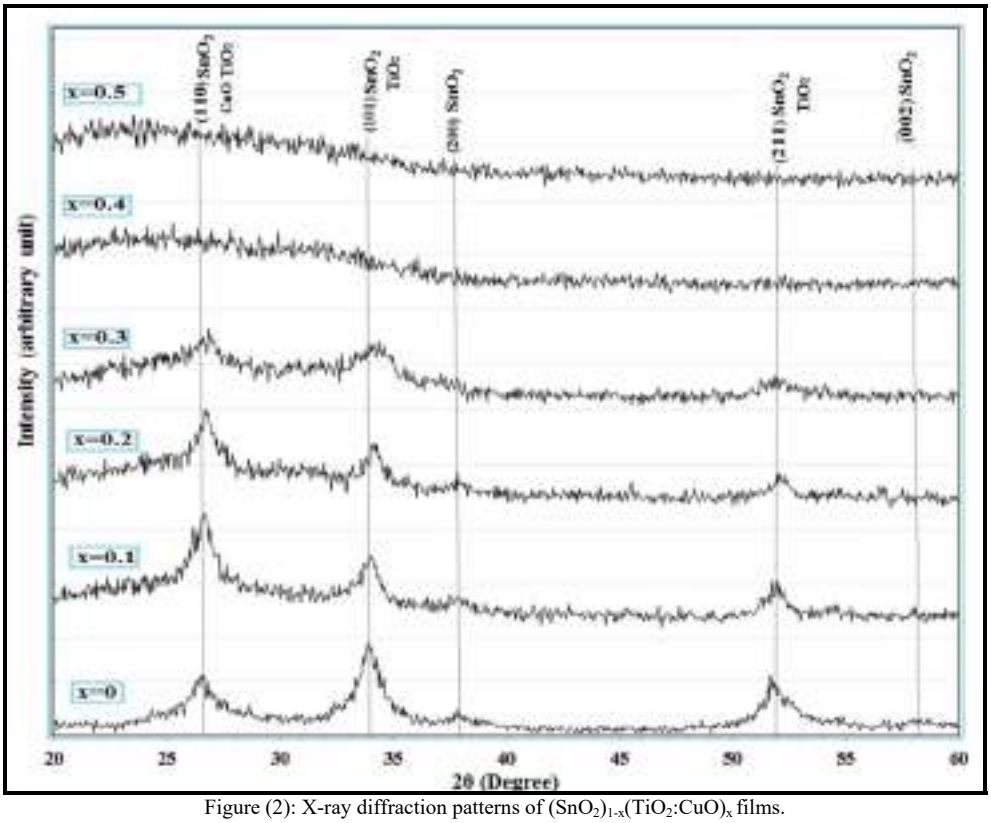

Figure (2): X-ray diffraction patterns of $(SnO_2)_{1-x}(TiO_2:CuO)_x$ films.

The peaks of XRD patterns of SnO_2 thin film are polycrystalline with tetragonal structure were analyzed and compared with JCPDS standard card (No. 41-1445) [18]. The rutile phases of SnO_2 thin films has a tetragonal unit cell showing a preferred orientation along (110) which is in agreement with Liang et.al. [19] and Sharmaa et.al. [20]. Broad and well defined reflections corresponding to (110), (101), (200) and (211) planes of SnO_2 were observed at 2θ= 26.5803°, 33.886°, 37.875 °and 51.7098° ,respectively, which are in good agreement with [21].

The X-ray diffraction spectra revealed polycrystalline structure of mixed of $(SnO_2)_{1-x}(TiO_2:CuO)_x$ thin films at mixing ratios of $(TiO_2:CuO)_x$ where x values 0.1,0.2 and 0.3 which post annealed at 873K for one hour in air this result was in good agreement with Edelman et.al [22]. While thin films with mixing ratios of $(TiO_2:CuO)_x$ at x values 0.4 and 0.5 remain amorphous (declare no diffraction peaks). Indeed the crystallite size was decreased from 9.3 nm at 2θ =26.6321° to 5.6nm at 2θ= 26.7358° with increasing of mixing ratios $(TiO_2:CuO)_x$ from x=0.1 to x=0.3 .

Table (1) XRD patterns of $(SnO_2)_{1-x}(TiO_2:CuO)_x$ films.

Value of x	2θ (Deg.)	FWHM (Deg.)	d_{hkl}Exp. (Å)	C.S (nm)	hkl	d_{hkl}Std. (Å)	Phase
	26.5803	1.3472	3.3508	6.1	(110)	3.3498	SnO_2,TiO_2,CuO
0	33.8860	1.2436	2.6433	6.7	(101)	2.6439	SnO_2,TiO_2
	37.8756	0.9327	2.3735	9.0	(200)	2.3686	SnO_2
	51.7098	1.3990	1.7664	6.3	(211)	1.7642	SnO_2,TiO_2
	26.6321	0.8808	3.3444	9.3	(110)	3.3498	SnO_2,TiO_2,CuO
0.1	33.9896	0.9845	2.6354	8.4	(101)	2.6439	SnO_2,TiO_2
	37.8238	0.7254	2.3766	11.6	(200)	2.3686	SnO_2
	51.9171	0.9326	1.7598	9.5	(211)	1.7642	SnO_2,TiO_2
	26.6321	1.0363	3.3444	7.9	(110)	3.3498	SnO_2,TiO_2,CuO
0.2	34.1451	0.9326	2.6238	8.9	(101)	2.6439	SnO_2,TiO_2
	37.8756	0.6736	2.3735	12.5	(200)	2.3686	SnO_2
	52.0725	0.9844	1.7549	9.0	(211)	1.7642	SnO_2,TiO_2
	26.7358	1.4508	3.3317	5.6	(110)	3.3498	SnO_2,TiO_2,CuO
0.3	34.2487	1.6062	2.6161	5.2	(101)	2.6439	SnO_2,TiO_2
	51.9171	1.6580	1.7598	5.3	(211)	1.7642	SnO_2,TiO_2
0.4	Amorphous						
0.5	Amorphous						

Noteworthy the preferred orientation of the films depends on the substrate temperature, mixing concentration and time deposition. The possibility of interaction between SnO_2 and CuO, TiO_2 depend on the preparation technique leading to a homogeneous phase exists or may be due to the low thickness ∼150 nm of metal oxide obtained from RF- sputtering method [23].

2- Atomic Force Microscope (AFM) Results:

Figure (3) illustrate the surface morphology of pure SnO_2 and $(SnO_2)_{1-x}(TiO_2:CuO)_x$ thin films

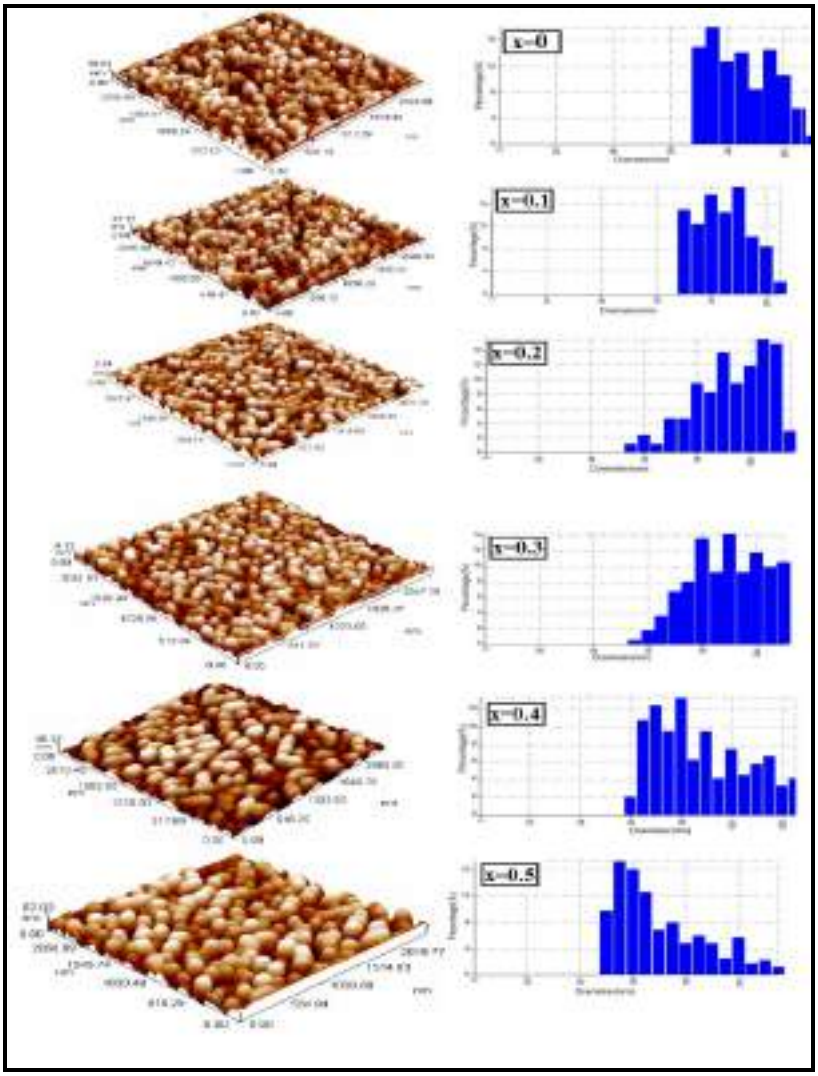

Figure (3): 3D AFM images of $(SnO_2)_{1-x}(TiO_2:CuO)_x$ films

3- Optical Properties:

3-1 Transmission and Absorption Coefficient:

The optical properties of pure SnO_2 and $(SnO_2)_{1-x}(TiO_2:CuO)_x$ thin films with different mixing ratios x=0.1, 0.2, 0.3, 0.4 and 0.5 were prepared by RF sputtering technique at 373K and annealed at 873K for 1 h were measured. The optical properties include the measurements of transmittance, absorption coefficient, optical energy gap (E_g) and optical constants such as extinction coefficient (k), refractive index (n) and dielectric constant (ε).The optical transmission of $(SnO_2)_{1-x}$ thin films measured in the wavelength range (300-1100nm) plotted in figure (4).

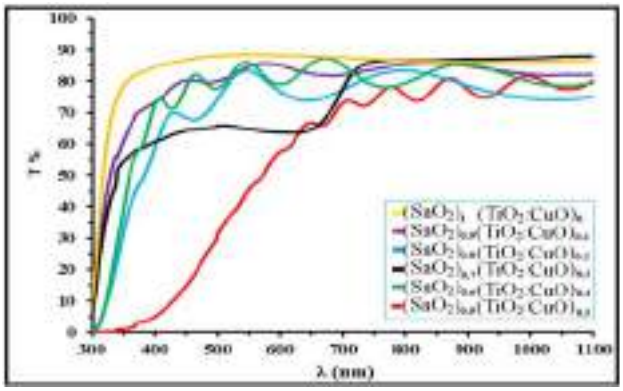

Figure (4): The transmission as a function of (λ) of ($SnO_2)_{1-x}(TiO_2:CuO)_x$ films.

It is clear that the transmission decreased with increasing of mixing ratio $(TiO_2:CuO)_x$, indeed the transmission decreased from 87.52% to 73.03% by increasing of x value from x=0 to x=0.5 , see Table(2).

The reduction of the transmission gives indication that the prepared thin films become more opaque to the incident light which giving rise to high absorption and consequently shift the optical energy gap to lower energy side as seen in the later section. Spectrum was formed due to occurrence of the phenomenon of overlap between film surface and the substrate surface. The presence of well-defined interference fringes pattern in the optical transmission spectra indicates the growth of good quality and homogeneous thin films [24].

Figure (5) shows the variation of the absorption coefficient α of $(SnO_2)_{1-x}(TiO_2:CuO)_x$ films. The absorption coefficient shows the valuable increase from (2963 to 20957) cm^{-1} at λ=500 nm with increasing of mixing ratio $(TiO_2:CuO)_x$ in prepare thin films. The increase of absorption coefficient related with the tail states established by oxide addition which responsible to the additional absorption.

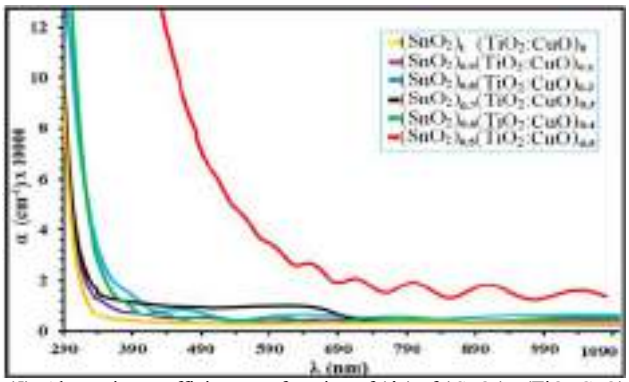

Figure (5): Absorption coefficient as a function of (λ) of ($SnO_2)_{1-x}(TiO_2:CuO)_x$ films

3-2 The Optical energy gap:

The values of optical band gap of $(SnO_2)_{1-x}$ $(TiO_2:CuO)_x$ films were estimated from the linear portion of Tauc plot which is between $\alpha h\nu^2$ and photon energy (hν) .A typical direct optical energy gap were determined in the highest absorption region were α $>10^4$ cm^{-1} by plotting $(\alpha h\nu)^{1/r} = 0$ where r = 0.5 for direct allowed transition. The value of E_g for pure SnO_2 was found to be about 3.6 eV which is close to the corresponding reported value for SnO_2 thin film by [25].

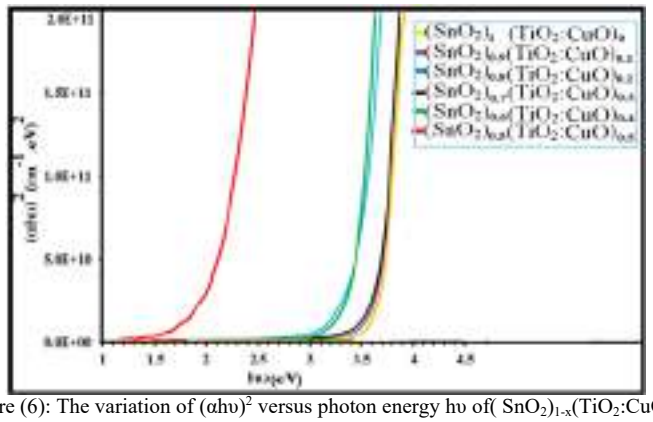

Figure (6): The variation of $(\alpha h\upsilon)^2$ versus photon energy hυ of($SnO_2)_{1-x}(TiO_2:CuO)_x$.

The optical energy gap was decreased by increasing of mixing ratio $(TiO_2:CuO)_x$. The decreasing of optical energy gap related with increasing of crystallite size. Also the localized states introduced by the two oxides responsible about the addition absorbance which lead to visual decrease of the optical energy gap [26].

When the mixing ratio increases, the edge of absorption shifted towards the long wavelengths (low energies). The values of E_g are given in Table (2).

3-3 The Extinction Coefficient and Refractive Index:

The variation of extintion coefficint with wavelength is shown in figure (7). It is clear that k gets to rise but non-systmatic manner as mixing ratio $(TiO_2:CuO)_x$ increased in the deposted thin films. Indeed k increased from 0.017 to 0.117 at λ=500 nm by increasing of x value from 0 to 0.5 , the increase of k related with the increase of α , the values of k are listed in Table (2).

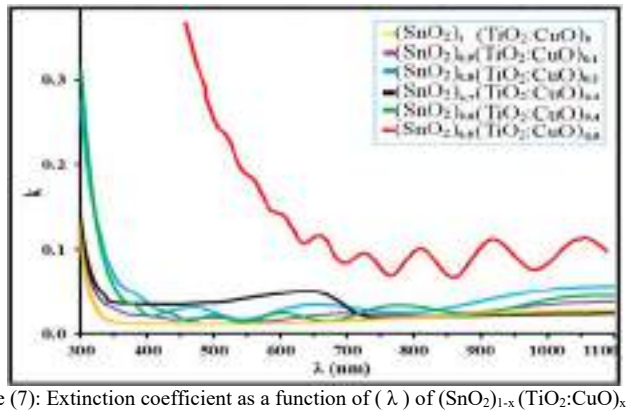

Figure (7): Extinction coefficient as a function of (λ) of $(SnO_2)_{1-x}(TiO_2:CuO)_x$ films.

The wavelength dependence of refractive index is shown in figure (8). The results show that n was increased in non-regular manner by increasing of mixing ratio $(TiO_2:CuO)_x$. The increase of n is attributed to the reduction of transmission giving rise to high opaque material while the reduction of n is related to the inverse manner.

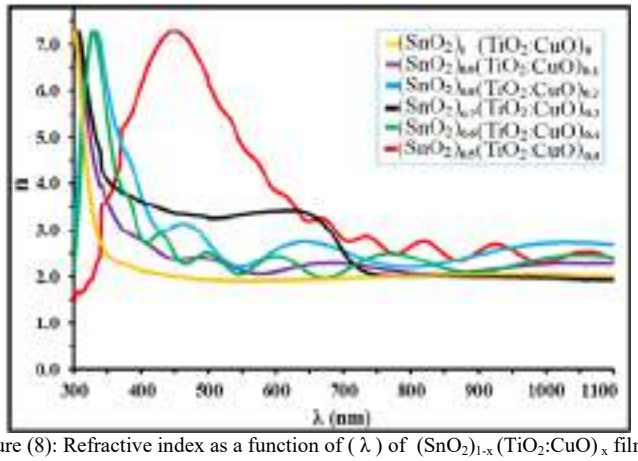

Figure (8): Refractive index as a function of (λ) of $(SnO_2)_{1-x}(TiO_2{:}CuO)_x$ films .

3-4 The Real and Imaginary Dielectric Constants:

Figure (9) and (10) show the change in the real and imaginary part of the dielectric constant with wavelength in the range (300–1100) nm for pure SnO_2 and $(SnO_2)_{1-x}(TiO_2{:}CuO)_x$ thin films with different concentrations. The variation of real dielectric constant ε_r has the same trend to that of n corresponding to eq.(9), thus similar explanation can be given to illustrate the behavior with SnO_2 concentration.

While the variation of imaginary dielectric constant ε_i has the same trend of the k corresponding to eq.(10), thus the increasing of ε_i related to the increase of absorption coefficient.

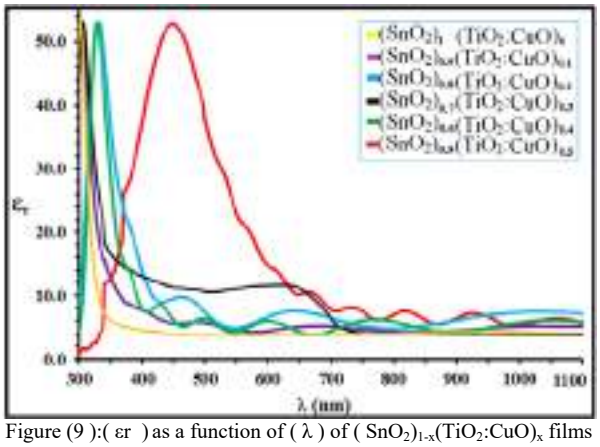

Figure (9):(εr) as a function of (λ) of ($SnO_2)_{1-x}(TiO_2{:}CuO)_x$ films

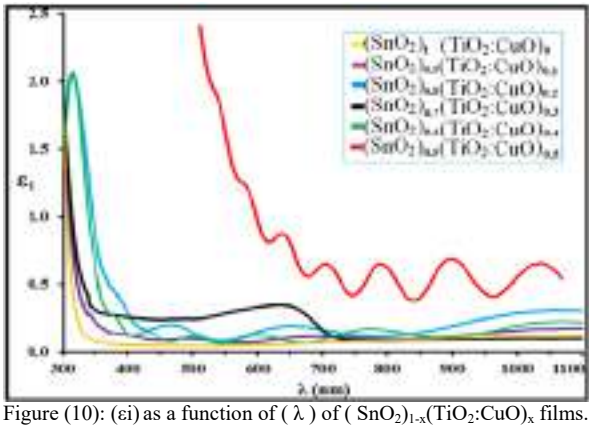

Figure (10): (εi) as a function of (λ) of ($SnO_2)_{1-x}(TiO_2:CuO)_x$ films.

Table (2) Values of optical energy gap and optical constants at λ=500 nm of $(SnO_2)_{1-x}$ $(TiO_2:CuO)_x$ films

Value of x	T%	α (cm^{-1})	k	n	ε_r	ε_i	E_g (eV)
0	87.52	2963	0.017	1.962	3.851	0.065	3.6
0.1	81.96	4422	0.025	2.275	5.177	0.112	3.5
0.2	77.30	5722	0.032	2.543	6.468	0.162	3.3
0.3	77.57	5645	0.031	2.528	6.389	0.159	3.45
0.4	85.05	3598	0.020	2.101	4.413	0.084	3.25
0.5	73.03	20957	0.117	2.799	7.819	0.654	1.9

4 Thin Films Gas Sensors:

4-1 Effect of Operation Temperature on the Sensor:

Figures (11) to (16) show the variation of resistance as a function of time with on/off gas valve for $(SnO_2)_{1-x}(TiO_2:CuO)_x$ thin films to NO_2 oxidizing gas at

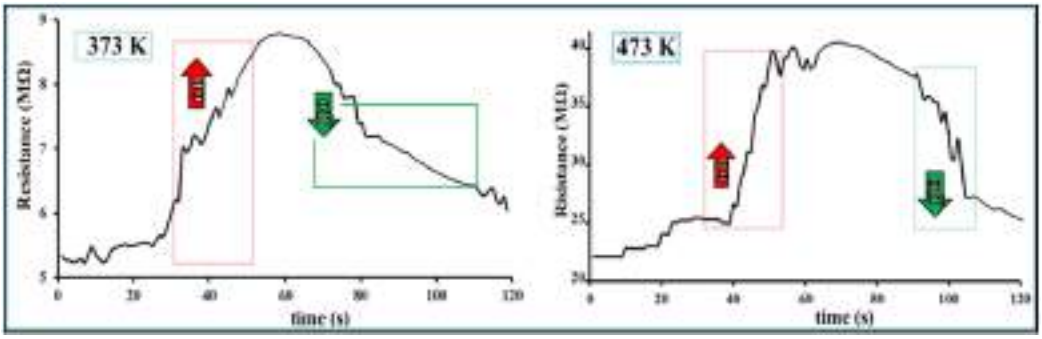

Figure (11): Variation of resistance as a function of time for pure SnO_2 deposited on n- Si at different temperatures.

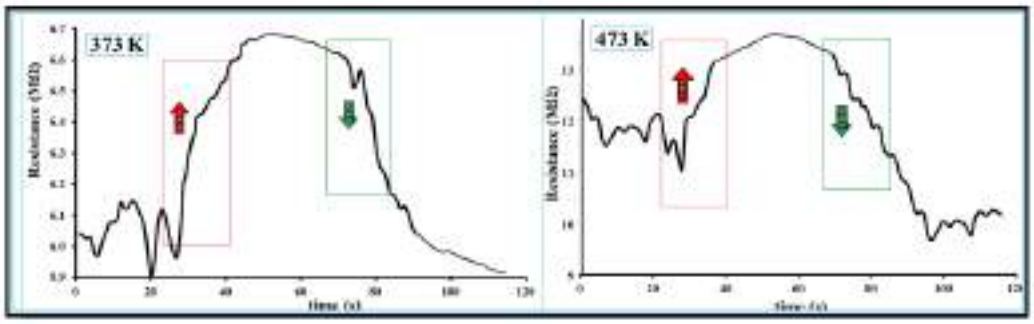

Figure (12): Variation of resistance as a function of time for $(SnO_2)_{0.9}(TiO_2{:}CuO)_{0.1}$ deposited on n- Si at different temperatures.

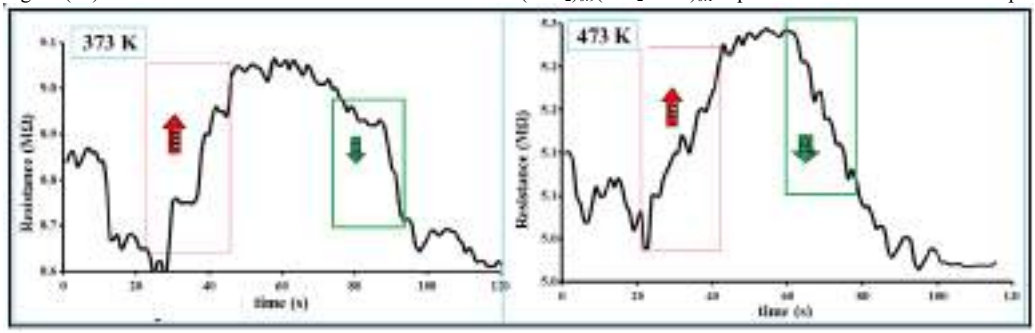

Figure (13): Variation of resistance as a function of time for $(SnO_2)_{0.8}(TiO_2{:}CuO)_{0.2}$ deposited on n- Si at different temperatures.

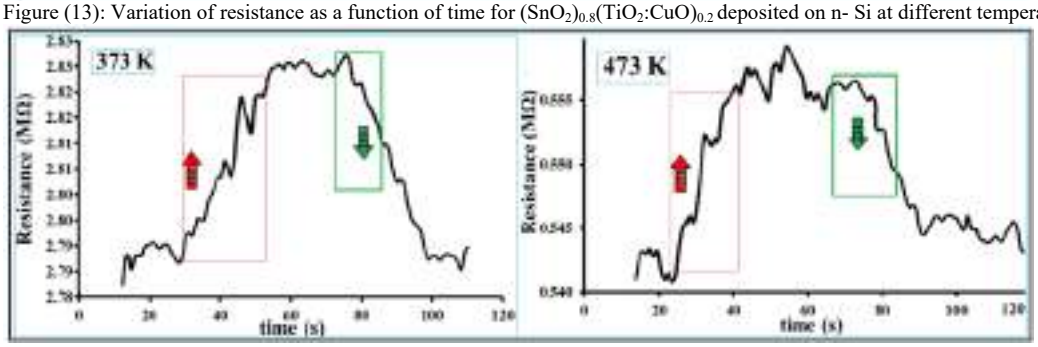

Figure (14): Variation of resistance as a function of time for $(SnO_2)_{0.7}(TiO_2{:}CuO)_{0.3}$ deposited on n- Si at different temperatures.

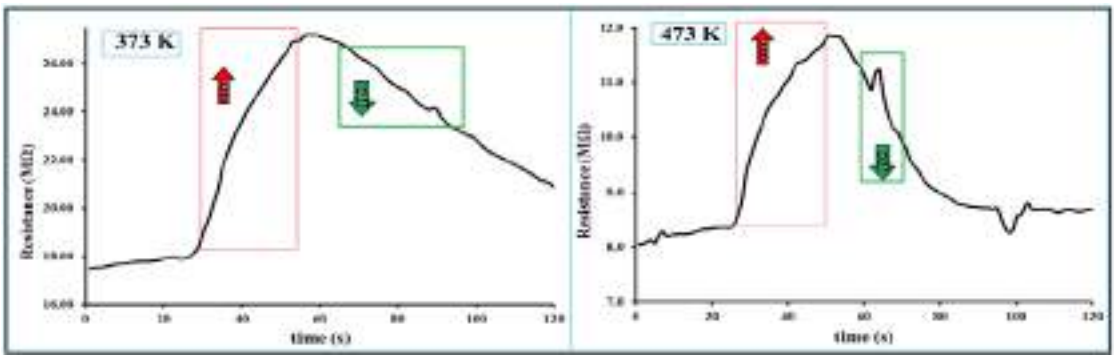

Figure (15): Variation of resistance as a function of time for $(SnO_2)_{0.6}(TiO_2{:}CuO)_{0.4}$ deposited on n- Si at different temperatures.

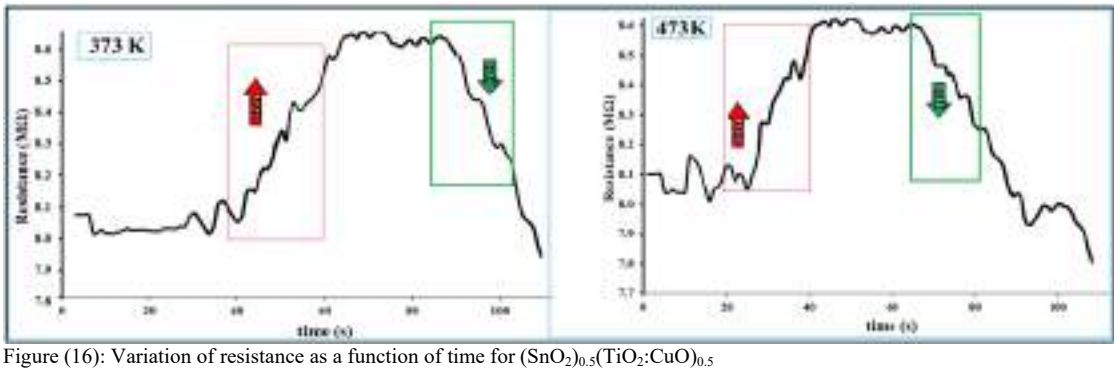

Figure (16): Variation of resistance as a function of time for $(SnO_2)_{0.5}(TiO_2:CuO)_{0.5}$ deposited on n- Si at different temperatures.

Note through the table (3) and figure (17) that the sensitivity was decreased by increasing the mixing ratio, but that the$(SnO_2)_{1-x}(TiO_2:CuO)_x$ sensor with mixing ratio $(TiO_2:CuO)_{0.4}$ has maximum value of sensitivity 57.14% at the operating temperature 373K and then start this value decrease by farther decreasing at mixing ratio $(TiO_2:CuO)_{0.5}$. The sensitivity for pure SnO_2 sensor 60% and then begin to decrease with increasing mixing ratio and then increase in $(TiO_2: CuO)_{0.4}$.

When we compare the results of the tables, we find that the sensitivity of the films to the gas was increased by increasing the operating temperature, indeed that sensitive of pure SnO_2 sensor was increased from 45.5% to 60% by increasing of operating temperature from 273K to 473K. The reducing of sensitivity by increasing of mixing ratio attributed to the presence of excess oxygen and slow conversion of CuO and TiO_2 during the detection of NO_2 gas [27,28].

Valueof x	Sensitivity (%)	Response Time (s)	Recover Time (s)
0	45.45	33.00	37.00
0.1	10.00	40.00	53.00
0.2	4.65	25.00	68.00
0.3	1.44	20.00	40.00
0.4	57.14	31.00	38.00
0.5	7.50	40.00	48.00

Table (3): Sensitivity, response and recovery time as a function of operating temperature 373K for $(SnO_2)_{1-x}$ $(TiO_2: CuO)_x$ films .

Value of x	Sensitivity (%)	Response Time (s)	Recover Time (s)
0	60.00	30.00	48.00
0.1	45.45	22.00	57.00
0.2	0.40	35.00	28.00
0.3	1.82	12.00	10.00
0.4	50.00	20.00	30.00
0.5	17.65	20.00	35.00

Table (4): Sensitivity, response and recovery time as a function of operating temperature 473 K $(SnO_2)_{0.5}$ $(TiO_2: CuO)_{0.5}$ films .

It could be observed from figure (17) that all the sensor structure and the sensor response was increased at a particular temperature, called the operating temperature (T_{op}), and then reduced with further increase in temperature.

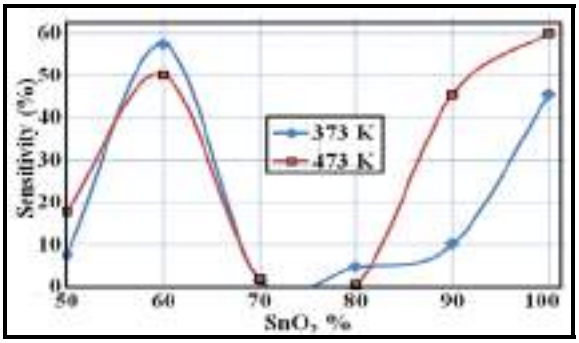

Figure (17): Sensitivity as function of SnO_2 content for $(SnO_2)_{1-x}$ $(TiO_2: CuO)_x$ films deposited on n- Si to NO_2 gas

4-2 Response and Recovery Times:

Figures (18) and (19) shows the variation in response time and recovery time with temperature of all prepared sensor which were exposed to NO_2 gas. During response time, NO_2 gas was desorbs as NO and O_2 molecules leaving behind the trapped electrons onto the sensor surface thereby, reducing the resistance value to the initial low resistance R_a value. It may be seen that with the incorporation of metal oxides thin film improves the sensor response time and recovery time which could be due to the increase in rate of adsorption of target NO_2 gas [29,30].

Further, with increasing the operating temperature, response time reduces slightly for all prepared sensors. It is important to note from figure (18) and (19) that incorporation of metal oxide improves the rate of desorption of target gas at both operating temperatures 373K and 473 K to a great extent giving low recovery time.

Table (3) and (4) shows that the response time and the recovery time get to change in non-regular manner with the increasing of mixing ratio, minimum values of response and recovery times obtained at $(TiO_2: CuO)_{0.3}$.

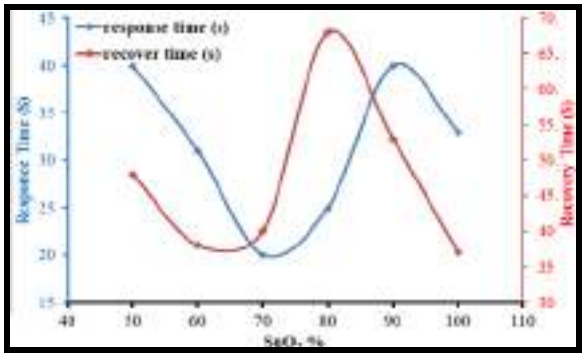

Figure(18): Response and recovery time as function of SnO_2 content for $(SnO_2)_{1-x}$ $(TiO_2:CuO)_x$ films at operating temperature 373K

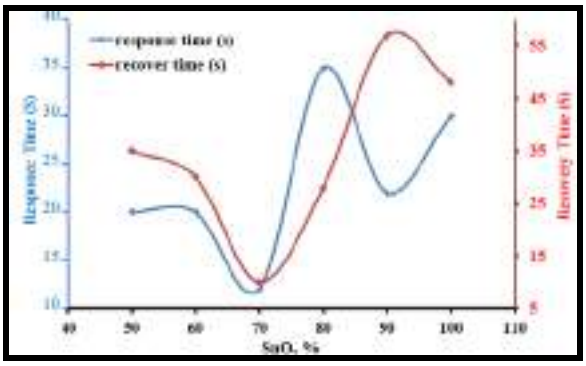

Figure(19): Response and recovery time as function of SnO_2 content for $(SnO_2)_{1-x}$ $(TiO_2: CuO)_x$ films at operating temperature(473K).

Eventully it is clear that the sensitivity of pure SnO_2 thin films gas sensors prepared by RF-sputtring exceeded those of thin films samples prepared by chemical spray pyrolysis .It was suggested that the low catalytic activity of SnO_2 with TiO_2 and CuO was related to the synergestic lack between Ti, Cu and Sn. Thus this suggested that improved sensitivity of RF-sputtering sensors higher operation temperature i.e < 473 K .It is well know that high response characteristics to any gas may attributed to the porocity of sensor structure which allow the sensing gas molecules to penetrate deeper in to the sensor structure and allowing embeded TiO_2 and CuO atoms to participate in the sensing phenomena, the reduction of sensitivity of gas sensors attributed to the low porocity and produced very smooth surface. This may be due to the effect of the temperature of the preparation[31,32]

4- Conclusion

1- RF-sputtering method produced amorphous thin films for all mixing ratio most of them convert to polycrystalline by annealing at 873K .
2- The average diameter and average roughness change in reverse manner with the increase of mixing ratio.
3- The increasing of titanium and copper oxides concentration made all thin films samples prepared more opaque for law mixing ratio throughout shifting the absorption edge to lower energies.
4- The increase of titanium and copper oxides at $(SnO_2)_{0.7}(TiO_2:CuO)_{0.3}$ thin film improves the crystallite, increases the grain size and lead to visual decrease of optical energy gap.
5- The sensitivity of $(SnO_2)_{1-x}(TiO_2:CuO)_x$ films was increased by increasing of operating temperature.

References

[1] Xiao Liu, Sitian Cheng , Hong Liu , Sha Hu , Daqiang Zhang and Huansheng Ning, "A Survey on Gas Sensing Technology",Sensors ,12(2012)9635-9665 .[2]Sofian M. Kanan, Oussama M. El-Kadri, Imad A. Abu-Yousef and Marsha C. Kanan," Semiconducting Metal Oxide Based Sensors for Selective Gas Pollutant Detection"Sensors,9(2009) 8158-8196.
[3] Alexander Larin , Phillip C. Womble And Vladimir Dobrokhotov "Hybrid Sno2/Tio2 Nanocomposites For Selective Detection Of Ultra-Low Hydrogen Sulfide Concentrations In Complex Backgrounds" Sensors 16(2016) 1-15.
[4] Low Jia Wei , Master Thesis " The Properties Of Sputtered Copper Oxide Thin Film For Sensing Application" Malaysia (2015)1-105.
[5] D. Haridas, K. Sreenivas and V. Gupta, "Improved response characteristics of SnO2 thin film loaded with nanoscale catalysts for LPG detection", Sensors 133(2008)270-275.
[6] Philip J. D. Peterson , Amrita Aujla , Kirsty H. Grant , Alex G. Brundle ,Martin R. Thompson , Josh Vande Hey and Roland J. Leigh ," Practical Use of Metal Oxide Semiconductor Gas Sensors for Measuring Nitrogen Dioxide and Ozone in Urban Environments" Sensors ,17(2017)1-25.
[7] Chapman, B. (1980) "Glow discharge processes"New York, John Wiley & Sons, Inc. ISBN = 0-471-07828-X.
[8] F. Ibrahim, "Design and Construction of Low-Pressure D.C.-Sputtering Plasma System For Preparing Gas Sensors", PhD Thesis, University of Baghdad, (2013)
[9] B. Chapman, "Glow Discharge Processes: Sputtering and Plasma Etching", New York: Wiley, PP.406, (1980).

[10] H. Urbassek and W. Eckstein, "Sputtering by Particles Bombardment Experiments and Computer Calculations From Threshold to Mev Energies" Springer, 110(2007) 21-31.
[11] A. Maheev, "Effect of Surface Morphology on the Sputtering Yield", Nuclear and Methods in Physics Research B., 222, (2004), 316-334.
[12] K. L. Chopra "Thin Film Phenomena" McGraw – Hill, New York (1969).
[13] E. Warren, "X-ray Diffraction", Addision Wesley Publishing Co.: London, 1969.
[14]Xiao, H., Xianogyan, Z., Uddin, A., Leu, C. B.," Thin Solid Films"4 (2005) 1-87.
[15] H. Liu,J. Huang and L. Meng, "The Dynamic Measurement of SnO_2 Gas Sensor and The IR Applications". Science and Technology of Chemiresistor Gas Sensors", New York, Ny, USA, (2007) 177-214.
[16] M. Boshta, F. Mahmoud and M. Sayed, "Characterization of Sprayed SnO_2:Pd Thin Films For Gas Sensing Applications", Journal of Ovonic Research 6 (2010) 93 – 98.
[17] N. Yamazoe , K. Shimanoe, "Review Article Receptor Function and Response of Semiconductor Gas Sensor ", Journal of Sensors (2009)1-21.
[18] Joint Committee on Powder Diffraction Standards (Jcpds), International Centre For Diffraction Data, 1997, Card No. 41-1445
[19] Xu, C., Jun Tamaki, J., Miura, N. & Yamazoe, N. , "Grain Size Effects on Gas Sensitivity of Porous SnO_2-Based Elements", Sens. Actuat. B 3,(1991) 147–155.
[20] A.Sharmaa, M. Tomarb, V.Gupta, "Enhanced Response Characteristics of SnO_2 Thin Film Based NO_2 Gas Sensor Integrated with Nanoscaled Metal Oxide Clusters", Sensors and Actuators B: Chemical 181 (2013) 735– 742.
[21] J. Sohn, S. Kim, Z. Kim, and Y.Yu, "H_2S Gas Sensing Properties of SnO_2:CuO Thin Film Sensors Prepared by E-Beam Evaporation", Transactions on Electrical and Electronic Materials, 10 (2009)135-139.
[22] F. Edelman, H. Hahn, S. Seifried, C.Alof, H. Hoche, A. Balogh, P. Werner, K. Zakrzewska, M. Radecka, P. Pasierb, A.Chack, V.Mikhelashvili and G.Eisenstein, "Structural Evolution of SnO_2_TiO_2 Nanocrystalline Films For Gas Sensors", Materials Science and Engineering, 70 (2000) 386–391.
[23] A. Chowdhuri, V. Gupta, and K. Sreenivas, "Response Speed of SnO_2 SnO_2-Based H_2S Gas Sensors with CuO Nanoparticles", Applied Physics Letters.84(2004)1180-1182.
[24] Sabah N. Mazhir, Noha. H. Har, Journal of Applied Physics, "Influence of Concentration on the Structural, Optical and Electrical Properties of TiO_2:CuO Thin Film Fabricate by PLD", 7(2015)14-21
[25] J. Sohn, S. Kim, Z. Kim, and Y.Yu, "H_2S Gas Sensing Properties of SnO_2:CuO Thin Film Sensors Prepared by E-Beam Evaporation", Transactions on Electrical and Electronic Materials, 10 (2009)135-139.
[26] M. Batal, G. Nashed, F. Jneed, "Electrical Properties of Nanostructure Tin Oxide Thin Film Doped with Copper Prepared by Sol-Gel Method", J. Phys. Educ., 6(2012)113-116.
[27] D. Mukhamedshina and N. Beisenkhanov, "Influence of Crystallization on the Properties of SnO_2 Thin Films", Institute of Physics and Technology, 9(2012),219-258.
[28] A. Chowdhuri, V. Gupta, and K. Sreenivas, "Response Speed of SnO_2 SnO_2-Based H_2S Gas Sensors with CuO Nanoparticles", Applied Physics Letters.84(2004)1180-1182.
[29] L. Jin, W. Chen, H. Zhang, G. Xiao, C. Yu and Q. Zhou, "Characterization of Reduced Graphene Oxide (Rgo)-Loaded SnO_2 Nanocomposite and Applications in C_2H_2 Gas Detection", Appl. Sci. ,7(2017)1-15
[30] V. Gupta, S.Mozumdar, A.Chowdhuri, K. Sreenivas, "Influence of CuO Catalyst in the Nanoscale Range on SnO_2 surface For H_2S Gas Sensing Applications", Indian Academy of Sciences,65(2005) 647–652
[31] J. Fraden, "Handbook of Modern Sensors Physics, Designs, and Applications", Springer New York(2003).
[32] A. Chowdhuri, V. Gupta, and K. Sreenivas, "Response Speed of SnO_2 SnO_2-Based H_2S Gas Sensors with CuO Nanoparticles", Applied Physics Letters.84(2004)1180-1182.

Available online at
http://namrc.uotechnology.edu.iq/index.php/

Nanotechnology and Advanced Materials Research Centre

Proceeding Articles Book 00 (2018) 000–000

6th International Scientific Conference on Nanotechnology, Advanced Materials and its Applications

Characterization and Electromagnetic Interference of Nickel Ferrite / polyaniline Composite

Muklis Ismail[1], Wasan Z.Khalaf[2], Sewench N. Rafeeq[1]

[1]Applied Science Department, University of Technology, Baghdad, Iraq

[2]State Company for Construction Industries (SCCI), Ministry of industry& Minerals, Baghdad, Iraq

Abstract

In the present work, polyaniline /Nickel ferrite composites in different weight percentage (5, 50 and 95 wt. %) were prepared and characterized. Nickel ferrite nanoparticles was synthesized by sol–gel auto combustion using two sintering temperature at (600,800)0C, while Polyaniline (PANI) in Emeraldine salt form was prepared by chemical oxidative polymerization of the appropriate monomeric aniline using Hydrochloric acid (HCL). X-ray diffraction results showed that all nickel ferrite samples are polycrystalline. Network analyzer device has been used to studying the microwaves absorption in the range of (X- band) with a frequency (8 -12 GHz), showed high absorbency for composite with high sintering temperature. Also the results showed that the permeability was enhancement when increasing nickel ferrite content in composite.

Keywords: Polyaniline, Nickel ferrite, Electromagnetic Interference.

1- Introduction

The Electromagnetic Interference (EMI) can affect to an electrical circuit of a device due to an electromagnetic radiation from another electrical circuit. The electromagnetic absorption is important in atmosphere engineering where the lightweight absorbing material development in a broad range of frequencies is a necessary part of the snatch technology. An absorber steeps the incident electromagnetic energy, thus reducing the net energy can be available for bounce back to radar. Metals are usually used for EMI as they have highly conductive and having the capacity to reflect the electromagnetic wave before being transferred. Nevertheless metals also have disadvantaged e.g. their weight, corrosion properties and weak in processing[1]. In the few past periods ineradicable conducting polymer (ICP) polyaniline (Pani) has been paid significant attention because of its high electrical conductivity, thermal stability, easiness of preparation, and good environmental constancy. This polymer has been found to be the most promising nominee for technological applications[2]. Soft ferromagnetic materials are used as microwave absorption materials according to their high exact resistance, high magnetic assuaging and low coercively. The properties which have made ferrite are very useful at radio and television frequencies also supply the key to their usage at microwave frequencies. Their high resistance enables an electromagnetic wave to infiltrate the material and the wave magnetic field component can react with the magnetic moment of the ferrite. The reaction is revealed by the notable behavior of the microwave ferrite permeability .The permeability displays a pronounced resonance at a frequency which is associated to the strength of the provided magnetic field within the ferrite[3]. Among numerous ferrites, which form a major component of the magnetic ceramic materials, nano-sized nickel ferrite has attractive properties for the application as soft magnets, central materials in power transformers and low loss materials at high frequencies. High permeability in the radio frequency area, high electrical resistivity, high Curie temperature and low eddy current loss are important properties of nickel ferrites, that make them appropriate for wide range of applications[4, 5]. Spinel ferrites like Nickel ferrite have high electrical resistivities and low dielectric losses. This has motivated us to carry out Electromagnetic Interference of nanocrystalline NiFe2O4 with a chosen polymer which have a permeability like polyaniline as a composite.

2- Materials and Method

2-1 Synthesis of Polyaniline (PANI)

Aniline (MERCK Schecharde) and Ammonium persulphate (APS)(NH4)2S2O8, were obtained from CDH, India. Hydrochloric acid (HCL) was obtained from Gain land Chemical Company (GCC).All was used to preparation Polyaniline doped with Hydrochloric acid. Doped Polyaniline (PANI-HCl) was chemically made by using aniline monomer and ammonium persulfate (NH4)2S2O8) as an oxidant. A particular amount of aniline was dissolved in aquatic solution of (HCl) acid (1M), and stirred by magnetic hot plat-stirrers model (SH-2) at (0 −5) ˚C for one hour (using an ice bath). Then ammonium persulphate was dissolved in (1M) hydrochloric acid, then added drop by drop to the stirred solution of aniline to make sure that the reaction was completed, the monomer to oxidizing agent ratio was kept at (1:1.35). The precipitate was washed with (HCL) (1M) and filtered until the filtrate becomes colorless and then was washed with ethanol to eliminate oligomeric impurities. Then it was washed with acetone, to remove water content. The precipitate was dried for four hours at (80)0C,then it was grinding into fine powder to produce emeraldine salt.

2-2 Synthesis of Ferrite nanoparticles

Ferric nitrate Fe(NO3)3.9H2O (MERCK Schecharde), Nickel nitrate Ni(NO3)2.6H2O, Citric acid(C6H8O7) and ammonia solution was used for prepare nickel ferrite.

In sol–gel auto combustion, suitable amount of Ferric nitrate (Fe(NO3)3·9H2O) and Nickel nitrate (Ni(NO3)2·6H2O) were dissolved in adequate amount of deionized water. The mixture was placed in a glass beaker and mixed with citric acid which acts as a burn agent with stirring by magnetic hot plat-stirrers. The solution pH was adjusted to be at (7) using ammonia solution that added in drops form with continuous stirring till the solution turned into brown color and the solution size became less and totally converted into a gel[6]. Also waiting for all gels to be completely burnt out to form a fluffy loose structure. This structure was powdered well in a mortar and calcined at (600 and 800) °C for 3 hours to get Nickel ferrite nanoparticles.

2-3 Synthesis of composite

The obtained powder from Polyaniline and Nickel ferrite preparation was mixed together with three ratio (95% NiFe2O4 + 5%PANI, 50% NiFe2O4 + 50%PANI, 5% NiFe2O4 + 95%PANI) and pressed by the piston oil at 5 tons in order to get samples as rectangular pellets of 2.2×0.9×1.2 cm dimensions, and the template was used to measure the Transmission/Reflection line method with a vector network analyzer (VNA).

The phase analysis of the samples was done by x-ray diffraction (XRD-6000) SHIMADZU, Japan, using a Cu target (λ =1.54 Å) with Current= 30 mA, Voltage = 40 KV and Scanning speed =5 deg/min). The range of the Braggs angles are taken (2θ=10˚- 80˚) for the samples. The average crystallite size (D) of the particles can be calculated from the X - Ray spectrum by means of Full Width at Half Maximum (FWHM) method (Scherrer relation). The average crystal size (D) of the samples can be estimated using Scherer's formula[7]:

$$D = 0.9\,\lambda \backslash ß \cos\theta \qquad (1)$$

Where, ß are the full width at half maximum in radian units, θ is Bragg diffraction angle of the XRD peak (degree). It is also called lattice constant, which represents the distance between the lattice points, it can be calculated using the relation[8]:

$$a = d\sqrt{h^2 + k^5 + l^2} \qquad (2)$$

Where (d) is the interplaner distance measured, (hkl) is Miller index.

The surface morphology of the samples, were determined using Atomic Force Microscope (AFM) type (CSPM-5000). The ac conductivity of the samples was carried out using LCR-meter for (capacitance, dissipation factor and dielectric constant). The equations below and the values of dielectric constant and dielectric loss factor was measured[9, 10]:

$$\sigma_{ac} = \omega\, \varepsilon_o\, \varepsilon'_r \tan\delta \qquad (3)$$

Where σac is the ac conductivity, ω is the angular frequency, ε_o is the permittivity of the air (8.854×10-12), ε'_r is the dielectric constant and tanδ is the loss tangent of the samples.

To calculate the absorbance of the prepared samples it is should first measuring the reflection and transmission coefficient using the vector network analyzer (VNA) this devise is widely used to measure the scattering parameters (S11, S12, S21, and S22) ,where S11 is (input reflection coefficient), S21 (forward transmission coefficient), S12 (reverse transmission coefficient) and S22 (output reflection coefficient)[11].

Permeabilityof Pani /NiFe2O4 composite

The NRW model is used for measuring the Permeability of Pani /NiFe2O4 composite. It requires at least two measured parameters (S11 and S21) and works well for lossy materials. The method is deduced from the following two equations for S11 and S21[12]:

$$C_1 = \frac{\mu_r}{\varepsilon_r} = \left(\frac{1+\Gamma}{1-\Gamma}\right)^2 \quad \text{..... (4)}$$

and

$$C_2 = \mu_r \varepsilon_r = -\left\{\frac{c}{wd}\ln\left(\frac{1}{\Gamma}\right)\right\}^2 \quad \text{..... (5)}$$

Therefore, we can find the permeability from the s-parameters $\mu r = \sqrt{C_1 C_2}$.

3- Results and discussion

3-1 X- ray Diffraction of Polyaniline.

The X-ray diffraction pattern of PANI is shown in Fig. 1. It found two diffraction peaks of about 2θ (13.08160 and 270) .The sharp peak around (270) is the characteristic peak of PANI.PANI is only partially crystalline with conducting metallic island separated by large amorphous regions[13]

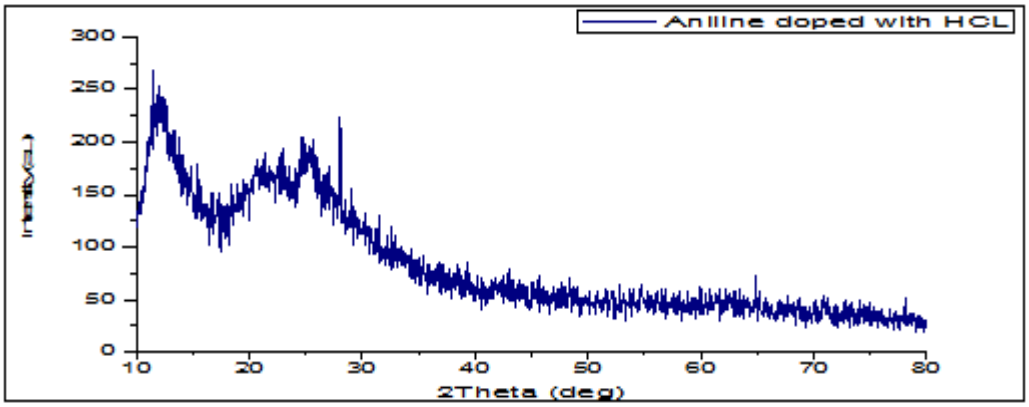

Fig (1): XRD pattern of PANI

3-2 X- ray diffraction (XRD) of Nickel ferrite

The X-ray diffraction patterns for NiFe2O4 at sintering temperature (Room temperature, 400, 600, 8000C) for the samples prepared by sol gel auto combustion, are shown in Figure (2). XRD data have been used to calculate structural parameters such as crystal size and lattice parameter of the prepared sample. The results shows matched perfectly with the international standard (ASTM /JCPDS Card No. (03-0875)) as shown in Tables (1) which indicate the formation of cubic spinel structure. Lattice parameter of the prepared samples was decreased with increasing sintering temperature. This may be due to compactness of the lattice in the crystal increases[14].

All peaks became more intense and sharp with the increase in sintering temperature suggesting the increase in particle size and crystallinity[15]. In sol-gel method with above 4000C highly intense characteristic peaks was found, it showed that phase changes above 4000C sintering temperature, for this reason it was chosen sintering temperature at (600 and 8000C) for nickel ferrite.

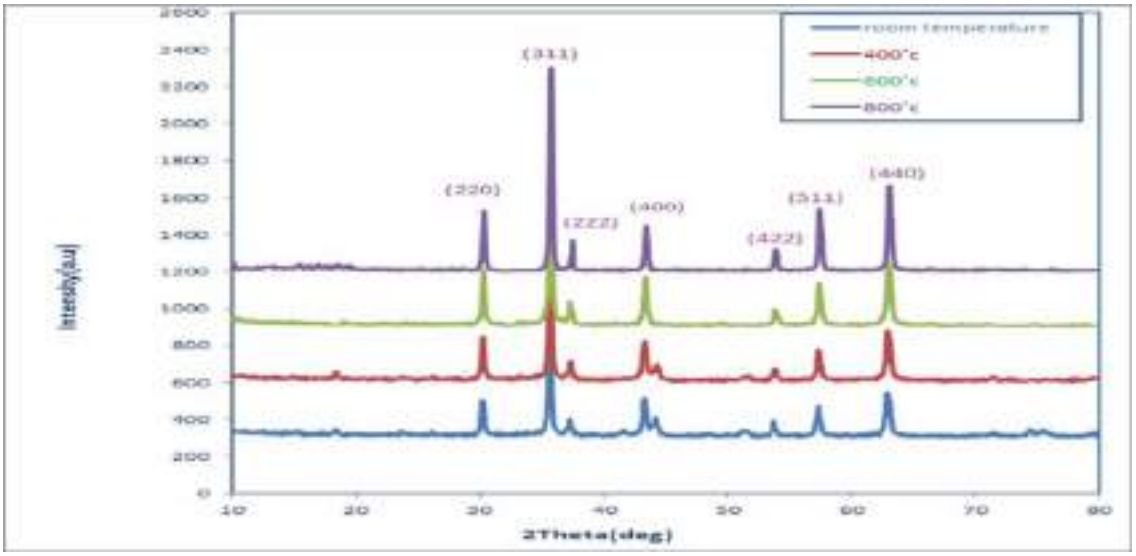

Figure (2): The XRD spectra of nickel ferrite prepared by sol-gel method at different temperature.

Table (1): structure parameters of NiFe2O4 samples prepared using Sol-Gel method

Temp (°C)	2θ°	d(Å) ASTM	a (Å)	C.S (nm)
Room Temperature	30.20	2.95168	8.36353	28.4
	35.628	2.51786	8.350791	31.1
	37.25	2.40873	8.35511	31.7
	43.35	2.08736	8.34241	24
	62.9148	1.47605	8.34982	27.5
400	30.2789	2.94943	8.34224	31.2
	35.7087	2.51241	8.33271	31.2
	37.265	2.41095	8.351787	32.3
	43.320	2.08697	8.34789	29
	53.75	1.70291	8.34801	26.6
	57.3	1.60585	8.34817	35.2
	62.9495	1.47532	8.34569	31.1
600	30.3708	2.94071	8.31759	33.7
	35.6615	2.51562	8.34338	31.7
	37.25	2.40825	8.35511	34.1
	43.37	2.08451	8.33804	31
	53.80	1.7012	8.34083	36.1
	57.400	1.60419	8.33486	35.4
	63.025	1.47373	8.336648	32
800	30.3	2.94492	8.33657	34.4
	35.7509	2.50954	8.323198	34.2
	37.4011	2.40252	8.322562	34.8
	43.4346	2.08174	8.32695	31.8
	53.8866	1.70003	8.32843	35.9
	57.434	1.60318	8.33034	36.4
	63.0712	1.47277	8.33124	37.4

The dielectric properties (ε') in the frequency range (250 Hz–5 MHz) for NiFe2O4 prepared by sol-gel auto combustion, are shown in Figure (4). The dielectric constant for all sintered samples show similar trends, decreases with increasing frequency. This fact shows a normal behavior of ferromagnetic materials[16]. The variation of dielectric constant with frequency may be explained on the basis of space-charge polarization phenomenon. The decrease can be explained using Koop's phenomenological theory. This theory considers the dielectric structure as an inhomogeneous medium of two layers of Maxwell–Wagner type, with the

first conducting layer consisting of large ferrite grains and the second, made up of grain boundaries, is a poor conductor. The electronic exchange between Fe+2 and Fe+3 ions, which produce local displacements in the direction of the applied external fields, results in polarization. Above certain frequencies this electronic exchange does not follow the applied field and this caused a decrease in the dielectric constant. The loss factor is caused by the lag in polarization of the applied electric field, which results in energy loss. This is caused by impurities and imperfections in the crystal lattice. At the higher frequency end, the loss factor is caused by the conversion of movement of charges into vibration of the lattices[17] .Now, with increasing sintering temperature; partial reduction of Fe+3 to Fe+2 takes place. Thus, the value of dielectric constant increases with increasing sintering temperature.

Figures (5) shows decrease dielectric loss (tan□) of NiFe2O4 with increasing frequency recorded small value at high frequencies. As the temperature rise, the mobility of localized charge carriers can be activated and this increases the hopping probability or as temperature increases maximum relaxation frequency, must move toward higher frequencies.

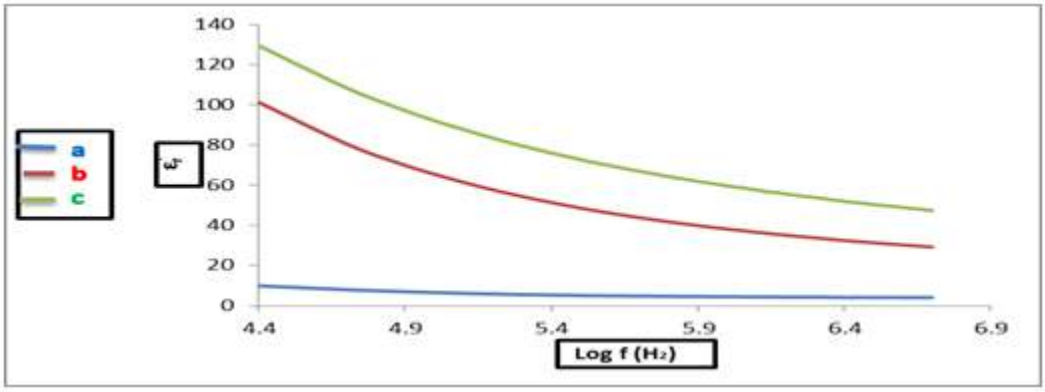

Figure(4): dielectric constant of nickel ferrite prepared by sol-gel method at (a) room temperature, (b) 600 and (c) 800)0C as a function of frequency

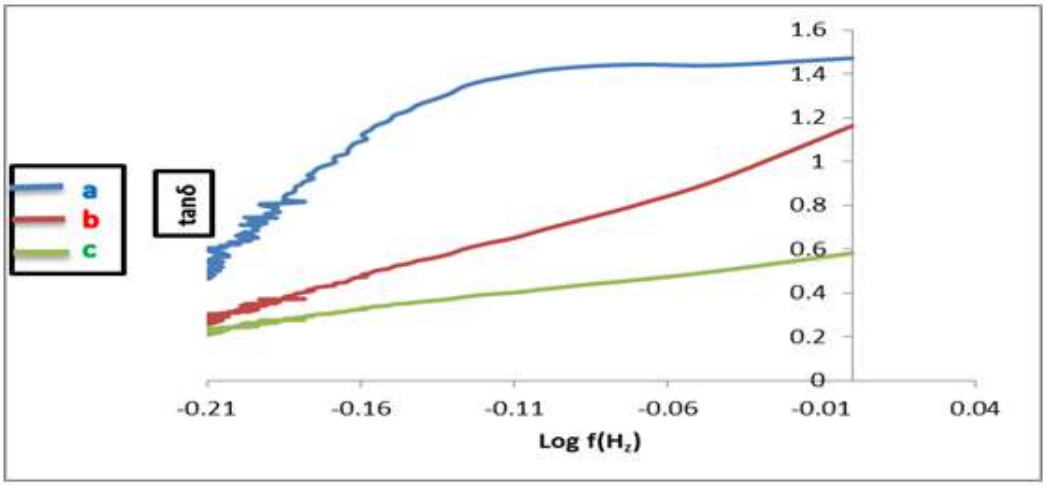

Figure(5): loss tangent of nickel ferrite prepared by sol-gel method at (a) room temperature, (b) 600 and (c) 800oC as a function of frequency

The variation of σac for NiFe2O4 as a function of frequency from 250Hz to 5 MHz is shown in Figure (6).The conductivity of nickel ferrites is increases with increasing frequency. The variation of ac conductivity with applied frequency could be explained on the basis of Koops model. According to this model, the AC conductivity at low frequency is due to the conducting grain boundaries while, the conductivity at higher frequencies due to conducting grains. As the frequency of the applied field increases, hopping of charge carriers also increases, thereby increasing the conductivity. Since the high density of interfacial states in nano system can serve as charge carriers due to with respect to the bulknization and also function as conduction centers for transport of charge carriers, ac conductivity in these system is at variance with respect to the bulk and conductivity is found to be higher[18]. It was observed that at higher frequency the (σac) conductivity became more active by encouraging the hopping of electrons between Fe+3 and Fe+2 ions[19].

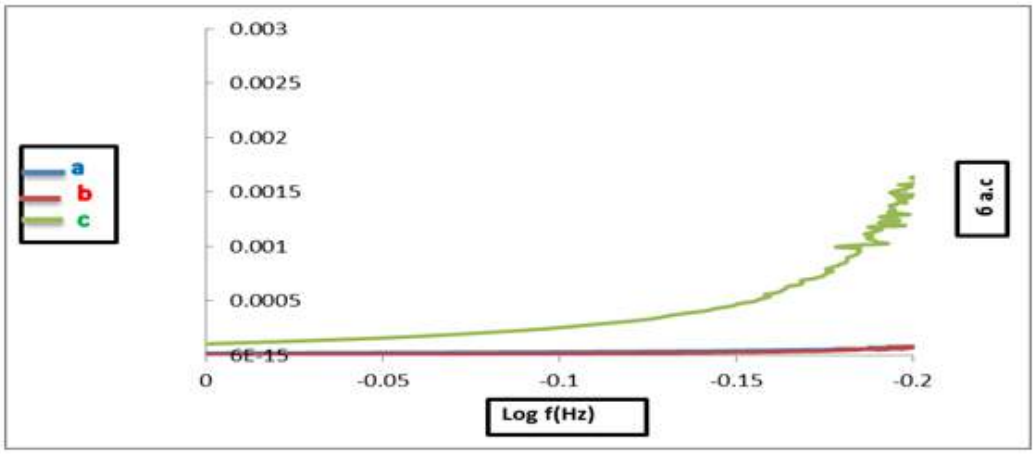

Figure(6): AC conductivity of nickel ferrite prepared by sol-gel method at (a) room temperature, (b) 600 and (c) 800oC as a function of frequency

3-3 Characterization of polyaniline-nickel ferrite composite

Figures (7) shows the absorbance, transmission coefficient (S21), reflection coefficient (S11) and attenuation coefficient as a function of frequency for composite prepared at 800oC. The highest values of the reflection coefficient at for (95%) nickel ferrite and 5% polyaniline are (-5) dB at frequencies (11) GHz. It may be that the spinel ferrite needs high sintering temperature for the complete formation of ferrite and getting best absorbance because of high temperature sintering cancels all secondary phases that made up with ferrite.

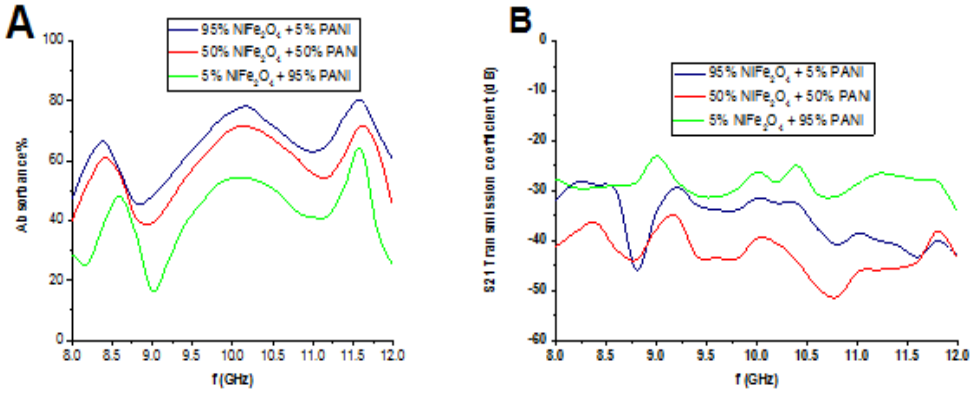

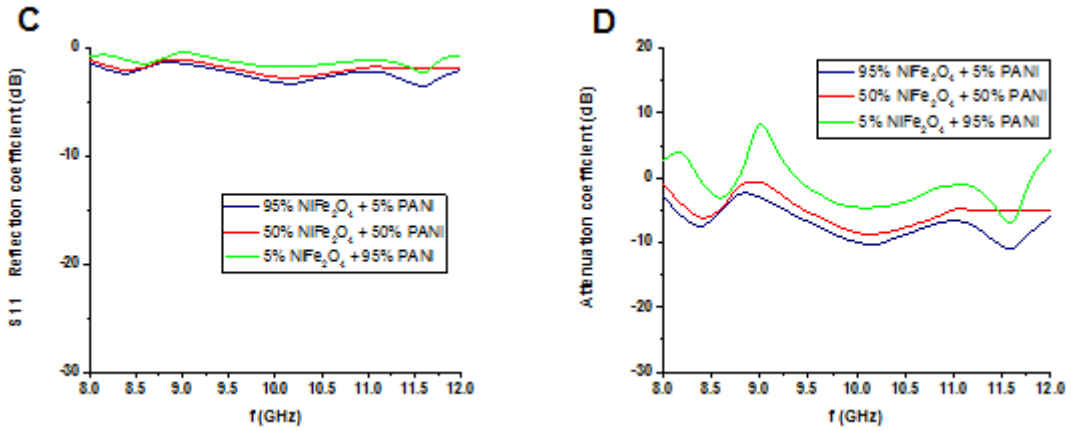

Figure (7): The absorbance, transmission coefficient (S21), reflection coefficient (S11) and attenuation coefficient as a function of frequency for composite calcined at 800oC.

3-4 Permeability Measurement

The permeability of PANI (μ) as a function of frequency with different amounts of NiFe2O4 nanoparticles were obtained from scattering parameters (S11 and S21) is shown in Fig. 8 and 9. The values of permeability for PANI was (7.3-9.6). As compared with NiFe2O4/PANI composites, the values of permeability were increase with increasing of ferrites content, to reach highest value up to (6000) as shown in Figure (9). This is because PANI itself is slightly magnetic in nature and ferrites are ferromagnetic in nature so magnetic dipole moment of both gets coupled with each other and may cause lesser value of net resultant dipole. This leads to diamagnetism, causing lesser value of magnetic saturation on increasing PANI content.

It is evident that permeability values obtained at higher temperatures are higher than the ones at the lower temperatures, this attributed to the domain wall contribution, which was controlled by the increased grain size induced by higher post-sintering density. Therefore, the high initial permeability could also be controlled through the microstructure. The relationship between the grain size and permeability is generally linear when the grain growth is normal. Both the density and the grain size of the ferrites increased when the sintering temperature increased as many pores and open crystal structures had become closed. As a result, fewer grain boundaries and larger grains led to the higher initial permeability, so the highest values of permeability was for NiFe2O4/PANi composite at 800oC as shown in Fig 9, this is because of the high grain size recorded at these temperature.

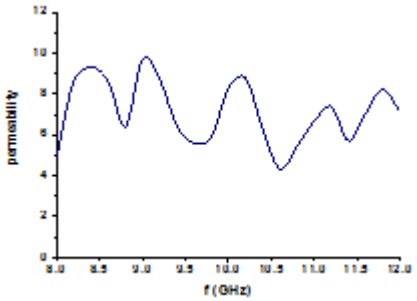

Figure(8): Permeability of PANI

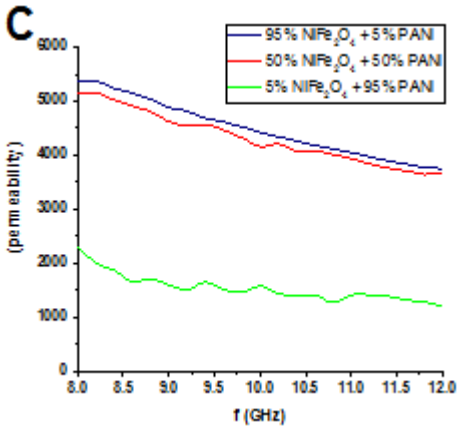

Figure (9): Permeability for PANI\NiFe2O4 composite as a function of frequency calcined at 800oC.

4- Conclusions

The sintering temperatures of prepared Nickel ferrite is 8000C was used to prepare a composite with PANI in three ratio. It is found that the Nickel ferrite \ Polyaniline composite was almost zero reflection value which is very useful in radar absorption application. Permeability value also found for all composites.

References

[1] S.P. Gairola, V. Verma, L. Kumarb, M. Abdullah Dara, S. Annapoorni and R.K. Kotnala, "Enhanced microwave absorption properties in polyaniline and nano-ferrite composite in X-band", Synthetic Metals 160 , 2315–2318,India,(2010).

[2] Milind Kulkarni, Bharat Kale, Sanjay Apte, Sonali Naik, Uttam Mulik and Dinesh Amalnerkar, "Synthesis and Characterization of Polyaniline Nanofibers by rapid Liquid-Liquid Interfacial Polymarization Method", Chemistry & Chemical Technology, Vol. 5, No. 1 ,India,(2011).

[3] P. J. B. Clarricoats," Handbook of Microwave Ferrites", Chapman &Hall, London, PP. 2, (1961).

[4] Daliya S. Mathew, Ruey-Shin Juang," An overview of the structure and magnetism of spinel ferrite nanoparticles and their synthesis in microemulsions",Chemical Engineering Journal 129 , 51–65,(2007).

[5] M. M. Ismail, N. A. Jaber, "Influences of Cation Distribution of Zinc Substituted on Inverse Spinal Nickel Ferrite Nanoparticle for Superparamagnetic Approach" Surface Review and Letters, (2017) doi.org/10.1142/S0218625X18500762.

[6] Sewench N. Rafeeq, Mukhils M. Ismail, Jameel M. A. Sulaiman, "Magnetic and Dielectric Properties of $CoFe_2O_4$ and $CoxZn1-xFe_2O_4$ Nanoparticles Synthesized Using Sol-Gel Method" Journal of Magnetics 22(3),9 (2017).

[7] Patil Basavani K.1, Rathod Sopan M," Synthesis, Characterization and Magnetic Properties of Co2+ Substituted Ni Nano ferrite by Sol-Gel Auto combustion Method", International Journal of Innovative Research in Science, Engineering and Technology,Vol. 3, Issue 6, June (2014).

[8] Mukhlis M. Ismail, Nasma A. Jaber," Structural Analysis and Magnetic Properties of Lithium-Doped Ni-Zn Ferrite Nanoparticle", J Supercond Nov Magn., (2017) https://doi.org/10.1007/s10948-017-4428-3.

[9] Md. Dilwar Alam Khan, Arshia Akhtar and Syed Ashfaq Nabi," Investigation of the electrical conductivity and optical property of polyaniline-based nanocomposite and its application as an ethanol vapor sensor", New Journal of Chemistry, 39, 3728-3735, Issue 5, (2015).

[10] Salma M. Hassan, Amera Ghareeb Baker, and Harith I. Jafaar," A.C Electrical Conductivity for Polyaniline Prepared in Different Acidic Medium", International Journal of basic and Applied Science, Vol. 01, No. 02 ,Oct (2012).

[11] Ersel Ozkazanc, Sibel Zor & Hatice Ozkazanc," Synthesis, Characterization, and AC Conductivity of Polyaniline/Selenium Composites", Journal of Macromolecular Science, Part B: Physics, 51:2122–2132, (2012).

[12] Smith, B., Carpentier, M.H.," The Microwave Engineering Handbook", Edited by Bradford L. Smith and Michel-Henri Carpentier ", Vol. 3, (1993).

[13] Haisel Mathew,Vrinda S Punnackal,Sunny Kuriakose,B.Syamala Kumari and Ancy Manuel,"Synthesis and Electrical Characterization of Polyaniline –Multiwalled Carbon Nanotube Composites with different Dopants",International Journal of Scientific and research Publications, Volume 3,Issue 8,(2013).

[14] Khalil J. Hamam," Dielectric Response of Polyaniline Derivatives and its Effect on the Absorption Spectrum of Modified Copper Phathlocyanine", Modern Applied Science; Vol. 8, No. 6(2014).

[15] S.K. Emdadul Islam, Pankaj Sharma, "Synthesis and Characterization of Nickel Ferrite: Role of Sintering Temperature on Structural Parameters", Journal of Nano-and electronic physics Vol. 6 No 1, 01008(4pp), (2014).

[16] Gagan Dixit, J P Singh, R C Srivastava, H M Agrawal, R J Choudhary and Ajay Gupta, "Structure and magnetic behavior of NiFe2O4 thin film grown by pulsed laser deposition", Indian Journal of Pure &Applied Physics,Vol.48, PP.287-291, April (2010).

[17] Shamima Choudhury, Mahabub Alam Bhuiyan and Sheikh Manjura Hoque," Retracted: Effect of sintering temperature on apparent density and transport properties of NiFe2O4: synthesized from nanosize powder of NiO and Fe2O3", International Nano Letters,2:6,2012.
[18] I. H. Gul and E. Pervaiz," Comparative study of NiFe2-XAlXO4 Ferrite nanoparticles synthesized by chemical co-precipitation and sol-gel combustion techniques ", Materials Research Bulletin, Volume 47, Issue 6, June (2012).
[19] M . Raghasudha, D. Ravinder, P. Vee rasomaiah," FTIR Studies and Dielectric Properties of Cr Substituted Cobalt Nano Ferrites Synthesized by Citrate-Gel Method", Nanoscience and Nanotechnology2013, 3(5): 105-114

Available online at
http://namrc.uotechnology.edu.iq/index.php/

Nanotechnology and Advanced Materials Research Centre

Proceeding Articles Book 00 (2018) 000–000

6th International Scientific Conference on Nanotechnology, Advanced Materials and its Applications

Electrical and Detection Properties of Nano and Micro Copper Oxide prepared by RPLD

Makram A. Fakhri[1], Ban A. Bader2, Farah G. Khalid[3] , Evan T. Salim[4],Mariam M. Hassan[5]
[1]Laser and Optoelectronic department, University of Technology, Baghdad, Iraq
[2]collage of Science, University of Al-Hamdaniyah,
[3]Collage of Agriculture, University of Baghdad, Baghdad, Iraq
[4]Applied Science Department, University of Technology, Baghdad, Iraq
[5]Ministry of Health, Baghdad, Iraq
Corresponding auther:mokaram_76@yahoo.com

Abstract

In this work, the effect of different substrate temperatures on the electrical and detection properties of Cu_2O copper oxide thin film has been carried out using Reactive Pulsed Laser Deposition technique (RPLD). λ = 1046 nm Q-switch Nd-YAG laser with (1000 MJ) laser energy's has been used to ablated pure copper target and deposited on the Silicon substrates. The CV results present an abrupt junction as a linear relationship between the $1/C^2$ and the V at the optimum preparing condition of 0.77 V essentially equal to the diffusion potential within the Cu_2O side, the responsivity results shows a two peaks one for the copper oxide responsivity for red region wavelength and the second one for the silicon and that is responsivity for IR region wavelength.

Keywords: copper Oxide; RPLD; herostructure; detector parameters

1- Introduction

There are many well-known transparent conductive oxide (TCO) materials and their doped derivatives. TCOs such as e In_2O_3, SnO_2 are n-type materials and are used, for example, as transparent electrodes in flat panel displays, solar cells, and touch panels. These materials need to have good optical transparency and electrical conductivity for their applications [1].

There are, however, new TCOs with p-type conductivity. Indeed, the development of p-type transparent conducting oxides is one of the key technologies for p–n junction-based oxide devices, such as diodes, transistors and light-emitting diodes [2].

Cuprous oxide (Cu_2O), a p-type semiconductor, has brown colour and possesses direct band gap around 2 eV. A crystal of Cu_2O has a cubic structure. It has high specific electrical resistivity and optical transmittance in the visible region of the solar spectrum which makes it useful for various applications such as solar cells, photodetectors, and phototransistors.

In addition, the Cu_2O, films have been attractive in the field of gas sensors made by employing the hetero-structure with SnO_2.

Thin films Cu_2O has been prepared using various techniques, for instance, reactive magnetron sputtering [4], reactive evaporation [5], RF sputtering [6], ion beam sputtering [7], plasma evaporation [8], and molecular beam epitaxy[11].

In this study, we report the fabrication and characterization of nanostructured copper oxide thin films deposited on silicon substrates by using the PLD technique.

2- Materials and Method

Undoped Cu_2O hetrostructure were prepared and deposited on a cleaned wafer of N-Si as a substrate using a tattoo removal Nd: YAG laser at different substrate temperatures. The pulse duration of the Q-switched Nd: YAG laser is 7 ns (FWHM) with wavelength= 1.064 nm, the laser beam was focused through a lens with a focal length=10 cm spotted on a silver target (99.999% provided from Fluka com.). The targets spin at a rate of one cycle per minute. The energy of the pulsed laser at the target surface was maintained within the 900 mj. All the deposited thin films were created by 50 laser shots at the temperature of the substrate arranged 200-600 C^o. A (P-type) Cooper oxide (Cu_2O) nanostructure thin film was deposited using the RPLD technique, with the aid of halogen lamp at oxidation temperature of (623 K) and (90 sec) as an oxidation time. The calcinations process was done at 250 °C for 30 min in static air within oxygen atmosphere to remove any organics. (Lenton VTF/12/60/700) tube furnace..

The white light response of the photodiode was tested by placing it under illumination of a (100W) tungsten filament lamp, placed 15 cm away. The I-V characteristics were measured using a DC power supply and Keithley electrometer. The spectral responsivity of the photodiode was measured for the spectral range (450-900nm) using a calibrated monochromator. All measurements were carried out at room temperature. The Photoconductive property of semiconductors can be used to determine the excess minority carriers lifetime.

3- Results and discussion

Electrical measurements of constructed device

Current-Voltage characteristics

The results in figure 1a give the I-V charecterisic behavior of the Cu_2O/N-Si heterojunctions in the forward bias. Two regions are recognized; the first one represents recombination current while the second represents the tunneling current. Figure (1a) gives a comparison between the results obtained at substrate temperature and different forward voltage for two junctions.

Most of the samples prepared at various deposition temperatures exhibit good rectification behavior and their leakage currents tend to increase with the substrate temperature.

Using n-type silicon substrate Cu_2O/Si heterojunction device was deposited, the results of the current-voltage (I-V) measurements in the dark for the prepared heterojunctions was present on the figure (1). These characteristics are very important to describe the heterojunction performance and all heterojunction parameters depending on these characteristics.

Fig. 1b presented curves, for the I-V characteristics under reverse bias, it is clear that the curve contains two regions; the first is the generation region where the reverse current is slightly increased with the applied voltage and this leads to generation of electron-hole pairs at low bias.

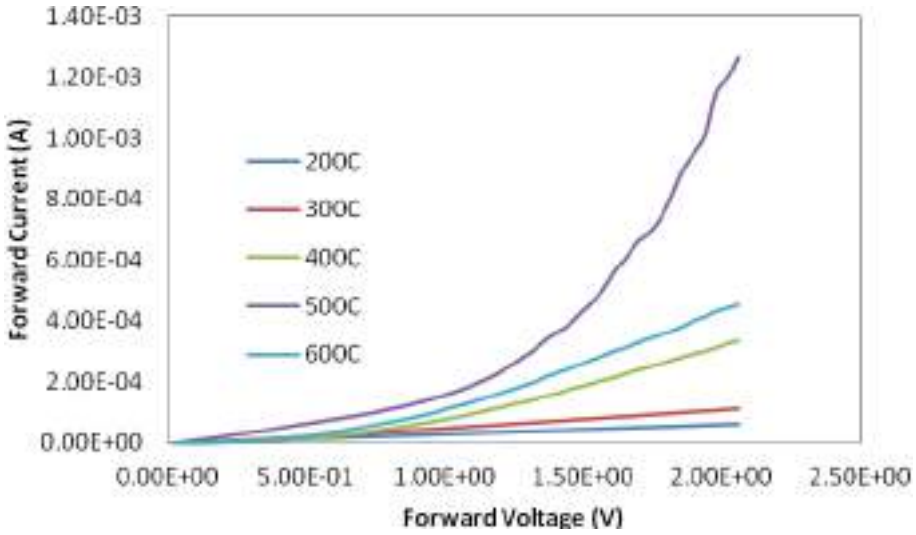

(a)

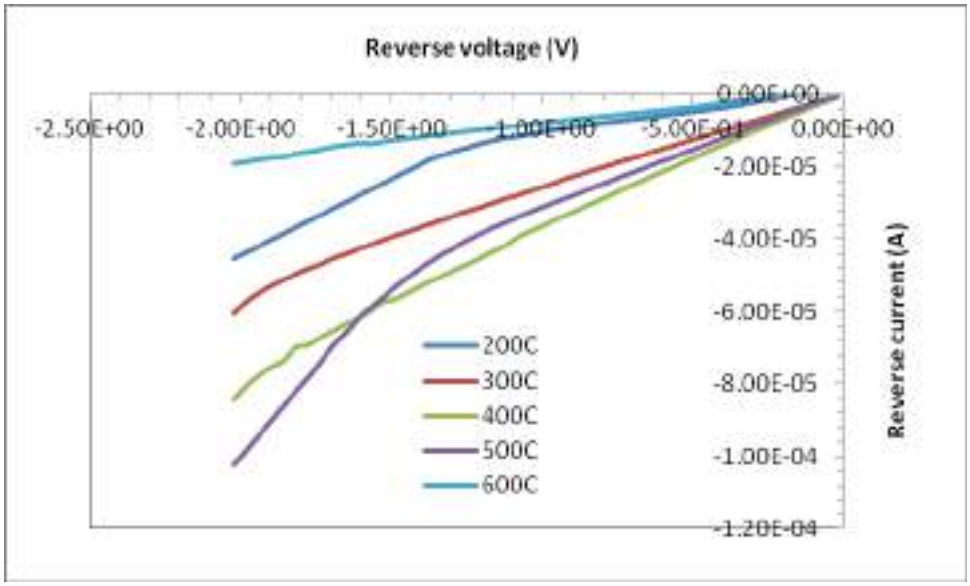

(b)

Figure (1) I-V characteristic under forward and reverse baise

It is one of the most important measurements since it determines different parameters such as built-in potential, junction capacitance and junction type.

give the C-V and C^{-2}-V measurements for both junctions at optimum substrate temperatures and O_2 pressures. Results show that the junction capacitance is inversely proportional to the bias voltage for all prepared samples. The reduction in the junction capacitance with increasing bias voltage is resulted from the expansion of depletion layer with the built-in potential. The depletion layer capacitance refers to the increment in charge per unit area to the incremental change of the applied voltage. This property gives an indication about the behavior of the charge transition from the donor to the acceptor region, which was found to be "**abrupt**" and this is confirmed when the relation between $1/C^2$ and reverse bias is a straight line.
Figure 2 present the *C-V* plot and C^{-2} –V of the nano and micro grown silver oxide hetrostructure deposited on the Si substrate at 40 kHz, this fig present an (abrupt junction) as a linear relationship between the $1/C^2$ and the V at the optimum preparing condition to the *x*-axis (0.77 V) essentially equal to the diffusion potential within Cu_2O side.

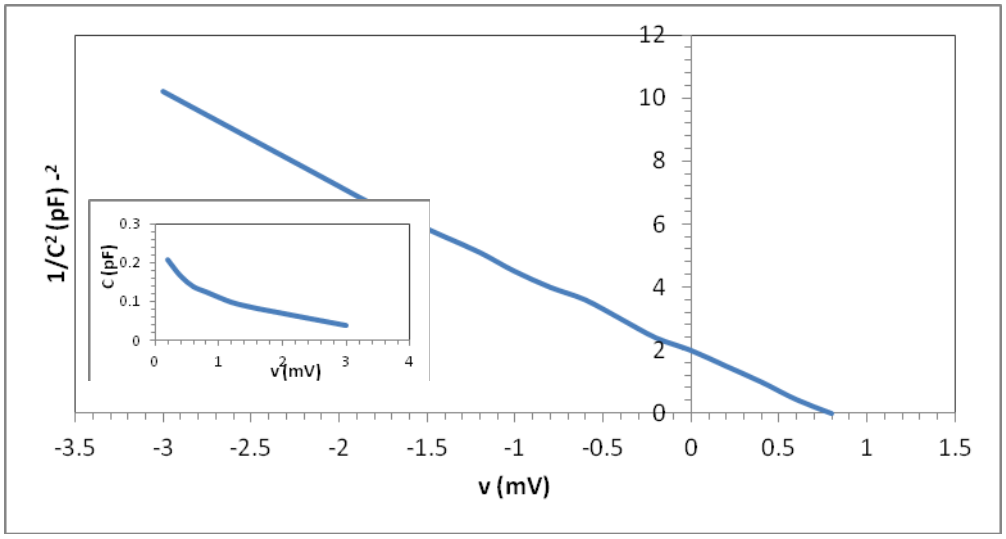

Figure (2) C-V C^{-2}–V plot of Cu_2O/Si HJ.

Measurements of device Parameters

Spectral Responsivity (R□)

The spectral responsivity represents the ratio between the output generated current to the incident power and it is very important because it specifies the performance range of detector.

The presented results of the spectral responsivity were performed using the double-beam UIR-210A spectrophotometer operating within the range (0.15-1.1)□m of the wavelengths while the current measurements were performed using the Fluke digital millimeter (8010 DMM). The values of the spectral responsively were calculating using the following equation:

$$R_\lambda = \frac{I_{ph}}{P_l} \quad \text{A/W} \qquad (2)$$

where Iph is the measured photocurrent and Pl is the incident optical power

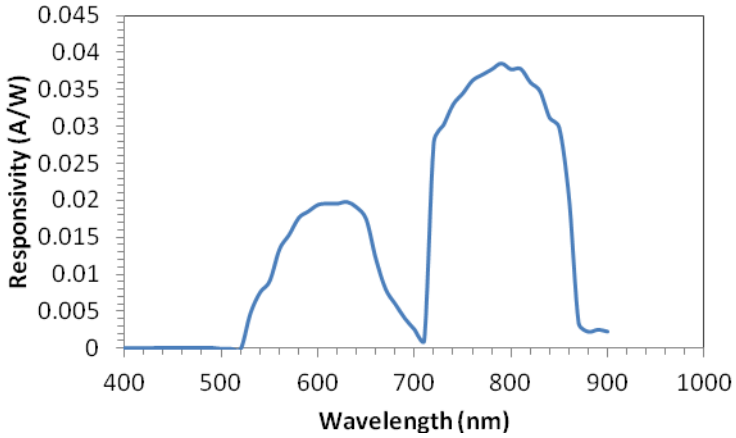

Figure **3** the responsivity characteristics at optimum substrates temperature

We have two packs in this result as it's responsive to the wavelength that used in the prtesented curve:

One for the copper oxide that responsive for red region wavelength

One for the silicon and that is responsive for IR region wavelength

Figure (4) present the open voltage decay pulse of the Cu_2O/ Si hetrostructure and we could recognize the value of the carries life time of about (113 sec) which give rise in the enhancement of other device photocurrent and quantum efficiency.

FIGURE (4) The rise time pulse of Cu_2O film

Figure (5) presents the obtain the response time pulse from fabricated detector device, which find to be (5.48 μs),

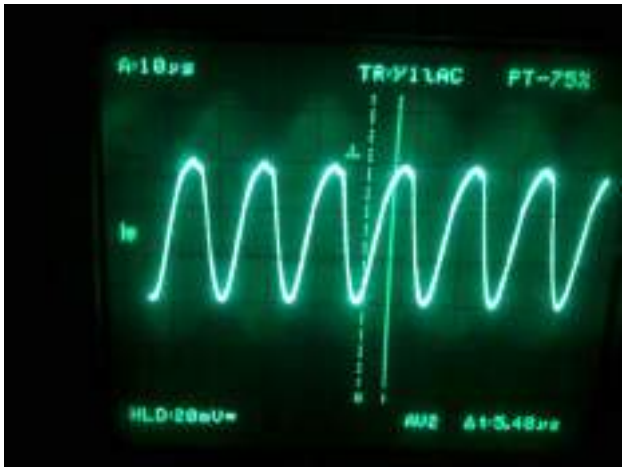

Figure (7) device rise time

4- Conclusion

The encouraged optoelectronic properties of this heterojunction suggest that it candidate to be visible- enhanced photo detectors. The method of fabricating Cu_2O layer by RPLD method are, cheep, and it is hoped it can be improved either by doping or annealing. According to the obtained electrical properties a good enhancement in the device performance could be achieve and it could recognize clearly that device has two main peak of the Responsivity, at (600nm). The encouraged optoelectronic properties of this heterojunction suggest that it candidate to be visible- enhanced photo detectors. The photodiode exhibited good rectifying characteristics and the turn-on voltage was around I-V. The C-V measurements showed an abrupt type junction and a diffusion potential of I-V.

References

1. A. H. Hammad, M. S. Abdel-Wahab, A. Alshahrie, Digest Journal of Nanomaterials and Biostructures 11(4): 1245-1252 (2016)
2. W. Wu , C.C. Tseng , C. Li, C.K. Chang, J.H. Hsieh, Vacuum 118 (2015) 147-151
3. L.A.A. Pettersson , P.G. Snyder, Thin Solid Films 270 (1995) 69-72
4. T.C. Kaspar, T.C. Droubay, S.A. Chambers, Thin Solid Films 519 (2010) 635–640
5. C.C. Tseng, J.H. Hsieh, W. Wu, Thin Solid Films 519 (2011) 5169–5173
6. Esben Lund, AugustinasGaleckas, Alexander Azarov, Edouard V. Monakhov, Bengt G. Svensson, Thin Solid Films 536 (2013) 156–159
7. Yang You, Long Wan, Shiying Zhang, DifaXu, Materials Research Bulletin 45 (2010) 1850–1854
8. K.Lalitha, J. K.Reddy,M. V. P. Sharma, V. D.Kumari,M.SubrahmanyamInternational Journal of hydrogen energy 35:3991-4001 (2010).
9. Jonathan Derouin, Rachael G. Farber, Stacy L. Heslop, Daniel R. Killelea, Surface Science 641 (2015) L1–L4
10. X.Gao, S.Wang, J. Li, Y.Zheng, R. Zhang, P. Zhou, Y.Yang, L.Chen, Thin Solid Films 455 –456 (2004) 438–442
11. F.X. Bocka, T.M. Christensenb, S.B. Riversc, L.D. Doucettea, R.J. LadaThin Solid Films 468 (2004) 57– 64.
12. S.B. Rivers a, G. Bernhardt b, M.W. Wright c, D.J. Frankel b, M.M. Steeves c, R.J. Lad, Thin Solid Films 515 (2007) 8684–8688
13. G.Xiaoyong, Z.Mengke, Z.Zengyuan, C. Chao, M.Jiaomin, L.Jingxiao, Thin Solid Films 519 (2011) 6620–6623

Available online at
http://namrc.uotechnology.edu.iq/index.php/

Nanotechnology and Advanced Materials Research Centre

Proceeding Articles Book 00 (2018) 000–000

6th International Scientific Conference on Nanotechnology, Advanced Materials and its Applications

Study the Effect of SiO_2 Particles on Flexural properties of Epoxy Reinforced by Glass Fiber Composites

Ali Q. kadhum[1], Harith I. Jaafer[2], Ehsan A.Mohammed[3] and Zainab R. Muslim[4]
Sciendce college, University of Baghdad, Baghdad, Iraq
*aliqassim99@yahoo.com

Abstract

The effect of addition of micro and nano SiO_2 particles on Young modulus and flexural strength for epoxy resin composites reinforced with glass fiber type woven roving mat [M] have been studied. Specimens were prepared using hand-lay-up technique arranged with 16 plies. Young modulus and flexural strength were measured using transverse loading. The specimens were cut along the y-direction to study the flexural modulus and flexural strength by using 3- point bending test. Higher flexural modulus is observed for (6 and 8) wt. % and higher flexural strength is found for 10 wt. % for micro composites. For nano composites it was found that the higher flexural modulus were observed for 6 wt. % and 10wt. %, higher flexural strength are observed for 10 wt. % .

Keywords: SiO_2, Young modulus, Flexural strength, and Nano Composites

1- Introduction

In materials science, laminated composites are assemblies of layers of fibrous composite materials . They are being used in critical engineering structures due to their high specific stiffness and specific strength. One of the fundamental advantages of laminates is their ability to adapt and control the orientation of fibers so that the material can best resist loadings. It is therefore important to know how the plies contribute to the laminate resistance, taking into account their relative orientation with respect to the loading direction [1]. Tadaharu et al. (2008) studied the effect of particle size and volume fraction on mode- I fracture toughness of Epoxy composites filled with SiO_2 micro and nano particles, which increased as volume fraction increased and particle diameter decreased [2].Lauke (2008) studied the Fracture toughness of particle reinforced polymers which was affected by the size of particles. It can be improved or reduced depending on the materials used and the particle volume fractions [3]. Abd (2012) studied the effect of mixing different ratios of micro and nano SiO_2 particles of volume fractions (1,2,3,4,5,7,10,15 and 20)wt.% with epoxy resin on the flexural properties .It was shown that maximum flexural strength was (96.9 MPa) and Young modulus was (3.43 GPa) at 4%vol of nanofiller as compared to microcomposites in which 20%wt of micro filler have (25.5 MPa) of flexural strength and (4.69 GPa) of flexural modulus .These results differed from epoxy resin flexural strength (67.4 MPa) and flexural modulus(1.42 GPa) [4]. Singh et al. (2018) investigated properties of SiO_2/epoxy nanocomposites increases with the increasing nanoparticles dispersion up to 4 wt.% SiO_2 nanoparticles and deterioration in the mechanical properties is realized above 4 wt.% [5]. This may be due to the significant increase in agglomeration and settlement of the SiO_2 nanoparticles during the long curing time. The tensile strength increases by 30.57 %, flexural strength by 17 % and flexural modulus by 76 % for 4 wt. % dispersion of SiO_2. Minh et al. (2019) study the morphology and gel fraction content of the unmodified nanosilica and nanosilica modified by an isopropyl tri[di(octyl) phosphate] titanate coupling agent, nanocomposites were analyzed with transmission electron microscopy and scanning electron microscopy methods. The viscosity, mechanical properties, gel fraction content, and morphology results of the cured epoxy–m-silica–TBuT nanocomposites confirm that 5 wt % m-nanosilica was the most suitable for improving the dispersion of m-nanosilica in the epoxy matrix and the properties of these materials [6]. The aim of this research is to study the effect of addition of nano and micro silica as energy absorption materials on flexural properties of epoxy composites in transverse direction, this materials in aerospace applications, as a strong need to reduce weight of structurally critical components with significant retention of mechanical strength.

2- Materials and Method

Matrix Materials

Epoxy resin type (Quick mast 105) was provided by DCP Company / Jordan with specific gravity (1.04) is used with its hardener in ratio (1:3).The epoxy was mixed with a hardener in a container to form a mixture was used to prepare nano composites. Electronic balance type (Sartorius BL 210 S /Germany) was used with sensitivity of 10^{-2} g and with a range up to 2 kg**.**

Fiber Materials

E-glass type Woven Roving Mat(WRM) i.e. (0-90) with surface density 450 g/m^2 was used. **Particulate Materials**

Two inorganic materials micro and nano SiO_2 particles were used as toughening materials; Hydrophilic silica nanoparticles by Aerosil pharma (hydrophilic silica) and microsilica particles (Mallinckrodt 2847) by Cambridge lab. , the specifications of these particulates were and analyzed using AFM as listed in Table (1).

Table (1) Specification of particulate materials

Particulate Materials	**Density (g/cm^3)**	**Surface area (m^2/g)**	**Particle Size**	**Purity**
Micro SiO_2	2.1	-----	100 μ m	99.99
Nano SiO_2	0.05	200± 25	12 nm	99.8

Direction of Cutting

The direction of cutting for flexural test specimen is along the y-axis. (i.e. transverse direction) as shown in Fig. (1), the directions of load on specimens was shown in figure.

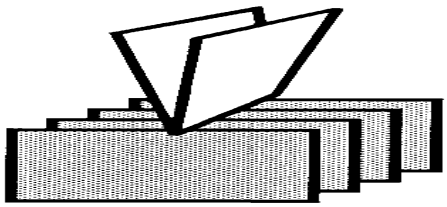

Fig (1): transverse direction

Preparation of Micro and Nanocomposites

SiO_2 micro particles were used with different weight percentages (2, 4, 6, 8 and 10)wt.% .A mixture of Epoxy resin with SiO_2 microparticles were mixed in a clean container using magnetic stirrer, hardener was added to the mixture of epoxy resin and micro silica particles.

To prepare microcomposites, a thin layer of mixture was spread on glass plate mould using a brush. One sheet of glass fiber was stuck on glass plate, and a rolling brush was used to remove the entrapped air bubbles from specimen. The above stage was repeated until 16-plies were reached; the specimens were left in room temperature for 24 hours for curing, they were casted in an oven for 1 hour at 50 °C. The specimens were cut according to ASTM (D790-02) for 3-point bending test [7]. The same procedures were repeated for nanocomposites but by using ultrasonic method.

3- Results and Discussion

Flexural Properties of Microcomposites

Epoxies are favorable as matrices in fiber reinforced composites due to their high crosslinking densities. This results in good thermal stability and creep resistance. However, this also results in the composite being brittle and having a poor resistance to fracture and delamination.

The effect of transverse loading is studied for SiO_2 microcomposites with different weight percentages (2, 4, 6, 8, and 10) wt. %. It is shown that higher flexural modulus are observed for (6 and 8) wt.% , as shown in Table (2), because of the good interlocking between the fiber and the matrix and because of better dispersion of silica microparticle , the lower strength of 4 wt.% was due to lower filler content which restrict the movement of crack propagation ,leading to debonding and buckling ,Fig.(2) .

Fig.(2): Failure in 4wt.% of microcomposites

Higher flexural strength is found for epoxy reinforced with micro silica 10wt. %, it means that the increasing filler content up to 10wt. % here the micro particle act as barrier for crack propagation and consequently have an important role in the increasing of the strength for epoxy composites [8-10]

Table (2) Flexural modulus and flexural strength for microcomposites under transverse loading

Micro SiO_2)%(wt	Flexural strength (MPa)	Flexural Modulus (GPa)
0	294	4.74
2%	370	3. 45
4%	281	7.82
6%	370	9.28
8%	374	8.88
10%	398	8.29

Flexural Properties for Nanocomposites

The effect of transverse loading for epoxy reinforced with nano SiO_2 filler of different weight percentages (2, 4, 6, 8 and 10) wt. % on flexural modulus and flexural strength is studied, Table (3).

It is shown that flexural modulus increases with increasing in filler content but higher flexural modulus were obtained for epoxy reinforced with nano SiO_2 filler of 6wt. % and for epoxy reinforced with nano SiO_2 filler of 10wt. % ,this is because the nanoparticle are distributed between intermolecular spacing for epoxy chains , so that when the load is applied , the nanoparticle will restrict the movement of these chains ,so the modulus of elasticity increases . Higher flexural strength is observed for for epoxy reinforced with nano SiO_2 filler of 10wt. %, in this case the aggregation of nanoparticles in high filler content give a behavior similar to that in microcomposites so the stiffness increases due to agglomeration , and the higher surface area, which may improve the interfacial properties between the matrix and the nano filler, Fig .(3) shows the good distribution for 10wt.% nano silica composites .

Table (3) Flexural modulus and flexural strength for nanocomposites under transverse loading

Nano SiO_2 %wt	Flexural strength (MPa)	Flexural Modulus (GPa)
0	294	4.74
2%	252	5.81
4%	209	5.61
6%	215	15.4
8%	289	10.3
10%	377	14.1

Figure (3): The distribution of nanosilica composites of 10 wt.%

Many phenomena have observed when specimen test in bending methods .Two modes will seen on bending sample , the upper area under compression mode but the lower area under tension mode , so that ,long fibers will split from lower area and some of laminates splitting in transverse direction at edges of specimen with buckling . Fiber debonding and pull –out were occur as a result of delamination cracks which were generated in above and below the layers , as it shown in Fig. (4).

Fig (4): Fiber debonding and pull –out

From these results, it is shown the flexural strength for microcomposites are higher than those of nanocomposites, while the modulus of elasticity for nanocomposites is higher than that of microcomposites.

4-Conclusion

The flexural properties can be improved by adding micro and nano silica particles .Higher flexural strength are observed for microcomposites because of the good interlocking between the fiber and the matrix and because of better dispersion of silica microparticle ,but higher flexural modulus were observed for nanocomposites because the nanoparticle will restrict the movement of these chains ,so the modulus of elasticity increases.

References

[1] Vasiliev,V.,"Advanced Mechanics of Composite Materials",(2007), Elsevier Ltd., (UK),pp.9.
[2] Tadaharu,A. ,M. Osaki 1 , W. Araki and S. Kwon, "Fracture toughness of nano and micro- spherical silica particle filled epoxy composites" , Acta Materialia,(2008), (56), P:2101-2109.
[3] Lauke,B, "On the effect of particle size on fracture toughness of polymer composites" , Composites Science and Technology ,(2008), 68, pp.3365–3372.
[4] M.M. Abd ,"Comparison study of some mechanical & dielectrical properties of TiO_2 &SiO_2 (Nano –Micro) particles /Epoxy composites ", (2012),Ph.D Thesis ,University of Baghdad ,Iraq.
[5] S. K. Singh, A. Kumar and A. Jain ,"Improving tensile and flexural properties of SiO_2-epoxy polymer nanocomposite", materials today, 5, 2, (2018) PP. 6339-6344.

[6] H. N. Minh ,N. T. Chinh ,T. T. Van and T. Hoang , "Ternary nanocomposites based on epoxy, modified silica, and tetrabutyl titanate: Morphology, characteristics, and kinetics of the curing process", J. Appl. Polym. Sci. 136, 16 (2019) 47412.

[7] ASTM (D790-02) ,"Standard test methods for flexural properties of unreinforced and reinforced plastics and electrical insulating materials"., Philadelphia, PA: American Society for Testing and Materials(2002).
[8] A. C. Johnson,"The role of matrix cracks and fiber/matrix debonding on the stress transfer between fiber and matrix in a single fiber fragmentation test", Composites: Part A 43 (2012) 65–72.
[9] K. K. Singh,S. K. Chaudhary and R. Venugopal," Enhancement of flexural strength of glass fiber reinforced polymer laminates using multiwall carbon nanotubes", Polymer engineering and science,59,51(2019)PP.248-261.
[10]Y. Liu ,"Role of matrix modification on interlaminar shear strength of glass fiber/epoxy composites", Composites: Part B 43 (2012) 95–98.